DOT/FAA/AR-09/8

Air Traffic Organization
NextGen & Operations Planning
Operations Planning
Office of Research and
Technology Development
Washington, DC 20591

Crashworthiness of Composite Fuselage Structures—Material Dynamic Properties, Phase I

November 2010

Final Report

This document is available to the U.S. public through the National Technical Information Service (NTIS), Springfield, Virginia 22161.

This document is also available from the Federal Aviation Administration William J. Hughes Technical Center at actlibrary.tc.faa.gov.

U.S. Department of Transportation
Federal Aviation Administration

NOTICE

This document is disseminated under the sponsorship of the U.S. Department of Transportation in the interest of information exchange. The United States Government assumes no liability for the contents or use thereof. The United States Government does not endorse products or manufacturers. Trade or manufacturer's names appear herein solely because they are considered essential to the objective of this report. This document does not constitute FAA certification policy. Consult your local FAA aircraft certification office as to its use.

This report is available at the Federal Aviation Administration William J. Hughes Technical Center's Full-Text Technical Reports page. actlibrary.tc.faa.gov in Adobe Acrobat portable document format (PDF).

Technical Report Documentation Page

1. Report No.	2. Government Accession No.	3. Recipient's Catalog No.
DOT/FAA/AR-09/8		

4. Title and Subtitle	5. Report Date
CRASHWORTHINESS OF COMPOSITE FUSELAGE STRUCTURES—MATERIAL DYNAMIC PROPERTIES, PHASE I	November 2010
	6. Performing Organization Code
7. Author(s)	8. Performing Organization Report No.
K. S. Raju and J. F. Acosta	
9. Performing Organization Name and Address	10. Work Unit No. (TRAIS)
National Institute for Aviation Research Wichita State University 1845 Fairmount Wichita, KS 67260-0093	
	11. Contract or Grant No.
12. Sponsoring Agency Name and Address	13. Type of Report and Period Covered
U.S. Department of Transportation Federal Aviation Administration Air Traffic Organization NextGen & Operations Planning Office of Research and Technology Development Washington, DC 20591	Final Report
	14. Sponsoring Agency Code ANM-100

15. Supplementary Notes

The Federal Aviation Administration Airport and Aircraft Safety R&D Division COTR was Allan Abramowitz.

16. Abstract

The use of composite materials for airframe structural applications is widespread in the commercial, business, and general aviation industries. Crashworthiness of metallic airframe structures investigations, using experiments at the coupon, subcomponent, and large-scale structural levels, and preliminary evaluations of analytical modeling of the dynamic impact event exist in open literature. The results of a limited number of dynamic and drop tests performed on fully composite fuselage structures indicated differences in the crush patterns, failure modes, stiffness, and other structural properties compared to traditional metallic fuselage structures. The differences observed between the composite and metallic structures under dynamic loads have often been attributed to the strain rate sensitivity of composites. An understanding of the strain rate effects at the materials level is necessary to facilitate a building-block approach for designing crashworthy airframe structures. In this study, the continuous fiber-reinforced composite material systems' sensitivity to strain rates was investigated experimentally. The in-plane tension, compression, and shear properties of seven composite material systems were characterized at different strain rates. The details of the test methods, test data, and observations related to the strain rate sensitivity of the materials are presented in this report.

17. Key Words	18. Distribution Statement
Crashworthiness, Dynamic properties, Composites, Strain rate, Stroke rate	This document is available to the U.S. public through the National Technical Information Service (NTIS), Springfield, Virginia 22161. This document is also available from the Federal Aviation Administration William J. Hughes Technical Center at actlibrary.tc.faa.gov.

19. Security Classif. (of this report)	20. Security Classif. (of this page)	21. No. of Pages	22. Price
Unclassified	Unclassified	303	

Form DOT F 1700.7 (8-72) Reproduction of completed page authorized

ACKNOWLEDGEMENTS

The authors appreciate the useful technical inputs and encouragement from the FAA monitors, Allan Abramowitz, John Zvanya, and Curtis Davies, who were instrumental to the success of this program. The authors appreciate the inputs of Ian Won on the technical content and documentation of this report. The authors would like to thank Dr. John Tomblin, Executive Director of the National Institute for Aviation Research, for providing the proper infrastructure required for the successful execution of this project. The efforts of Art Porter and Mark Murrell in machining quality parts for the experimental apparatus are appreciated. The authors also thank Mr. Kim-Leng Poon for his guidance and coordination during the machining of test specimens. The efforts of the following graduate students in conducting and documenting the experiments are greatly appreciated—Anand Deshpande, Satish Dandayudhapani, Manoj Thotakuri, and Mohan Ghimire.

TABLE OF CONTENTS

		Page
EXECUTIVE SUMMARY		xvii
1.	INTRODUCTION	1
2.	OBJECTIVES	1
2.1	Literature Review	1
2.2	Material Systems	7
2.3	Test Methods	7
3.	TENSION TESTS AT HIGH STRAIN RATES	8
3.1	Test Apparatus	8
3.2	Signal Conditioning and Data Acquisition	12
3.3	Test Matrix	13
3.4	Test Specimen Geometry and Fabrication	13
3.5	Strain and Stroke Rates	14
3.6	Test Results	18
3.6.1	Quasi-Static Tests	18
3.6.2	High-Rate Tests	19
3.6.3	Failure Modes	24
4.	IN-PLANE SHEAR TESTS	31
4.1	Test Apparatus	32
4.2	Test Results	34
4.2.1	Shear Strain Rates	34
4.2.2	Stress-Strain Behavior	35
4.2.3	In-Plane Shear Strengths	37
4.3	Failure Modes	39
5.	COMPRESSION TESTS	42
5.1	Test Matrix	43
5.2	Specimen Geometry	44
5.3	Quasi-Static and Medium-Rate Tests	44
5.4	Split-Hopkinson Pressure Bar Apparatus	45
5.4.1	The SHPB Apparatus at NIAR/WSU	45

5.4.2 Specimen Alignment Technique 49
5.4.3 Data Acquisition 50
5.4.4 Strain Gage Data Filtering 52
5.4.5 Stress, Strain, and Strain Rates in the Specimen 52
5.4.6 Pulse Shaping 53

5.5 Test Results 54

5.5.1 Toray T800S/3900-2B Unitape 55
5.5.2 Toray T700G-12K-50C/3900-2 PWCF 59
5.5.3 Newport NB321/7781 Fiberglass 63
5.5.4 Newport NB321/3K70 PWCF 67
5.5.5 Newport NCT321/G150 Unitape 71
5.5.6 Cytec T300/97714AC 3KNT PWCF 75
5.5.7 Fibercote 3KPW-E365 PWCF 79

6. CONCLUSIONS 83

7. REFERENCES 84

APPENDICES

A—Tension Test Data
B—Shear Test Data
C—Compression Test Data

LIST OF FIGURES

Figure		Page
1	Typical EA Devices	2
2	Building-Block Approach Characterizing Rate Effects on Composite Airframe Structures	6
3	High-Rate, Servo-Hydraulic Test Machine and Test Setup for Tension Tests	9
4	Schematic Diagram of the Tension Test Arrangement Showing the Slack Inducer Mechanism	10
5	The Operating Principle of the Slack Inducer Mechanism	11
6	Multidegree of Freedom Idealization Corresponding to Slack Inducer Mechanism, Grips, and Specimen Assembly	12
7	Geometry of Tension Specimens	14
8	Parent Laminate Geometry and Tabs Used for Specimen Fabrication	14
9	Variation of Strain in Tension Tests Conducted at Different Stroke Rates	15
10	Comparison of Strain Levels Achieved Relative to the Ideal	16
11	Comparison of Strain Rate Computed Using Different Methods for Quasi-Static Loading	17
12	Comparison of Strain Rate Computed Using Different Methods for Dynamic Loading at a Stroke Rate of 1 in/s	17
13	Average Values of Tensile Strength as a Function of Orientation for Different Material Systems Under Quasi-Static Loading	18
14	Average Values of Tensile Modulus as a Function of Orientation for Different Material Systems Under Quasi-Static Loading	19
15	Stress-Strain Behavior of Toray Unitape Specimens at Different Stroke Rates	20
16	Tensile Strength of Toray T800S/3900-2B Unitape Specimens With Different Orientations as a Function of Stroke Rate	21
17	Tensile Strength of Toray T700G-12k-PW/3900-2 Fabric Specimens With Different Orientations as a Function of Stroke Rate	21
18	Tensile Strength of Newport NB321/7781 Fiberglass Fabric Specimens With Different Orientations as a Function of Stroke Rate	22

19 Tensile Strength of Newport NB321/3K70 PWCF Specimens With Different Orientations as a Function of Stroke Rate 22

20 Tensile Strength of Newport NCT321/G150 Unitape Specimens With Different Orientations as a Function of Stroke Rate 23

21 Tensile Strength of Fibercote 3KPW-E365 PWCF Specimens With Different Orientations as a Function of Stroke Rate 23

22 Tensile Strength of Cytec T300/7714AC 3KNT PWCF Specimens With Different Orientations as a Function of Stroke Rate 24

23 Failure Modes in $[0°]_2$ Toray T800S/3900-2B Unitape Specimens 25

24 Failure Modes in $[0°]_4$ Toray T700G-12K-PW/3900-2 Fabric Specimens 25

25 Failure Modes in $[0°]_4$ Newport NB321/7781 Fiberglass Specimens 26

26 Failure Modes in $[0°]_4$ Newport NB321/3K70 PWCF Specimens 26

27 Failure Modes in $[0°]_4$ Newport NCT321/G150 Unitape Specimens 26

28 Failure Modes in $[0°]_4$ Fibercote 3KPW-E365 PWCF Specimens 27

29 Failure Modes in $[+15°/-15°]_{2S}$ Toray Specimens Tested at Different Stroke Rates 27

30 Failure Modes in $[+15°/-15°]_{2S}$ Newport Specimens Tested at Different Stroke Rates 28

31 Failure Modes in $[+15°/-15°]_{2S}$ Fibercote 3KPW-E365 PWCF Specimens Tested at Different Stroke Rates 28

32 Failure Modes in $[+30°/-30°]_{2S}$ Toray Specimens Tested at Different Stroke Rates 29

33 Failure Modes in $[+30°/-30°]_{2S}$ Newport Specimens Tested at Different Stroke Rates 29

34 Failure Modes in $[+30°/-30°]_{2S}$ Fibercote 3KPW-E365 PWCF Specimens Tested at Different Stroke Rates 30

35 Failure Modes in $[+45°/-45°]_{2S}$ Toray Specimens Tested at Different Stroke Rates 30

36 Failure Modes in $[+45°/-45°]_{2S}$ Newport Specimens Tested at Different Stroke Rates 31

37 Failure Modes in $[+45°/-45°]_{2S}$ Fibercote 3KPW-E365 PWCF Specimens Tested at Different Stroke Rates 31

38 Test Fixture for V-Notch Rail Shear Tests 32

39 Test Specimen Geometry and Nominal Dimensions for V-Notch Rail Shear Tests 33

40	Test Arrangement for High Strain Rate Tests of In-Plane Shear Specimens	33
41	Variation of Shear Strain With Time for Tests Conducted at Different Nominal Stroke Rates	34
42	Variation of Shear Strain Rate With Shear Strain for Tests Conducted at Different Stroke Rates	35
43	Shear Stress-Displacement and Shear Stress-Strain Behavior Under Quasi-Static Loading	36
44	Shear Stress-Strain Behavior at Different Test Rates	36
45	In-Plane Shear Strengths of Toray Materials at Different Stroke Rates	37
46	In-Plane Shear Strengths of Newport Materials at Different Stroke Rates	38
47	In-Plane Shear Strengths of Cytec and Fibercote Materials at Different Stroke Rates	38
48	Failure Modes of Newport NB321/7781 Fiberglass Specimens Tested at Different Stroke Rates	39
49	Failure Modes of Newport NB321/3K70 PWCF Specimens Tested at Different Stroke Rates	40
50	Failure Modes of Newport NCT321/G150 Unitape Specimens Tested at Different Stroke Rates	40
51	Failure Modes of Toray Unitape Specimens Tested at Different Stroke Rates	41
52	Failure Modes of Toray Fabric Specimens Tested at Different Stroke Rates	41
53	Failure Modes of Cytec Specimens Tested at Different Stroke Rates	42
54	Failure Modes of Fibercote Specimens Tested at Different Stroke Rates	42
55	Specimen Geometry for Compression Tests Using an SHPB Apparatus	44
56	Schematic of the SHPB Apparatus	45
57	Schematic of SHPB Apparatus at NIAR/WSU	46
58	The NIAR/WSU SHPB Apparatus as Viewed From the Pressure Chamber End	46
59	Cross-Section of the NIAR/WSU SHPB Support Assembly	46
60	Details of SHPB Propulsion and Trigger System Used to Propel Projectile	47
61	Geometric Details of Typical SHPB Projectile Assembly	48

62 Geometric Details of SHPB Gun Barrel 49

63 The SHPB and Specimen Alignment Technique 50

64 The SHPB Wheatstone Bridge Balancing Circuit 50

65 The SHPB Instrumentation and Data Acquisition 51

66 Oscilloscope Window—Recorded Incident, Reflected, and Transmitted Pulses 51

67 Incident Pulse Before and After Filtering 52

68 Loading End Schematic of an SHPB With Pulse Shaper 53

69 Incident Pulses Recorded for Three Copper Disc Thicknesses 54

70 Failure Strength vs Average Strain Rate for Toray T800S/3900-2B Unitape Material 55

71 Stress-Strain Behavior of Toray T800S/3900-2B $[0°]_N$ Specimens 56

72 Stress-Strain Behavior of Toray T800S/3900-2B $[+15°/-15°]_{NS}$ Specimens 56

73 Stress-Strain Behavior of Toray T800S/3900-2B $[+30°/-30°]_{Ns}$ Specimens 57

74 Stress-Strain Behavior of Toray T800S/3900-2B $[+45°/-45°]_{NS}$ Specimens 57

75 Characteristic Failure Modes in Toray T800S/3900-2B $[0°]_N$ Specimens 58

76 Characteristic Failure Modes in Toray T800S/3900-2B $[+15°/-15°]_{NS}$ Specimens 58

77 Characteristic Failure Modes in Toray T800S/3900-2B $[+30°/-30°]_{NS}$ Specimens 58

78 Characteristic Failure Modes in Toray T800S/3900-2B $[+45°/-45°]_{NS}$ Specimens 59

79 Failure Strength vs Average Strain Rate for Toray T700G-12K-50C/3900-2 PWCF Material 59

80 Stress-Strain Behavior of Toray T700G-12K-50C/3900-2 $[0°]_N$ Specimens 60

81 Stress-Strain Behavior of Toray T700G-12K-50C/3900-2 $[+15°/-15°]_{NS}$ Specimens 60

82 Stress-Strain Behavior of Toray T700G-12K-50C/3900-2 $[+30°/-30°]_{NS}$ Specimens 61

83 Stress-Strain Behavior of Toray T700G-12K-50C/3900-2 $[+45°/-45°]_{NS}$ Specimens 61

84 Characteristic Failure Modes in Toray T700G-12K-50C/3900-2 $[0°]_N$ Specimens 62

85 Characteristic Failure Modes in Toray T700G-12K-50C/3900-2 $[+15°/-15°]_{NS}$ Specimens 62

86 Characteristic Failure Modes in Toray T700G-12K-50C/3900-2 $[+30°/-30°]_{NS}$ Specimens 62

87 Characteristic Failure Modes in Toray T700G-12K-50C/3900-2 $[+45°/-45°]_{NS}$ Specimens 62

88 Average Failure Strength vs Average Strain Rate for Newport NB321/7781 Fiberglass Material 63

89 Stress-Strain Behavior of Newport NB321/7781 $[0°]_N$ Specimens 64

90 Stress-Strain Behavior of Newport NB321/7781 $[+15°/-15°]_{NS}$ Specimens 64

91 Stress-Strain Behavior of Newport NB321/7781 $[+30°/-30°]_{NS}$ Specimens 65

92 Stress-Strain Behavior of Newport NB321/7781 $[+45°/-45°]_{NS}$ Specimens 65

93 Characteristic Failure Modes in Newport NB321/7781 $[0°]_N$ Specimens 66

94 Characteristic Failure Modes in Newport NB321/7781 $[+15°/-15°]_{NS}$ Specimens 66

95 Characteristic Failure Modes in Newport NB321/7781 $[+30°/-30°]_{NS}$ Specimens 66

96 Characteristic Failure Modes in Newport NB321/7781 $[+45°/-45°]_{NS}$ Specimens 67

97 Failure Strength vs Average Strain Rate for Newport NB321/3K70 PWCF Material 67

98 Stress-Strain Behavior of Newport NB321/3K70 PWCF $[0°]_N$ Specimens 68

99 Stress-Strain Behavior of Newport NB321/3K70 PWCF $[+15°/-15°]_{NS}$ Specimens 68

100 Stress-Strain Behavior of Newport NB321/3K70 PWCF $[+30°/-30°]_{NS}$ Specimens 69

101 Stress-Strain Behavior of Newport NB321/3K70 PWCF $[+45°/-45°]_{NS}$ Specimens 69

102 Characteristic Failure Modes in Newport NB321/3K70 PWCF $[0°]_N$ Specimens 70

103 Characteristic Failure Modes in Newport NB321/3K70 PWCF $[+15°/-15°]_{NS}$ Specimens 70

104 Characteristic Failure Modes in Newport NB321/3K70 PWCF $[+30°/-30°]_{NS}$ Specimens 70

105 Characteristic Failure Modes in Newport NB321/3K70 PWCF $[+45°/-45°]_{NS}$ Specimens 71

106 Failure Strength vs Average Strain Rate for Newport NCT321/G150 Unitape Material 71

107 Stress-Strain Behavior of Newport NCT321/G150 $[0°]_N$ Specimens 72

108 Stress-Strain Behavior of Newport NCT321/G150 $[+15°/-15°]_{NS}$ Specimens 72

109 Stress-Strain Behavior of Newport NCT321/G150 $[+30°/-30°]_{NS}$ Specimens 73

110 Stress-Strain Behavior of Newport NCT321/G150 $[+45°/-45°]_{NS}$ Specimens 73

111 Characteristic Failure Modes in Newport NCT321/G150 $[0°]_N$ Specimens 74

112 Characteristic Failure Modes in Newport NCT321/G150 $[+15°/-15°]_{NS}$ Specimens 74

113 Characteristic Failure Modes in Newport NCT321/G150 $[+30°/-30°]_{NS}$ Specimens 74

114 Characteristic Failure Modes in Newport NCT321/G150 $[+45°/-45°]_{NS}$ Specimens 74

115 Failure Strength vs Average Strain Rate for Cytec T300/97714AC 3KNT PWCF Material 75

116 Stress-Strain Behavior of Cytec T300/97714AC 3KNT PWCF $[0°]_N$ Specimens 76

117 Stress-Strain Behavior of Cytec T300/97714AC 3KNT PWCF $[+15°/-15°]_{NS}$ Specimens 76

118 Stress-Strain Behavior of Cytec T300/97714AC 3KNT PWCF $[+30°/-30°]_{NS}$ Specimens 77

119 Stress-Strain Behavior of Cytec T300/97714AC 3KNT PWCF $[+45°/-45°]_{NS}$ Specimens 77

120 Characteristic Failure Modes in Cytec T300/97714AC 3KNT PWCF $[0°]_N$ Specimens 78

121 Characteristic Failure Modes in Cytec T300/97714AC 3KNT PWCF $[+15°/-15°]_{NS}$ Specimens 78

122 Characteristic Failure Modes in Cytec T300/97714AC 3KNT PWCF $[+30°/-30°]_{NS}$ Specimens 78

123 Characteristic Failure Modes in Cytec T300/97714AC 3KNT PWCF $[+45°/-45°]_{NS}$ Specimens 79

124 Failure Strength vs Average Strain Rate for Fibercote 3KPW-E365 PWCF Material 79

125 Stress-Strain Behavior of Fibercote 3KPW-E365 PWCF $[0°]_N$ Specimens 80

126 Stress-Strain Behavior of Fibercote 3KPW-E365 PWCF $[+15°/-15°]_{NS}$ Specimens 80

127 Stress-Strain Behavior of Fibercote 3KPW-E365 PWCF $[+30°/-30°]_{NS}$ Specimens 81

128 Stress-Strain Behavior of Fibercote 3KPW-E365 PWCF $[+45°/-45°]_{NS}$ Specimens 81

129 Characteristic Failure Modes Over Five Strain Rates in Fibercote 3KPW-E365 PWCF $[0°]_{N}$ Specimens 82

130 Characteristic Failure Modes Over Five Strain Rates in Fibercote 3KPW-E365 PWCF $[+15°/-15°]_{NS}$ Specimens 82

131 Characteristic Failure Modes Over Five Strain Rates in Fibercote 3KPW-E365 PWCF $[+30°/-30°]_{NS}$ Specimens 82

132 Characteristic Failure Modes Over Four Strain Rates in Fibercote 3KPW-E365 PWCF $[+45°/-45°]_{NS}$ Specimens 83

LIST OF TABLES

Table		Page
1	Test Matrix for Tension Tests	13
2	Test Matrix for In-Plane Shear Tests	32
3	Test Matrix for Compression Tests	43

LIST OF ACRONYMS

EA	Energy absorption
FFT	Fast Fourier Transform
MTS	MTS Systems Corporation
NIAR	National Institute for Aviation Research
PWCF	Plain weave carbon fabric
rad/s	Radians per second
SEA	Specific energy absorption
SHPB	Split-Hopkinson Pressure Bar
UD	Unidirectional
WSU	Wichita State University

EXECUTIVE SUMMARY

The use of composite materials for airframe structural applications is widespread in the commercial, business, and general aviation industries. The tailorability of composites, their attributes of high strength-to-weight and stiffness-to-weight ratios, corrosion resistance, and superior fatigue properties have made them attractive in the development of new aircraft fuselage structures. Crashworthiness of metallic airframe structures investigations, using experiments at the coupon, subcomponent, and large-scale structural levels, and preliminary evaluations of analytical modeling of dynamic impact events exist in open literature. The results of a limited number of dynamic drop tests performed on fully composite fuselage structures have indicated differences in the crush patterns, failure modes, stiffness, and other structural properties compared to traditional metallic fuselage structures. The differences observed between the composite and metallic structures under dynamic loads have often been attributed to the strain rate sensitivity of composites. A good understanding of the strain rate effects at the materials level is necessary to facilitate a building-block approach for designing crashworthy airframe structures. The inclusion of dynamic material properties in the analysis of airframe structures under crash loads will decrease the number of expensive and time-consuming tests required to develop such structures.

In this study, the continuous fiber-reinforced composite material systems' sensitivity to strain rates was investigated experimentally. The in-plane tension, compression, and shear properties were generated by conducting tests at different strain rates. The test apparatus and fixtures required to facilitate high-rate tests were designed based on existing literature on high-rate tests. A high-rate, servo-hydraulic test machine capable of stroke rates up to 500 in/s was augmented with a slack inducer mechanism to achieve constant strain rate tension testing. The advantages and limitations of the mechanism are highlighted in this document. The high-rate tests performed using this mechanism did not produce a constant strain rate test; however, the strain rates tended to approach an asymptote with increasing strain levels during the tests. The following seven material systems were investigated: Toray T800S/3900-2B unitape, Toray T700G-12K-PW/3900-2 fabric, Newport NB321/7781 fiberglass, Newport NB321/3k90 plain weave carbon fabric, Newport NCT321/G150 unitape, Fibercote 3KPW-E365, and Cytec T300/7714A 3KNT. Test specimens with stacking sequences of $[0°]_N$, $[+\theta/-\theta]_{NS}$ (θ = 15°, 30°, and 45°), were tested in tension, and test specimens with a stacking sequence of $[0°]_N$ were tested under in-plane shear at nominal stroke rates of 10^{-3}, 1, 10, 100, 250, and 500 in/s. The compression tests were conducted using a servo-hydraulic test machine at quasi-static (10^{-3} in/s) and medium (1 and 10 in/s) rates, and a Split-Hopkinson Pressure Bar (SHPB) apparatus was used for higher strain rates. Based on existing literature, an SHPB apparatus was fabricated at Wichita State University to conduct the high strain rate tests. The SHPB apparatus used a pneumatic propulsion system to propel a projectile at speeds required to generate stress waves in the incident bars at desired strain rates.

The material systems investigated exhibited rate sensitivity in the form of changes in strength and stiffness under tension, compression, and shear loading. However, the nature and extent of these effects were dependent on the stacking sequence and the loading type. The tensile strength of the materials increased with stroke rate, up to a stroke rate of 100 in/s. At higher rates, the strength either increased or decreased, depending on the material and stacking

sequence. It was concluded that, in addition to the material effects, the observed results at higher rates could be an artifact of the load measurement and test fixture arrangement as well as the material behavior. The Newport NB321/7781 fiberglass material was the most rate-sensitive material, with the $[+45°/-45°]_{NS}$ laminates experiencing a strength increase by a factor of 3. The failure modes were consistent across the test rates, with the failure mode being relatively diffuse at higher rates.

The in-plane shear strength of the seven materials exhibited trends that were similar to the tensile strengths up to 100 in/s. However, at higher rates, the behavior was material-dependent. Some materials exhibited an increase in strength while the others decreased. A change in failure mode was observed for the Newport and Toray materials reinforced by fabrics, where the fracture path meandered away from that of the minimum section, indicating a different failure mechanism and wave propagation effects. Additional investigation into dynamic loading and failure propagation is warranted to rule out the possibility of fixture-related effects on the failure modes at the higher rates.

The in-plane compression tests revealed the dependence of both strength and modulus of the materials on strain rates. However, the increases in strength were not as appreciable as the tensile and shear results. This supports the observations of rate insensitivity of energy absorption devices, wherein the primary loading occurs in compression. It was noted that the failure modes depended on the type of reinforcement and strain rate. The unidirectional material tended to undergo end-crushing-initiated split across interlaminar planes and along planes parallel to the fiber direction in off-axis specimens. However, the material systems reinforced by fabrics exhibited the formation of kink bands at certain strain rates, while in an equal number of instances, interlaminar splitting. The stiffness of all material systems exhibited a pronounced sensitivity to the strain rate.

1. INTRODUCTION.

The use of composite materials for airframe structural applications is widespread in the commercial, business, and general aviation industries. The tailorability of composites, their attributes of high strength-to-weight and stiffness-to-weight ratios, corrosion resistance, and superior fatigue properties have made them attractive in the development of new aircraft fuselage structures. Some airplanes that use composite materials for their primary structures are the Boeing 787, Hawker Beechcraft Hawker Horizon, and Premier I.

Crashworthiness of metallic airframe structures investigations, using experiments at the coupon, subcomponent, and large-scale structural levels, and preliminary evaluations of analytical modeling of dynamic impacts exist in open literature. The results of the limited number of dynamic drop tests performed on fully composite fuselage structures have indicated differences in the crush patterns, failure modes, stiffness, and other structural properties compared to traditional metallic fuselage structures. The differences observed between the composite and metallic structures under dynamic loads have often been attributed to the strain rate sensitivity of composites. A good understanding of the strain rate effects at the materials level is necessary to facilitate a building-block approach for designing crashworthy airframe structures. The inclusion of dynamic material properties in the analysis of airframe structures under crash loads will assist in decreasing the number of expensive and time-consuming, full-scale tests required to develop crashworthy structures.

2. OBJECTIVES.

The objectives and deliverables for this program were identified based on meetings with an advisory group that included the program monitor(s) and representatives from the aircraft industry. The objectives of the program are listed below.

- Conduct a literature survey of the past research addressing crashworthiness, strain rate sensitivity of composite materials, test methods, and observations.
- Identify material systems based on their usage in the aircraft industry.
- Based on existing literature, identify, design, and develop test apparatus to facilitate material tests at high strain rates.
- Generate material properties such as in-plane tension, compression, and shear strength at different strain rates.

2.1 LITERATURE REVIEW.

The open literature contains documentation of investigations that primarily address the rate sensitivity of material systems and the characteristics of energy absorption (EA) devices. The investigations studying EA devices primarily focus on the effects of variables, such as materials, geometry, and trigger mechanisms, with a secondary focus on rate effects. A brief review of the literature addressing rate sensitivity of EA devices and material systems are presented in this section.

Using composite materials formed as tubes, sandwich panels, and honeycomb core for EA devices has been reported [1-9]. The geometric configurations of representative EA devices [10-12] used in the past are shown in figure 1. The EA devices that were investigated include tubes, sine-wave beams, box beams, frusta, angles, channels, etc. Typically, the EA devices were experimentally characterized under quasi-static loading. However, the EA devices are subjected to dynamic loads in real-life applications. The strain rates experienced by the EA devices are several orders of magnitude higher than the quasi-static strain rates. Farley [13] investigated the effects of loading rate on the specific energy absorption (SEA) of $[\pm\theta]_3$ and $[0°/\pm\theta]_2$ carbon/epoxy and aramid/epoxy tubes. The SEA in $[\pm\theta]_3$ carbon/epoxy tubes, which was primarily due to interlaminar crack growth, was increased by up to 35% for a loading rate increase from 0.01 m/s to 12 m/s. On the other hand, the EA of $[0°/\pm\theta]_2$ carbon/epoxy tubes, dominated by the 0° plies resulting in lamina bundle fractures, was independent of loading rate. With an increased loading rate, the $[\pm\theta]_3$ and $[0°/\pm\theta]_2$ aramid/epoxy tubes exhibited increases of 20% and 45% in SEA. This study highlights that the rate dependence of an EA device could be influenced by the material system and the orientation of the plies relative to the loading direction.

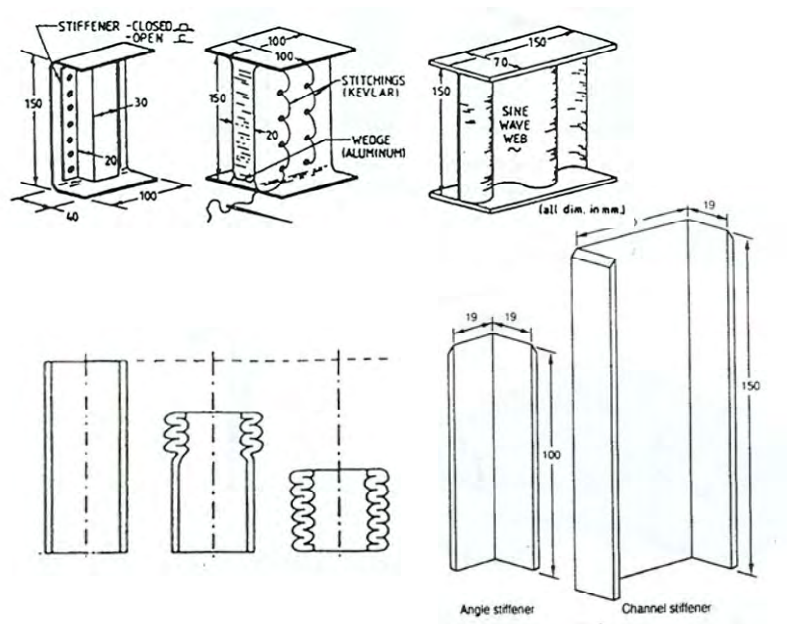

Figure 1. Typical EA Devices

Mamalis, et al. [14], investigated the effects of loading rates on the EA of random chopped glass mat-reinforced polyester tubes and frusta. In this investigation, the SEA decreased for thick-walled tubes and frusta with increasing crush rate (up to 24 m/s), while the thin-walled members did not exhibit a clear dependence on the loading rate. The authors, however, observed change in failure mechanism with loading rates, with the matrix behaving in a brittle manner with increasing crush rates.

Boitnott and Kindervater [15] investigated the crashworthy behavior of composite materials and generic structural elements under static and dynamic loads. Sine-wave beams, fabricated using carbon fiber composite (CFC), aramid fiber composite (AFC) and hybrid (AFC/CFC) material,

were tested under static and dynamic loading. The dynamic loading was accomplished through a drop test device that produced an initial impact velocity of approximately 10 m/s. No comparable effects of load rate on the specific crushing stress was evident from the test data. The authors observed that if the characteristic failure mode (folding and crushing) occurred in a uniform manner, it resulted in a higher crushing stress. A similar observation was made by Kellas [16], who investigated the performance of composite beam webs for aircraft subfloor applications. Kellas reported that the transition from a compact- to a non-compact-folding behavior of the cell cross-section was prevalent in dynamically loaded specimens. The EA was, in general, higher than that of the static tests, provided that a compact-folding (viz., accordion) behavior prevailed. However, unlike the static response, the dynamic response of the tested specimens were absent of a load minimum (valley) following the crush initiation load. This particular response was attributed to the increase in specific crush load under dynamic testing.

Johnson, et al. [17], reported the results from the finite element modeling of composite cruciform elements using the dynamic explicit code PAM-CRASH [18]. The predicted load levels and EA were about 50% below the dynamic test results, with the differences attributed to deficiencies in dynamic modeling of laminates. The report expressed the need for additional test data to better model the material response under dynamic loads.

Carruthers, et al. [19], provided a detailed review of the EA capabilities and crashworthiness of composite structures. The report highlighted that the bulk of the existing work on EA of fiber-reinforced plastics has been focused on behavior of tubular specimens. The report pointed out that the influence of the loading rate on the EA capability is a contentious issue and that previous investigations showed contradicting trends about rate effect on EA. Based on the review of previous studies, it was concluded that the rate effect was specific to the particular material and geometric configuration, and it would be difficult to draw broad conclusions. The report further cautions that the use of static test data for predicting dynamic performance can produce discrepancies of up to 30% in either direction.

While the effects of load rates on the EA of composite structures and subcomponents have been reported to be contradictory, no focused attempt has been made to identify and quantify the various factors and mechanisms that may or may not contribute to the sensitivity or nonsensitivity to the rate effects. In the instances where rate effects were evident, no attempt was made to quantify the strain rates or the contribution of mechanisms that were attributed for the effects. It should be noted that a majority of the reports do not associate a strain rate value with the observed behavior, but rather, specify a stroke rate. It should also be noted that the strain rate and stroke rate may or may not be linearly related, depending on the geometry of the device or component being tested.

The widespread studies into the strain rate sensitivity of composite materials deal with, not only characterization of composite material properties, but to a large extent, adaptation and the development of test methods used for characterization. A brief review of the past studies addressing testing and characterization of composites at different rates of loading is presented in the following paragraphs.

The effect of strain rate on the mechanical properties of fiber-reinforced polymer composites has been investigated by various authors [20-26]. Typical strain rates used in the previous investigations ranged between 1 s^{-1} to above 2000 s^{-1}. The loading devices used for high strain rate tests are servo-hydraulic test machines (10^{-3} to 50 s^{-1}) [20-26], drop-weight impact test machines (<10 s^{-1}), Split-Hopkinson Pressure Bar (SHPB) or Kolsky Pressure Bar apparatuses (between 10^2 to 10^4 s^{-1}) [27], and a Modified Charpy Pendulum (<100 s^{-1}) [11]. Li and Lambros [28] reported a consistent and accurate data reduction procedure for SHPB, which accounts for dispersion, selection of starting points, and stress homogeneity. A summary of the advantages and disadvantages associated with the above test apparatuses are discussed by Barré, et al. [29].

The effect of strain rate on the tensile, compressive, and shear properties of composite materials has been studied by various investigators using the above apparatuses at different strain rates. Rotem and Llifshitz [30] investigated the strain rate effect on the stiffness and strength of unidirectional (UD) and cross-ply E-glass/epoxy composites. This investigation showed a three-fold increase in the strength and a 50% increase in modulus over that of the static tests, when the UD E-glass/epoxy was tested at a strain rate of 30 s^{-1}. The angle-ply laminates exhibited a 20% to 30% increase in failure stress without a significant change in modulus. However, Armenakas and Sciammarella [31] reported a linear increase in elastic modulus with strain rate, and a decrease in ultimate strain and strength for glass/epoxy UD composites loaded up to a strain rate of 500 s^{-1}.

Oguni and Ravichandran [24] employed a modified Kolsky Pressure Bar to study the response of UD E-glass vinyl-ester composites at various strain rates, up to 3000 s^{-1}. This study showed that the compressive strength increased with increasing strain rates. Using an energy-based model, the authors attributed the strength increase to the increase in modulus of the matrix material and the decrease of the surface energy due to a loading rate increase.

Tsai and Sun [25] studied the strain rate effect on the dynamic compressive failures in off-axis glass/epoxy (S2/8552) composites. An increase in compressive strength was reported when the strain rate was increased from 10^{-4} s^{-1} to 1100 s^{-1}. Also reported was a change in failure mode in 15º off-axis specimens from a fiber microbuckling-dominated failure at strain rates below 0.01 s^{-1} to a matrix shearing failure at higher strain rates.

Hsiao and Daniel [26] investigated the effects of strain rate on the transverse compressive and shear behavior of UD carbon/epoxy (IM6G/3501-6) laminates. Off-axis specimens were also used in the compression tests to study the in-plane shear behavior. Strain rates ranging from 10^{-4} s^{-1} up to 1800 s^{-1} were used in the study. The authors observed that the transverse strength and modulus increase with strain rate without any significant increase in ultimate strain. The stress-strain curves for the off-axis tests were observed to significantly stiffen in the nonlinear region for strain rates between 10^{-4} s^{-1} to 1 s^{-1}. The matrix-dominated shear stress-strain behavior was found to exhibit high nonlinearity with a plateau region at a stress level that increased with strain rate.

Hayes and Adams [32] conducted tensile tests at various tests speeds and load levels to characterize the tensile-impact behavior and rate sensitive material properties of UD glass/epoxy and graphite/epoxy composites. An instrumented tensile-impact test system with partial loading

capabilities was developed and tested. A standard pendulum-type impact test machine was modified for these tests. The various test speeds used in this research were 2.7, 3.4, 3.8, 4.5, and 4.9 m/s. The micromechanics of fracture within the composite caused by impact were studied using partially loaded impact test specimens and scanning electron microscopy. The glass/epoxy material exhibited a considerable increase in the strength and modulus as the strain rates were increased, but in case of the graphite/epoxy material system, the results were opposite.

The effects of strain rate on the mechanical behavior of Scotchply type 1002 glass/epoxy angle-ply laminates were investigated by Staab and Gilat [33]. Tests were conducted at high strain rates of approximately 10^3 s^{-1} using a direct-tension SHPB apparatus. Quasi-static tests at a strain rate of 10^{-4} s^{-1} were conducted using a servo-hydraulic test machine. Results showed that maximum normal stress experienced by glass/epoxy laminates was higher for dynamic-loading than for quasi-static loading conditions. Both fibers and matrix are reported to be sensitive to strain rates, with the fibers dominating the laminate properties at higher rates.

Strain rate-dependent behavior of IM7/977-2 carbon/epoxy matrix composite in tension was studied by Gilat and Goldberg [34] by testing various laminate configurations at strain rates up to 400-600 s^{-1}. High strain rate tests were conducted using an SHPB, and the low strain rate tests were conducted on a conventional servo-hydraulic test machine. To avoid the uncertainties in the data interpretation due to different test apparatus, the specimen geometry was the same for all tests. The authors observed an increase in both the strength and stiffness of the material with increasing strain rates.

Papadakis, et al. [35], investigated the characterization of the in-plane shear properties of glass fiber-reinforced thermoplastic composite laminates over a range of strain rates. Twenty-two $[45°]_{2s}$ specimens were tested at 5, 50, and 500 mm/min crosshead displacement rates using a universal test machine. The longitudinal and transverse strains were obtained experimentally using extensometer apparatus and then transformed to the ply axis using classical laminate theory. The shear modulus decreased with increasing strain rate, while the shear failure stress increased for increasing strain rate. The opposing trends of in-plane shear modulus and shear failure stress was attributed to the rate dependence of shear damage evolution.

Based on the existing literature, composite material strength and stiffness are indeed dependent on strain rates, albeit the different or opposing trends. However, it should be noted that the comparisons between different investigations are difficult due to the differences in material systems, strain rate ranges, test specimen geometries, test methods, and the equipment used. In addition, most studies report a wide range (the limits of which are material-dependent) of strain rates over which no significant rate effects are discernible. Further, the tensile, compression, and shear properties are not all sensitive to strain rate to the same extent. It is reasonable to speculate that the strain rates achieved in some of the aforementioned crashworthiness investigations may have been within the range where rate effects are negligible. In addition, the EA modes may have been dominated by loading modes that are least sensitive to strain rate. A thorough investigation addressing the rate effects of a material under different loading modes would be necessary to quantify the strain rate-induced trends in EA devices and crashworthy airframes under dynamic loading.

While the previous studies addressed the rate sensitivity, either at the material or the EA device level, no concerted effort was made to connect the two. This led to speculations about the source of rate sensitivity (or lack) of EA devices. While it may seem logical to support the previous investigations of EA devices by adding rate sensitive material properties, the lack of strain rate information from the experiments conducted on EA devices defeats this approach. The common shortcomings of all the previous investigations on EA devices is the lack of strain data collection and the rate sensitive material behavior at the lamina or laminate levels. In the present investigation, the building-block approach illustrated in figure 2 was embraced to study the rate effects on the behavior of composite airframe structures.

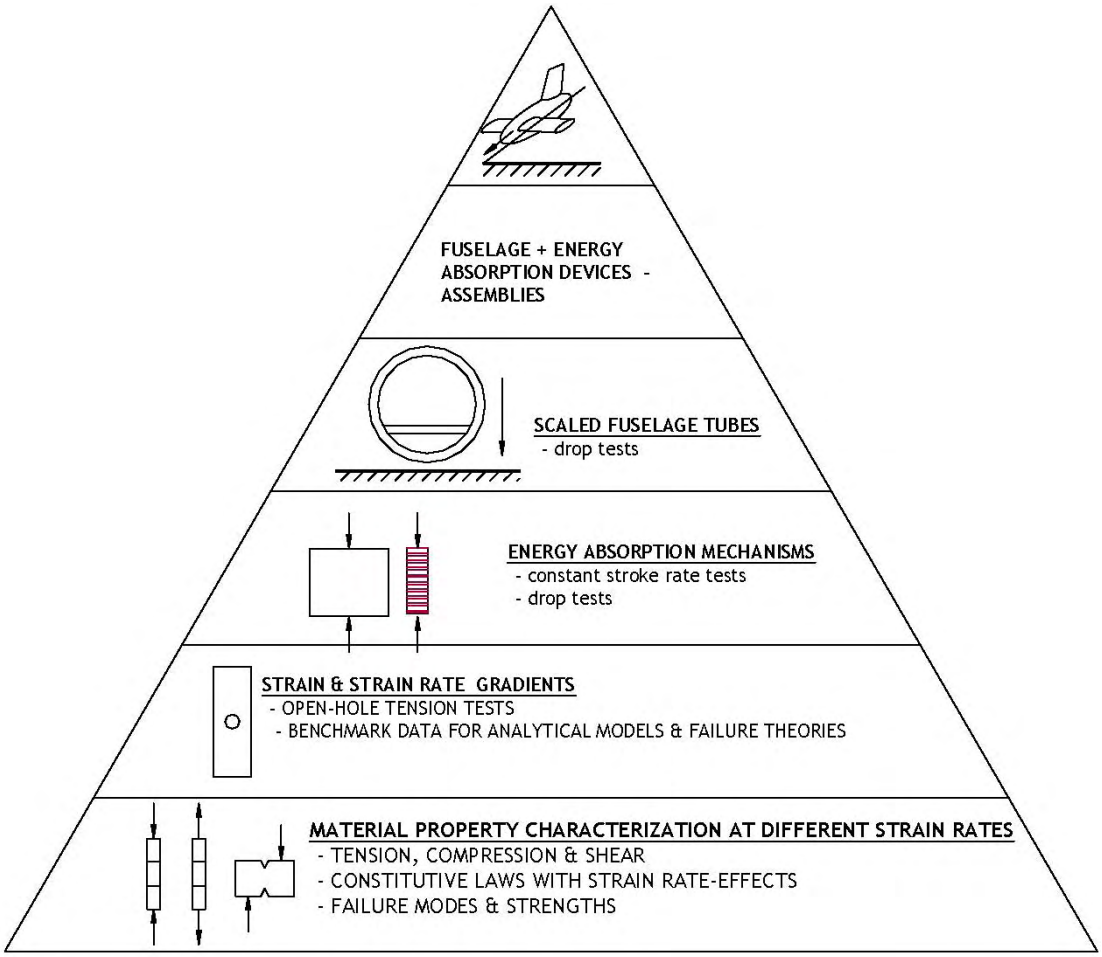

Figure 2. Building-Block Approach Characterizing Rate Effects on Composite Airframe Structures

While this philosophy was used in the static characterization of composite materials, it was seldom applied to address rate sensitivity. This approach addresses the contribution of material rate sensitivity to that in EA devices and structures. The rate effects (i.e., strain rate effects) are characterized at the fundamental ply level, since for most numerical analysis, the material properties are specified at this level. The material tests at this level included the characterization along the primary ply directions and off-axis specimen tests. The off-axis specimen tests are

intended to simulate a combined stress state in the plies and not to characterize material property. This combined stress state could be used for benchmarking material models in the future. The next level of tests included cases where strain and strain rate gradients existed, e.g., open-hole tension, which served as benchmark data for the material failure models. Moving up the building block pyramid, small components and component assembly are characterized under dynamic loading, culminating in characterization of scaled aircraft structures, which would be the most expensive. The understanding of rate effects at the ply level helped identify whether the rate effects in structural components and their assemblies were due to geometric effects or material rate sensitivity.

This investigation initially characterized, experimentally, the effects of strain rate on the in-plane tension, compression, and shear properties of selected composite material systems. A limited number of off-axis tension tests were also conducted to investigate the rate effects[1] under combined stress states. Considerable effort was focused on researching the appropriate method for high-rate tests and the design, fabrication, and assembly of apparatus for the current program. The details of the objectives of the test program, test apparatus, material systems, and test results are presented in this report.

2.2 MATERIAL SYSTEMS.

In the current study, a total of seven material systems were identified by an industry advisory committee comprised of representatives from Cessna Aircraft Company, Hawker Beechcraft, and The Boeing Company. The material systems selected for the investigation are listed below.

- Toray T800S/3900-2B unitape system[2] [36]
- Toray T700G-12K-PW/3900-2 (fabric)[2] [36]
- Newport NB321/7781 satin weave glass fiber or SWGF (fiberglass)[2] [37]
- Newport NB321/3K70 plain weave carbon fabric (PWCF)[2] [37]
- Newport NCT 321/G150 Carbon Fiber unitape [37]
- Fibercote 3KPW-E365 PWCF [38]
- Cytec T300/7714AC 3KNT PWCF [39]

The choice of material systems was based on different combinations of reinforcements and matrix materials. The Toray material systems share the same resin system but differ in reinforcement style. These materials are used in a wide variety of applications in commercial and general aviation airframes. The Newport material systems share the same resin system but differ in reinforcement material and style and are popular among general aviation airframes.

2.3 TEST METHODS.

The composite materials tension tests were conducted using constant stroke rate machines, impact test machines, and modified SHPB apparatuses by past researchers. The maximum strain rates achieved using the constant stroke rate machines (servo-hydraulic and electromechanical

[1] Henceforth, rate shall be associated with strain unless otherwise mentioned.

[2] The tests of these material systems were cost-shared with funding from the NIAR/industry/ State of Kansas (NIS) program.

machines) were typically less than $1s^{-1}$ due to lack of faster machines. High strain rate tension tests using SHPB apparatus pose a problem of proper specimen design due to the low shear capability of composites and the compact (small) size of the specimen required for SHPB tests. Thus, in this investigation, the composite materials tension test were carried out using a high-rate, servo-hydraulic test machine available at the National Institute for Aviation Research (NIAR), located at the Wichita State University (WSU). Compression properties were characterized using a standard servo-hydraulic test machine for quasi-static and medium strain rates. An SHPB apparatus was used for strain rates above $100s^{-1}$ to $900s^{-1}$. The in-plane shear tests were characterized using the V-notch rail shear method on the high-rate, servo-hydraulic test machine, which required a tensile loading mode suitable for safe testing at high stroke rates. The details of the test methods, apparatus, test procedures, and results are discussed in the following sections.

3. TENSION TESTS AT HIGH STRAIN RATES.

The laminated composites tension tests were conducted at different strain rates to study the strain rate effects on the strength and stiffness of the material. Tension tests were conducted along the in-plane fiber direction, and a limited number of off-axis tests were conducted to study the rate effects under combined loading. Balanced and symmetric laminates were used for off-axis tests to circumvent the in-plane extension-shear and -bending coupling. The off-axis laminates were intended to generate a combined stress state in the lamina relative to the fiber direction. The presence of free-edge effects in off-axis laminates are recognized, but the effects were minimized by avoiding ply grouping. The details of the design and development of test apparatus, test matrix, specimen geometry, test procedure, and test results are summarized in the following sections.

3.1 TEST APPARATUS.

The tension tests were conducted using a high stroke rate MTS Systems Corporation (MTS) [40] servo-hydraulic test machine shown in figure 3. The test machine is capable of maximum speeds up to 500 in/s. The test machine can apply sustained loads up to 5000 pound force (lbf) at maximum speed and up to 9000 lbf sustained when the speed is reduced to quasi-static range (less than 1 in/s).

Figure 3. High-Rate, Servo-Hydraulic Test Machine and Test Setup for Tension Tests

Testing composite specimens at constant strain rates is desirable for material characterization. This requires that the actuator speed be at the desired speed when the specimen loading begins. However, any actuator requires a finite period of acceleration to achieve a desired speed. The amount of displacement required to reach a particular speed is proportional to the speed itself. Thus, if a specimen is directly attached (e.g., using a grip) to the actuator, the specimen will fail[3] even before the actuator reaches the desired speed. Thus, it is desirable that the specimen be engaged (loaded) after the actuator has achieved the required speed. To accomplish this, a simple slack inducer mechanism was designed and fabricated at NIAR/WSU. The slack inducer mechanism is illustrated in figure 4.

[3] The typical failure strain for composite materials is approximately 0.015, which translates to an extension of about 0.03 inch over a gage length of 2 inches.

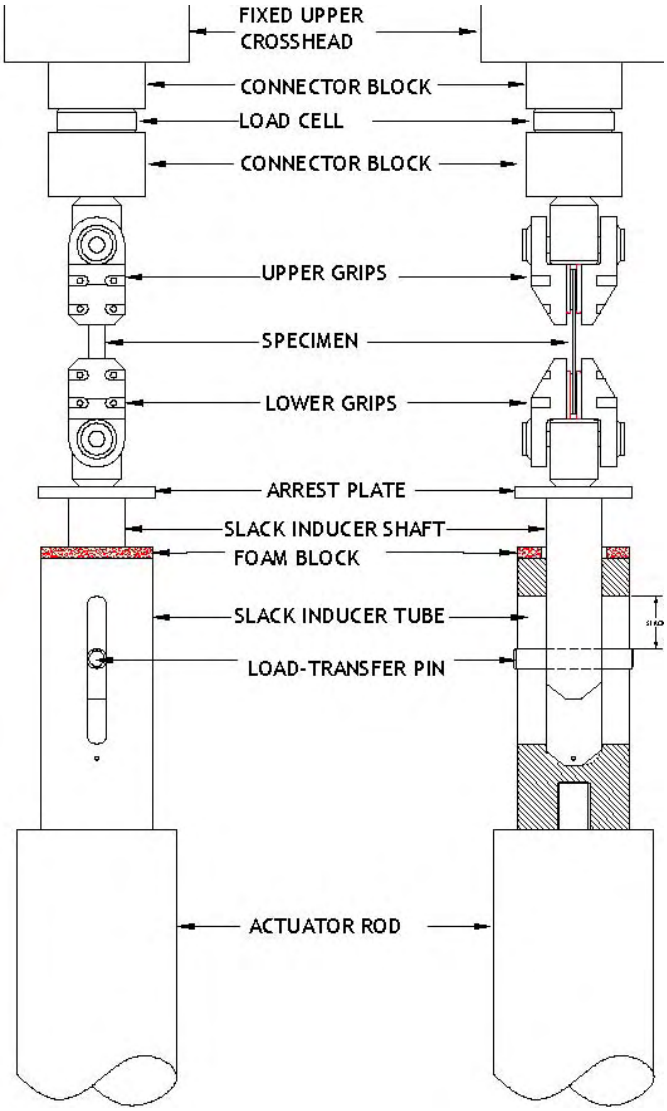

Figure 4. Schematic Diagram of the Tension Test Arrangement Showing the Slack Inducer Mechanism

The slack inducer mechanism consists of a cylindrical slack inducer tube that has a longitudinal through-slot for a certain portion of its length. The length of the slot governs the amount of permissible slack in the system. One end of the tube is fastened to the end of the actuator. The cylindrical bore of the slack inducer tube houses a slack inducer rod, which is free to translate along the axis of the bore. As shown in figure 4, a load-transfer pin is inserted on one end of the rod. This pin rides the slot in the tube and prevents the rotation of the rod relative to the tube. The free end of the slack inducer rod is attached to a specimen-gripping device (e.g., grips). An arrest plate is secured in between the gripping device and the rod. The operation of the device is described in the following paragraph.

As shown in figure 5, the tension tests begin with a known slack distance between the load-transfer pin and the end of the slot in the tube. The slack distance is governed by the desired final speed. The slack distance required to achieve a specified speed is obtained by

characterizing the performance of the actuator. Once the test commences, the slack inducer tube starts moving away from the load-transfer pin until the pin contacts the end of the slot. At this point, the actuator has already achieved the desired speed. The loading of the specimen begins when the pin engages the end of the slot. The loading continues until the specimen breaks, after which, the slack inducer shaft starts accelerating towards the slack inducer tube and actuator. The kinetic energy of the actuator is dissipated by the hydraulic cushions provided in the actuator. However, the kinetic energy of the slack inducer shaft (along with the grips) must be dissipated to avoid catastrophic failure of the shaft/grip assembly. The kinetic energy of the shaft/grip assembly is dissipated by crushing a sacrificial foam ring placed between the arrest plate and the end of the slack inducer tube. The foam crushes at an almost constant load and absorbs the energy.

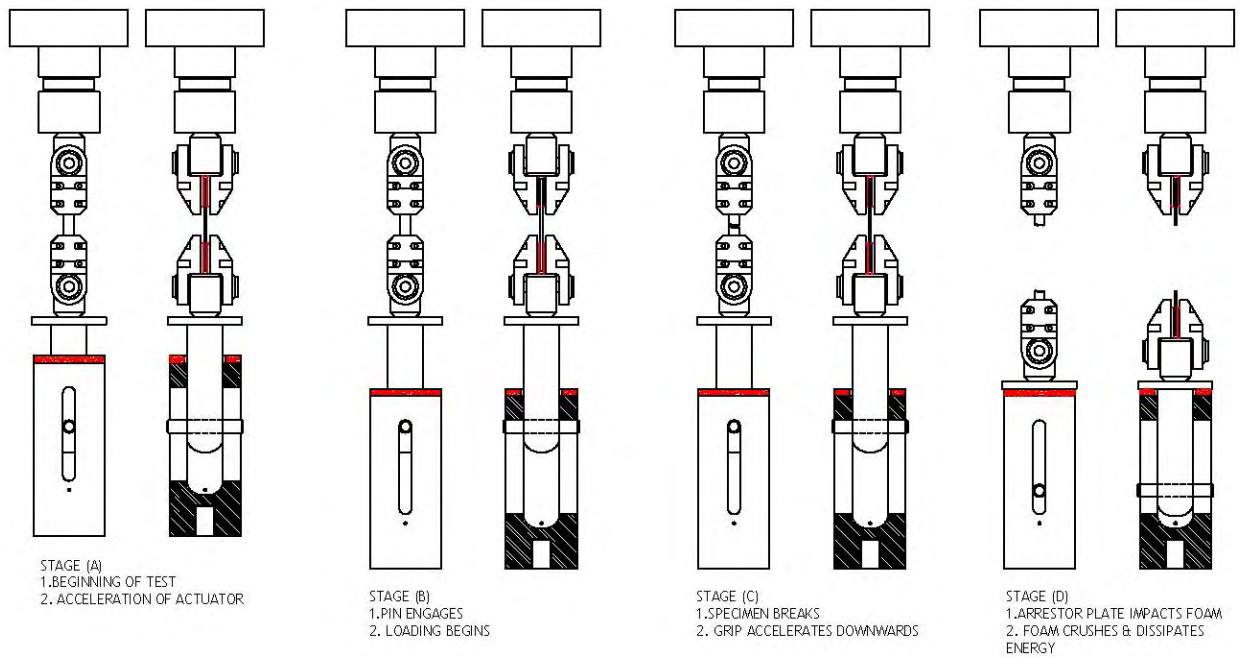

Figure 5. The Operating Principle of the Slack Inducer Mechanism

In an ideal situation, the various parts of the mechanism are rigid. However, the flexibility of the various components, in particular, the pins and the fasteners (studs), render the system less than perfect. The entire system now constitutes a multidegree of freedom arrangement of springs and masses, as shown in figure 6. This implies that the constant actuator speed is not translated to the specimen, resulting in tension tests at strain rates that vary throughout the tests. A preliminary analysis of the linearized spring-mass model of the system indicated that the mass of the grip should be minimized. A smaller grip mass is also favorable for the EA process during the recoil. A simple wedge grip assembly, shown in figures 3 to 5, weighing 2.6 lb was designed and fabricated at WSU. The gripping forces are generated by the four fasteners that pull the two halves together along with the wedge action created by the wedges due to axial loading.

K_{SR} - stiffness of stud connecting grips to load cell/rod
K_{SP} - stiffness of specimen
K_R - stiffness of rod
K_P - stiffness of load transfer pin
K_T - stiffness of tube

M_{SR} - effective lumped mass of grips and stud
M_{ROD} - effective lumped mass of rod
M_{PIN} - effective lumped mass of pin
M_{TUBE} - effective lumped mass of tube
M_{ACT} - effective lumped mass of actuator
xi - displacements

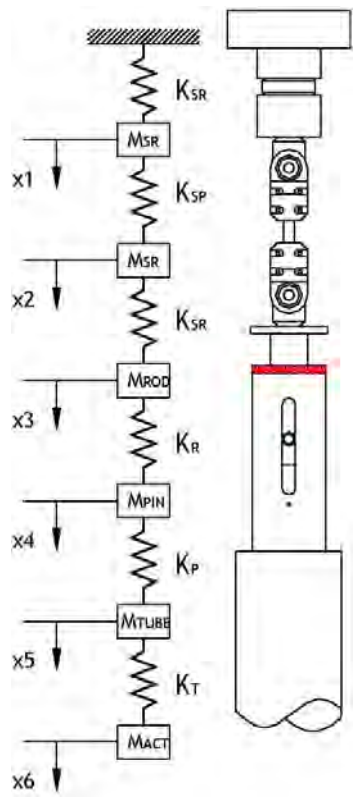

Figure 6. Multidegree of Freedom Idealization Corresponding to Slack Inducer Mechanism, Grips, and Specimen Assembly

3.2 SIGNAL CONDITIONING AND DATA ACQUISITION.

The test duration[4] for high strain rate tension tests can range between 100 μs to 50 ms for specimen elongation rates ranging between 1 and 500 in/s. A bandwidth of approximately 100 kHz is required to condition the strain and load signals encountered during high-rate tests. A Vishay [41] model 2210 signal conditioner amplifier with a frequency range in excess of 100 kHz for gains lower than 100, was used for conditioning strain gage signals. PCB Piezotronics, Inc. [42] model 206M33 ICP® load sensor and model 484B series ICP signal conditioner were used for dynamic force measurement. The load cell had a calibrated force measurement range of ±10,000 lbf and a frequency limit of 40 kHz.

The data acquisition for high-rate tests was accomplished using National Instruments [43] model PCI 6110 simultaneous sampling data acquisition board with 12-bit resolution and maximum data acquisition speed of 5 MHz. The data acquisition board was capable of sampling four channels of data simultaneously. Depending on the stroke rate, sampling rates ranged from 100 kHz to 2 MHz. Data acquisition was automatically triggered by the MTS test control software at the start of the test. A considerable amount of extraneous data was recorded before loading and after failure of the specimen. A visual data decimation computer program provided by MTS was used posttest to remove the extraneous data.

[4] A specimen gage length of 2.00 inches and failure strain of 0.02 in/in is assumed.

3.3 TEST MATRIX.

The tension tests used to determine the in-plane strength and stiffness of the material systems identified in section 2 were carried out at nominal actuator stroke rates of 10^{-3}, 1, 10, 100, 250, and 500 in/sec. The tests were conducted along principal material directions, and balanced and symmetric off-axis specimens were tested to investigate the rate effects under combined stress states. The total number of plies for [0°]N and $[+15°/-15°]_{NS}$ specimens differed between materials to reduce the load levels required to fail the specimens within the limits of the test machine. Three replicates were used for each specimen type and stroke rate. The test matrix for the three material systems investigated is summarized in table 1. A total of 502 tension tests were conducted in this study.

Table 1. Test Matrix for Tension Tests

Stacking Sequence	Nominal Stroke Rate (in/s)					
	0.001	1	10	100	250	500
$[0°]_n$	×3	×3	×3	×3	×3	×3
$[+15°/-15°]_{NS}$	×3	×3	×3	×3	×3	×3
$[+30°/-30°]_{2S}$	×3	×3	×3	×3	×3	×3
$[+45°/-45°]_{2S}$	×3	×3	×3	×3	×3	×3

3.4 TEST SPECIMEN GEOMETRY AND FABRICATION.

The strain rate achieved during a constant stroke rate test, as a first-order approximation, is inversely proportional to the gage length of the specimen. Therefore, minimizing the gage length will maximize the strain rates that can be achieved during the constant stroke rate test. However, minimizing the gage length can introduce constraint effects due to the presence of tabs and gripping of the specimen in the tab region. Therefore, for the current investigation, the reduced gage length was fixed at 2.00 inches, while the width of the gage section was maintained at 0.5 inch. The typical tension specimen geometry used in the investigation is shown in figure 7. The specimen geometry is based on ASTM D 3039 [44] with modifications to accommodate high strain rate tests. The specimens were tabbed at the ends using fiberglass tabs, which consisted of two layers of fiberglass/epoxy (NB321/7781) at ±45º to the loading direction.

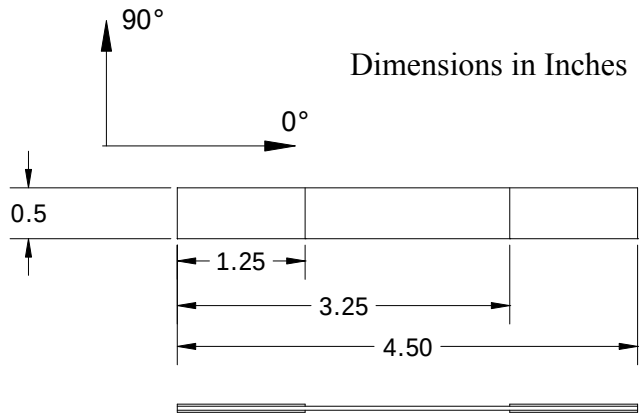

Figure 7. Geometry of Tension Specimens

Laminated panels measuring 8 inches by 20 inches (see figure 8) were assembled and cured using an autoclave cycle recommended by the prepreg manufacturers [36-39]. Fiberglass tabs measuring 2 inches by 20 inches were subsequently bonded to the laminates (using Hysol® EA9394 paste adhesive) and cured at room temperature. The tabs specimens were then cut into specimen blanks and surface-ground to the final dimensions shown in figure 7.

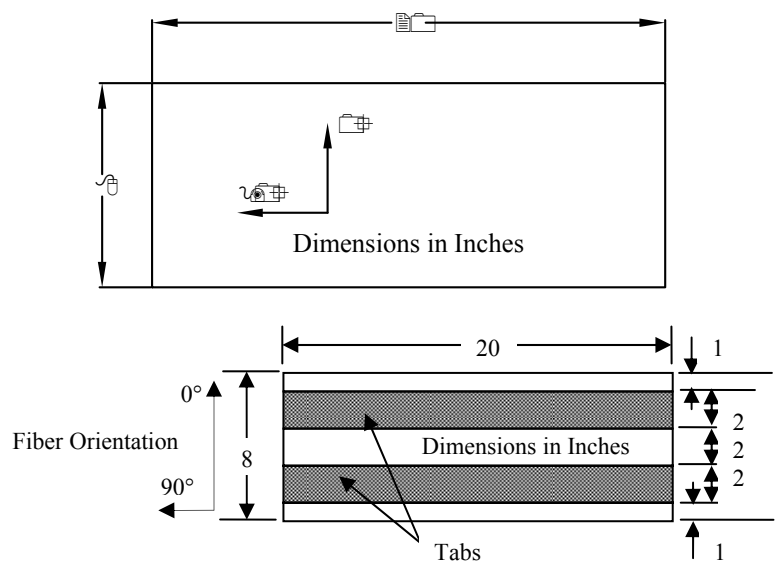

Figure 8. Parent Laminate Geometry and Tabs Used for Specimen Fabrication

3.5 STRAIN AND STROKE RATES.

The tensile tests were carried out under displacement (stroke) control at various actuator speeds. Assuming that the stiffness of the load train is several orders of magnitude higher than the test specimen, the strain in the test specimen with gage length L_o can be approximated by

$$\varepsilon(t) = \frac{u(t)}{L_o} \tag{1}$$

where $u(t)$ is the displacement (stroke) of the actuator. If the stroke rate $\frac{du}{dt}$ is a constant throughout the test, the associated strain rate is given by

$$\frac{d\varepsilon}{dt} = \frac{1}{L_o}\frac{du}{dt} \tag{2}$$

Due to the flexibility and inertial effects of the members of the load train, the above condition is seldom satisfied. The strain rate, $\dot{\varepsilon}$, varies over the duration of the test and will be a function of the nominal actuator speed and stiffness of the test specimen, provided that the rest of the test apparatus remains unchanged. The variation of strain as a function of time is compared for the tests conducted at different actuator speeds shown in figure 9. Since the durations of the tests differ by orders of magnitude, the strain data is compared on a normalized time scale, the normalization performed by the time required to achieve the maximum strain. It is shown that even the quasi-static test does not produce a linear strain variation with respect to time. The test apparatus was observed to produce a spurious behavior at a stroke rate of 10 in/s, and is a function of the system. The strain was observed to oscillate rather than approach a linear behavior similar to the rest of the test speeds. This can be remedied by altering the mass and/or stiffness of some of the members in the load train. However, this will result in shifting this particular type of behavior to another test speed. A comparison of system behavior relative to the ideal scenario described by equation (1) is shown in figure 10. Except at the quasi-static rate (0.001 in/s), the strains during initial loading are much less than the ideal values. However, with increasing time, the strains tend to approach the ideal levels. The rate at which the ideal value is approached was observed to be a function of the test speed.

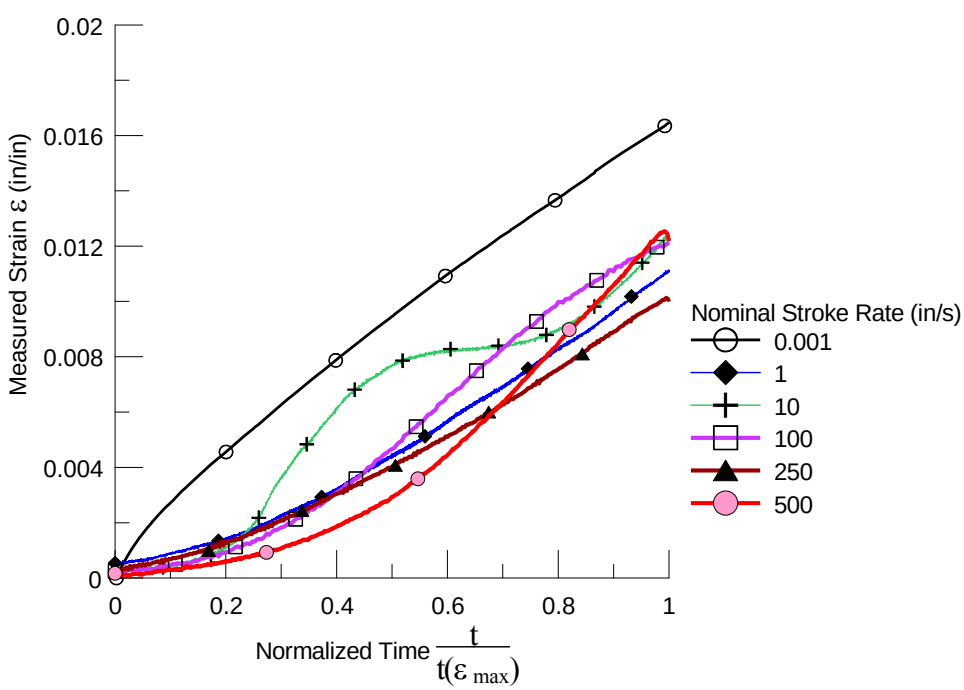

Figure 9. Variation of Strain in Tension Tests Conducted at Different Stroke Rates

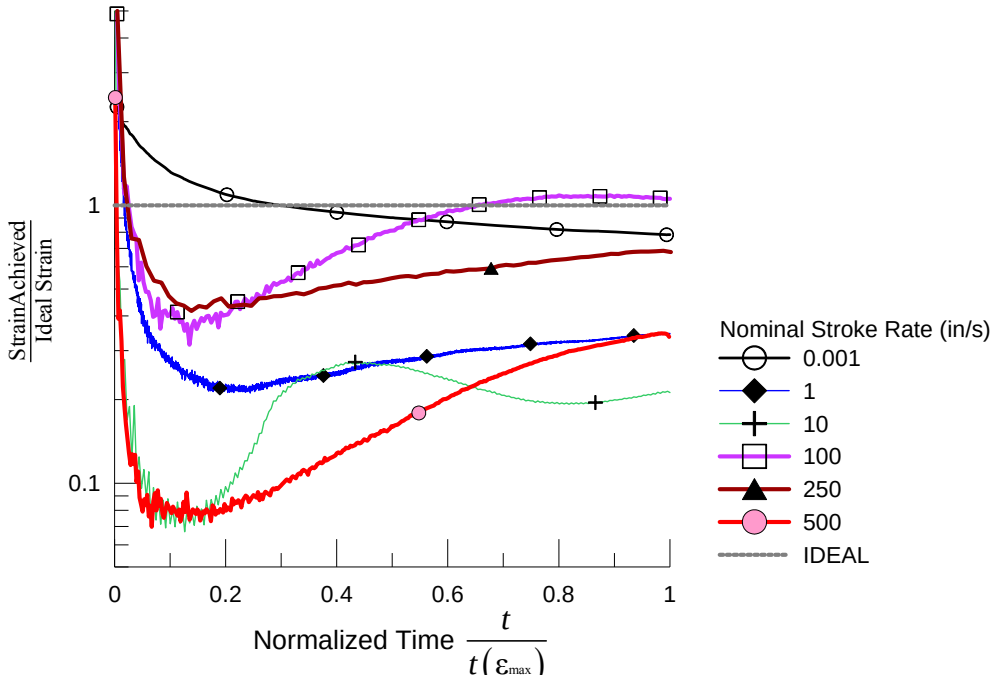

Figure 10. Comparison of Strain Levels Achieved Relative to the Ideal

The calculation of strain rate using discrete test data could be accomplished using numerical differentiation methods. The typical methods include the direct-fit polynomial method, Newton polynomials, and Taylor series approach [45]. High-frequency noise is characteristic of test data, and obtaining derivatives at each step using the test data directly will amplify the noise leading to an erroneous, less informative picture of the strain rate. Using a direct-fit polynomial to estimate the strain rate would be appropriate if the degree of the polynomial is less than four [45]. The use of higher-order Taylor series-based difference formulas would provide a better estimate, but would amplify the noise inherent in the strain data. To alleviate the noise, running averages of the strain data was used. A seven-point average was found to produce a satisfactory estimate of the strain rate. The strain rates obtained based on raw and smoothed data, and the best-fit polynomial, are compared in figure 11 for a quasi-static test. It is shown that even though the raw strain data appears smooth, its first derivative has a significant amount of noise. The best-fit polynomial captures the trends associated with variation of strain rate, but the rates predicted by this method will deviate significantly at several locations. This will become a bigger concern when the degree of polynomial becomes higher as shown in figure 12. This figure presents the strain rate data for a test conducted at an actuator speed of 10 in/s. The dynamic effects of the load train are evident in figure 12.

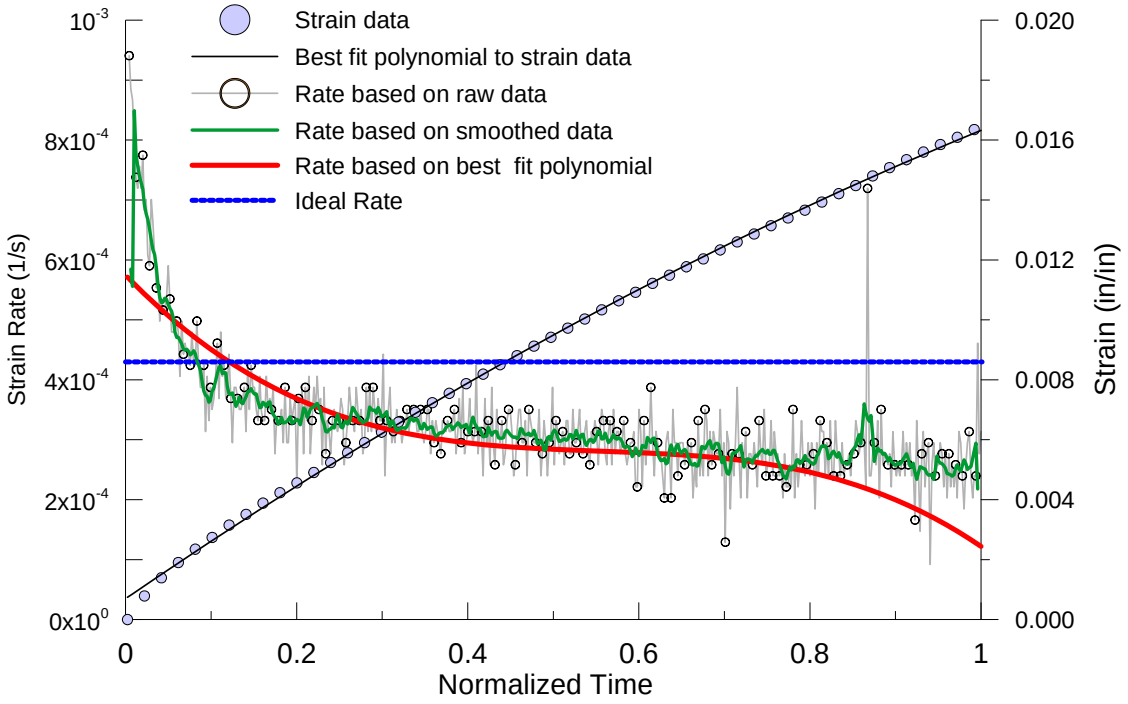

Figure 11. Comparison of Strain Rate Computed Using Different Methods for Quasi-Static Loading

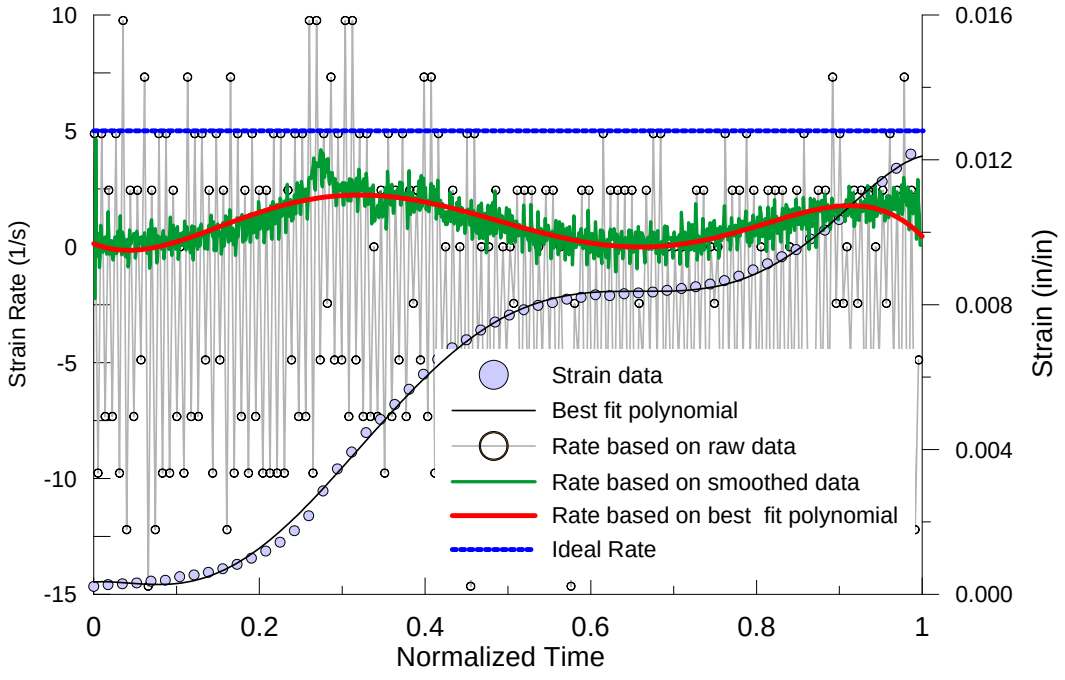

Figure 12. Comparison of Strain Rate Computed Using Different Methods for Dynamic Loading at a Stroke Rate of 1 in/s

The comparison of test data obtained at different test speeds requires a nominal value of the strain rate to be associated with each set of test data. In this study, an average strain rate was computed by taking the average of the strain rate data for the three series of tests. It showed that the value of the average strain, based on raw and smooth rate data, differed by less than 1%. The average strain rates achieved for individual tests are tabulated in appendix A. The average strain rate achieved during a test at a given stroke rate was inversely proportional to the test specimen's stiffness.

3.6 TEST RESULTS.

3.6.1 Quasi-Static Tests.

In this section, a summary of the test data obtained from quasi-static tests are presented. The average tensile strengths and modulus of different material systems are plotted as a function of fiber orientation and shown in figures 13 and 14, respectively. The tabulated values for the individual specimens are in appendix A. The plots indicate that the materials chosen for this investigation represent a wide range of strength and stiffness combinations. The Toray unitape material was observed to possess the highest strength and stiffness (420 ksi and 9 Msi), while the Newport fiberglass was the material with least strength and stiffness (67 ksi and 3 Msi). The strengths of the materials with $[45°/-45°]_{NS}$ orientation, which is dominated by in-plane shear loading, varied between 25 ksi to 40 ksi, and stiffness varied between 1.8 Msi to 2.2 Msi. Unlike other orientations, no particular trend was observed with respect to materials and their strengths for this orientation.

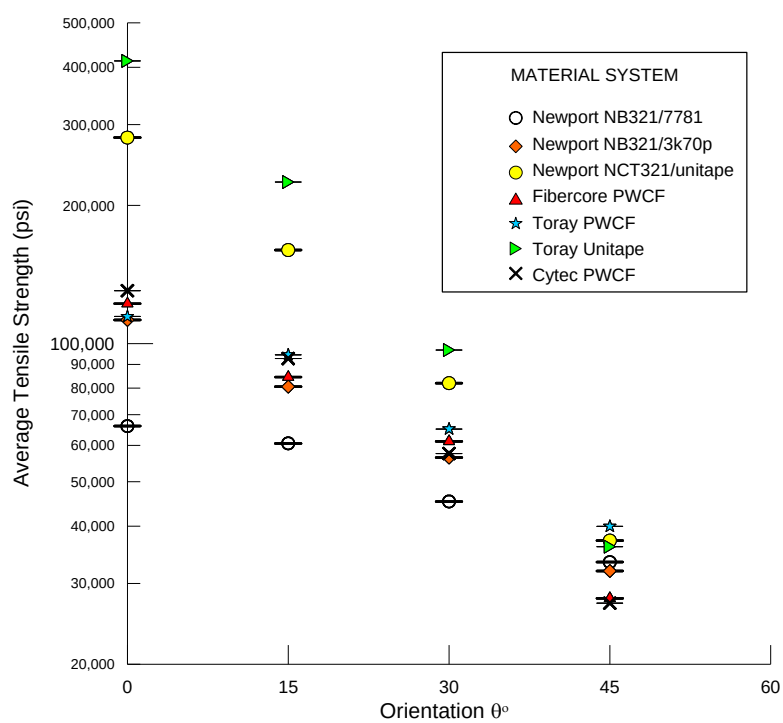

Figure 13. Average Values of Tensile Strength as a Function of Orientation for Different Material Systems Under Quasi-Static Loading

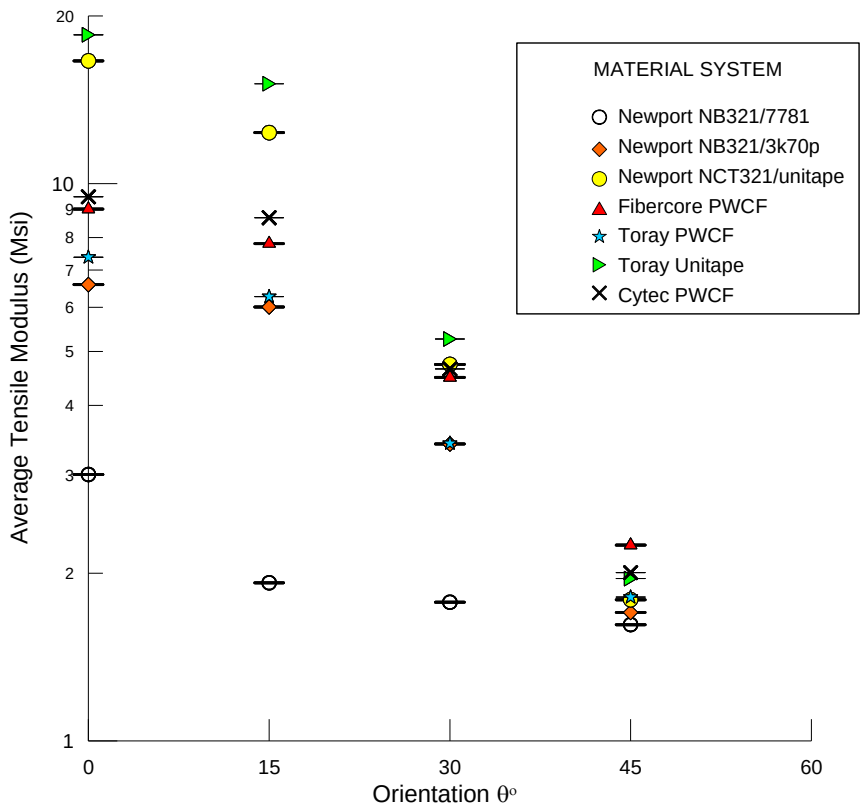

Figure 14. Average Values of Tensile Modulus as a Function of Orientation for Different Material Systems Under Quasi-Static Loading

3.6.2 High-Rate Tests.

The tension tests of the materials listed in section 2 were conducted at the nominal stroke rates listed in table 1. The typical stress-strain plots for Toray T800S/3900-2B unitape $[0°]_2$ specimens tested at different nominal stroke rates are shown in figure 15. The plots indicate that the tensile strength and modulus increase with stroke rate, while the failure strain decreases. Further, the stress-strain behaviors at a stroke rate of 100 in/s and above are different when compared to the lower stroke rates. The tests at a constant stroke rate do not represent constant strain rate tests due to the reasons discussed in section 3.1. Since the strain rates vary with time (or strain), the stiffness of the material at different stroke rates was not reported. The stress-strain data have to be resolved into constant strain rate curves prior to obtaining the stiffness properties.

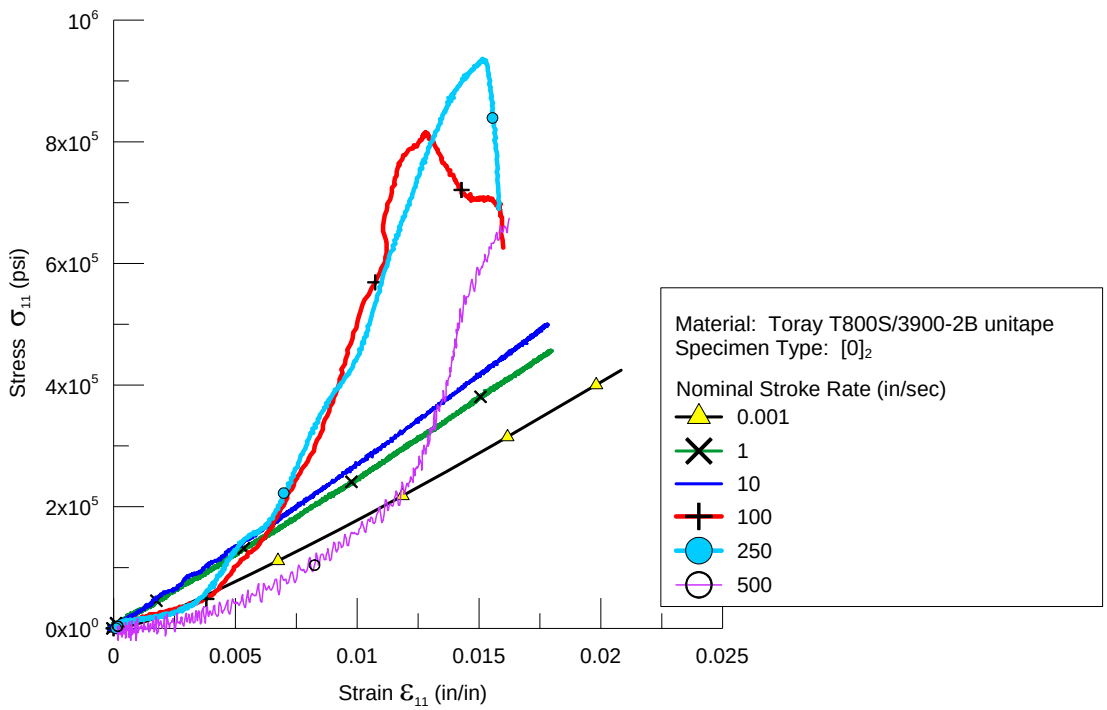

Figure 15. Stress-Strain Behavior of Toray Unitape Specimens at Different Stroke Rates

The tensile failure strengths of the seven material systems at different stroke rates and strain rates are summarized and presented in figures 16 to 22. The tabulated data for the seven material systems are presented in appendix A. All materials tested in this program exhibited different levels of sensitivity to strain rate. The strengths increased when the strain rate increased by an order of magnitude. The Toray unitape specimen exhibited a significant increase in strength for each increment of increase in stroke rate. The strength of 0º specimens approached 1 Msi at a stroke rate of 100 in/s. The strength of the material saturated or even decreased at stroke rates of 250 and 500 in/s. However, the strengths were still higher than those of the quasi-static rates. The strain rate sensitivity of Toray plain weave laminates were not as pronounced as the unitape material for stroke rates up to 1 in/s, but increased significantly at strain rates approaching 100 in/s. A significant amount of strength reduction was observed at stroke rates of 250 and 500 in/s, with strengths reducing to levels recorded at quasi-static test rates. However, the ±45° specimens exhibited a steady increase in strength with a strain rate similar to the unitape material.

The Newport materials exhibited rate sensitivity that was dependent on the fiber-reinforcement style (see figures 18-20). The Newport 7781 fiberglass material exhibited a perceptible increase in tensile strength for each increment of stroke rate, unlike the Newport carbon fabric. The strength increase for Newport carbon fabric specimens with 0°, ±15°, and ±30° orientations had stroke rates exceeding 10 in/s. The ±45° carbon fabric specimens behaved similarly to the corresponding fiberglass specimen. The tensile strength of both material systems decreased at stroke rates of 250 and 500 in/s. The Newport unitape material had a rate insensitivity up to a stroke rate of 1 in/s, and the behavior past this rate resembles that of the 3K70 PWCP material.

The tensile strengths of Fibercote and Cytec materials tested at different rates are summarized in figures 21 and 22, respectively. The Cytec material system had more rate sensitivity relative to the Fibercote and Newport (3K70P) materials, which have similar reinforcements.

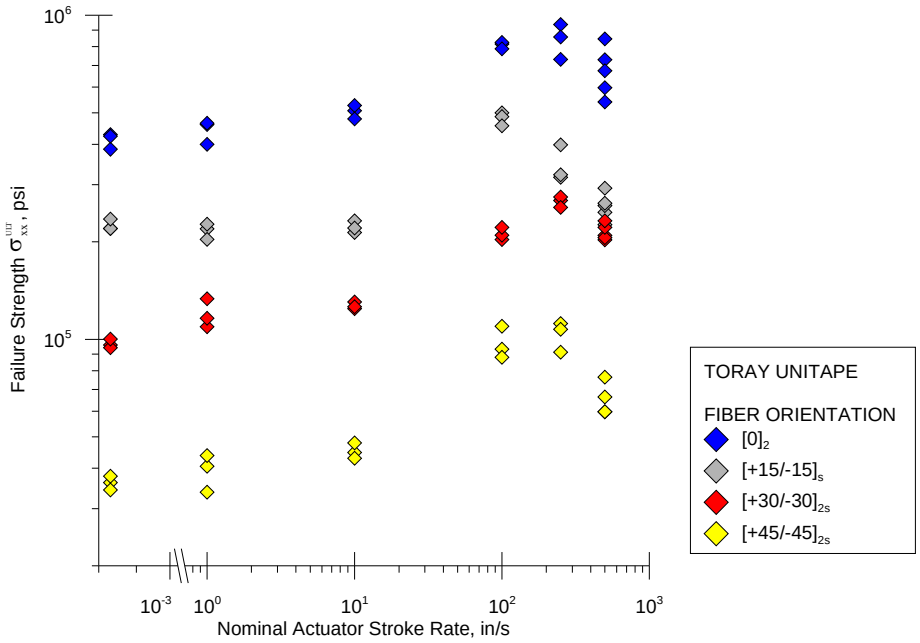

Figure 16. Tensile Strength of Toray T800S/3900-2B Unitape Specimens With Different Orientations as a Function of Stroke Rate

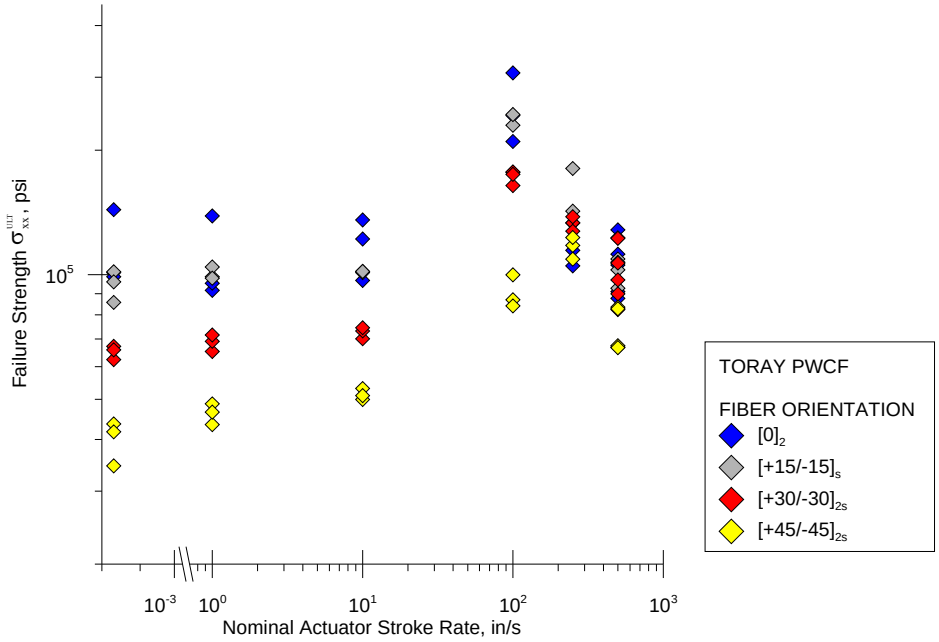

Figure 17. Tensile Strength of Toray T700G-12k-PW/3900-2 Fabric Specimens With Different Orientations as a Function of Stroke Rate

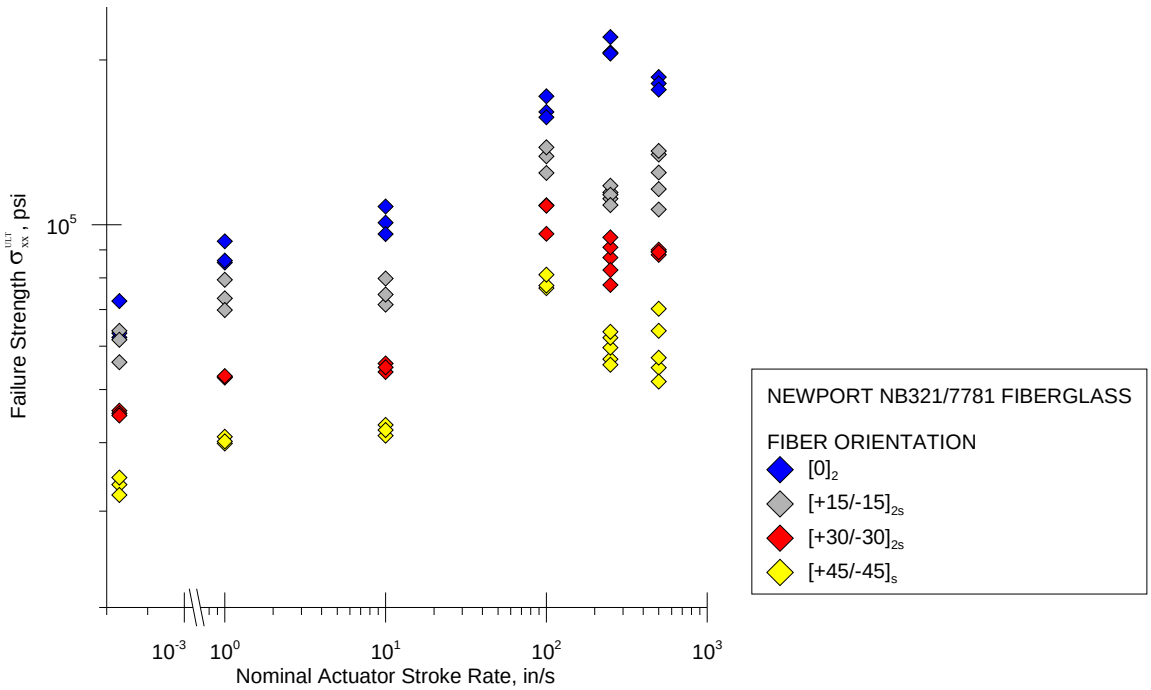

Figure 18. Tensile Strength of Newport NB321/7781 Fiberglass Fabric Specimens With Different Orientations as a Function of Stroke Rate

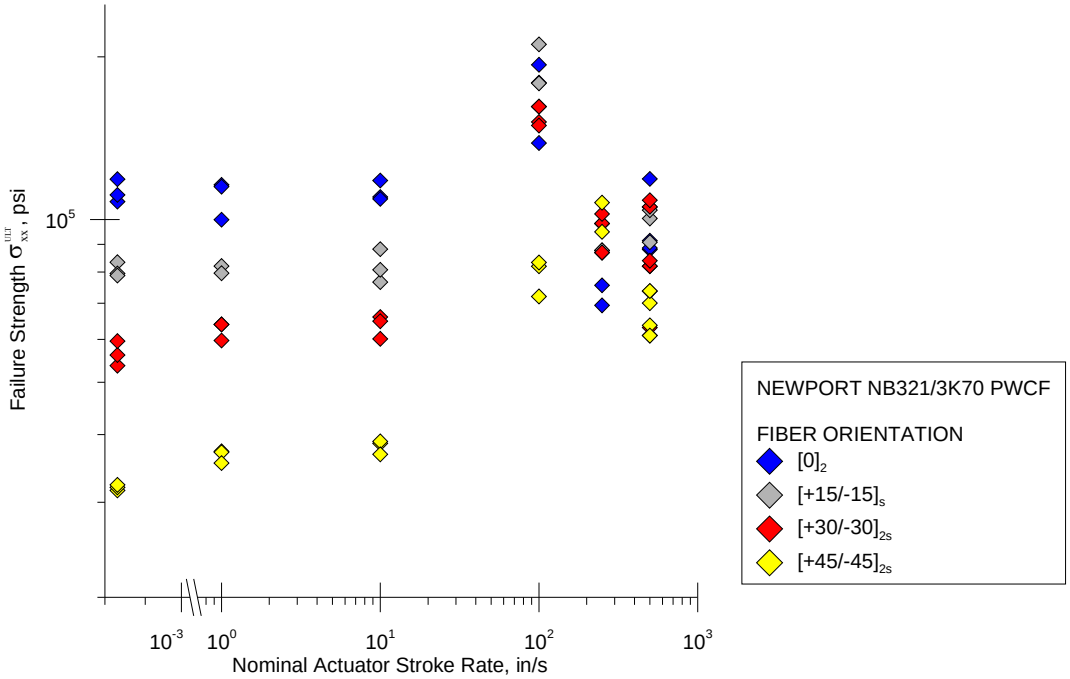

Figure 19. Tensile Strength of Newport NB321/3K70 PWCF Specimens With Different Orientations as a Function of Stroke Rate

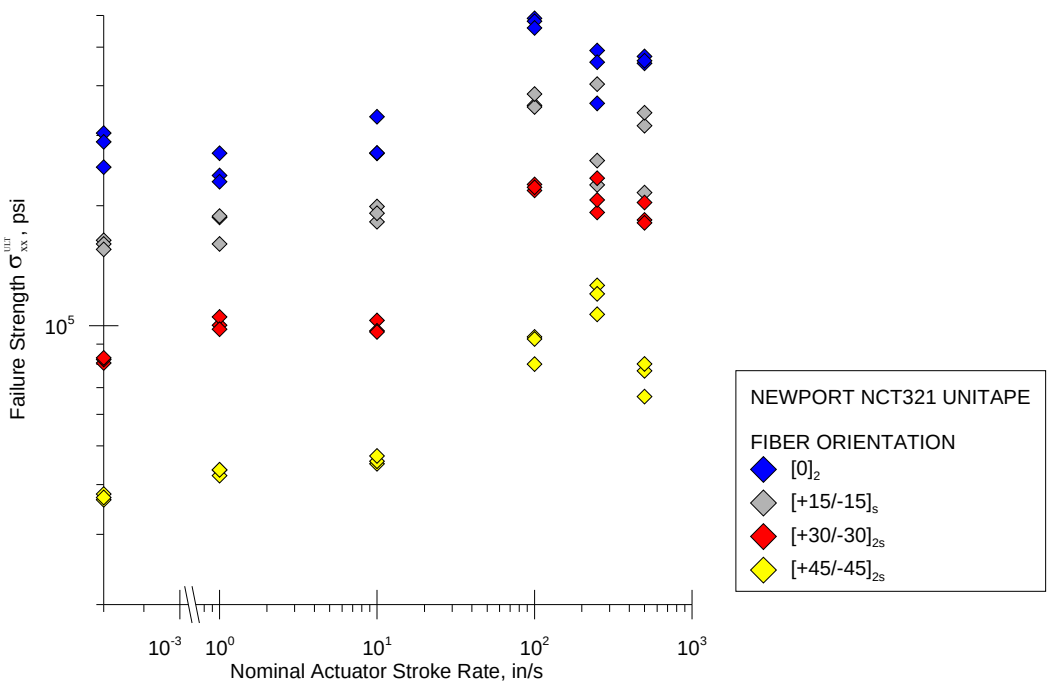

Figure 20. Tensile Strength of Newport NCT321/G150 Unitape Specimens With Different Orientations as a Function of Stroke Rate

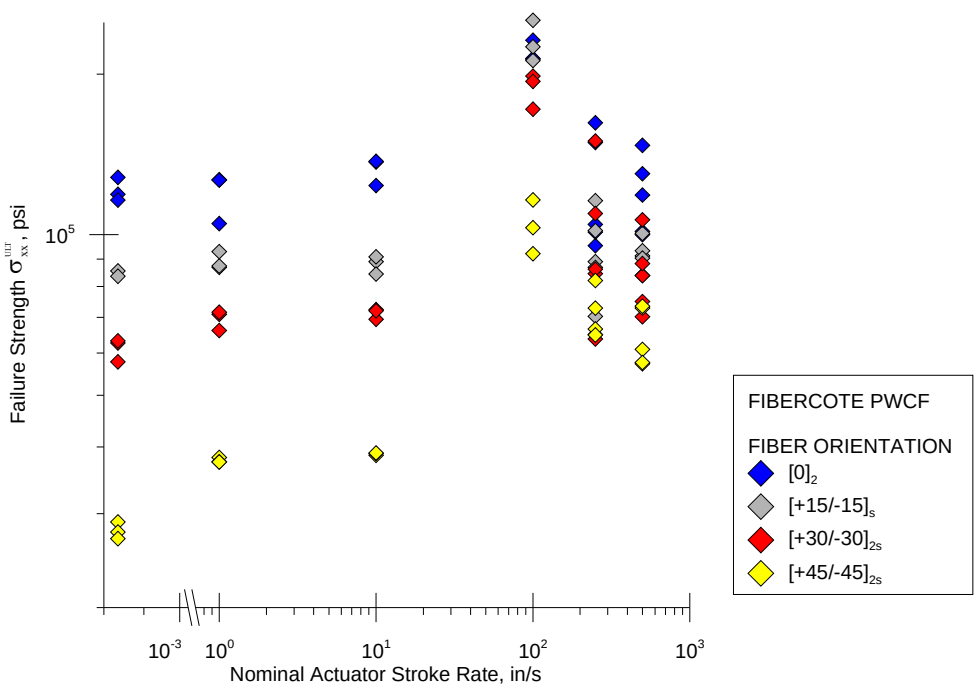

Figure 21. Tensile Strength of Fibercote 3KPW-E365 PWCF Specimens With Different Orientations as a Function of Stroke Rate

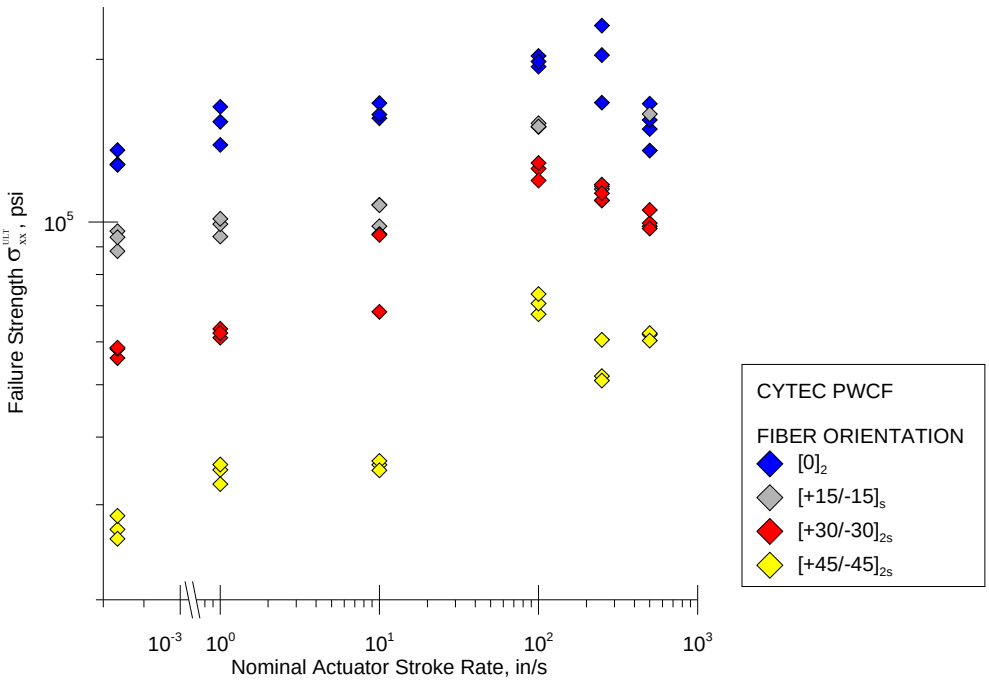

Figure 22. Tensile Strength of Cytec T300/7714AC 3KNT PWCF Specimens With Different Orientations as a Function of Stroke Rate

3.6.3 Failure Modes.

The failure modes in tension specimens were examined to study changes in failure mode, if any, as a function of strain rate. The images of failed specimens were digitally captured posttest and compared. The representative images of failed specimens with different lay-up schedules were tested at different stroke rates. The failure modes for different material systems and orientations are discussed in the following sections.

3.6.3.1 Failure Modes in $[0°]_N$ Specimens.

The failures modes observed in the specimens tested at different stroke rates are summarized in this section. The $[0°]_2$ Toray T800S/3900-2B unitape specimens exhibited explosive longitudinal splitting failure mode at all the stroke rates at which the specimens were tested, as shown in figure 23. The specimen failed at the edge of the tab region for the specimens tested at 500 in/s, indicating dominance of edge effects. The Toray T700G-12K-PW/3900-2 fabric exhibited net section failure along a section perpendicular to the loading direction, as shown in figure 24. These sections were located at a distance of at least that of the specimen width, away from the end of the tabs in a majority of the specimens. This indicated that the end effects due to tabs and the grips were minimal. The Newport NB321/7781 fiberglass specimens exhibited visible matrix cracking and net section failures at all stroke rates investigated. Delaminations around the net section fractures were observed in specimens with increasing stroke rates, as shown in figure 25. This indicated a possible change in failure mechanism(s) with increasing stroke rates. The Newport NB321/3K70 PWCF system exhibited net section fractures at locations well inside the gage region for test rates of up to 250 in/s, as shown in figure 26. However, the specimens tended to fail at the edge of the tab region at stroke rates of 500 in/s. The Newport

NCT321/G150 unitape system exhibited failure modes (figure 27) that were similar to the Toray unitape system, as shown in figure 23. The Fibercote specimens shown in figure 28, and Cytec (pictures unavailable) exhibited net section fractures at all rates tested.

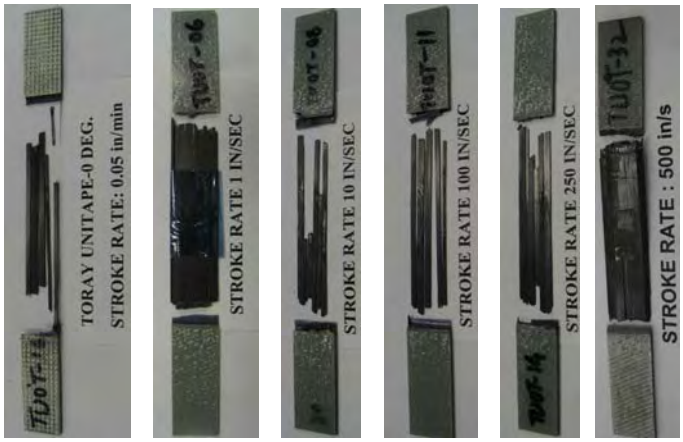

Figure 23. Failure Modes in $[0°]_2$ Toray T800S/3900-2B Unitape Specimens

Figure 24. Failure Modes in $[0°]_4$ Toray T700G-12K-PW/3900-2 Fabric Specimens

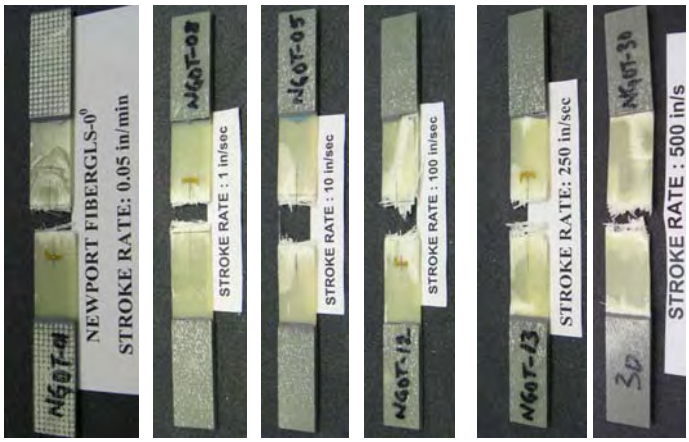

Figure 25. Failure Modes in $[0°]_4$ Newport NB321/7781 Fiberglass Specimens

Figure 26. Failure Modes in $[0°]_4$ Newport NB321/3K70 PWCF Specimens

Figure 27. Failure Modes in $[0°]_4$ Newport NCT321/G150 Unitape Specimens

Figure 28. Failure Modes in $[0°]_4$ Fibercote 3KPW-E365 PWCF Specimens

3.6.3.2 Failure Modes in $[+15°/-15°]_{NS}$ Specimens.

The failure modes in Toray unitape and plain weave $[+15°/-15°]_{NS}$ specimens tested at different stroke rates are shown in figure 29. The unitape specimen exhibited failures within the gage region with characteristic fractures along the fiber directions. No change in failure mode was observed with increasing test speed. The Toray fabric specimens exhibited net section fractures within the gage region at all rates tested.

T800S/3900-2B UNITAPE T700G-12K-PW/3900-2 FABRIC

Figure 29. Failure Modes in $[+15°/-15°]_{2S}$ Toray Specimens Tested at Different Stroke Rates

The failure modes in Newport fiberglass, PWCF, and unitape $[+15°/-15°]_{NS}$ specimens tested at different rates are shown in figure 30. Net section failures in 7781 fiberglass specimens occurred at regions both away from and close to the tabs. No preference of location was observed at any particular rate. At the higher rates, a pronounced whitening of the longitudinal edges of the specimen was observed, indicating a presence of interlaminar failure modes. The Newport 3K70P fabric and G150 unitape specimens failed across the gage region, with the unitape specimens displaying characteristic fractures along the fiber direction.

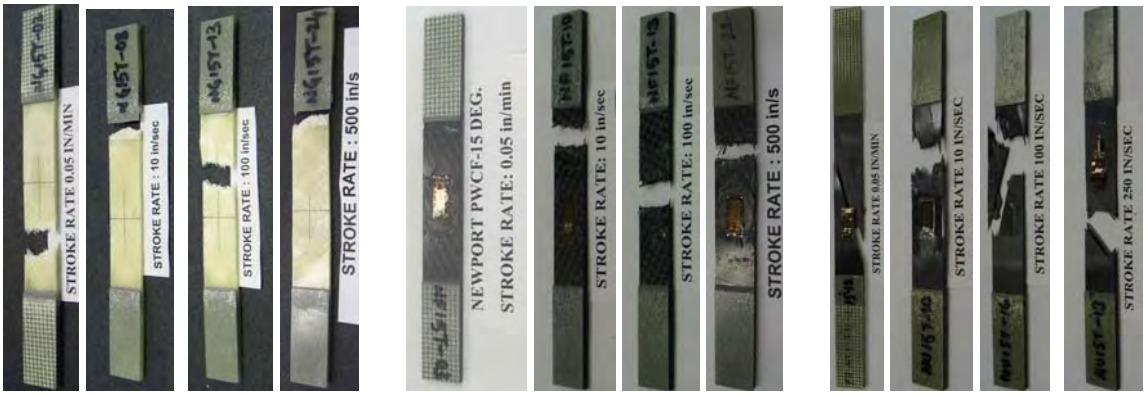

NB321/7781 FIBERGLASS NB321/3K70 PWCF NCT321/G150 UNITAPE

Figure 30. Failure Modes in $[+15°/-15°]_{2S}$ Newport Specimens Tested at Different Stroke Rates

The failure modes in Fibercote and Cytec (pictures not available) specimens were similar to the Newport 3K70P system with no significant changes in failure modes observed with increasing test speeds. The failure modes in Fibercote specimens at different representative stroke rates are shown in figure 31.

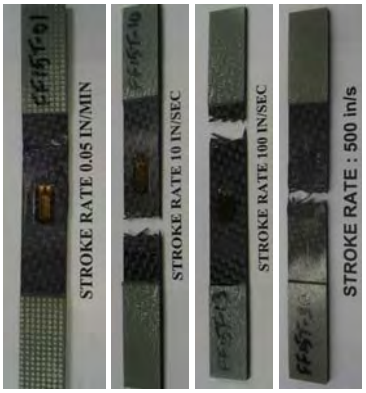

Figure 31. Failure Modes in $[+15°/-15°]_{2S}$ Fibercote 3KPW-E365 PWCF Specimens Tested at Different Stroke Rates

3.6.3.3 Failure Modes in $[+30°/-30°]_{NS}$ Specimens.

The failure modes in Toray unitape and plain weave $[+30°/-30°]_{NS}$ specimens tested at different stroke rates are shown in figure 32. The unitape specimen exhibited failures within the gage region, with characteristic fractures along the fiber directions. The failure zone was spread over a larger region at higher rates of loading. The Toray fabric specimens exhibited net section fractures within the gage region at all rates tested with no discernible differences in the mode of failure.

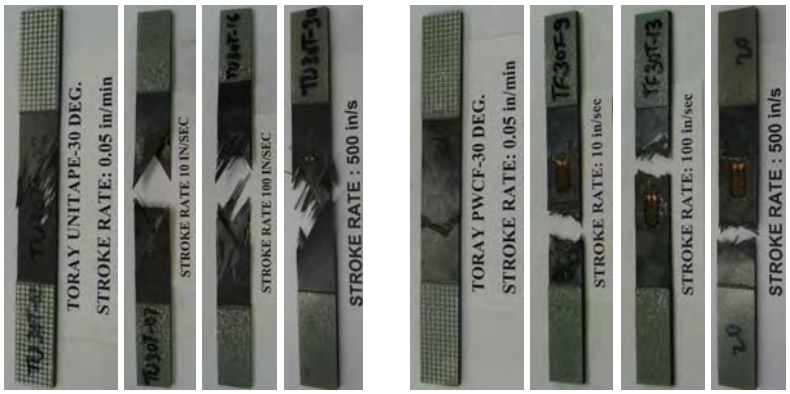

T800S/3900-2B UNITAPE T700G-12K-PW/3900-2 FABRIC

Figure 32. Failure Modes in $[+30°/-30°]_{2S}$ Toray Specimens Tested at Different Stroke Rates

The failure modes in Newport fiberglass, PWCF and unitape $[+30°/-30°]_{NS}$ specimens tested at different rates are shown in figure 33. The failures in 7781 fiberglass specimens ranged from net section failures at regions away from and close to the tab regions. No preference of location was observed at any particular rate. At the higher rates, a pronounced whitening of the longitudinal edges of the specimen and regions close to the tabs indicated the presence of interlaminar failure modes. The failure zone was spread over a larger region at higher rates of loading. The Newport 3K70P fabric and G150 unitape specimens failed across the gage region, with the unitape specimens displaying characteristic fractures along the fiber direction.

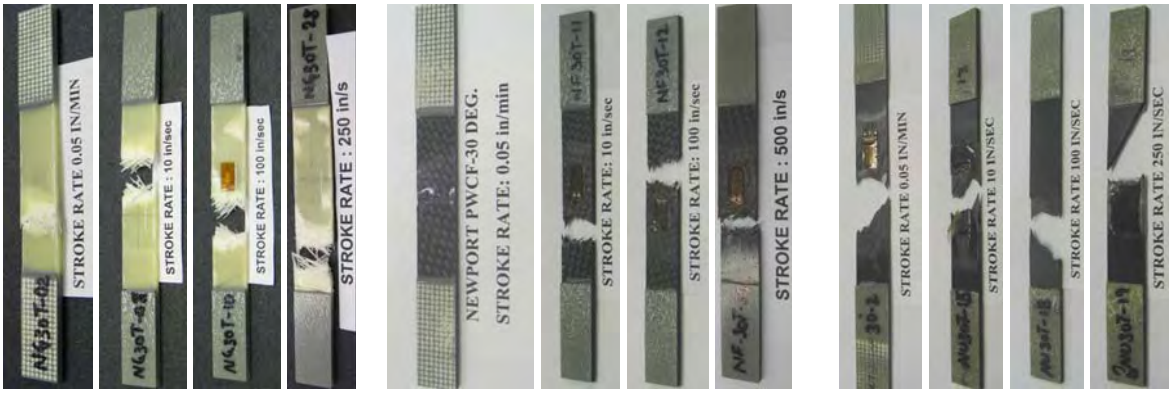

NB321/7781 FIBERGLASS NB321/3K70 PWCF NCT321/G150 UNITAPE

Figure 33. Failure Modes in $[+30°/-30°]_{2S}$ Newport Specimens Tested at Different Stroke Rates

The failure modes in Fibercote and Cytec (pictures not available) specimens were similar to the Newport 3K70P system with no significant changes in failure modes observed with increasing test speeds. The failure modes in Fibercote specimens at different representative test speeds are shown in figure 34.

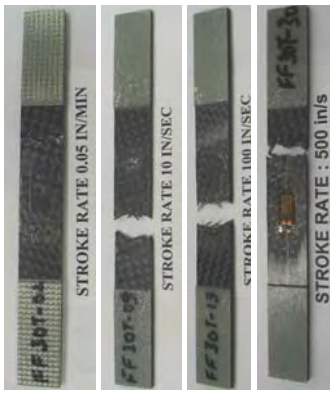

Figure 34. Failure Modes in $[+30°/-30°]_{2S}$ Fibercote 3KPW-E365 PWCF Specimens Tested at Different Stroke Rates

3.6.3.4 Failure Modes in $[+45°/-45°]_{NS}$ Specimens.

The failure modes in Toray unitape and plain weave $[+45°/-45°]_{NS}$ specimens tested at different stroke rates are shown in figure 35. The unitape specimen exhibited failures within the gage region, with characteristic fractures along the fiber directions. The failure zone was observed to be spread over a larger region at higher rates of loading. The Toray fabric specimens exhibited net section fractures within the gage region at all rates tested with no discernible differences in the mode of failure.

T800S/3900-2B UNITAPE T700G-12K-PW/3900-2 FABRIC

Figure 35. Failure Modes in $[+45°/-45°]_{2S}$ Toray Specimens Tested at Different Stroke Rates

The failure modes in Newport fiberglass, PWCF, and unitape $[+45°/-45°]_{NS}$ specimens tested at different stroke rates are shown in figure 36. The failures in 7781 fiberglass specimens ranged from net section failures at region away from and close to the tab regions. No preference of location was observed at any particular rate. At the higher rates, a pronounced whitening of the longitudinal edges of the specimen and regions close to the tabs was observed indicating presence of interlaminar failure modes. The failure zone was spread over a larger region at higher rates of loading. The Newport 3K70P fabric and G150 unitape specimens failed across the gage region, with the unitape specimens displaying characteristic fractures along the fiber direction.

The failure modes in Fibercote and Cytec (pictures not available) specimens were similar to the Newport 3K70P system with no significant changes in failure modes observed with increasing stroke rates. The failure modes in Fibercote specimens at different representative stroke rates are shown in figure 37.

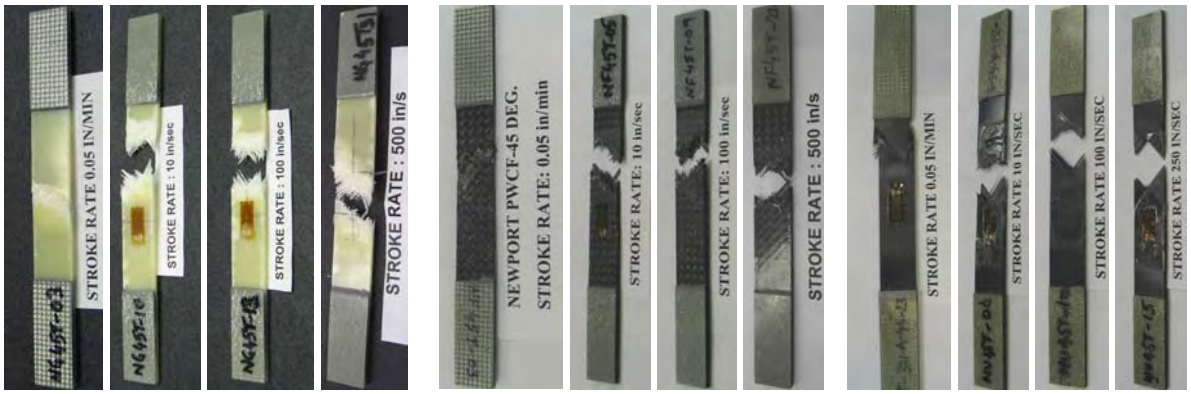

NB321/7781 FIBERGLASS NB321/3K70 PWCF NCT321/G150 UNITAPE

Figure 36. Failure Modes in $[+45°/-45°]_{2S}$ Newport Specimens Tested at Different Stroke Rates

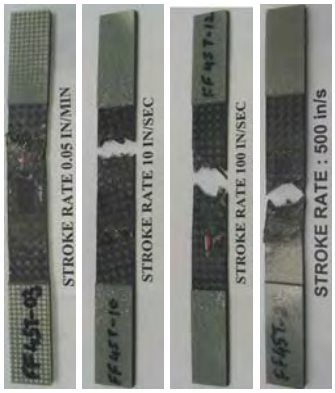

Figure 37. Failure Modes in $[+45°/-45°]_{2S}$ Fibercote 3KPW-E365 PWCF Specimens Tested at Different Stroke Rates

4. IN-PLANE SHEAR TESTS.

The in-plane shear tests of the seven material systems listed in section 2 were carried out using the V-notch rail shear method [46]. The tests were conducted at nominal actuator stroke rates of 0.001, 1, 10, 100, 250, and 500 in/s. The test matrix for the in-plane shear tests is summarized in table 2. A stacking sequence of $[0°]_{12}$ was used for the specimens. Three specimens were tested at each stroke rate per material for a total of 126 tests.

Table 2. Test Matrix for In-Plane Shear Tests

Material	Nominal Stroke Rate (in/s)					
	0.001	1	10	100	250	500
NB321/7781	×3	×3	×3	×3	×3	×3
NB321/3K70 PWCF	×3	×3	×3	×3	×3	×3
NCT321/G150 Unitape	×3	×3	×3	×3	×3	×3
T800S/3900-2B Unitape	×3	×3	×3	×3	×3	×3
T700G-12K-PW/3900-2	×3	×3	×3	×3	×3	×3
3KPW-E365 PWCF	×3	×3	×3	×3	×3	×3
T300/7714AC 3KNT	×3	×3	×3	×3	×3	×3

4.1 TEST APPARATUS.

The V-notch rail shear method [46] was preferred over the ASTM D 5379 (Iosipescu shear) method [47], due to the tensile nature of applied load, which lends itself to high-rate tests using servo-hydraulic machines. The V-notch rail shear test fixture and test specimen geometry is shown in figures 38 and 39, respectively. The shear loading of the specimen is achieved by pulling the two fixture halves apart. Upon failure of the specimen, the two halves of the fixture move away from each other, unlike the Iosipescu fixture.

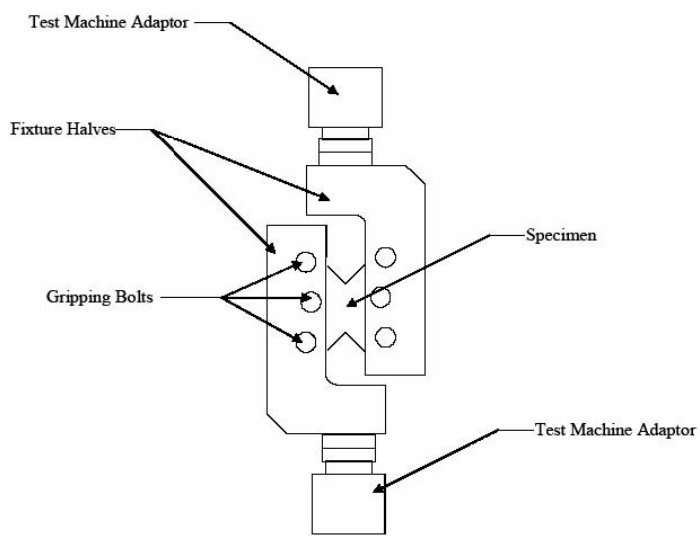

Figure 38. Test Fixture for V-Notch Rail Shear Tests

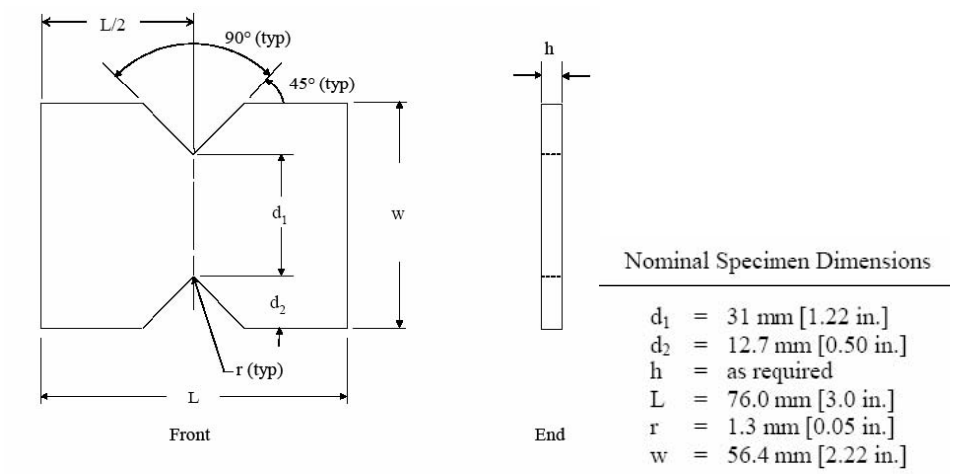

Figure 39. Test Specimen Geometry and Nominal Dimensions for V-Notch Rail Shear Tests

The test arrangement for the high-rate shear tests is shown in figure 40. The test setup uses a slack inducer mechanism similar to the tension test. However, the two halves of the test fixture are heavier than the tension grips and will further influence the strain rate achieved during the test. The test specimens were mounted into the fixture in situ, and the clamping bolts were torqued to 600 in-lb to avoid specimen slipping during the test. The strain gages were monitored while the bolts were torqued; twisting of the specimen was minimized by maintaining the two strain gage readings within 5% of each other.

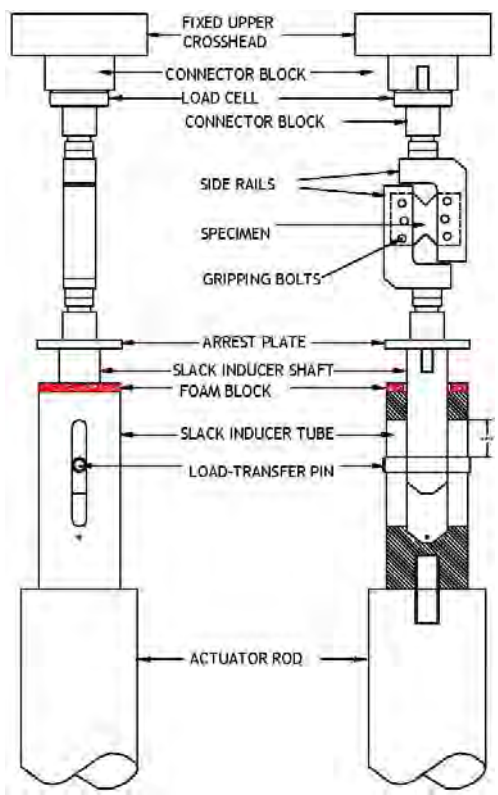

Figure 40. Test Arrangement for High Strain Rate Tests of In-Plane Shear Specimens

The test specimens were instrumented using Vishay model EA-06-125TH-120 shear rosettes for shear strain measurement. The strain signals were conditioned using a Vishay model 2100 signal conditioner. An excitation voltage of 10V was used for the strain gage circuits to accommodate a low amplification, which maximizes the available bandwidth. Due to the high levels of excitation signal and low thermal conductivity of composites, heat buildup of approximately 25ºF was observed during the tests. To avoid thermal effects on this behavior, the excitation voltage was turned down after balancing the specimen, and the gages were allowed to cool down for about 15 minutes. Since, the high-rate tests last for a fraction of a second, the excitation voltage was turned on just prior to the test, thus minimizing the thermal effects.

4.2 TEST RESULTS.

4.2.1 Shear Strain Rates.

The shear strain tests conducted at constant stroke rates did not produce constant shear strain rate data, due to the nonlinear relation between the shear strain and the relative displacement of the test fixture halves. The variation of strain as a function of time for Newport NB321/3K70 PWCF material tested at different nominal stroke rates is shown in figure 41. Since the test durations differ by orders of magnitude, the time is normalized by the time required to reach a shear strain level of 0.08 radians. It should be noted that the strain gage data represents approximately 1/6 of the total test, since the strain gages reach their physical limits at this point. The shape of the strain-time curve appears to be similar for tests conducted at quasi-static, 1, 250, and 500 in/s, while the tests conducted at 10 in/s and 100 in/s exhibited the dynamic effects associated with the load train.

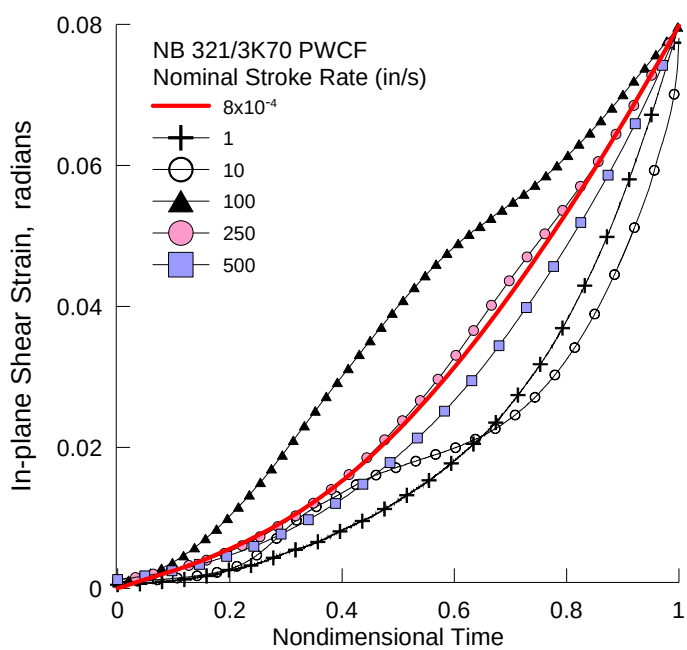

Figure 41. Variation of Shear Strain With Time for Tests Conducted at Different Nominal Stroke Rates

The variation of shear strain rates as a function of the shear strain in the specimen is shown in figure 42 for Newport NB321/7781 specimens. The variation of shear strain rate with strain depended on the stroke rate. The dynamic effects of the loading mechanism are evident in the tests conducted at stroke rates of 10, 100, and 250 in/s. The maximum strain rates achieved during the tests range from 0.0016 radians per second (rad/s) to over 1000 rad/s. However, the average strain rates are much lower than these values. The average strain rates achieved during the tests are shown in appendix B.

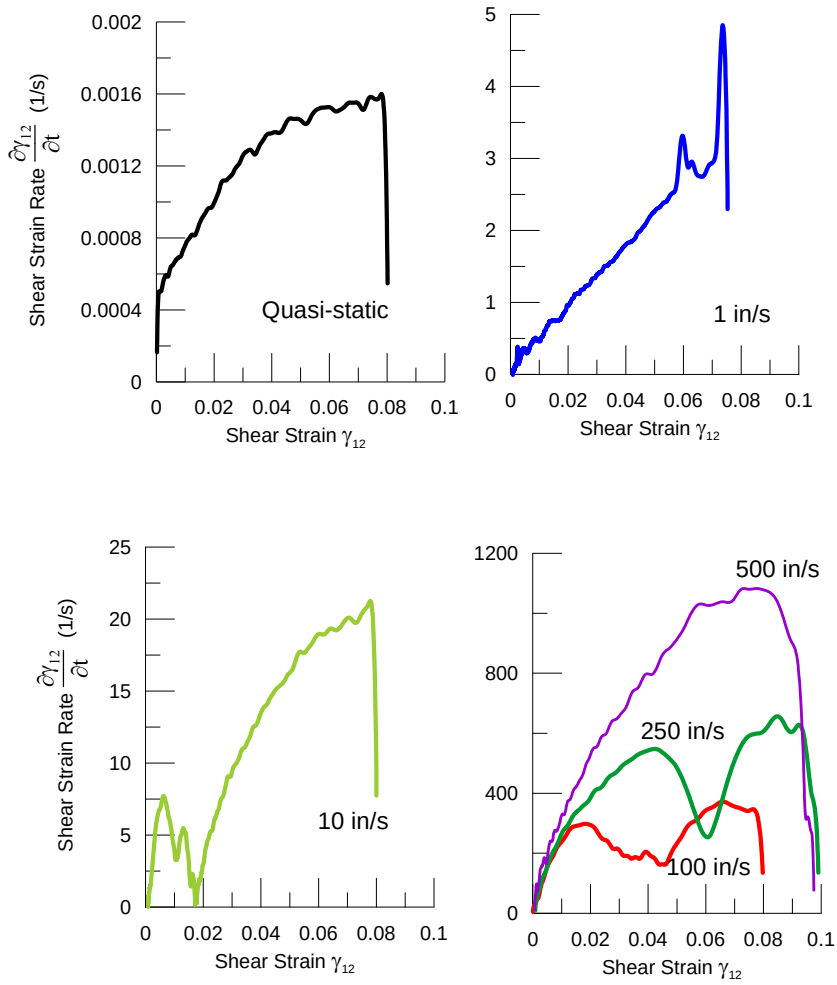

Figure 42. Variation of Shear Strain Rate With Shear Strain for Tests Conducted at Different Stroke Rates

4.2.2 Stress-Strain Behavior.

The typical shear stress versus shear strain behavior of Newport NB321/7781 fiberglass and NB321/3K70 PWCF carbon fabric specimens at different stroke rates are shown in figure 43. The stress-strain plots are shown, up to a maximum shear strain value of 0.08 radians, due to the physical limitations of the strain gages. The materials, however, possess load-bearing capability past the physical limit of the strain gages, which is also shown in figure 43. Further, the nonlinear behavior under shear loading begins much earlier than is evident from the

stress-displacement plots. In practice, the limit of strain gages (shear strain of 0.1 radians or 5.7°) is seldom exceeded, and the strain rate data within this region would still be useful.

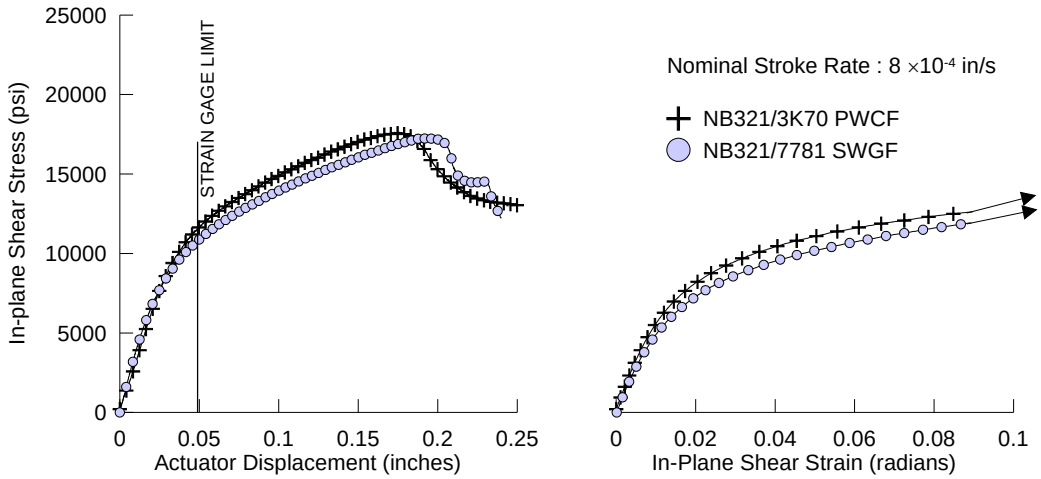

Figure 43. Shear Stress-Displacement and Shear Stress-Strain Behavior Under Quasi-Static Loading

A comparison of the stress-strain behavior of Newport NB321/7781 material tested at different stroke rates is shown in figure 44. While maintaining the overall shape of the curve, the shear stresses increase for a given shear strain level for stroke rates up to 10 in/s. However, a change in behavior was observed at stroke rates of 100 in/s and higher, with the specimen exhibiting lower stiffness during the initial stages. It should be noted that these curves are not constant strain rate curves; rather, the strain rate varies with strain, as discussed previously. The stress-strain plots for individual tests at different stroke rates are shown in appendix B.

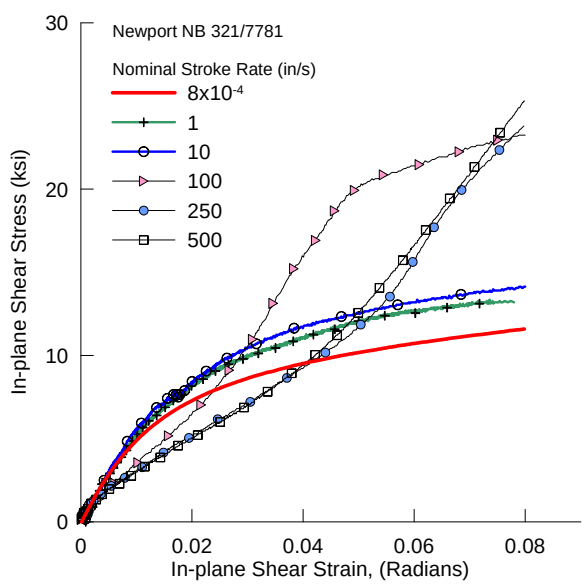

Figure 44. Shear Stress-Strain Behavior at Different Test Rates

4.2.3 In-Plane Shear Strengths.

The variation of in-plane shear strength as a function of actuator stroke rate for the different material systems investigated are shown in figures 45, 46, and 47. The tabulated strengths for individual materials can be found in appendix B. All material systems exhibited an increase in shear strength for stroke rates up to 100 in/s. Beyond this rate, the increase or decrease in strength depended on the material system. The Toray T700G-12K-PW/3900-2 system exhibited an increasing trend, up to 500 in/s, while the Toray T800S/3900-2 unitape system exhibited a decrease in strength at the highest rate tested. Similarly, the Newport material systems reinforced by fabrics (3K70P and 7781) exhibited increase in shear strengths for the entire range of stroke rates, while a reduction in strength was observed for the Newport unitape material at test speeds of 250 and 500 in/s. The shear strengths of the Cytec and Fibercote materials increased with stroke rate for rates up to 100 in/s, beyond which, the strengths decreased. While the test data indicates specific trends associated with shear strengths, they should be interpreted with caution for stroke rates above 100 in/s. Due to the heavy mass of the test fixture, the load signal modulation may be significant at higher rates.

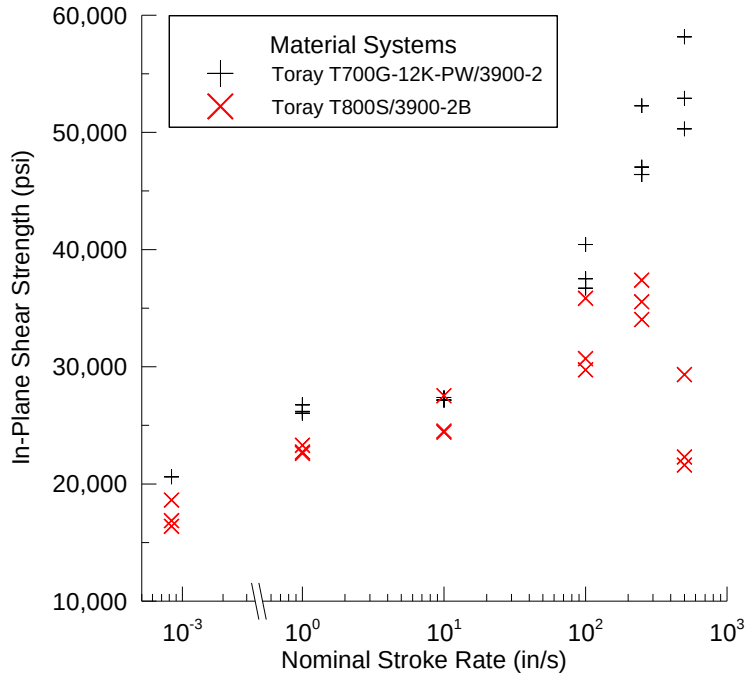

Figure 45. In-Plane Shear Strengths of Toray Materials at Different Stroke Rates

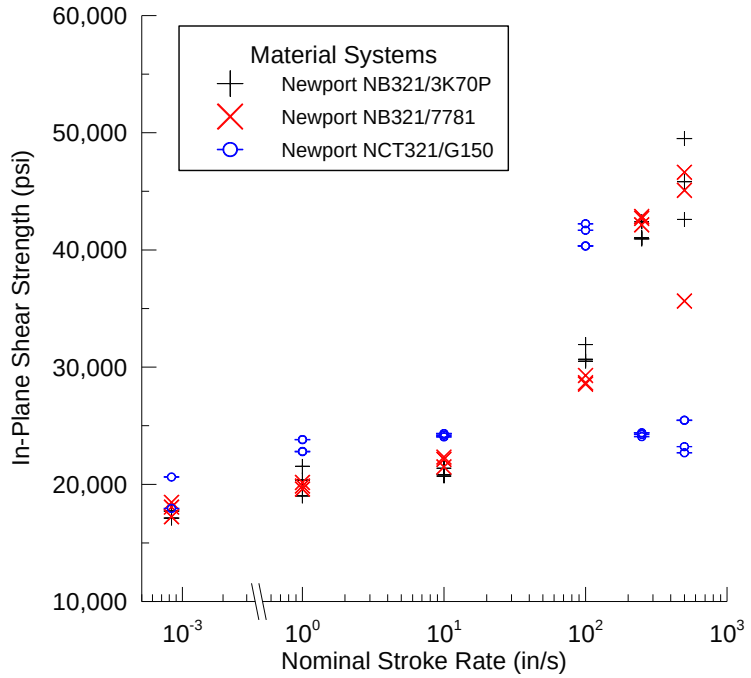

Figure 46. In-Plane Shear Strengths of Newport Materials at Different Stroke Rates

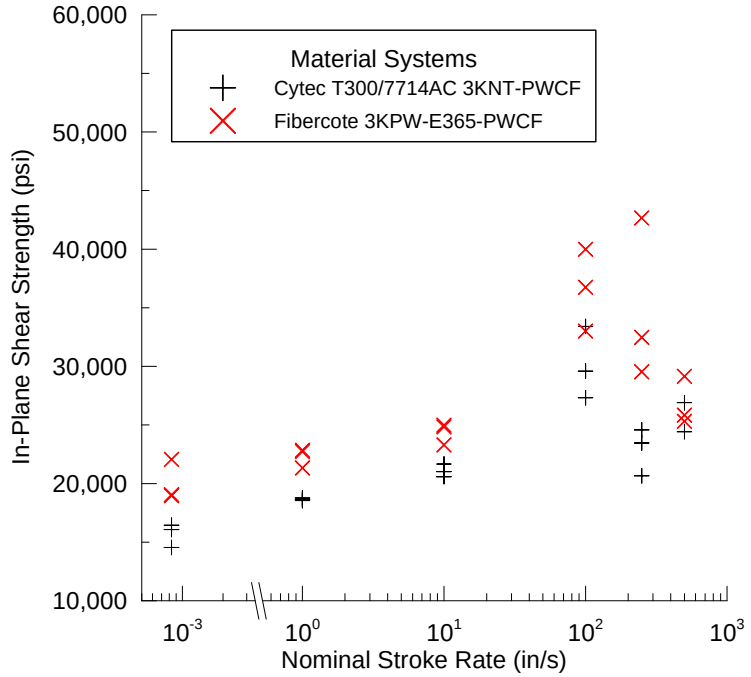

Figure 47. In-Plane Shear Strengths of Cytec and Fibercote Materials at Different Stroke Rates

4.3 FAILURE MODES.

The specimens were examined posttest for any changes in the failure modes with increasing strain rates. The pictures of failed specimens tested at different stroke rates are shown in figures 48 through 54 for the seven materials investigated. The failure modes in Newport NB321/7781 fiberglass specimens tested at different rates are shown in figure 48. The failure mode at a quasi-static rate consists of a band of matrix failure extending between the two notches and regions of fiber fracture that typically connect the notches. The primary fracture occurs across the notches while secondary fractures, when present, propagate toward the fixture halves, as shown in the figure. At higher stroke rates, a band of matrix failure similar to the quasi-static case exists, but the fiber fracture zone tends to deviate from the line joining the two notches, indicating the presence of other dominant failure modes (tensile), which needs to be investigated further. At test rates of 100 in/s and above, the test specimen fractures along the lines closer to the gripping region. Thus, the shear strength of the material might be higher than that indicated by the test data.

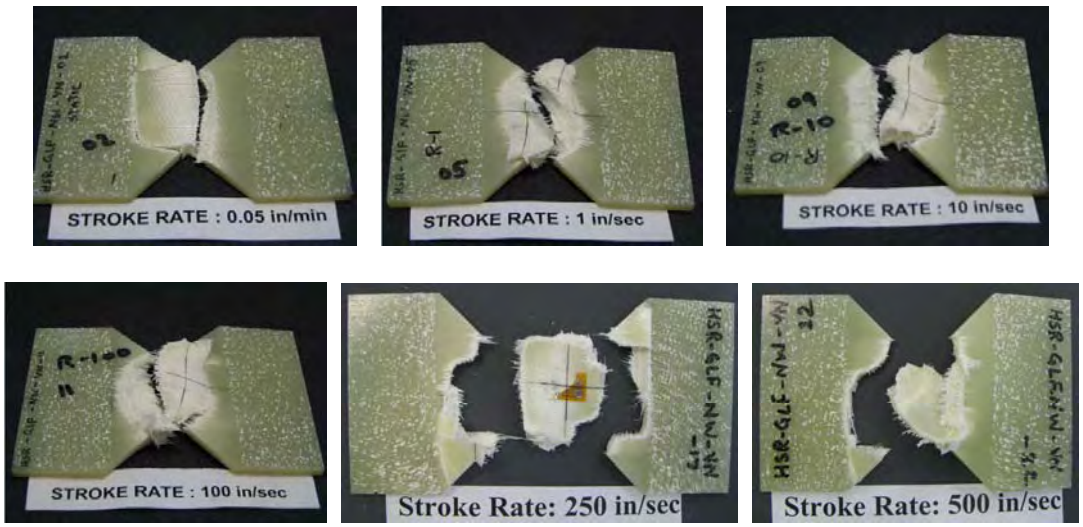

Figure 48. Failure Modes of Newport NB321/7781 Fiberglass Specimens Tested at Different Stroke Rates

The failure modes in Newport NB321/3K70 PWCF specimens at different stroke rates are shown in figure 49. The failure modes were similar for test rates up to 100 in/s with a diffuse failure zone surrounding the fracture across the minimum section. A significant amount of fiber pull-out was evident at these rates. At test rates of 250 in/s, the fracture initiated at the notch but propagated away from the minimum section, leaving a fragment similar to the fiberglass specimen. At the highest test rate, the fracture initiation and propagation were both away from the minimum section, indicating the dominance of a different failure mechanism.

The failure modes in Newport NCT321/G150 unitape specimens tested at different rates are shown in figure 50. Unlike the fiberglass and carbon fabric systems, this material system did not exhibit changes in overall failure mode with increasing test speed.

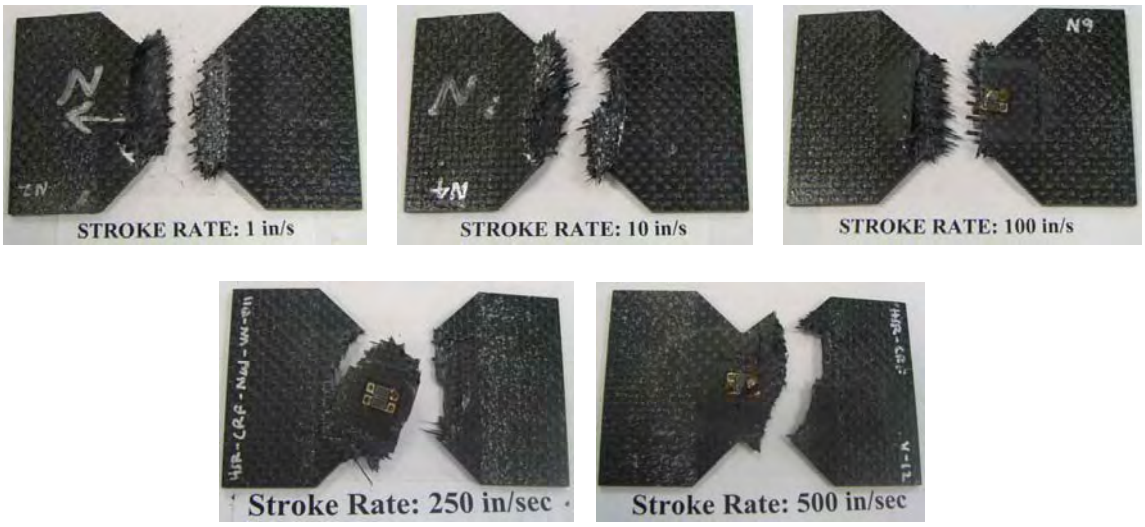

Figure 49. Failure Modes of Newport NB321/3K70 PWCF Specimens Tested at Different Stroke Rates

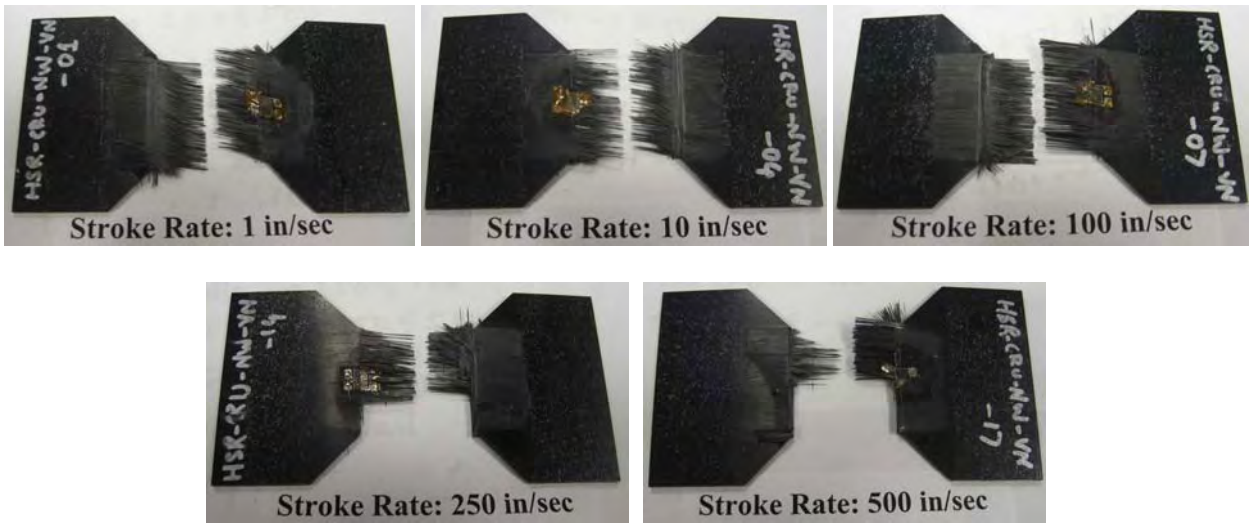

Figure 50. Failure Modes of Newport NCT321/G150 Unitape Specimens Tested at Different Stroke Rates

The failure modes in Toray T800S/3900-2 unitape and Toray T700G-12K-PW/3900-2 fabric specimens tested at different speeds are shown in figures 51 and 52, respectively. Similar to the Newport unitape specimens, the failure mode in Toray unitape specimens did not change with increasing test speeds. However, the Toray fabric specimen exhibited a failure mode change at test speeds of 250 and 500 in/s. The fracture path deviated away from the minimum section similar to the Newport fiberglass and carbon fabric specimens.

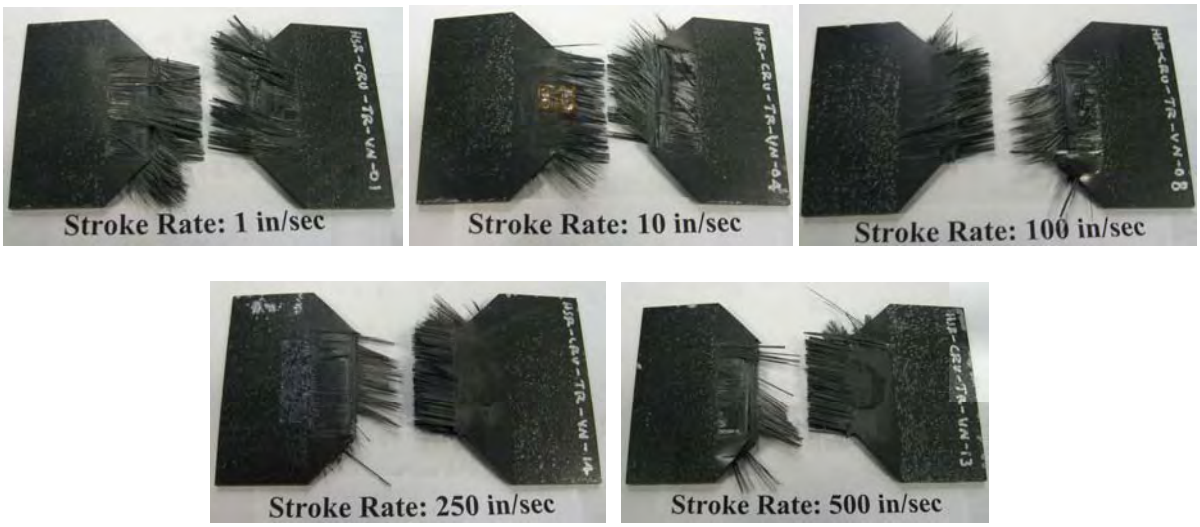

Figure 51. Failure Modes of Toray Unitape Specimens Tested at Different Stroke Rates

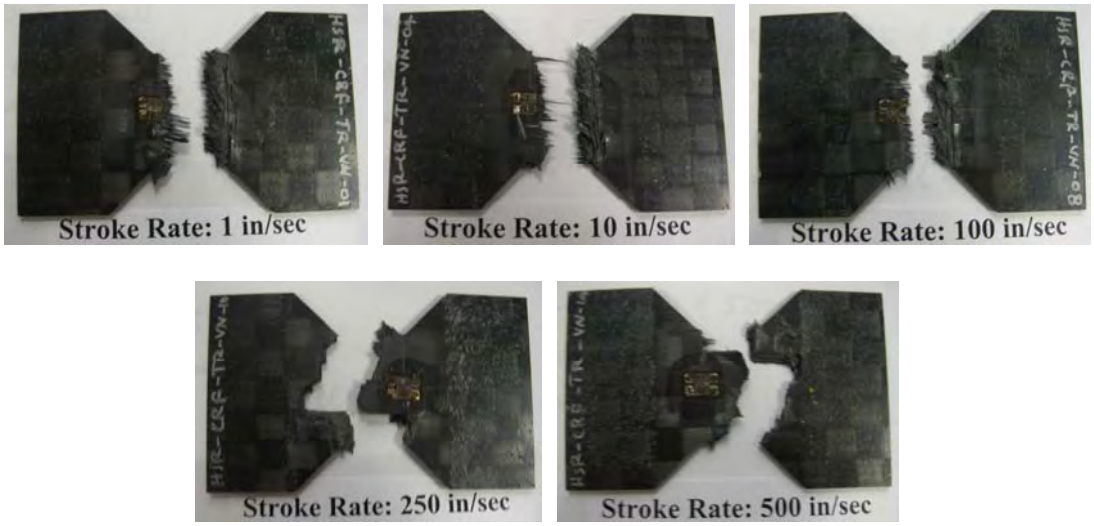

Figure 52. Failure Modes of Toray Fabric Specimens Tested at Different Stroke Rates

The failure modes in Cytec and Fibercote specimens tested at different rates are shown in figures 53 and 54, respectively. Unlike the previous material systems with fabric reinforcement where the failure modes changed at higher test speeds, the Cytec and Fibercote material systems always failed across the minimum section. A slight deviation in the fracture path from the minimum section was observed in the Fibercote specimens tested at 250 in/s and 500 in/s, but this deviation was not as significant as those with the other material systems.

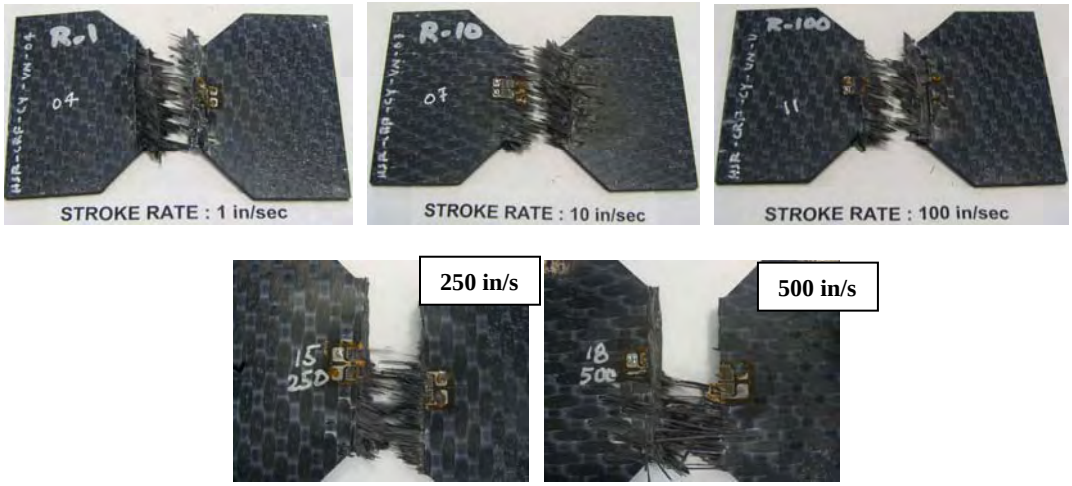

Figure 53. Failure Modes of Cytec Specimens Tested at Different Stroke Rates

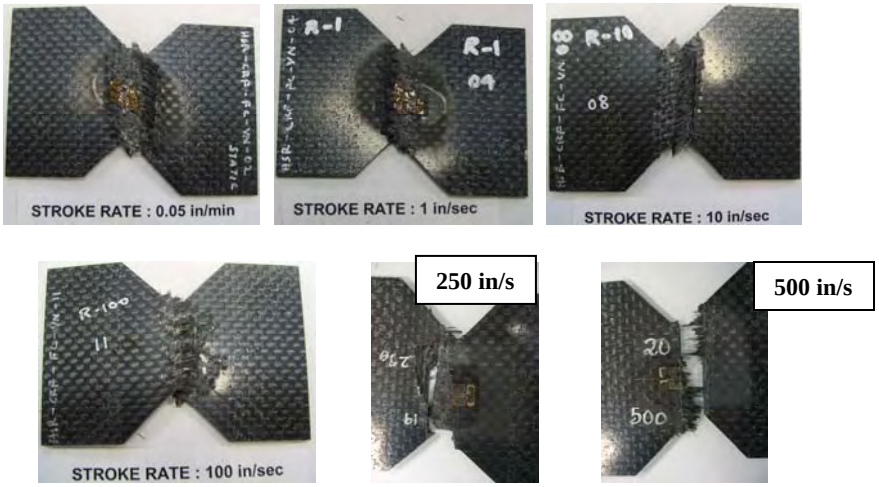

Figure 54. Failure Modes of Fibercote Specimens Tested at Different Stroke Rates

5. COMPRESSION TESTS.

To date, various test methods for material characterization of composites have advantages and limitations. Typically, servo-hydraulic systems are frequently used; typical systems are limited to low strain rates (0.00167 - 10 s^{-1}). Drop towers can accommodate different specimen geometries and achieve relatively high strain rates. Difficulties arise from the existence of nonuniform stress fields and multiple types of damage. An SHPB apparatus can achieve uniaxial, homogeneous state of stress at high rates; however, contact surfaces' conditions are very critical and specimens must be short to minimize wave propagation effects. Most of the high strain rate compressive properties reported to date were obtained by means of an SHPB apparatus.

The present work evaluated the stress-strain behavior of seven different composite material systems over a wide range of strain rates. Five strain rate levels, ranging from 0.00167 s^{-1} (quasi-static loading) to 900 s^{-1} (maximum dynamic loading), were used. Due to the wide range

of strain rates, two different test apparatuses were used. Quasi-static tests and tests at a medium strain rate of 1 s^{-1} were carried out on a standard 22-kip servo-hydraulic MTS test machine. Strain rates above 100 s^{-1} to 900 s^{-1} were achieved using a compression SHPB apparatus.

5.1 TEST MATRIX.

The strain rate behavior of the seven material systems listed in section 2 was investigated. Each material system followed a typical test matrix, which is summarized in table 3. Every material system was fabricated in four stacking sequences. A laminate measuring 12″ by 12″ was manufactured for each stacking sequence. Rectangular specimens were cut from each laminate and tested over five strain rates. Rate one (R_1), the lowest rate, is referred to as quasi-static and corresponds to 0.00167 s^{-1}. Rate two (R_2), is referred to as medium and corresponds to 1 s^{-1}. Rates three (R_3), four (R_4), and five (R_5) varied on average from 353 s^{-1} to 852 s^{-1}. Quasi-static rate R_1 and medium rate R_2 were performed on a standard 22-kip servo-hydraulic MTS system. Strain rates R_3, R_4, and R_5 were performed using an SHPB apparatus. Three replicate tests were conducted at every rate for a total of 15 specimens per laminate (orientation), 60 specimens per material system, and 420 specimens for the entire material characterization.

Table 3. Test Matrix for Compression Tests

Orientation	Rate	No. of Replicates
$[0°]_N$	R_1	×3
	R_2	×3
	R_3	×3
	R_4	×3
	R_5	×3
$[+15°/-15°]_{Ns}$	R_1	×3
	R_2	×3
	R_3	×3
	R_4	×3
	R_5	×3
$[+30°/-30°]_{Ns}$	R_1	×3
	R_2	×3
	R_3	×3
	R_4	×3
	R_5	×3
$[+45°/-45°]_{Ns}$	R_1	×3
	R_2	×3
	R_3	×3
	R_4	×3
	R_5	×3

5.2 SPECIMEN GEOMETRY.

The operation principle of an SHPB apparatus requires that the specimen reaches equilibrium at an early stage during the test [48]. For this requirement to be satisfied, the stress distribution on the specimen and the failure process expected to predominate needs to be well understood. Several in-plane compression tests were performed aiming to characterize the static material response and to generate the static failure loads. Static failure strengths provided with a lower bound for load requirement during dynamic tests and in sizing the specimen geometry. Specimen shape and size were selected, taking into account several factors, i.e., specimen length required for stress equilibrium, composites machining difficulty, and specimen's cross-sectional area relative to bar's cross-sectional area. The test specimen geometry is shown in figure 55. Rectangular cross-section specimens for quasi-static and dynamic compression tests were machined from the laminated panels using a lubricated diamond wheel. Specimen-loading surfaces were polished on a grinding table. Specimen dimensions and perpendicularity were checked before testing, according to SHPB technique requirements. The loading direction corresponds to the 0° direction, as shown in figure 55.

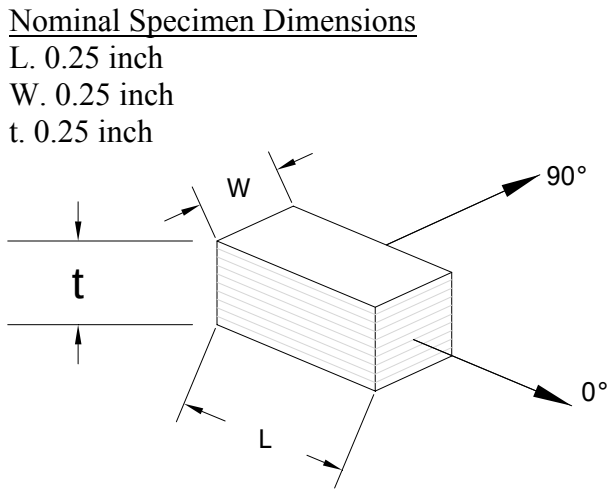

Figure 55. Specimen Geometry for Compression Tests Using an SHPB Apparatus

5.3 QUASI-STATIC AND MEDIUM-RATE TESTS.

A 22-kip MTS servo-hydraulic test machine was used to perform the test at the quasi-static and medium strain rates. The compression tests were conducted under displacement control at a constant rate of 0.05 in/min for the quasi-static rate and at 15 in/min for the medium rate. Rectangular specimens were placed (sandwiched) in between two flat stainless steel platens and compressed. Specimens were centered on the platens, and grease was applied on the contact surfaces to minimize friction. Time, actuator displacement, and force data were acquired during the test. A medium-rate compression test was conducted with an initial gap between the specimen and one of the platens. This gap allowed the actuator to reach a constant velocity before the platen came into contact with the test specimen. The force data, actuator displacement, and time were recorded during each test. The stress and strain values were computed based on the undeformed dimensions of the specimen. A limited number of specimens for each combination of material system and orientation were bonded with strain

gages to monitor the strains due to compressive loading. The stress-strain data from these tests were used for comparisons across different strain rates.

5.4 SPLIT-HOPKINSON PRESSURE BAR APPARATUS.

The SHPB apparatus is the most reliable device for measuring the stress-strain response of solid materials at high strain rates. It is the most frequently used method for testing material at strain rates between 100 s^{-1} and 2000 s^{-1}. A compression SHPB apparatus is comprised of three separate bars, the striker, the incident or input bar, and the transmitted bar, as shown in figure 56. The striker bar is accelerated using compressed air or a gas gun. An elastic-stress pulse is imparted to the incident bar by impacting it with a striker bar of the same cross-sectional area and modulus. The wavelength of the generated wave is equal to twice the length of the striker bar and propagates through the incident bar with the velocity of sound in the bar. The elastic wave propagates uninterrupted along the incident bar until it reaches the bar-sample interface. When the elastic wave reaches the specimen incident bar interface, part of it is reflected back, and part of it is transmitted through the specimen and into the transmitted bar. The velocity of the striker controls the strain rate achieved, while the length determines the duration of the test. The impact velocity can be controlled by changing the pressure of the gas gun.

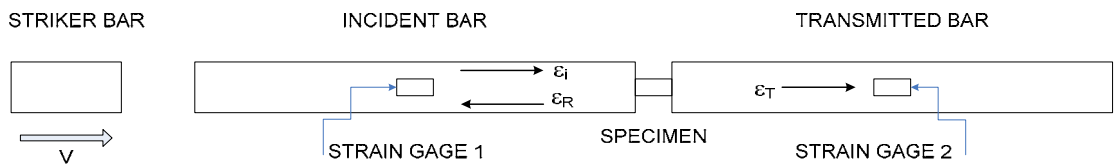

Figure 56. Schematic of the SHPB Apparatus

To determine the strain within the specimen, strain gages are mounted on both the incident and transmitted bar. Strain gages are placed in a position where no superposition between the reflected wave and incident wave will occur over the duration of the test. Since the pulse wavelength is twice the length of the striker, the incident bar must be larger than two times the length of the striker. This also implies that the strain gages must be located at the length of the striker, or greater, from the bar end to avoid superposition of the waves (see figure 56).

5.4.1 The SHPB Apparatus at NIAR/WSU.

The schematic of the SHPB apparatus designed and fabricated at NIAR/WSU is shown in figure 57, and the photograph of the physical assembly is shown in figure 58. The SHPB assembly is mounted on a W10×60 steel beam that rests on eight cylindrical aluminum legs (not shown in the figure). The SHPB apparatus consists of a compressed air chamber, muzzle, and gun barrel that are coaxial with the incident and transmitter bars. The incident and transmitter bars are supported by bearing blocks at regular intervals of 10 to 15 inches. The bearing blocks are fastened to bearing mount blocks, which are, in turn, fastened to the mounting plate, as shown in figure 59. Additionally, the mounting plate is fastened to a 6″ by 6″ square tube made of 6061 aluminum. A momentum trap consisting of an aluminum block and a sacrificial layer of foam is mounted on the free end of the transmitter bar to dissipate energy at the end of the test, as shown in figure 57.

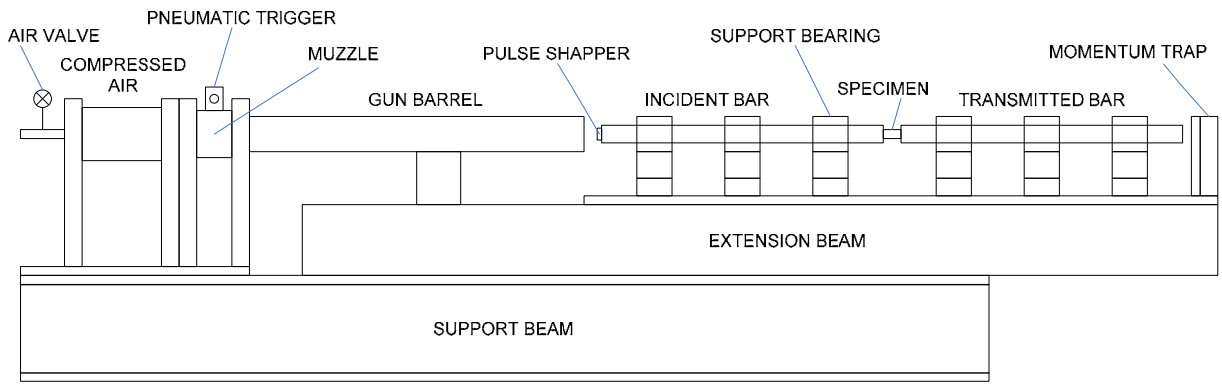

Figure 57. Schematic of SHPB Apparatus at NIAR/WSU

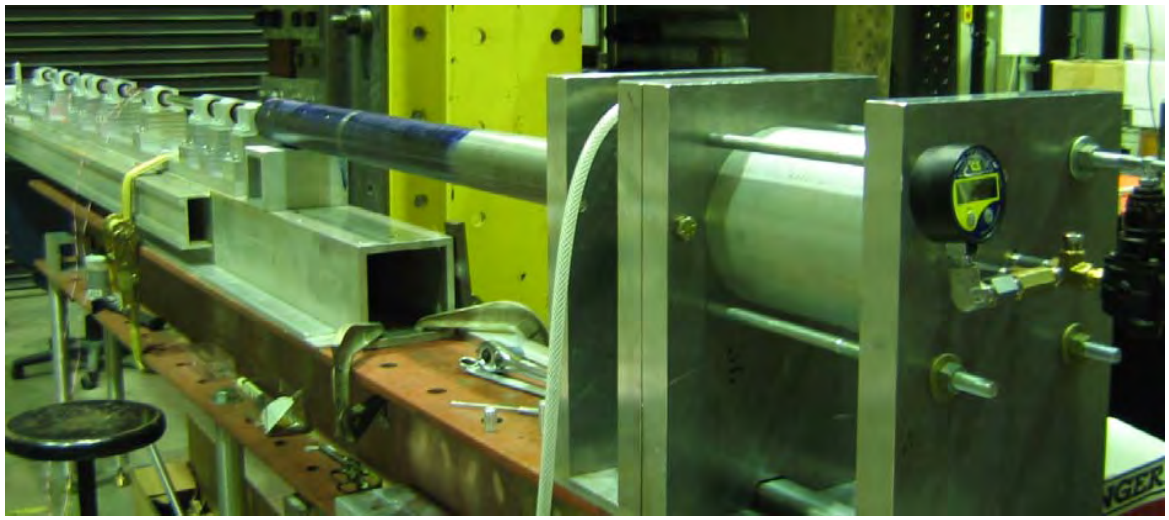

Figure 58. The NIAR/WSU SHPB Apparatus as Viewed From the Pressure Chamber End

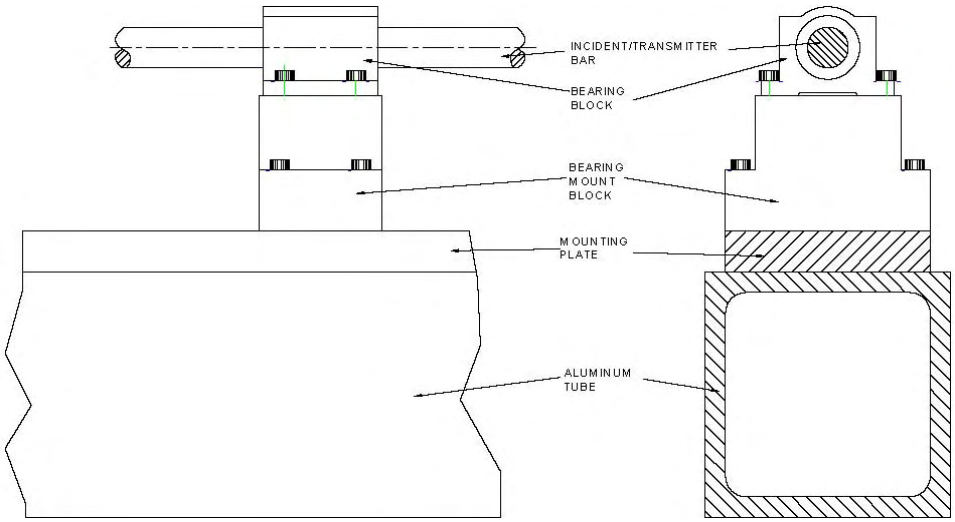

Figure 59. Cross-Section of the NIAR/WSU SHPB Support Assembly

The design of the incident and transmitter bars is dictated by the requirements for enforcing a one-dimensional wave in the bars. A length-to-diameter ratio in excess of 10 is desired to enforce one-dimensional wave propagation. The diameter of the bars is based on the maximum strain levels required during the tests and the minimum strain levels that can be amplified using the signal-conditioning circuits without loss of useful information. In the current design, bar diameters of 1.0 inch were chosen, with the incident and transmitter bars measuring 48 and 36 inches long, respectively. The bars were fabricated from Vascomax-350 maraging steel, which has a yield stress exceeding 300 ksi.

A 10″ long, 6″ in diameter, 6061 aluminum tube with 0.25″ thick walls was secured between two flat 7075 aluminum plates to form the compressed air chamber. One end of the assembly provided inlet to the compressed air. A compressed air regulator and pressure gage (figure 58) were used to control the pressure in the chamber. The chamber was connected to the muzzle, which consisted of a 4″ long, 2″ by 2″ square aluminum tube that opened into the gun barrel (figure 60). A pneumatic-actuated cylinder with an attached trigger rod was mounted on the muzzle. The trigger rod was used to hold the projectile in position and to release the projectile. The muzzle and the pressure chamber are connected using a pair of split plates, as shown in figure 60. The split plates are separated to load the barrel with the projectile; then the two split plates are bolted together and the air chamber is pressurized. At the start of the test, the pressure in the pneumatic cylinder is released and the trigger rod retracts into the cylinder. This releases the projectile, which accelerates down the gun barrel and impacts the free end of the incident bar to generate the stress pulse.

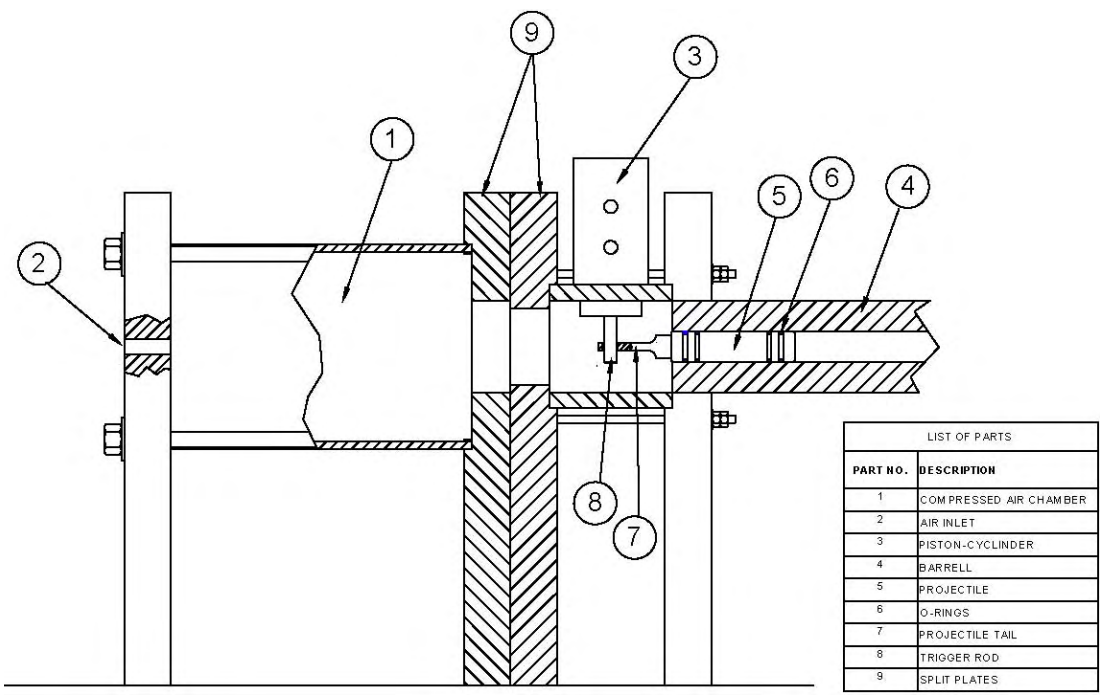

Figure 60. Details of SHPB Propulsion and Trigger System Used to Propel Projectile

The typical projectile geometry used in the current investigation is shown in figure 61. The projectile is cylindrical with a nominal diameter of 0.99″. The projectiles are machined from

Vascomax-350 maraging steel rod stock of 1.00′ diameter. The projectiles contain grooves for mounting O-rings, which facilitate sealing the breech chamber and reduce the friction between the projectile and the barrel surface. The rear end of the projectiles contains tapped holes for mounting tails (aluminum) used to secure the projectiles in the breech chamber. The typical projectile assembly is shown in figure 60. Projectiles of 1.5″, 2″, 4″, 6″, and 12″ in length are currently available at WSU.

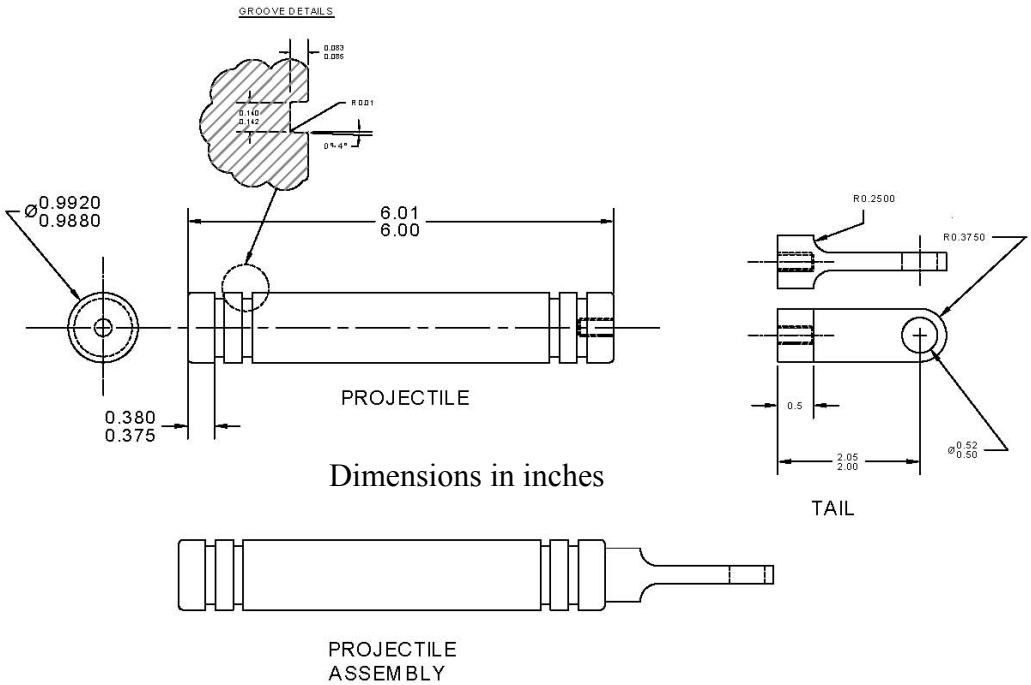

Figure 61. Geometric Details of Typical SHPB Projectile Assembly

The gun barrel used was 48″ long and has an internal bore of 1.00″, as shown in figure 62. The barrel was machined using 3″ diameter stock of 416R stainless steel. The gun barrel is machined with pressure-relief holes of 0.25″ diameter at one end. The pressure-relief holes are located on the end where the projectile impacts the incident bar. The relief holes are intended to relieve the pressure behind the projectile after the impact, thus reducing the chances of multiple impacts on the incident bar.

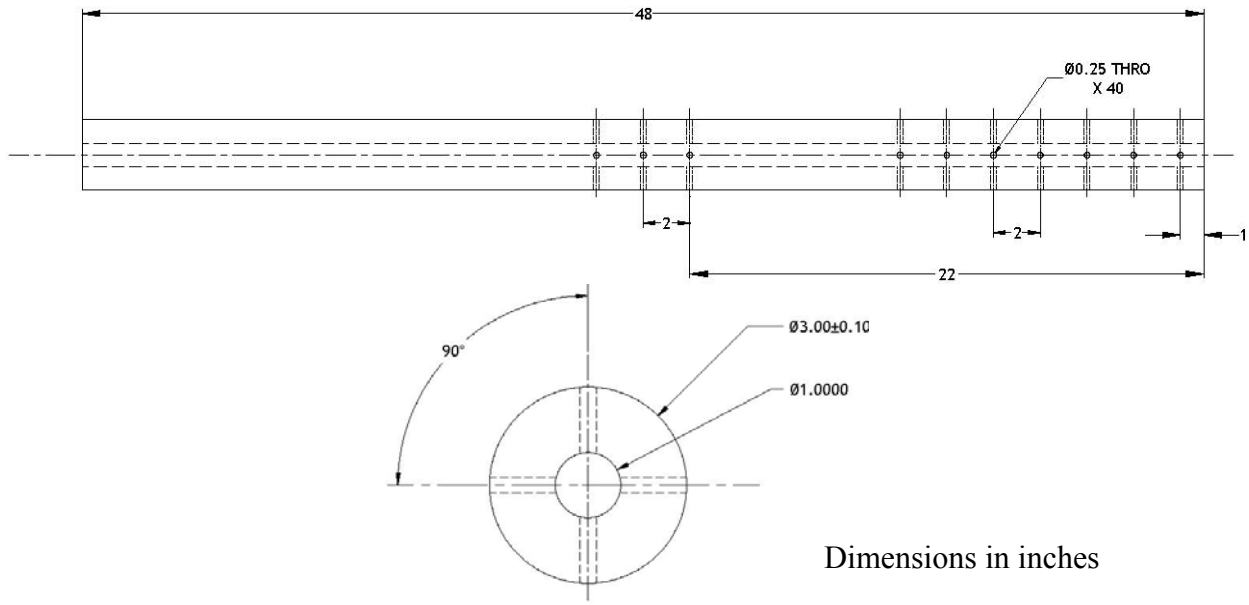

Figure 62. Geometric Details of SHPB Gun Barrel

5.4.2 Specimen Alignment Technique.

One of the keys to the success of the SHPB test is the alignment of the specimen axis with the bars.

Centering the specimens on the bar cross-section was critical for proper load transfer. Any misalignment between the specimen and the bars could induce premature and undesirable failure modes due to eccentric loading. To properly align the specimen on the bar cross-section, a centering procedure was implemented. A circular disc was machined with a precise rectangular cutout at the center so it would match the specimen cross-section geometry. The specimen was placed on the centering disc and slid into the alignment holder (figure 63). The alignment holder is a hollow circular piece, which has an inner diameter with a close tolerance with the pressure bar diameter. The assembly that included the specimen, centering disc, and holder was then slid onto the bar, centering the specimen precisely with respect to the bar cross-section. With the specimen in place, the alignment fixture was removed, leaving the specimen in place. The grease applied to the end of the rod aided in holding the specimen in place while the alignment apparatus was being removed. Grease was also applied on the bars' contact surfaces to minimize friction.

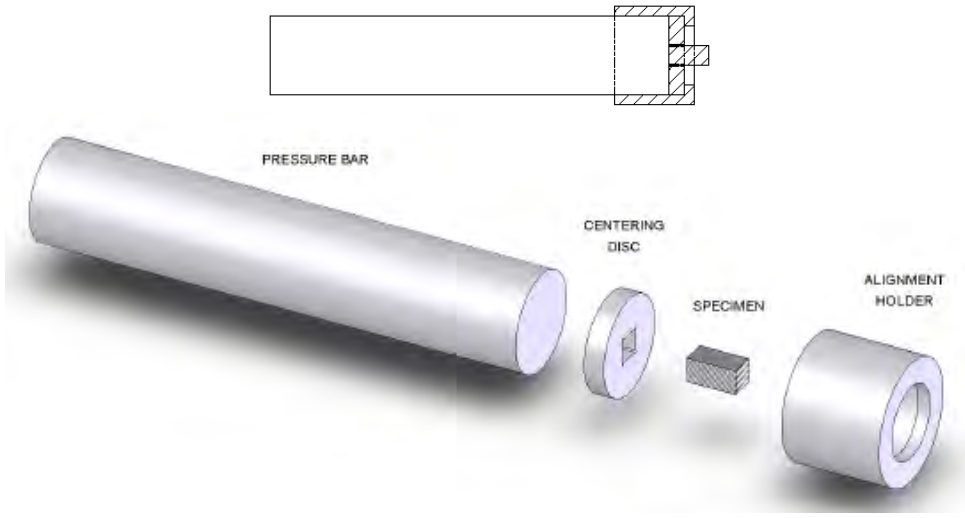

Figure 63. The SHPB and Specimen Alignment Technique

5.4.3 Data Acquisition.

Strain waves propagating in the incident and transmitted bar were recorded from Vishay model EA-00-060EK-350-LE 350Ω strain gages mounted on each bar. Two strain gages were mounted on each bar diametrically opposite from each other to complete a Wheatstone™ half-bridge configuration. This configuration senses the change in resistance that occurs from axial loading while minimizing the sensitivity to bending-induced strains. In this case, any bending strain in the bar would be eliminated. This was achieved by having two opposite arms of the bridge active. Figure 64 shows R_1 and R_3 as the active resistors (strain gages), and R_2 and R_4 are precision resistors of equal resistance. A differential balance arrangement was used to balance the bridge.

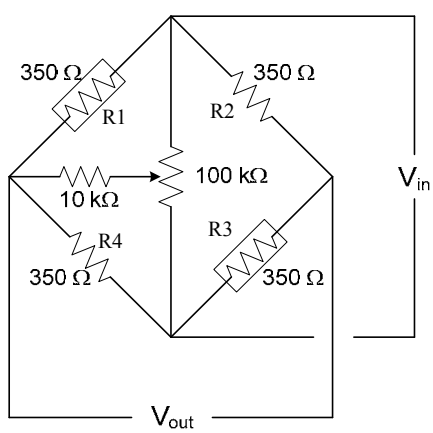

Figure 64. The SHPB Wheatstone Bridge Balancing Circuit

Low-voltage strain gage signals were amplified using Ectron model 778 wideband conditioner amplifier. The transducer excitation was set to 15 volts, resulting in 5-mV signal resolution. Amplifier gain was set to ×100 for the strain gages mounted on the incident bar, and ×500 for the

strain gages mounted on the transmitted bar. The gain on the signal from the transmitter bar was set to a higher number, as the amplitude of the transmitted signal is less than the incident signal. Strain gage signals were recorded using Tektronix TDS 3034B digital oscilloscope. The sampling rate on the oscilloscope was set to 10 MHz. The incident pulse was used as a trigger signal for the data collection. After the output voltage from the bridge was processed on the amplifier, the strain gage's raw data was recorded by the oscilloscope. This arrangement is shown in figure 65. Typical incident, reflected, and transmitted signals, as displayed on the oscilloscope window, are shown in figure 66. Incident and reflected strain data are contained in the same raw data signal recorded from the incident bar. The short delay of the transmitted pulse relative to the reflected pulse was observed. The timing between the reflected pulse and the transmitted pulse strongly affects interpretation of the test results in the SHPB test.

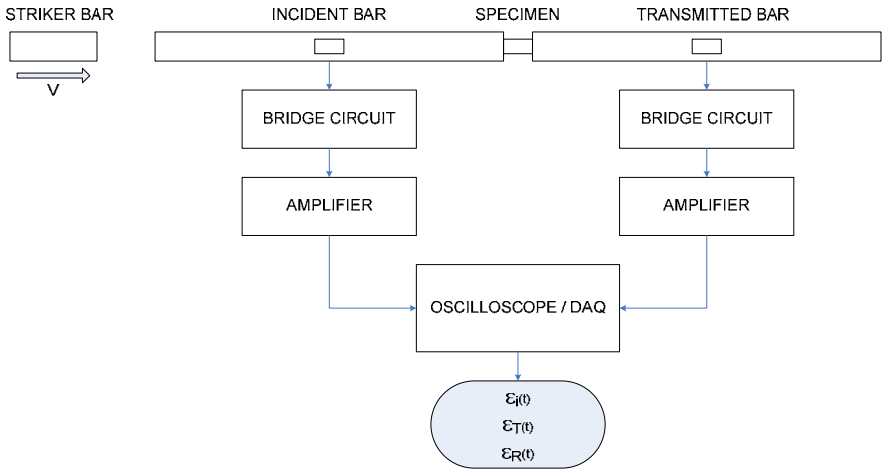

Figure 65. The SHPB Instrumentation and Data Acquisition

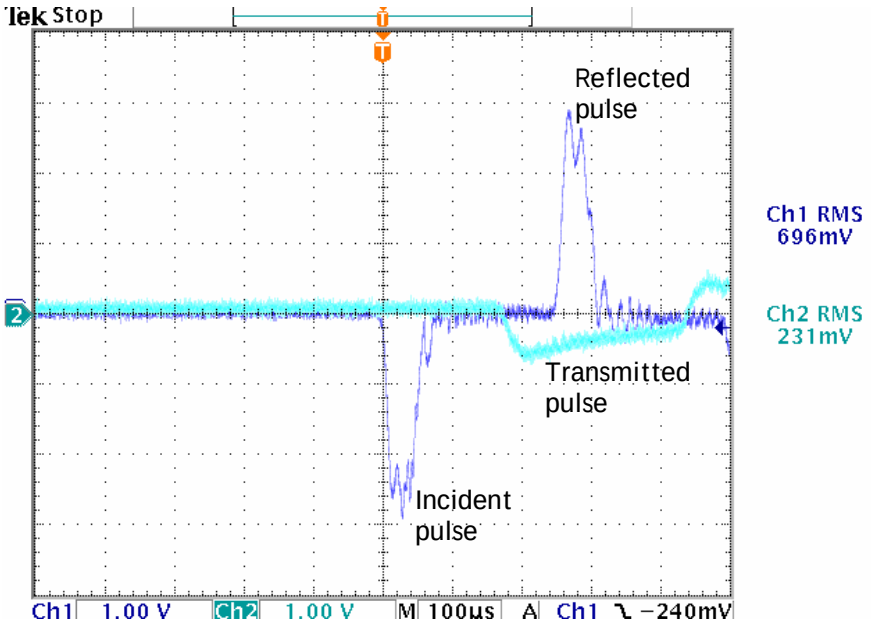

Figure 66. Oscilloscope Window—Recorded Incident, Reflected, and Transmitted Pulses

5.4.4 Strain Gage Data Filtering.

Processing raw strain gage data into engineering data is not straightforward. Several sources introduce high-frequency components into the strain gage signal. The strain history of a wave traveling in the incident bar is comprised of the incident pulse and its reflection. Without noise, the wave shapes should be identical but of opposite sign. In reality, this is not the case. Figure 66 shows that an incident pulse and its reflection are not identical. The dispersive nature of the bars, along with radial inertia, friction, specimen geometry, noise, etc., introduces high-frequency components to the strain gage signal. It is a common practice in signal processing to filter raw data by eliminating high-frequency components. This is done using a low-pass filter. To specify what frequencies are to be removed, cutoff frequencies must be defined. High-frequency components are identified by transforming the data into the frequency domain using a Fast Fourier Transform (FFT). The unwanted frequency components are eliminated by multiplying the FFT values at these frequencies by zero. The modified frequency domain data is then transformed back into time-domain using an inverse FFT. Figure 67 shows an incident pulse before and after the high-frequency components were eliminated. A significant noise reduction is observed without compromising the shape of the pulse. Altair® HyperGraph® [49] software was used to filter the data.

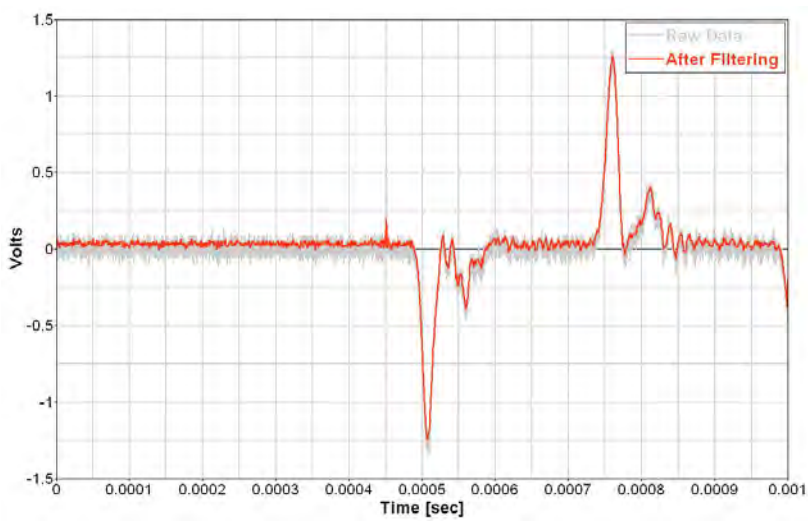

Figure 67. Incident Pulse Before (gray line) and After Filtering (red line)

5.4.5 Stress, Strain, and Strain Rates in the Specimen.

One-dimensional elastic wave theory [50] is used to determine the stress and particle velocity at the end of the bars in contact with the specimen. The velocity difference across the ends of the specimen and its integral with respect to time are used to compute the strain rate and strain. The travel time of a compressive wave in the specimen is short enough compared to the total pulse duration. For the specimen to be in equilibrium, it must experience multiple reflections of the waves so the stress and strain field can be considered uniform. This is achieved by ensuring that the pulse rise time is at least five times the travel time of the pulse through the specimen.

A one-dimensional analysis of the SHPB provides stress, strain rate, and strain in the specimen, as follows [50]:

$$\sigma(t) = \frac{A_b \cdot E}{A_s} \cdot \varepsilon_T(t) \tag{3}$$

$$\dot{\varepsilon}(t) = -\frac{2c}{L_s} \cdot \varepsilon_R(t) \tag{4}$$

$$\varepsilon(t) = \int_0^t \dot{\varepsilon}(\tau)\, d\tau \tag{5}$$

where A_b is the bar cross-sectional area, E is the Young's modulus of the bar, c is the wave speed in the bar, L_s is the specimen length, and A_s is the cross-sectional area of the specimen. Notice that the stress in the specimen is directly related to the amplitude of the transmitted pulse. The strain within the specimen is related to the time integral of the amplitude of the reflected pulse. The latter equations provide the means to determine the dynamic stress-strain behavior of the specimen simply by strain measurements made on the surface of the pressure bars.

5.4.6 Pulse Shaping.

The elastic stress pulse imparted by direct impact of a projectile on the incident bar of a conventional SHPB apparatus has a high level of oscillation superimposed on the trapezoidal-shaped pulse. These oscillations are a consequence of the short rise time of the loading pulse [51]. Such oscillations cause difficulty in the interpretation of the stress-strain results. A slowly rising incident pulse is preferred to a pulse that rises steeply to minimize the effect of dispersion and allow the sample to achieve dynamic stress equilibrium [52]. Longer rise times also reduce inertial effects in the specimen [53].

A modification of the conventional SHPB is done by simply placing a thin disc of annealed copper on the impact surface of the incident bar (see figure 68). This increases the impact rise time and reduces the amplitude of the oscillations by softening the impact. When preimpacting a copper disc, the resulting smooth-loading pulse generates a nearly constant strain rate in the sample.

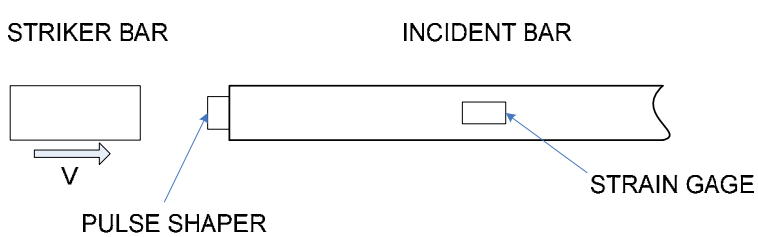

Figure 68. Loading End Schematic of an SHPB With Pulse Shaper

A study was conducted to identify the appropriate dimensions of the copper disc to achieve a desired strain rate. Several tests were conducted with free-end conditions, i.e., the incident bar was impacted without the specimen or transmitted bar in the assembly. The thickness and diameter of the copper discs were varied to study the rise time of each impact event. Strain gage signals show larger rise times for thicker copper discs, as shown in figure 69. Larger rise times improved data collection at the early loading stages, where strain rate sensitivity interpretation is fundamental. The thicker copper discs, however, precipitated lower pulse amplitude, thus requiring higher impact velocities for higher strain rates and strain levels. In the current investigation, 0.016-inch-thick copper discs were selected since they produced larger rise times than direct impact without significant reduction in pulse amplitude. The selected copper disc diameter was 0.283 in.

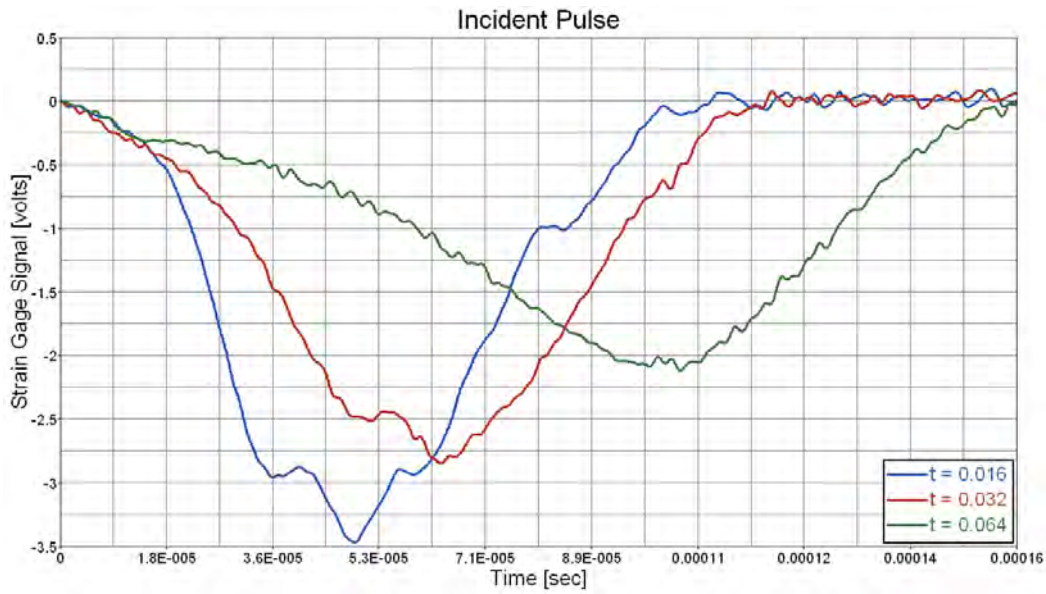

Figure 69. Incident Pulses Recorded for Three Copper Disc Thicknesses

5.5 TEST RESULTS.

Seven material systems were evaluated in the present investigation. Experiments were performed on rectangular cross-section specimens with four characteristic stacking sequences, [0°], $[+15°/-15°]_{NS}$, $[+30°/-30°]_{NS}$, and $[+45°/-45°]_{NS}$. The strain rate effect on failure strength was characterized, and the dynamic stress-strain curves were generated. Failure modes for each fiber orientation were recorded using an optical microscope.

The test results for each material system are presented individually for clarity. Results are presented in three main subdivisions, i.e., failure strength, stress-strain behavior, and failure modes. The failure strength section summarizes failure strengths at each of the five strain rates tested. Stacking sequences of each of the material systems, $[0°]_N$, $[+15°/-15°]_{NS}$, $[+30°/-30°]_{NS}$, and $[+45°/-45°]_{NS}$, are clearly differentiated and compared in each plot. The stress-strain behavior section presents the material response at each of the actual strain rates tested for every stacking sequence. The failure mode section provides a graphical characterization of the failures modes.

5.5.1 Toray T800S/3900-2B Unitape.

5.5.1.1 Failure Strength.

The failure strengths are presented in figure 70 for five different strain rates. The tabulated values for each test are in appendix C. The strengths of $[0°]_N$ specimens exhibited an increasing trend between the quasi-static rates and $500s^{-1}$. Beyond this value, no significant differences were observed up to strain rates of about $800s^{-1}$. The $[+15°/-15°]_{NS}$ specimens exhibited a slight increase in strength at strain rates up to 500 s^{-1} and no trends could be identified beyond this strain rate due to scatter in the test data. The $[+30°/-30°]_{NS}$ and $[+45°/-45°]_{NS}$ specimen strengths exhibited a flat response with strain rate.

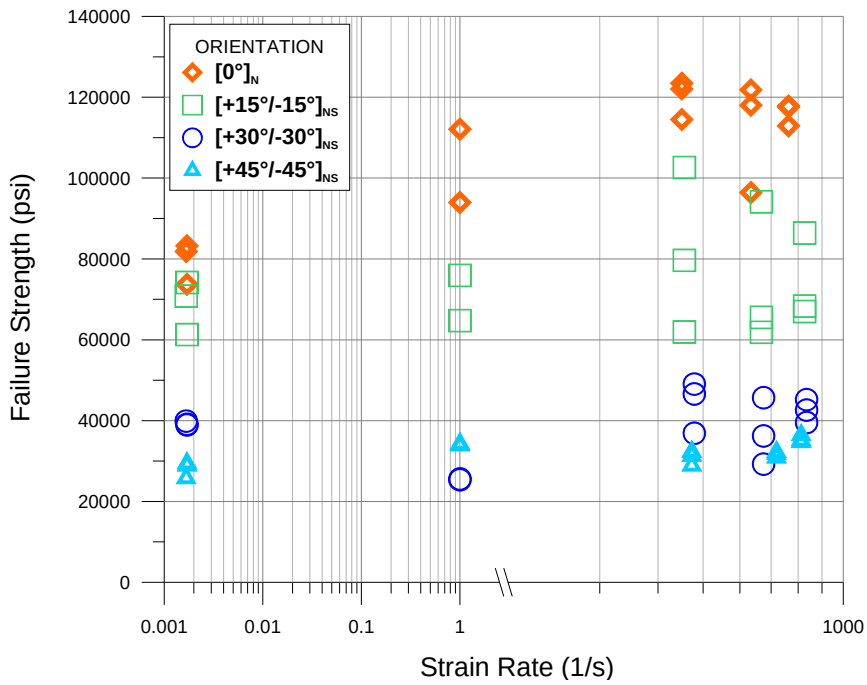

Figure 70. Failure Strength vs Average Strain Rate for Toray T800S/3900-2B Unitape Material

5.5.1.2 Stress-Strain Behavior.

The dynamic stress-strain behavior of Toray T800S/3900-2B Unitape material system is shown in figures 71 to 74 for different stacking sequences. The stress-strain response of individual tests and the variation of strain rate during the tests are in appendix C. A steeper response, indicating stiffening behavior, is observed as the strain rate increases for $[0°]_N$, $[+30°/-30°]_{NS}$, and $[+45°/-45°]_{NS}$ specimens. No significant differences could be observed for the $[+15/-15]_{NS}$ specimens and may be attributed to scatter in test data. The failure strains were observed to decrease with increasing strain rates. The nonlinear region associated with the behavior of $[+45°/-45°]_{NS}$ was considerably reduced at higher strain rates.

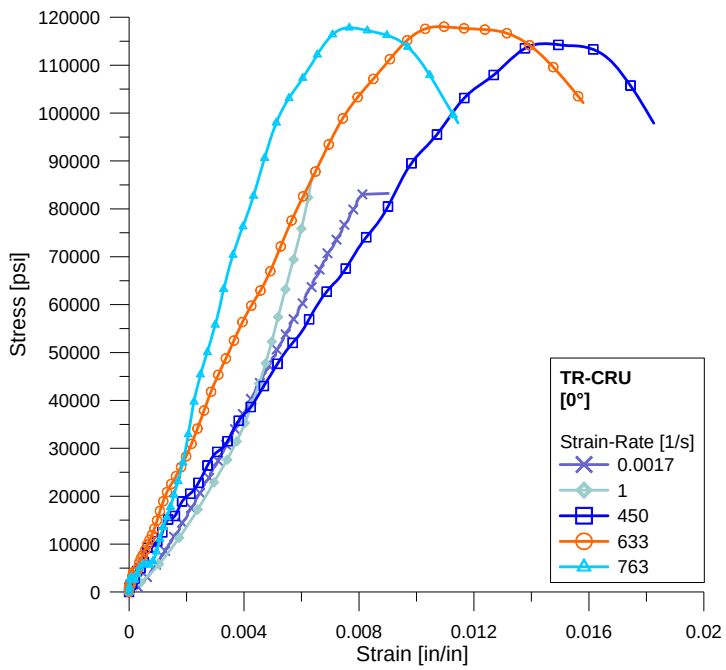

Figure 71. Stress-Strain Behavior of Toray T800S/3900-2B $[0°]_N$ Specimens

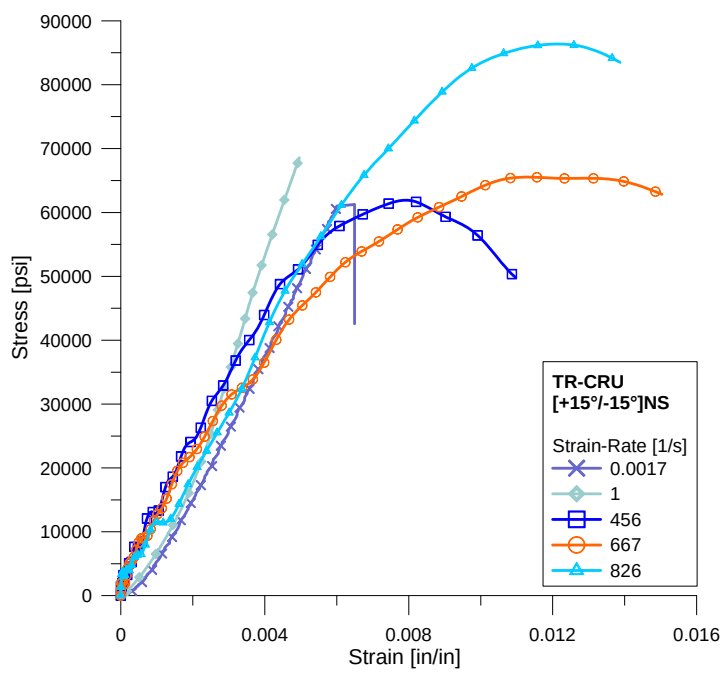

Figure 72. Stress-Strain Behavior of Toray T800S/3900-2B $[+15°/-15°]_{NS}$ Specimens

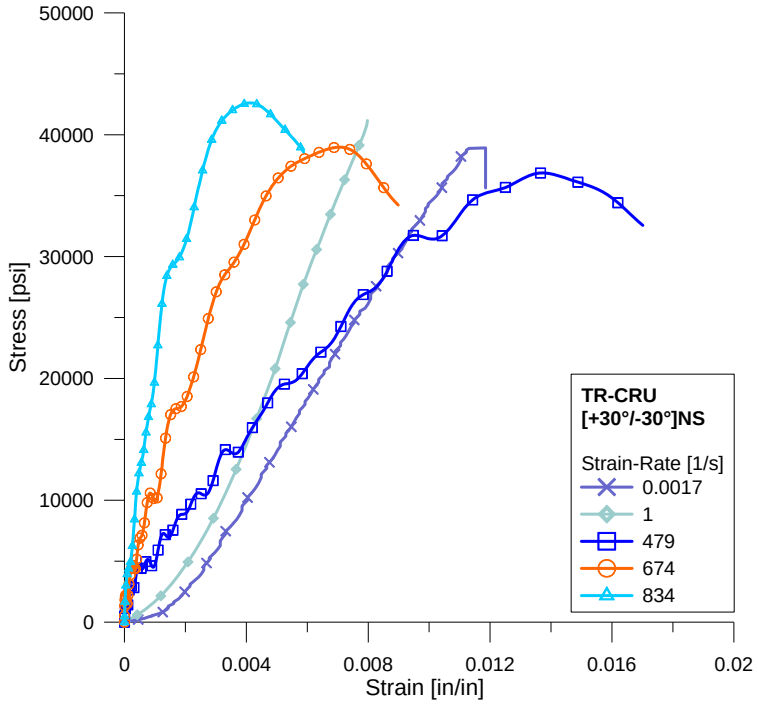

Figure 73. Stress-Strain Behavior of Toray T800S/3900-2B $[+30°/-30°]_{Ns}$ Specimens

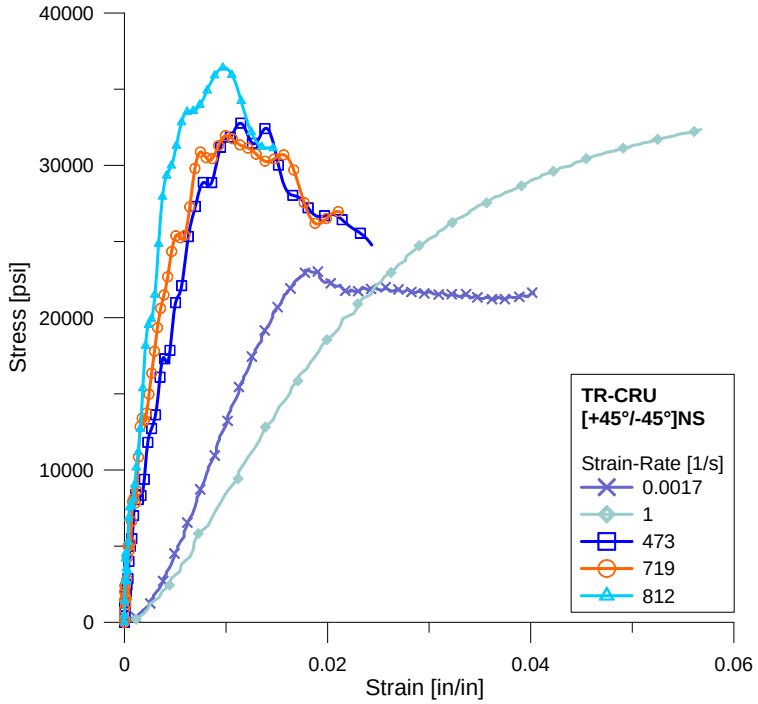

Figure 74. Stress-Strain Behavior of Toray T800S/3900-2B $[+45°/-45°]_{NS}$ Specimens

5.5.1.3 Failure Modes.

The representative failure modes at different test rates are shown in figures 75 through 78 for the four material orientations. The $[0°]_N$ specimens exhibited end-crushing-initiated failure accompanied by longitudinal splitting at higher rates. The $[+\theta/-\theta]_{NS}$ specimens exhibited splitting across planes along the fiber directions and, on certain occasions, across interlaminar planes. At higher rates, for certain stacking sequences, the specimen failed in an explosive manner, and the fragments could not be salvaged or the specimen was pulverized. Thus, the failure modes for these specimens could not be recorded.

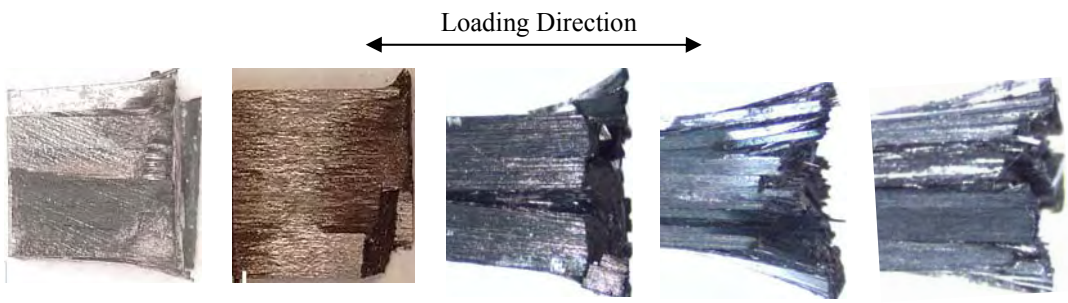

a) 0.0017 s^{-1} b) 1 s^{-1} c) 450 s^{-1} d) 633 s^{-1} e) 763 s^{-1}

Figure 75. Characteristic Failure Modes in Toray T800S/3900-2B $[0°]_N$ Specimens

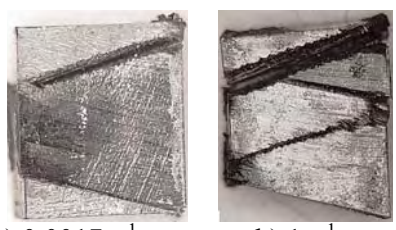

a) 0.0017 s^{-1} b) 1 s^{-1}

Figure 76. Characteristic Failure Modes in Toray T800S/3900-2B $[+15°/-15°]_{NS}$ Specimens

a) 0.0017 s^{-1} b) 1 s^{-1} c) 1 s^{-1} (side view)

Figure 77. Characteristic Failure Modes in Toray T800S/3900-2B $[+30°/-30°]_{NS}$ Specimens

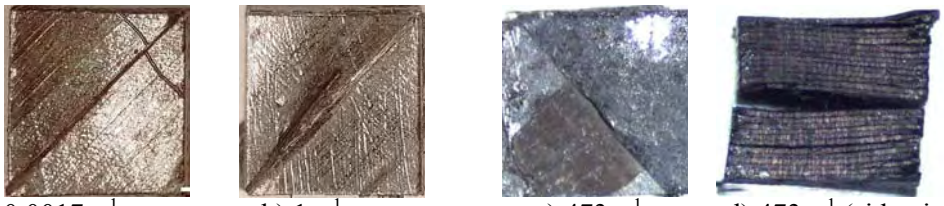

a) 0.0017 s^{-1} b) 1 s^{-1} c) 473 s^{-1} d) 473 s^{-1} (side view)

Figure 78. Characteristic Failure Modes in Toray T800S/3900-2B $[+45°/-45°]_{NS}$ Specimens

5.5.2 Toray T700G-12K-50C/3900-2 PWCF.

5.5.2.1 Failure Strength.

The failure strengths are presented for five different strain rates in figure 79. The tabulated values for each test are in appendix C. The scatter in the test data was lower compared to the UD specimens. The $[0°]_N$, $[+15°/-15°]_{NS}$, and $[+30°/-30°]_{NS}$ specimens exhibited an increase in strength up to 500-600 s^{-1} and a reduction in strength at strain rates beyond 500-600 s^{-1}. The strength of the $[+45°/-45°]_{NS}$ specimens was comparable at the quasi-static and medium rate. However, the strengths of the $[+45°/-45°]_{NS}$ specimens at low and medium rates were higher than those obtained using the SHPB apparatus. The strengths of $[0°]_N$ specimens at quasi-static and medium rates were similar to those of $[+15°/-15°]_{NS}$, due to the premature failure initiation in the form of end crushing, which promotes a interlaminar splitting-type failure. The sublaminates formed due to interlaminar splits are unstable, and thus, have a reduced load carrying capability. The interlaminar splitting is governed by the matrix properties, resulting in low strengths.

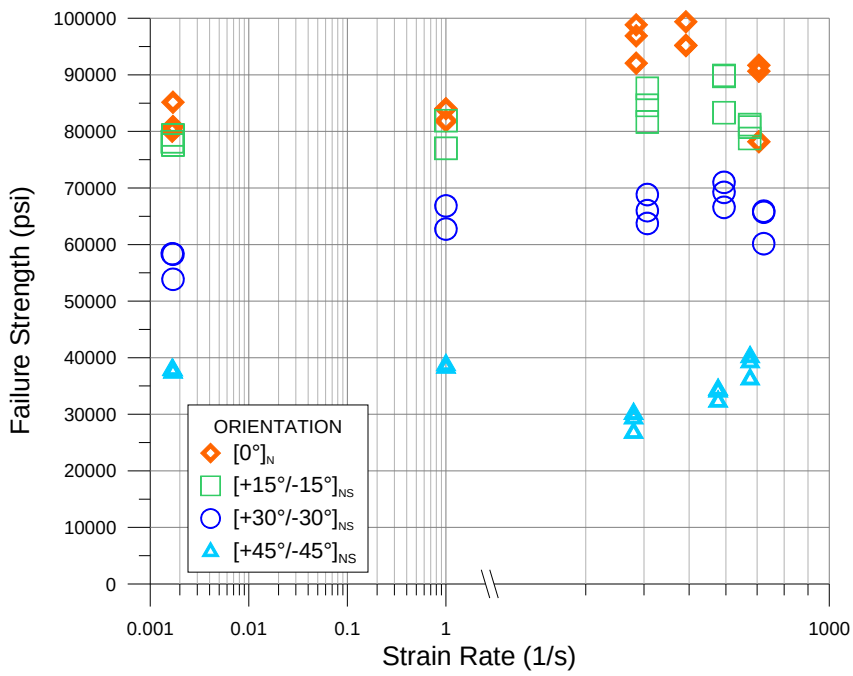

Figure 79. Failure Strength vs Average Strain Rate for Toray T700G-12K-50C/3900-2 PWCF Material

5.5.2.2 Stress-Strain Behavior.

The dynamic stress-strain behavior of Toray T700G-12K-50C/3900-2 PWCF material system is shown in figures 80 to 83 for different stacking sequences. The stress-strain response of individual tests and the variation of strain rate during the tests are in appendix C. A steeper response, indicating stiffening behavior, is observed as the strain-rate increases regardless of the orientation. The stress-strain curves for the $[+45°/-45°]_{NS}$ specimens exhibited no significant differences at the quasi-static and medium rates; however, an increase in stiffness and stress levels are evident at higher rates of loading.

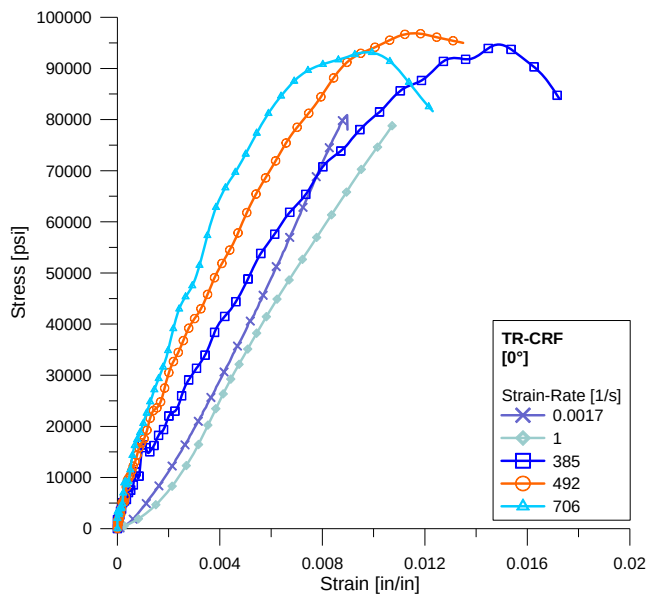

Figure 80. Stress-Strain Behavior of Toray T700G-12K-50C/3900-2 $[0°]_N$ Specimens

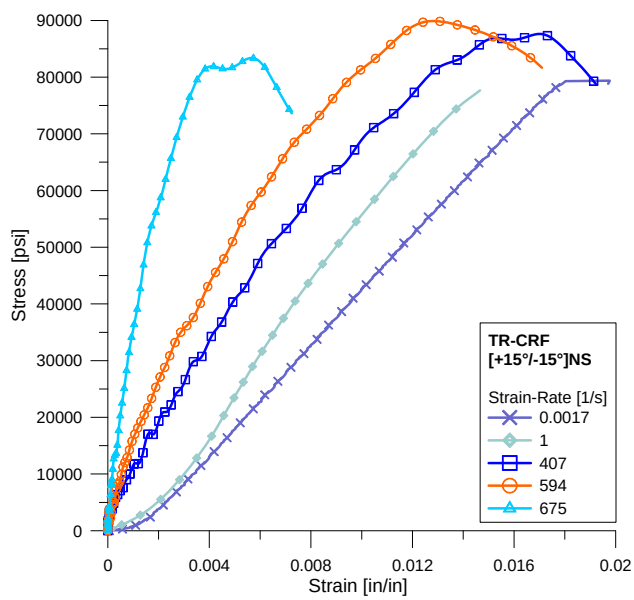

Figure 81. Stress-Strain Behavior of Toray T700G-12K-50C/3900-2 $[+15°/-15°]_{NS}$ Specimens

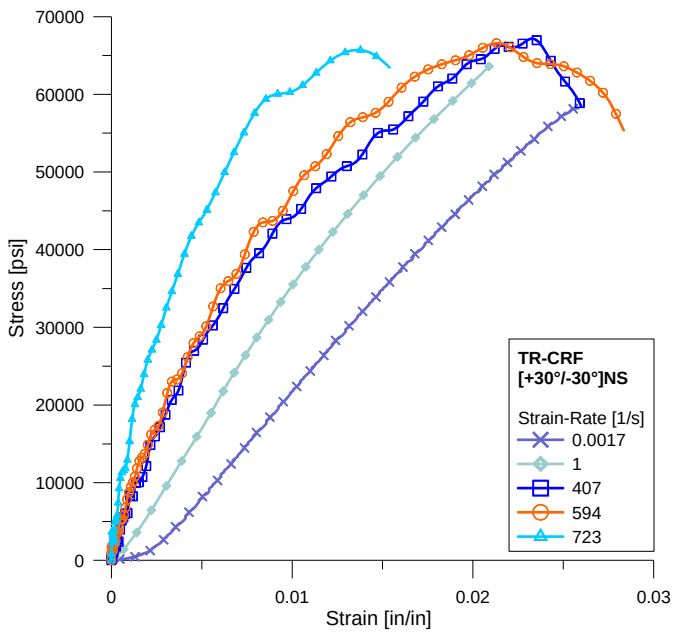

Figure 82. Stress-Strain Behavior of Toray T700G-12K-50C/3900-2 $[+30°/-30°]_{NS}$ Specimens

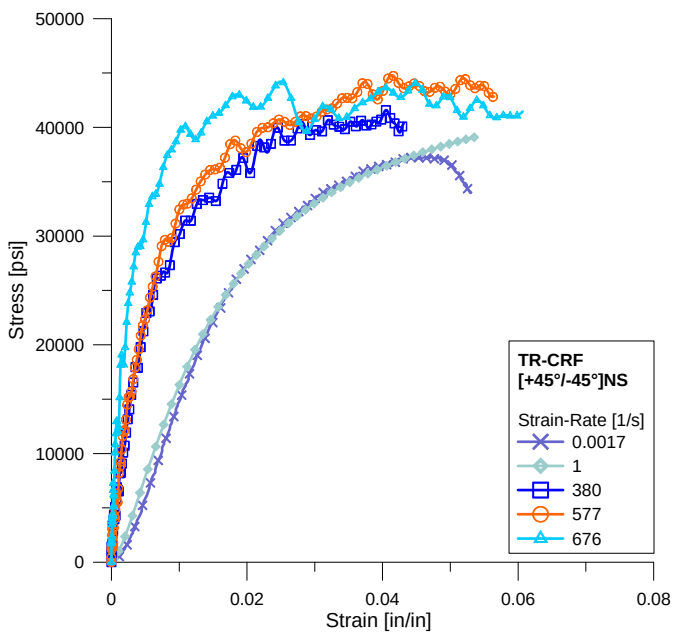

Figure 83. Stress-Strain Behavior of Toray T700G-12K-50C/3900-2 $[+45°/-45°]_{NS}$ Specimens

5.5.2.3 Failure Modes.

The representative failure modes at different test rates are shown in figures 84 through 87 for the four material orientations. The [0°]n specimens exhibited end-crushing-initiated failure accompanied by longitudinal splitting across interlaminar planes at higher rates. The $[+\theta/-\theta]_{NS}$ specimens exhibited splitting across interlaminar planes with evidence of end crush.

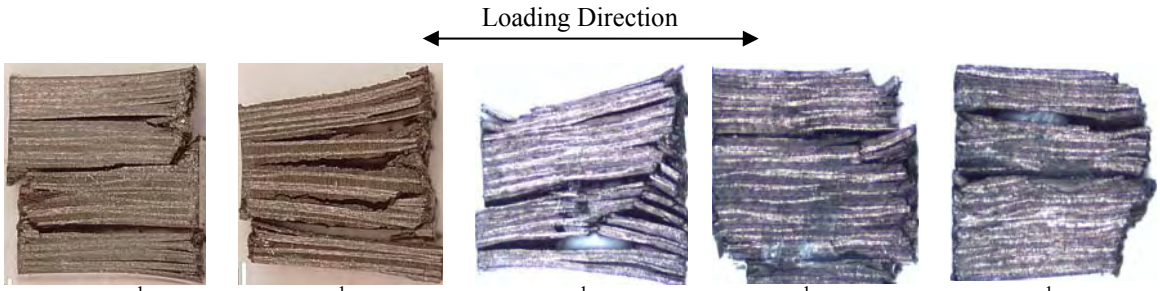

a) 0.0017 s^{-1} b) 1 s^{-1} c) 385 s^{-1} d) 492 s^{-1} e) 706 s^{-1}

Figure 84. Characteristic Failure Modes in Toray T700G-12K-50C/3900-2 $[0°]_N$ Specimens

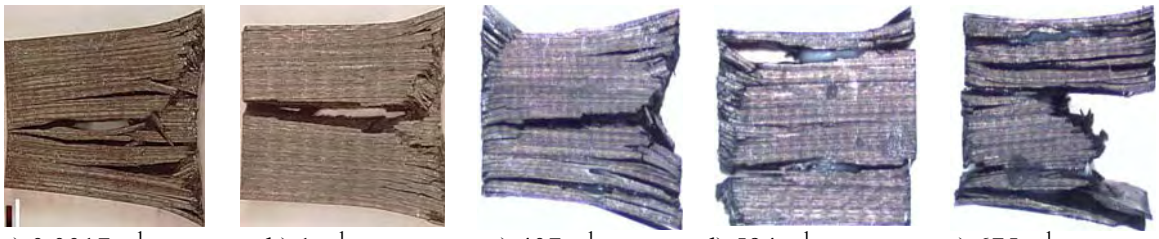

a) 0.0017 s^{-1} b) 1 s^{-1} c) 407 s^{-1} d) 594 s^{-1} e) 675 s^{-1}

Figure 85. Characteristic Failure Modes in Toray T700G-12K-50C/3900-2 $[+15°/-15°]_{NS}$ Specimens

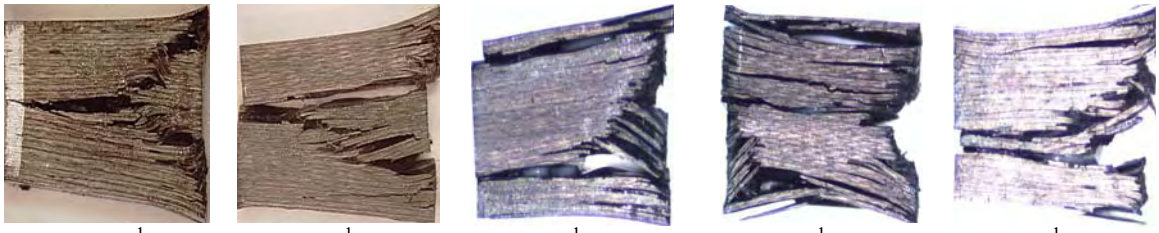

a) 0.0017 s^{-1} b) 1 s^{-1} c) 407 s^{-1} d) 594 s^{-1} e) 723 s^{-1}

Figure 86. Characteristic Failure Modes in Toray T700G-12K-50C/3900-2 $[+30°/-30°]_{NS}$ Specimens

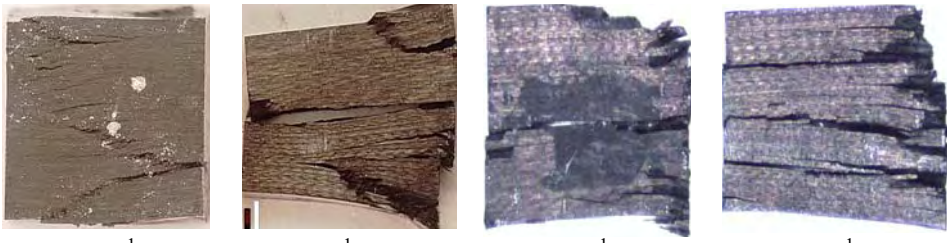

a) 0.0017 s^{-1} b) 1 s^{-1} c) 577 s^{-1} d) 676 s^{-1}

Figure 87. Characteristic Failure Modes in Toray T700G-12K-50C/3900-2 $[+45°/-45°]_{NS}$ Specimens

5.5.3 Newport NB321/7781 Fiberglass.

5.5.3.1 Failure Strength.

The failure strengths are presented in figure 88 for five different strain rates. The tabulated values for each test are in appendix C. The strength of $[0°]_N$ specimens increased over the entire range of strain rates tested, and the strength was observed to increase by a factor of 1.3 at the highest strain rate. The $[+15°/-15°]_{NS}$ specimens exhibited a similar increase in strength, albeit a significant amount of scatter. The strength of $[0°]_N$ specimens at quasi-static and medium rates were similar to those of $[+15°/-15°]_{NS}$ specimens, due to the premature failure initiation in the form of end crushing. The strength of $[+30°/-30°]_{NS}$ and $[+45°/-45°]_{NS}$ specimens did not follow a clear trend. However, an increase in strength was observed with strain rates, among the specimens tested with SHPB apparatus. However, their strengths at low and medium rates were higher than those obtained using the SHPB apparatus.

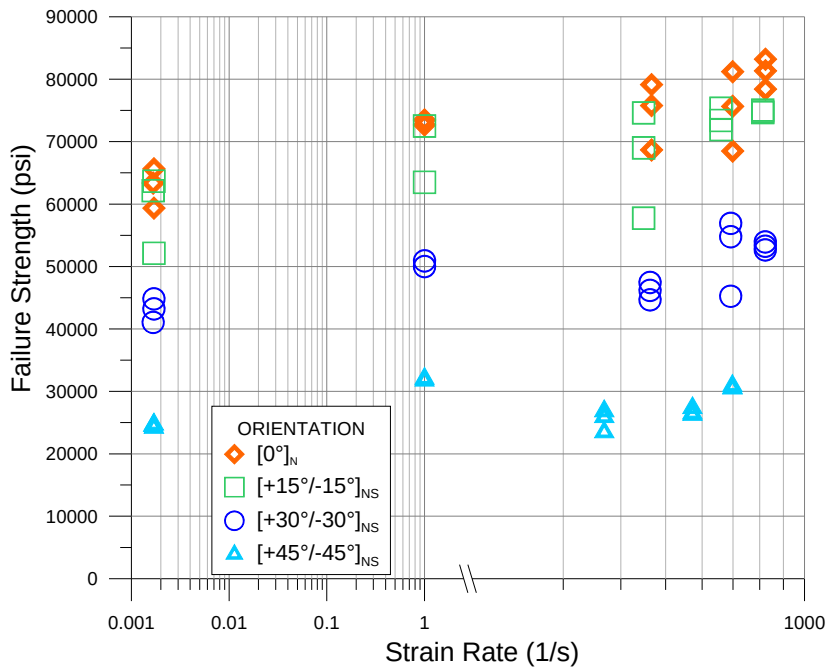

Figure 88. Average Failure Strength vs Average Strain Rate for Newport NB321/7781 Fiberglass Material

5.5.3.2 Stress-Strain Behavior.

The dynamic stress-strain behavior of Newport NB321/7781 fiberglass material system is shown in figures 89 to 92 for different stacking sequences. The stress-strain response of individual tests and the variation of strain rate during the tests are in appendix C. A clear increase in stiffness may be observed as the strain-rate increases regardless of the orientation. The failure strains were observed to decrease with increasing strain rates.

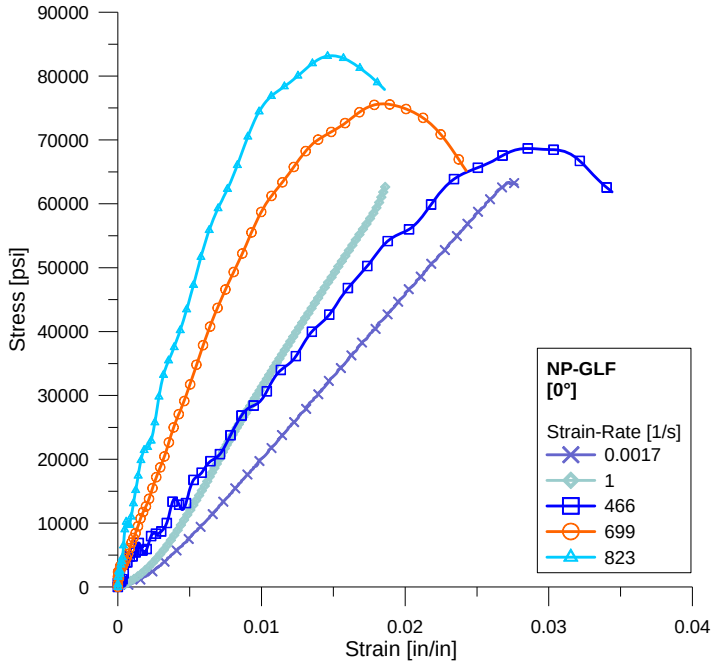

Figure 89. Stress-Strain Behavior of Newport NB321/7781 $[0°]_N$ Specimens

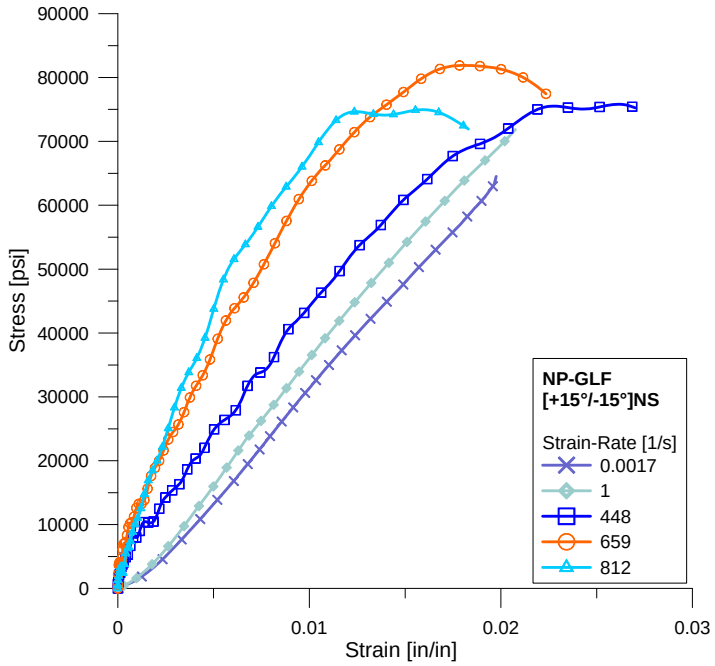

Figure 90. Stress-Strain Behavior of Newport NB321/7781 $[+15°/-15°]_{NS}$ Specimens

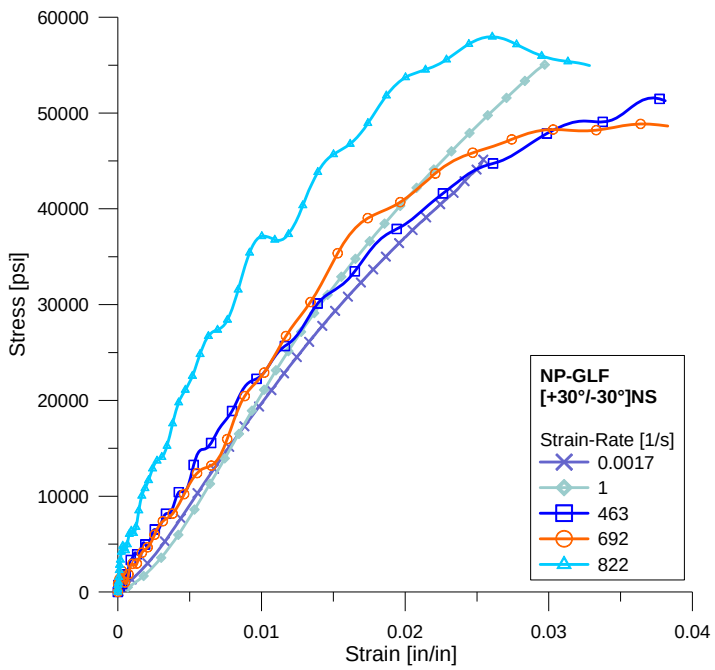

Figure 91. Stress-Strain Behavior of Newport NB321/7781 $[+30°/-30°]_{NS}$ Specimens

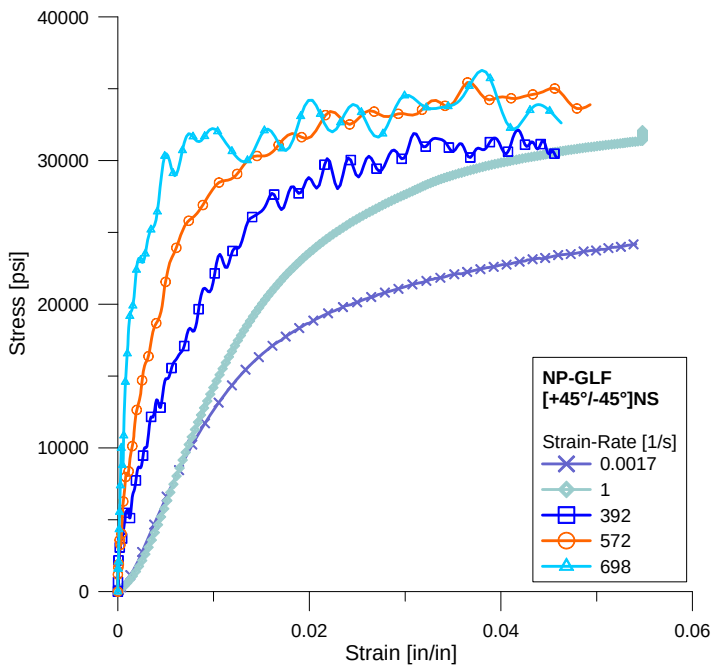

Figure 92. Stress-Strain Behavior of Newport NB321/7781 $[+45°/-45°]_{NS}$ Specimens

5.5.3.3 Failure Modes.

The representative failure modes at different test rates are illustrated in figures 93 through 96 for the four material orientations. The $[0°]_N$ specimens exhibited end-crushing-initiated failure accompanied by failure across planes that were inclined to the interlaminar planes. The formation of kink bands was evident along the planes of failure. The $[+\theta/-\theta]_{NS}$ specimens exhibited a considerable amount of matrix whitening, indicating extensive matrix cracking prior to failure. In addition, kink bands were also observed in these specimens across inclined planes. However, no trend could be observed relating the orientation of the kink bands relative to the loading axis as a function of stacking sequence and/or the strain rates.

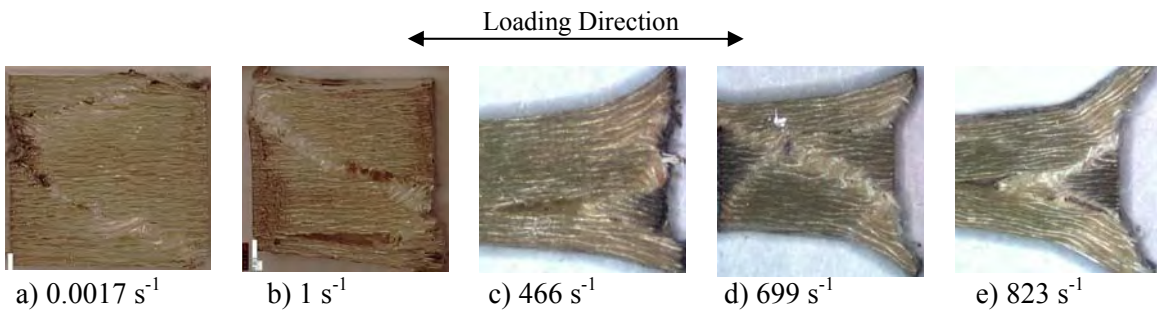

Figure 93. Characteristic Failure Modes in Newport NB321/7781 $[0°]_N$ Specimens

Figure 94. Characteristic Failure Modes in Newport NB321/7781 $[+15°/-15°]_{NS}$ Specimens

Figure 95. Characteristic Failure Modes in Newport NB321/7781 $[+30°/-30°]_{NS}$ Specimens

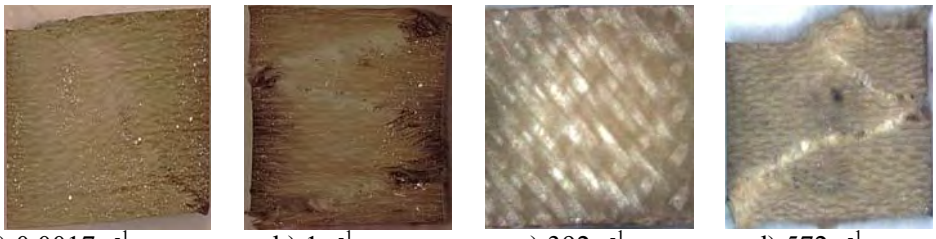

a) 0.0017 s^{-1} b) 1 s^{-1} c) 392 s^{-1} d) 572 s^{-1}

Figure 96. Characteristic Failure Modes in Newport NB321/7781 $[+45°/-45°]_{NS}$ Specimens

5.5.4 Newport NB321/3K70 PWCF.

5.5.4.1 Failure Strength.

The failure strengths are presented in figure 97 for five different strain rates. The tabulated values for each test are in appendix C. The strengths of $[0°]_N$ specimens at quasi-static and medium rates were similar to those of $[+15°/-15°]_{NS}$, due to the premature failure initiation in the form of end crushing, which promotes a interlaminar splitting-type failure. The increase in strengths as a function strain rates for the $[0°]_N$ and $[+15°/-15°]_{NS}$ specimens were not as conspicuous as the Newport NB321/7781 material system. The strengths at strain rates of around 400s^{-1} and above were sometimes lower than the low strain rates. The $[+30°/-30°]_{NS}$ and $[+45°/-45°]_{NS}$ specimens, however, indicated a slight increasing trend over the range of strain rates used in the experiments.

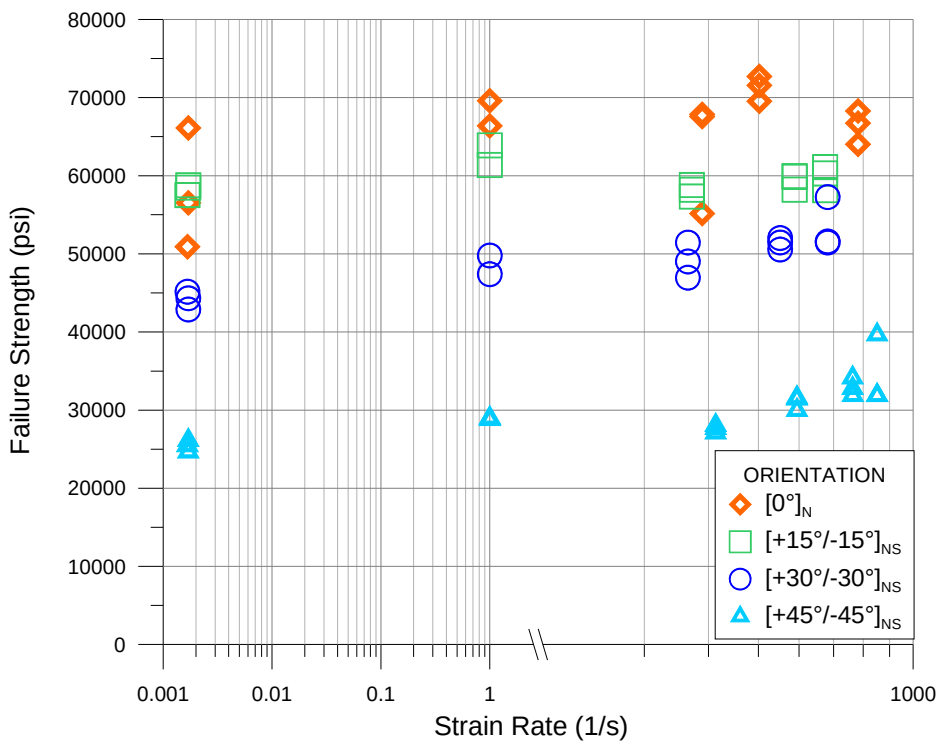

Figure 97. Failure Strength vs Average Strain Rate for Newport NB321/3K70 PWCF Material

5.5.4.2 Stress-Strain Behavior.

The dynamic stress-strain behavior of Newport NB321/3K70 PWCF material system is shown in figures 98 to 101 for different stacking sequences. The stress-strain response of individual tests and the variation of strain rate during the tests are shown in appendix C. A steeper response, indicating stiffening behavior, was observed as the strain rate increased, regardless of the orientation. The failure strains decreased with increasing strain rates. The nonlinear region associated with the behavior of $[+45°/-45°]_{NS}$ was considerably reduced at higher strain rates.

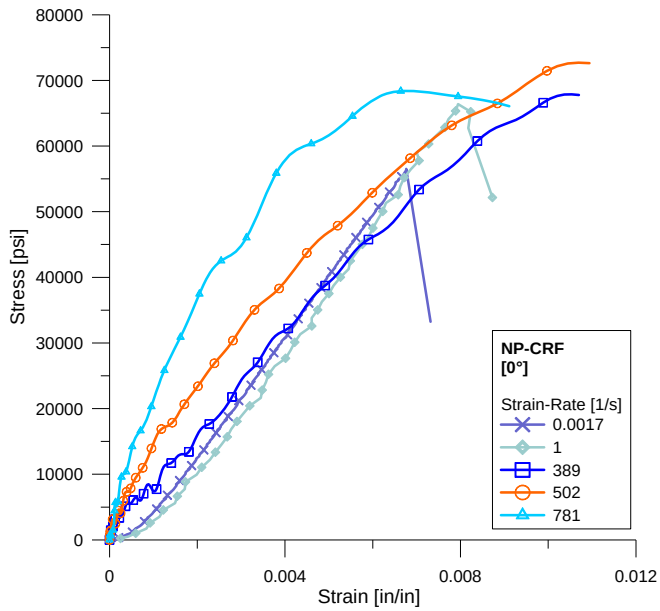

Figure 98. Stress-Strain Behavior of Newport NB321/3K70 PWCF $[0°]_N$ Specimens

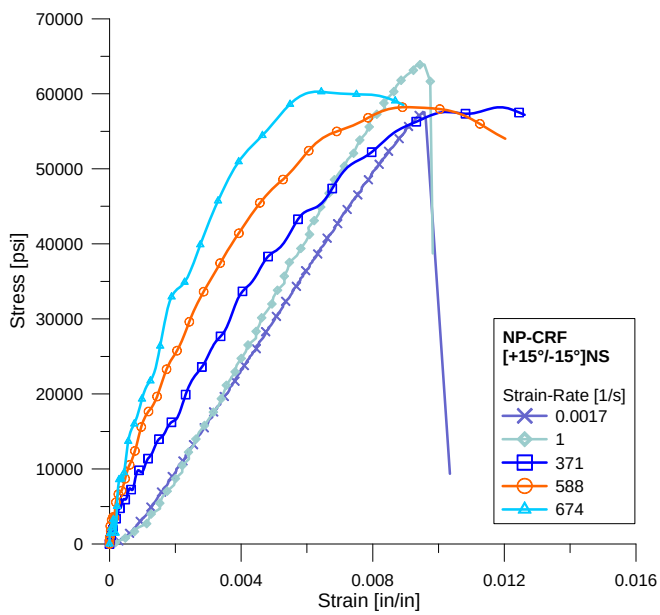

Figure 99. Stress-Strain Behavior of Newport NB321/3K70 PWCF $[+15°/-15°]_{NS}$ Specimens

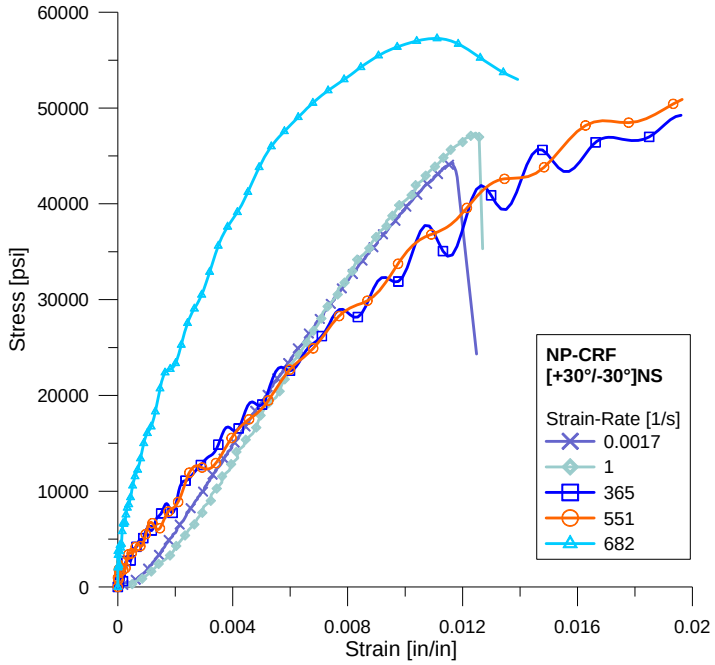

Figure 100. Stress-Strain Behavior of Newport NB321/3K70 PWCF $[+30°/-30°]_{NS}$ Specimens

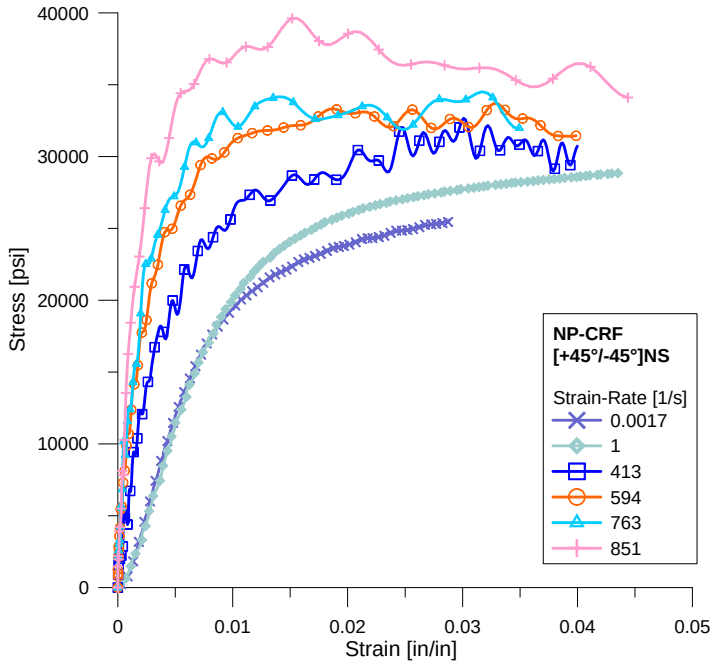

Figure 101. Stress-Strain Behavior of Newport NB321/3K70 PWCF $[+45°/-45°]_{NS}$ Specimens

5.5.4.3 Failure Modes.

The representative failure modes at different test rates are shown in figures 102 through 105 for the four material orientations. The $[0°]_N$ specimens exhibited end-crushing-initiated failure accompanied by failure across planes that were either inclined or parallel to the interlaminar planes. The formation of kink bands was evident along the planes of failure in $[+30°/-30°]_{NS}$ and $[+45°/-45°]_{NS}$ specimens. In addition, an equal number of cases were observed where splitting across interlaminar planes occurred.

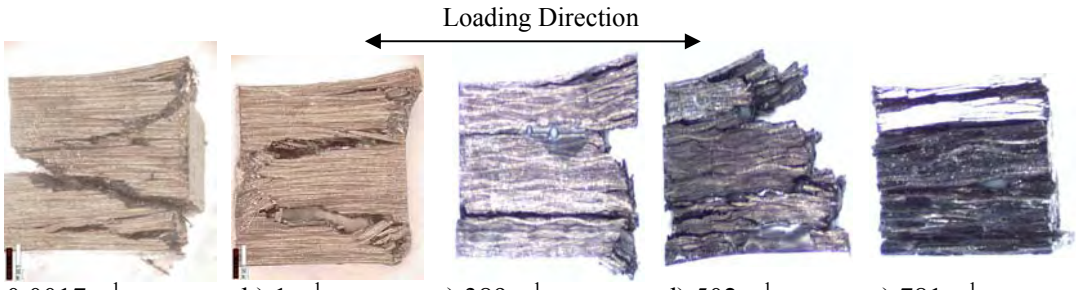

a) 0.0017 s^{-1} b) 1 s^{-1} c) 389 s^{-1} d) 502 s^{-1} e) 781 s^{-1}

Figure 102. Characteristic Failure Modes in Newport NB321/3K70 PWCF $[0°]_N$ Specimens

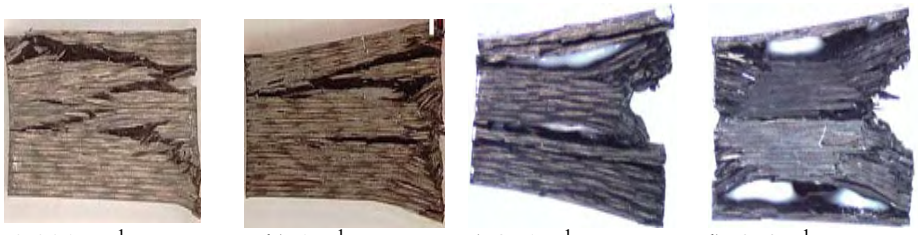

a) 0.0017 s^{-1} b) 1 s^{-1} c) 371 s^{-1} d) 674 s^{-1}

Figure 103. Characteristic Failure Modes in Newport NB321/3K70 PWCF $[+15°/-15°]_{NS}$ Specimens

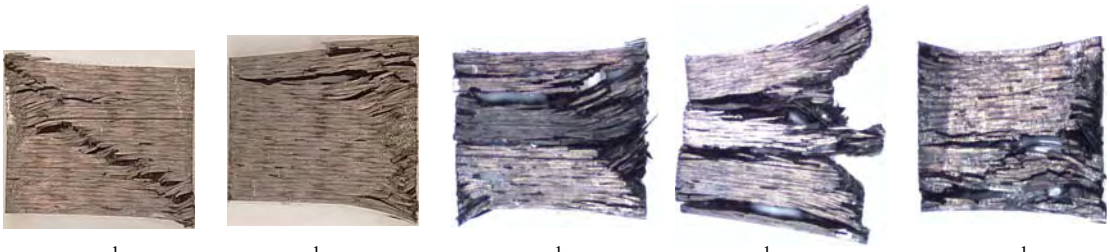

a) 0.0017 s^{-1} b) 1 s^{-1} c) 365 s^{-1} d) 551 s^{-1} e) 682 s^{-1}

Figure 104. Characteristic Failure Modes in Newport NB321/3K70 PWCF $[+30°/-30°]_{NS}$ Specimens

a) 0.0017 s^{-1} b) 1 s^{-1} c) 594 s^{-1} d) 763 s^{-1} e) 851 s^{-1}

Figure 105. Characteristic Failure Modes in Newport NB321/3K70 PWCF $[+45°/-45°]_{NS}$ Specimens

5.5.5 Newport NCT321/G150 Unitape.

5.5.5.1 Failure Strength.

The failure strengths are presented in figure 106 for five different strain rates. The tabulated values for each test are in appendix C. The strengths of $[0°]_N$ and $[+15°/-15°]_{NS}$ specimens were similar, except at the highest rate of loading. At the higher rates, the strengths of $[0°]_N$ specimens were observed to increase with strain rates, whereas the strength of the $[+15°/-15°]_{NS}$ specimens decreased and fell below the quasi-static value at the highest strain rate (~700s^{-1}). The strengths of the $[+30°/-30°]_{NS}$ and $[+45°/-45°]_{NS}$ specimens from dynamic testing were higher than the quasi-static values, but no specific trends could be identified.

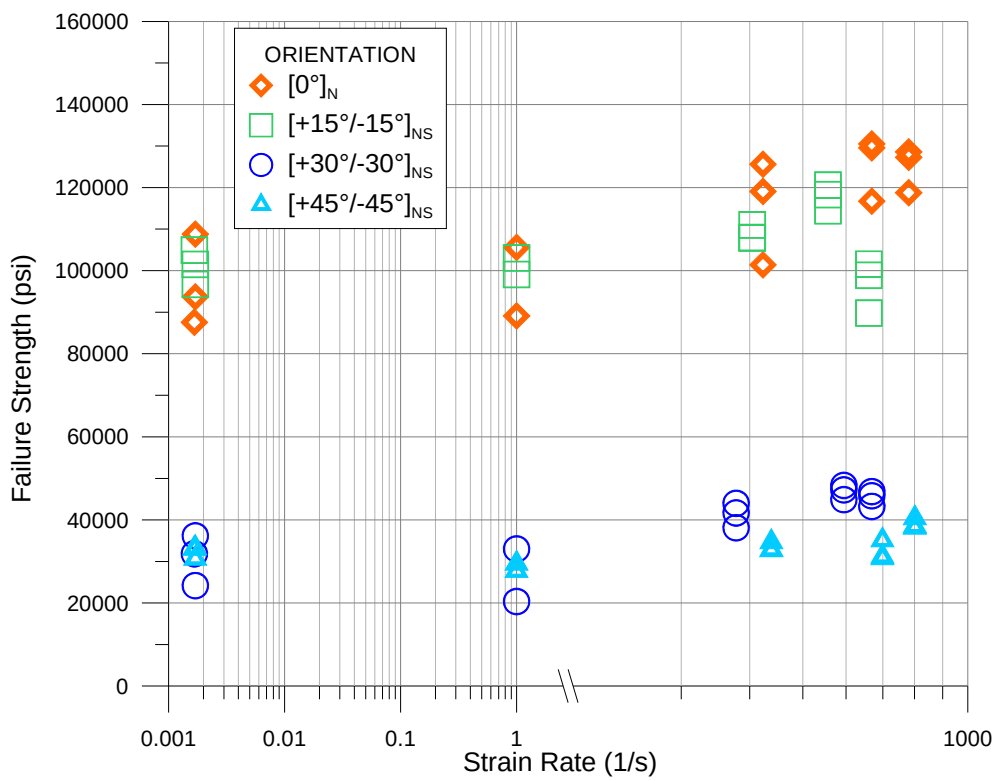

Figure 106. Failure Strength vs Average Strain Rate for Newport NCT321/G150 Unitape Material

5.5.5.2 Stress-Strain Behavior.

The dynamic stress-strain behavior of Newport NCT321/G150 unitape material system is shown in figures 107 to 110 for different stacking sequences. The stress-strain response of individual tests and the variation of strain rate during the tests are in appendix C. A steeper response, indicating stiffening behavior, is observed as the strain rate increases regardless of the orientation. The stress-strain behavior at a strain rate of approximately $400s^{-1}$ appears to deviate from the trends and is attributed to scatter in the test data.

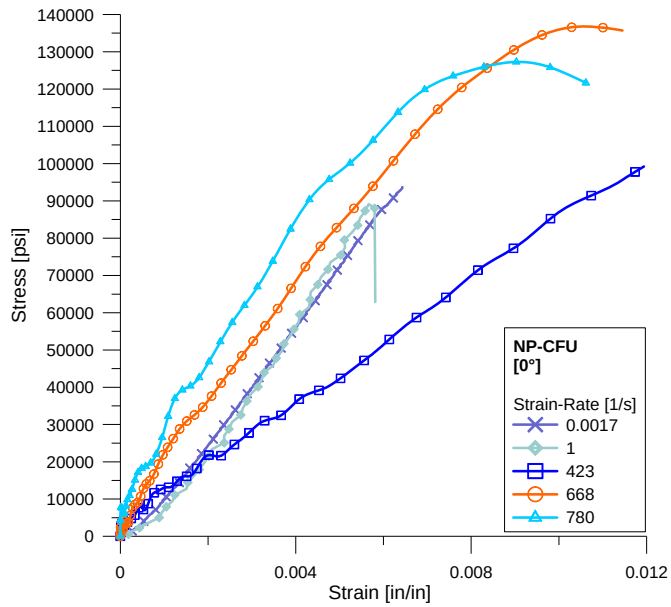

Figure 107. Stress-Strain Behavior of Newport NCT321/G150 $[0°]_N$ Specimens

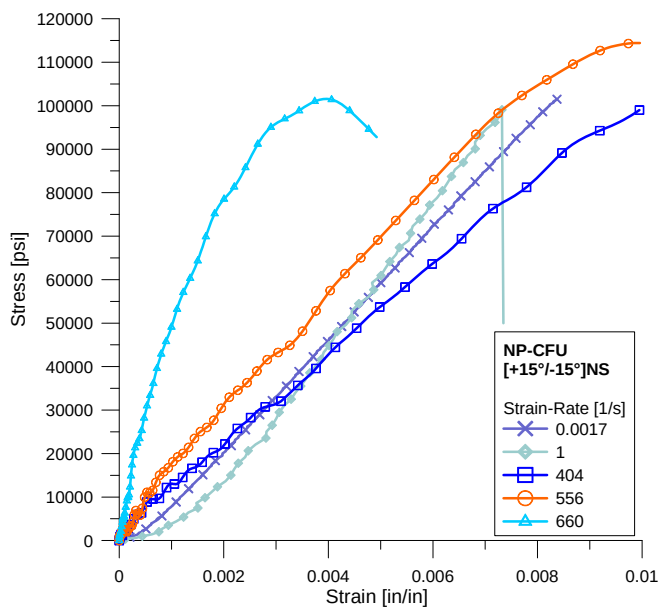

Figure 108. Stress-Strain Behavior of Newport NCT321/G150 $[+15°/-15°]_{NS}$ Specimens

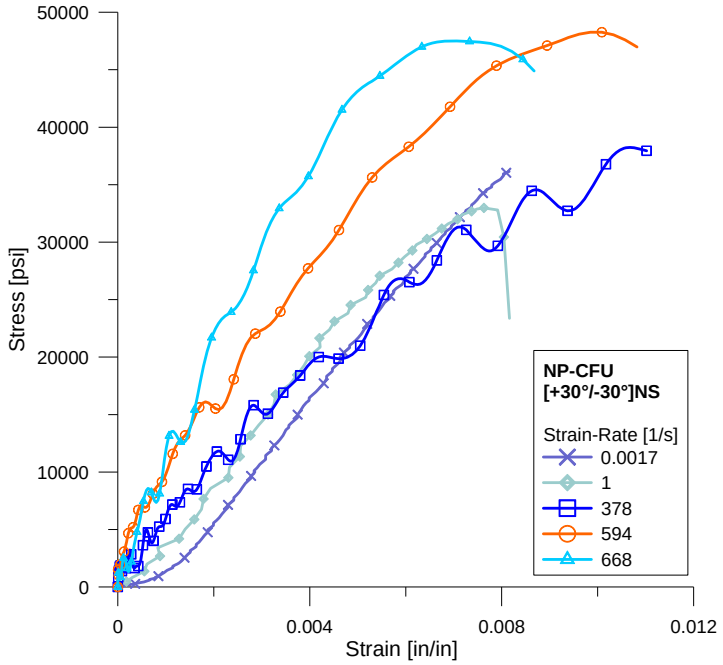

Figure 109. Stress-Strain Behavior of Newport NCT321/G150 $[+30°/-30°]_{NS}$ Specimens

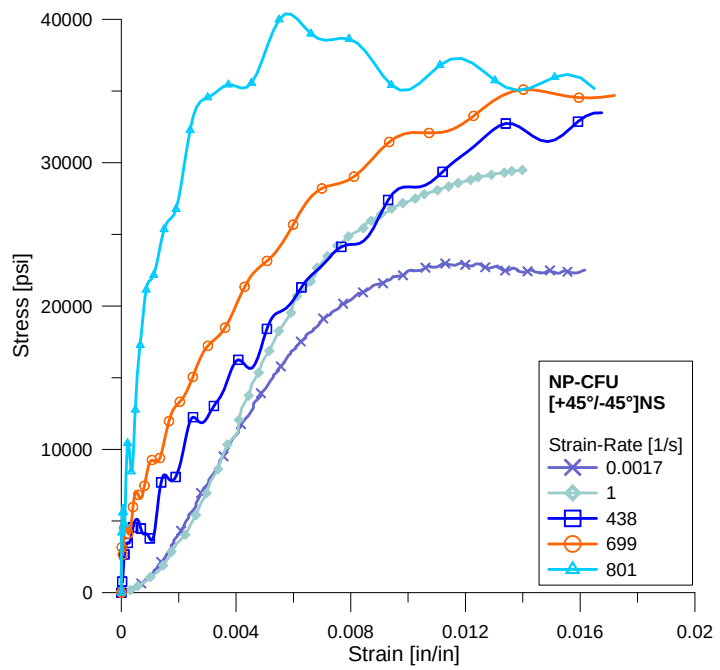

Figure 110. Stress-Strain Behavior of Newport NCT321/G150 $[+45°/-45°]_{NS}$ Specimens

5.5.5.3 Failure Modes.

The representative failure modes at different test rates are shown in figures 111 through 114 for the four material orientations. The $[0°]_N$ specimens exhibited end-crushing-initiated failure accompanied by longitudinal splitting. Due to the explosive nature of the failure, the fragments

of the specimen were either not recoverable or assembled postfailure to study the failure modes. Translaminar splits across the specimen width, along planes parallel to fiber orientation, were observed in $[+15°/-15°]_{NS}$, $[+30°/-30°]_{NS}$, and $[+45°/-45°]_{NS}$ specimens. The fragments of $[+45°/-45°]_{NS}$ specimens were not recoverable at higher strain rates.

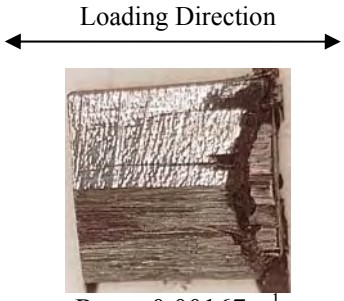

Rate. 0.00167 s^{-1}

Figure 111. Characteristic Failure Modes in Newport NCT321/G150 $[0°]_N$ Specimens

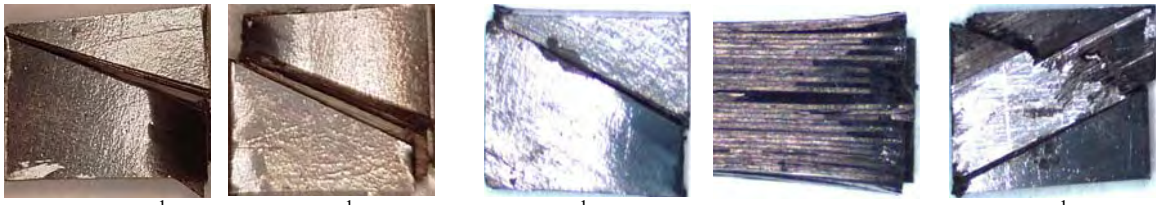

a) 0.00167 s^{-1} b) 1 s^{-1} c) 404 s^{-1} d) 404 (side view) e) 660 s^{-1}

Figure 112. Characteristic Failure Modes in Newport NCT321/G150 $[+15°/-15°]_{NS}$ Specimens

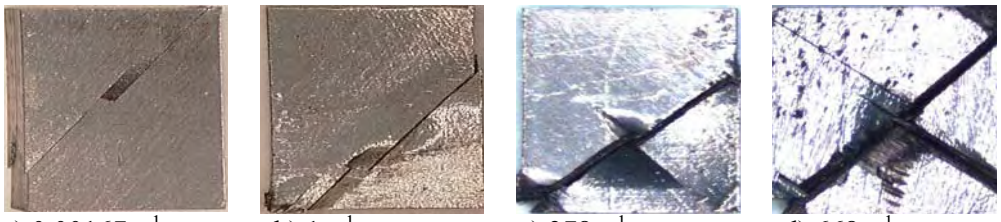

a) 0.00167 s^{-1} b) 1 s^{-1} c) 378 s^{-1} d) 668 s^{-1}

Figure 113. Characteristic Failure Modes in Newport NCT321/G150 $[+30°/-30°]_{NS}$ Specimens

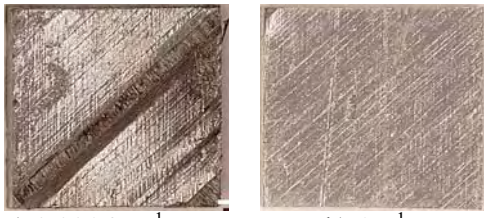

a) 0.00167 s^{-1} b) 1 s^{-1}

Figure 114. Characteristic Failure Modes in Newport NCT321/G150 $[+45°/-45°]_{NS}$ Specimens

5.5.6 Cytec T300/97714AC 3KNT PWCF.

5.5.6.1 Failure Strength.

The failure strengths are presented in figure 115 for five different strain rates. The tabulated values for each test are in appendix C. The compressive strengths of $[0°]_N$ specimens exhibited moderately increasing trends with strain rate. The strengths of $[+15°/-15°]_{NS}$ specimens were observed to be insensitive to strain rates, whereas the $[+30°/-30°]_{NS}$ specimens exhibited a gradual increase in strength with strain rate. The $[+45°/-45°]_{NS}$ specimens exhibit a reduction in strength when the strengths obtained from SHPB test are compared to those obtained from quasi-static and medium rate tests. However, an increasing trend was observed for the test conducted at strain rates of 300 s^{-1} and higher.

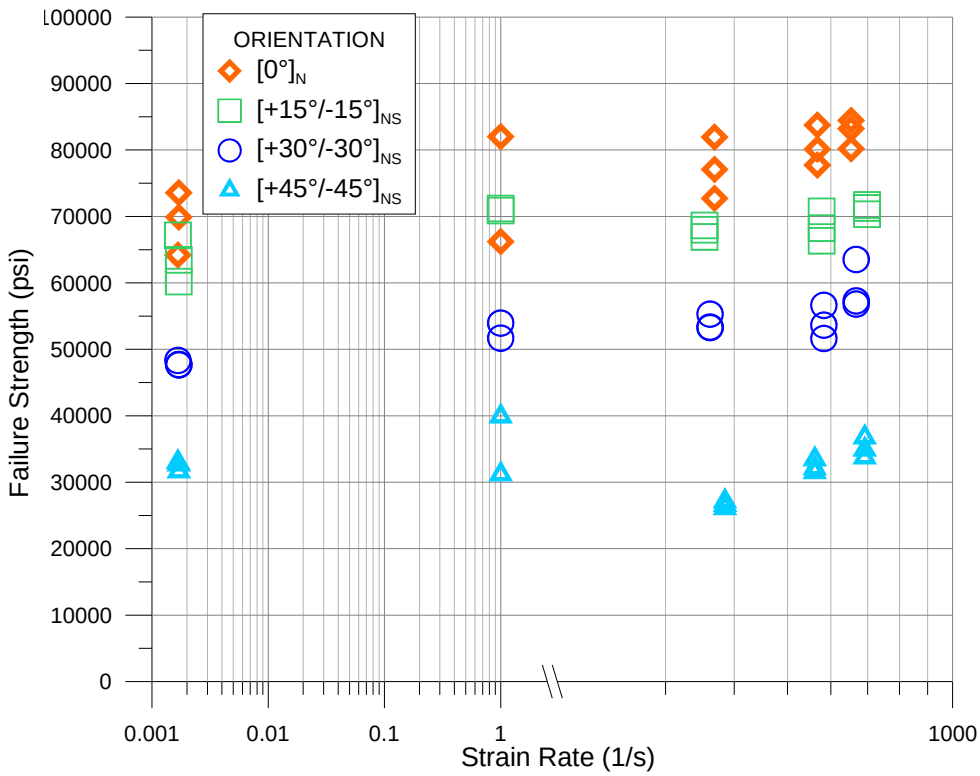

Figure 115. Failure Strength vs Average Strain Rate for Cytec T300/97714AC 3KNT PWCF Material

5.5.6.2 Stress-Strain Behavior.

The dynamic stress-strain curves for Cytec PWC T300/97714AC 3KNT material system are shown in figures 116 to 119 for different stacking sequences. The stress-strain response of individual tests and the variation of strain rate during the tests are in appendix C. A steeper response, indicating stiffening behavior, is observed as the strain rate increases regardless of the orientation. The failure strains were observed to decrease with increasing strain rates, whereas no appreciable increase in strength was observed.

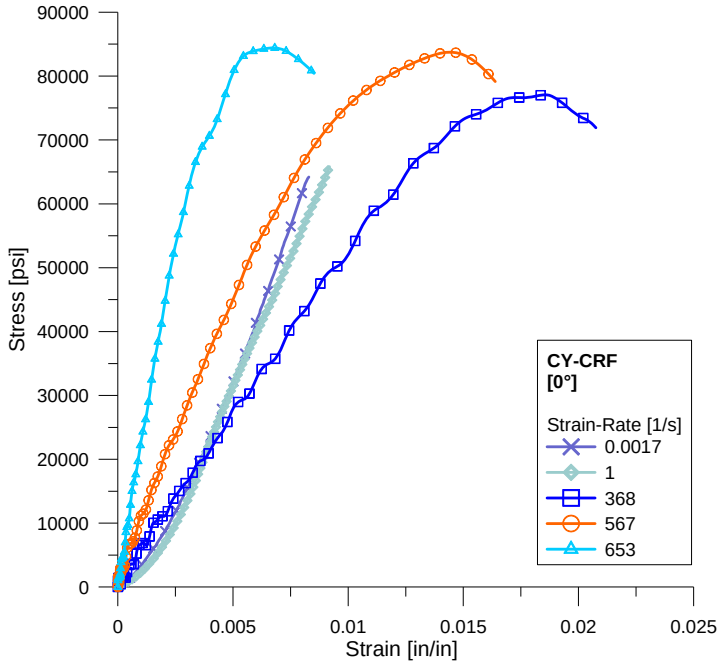

Figure 116. Stress-Strain Behavior of Cytec T300/97714AC 3KNT PWCF $[0°]_N$ Specimens

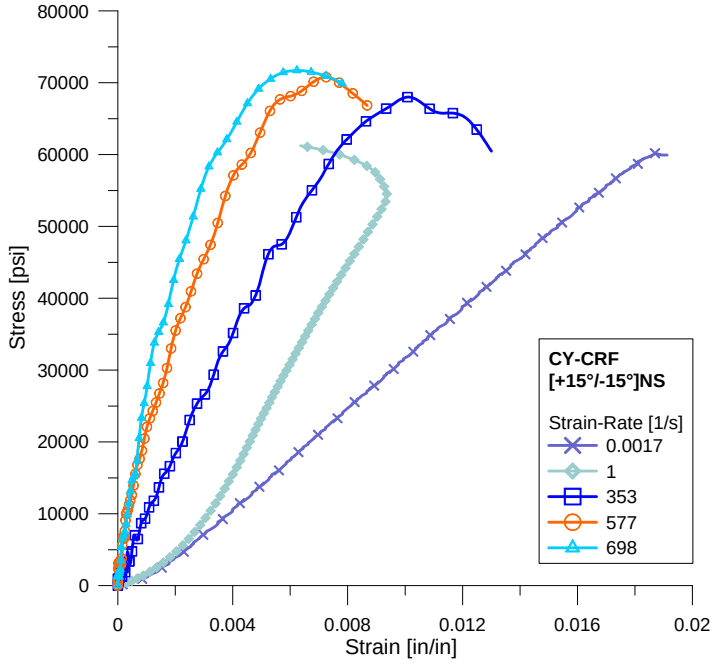

Figure 117. Stress-Strain Behavior of Cytec T300/97714AC 3KNT PWCF $[+15°/-15°]_{NS}$ Specimens

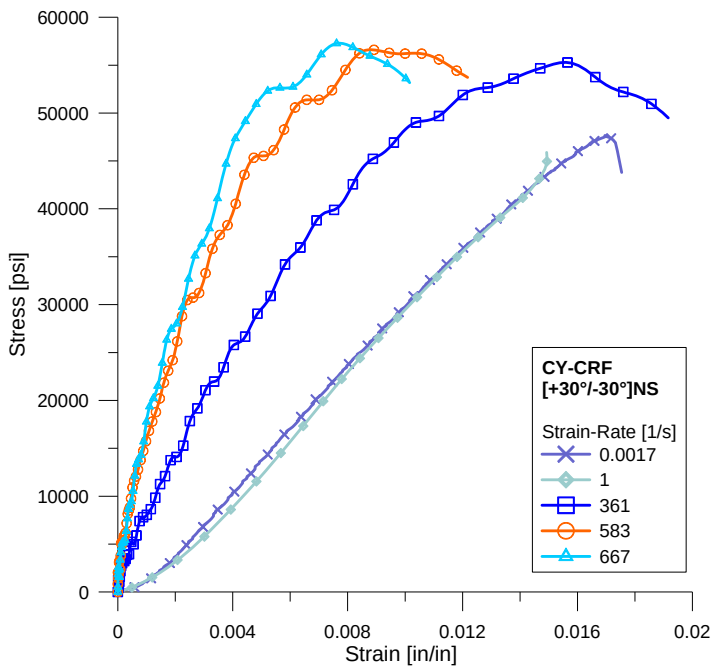

Figure 118. Stress-Strain Behavior of Cytec T300/97714AC 3KNT PWCF $[+30°/-30°]_{NS}$ Specimens

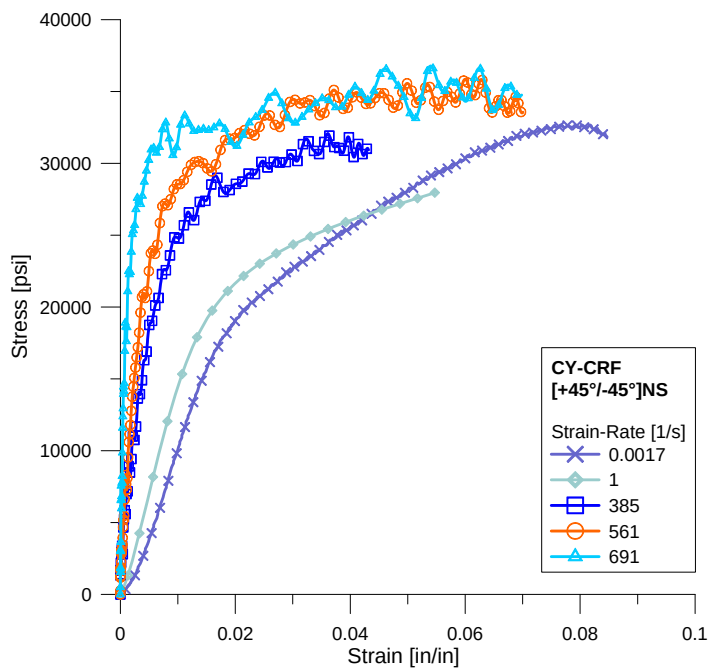

Figure 119. Stress-Strain Behavior of Cytec T300/97714AC 3KNT PWCF $[+45°/-45°]_{NS}$ Specimens

5.5.6.3 Failure Modes.

The representative failure modes at different test rates are shown in figures 120 through 123 for the four material orientations. The $[0°]_N$ specimens exhibited end-crushing-initiated failure accompanied by failure across planes parallel to the interlaminar planes. The formation of kink bands was evident along the planes of failure in $[+15°/-15°]_{NS}$, $[+30°/-30°]_{NS}$, and $[+45°/-45°]_{NS}$ specimens. In addition, an equal number of cases were observed where splitting across interlaminar planes occurred.

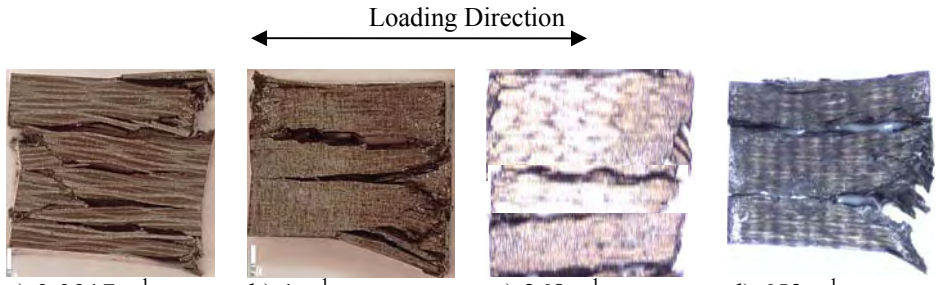

a) 0.0017 s^{-1} b) 1 s^{-1} c) 368 s^{-1} d) 653 s^{-1}

Figure 120. Characteristic Failure Modes in Cytec T300/97714AC 3KNT PWCF $[0°]_N$ Specimens

a) 0.0017 s^{-1} b) 1 s^{-1} c) 698 s^{-1}

Figure 121. Characteristic Failure Modes in Cytec T300/97714AC 3KNT PWCF $[+15°/-15°]_{NS}$ Specimens

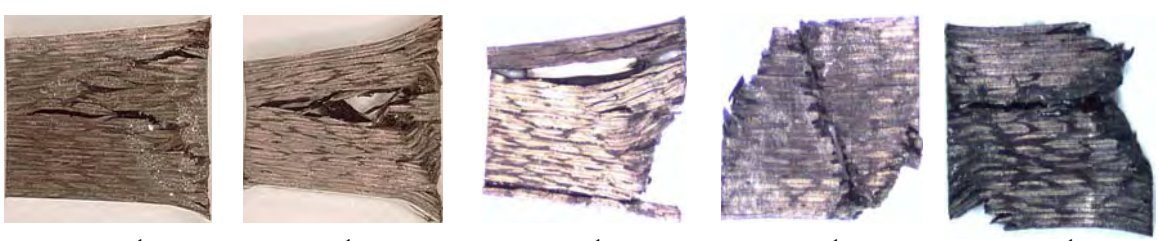

a) 0.0017 s^{-1} b) 1 s^{-1} c) 361 s^{-1} d) 583 s^{-1} e) 667 s^{-1}

Figure 122. Characteristic Failure Modes in Cytec T300/97714AC 3KNT PWCF $[+30°/-30°]_{NS}$ Specimens

a) 0.0017 s^{-1} b) 1 s^{-1} c) 691 s^{-1}

Figure 123. Characteristic Failure Modes in Cytec T300/97714AC 3KNT PWCF $[+45°/-45°]_{NS}$ Specimens

5.5.7 Fibercote 3KPW-E365 PWCF.

5.5.7.1 Failure Strength.

The failure strengths are presented in figure 124 for five different strain rates. The tabulated values for each test are in appendix C. The $[0°]_N$ specimens exhibit a slight increase in strength with strain rate, whereas the strength of $[+15°/-15°]_{NS}$ specimens tends to remain more or less constant with strain rate. High scatter was associated with the strengths of $[+15°/-15°]_{NS}$ specimens compared to the other orientations. The strength of $[+30°/-30°]_{NS}$ and $[+45°/-45°]_{NS}$ specimens exhibit an increasing trend at strain rates of 400 s^{-1} and beyond.

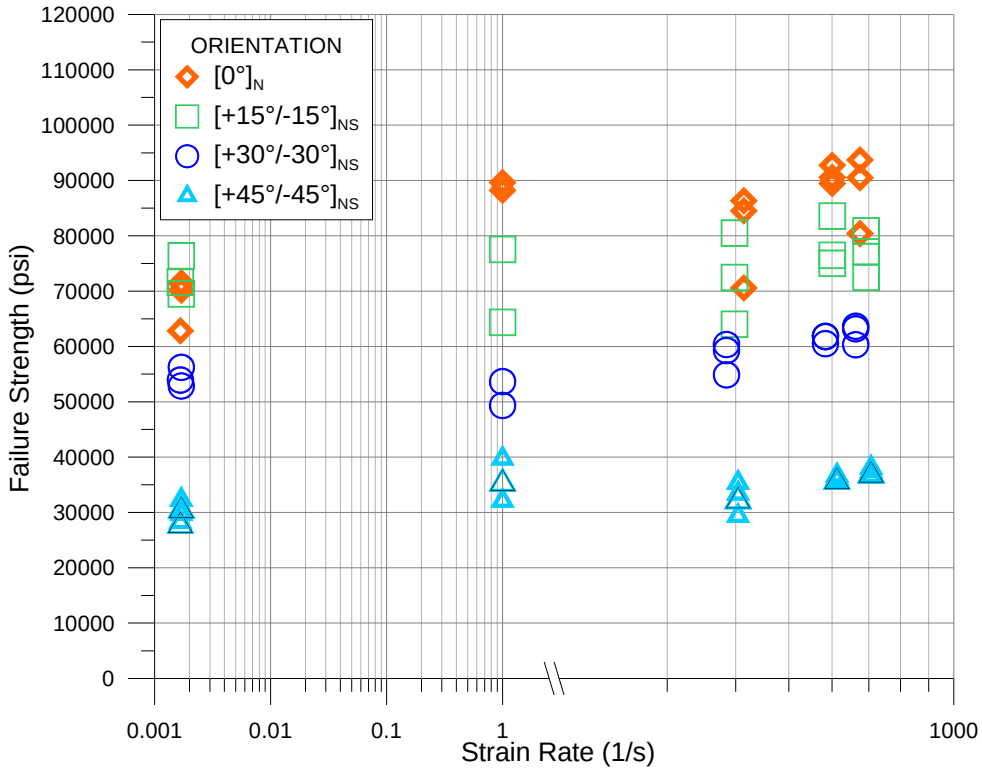

Figure 124. Failure Strength vs Average Strain Rate for Fibercote 3KPW-E365 PWCF Material

5.5.7.2 Stress-Strain Behavior.

The dynamic stress-strain curves for the Fibercote 3KPW-E365 PWCF material system are shown in figures 125 to 128 for different stacking sequences. The stress-strain response of individual tests and the variation of strain rate during the tests are in appendix C. A steeper response, indicating stiffening behavior, was observed as the strain rate increased, regardless of the orientation. The failure strains decreased with increasing strain rates, while no appreciable increase in strength was observed. The nonlinear region associated with the behavior of $[+45°/-45°]_{NS}$ was considerably reduced at higher strain rates.

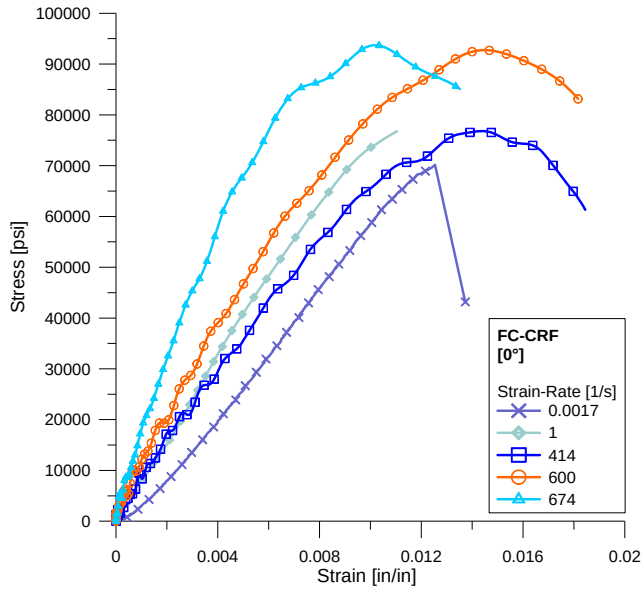

Figure 125. Stress-Strain Behavior of Fibercote 3KPW-E365 PWCF $[0°]_N$ Specimens

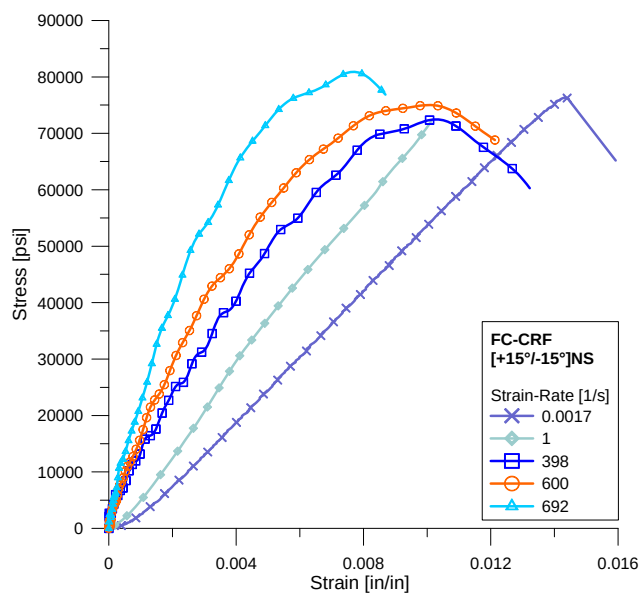

Figure 126. Stress-Strain Behavior of Fibercote 3KPW-E365 PWCF $[+15°/-15°]_{NS}$ Specimens

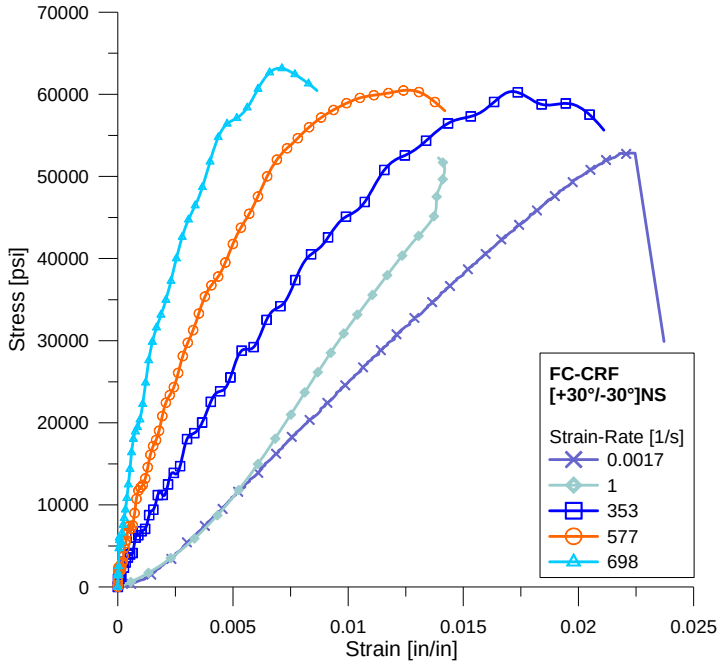

Figure 127. Stress-Strain Behavior of Fibercote 3KPW-E365 PWCF $[+30°/-30°]_{NS}$ Specimens

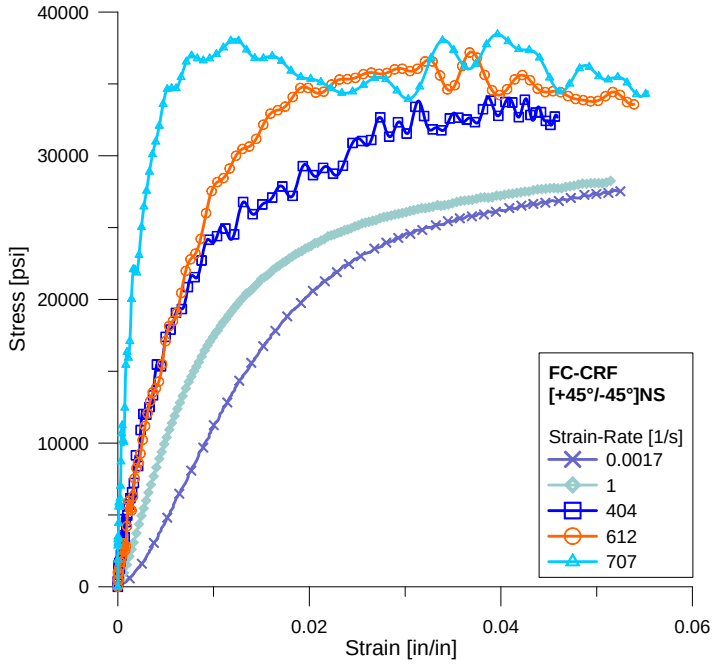

Figure 128. Stress-Strain Behavior of Fibercote 3KPW-E365 PWCF $[+45°/-45°]_{NS}$ Specimens

5.5.7.3 Failure Modes.

The representative failure modes at different test rates are shown in figures 129 through 132 for the four material orientations. The $[0°]_N$ specimens exhibited end-crushing-initiated failure accompanied by failure across planes parallel to the interlaminar planes. The formation of kink

bands was evident along the planes of failure in $[+15°/-15°]_{NS}$, $[+30°/-30°]_{NS}$, and $[+45°/-45°]_{NS}$ specimens. In addition, an equal number of cases were observed where splitting across interlaminar planes occurred.

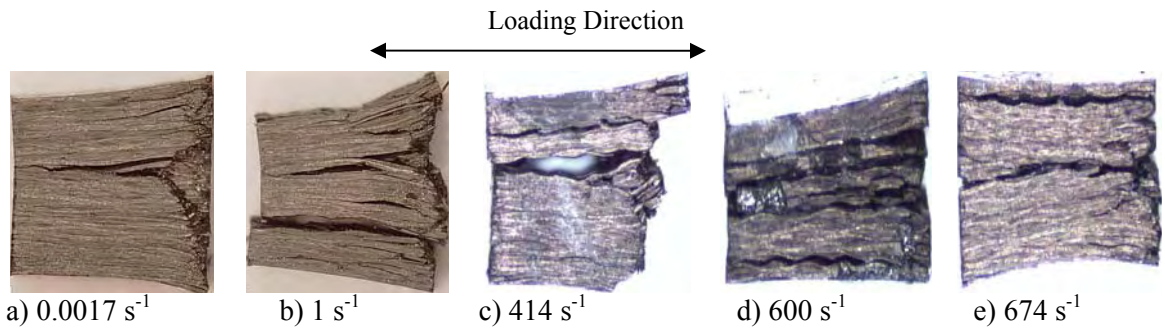

Figure 129. Characteristic Failure Modes Over Five Strain Rates in Fibercote 3KPW-E365 PWCF $[0°]_N$ Specimens

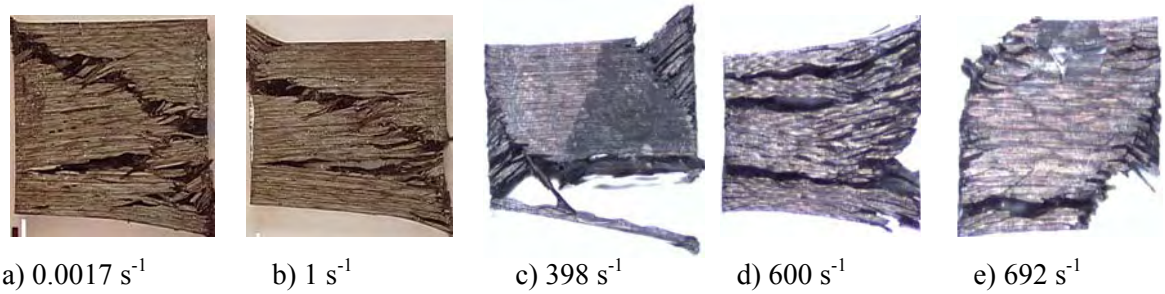

Figure 130. Characteristic Failure Modes Over Five Strain Rates in Fibercote 3KPW-E365 PWCF $[+15°/-15°]_{NS}$ Specimens

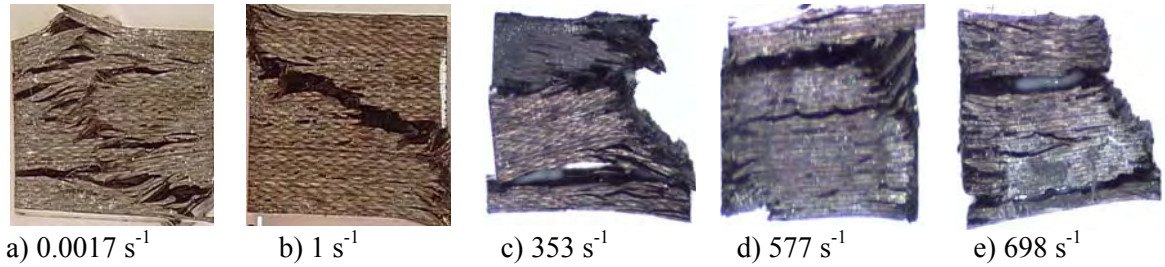

Figure 131. Characteristic Failure Modes Over Five Strain Rates in Fibercote 3KPW-E365 PWCF $[+30°/-30°]_{NS}$ Specimens

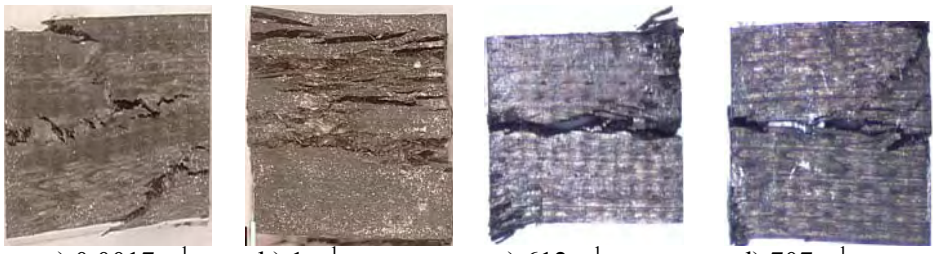

a) 0.0017 s^{-1} b) 1 s^{-1} c) 612 s^{-1} d) 707 s^{-1}

Figure 132. Characteristic Failure Modes Over Four Strain Rates in Fibercote 3KPW-E365 PWCF $[+45°/-45°]_{NS}$ Specimens

6. CONCLUSIONS.

Based on a literature review, the possible role of material rate sensitivity on the observed rate dependency of energy absorption (EA) devices and structures has been highlighted. Most investigations related to crashworthiness and EA do not report a measured strain rate but quote the material rate sensitivity as either a contributing or a negligible factor. Several investigations on rate sensitivity of composite material properties reveal that the materials are indeed rate dependent. However, the extent of sensitivity is often conflicting due to the differences in material systems, stacking sequences, test specimen geometry, apparatus, etc. used in each study.

In the current study, the sensitivity of seven continuous fiber-reinforced composite material systems to strain rates was investigated experimentally. Toray T800S/3900-2B unitape, Toray T700G-12K-PW/3900-2 fabric, Newport NB321/7781 fiberglass, Newport NB321/3k90 plain weave carbon fabric, Newport NCT321/G150 unitape, Fibercote 3KPW-E365 and Cytec T300/7714AC 3KNT material were investigated. These material systems possess different combinations of matrix systems and fiber reinforcement. The in-plane tension, compression, and shear properties were generated by conducting tests at different strain rates. The material systems investigated exhibited rate sensitivity in the form of increasing strength and stiffness under tension, compression, and shear loading. However, the extent of these effects was dependent on the stacking sequence and the loading type

The test apparatus and fixtures required to facilitate high-rate tests were designed based on existing literature on high-rate tests. A high-rate, servo-hydraulic test machine capable of stroke rates up to 500 in/s was augmented with a slack inducer mechanism to achieve constant strain rate tension and shear testing of composite materials. The advantages and limitations of the mechanisms were highlighted in view of the high-rate tests. The high-rate tests performed using this mechanism did not produce a constant strain rate test, but the strain rates tended to approach an asymptote with increasing strain levels during the tests.

The tension tests were conducted at stroke rates ranging between 10^{-3} and 500 in/s and strain rates ranging between 10^{-3} and 200 s^{-1}. The strain rates achieved during a test depended on the stiffness of the test specimen and the stroke rate. The tensile strength of the materials was observed to increase with stroke rates up to 100 in/s. At higher rates, depending on the material and stacking sequence, the strength either increased or decreased. It was concluded that the trends at higher strain rates could be an artifact of the load measurement or test fixture

arrangement as well as the material rate effects. The Newport NB321/7781 fiberglass material was the most rate-sensitive material, with the $[+45°/-45°]_{NS}$ laminates experiencing a strength increase by a factor of 3. The failure modes were consistent across the different test rates, and the failure mode was relatively diffuse at higher rates.

The strain rate measurement was possible up to a shear strain value of 0.1 radian, which is the physical limit of the strain gage. A maximum shear strain rate approaching 800 s^{-1} was observed during the test. The in-plane shear strength of the seven materials exhibited trends that were similar to the tensile strengths up to 100 in/s. However, at higher rates, the behavior was observed to be material dependent. Some materials exhibited an increase in strength, while the rest suffered a decrease in strength. A change in failure mode was observed for the fabric-reinforced Newport and Toray materials, where the fracture path meandered away from the minimum section, indicating a change in failure mechanism. Additional investigation into dynamic loading and failure propagation is warranted to rule out the possibility of fixture-related effects on the failure modes at the higher rates.

The in-plane compression tests revealed the dependence of both strength and modulus of the materials on strain rates. The increases in strength were not as significant as the tensile and shear properties, which supports the observations of rate insensitivity of EA devices, wherein the primary loading occurs in compression. However, the failure modes were observed to depend on the type of reinforcement and strain rate. The unidirectional material tended to undergo end-crushing-initiated split across interlaminar planes and along planes parallel to the fiber direction in off-axis specimens. However, the material systems reinforced by fabrics exhibited the formation of kink bands at certain strain rates, while in an equal number of instances exhibited interlaminar splitting. The stiffness of all material systems exhibited a pronounced sensitivity to the strain rate.

Constant strain rate sensitivity of composite materials during compressive loading was determined using a standard size test coupon and the high-rate, servo-hydraulic test machine. High strain rate sensitivity of composite materials during compressive loading used subscale specimens and a Split-Hopkinson Pressure Bar apparatus. The small specimen size may be prone to end and edge effects due to constraints in the load introduction region—gripping for tension tests and contact deformation for compression tests. These constraints may produce three dimensional stress fields that may not dissipate in the gage region. The rate effects and failure modes could be influenced by these constraint effects. A study addressing the scaling of specimen size (length and width) must be conducted in subsequent phases to validate the current observations or impose restrictions on their use.

7. REFERENCES.

1. Farley, G.L., Bird, R.K., and Modlin, J.T., "The Role of Fiber and Matrix in Crash Energy Absorption of Composite Materials," *Journal of the American Helicopter Society*, April 1989.

2. Farley, G.L., "Energy Absorption Capability and Scalability of Square Cross-Section Tube Specimens," *Journal of the American Helicopter Society*, April 1989.

3. Carden, Huey D. and Hayduk, R.J., "Airplane Subfloor Response to Crash Loadings," *SAE Technical Paper 810614*.

4. Farley, G.L., "Crash Energy Absorbing Sub-Floor Beam Structures," *Journal of the American Helicopter Society*, October 1987.

5. Farley, G.L. and Jones, R.M., "Crushing Characteristics of Composite Tubes With 'Near Elliptical' Cross-Sections," *Journal of Composite Materials*, Vol. 26, No. 12, 1992, pp. 1741-1751.

6. Karbhari, V.M., "Progressive Crush Response of Multi-Element Foam Filled Perform RTM Structures," *Journal of Composite Materials*, Vol. 29, No. 6, 1996, pp. 734-750.

7. Raju, S. and Tomblin, J.S., "Energy Absorption Characteristics of Stitched Composite Sandwich Panels," *Journal of Composite Materials*, Vol. 33, No. 8, 1999, pp. 712-728.

8. Thornton, P.H., "Energy Absorption in Composite Structures," *Journal of Composite Materials*, Vol. 13, 1979.

9. Quek, C. and Waas, A.M., "Energy Absorption of Braided Glass Reinforced Composite Tubes," *Dynamic Failure in Composite Materials and Structures*, ASME 2000 AMD-Vol. 243.

10. Hull, D., "A Unified Approach to Progressive Crushing of Fibre-Reinforced Composite Tubes," *Composites Science & Technology*, Vol. 40, 1991.

11. Bannerman, D.C. and Kindervater, C.M., "Crashworthiness Investigation of Composite Aircraft Subfloor Beam Sections," *Structural Impact and Crashworthiness*, Vol. 2, Morton J., ed., Elsevier Applied Science Publication, 1984.

12. Bolukbasi, A.O. and Laananen, D.H., "Energy Absorption in Composite Stiffeners," *Composites*, Vol. 26, 1995.

13. Farley, G.L., "The Effects of Crushing Speed on the Energy Absorption Capability of Composite Tubes," *Journal of Composite Materials*, Vol. 25, 1991.

14. Mamalis A.G., Yuan Y.B., and Viegelahn, G.L., "Collapse of Thin-Wall Composite Sections Subject to High Speed Axial Loading," *International Journal of Vehicle Design*, Vol. 13, 1992.

15. Boitnott, R.L. and Kindervater, C., "Crashworthy Design of Helicopter Airframe Structures," U.S. Army Aviation Research and Technology Activity, Langley Research Center, Hampton, Virginia, 1989.

16. Kellas, S., "An Experimental Investigation Into the Energy Absorption Performance of Composite Beam Webs for Aircraft Subfloor Applications," Proceedings, National Technical Specialists' Meeting on Advanced Rotorcraft Structures, American Helicopter Society, 1995.

17. Johnson, A.F., Kindervater, C.M., and Jackson, K.E., "Multifunctional Design Concepts for Energy Absorbing Composite Fuselage Sub-Structures," *53rd Annual Forum*, American Helicopter Society, 1997.

18. PAM-CRASH, Engineering Systems International SA, F-94588 Rungis, France.

19. Carruthers, J.J., Kettle, A.P., and Robinson, A.M., "Energy Absorption Capability and Crashworthiness of Composite Material Structures," *Applied Mechanics Reviews*, Vol. 51, No. 10, October 1998.

20. Hayes, S.V. and Adams, D.F., "Rate Sensitive Impact Properties of Fully and Partially Loaded Unidirectional Composites," *Journal of Testing and Evaluation*, Vol. 10, No. 2, 1982, pp. 61-68.

21. Daniel, I.M. and Liiber, T., "Testing Fiber Composites at High Strain Rates," *Proc. 2nd International Conference on Composite Materials*, ICCM-II, Toronto, Canada, 1978, pp. 1003-1018.

22. Peterson, B.L., Pangborn, R.N., and Pantano, C.G., "Static and High Strain Rate Response of a Glass Fiber Reinforced Thermoplastic," *Journal of Composite Material*, Vol. 25, 1991, pp. 887-906.

23. Peijs, T., Smets, E.A.M., and Govaert, L.E., "Strain Rate and Temperature Effects on Energy Absorption of Polyethylene Fibers and Composites," *Applied Composite Materials*, Vol. 11, 1994, pp. 35-54.

24. Oguni, K. and Ravichandran, G., "Dynamic Compressive Failure of Unidirectional E-Glass/Vinylester Composites," *Dynamic Failure in Composite Materials and Structures*, AMD- Vol. 243, ASME 2000, pp. 1-11.

25. Tsai, Jialin and Sun, C.T., "Strain Rate Effect on Dynamic Compressive Failures in Off-Axis Glass-Epoxy Composites," *Dynamic Failure in Composite Materials and Structures*, AMD- Vol. 243, ASME 2000, pp. 13-24.

26. Hsiao, H.M., Daniel, I.M., and Cordes, R.D., "Strain Rate Effects on the Transverse Compressive and Shear Behavior of Unidirectional Composites," *Journal of Composite Materials*, Vol. 33, No.17, 1999, pp. 1620-1642.

27. Kolsky, H., "An Investigation of the Mechanical Properties of Materials at Very High Rates of Loading," *Proceedings of the Royal Society*, London, Vol. 58, 1949, pp.1405-1410.

28. Li, Zhouhua and Lambros, John, "Determination of the Dynamic Response of Brittle Composites by the use of the Split Hopkinson Pressure Bar," *Composites Science and Technology*, Vol. 59, No. 7, 1999, pp. 1097-1107.

29. Barre S., Chotard T., and Benzeggagh M.L., "Comparative Study of Strain Rate Effects on Mechanical Properties of Glass Fibre-Reinforced Thermoset Composites," *Composites* Part A 996; 27A.1169

30. Rotem, A. and Lifshitz, J.M., "Longitudinal Strength of Unidirectional Fibrous Composites Under High Rate of Loading," *Proc. 26th Annual Tech. Conf., Soc. Plastics Industry, Reinforced Plastics/Composites Division*, Washington, DC, 1971, Section 10G, pp. 1-10.

31. Armenakas, A.E. and Sciammarella, C.A., "Response of Glass-Fiber Reinforced Epoxy Specimens to High Rates of Tensile Loading," *Experimental Mechanics*, Vol. 13, 1973, pp. 433-440.

32. Hayes, S.V. and Adams, D.F., "Rate Sensitive Tensile Impact Properties of Fully and Partially Loaded Unidirectional Composites," *Journal of Testing and Evaluation*, Vol. 10, No.2, 1982, pp. 61-68.

33. Staab, H. and Gilat, A., "High Strain Rate Response of Angle-Ply Glass/Epoxy Laminates," *Journal of Composite Materials*, Vol. 29, No. 10, 1995.

34. Gilat, A. and Goldberg, R.K., "Experimental Study of Strain Rate Dependent Behavior of Carbon/Epoxy Composite," *Composites Science and Technology*, Vol. 62, 2002, pp 1469-1476.

35. Papadakis, N., Reynolds, N., Pharaoh, M.W., Wood, P.K.C., and Smith, G.F., "Strain Rate Effects on the Shear Mechanical Properties of a Highly Oriented Thermoplastic Composite Material Using a Contacting Displacement Measurement Methodology," *Composites Science and Technology*, Vol. 64, Issue 5, April 2004, pp. 729-738.

36. Toray Composites (America), Inc., 19002 50th Avenue East, Tacoma, Washington 98446.

37. Newport Adhesives & Composites, Inc., 1822 Reynolds Avenue, Irvine, California 92614-5714.

38. Nelcote, Inc., 172 East Aurora Street, Waterbury, Connecticut 06708.

39. Cytec Engineered Materials, Inc., 4300 Jackson Street, Greenville, Texas 75401.

40. MTS Systems Corporation, Eden Prairie, Minnesota 55344.

41. Vishay Intertechnology, Inc., 63 Lancaster Avenue, Malvern, Pennsylvania 19355-2143.

42. PCB Piezotronics, Depew, New York 14043-2495. www.pcb.com

43. National Instruments, 11500 N. Mopac Expressway, Austin, Texas 78759-3504.

44. ASTM D 3039, "Standard Test Method for Tensile Properties of Polymer Matrix Composite Materials," ASTM International, 100 Barr Harbor Drive, P.O. Box C700, West Conshohocken, Pennsylvania 19428-2959.

45. Hoffman, J.D., *Numerical Methods for Engineers and Scientists*, McGraw Hill, Inc., 1992.

46. ASTM D 7078/D 7078M-05, "Standard Test Method for Shear Properties of Composite Materials by V-Notched Rail Shear Method," *ASTM Book of Standards*, Vol. 15.03, 2005.

47. ASTM D 5379/D 5379M-05 Standard Test Method for Shear Properties of Composite Materials by V-Notched Beam Method, ASTM Book of Standards, Vol. 15.03, 2005.

48. Ruiz, C. and Harding, J., *Modeling Impact of Composite Structures Using Small Specimens, Chapter 3, Impact Behavior of Fibre-Reinforced Composite Materials and Structures*, Reid, S.R. and Zhou, G., ed., CRC Press, 2000.

49. Altair Engineering, Inc., 1820 Big Beaver Road, Troy, Michigan 48085.

50. Graff, K.F., *Wave Motion in Elastic Solids*, Dover Publications.

51. Parry, D.J., Walker, A.G., and Dixon, P.R., "Hopkinson Bar Pulse Smoothing," *Measured Science and Technology*, Vol. 6, 1995, pp. 443-446.

52. Frew, D.J., Forrestal, M.J., and Chen, W., "Pulse Shaping Techniques for Testing Brittle Materials With a Split-Hopkinson Pressure Bar," *Experimental Mechanics*, 2000, pp. 93-105.

53. Bertholf, L.D. and Karnes, C.H., "Two Dimensional Analysis of the Split Hopkinson Pressure Bar System," *J. Mech. Phys. Solids*, Vol. 23, 1974, pp. 1-19.

APPENDIX A—TENSION TEST DATA

Table A-1. Tensile Strengths at Quasi-Static Rate of Testing

Material	Specimen Orientation			
	$[0°]_N$	$[+15°/-15°]_{NS}$	$[+30°/-30°]_{NS}$	$[+45°/-45°]_{NS}$
Newport NB321/7781	62.29 63.41 72.58	56.12 64.03 61.68	45.75 45.24 44.86	33.55 34.53 32.10
Newport NB321/3K70P	107.93 111.02 118.73	83.39 79.46 78.79	53.67 56.18 59.59	31.55 31.96 32.31
Newport NCT321/G150 Unitape	304.20 289.25 249.86	163.89 160.34 155.48	80.65 82.30 83.07	37.85 36.62 37.13
Toray T800S/3900-2B Unitape	428.40 386.31 423.75	219.76 229.76 235.11	96.06 94.23 100.21	36.16 34.26 37.83
Toray T700G-12K- PW/3900-2	101.21 98.83 143.64	101.66 96.10 85.75	62.37 67.16 65.85	43.63 34.54 41.72
Fibercote 3KPW-E365-PWCF	116.16 128.10 *	85.51 83.61 *	62.70 63.21 57.78	28.94 27.70 26.92
Cytec T300/7714AC 3KNT	127.86 135.86 127.60	88.37 96.21 93.72	56.00 58.26 58.53	27.00 28.61 25.94

Note: Units of strength: $\times 10^3 \text{lbf/in}^2$
*Invalid test—strength data not available

Table A-2. Tensile Modulii at Quasi-Static Rate of Testing

Material	Specimen Orientation			
	$[0°]_N$	$[+15°/-15°]_{NS}$	$[+30°/-30°]_{NS}$	$[+45°/-45°]_{NS}$
Newport NB321/7781	2.837 3.113 3.072	1.931 1.951 1.885	1.732 1.800 1.790	1.622 1.612 1.617
Newport NB321/3K70 PWCF	6.649 6.887 6.226	5.536 6.545 5.948	3.411 3.569 3.253	* 1.674 1.727
Newport NCT321/G150 Unitape	16.20 16.95 16.68	12.380 12.389 12.271	4.708 4.749 4.756	1.791 1.792 1.796
Toray T800S/3900-2B Unitape	17.19 19.17 19.15	14.971 15.170 15.172	5.150 5.200 5.440	1.891 1.930 2.050
Toray T700G-12K-PW/3900-2	7.297 6.779 8.060	6.470 6.050 6.288	3.205 3.558 3.493	1.771 1.823 1.840
Fibercote 3KPW-E365 PWCF	9.178 9.095 8.738	7.634 7.979 *	4.349 4.606 4.512	2.275 2.236 2.229
Cytec T300/7714AC 3KNT	9.495 9.515 9.399	8.688 8.604 8.768	4.715 4.451 4.790	1.947 2.073 1.995

Note: Units of modulus equal $\times 10^6$ psi.
*Strain gage failure/invalid test.

Table A-3. Summary of Tensile Strength for Newport NB321/7781 Fiberglass Material

Nominal Stroke Rate (in/s)	Orientation			
	$[0°]_N$	$[+15°/-15°]_{NS}$	$[+30°/-30°]_{NS}$	$[+45°/-45°]_{NS}$
1	85.37	73.40	52.74	41.00
	93.29	69.86	52.58	39.90
	86.06	79.37	52.90	40.22
10	100.94	71.46	53.86	43.10
	108.02	79.76	55.82	41.22
	96.16	74.63	54.93	42.18
100	171.63	133.33	108.55	76.59
	160.73	138.50	96.31	77.45
	157.12	124.34	108.35	81.09
250	206.45	114.57	87.11	56.84
	205.50	111.59	77.65	55.54
	220.27	117.80	82.71	59.66
		113.42	90.97	62.19
		108.65	94.84	63.77
500	186.16	116.23	89.38	54.83
	181.19	134.39	88.13	51.73
	176.53	106.65	90.07	57.20
	171.90	136.45	89.16	64.05
	172.29	124.63		70.27

Note: Units of strength: $\times 10^3 \text{lbf/in}^2$

Table A-4. Summary of Tensile Strength for Newport NB321/3K70 Plain Weave Carbon Fabric (PWCF) Material

Nominal Stroke Rate (in/s)	Orientation			
	$[0°]_N$	$[+15°/-15°]_{NS}$	$[+30°/-30°]_{NS}$	$[+45°/-45°]_{NS}$
1	99.96	82.01	59.76	37.24
	115.97	79.56	64.00	37.10
	115.10	*	63.94	35.44
10	110.05	88.18	60.15	38.54
	109.20	76.65	66.00	38.85
	118.09	80.74	64.84	36.79
100	138.53	211.00	161.84	81.96
	193.33	178.67	151.52	83.25
	179.14	161.83	149.20	72.07
250	75.55	86.82	86.90	107.48
	87.68	98.27	98.39	*
	69.38	87.68	102.48	94.89
500	91.39	81.97	82.04	61.02
	88.00	73.70	83.91	63.72
	88.61	90.78	105.56	61.01

Note: Units of strength: $\times 10^3 \text{lbf/in}^2$
*Invalid test—strength data not available

Table A-5. Summary of Tensile Strength for Newport NCT321/G150 Unitape Material

Nominal Stroke Rate (in/s)	Orientation			
	$[0°]_N$	$[+15°/-15°]_{NS}$	$[+30°/-30°]_{NS}$	$[+45°/-45°]_{NS}$
1	271.05	187.01	100.35	43.46
	238.26	188.42	105.30	42.09
	229.62	160.41	97.99	43.53
10	270.61	182.27	103.17	45.08
	334.29	199.07	97.11	45.76
	271.42	191.59	96.56	47.16
100	590.43	357.18	226.17	93.79
	580.25	353.81	218.45	80.21
	557.85	381.45	222.53	92.68
250	489.98	*	192.55	106.92
	361.04	225.43	206.71	126.19
	458.35	259.76	234.46	120.31
500	473.59	215.66	184.32	77.11
	455.33	317.23	181.18	66.45
	462.21	342.30	203.75	80.25

Note: Units of strength: $\times 10^3$ lbf/in^2
*Invalid test—strength data not available

Table A-6. Summary of Tensile Strength for Toray T800S/3900-2B Unitape Material

Nominal Stroke Rate (in/s)	Orientation			
	$[0°]_N$	$[+15°/-15°]_{NS}$	$[+30°/-30°]_{NS}$	$[+45°/-45°]_{NS}$
1	459.97	219.31	133.55	40.54
	400.02	226.66	109.31	33.77
	464.60	203.54	116.14	43.77
10	508.02	232.25	124.49	44.78
	527.20	213.74	130.46	47.90
	478.91	220.77	126.20	42.96
100	815.61	499.91	203.18	93.36
	824.76	486.83	209.50	88.00
	787.95	456.08	221.59	109.76
250	936.48	398.29	268.05	112.01
	857.07	316.35	275.05	107.45
	731.12	322.17	255.39	91.25
500	729.31	246.47	202.79	59.77
	674.21	258.50	209.35	59.81
	846.35	225.89	205.99	66.42
		292.81	221.64	76.49
		263.29	232.26	

Note: Units of strength: $\times 10^3$ lbf/in^2

Table A-7. Summary of Tensile Strength for Toray T700G-12K-PW/3900-2 Material

Nominal Stroke Rate (in/s)	Orientation			
	$[0°]_N$	$[+15°/-15°]_{NS}$	$[+30°/-30°]_{NS}$	$[+45°/-45°]_{NS}$
1	138.70	98.85	65.21	48.76
	91.68	104.45	69.04	43.47
	95.38	98.05	71.48	46.58
10	135.60	101.82	70.03	53.12
	122.01	101.24	73.14	49.96
	96.86	101.85	74.47	51.07
100	242.57	176.93	164.24	87.02
	307.25	229.75	176.90	84.12
	209.85	243.95	174.86	99.99
250	114.54	133.32	133.53	109.10
	105.09	142.39	138.08	117.74
	*	180.59	127.42	123.04
500	112.10	92.76	82.41	66.92
	128.40	109.14	89.89	67.42
	87.66	102.83	97.19	66.66
		122.82	106.72	83.50

Note: Units of strength: $\times 10^3 \text{lbf/in}^2$
*Invalid test—strength data not available

Table A-8. Summary of Tensile Strength for Fibercote 3KPW-E365 PWCF Material

Nominal Stroke Rate (in/s)	Orientation			
	$[0°]_N$	$[+15°/-15°]_{NS}$	$[+30°/-30°_{NS}$	$[+45°-45°_{NS}$
1	126.78	86.88	70.96	38.23
	104.90	92.98	66.14	37.52
	126.59	87.36	71.57	37.49
10	136.85	89.07	72.40	38.58
	137.29	90.92	69.42	38.89
	123.62	84.39	72.02	38.97
100	213.30	212.11	198.32	92.14
	239.70	252.29	171.98	103.09
	231.65	225.11	193.82	116.23
250	95.39	70.29	63.76	65.00
	101.17	89.07	84.55	66.54
	104.56	86.79	86.17	64.88
	162.09			72.83
	148.87			82.08
500	101.37	91.26	83.77	57.31
	100.04	83.92	74.93	60.97
	118.68	93.33	70.19	57.61
	130.11	90.39	88.32	72.88
	147.10	100.60		73.44

Note: Units of strength: $\times 10^3$ lbf/in^2

Table A-9. Summary of Tensile Strength for Cytec T300/7714AC 3KNT Material

Nominal Stroke Rate (in/s)	Orientation			
	$[0°]_N$	$[+15°/-15°]_{NS}$	$[+30°/-30°]_{NS}$	$[+45°/-45°]_{NS}$
1	163.33	93.99	63.43	34.79
	138.88	99.09	61.13	35.59
	153.25	101.44	62.31	32.75
10	155.61	107.60	95.02	35.56
	165.97	107.51	94.65	36.15
	158.06	98.25	68.19	34.73
100	202.85	152.34	125.49	67.51
	193.82	120.25	119.35	70.66
	198.05	150.25	128.60	73.57
250	203.67	109.64	117.24	60.53
	166.25	115.06	109.63	51.86
	230.87	116.34	113.00	50.88
500	135.54	98.22	99.49	61.89
	165.49	158.39	97.29	62.30
	148.57	*	105.24	60.36
	154.41			

Note: Units of strength: $\times 10^3 \text{lbf/in}^2$
*Invalid test—strength data not available

Table A-10. Summary of Failure Strains and Average Strain Rate for Newport NB321/7781 Fiberglass Material

Nominal Stroke Rate (in/s)	Orientation							
	$[0°]_N$		$[+15°/-15°]_{NS}$		$[+30°/-30°]_{NS}$		$[+45°/-45°]_{NS}$	
8×10^{-4}	0.0278	(0.00039)	0.0268	(0.00033)	0.0428	(0.00041)	-	(0.00038)
	0.0259	(0.00036)	0.0312	(0.00033)	0.0424	(0.00040)	-	(0.00041)
	0.0285	(0.00037)	0.0300	(0.00033)	0.0404	(0.00038)	-	(0.00041)
1	0.0252	(0.28)	0.0303	(0.22)	0.0425	(0.3)	-	(0.4)
	0.0272	(0.27)	0.0297	(0.22)	0.0418	(0.29)	-	(0.42)
	0.0128	(0.16)	0.0291	(0.22)	0.0420	(0.3)	-	(0.4)
10	0.0222	(2.06)	0.0287	(1.59)	0.0403	(2.32)	-	(2.59)
	0.0286	(2.25)	0.0310	(1.66)	0.0443	(2.59)	-	(3.33)
	0.0321	(2.31)	0.0295	(1.54)	0.0357	(2.43)	-	(3.33)
100	0.0183	(52.14)	0.0351	(47.11)	0.0432	(60.44)	-	(82.9)
	0.0357	(58.19)	0.0325	(47.43)	0.0311	(59.44)	-	(68.9)
	0.0390	(51.09)	0.0375	(50.07)	0.0420	(56.3)	-	(82.69)
250	0.0366	(88.9)	0.0275	(90.89)	0.0290	(130.86)	-	(154.95)
	0.0299	(99.51)	0.0217	(115.02)	0.0280	(141.82)	-	(158.83)
	0.0326	(89.75)	0.0178	(129.8)	0.0389	(129.15)	-	(144.66)
500	0.0396	(140.68)	0.0231	(113.19)	0.0379	(150.33)	-	(158.45)
	0.0117	(144.19)	0.0344	(116.05)	0.0410	(145.21)	-	(118.86)
	0.0296	(163.37)	0.0306	(115.23)	0.0336	(157.8)	-	(184.62)

Note: The number in the parenthesis is the average strain rate. The failure strain for $[+45°/-45°]_{NS}$ exceeded the capability of the strain gage and thus is not reported.

Table A-11. Summary of Failure Strains and Average Strain Rate for Newport NB321/3K70 PWCF

Nominal Stroke Rate (in/s)	Orientation							
	$[0°]_N$		$[+15°/-15°]_{NS}$		$[+30°/-30°]_{NS}$		$[+45°/-45°]_{NS}$	
8×10^{-4}	0.0146	(.000330)	0.0142	(.000277)	0.0185	(.000349)	-	(.000895)
	0.0148	(.000320)	0.0124	(.000256)	0.0198	(.000368)	-	(.000695)
	0.0165	(.000316)	0.0133	(.000279)	0.0074	(.000126)	-	(.000597)
1	0.0111	(.180)	0.0106	(.15)	0.0167	(.22)	-	(.28)
	0.0126	(.175)	0.0113	(.16)	0.0170	(.23)	-	(.40)
	0.0123	(.174)	*	*	*	*	-	(.42)
10	0.0125	(1.225)	0.0112	(1.06)	0.0149	(1.42)	-	(3.29)
	0.0118	(1.215)	0.0103	(.98)	0.0177	(1.57)	-	(3.17)
	0.0121	(1.229)	0.0109	(1.01)	0.0146	(1.42)	-	(3.33)
100	0.0111	(59.318)	0.0113	(42.23)	0.0177	(49.19)	-	(64.62)
	0.0123	(61.306)	0.0113	(48.03)	0.0182	(55.91)	-	(72.93)
	0.0121	(61.513)	0.0123	(52.60)	0.0179	(59.49)	-	(75.22)
250	*	*	0.0115	(91.99)	0.0166	(102.75)	-	(131.15)
	*	*	0.0120	(93.11)	0.0195	(116.54)		
	*	*	0.0117	(94.36)	0.0178	(98.90)	-	(121.78)
500	0.0125	(111.691)	0.0101	(96.42)	0.0172	(138.62)	-	(146.76)
	0.0189	(149.682)	0.0112	(89.94)	0.0182	(113.70)	-	(161.20)
	0.0119	(100.830)	0.0116	(93.99)	0.0183	(113.41)	-	(480.10)

Note: The number in the parenthesis is the average strain rate. The failure strain for $[+45°/-45°]_{NS}$ exceeded the capability of the strain gage and is thus not reported.
*Strain gage failure

Table A-12. Summary of Failure Strains and Average Strain Rate for Newport NCT321/G150 Unitape Material

Nominal Stroke Rate (in/s)	Orientation							
	$[0°]_N$		$[+15°/-15°]_{NS}$		$[+30°/-30°]_{NS}$		$[+45°/-45°]_{NS}$	
8×10^{-4}	0.0135	(0.0004)	0.0134	(0.0001)	0.0270	(0.0003)	-	(0.0004)
	0.0101	(0.0004)	0.0131	(0.0001)	0.0296	(0.0003)	-	(0.0004)
	0.0139	(0.0004)	0.0128	(0.0001)	0.0298	(0.0003)	-	(0.0003)
1	0.0139	(0.16)	0.0123	(0.13)	0.0221	(0.26)	-	(.31)
	0.0131	(0.17)	0.0124	(0.12)	0.0235	(0.26)	-	(.35)
	0.0115	(0.16)	0.0108	(0.12)	0.0253	(0.28)	-	(.31)
10	0.0138	(1.00)	0.0119	(0.71)	0.0232	(1.81)	-	(3.43)
	0.0156	(0.90)	0.0120	(0.7)	0.0259	(2.04)	-	(3.55)
	0.0134	(1.05)	0.0131	(0.74)	0.0212	(1.77)	-	(3.43)
100	0.0157	(39.47)	0.0129	(34.9)	0.0218	(56.29)	-	(77.53)
	0.0134	(18.97)	0.0118	(37.39)	0.0204	(52.1)	-	(80.81)
	0.0149	(38.34)	0.0130	(34.52)	0.0206	(52.35)	-	(80.52)
250	0.0137	(74.36)	0.0120	(66.34)	0.0201	(98.14)	-	(138.23)
	0.0132	(84.25)	0.0111	(85.66)	0.0226	(104.25)	-	(107.14)
	0.0140	(86.83)	0.0102	(90.49)	0.0264	(119.1)	-	(111.83)
500	0.0146	(116.22)	0.0115	(94.03)	0.0246	(130.03)	-	(180.42)
	0.0128	(120.34)	0.0103	(46.51)	0.0250	(134.86)	-	*
	0.0130	(100.27)	0.0115	(81.07)	0.0250	(188.98)	-	(191.93)

Note: The number in the parenthesis is the average strain rate. The failure strain for $[+45°/-45°]_{NS}$ exceeded the capability of the strain gage and is thus not reported.

Table A-13. Summary of Failure Strains and Average Strain Rate for Toray T800S/3900-2B Unitape Material

Nominal Stroke Rate (in/s)	Orientation							
	$[0°]_N$		$[+15°/-15°]_{NS}$		$[+30°/-30°]_{NS}$		$[+45°/-45°]_{NS}$	
8×10^{-4}	0.0210	(0.0002)	0.0147	(0.0002)	0.0345	(0.0004)	-	(0.0004)
	0.0178	(0.0002)	0.0152	(0.0002)	0.0235	(0.0004)	-	(0.0006)
	0.0194	(0.0002)	0.0155	(0.0002)	0.0337	(0.0004)	-	(0.0004)
1	0.0180	(0.18)	0.0125	(0.16)	0.0273	(0.25)	-	(0.46)
	0.0158	(0.18)	0.0133	(0.17)	0.0243	(0.24)	-	(0.37)
	0.0168	(0.19)	0.0108	(0.16)	0.0328	(0.28)	-	(0.39)
10	0.0177	(1.06)	0.0135	(1.07)	0.0200	(1.42)	-	(2.99)
	0.0188	(1.13)	0.0120	(1.03)	0.0174	(1.40)	-	(3.03)
	0.0169	(1.17)	0.0114	(1.00)	0.0191	(1.42)	-	(3.33)
100	0.0173	(44.19)	0.0132	(42.33)	0.0200	(47.55)	-	(53.06)
	0.0182	(43.86)	0.0131	(50.77)	0.0217	(47.65)	-	(52.21)
	0.0168	(41.09)	0.0112	(48.95)	0.0260	(51.28)	-	(55.71)
250	0.0181	(76.14)	0.0144	(81.14)	0.0346	(99.20)	-	(90.70)
	0.0185	(86.96)	0.0128	(80.83)	*	*	-	(81.11)
	0.0160	(81.43)	0.0125	(73.97)	0.0101	(93.45)	-	(92.59)
500	0.0177	(108.99)	0.0139	(122.31)	0.0214	(125.23)	-	(164.00)
	0.0168	(101.65)	0.0140	(122.08)	0.0260	(132.72)	-	(172.24)
	*	*	0.0141	(127.54)	0.0255	(125.45)	-	(125.45)

Note: The number in the parenthesis is the average strain rate. The failure strain for $[+45°/-45°]_{NS}$ exceeded the capability of the strain gage and thus, is not reported.
*Strain gage failure

Table A-14. Summary of Failure Strains and Average Strain Rate for Toray T700G-12K-PW/3900-2 Material

Nominal Stroke Rate (in/s)	Orientation							
	$[0°]_N$		$[+15°/-15°]_{NS}$		$[+30°/-30°]_{NS}$		$[+45°/-45°]_{NS}$	
8×10^{-4}	0.0129	(.000335)	0.0154	(.000262)	0.0232	(.000379)	-	(.000582)
	0.0134	(.000339)	0.0154	(.000261)	0.0210	(.000316)	-	(.000391)
	0.0165	(.000304)	0.0130	(.000267)	0.0213	(.000325)	-	(.000553)
1	0.0121	(.17)	0.0124	(.16)	0.0164	(.21)	-	(.34)
	0.0098	(.16)	0.0137	(.16)	0.0164	(.21)	-	(.48)
	0.0098	(.16)	0.0123	(.15)	0.0176	(.22)	-	(.54)
10	0.0120	(1.17)	0.0125	(1.00)	0.0175	(1.55)	-	(2.76)
	0.0122	(1.21)	0.0131	(1.05)	0.0195	(1.69)	-	(3.48)
	0.0103	(1.14)	0.0122	(.96)	0.0170	(1.45)	-	(2.74)
100	0.0119	(52.59)	0.0109	(49.32)	0.0157	(54.64)	-	(68.29)
	0.0137	(53.12)	0.0122	(44.57)	0.0158	(52.74)	-	(64.10)
	0.0125	(57.26)	0.0101	(53.75)	0.0175	(53.76)	-	(68.65)
250	0.0063	(49.83)	0.0125	(79.15)	0.0187	(96.62)	-	(108.56)
	0.0112	(88.17)	0.0119	(75.54)	0.0192	(98.27)	-	(114.61)
	*	*	0.0136	(78.74)	0.0199	(100.95)	-	(108.64)
500	*	*	0.0122	(108.83)	0.0202	(129.47)	-	(195.94)
	0.0121	(97.97)	0.0123	(99.12)	0.0202	(129.47)	-	(157.82)
	*	*	0.0131	(107.39)	0.0204	(123.95)	-	(160.60)

Note: The number in the parenthesis is the average strain rate. The failure strain for $[+45°/-45°]_{NS}$ exceeded the capability of the strain gage and thus, is not reported.
*Strain gage failure

Table A-15. Summary of Failure Strains and Average Strain Rate for Fibercote 3KPW-E365 PWCF Material

Nominal Stroke Rate (in/s)	Orientation							
	$[0°]_N$		$[+15°/-15°]_{NS}$		$[+30°/-30°]_{NS}$		$[+45°/-45°]_{NS}$	
8×10^{-4}	0.0128	(0.0002)	0.0112	(0.0002)	0.0174	(0.0003)	-	(0.0004)
	0.0121	(0.0002)	0.0107	(0.0002)	0.0173	(0.0003)	-	(0.0004)
	0.0130	(0.0002)	*	*	0.0160	(0.0003)	-	(0.0006)
1	0.0075	(0.15)	0.0105	(0.14)	0.0078	(0.24)	-	(0.32)
	0.0104	(0.14)	0.0117	(0.13)	0.0178	(0.21)	-	(0.40)
	0.0128	(0.17)	0.0104	(0.13)	0.0415	(0.37)	-	(0.29)
10	0.0134	(1.23)	0.0103	(0.87)	0.0173	(1.46)	-	(2.43)
	0.0137	(1.22)	0.0110	(0.93)	0.0160	(1.41)	-	(1.41)
	0.0123	(1.21)	0.0092	(0.85)	0.0167	(1.45)	-	(2.73)
100	0.0133	(67.24)	0.0110	(45.70)	0.0174	(46.22)	-	(51.16)
	0.0128	(70.89)	0.0100	(43.11)	0.0162	(51.31)	-	(58.87)
	0.0125	(61.04)	0.0107	(40.73)	0.0167	(49.76)	-	(50.04)
250	0.0135	(122.08)	0.0158	(132.36)	0.0158	(139.00)	-	(120.59)
	0.0150	(134.47)	0.0110	(109.50)	0.0116	(113.73)	-	(136.78)
	0.0125	(122.86)	0.0119	(124.30)	0.0211	(152.04)	-	(120.80)
500	0.0141	(104.67)	0.0108	(92.95)	0.0175	(127.16)	-	(181.99)
	*	*	0.0113	(94.78)	0.0159	(111.68)	-	(176.39)
	0.0180	(160.99)	0.0112	(89.68)	0.0178	(159.14)	-	(182.51)

Note: The number in the parenthesis is the average strain rate. The failure strain for $[+45°/-45°]_{NS}$ exceeded the capability of the strain gage and thus, is not reported.
*Strain gage failure

Table A-16. Summary of Failure Strains and Average Strain Rate for Cytec T300/7714AC 3KNT Material

Nominal Stroke Rate (in/s)	Orientation							
	$[0°]_N$		$[+15°/-15°]_{NS}$		$[+30°/-30°]_{NS}$		$[+45°/-45°]_{NS}$	
8×10^{-4}	0.0128	(0.00019)	0.0106	(0.00016)	0.0172	(0.0003)	-	(0.0003)
	0.0138	(0.0002)	0.0119	(0.00016)	0.0167	(0.0002)	-	(0.0003)
	0.013	(0.0002)	0.0114	(0.00016)	0.0162	(0.0002)	-	(0.0004)
1	0.0149	(0.16)	0.012	(0.15)	0.0169	(0.11)	-	(0.34)
	0.0127	(0.15)	0.0114	(0.15)	0.0165	(0.11)	-	(0.35)
	0.0138	(0.16)	0.0115	(0.15)	0.0177	(0.13)	-	(0.24)
10	0.0137	(1.11)	0.0132	(1.07)	0.0038	(1.05)	-	(2.44)
	0.0141	(1.09)	0.0132	(1.07)	0.0046	(1.13)	-	(2.23)
	0.0143	(1.11)	0.0106	(0.93)	0.0182	(1.04)	-	(2.82)
100	0.0149	(44.54)	0.0129	(42.68)	0.0168	(45.73)	-	(30.28)
	0.0149	(44.61)	0.0114	(40.79)	0.0140	(41.55)	-	(37.97)
	0.0134	(47.07)	0.0115	(37.27)	0.0172	(39.71)	-	(57.73)
250	0.0141	(123.7)	0.0128	(108.44)	0.0150	(93.60)	-	(128.46)
	*	*	0.0097	(96.69)	0.0138	(83.79)	-	(124.05)
	*	*	*	*	0.0180	(87.29)	-	(111.05)
500	0.0126	(109.69)	0.0222	(116.96)	0.0163	(103.69)	-	(135.51)
	0.0313	(109.13)	0.0114	(92.49)	0.0174	(102.44)	-	(163.73)
	0.0126	(109.64)	0.0105	(77.12)	0.0179	(92.50)	-	(157.51)

Note: The number in the parenthesis is the average strain rate. The failure strain for $[+45°/-45°]_{NS}$ exceeded the capability of the strain gage and thus, is not reported.
*Insufficient strain data/gage failure

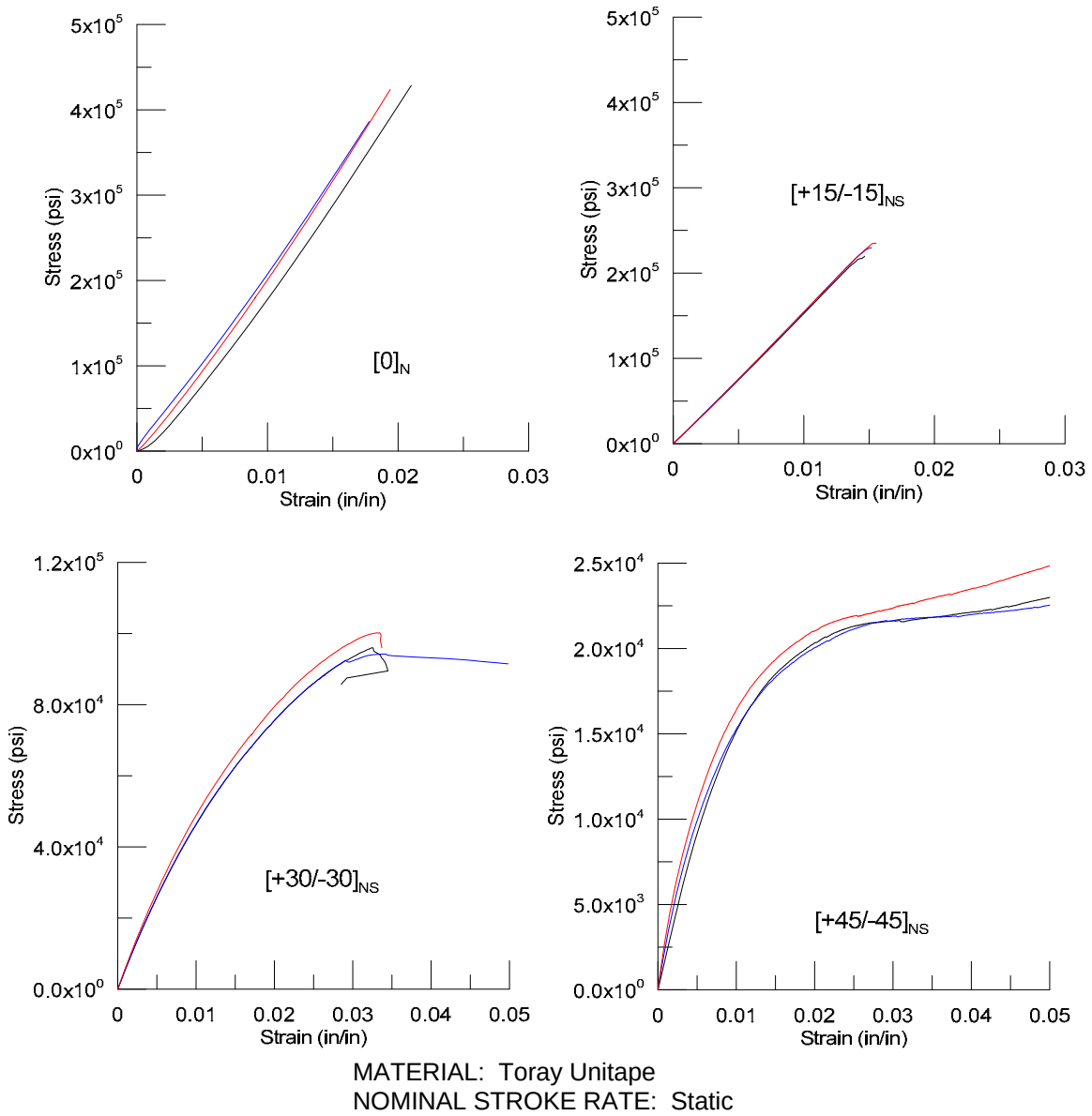

Figure A-1. Stress-Strain Diagrams for Toray Unitape Material Oriented at $[0°]_{NS}$, $[-15°/+15°]_{NS}$, $[-30°/+30°]_{NS}$, and $[-45°/+45°]_{NS}$ and Tested at a Rate of 0.001 in/s

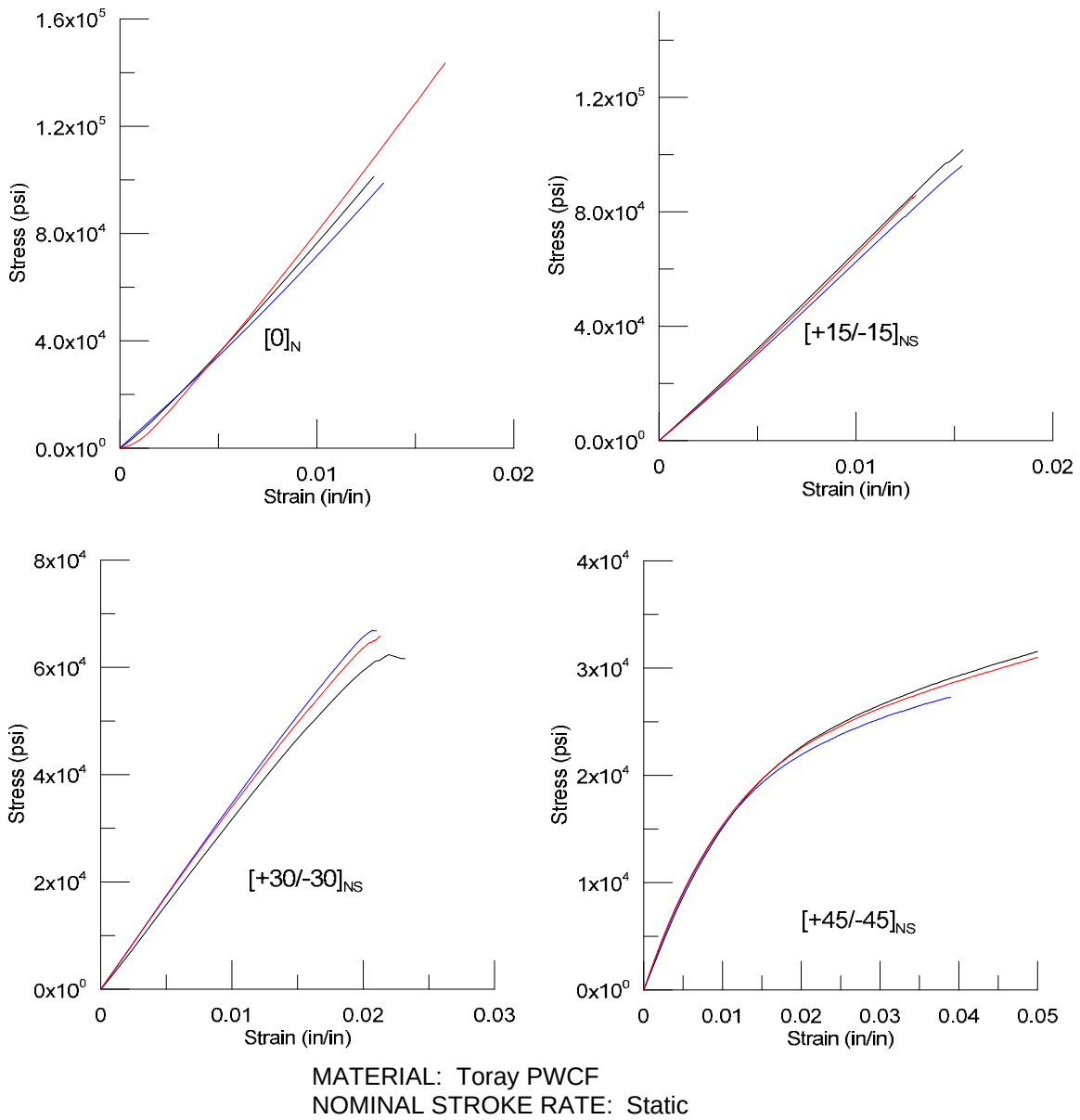

MATERIAL: Toray PWCF
NOMINAL STROKE RATE: Static

Figure A-2. Stress-Strain Diagrams for Toray PWCF Material Oriented at $[0°]_N$, $[-15°/+15°]_{NS}$, $[-30°/+30°]_{NS}$, and $[-45°/+45°]_{NS}$ and Tested at a Rate of 0.001 in/s

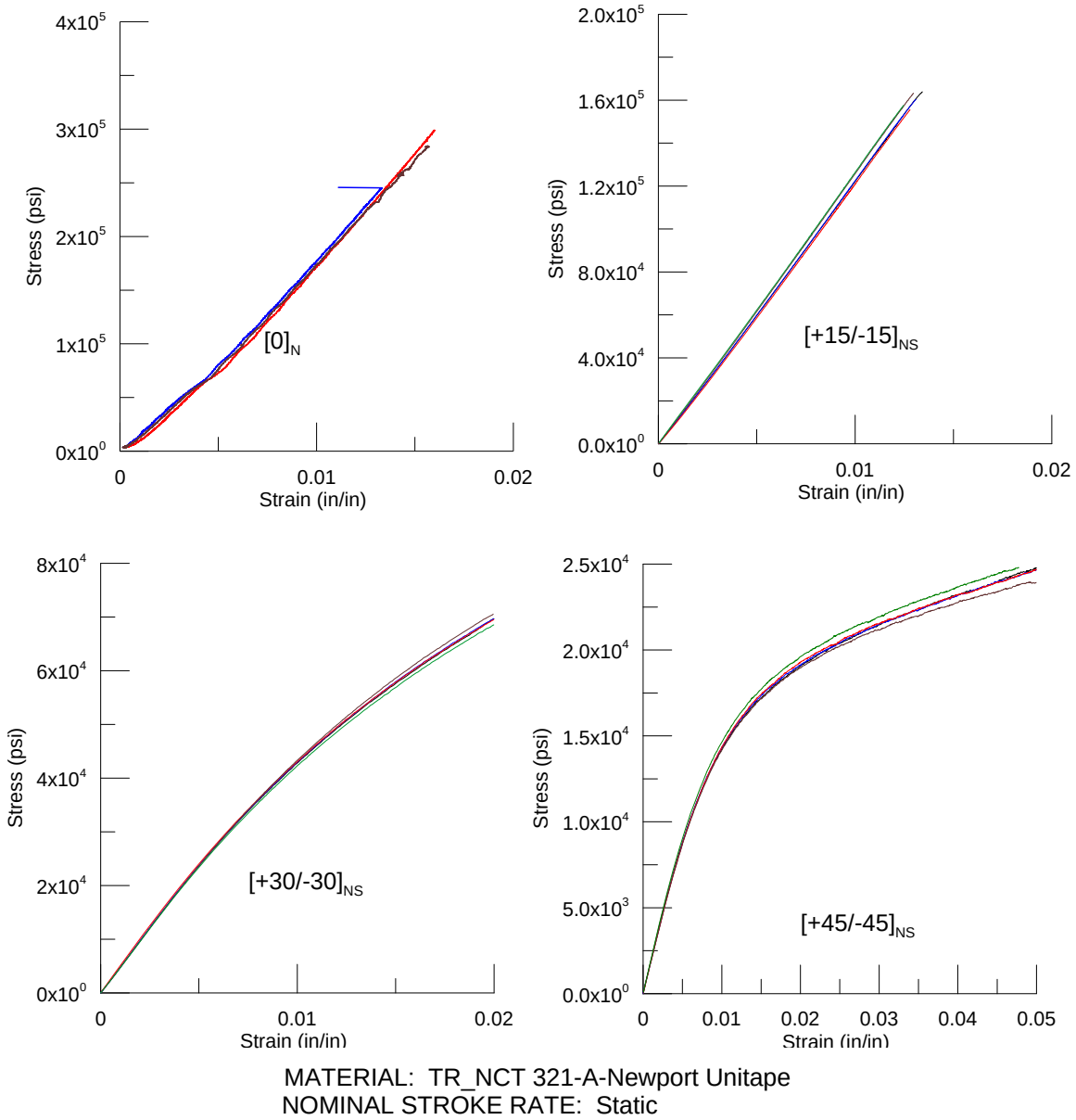

MATERIAL: TR_NCT 321-A-Newport Unitape
NOMINAL STROKE RATE: Static

Figure A-3. Stress-Strain Diagrams for Newport Unitape Material Oriented at $[0°]_N$, $[-15°/+15°]_{NS}$, $[-30°/+30°]_{NS}$, and $[-45°/+45°]_{NS}$ and Tested at a Rate of 0.001 in/s

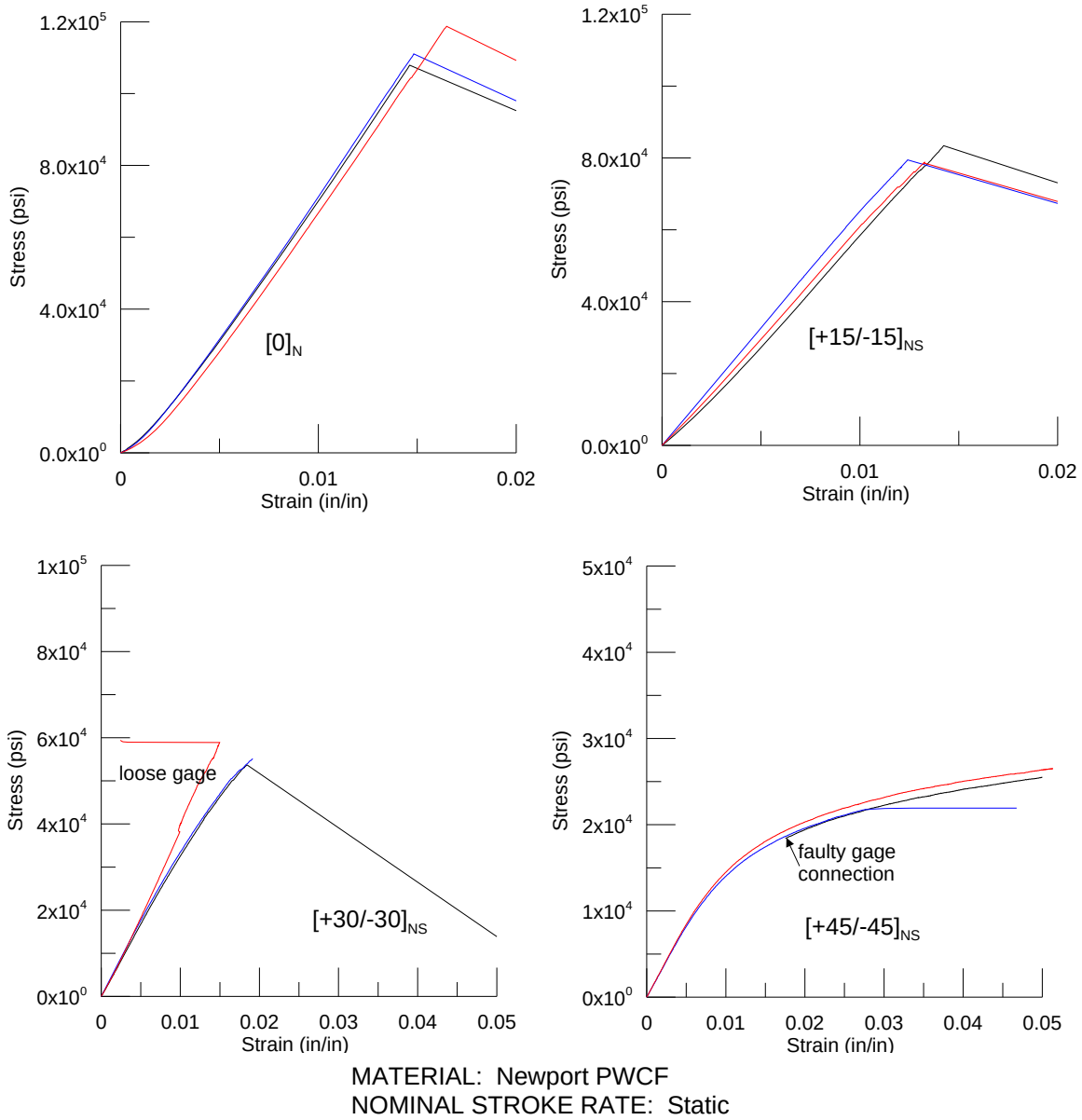

MATERIAL: Newport PWCF
NOMINAL STROKE RATE: Static

Figure A-4. Stress-Strain Diagrams for Newport PWCF Material Oriented at $[0°]_N$, $[-15°/+15°]_{NS}$, $[-30°/+30°]_{NS}$, and $[-45°/+45°]_{NS}$ and Tested at a Rate of 0.001 in/s

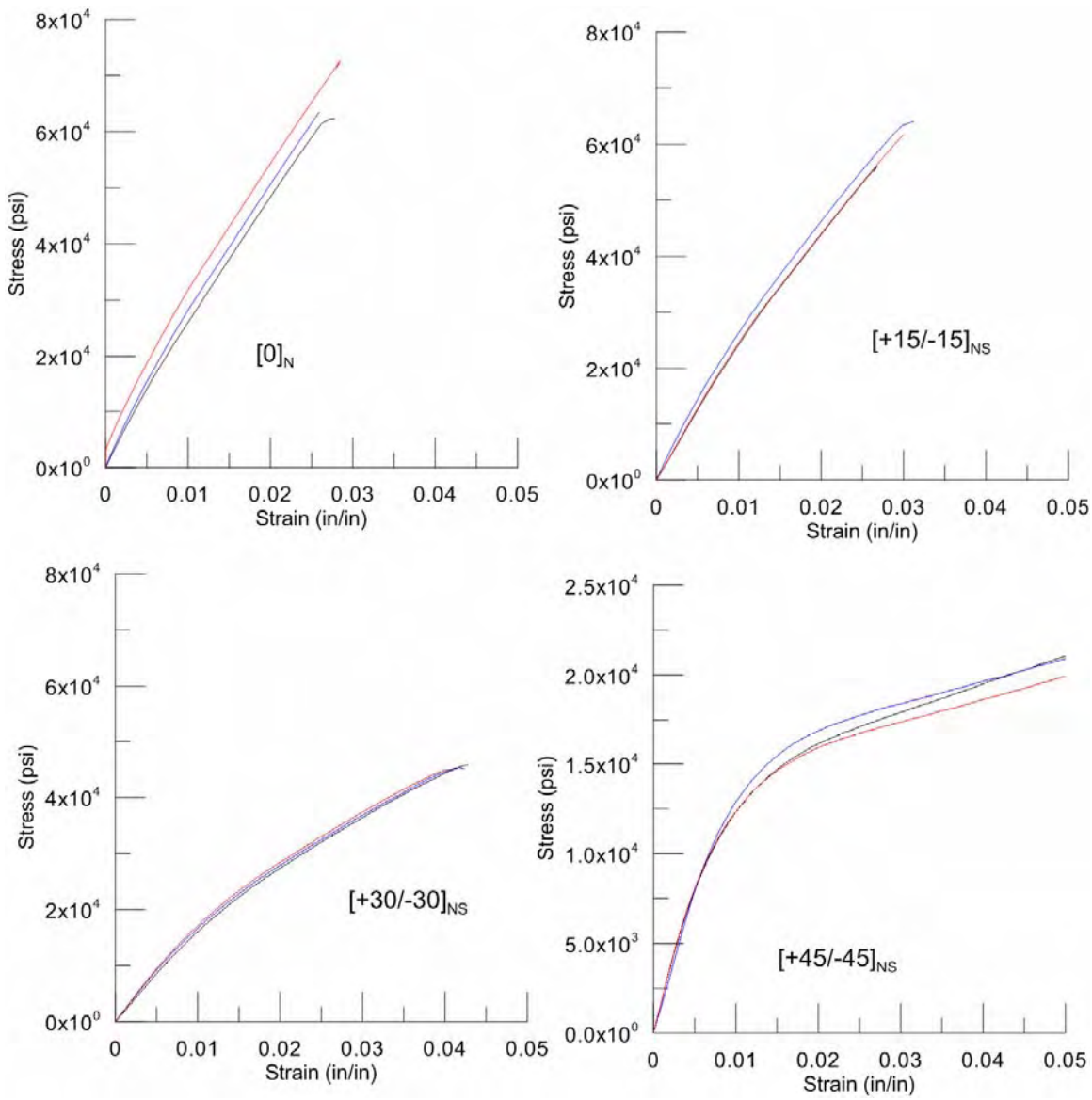

MATERIAL: Newport Glass Fiber
NOMINAL STROKE RATE: Static

Figure A-5. Stress-Strain Diagrams for Newport Glass Fiber Material Oriented at $[0°]_N$, $[-15°/+15°]_{NS}$, $[-30°/+30°]_{NS}$, and $[-45°/+45°]_{NS}$ and Tested at a Rate of 0.001 in/s

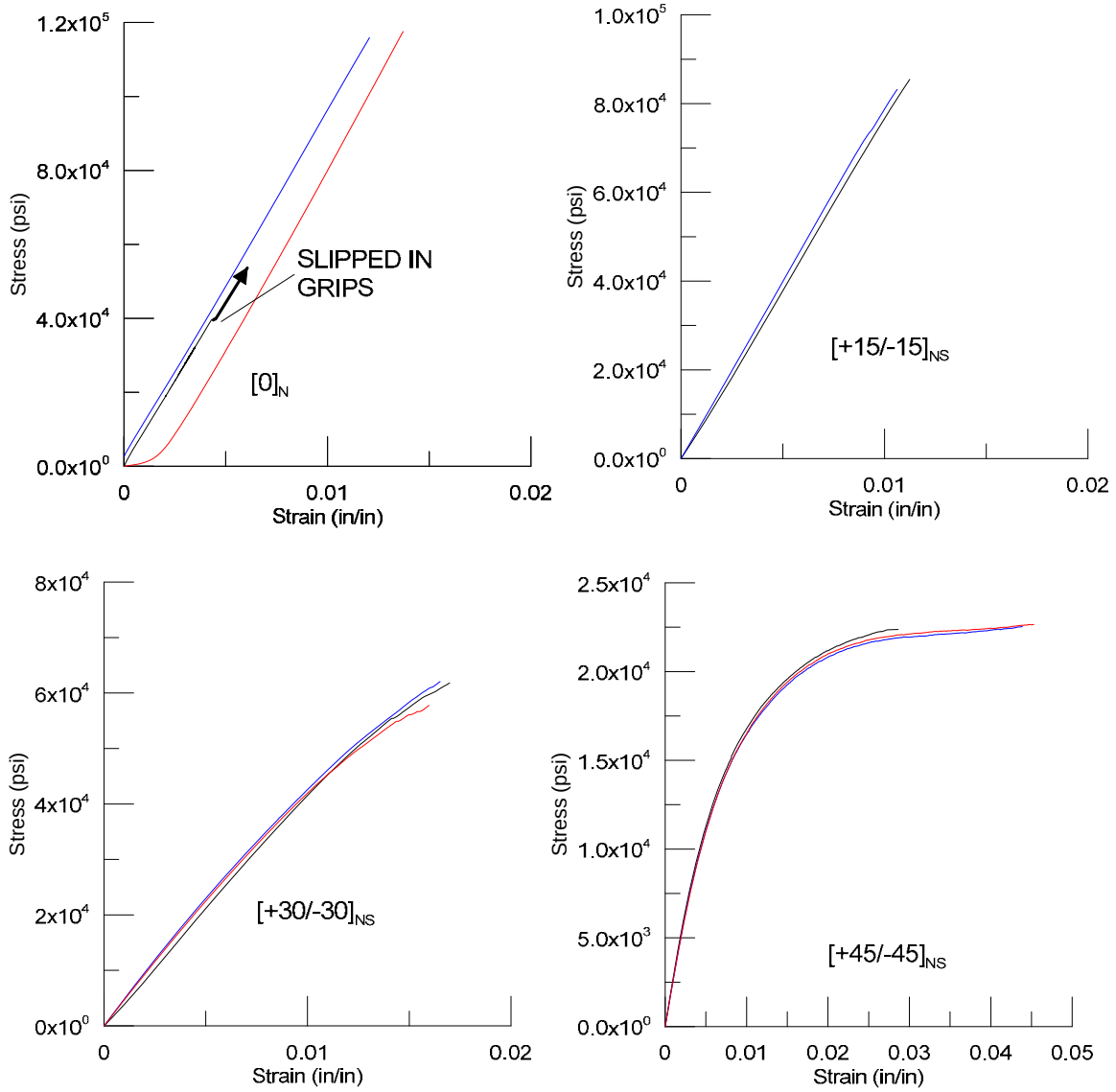

MATERIAL: Fibercote
NOMINAL STROKE RATE: Static

Figure A-6. Stress-Strain Diagrams for Fibercote Material Oriented at $[0°]_N$, $[-15°/+15°]_{NS}$, $[-30°/+30°]_{NS}$, and $[-45°/+45°]_{NS}$ and Tested at a Rate of 0.001 in/s

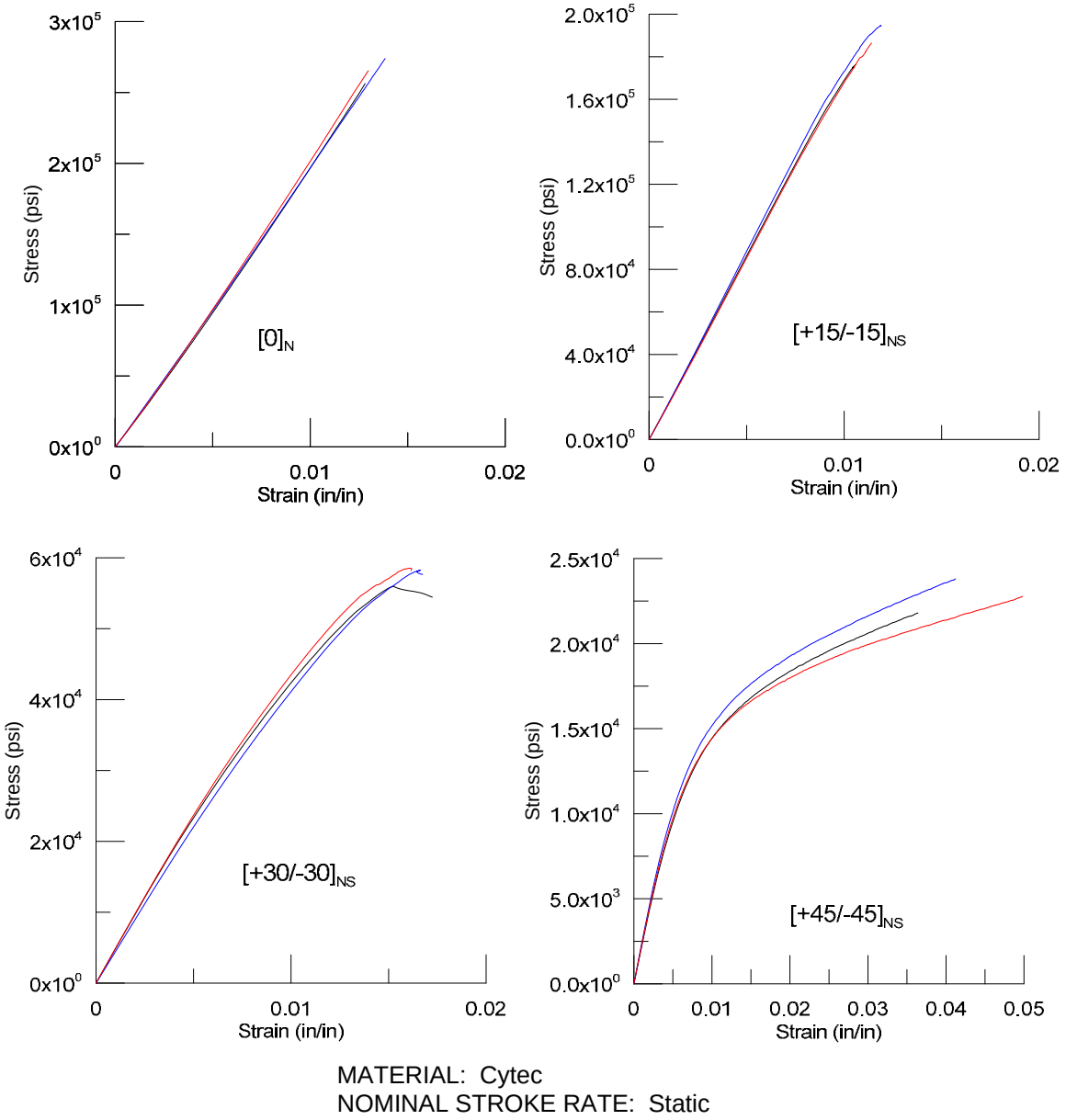

MATERIAL: Cytec
NOMINAL STROKE RATE: Static

Figure A-7. Stress-Strain Diagrams for Cytec Material Oriented at $[0°]_N$, $[-15°/+15°]_{NS}$, $[-30°/+30°]_{NS}$, and $[-45°/+45°]_{NS}$ and Tested at a Rate of 0.001 in/s

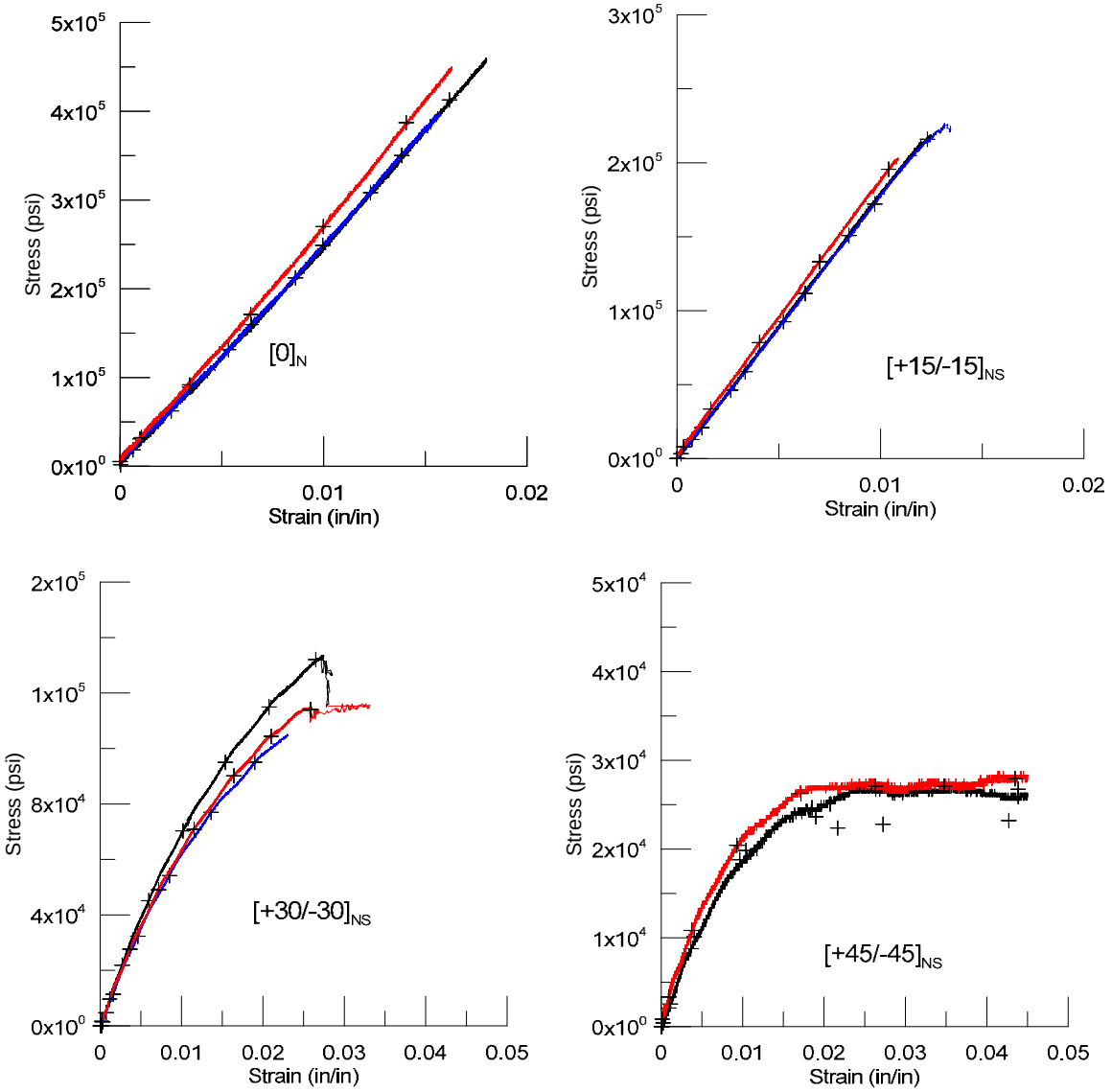

MATERIAL: Toray Unitape
NOMINAL STROKE RATE: 1 in/s

Figure A-8. Stress-Strain Diagrams for Toray Unitape Material Oriented at $[0°]_N$, $[-15°/+15°]_{NS}$, $[-30°/+30°]_{NS}$, and $[-45°/+45°]_{NS}$ and Tested at a Rate of 1 in/s

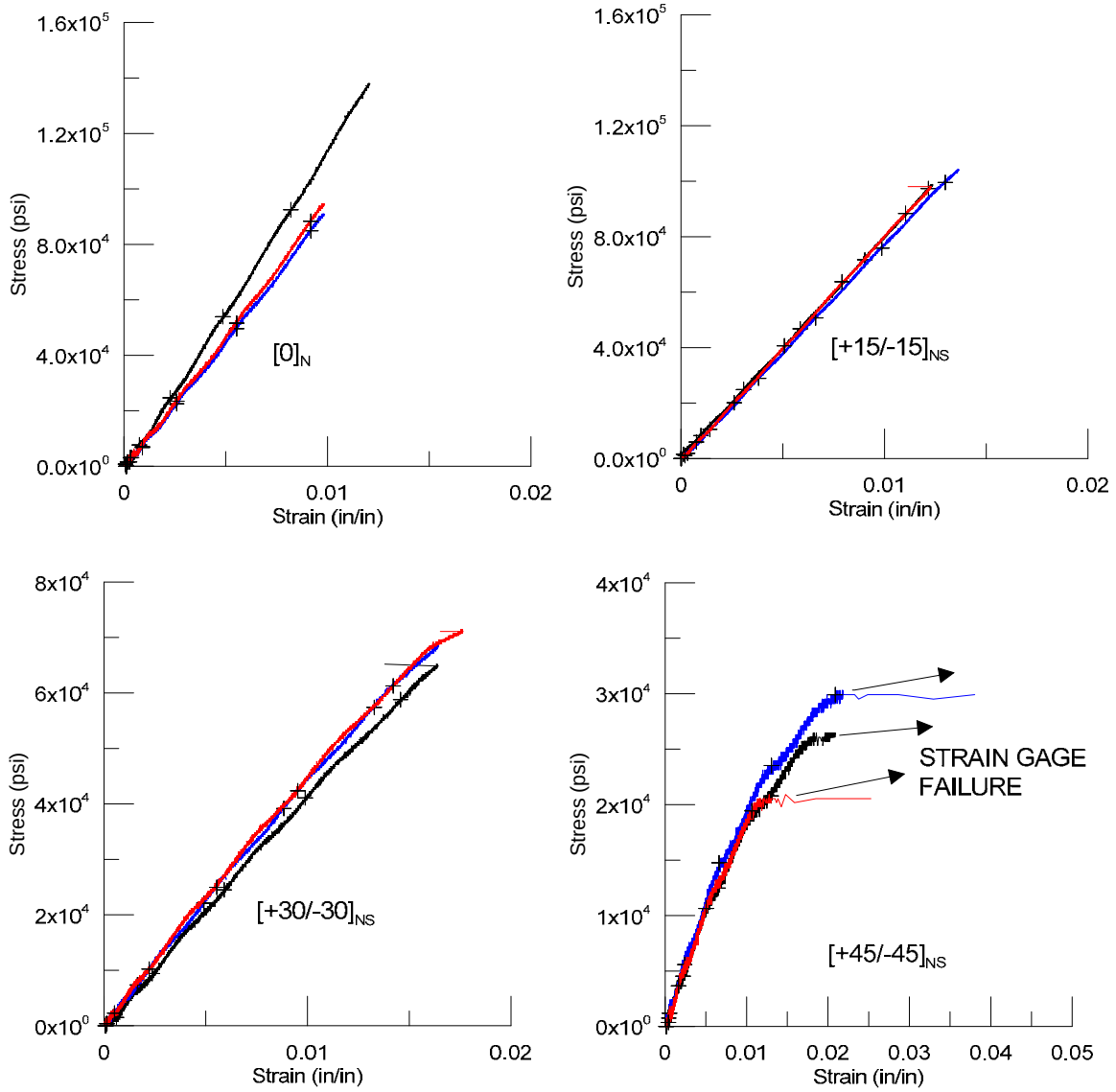

MATERIAL: Toray PWCF
NOMINAL STROKE RATE: 1 in/s

Figure A-9. Stress-Strain Diagrams for Toray PWCF Material Oriented at $[0°]_N$, $[-15°/+15°]_{NS}$, $[-30°/+30°]_{NS}$, and $[-45°/+45°]_{NS}$ and Tested at a Rate of 1 in/s

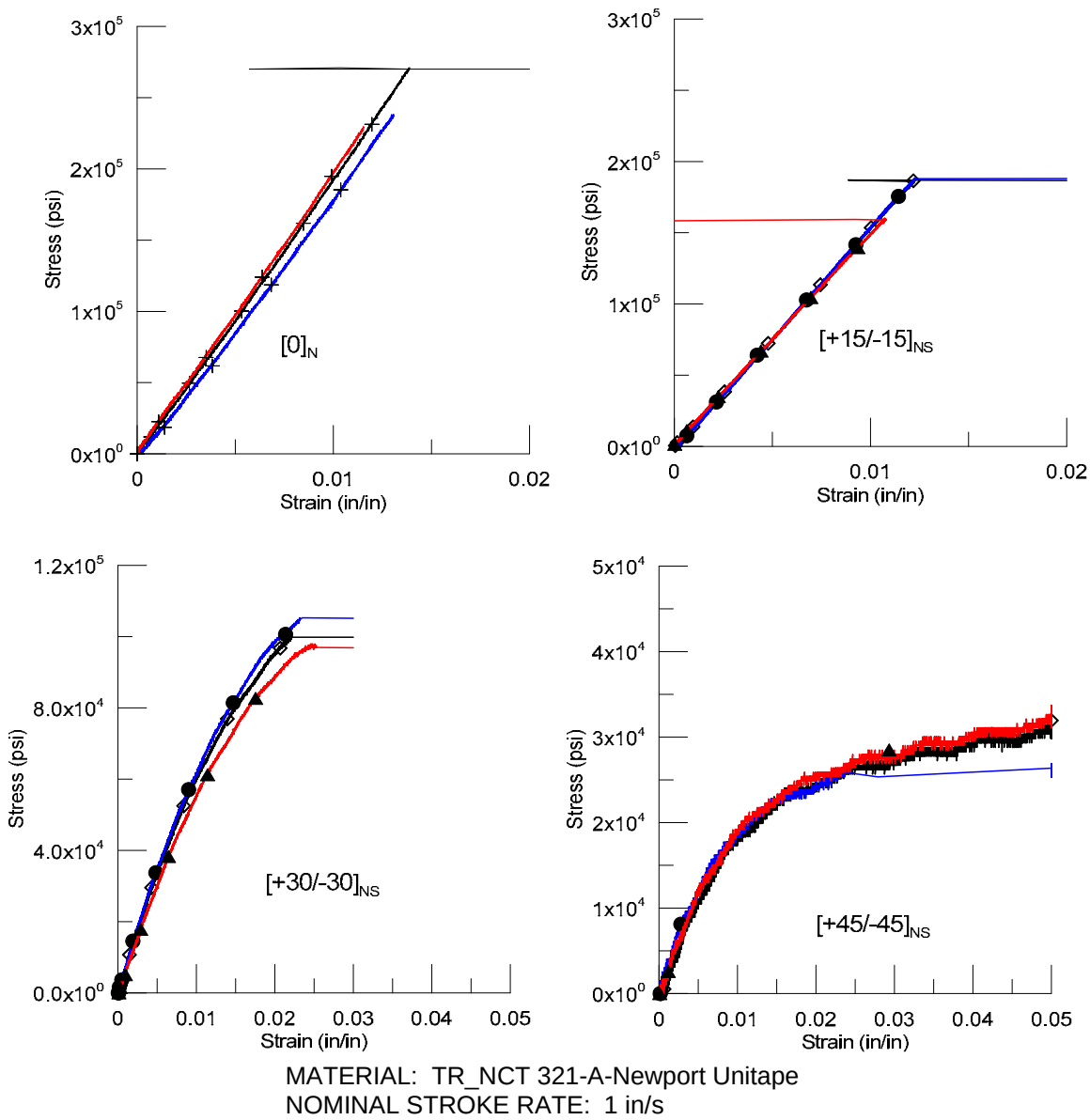

Figure A-10. Stress-Strain Diagrams for Newport Unitape Material Oriented at $[0°]_N$, $[-15°/+15°]_{NS}$, $[-30°/+30°]_{NS}$, and $[-45°/+45°]_{NS}$ and Tested at a Rate of 1 in/s

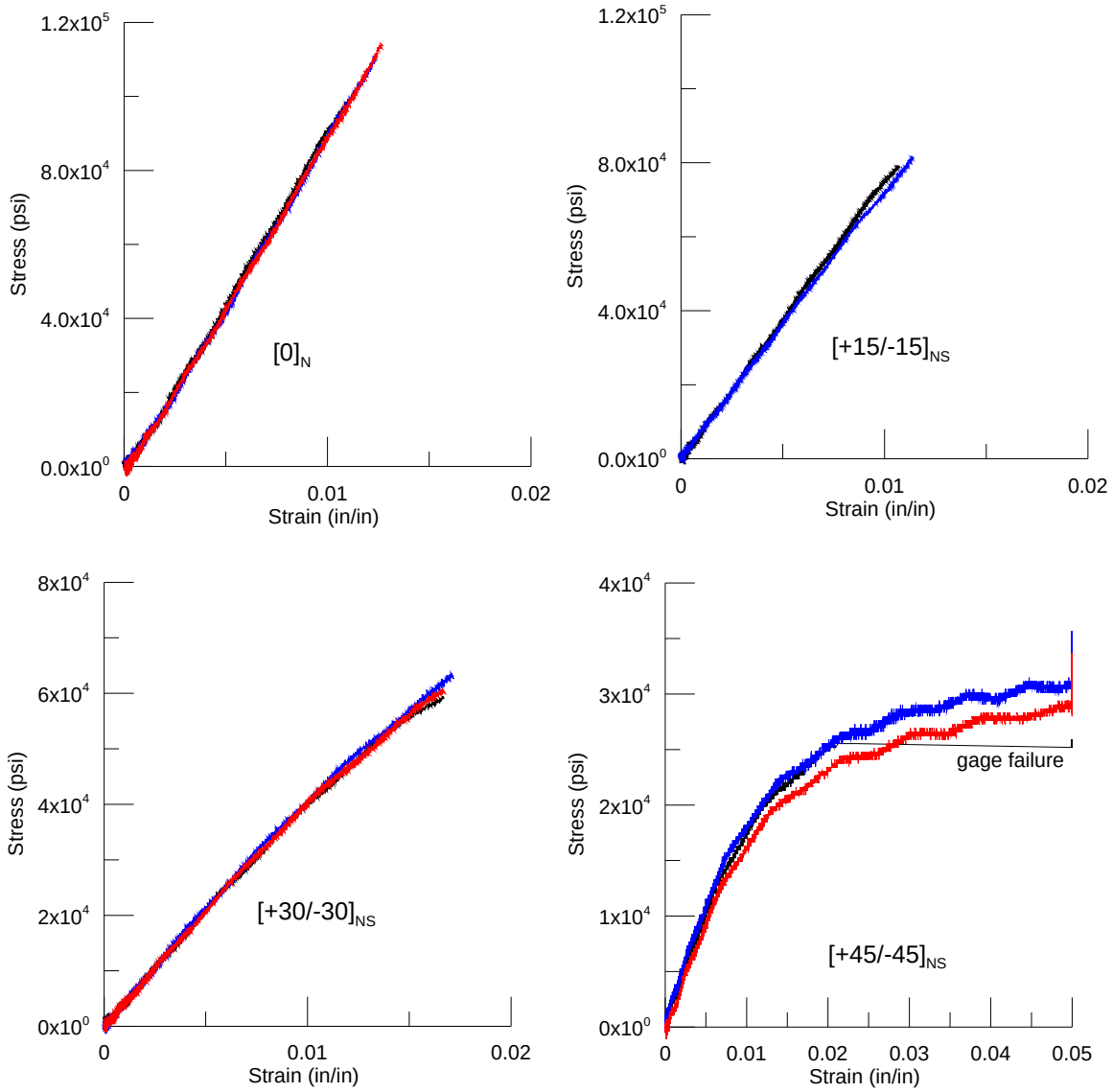

MATERIAL: Newport PWCF
NOMINAL STROKE RATE: 1 in/s

Figure A-11. Stress-Strain Diagrams for Newport PWCF Material Oriented at $[0°]_N$, $[-15°/+15°]_{NS}$, $[-30°/+30°]_{NS}$, and $[-45°/+45°]_{NS}$ and Tested at a Rate of 1 in/s

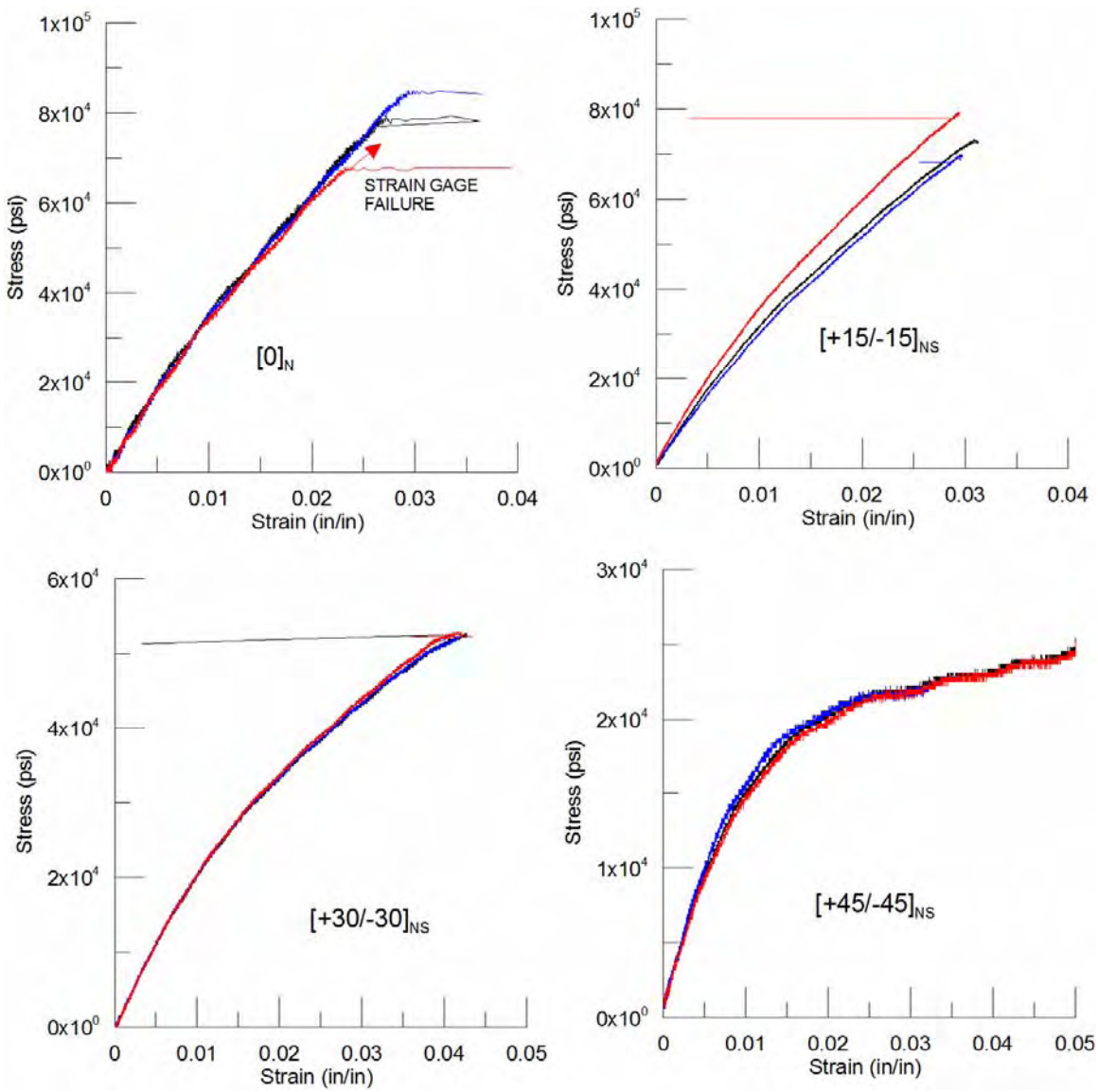

MATERIAL: Newport Glass Fiber
NOMINAL STROKE RATE: 1 in/s

Figure A-12. Stress-Strain Diagrams for Newport Glass Fiber Material Oriented at $[0°]_N$, $[-15°/+15°]_{NS}$, $[-30°/+30°]_{NS}$, and $[-45°/+45°]_{NS}$ and Tested at a Rate of 1 in/s

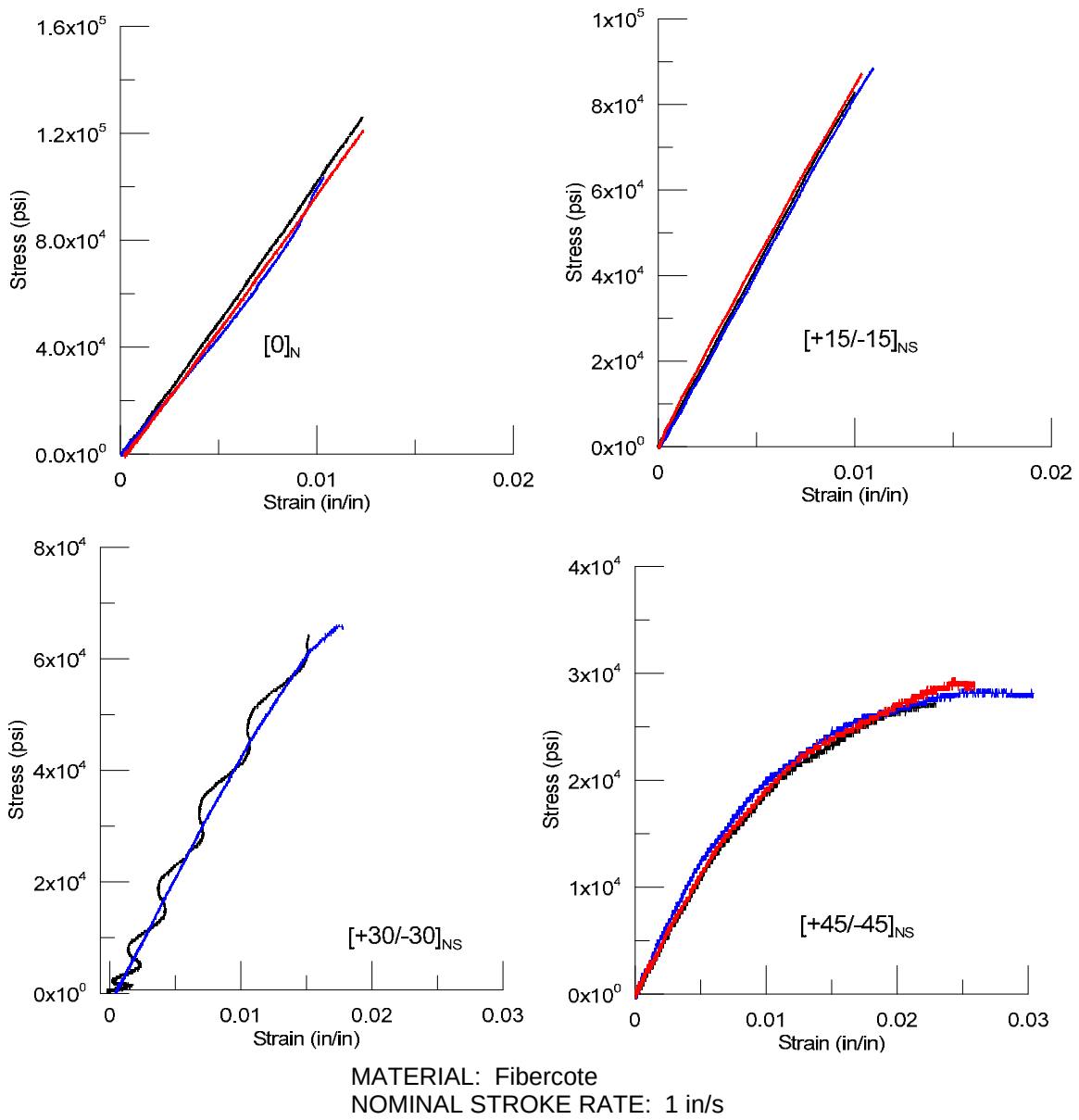

MATERIAL: Fibercote
NOMINAL STROKE RATE: 1 in/s

Figure A-13. Stress-Strain Diagrams for Fibercote Material Oriented at $[0°]_N$, $[-15°/+15°]_{NS}$, $[-30°/+30°]_{NS}$, and $[-45°/+45°]_{NS}$ and Tested at a Rate of 1 in/s

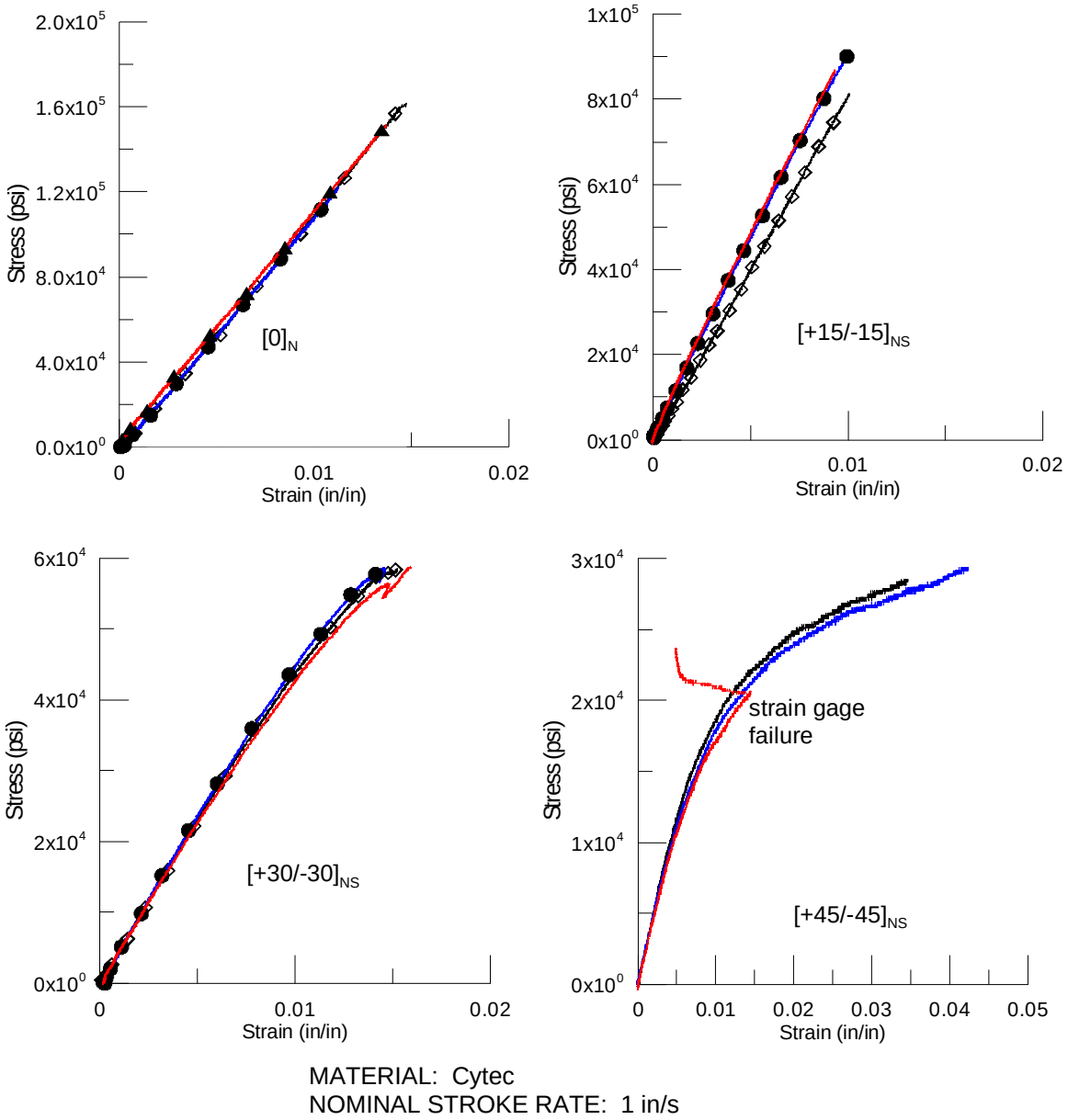

MATERIAL: Cytec
NOMINAL STROKE RATE: 1 in/s

Figure A-14. Stress-Strain Diagrams for Cytec Material Oriented at $[0°]_N$, $[-15°/+15°]_{NS}$, $[-30°/+30°]_{NS}$, and $[-45°/+45°]_{NS}$ and Tested at a Rate of 1 in/s

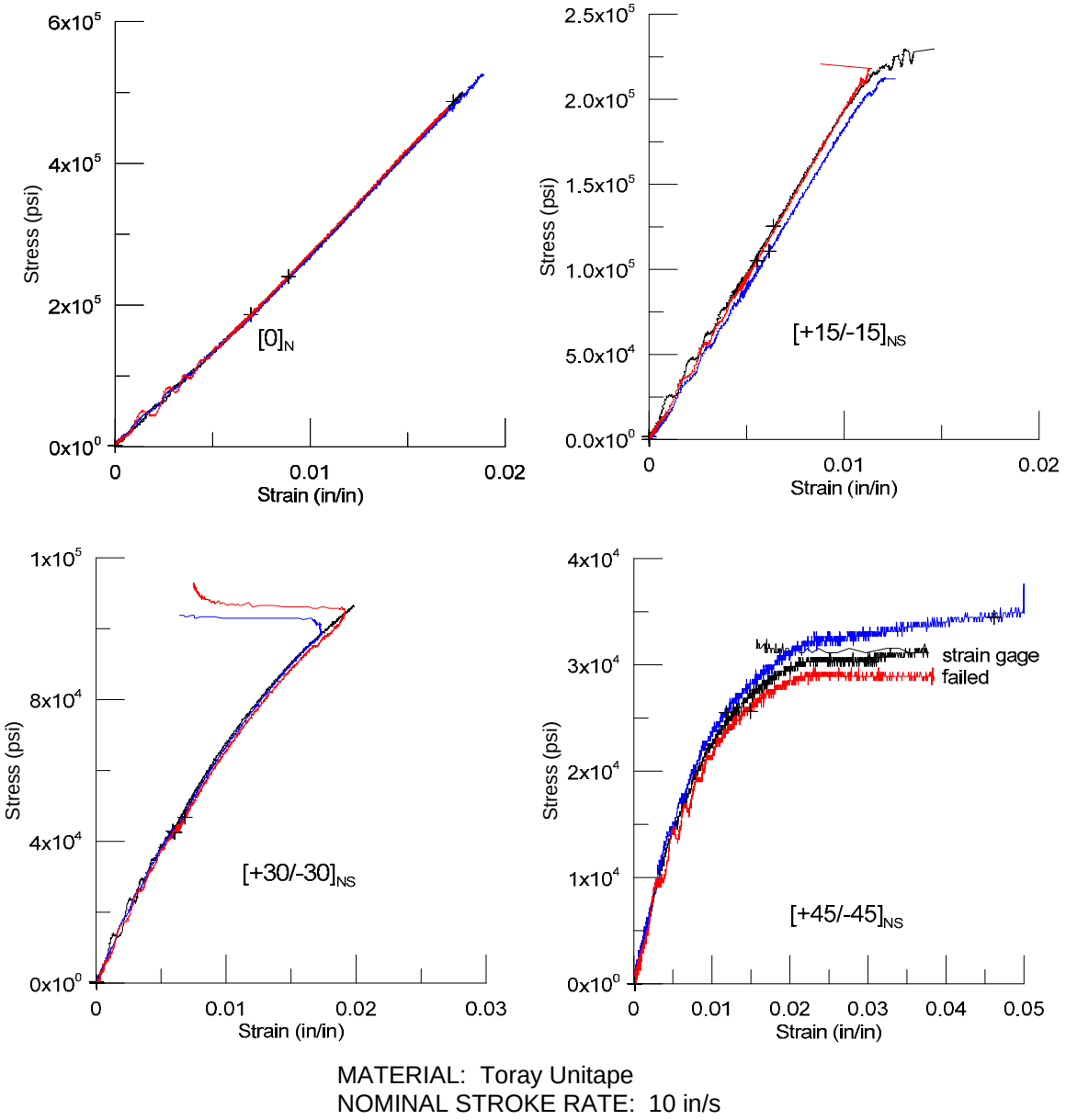

MATERIAL: Toray Unitape
NOMINAL STROKE RATE: 10 in/s

Figure A-15. Stress-Strain Diagrams for Toray Unitape Material Oriented at $[0°]_N$, $[-15°/+15°]_{NS}$, $[-30°/+30°]_{NS}$, and $[-45°/+45°]_{NS}$ and Tested at a Rate of 10 in/s

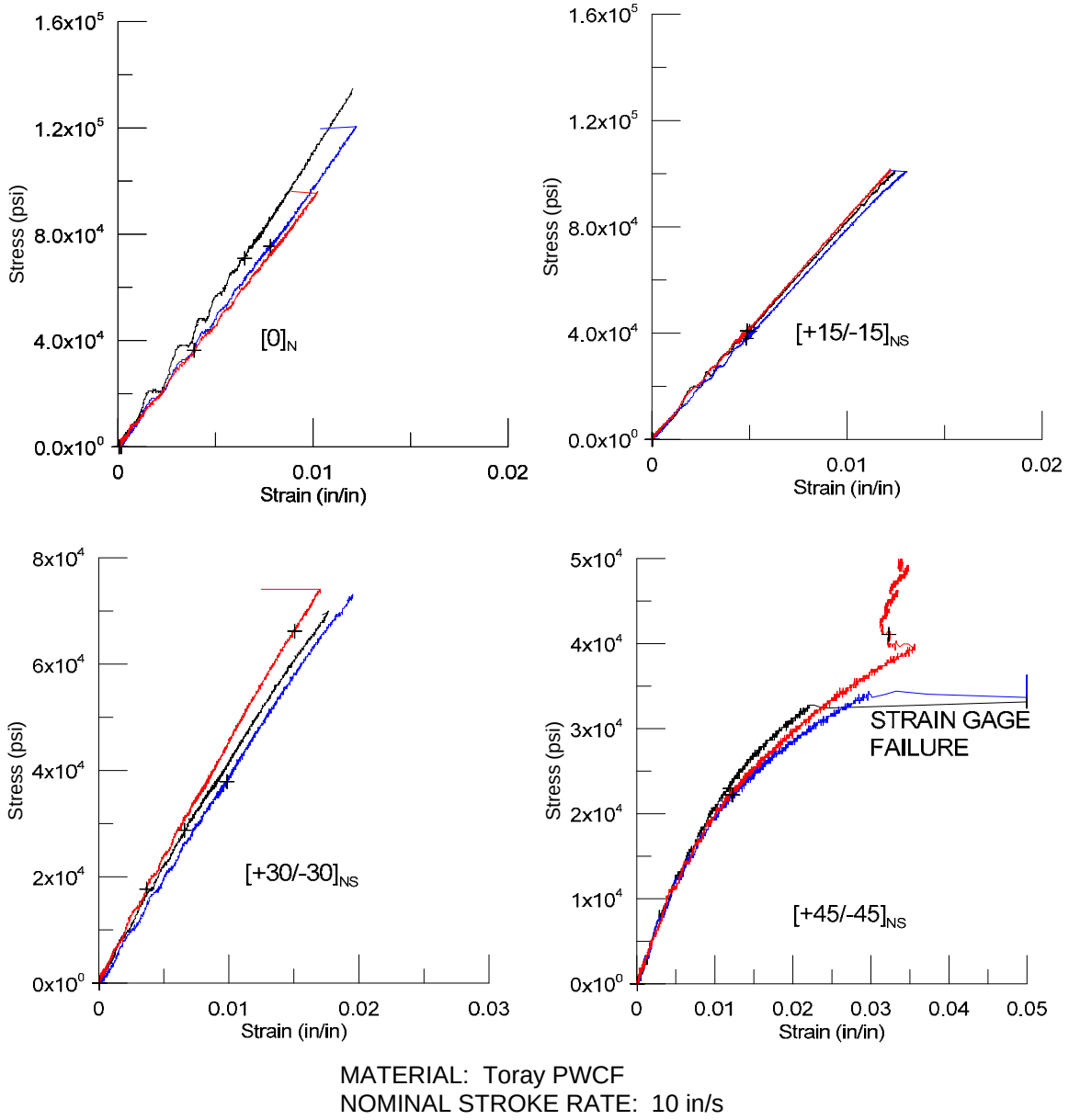

Figure A-16. Stress-Strain Diagrams for Toray PWCF Material Oriented at $[0°]_N$, $[-15°/+15°]_{NS}$, $[-30°/+30°]_{NS}$, and $[-45°/+45°]_{NS}$ and Tested at a Rate of 10 in/s

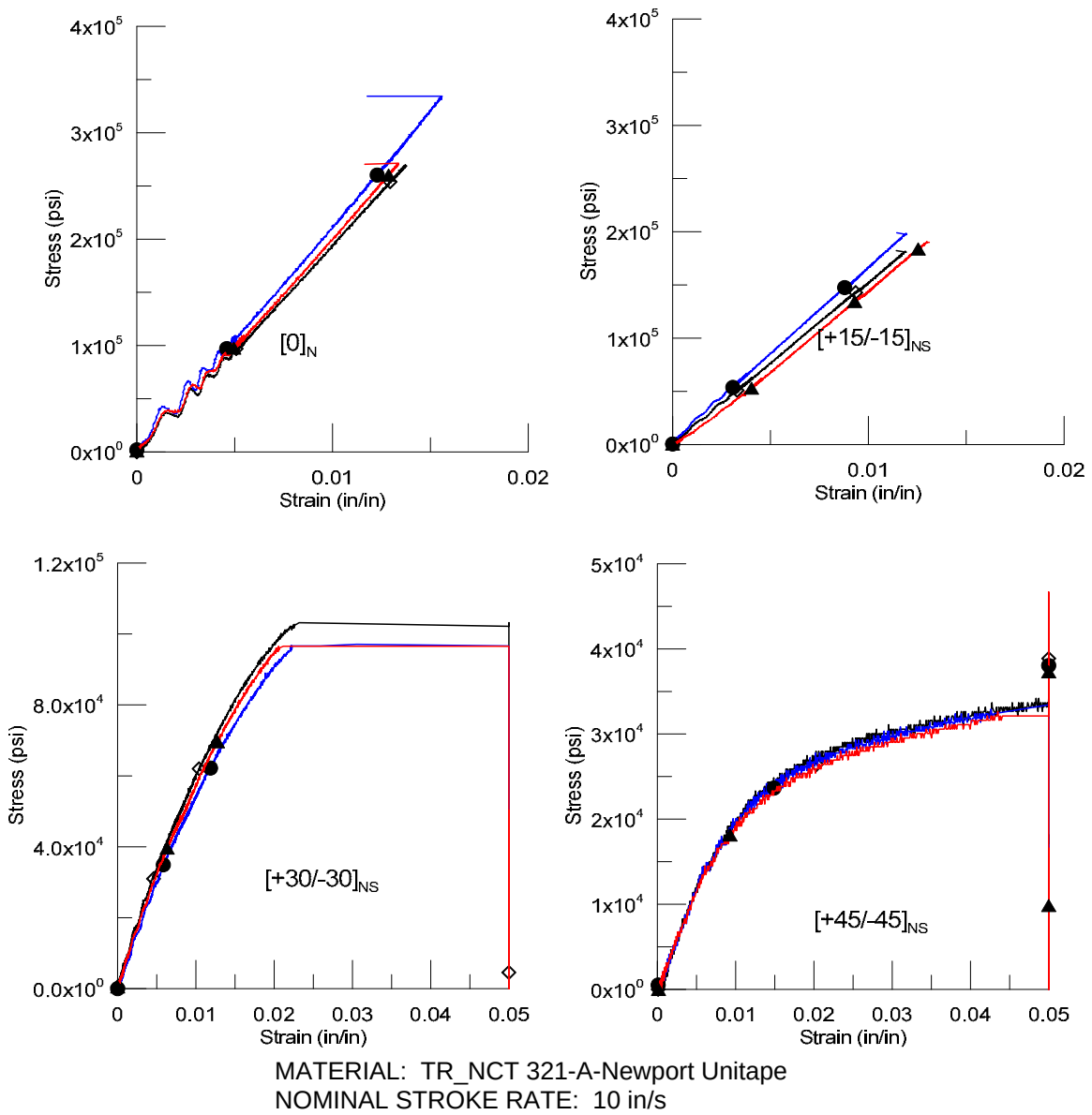

Figure A-17. Stress-Strain Diagrams for Newport Unitape Material Oriented at $[0°]_N$, $[-15°/+15°]_{NS}$, $[-30°/+30°]_{NS}$, and $[-45°/+45°]_{NS}$ and Tested at a Rate of 10 in/s

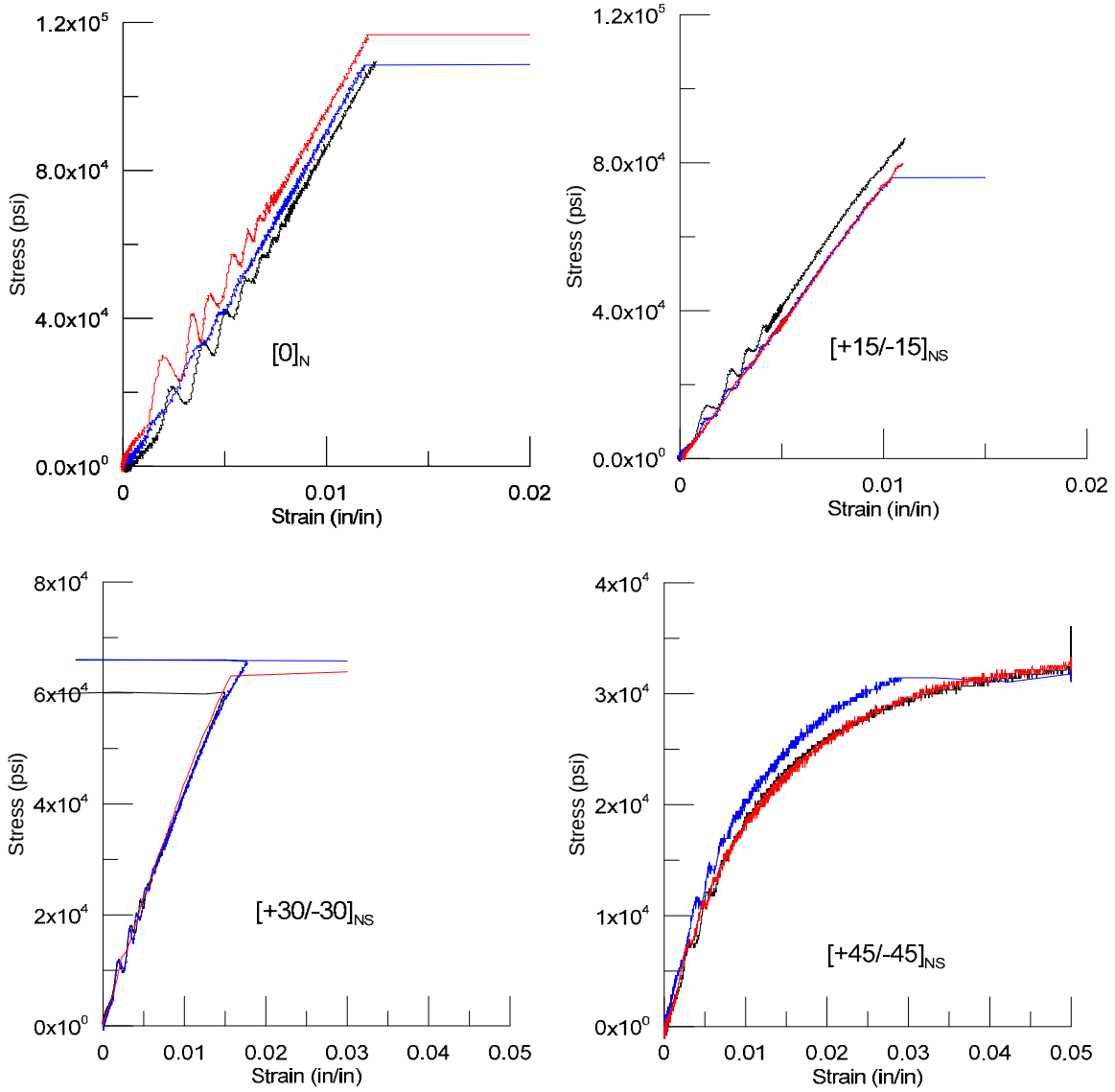

MATERIAL: Newport PWCF
NOMINAL STROKE RATE: 10 in/s

Figure A-18. Stress-Strain Diagrams for Newport PWCF Material Oriented at $[0°]_N$, $[-15°/+15°]_{NS}$, $[-30°/+30°]_{NS}$, and $[-45°/+45°]_{NS}$ and Tested at a Rate of 10 in/s

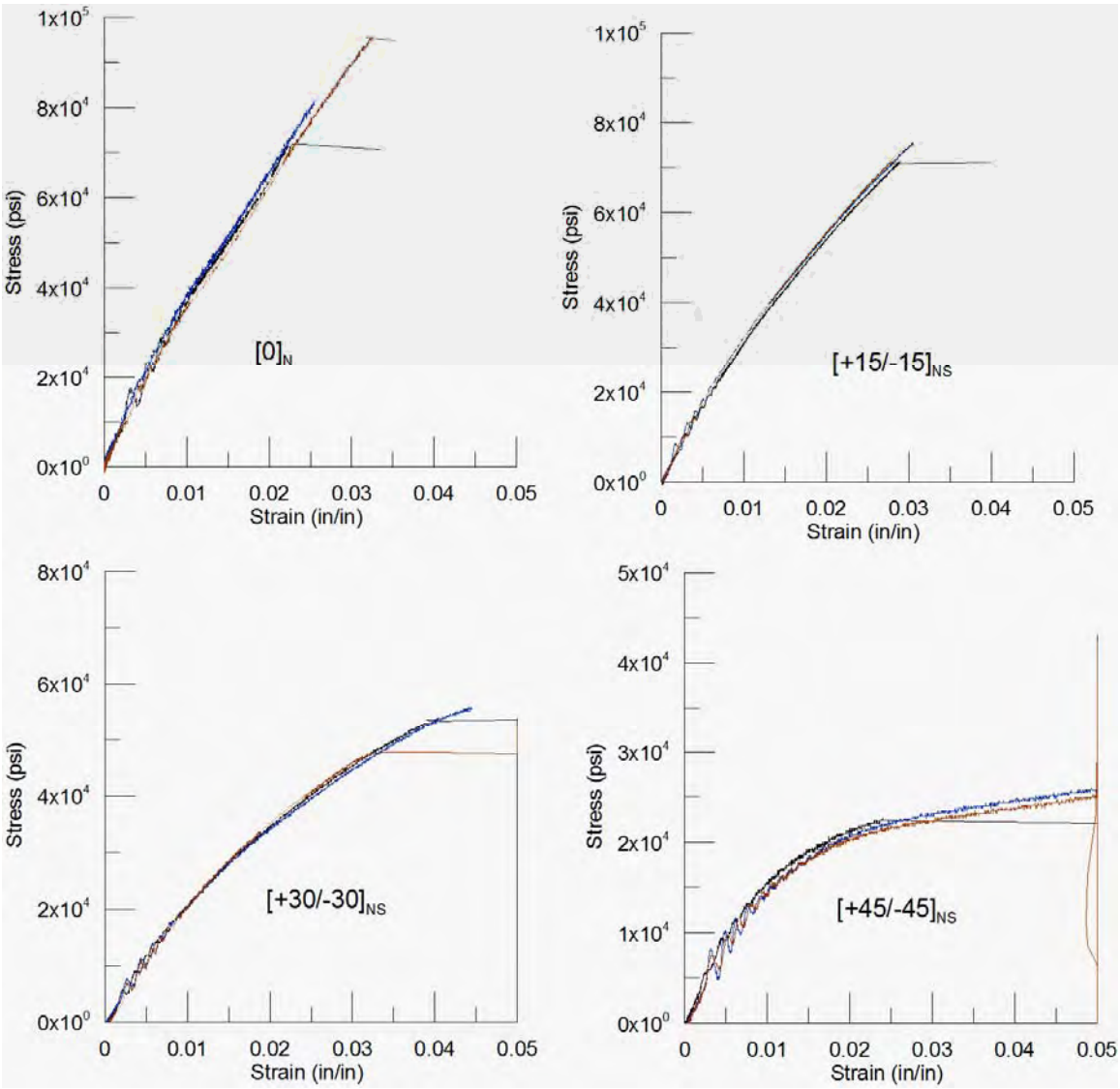

MATERIAL: Newport PWCF
NOMINAL STROKE RATE: 10 in/s

Figure A-19. Stress-Strain Diagrams for Newport Glass Fiber Material Oriented at $[0°_N$, $[-15°/+15°]_{NS}$, $[-30°/+30°]_{NS}$, and $[-45°/+45°]_{NS}$ and Tested at a Rate of 10 in/s

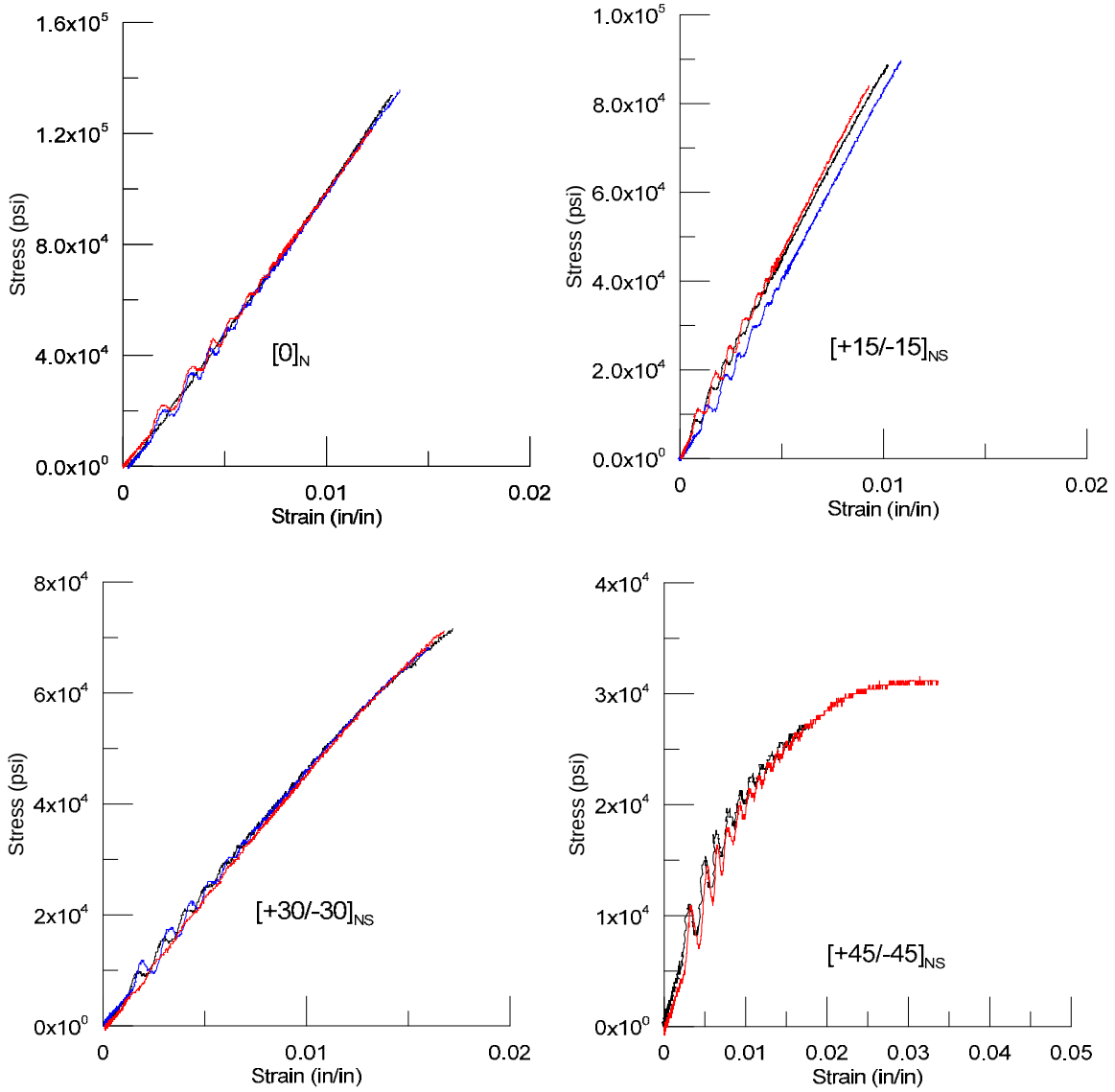

MATERIAL: Fibercote
NOMINAL STROKE RATE: 10 in/s

Figure A-20. Stress-Strain Diagrams for Fibercote Material Oriented at $[0°]_N$, $[-15°/+15°]_{NS}$, $[-30°/+30°]_{NS}$, and $[-45°/+45°]_{NS}$ and Tested at a Rate of 10 in/s

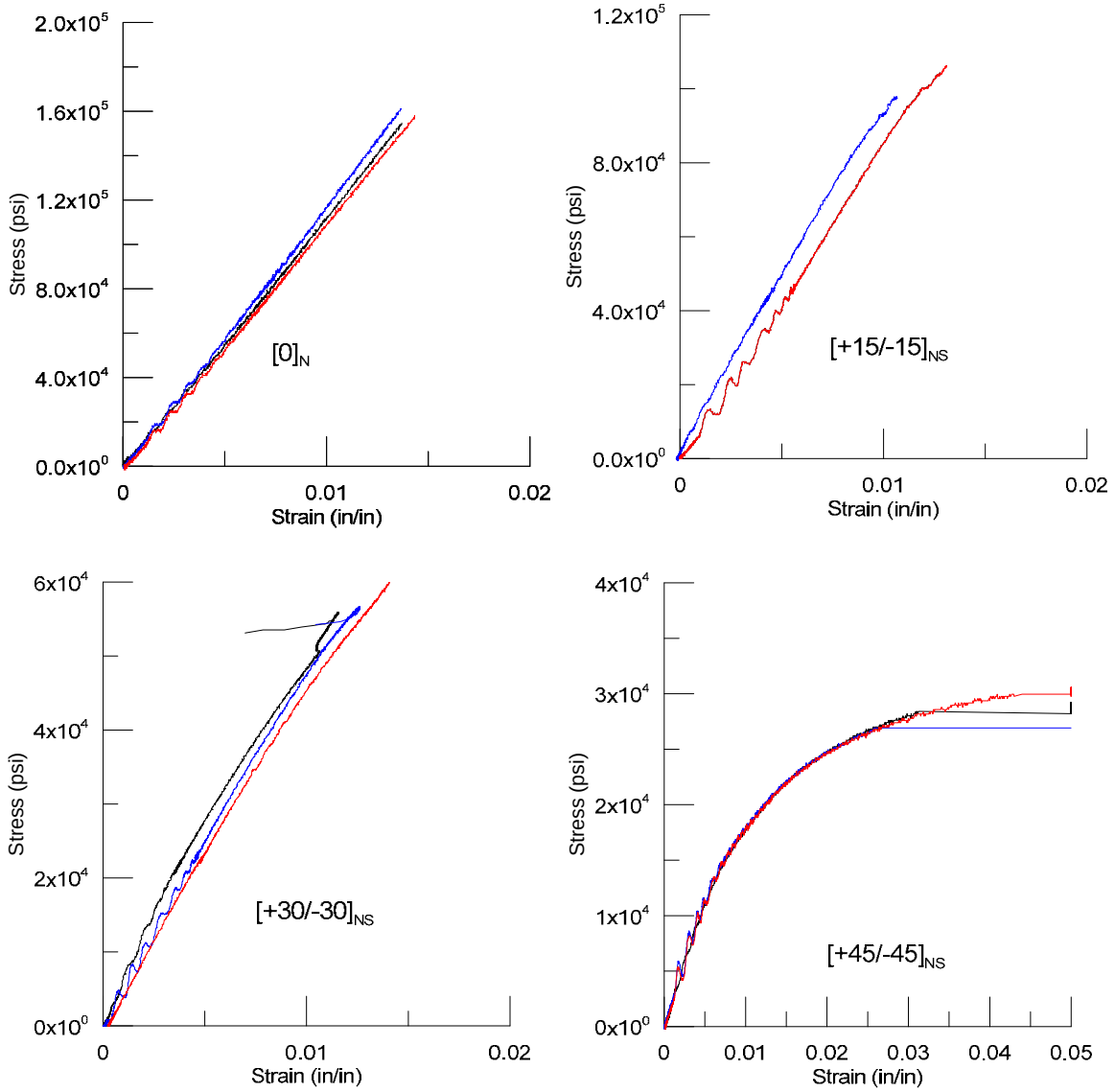

MATERIAL: Cytec
NOMINAL STROKE RATE: 10 in/s

Figure A-21. Stress-Strain Diagrams for Cytec Material Oriented at $[0°]_N$, $[-15°/+15°]_{NS}$, $[-30°/+30°]_{NS}$, and $[-45°/+45°]_{NS}$ and Tested at a Rate of 10 in/s

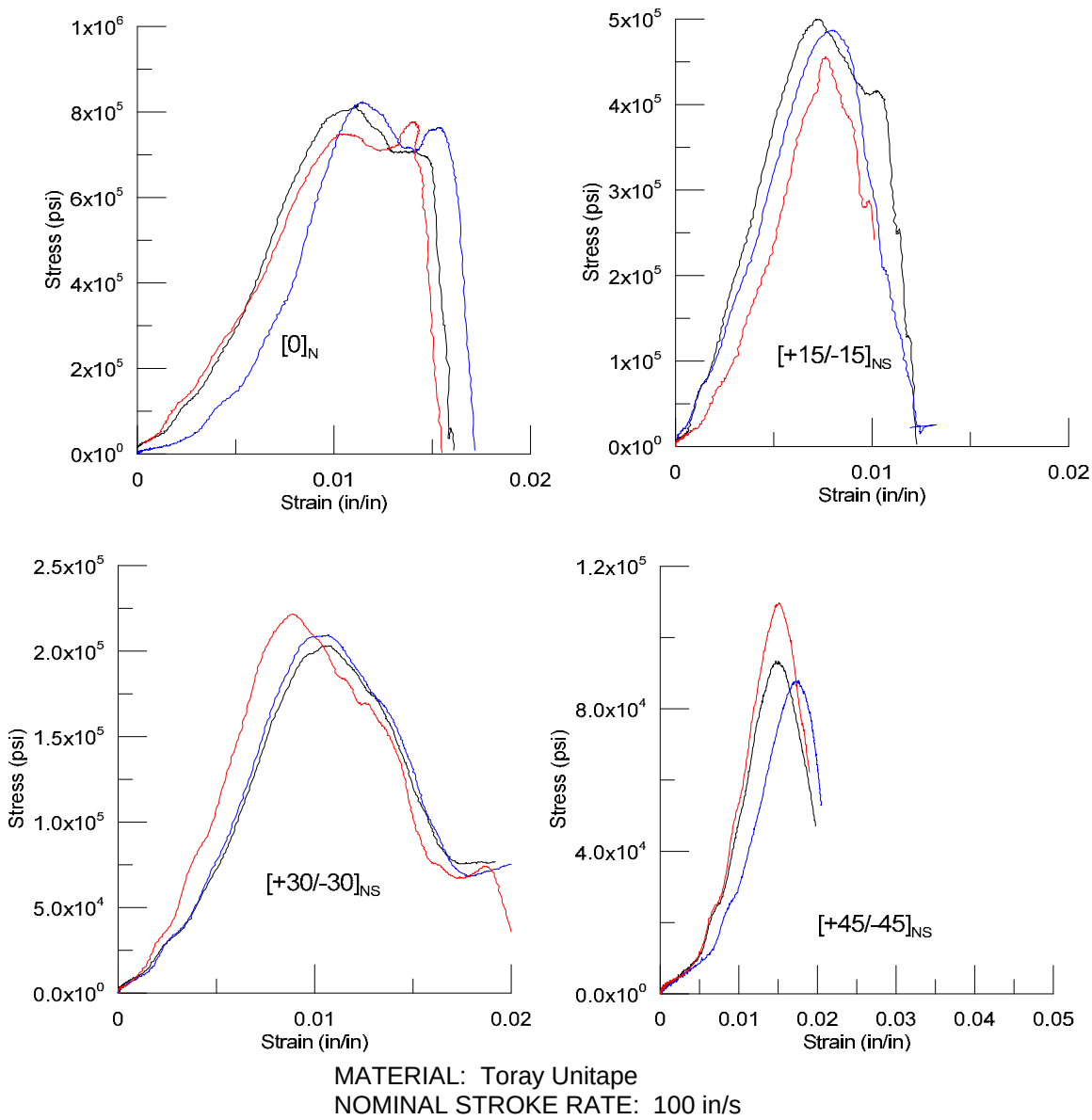

MATERIAL: Toray Unitape
NOMINAL STROKE RATE: 100 in/s

Figure A-22. Stress-Strain Diagrams for Toray Unitape Material Oriented at $[0°]_N$, $[-15°/+15°]_{NS}$, $[-30°/+30°]_{NS}$, and $[-45°/+45°]_{NS}$ and Tested at a Rate of 100 in/s

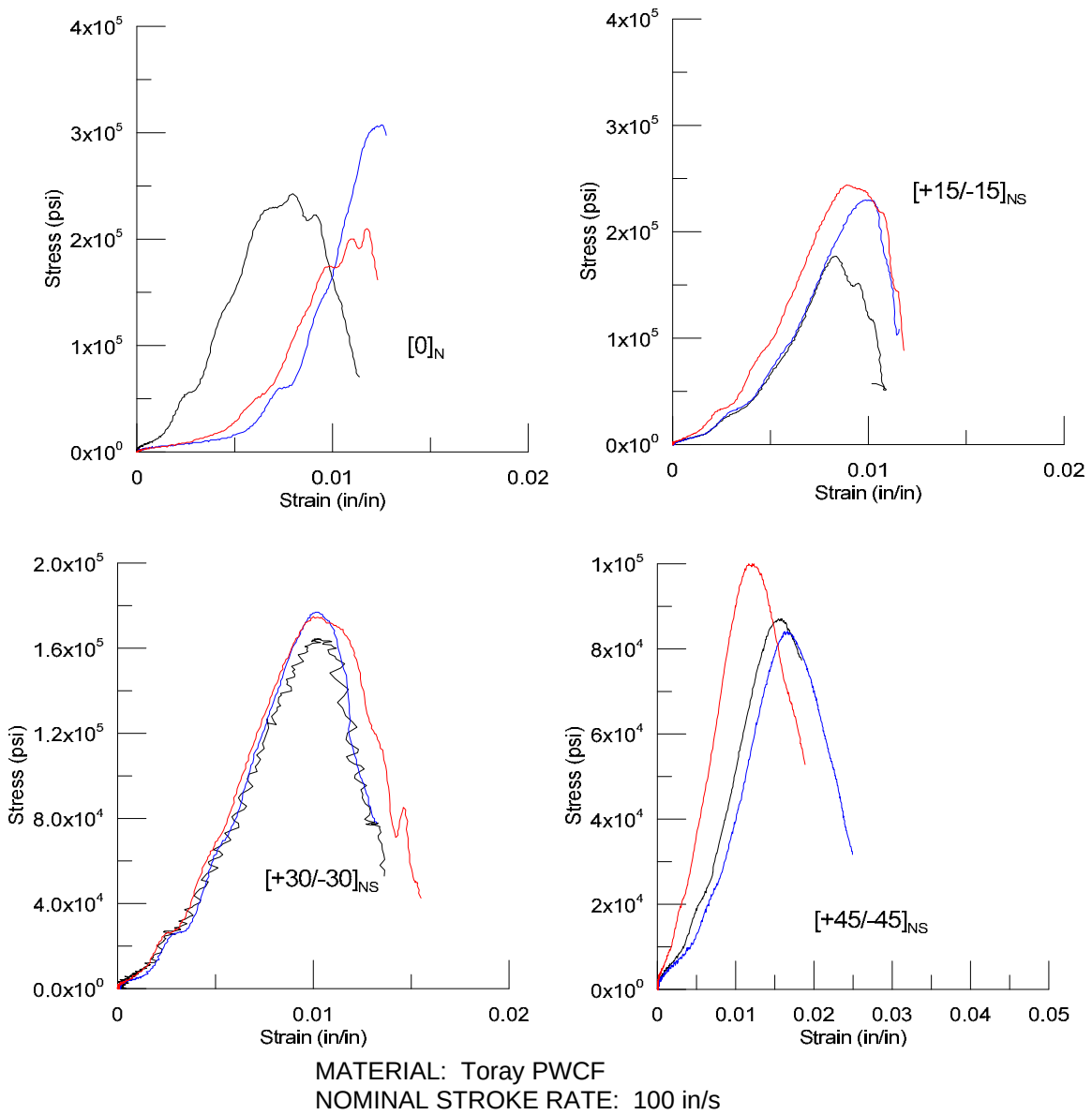

Figure A-23. Stress-Strain Diagrams for Toray PWCF Material Oriented at $[0°]_N$, $[-15°/+15°]_{NS}$, $[-30°/+30°]_{NS}$, and $[-45°/+45°]_{NS}$ and Tested at a Rate of 100 in/s

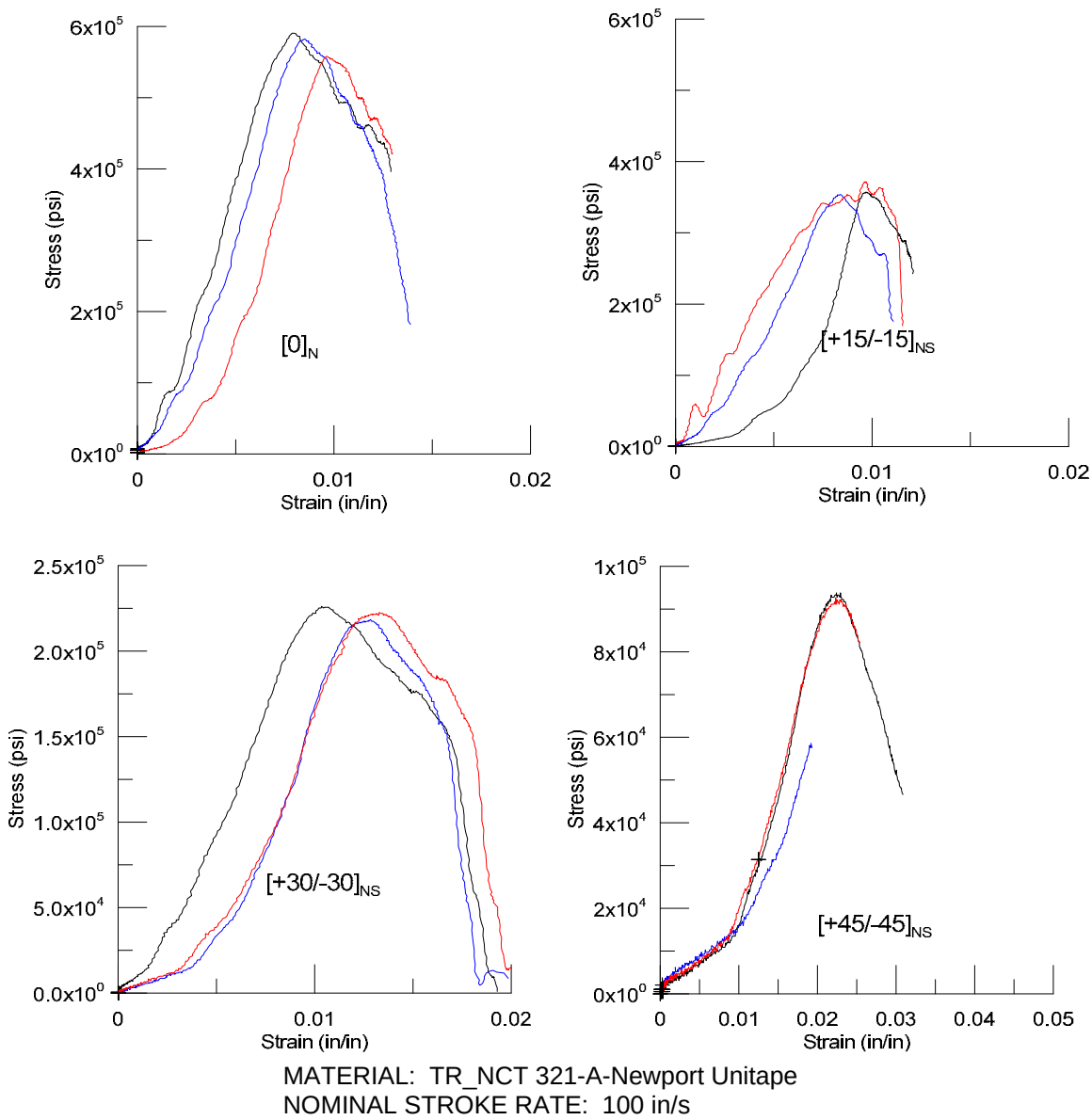

Figure A-24. Stress-Strain Diagrams for Newport Unitape Material Oriented at $[0°]_N$, $[-15°/+15°]_{NS}$, $[-30°/+30°]_{NS}$, and $[-45°/+45°]_{NS}$ and Tested at a Rate of 100 in/s

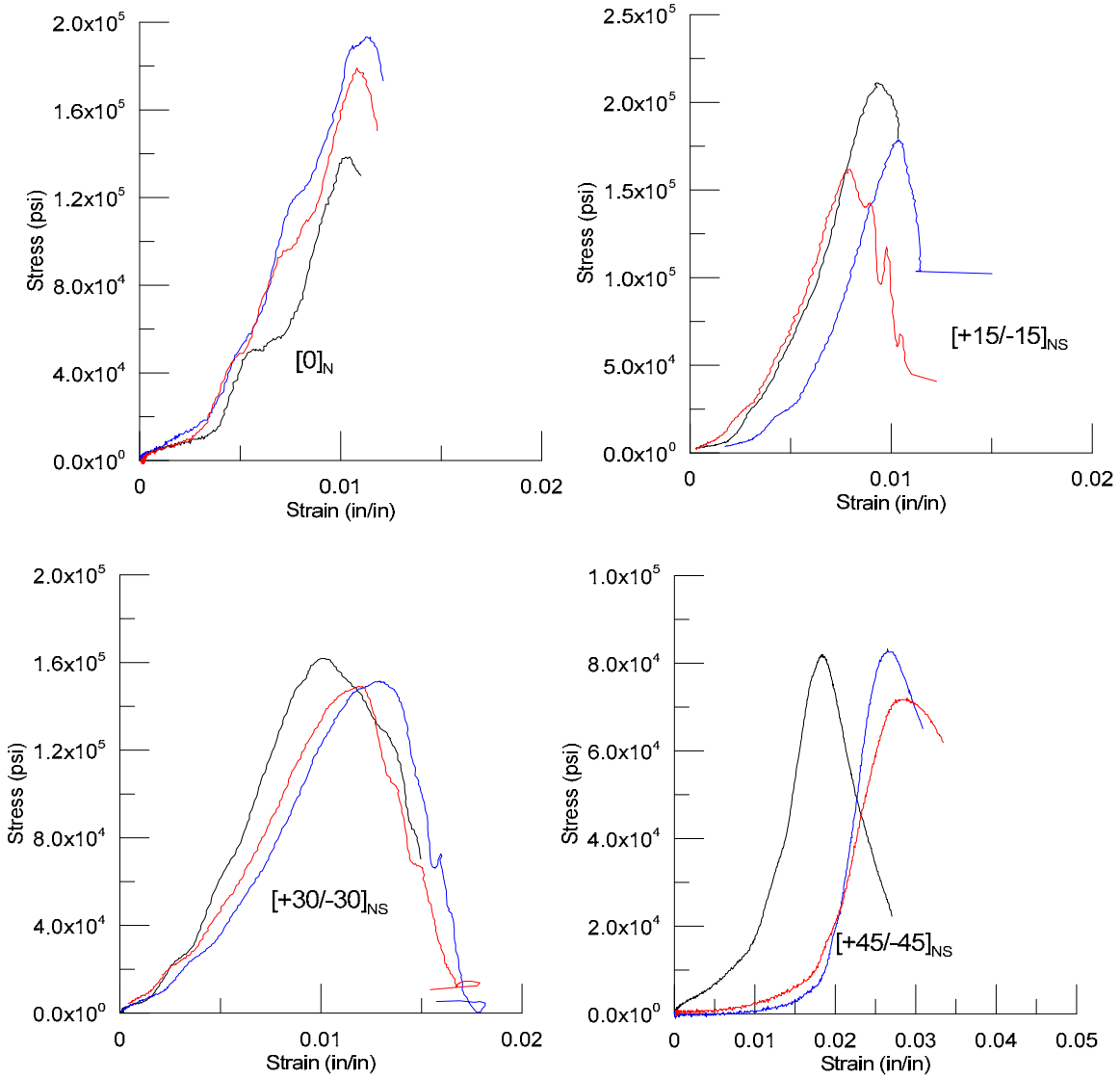

MATERIAL: Newport PWCF
NOMINAL STROKE RATE: 100 in/s

Figure A-25. Stress-Strain Diagrams for Newport PWCF Material Oriented at $[0°]_N$, $[-15°/+15°]_{NS}$, $[-30°/+30°]_{NS}$, and $[-45°/+45°]_{NS}$ and Tested at a Rate of 100 in/s

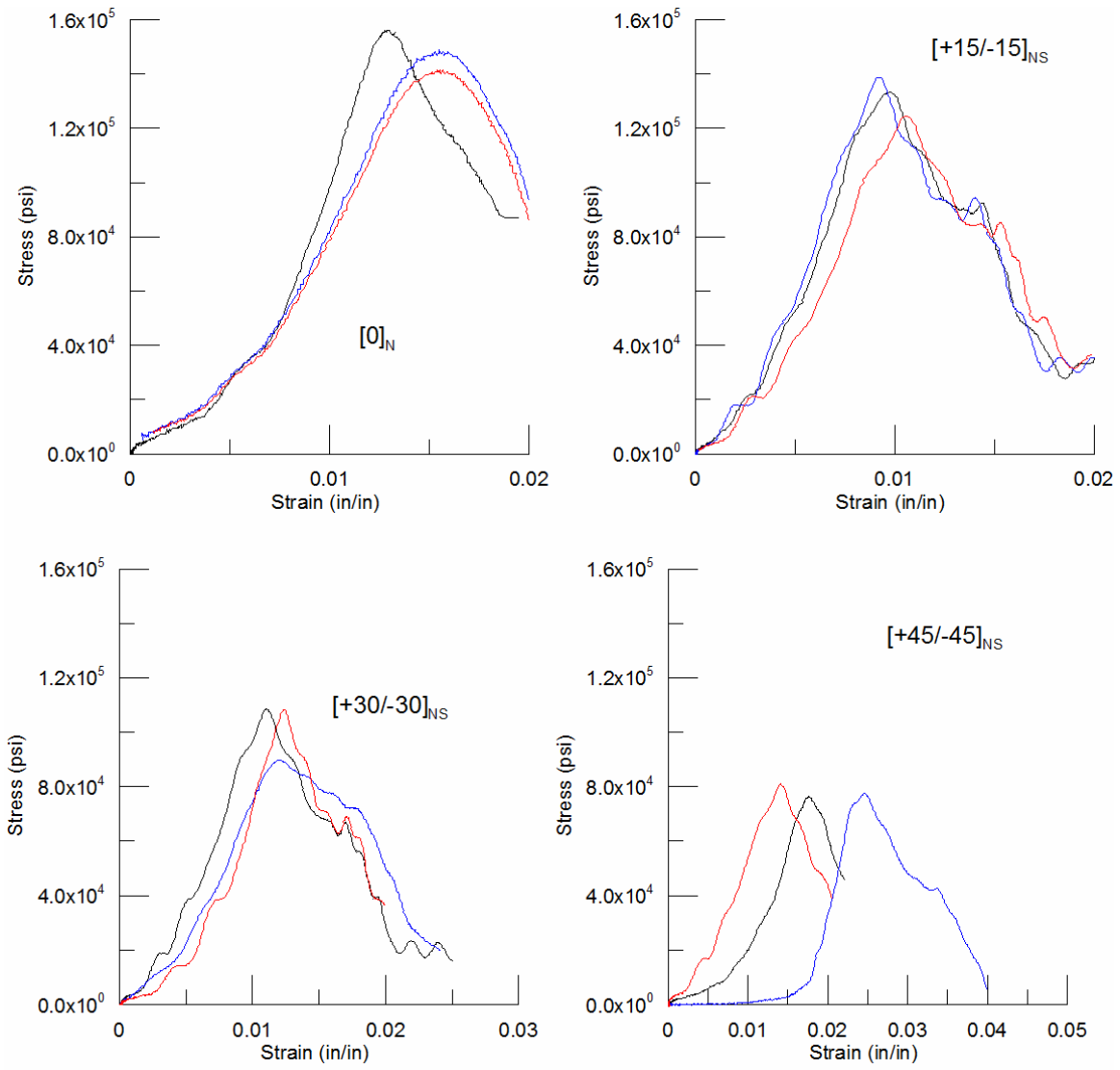

Figure A-26. Stress-Strain Diagrams for Newport Glass Fiber Material Oriented at $[0°]_N$, $[-15°/+15°]_{NS}$, $[-30°/+30°]_{NS}$, and $[-45°/+45°]_{NS}$ and Tested at a Rate of 100 in/s

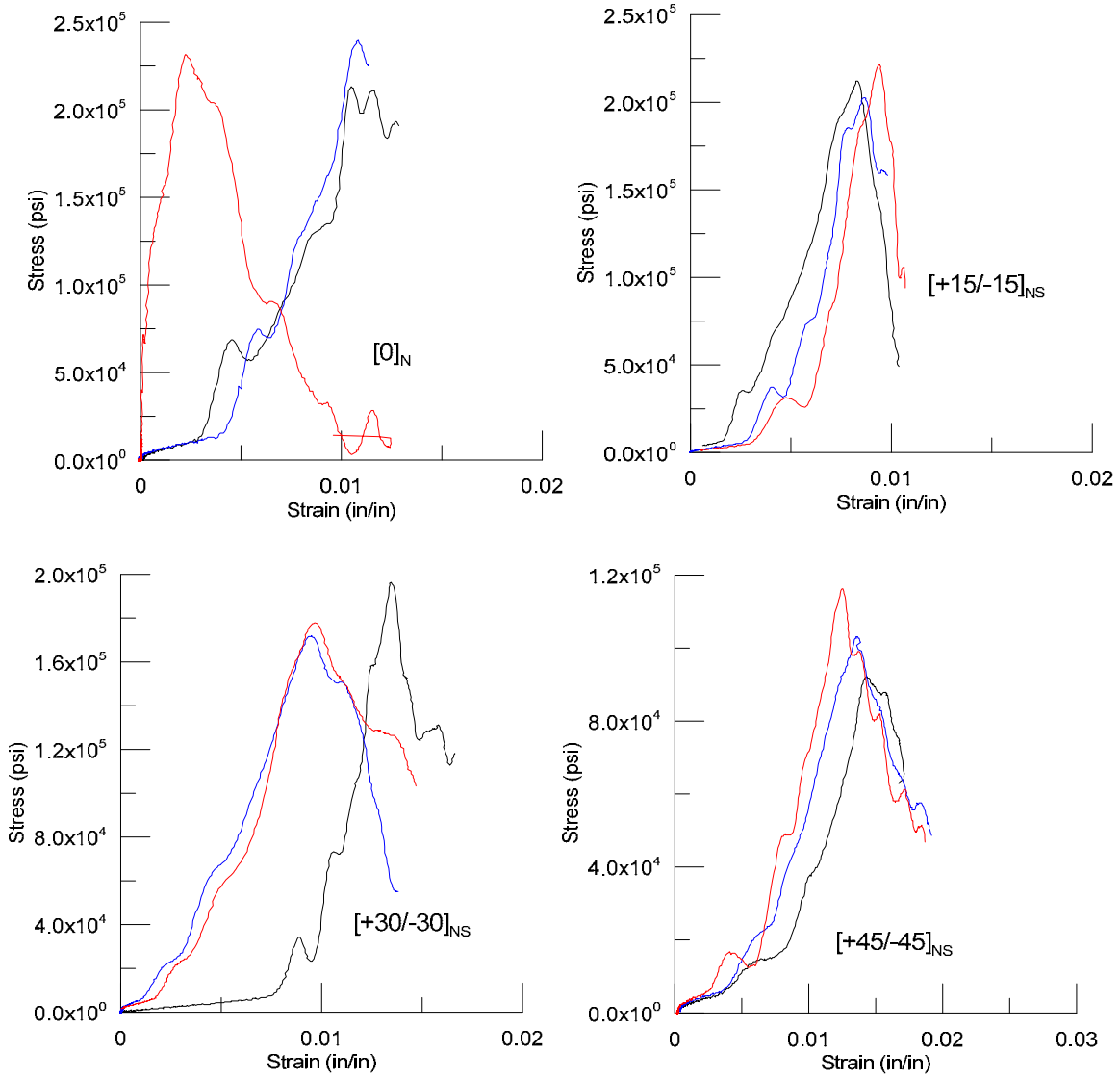

MATERIAL: Fibercote
NOMINAL STROKE RATE: 100 in/s

Figure A-27. Stress-Strain Diagrams for Fibercote Material Oriented at $[0°]_N$, $[-15°/+15°]_{NS}$, $[-30°/+30°]_{NS}$, and $[-45°/+45°]_{NS}$ and Tested at a Rate of 100 in/s

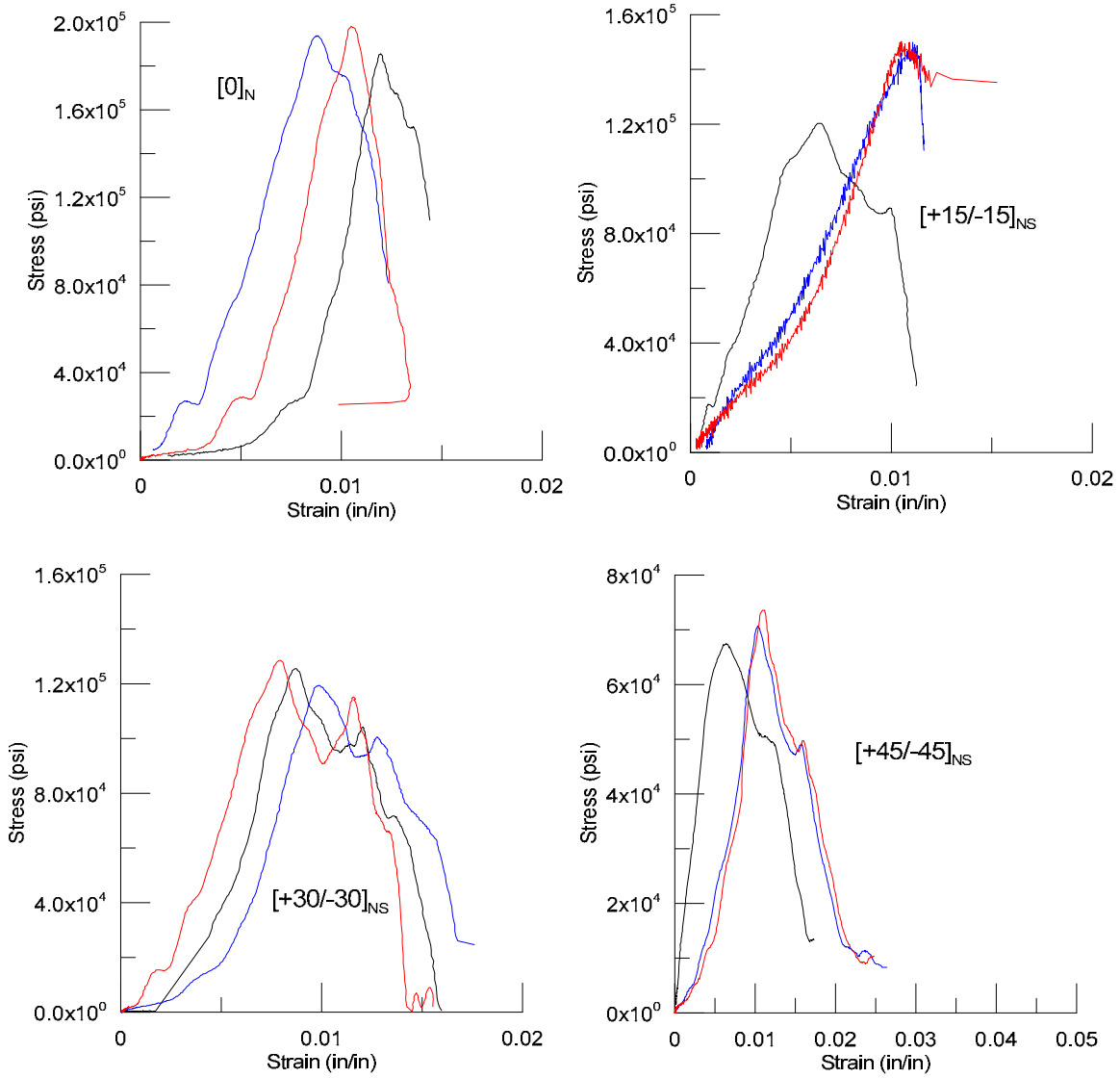

MATERIAL: Cytec
NOMINAL STROKE RATE: 100 in/s

Figure A-28. Stress-Strain Diagrams for Cytec Material Oriented at $[0°]_N$, $[-15°/+15°]_{NS}$, $[-30°/+30°]_{NS}$, and $[-45°/+45°]_{NS}$ and Tested at a Rate of 100 in/s

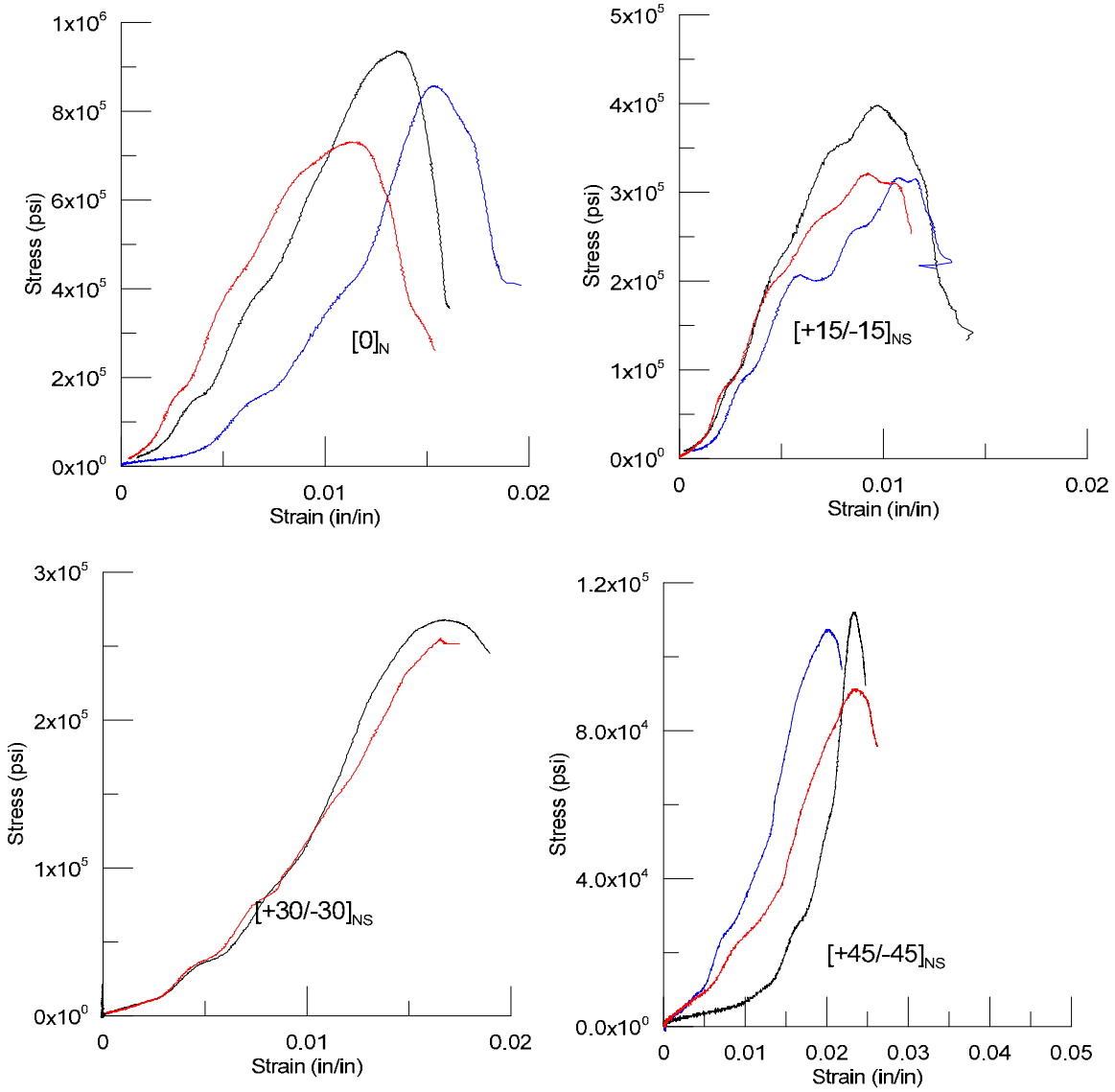

MATERIAL: Toray Unitape
NOMINAL STROKE RATE: 250 in/s

Figure A-29. Stress-Strain Diagrams for Toray Unitape Material Oriented at $[0°]_N$, $[-15°/+15°]_{NS}$, $[-30°/+30°]_{NS}$, and $[-45°/+45°]_{NS}$ and Tested at a Rate of 250 in/s

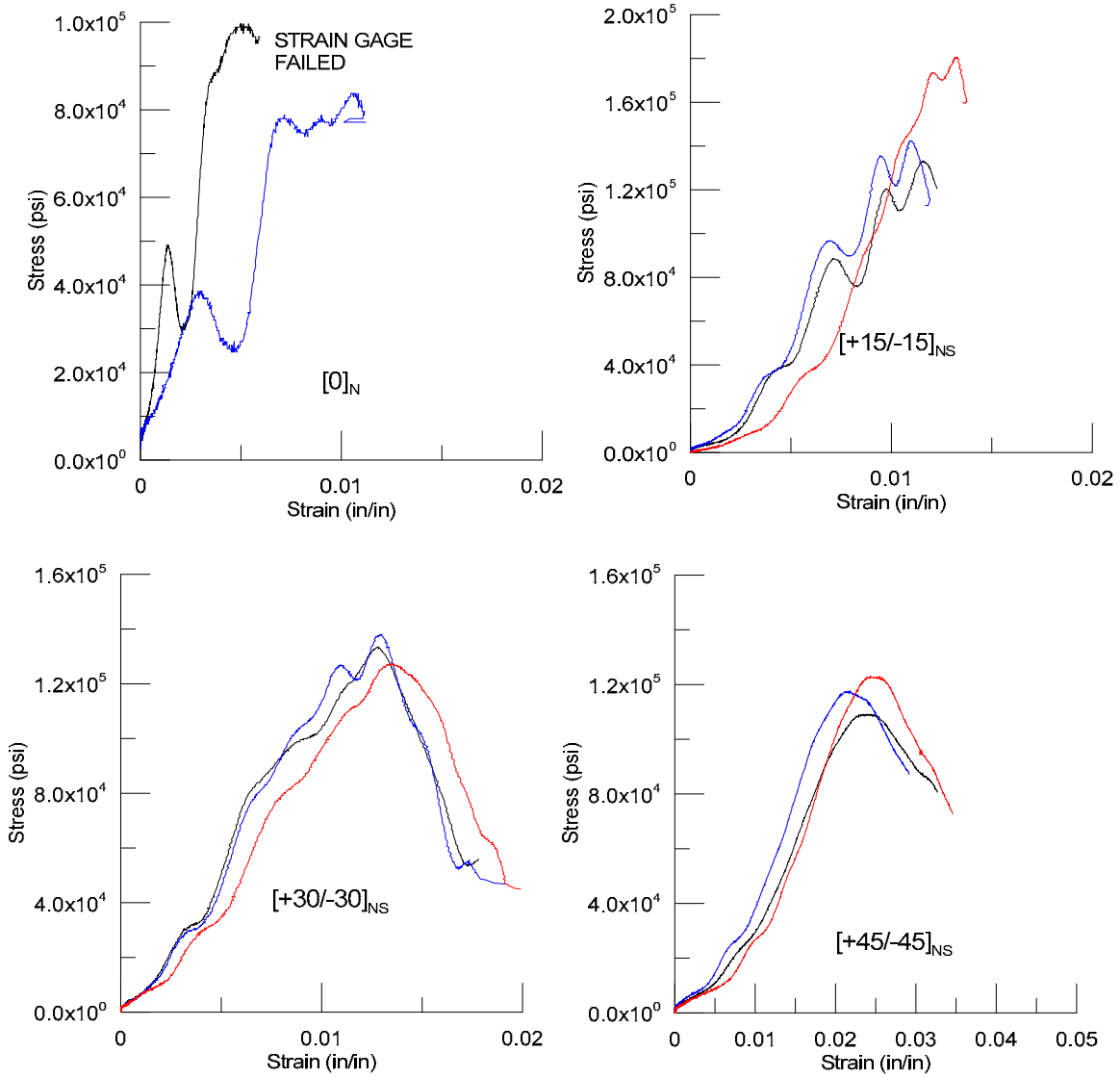

Figure A-30. Stress-Strain Diagrams for Toray PWCF Material Oriented at $[0°]_N$, $[-15°/+15°]_{NS}$, $[-30°/+°30]_{NS}$, and $[-45°/+45°]_{NS}$ and Tested at a Rate of 250 in/s

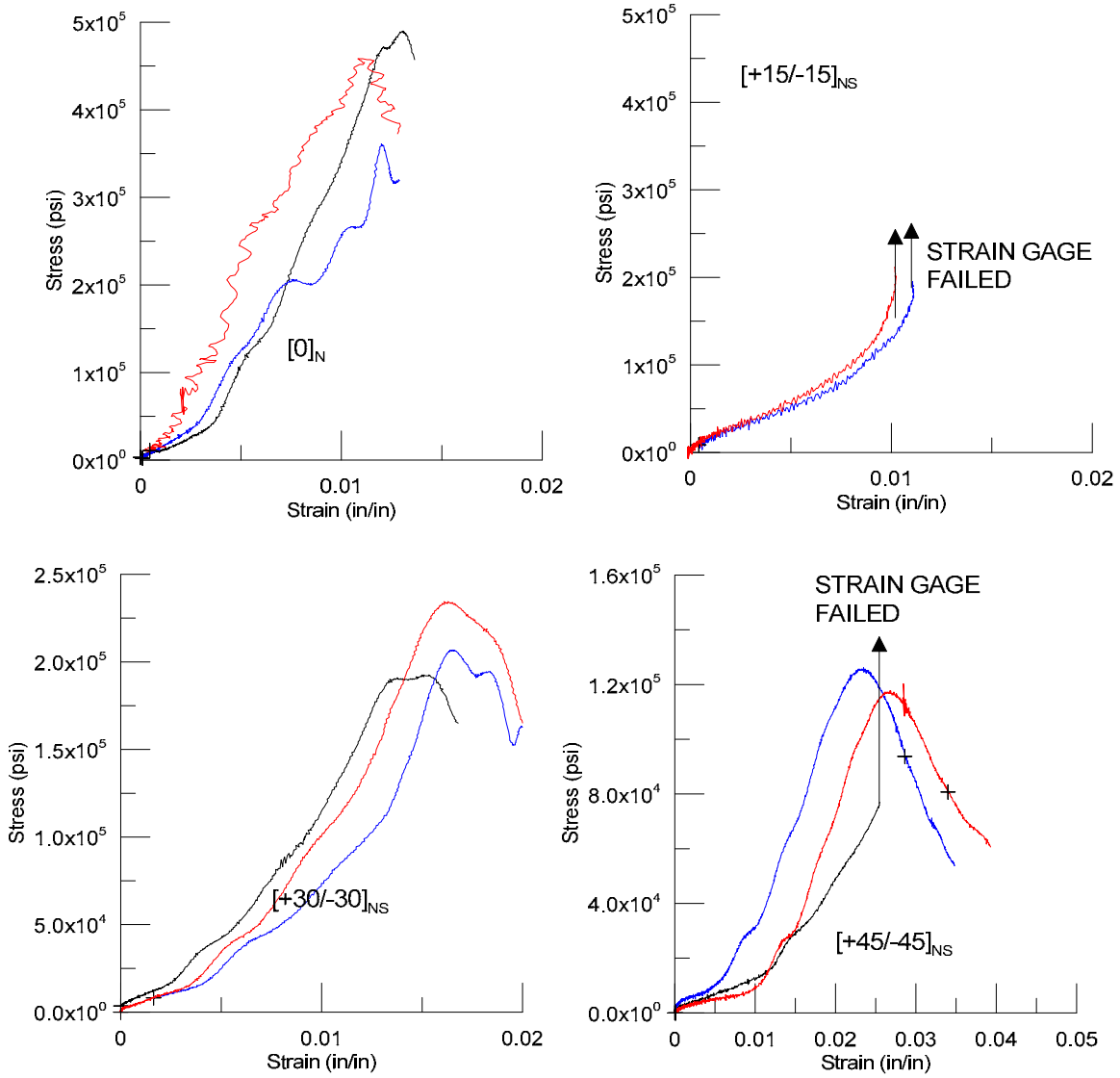

MATERIAL: TR_NCT 321-A-Newport Unitape
NOMINAL STROKE RATE: 250 in/s

Figure A-31. Stress-Strain Diagrams for Newport Unitape Material Oriented at $[0°]_N$, $[-15°/+15°]_{NS}$, $[-30°/+30°]_{NS}$, and $[-45°/+45°]_{NS}$ and Tested at a Rate of 250 in/s

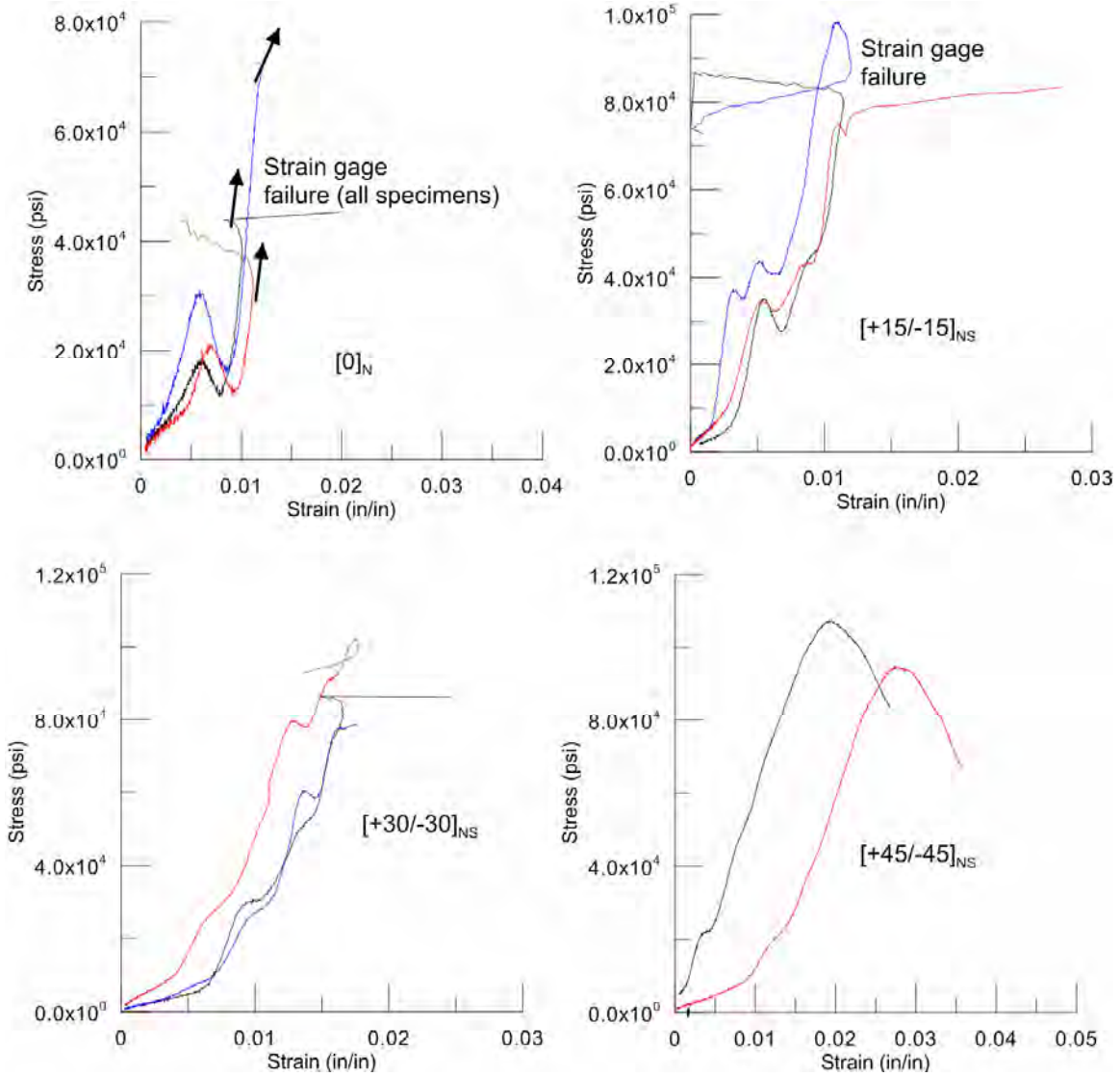

MATERIAL: Newport PWCF
NOMINAL STROKE RATE: 250 in/s

Figure A-32. Stress-Strain Diagrams for Newport PWCF Material Oriented at $[0°]_N$, $[-15°/+15°]_{NS}$, $[-30°/+30°]_{NS}$, and $[-45°/+45°]_{NS}$ and Tested at a Rate of 250 in/s

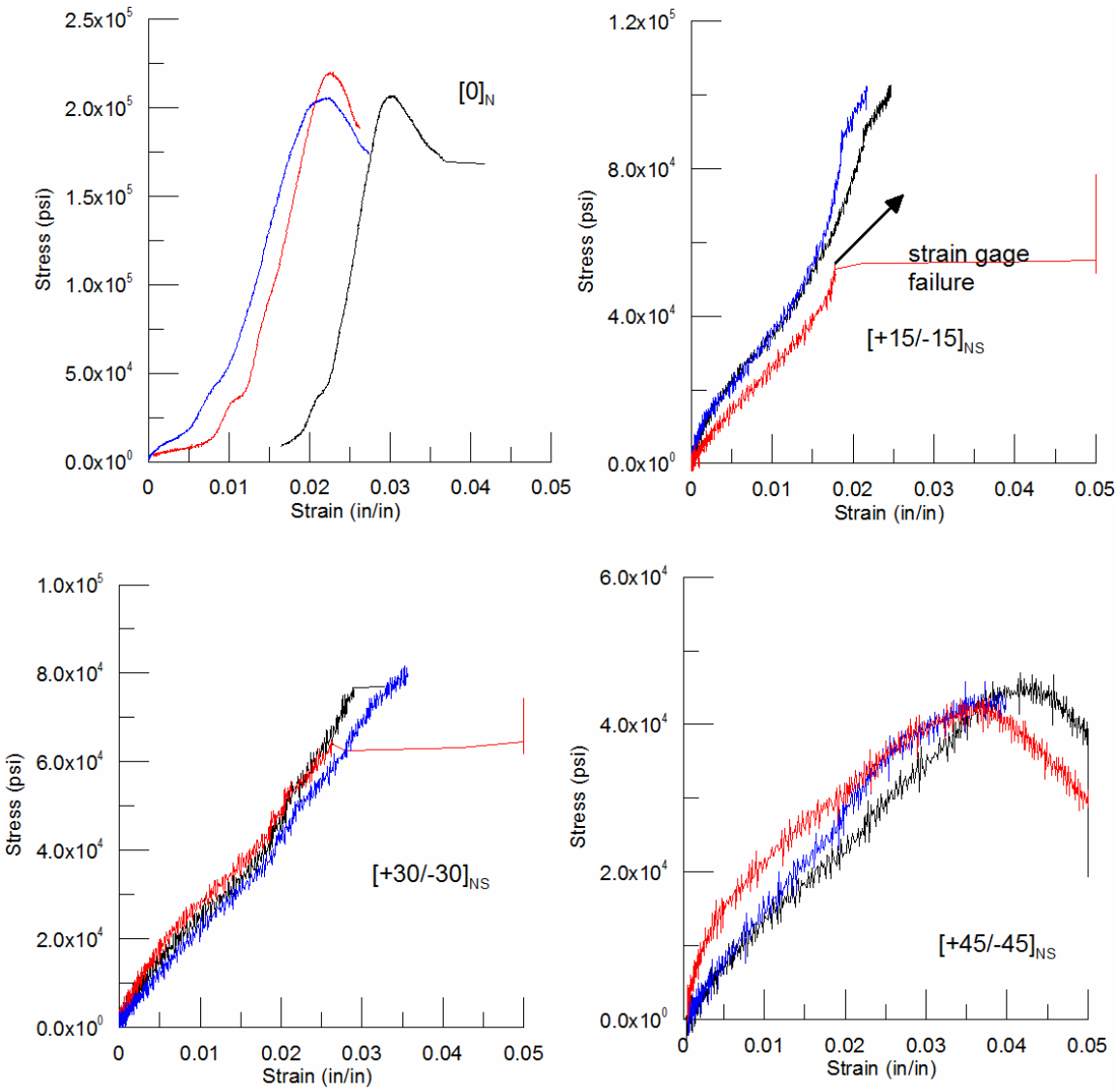

MATERIAL: Newport Glass Fiber
NOMINAL STROKE RATE: 250 in/s

Figure A-33. Stress-Strain Diagrams for Newport Glass Fiber Material Oriented at $[0°]_N$, $[-15°/+15°]_{NS}$, $[-30°/+30°]_{NS}$, and $[-45°/+45°]_{NS}$ and Tested at a Rate of 250 in/s

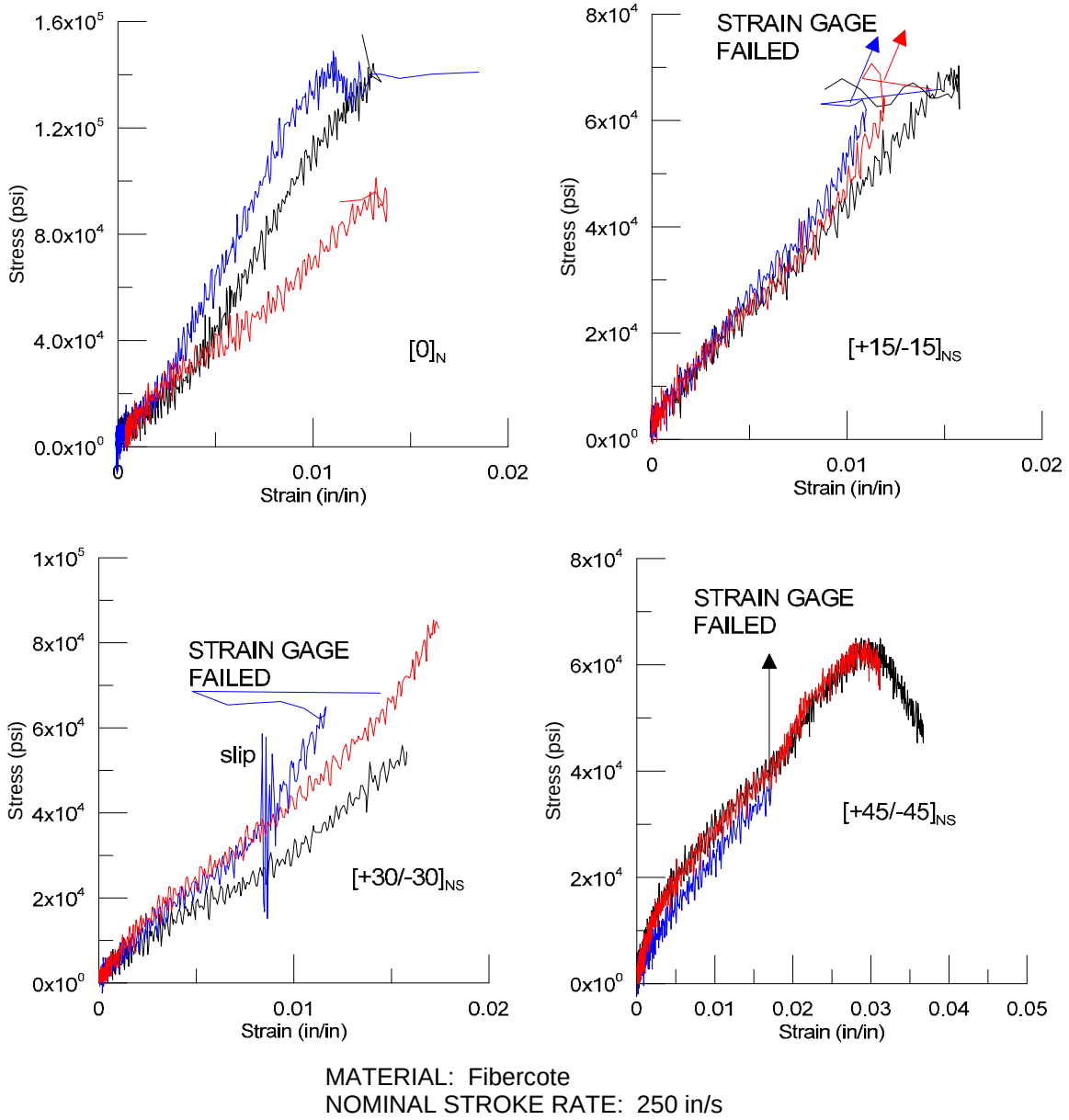

Figure A-34. Stress-Strain Diagrams for Fibercote Material Oriented at $[0°]_N$, $[-15°/+15°]_{NS}$, $[-30°/+30°]_{NS}$, and $[-45°/+45°]_{NS}$ and Tested at a Rate of 250 in/s

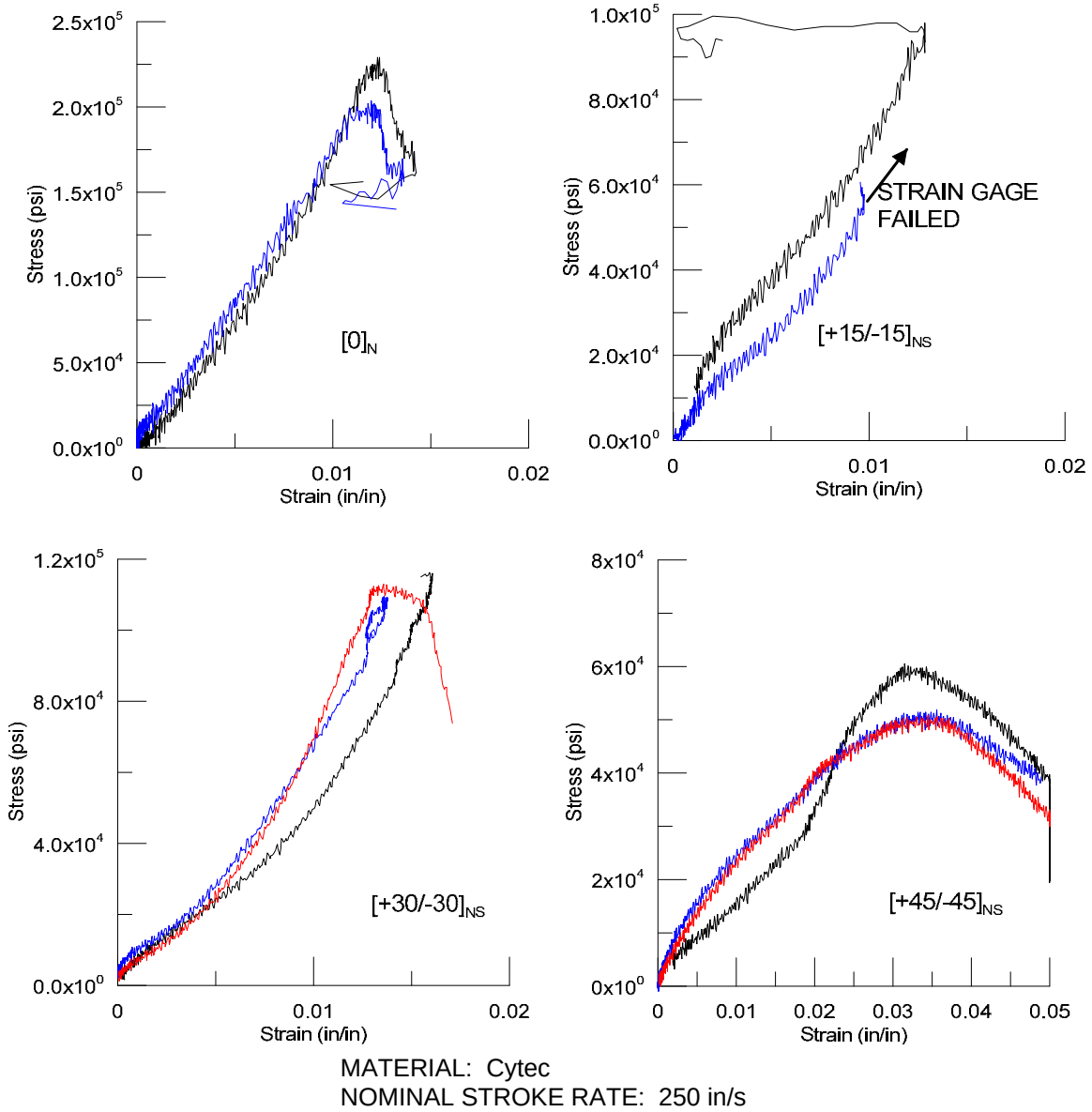

MATERIAL: Cytec
NOMINAL STROKE RATE: 250 in/s

Figure A-35. Stress-Strain Diagrams for Cytec Material Oriented at $[0°]_N$, $[-15°/+15°]_{NS}$, $[-30°/+30°]_{NS}$, and $[-45°/+45°]_{NS}$ and Tested at a Rate of 250 in/s

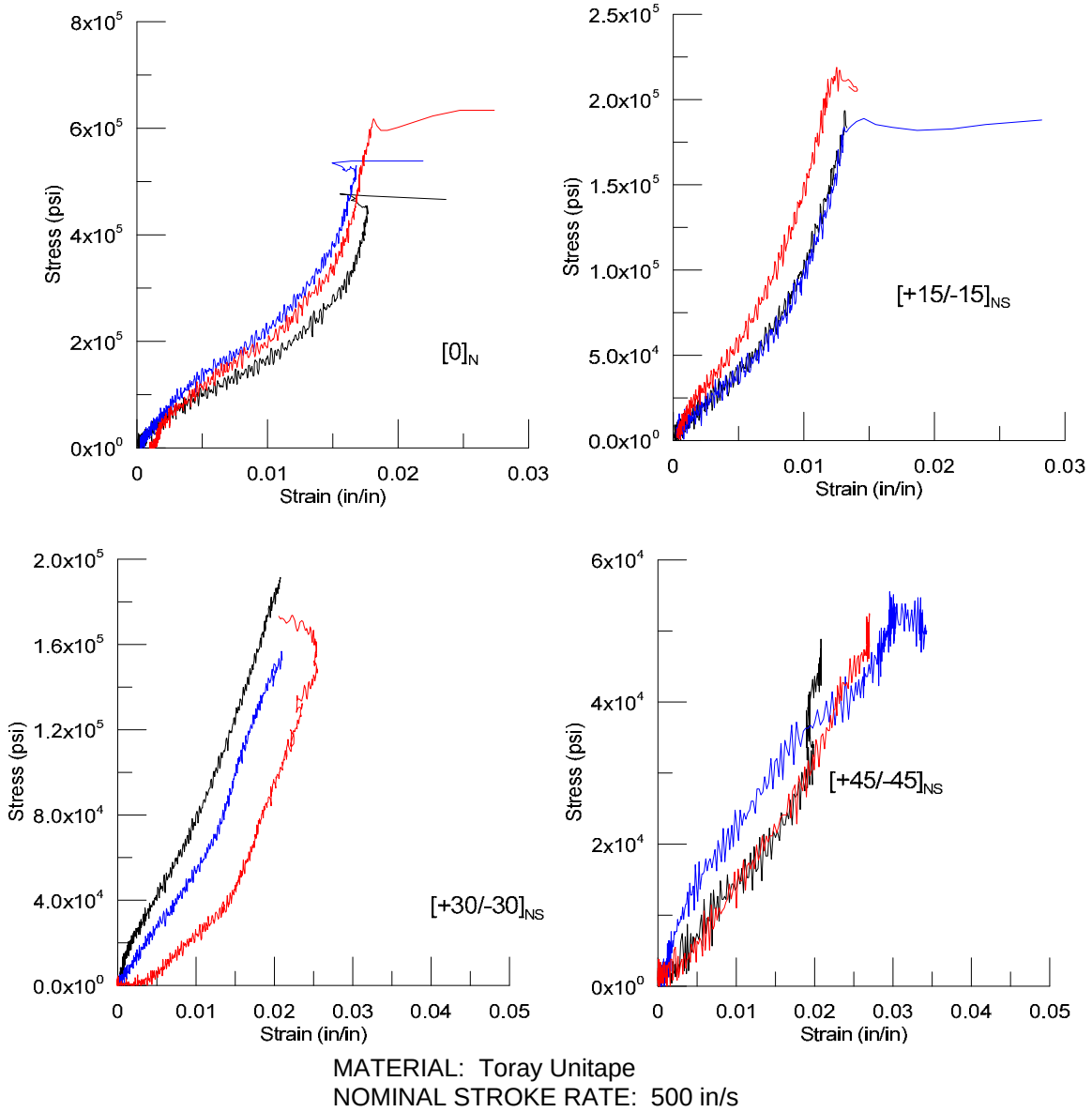

MATERIAL: Toray Unitape
NOMINAL STROKE RATE: 500 in/s

Figure A-36. Stress-Strain Diagrams for Toray Unitape Material Oriented at $[0°]_N$, $[-15°/+15°]_{NS}$, $[-30°/+30°]_{NS}$, and $[-45°/+45°]_{NS}$ and Tested at a Rate of 500 in/s

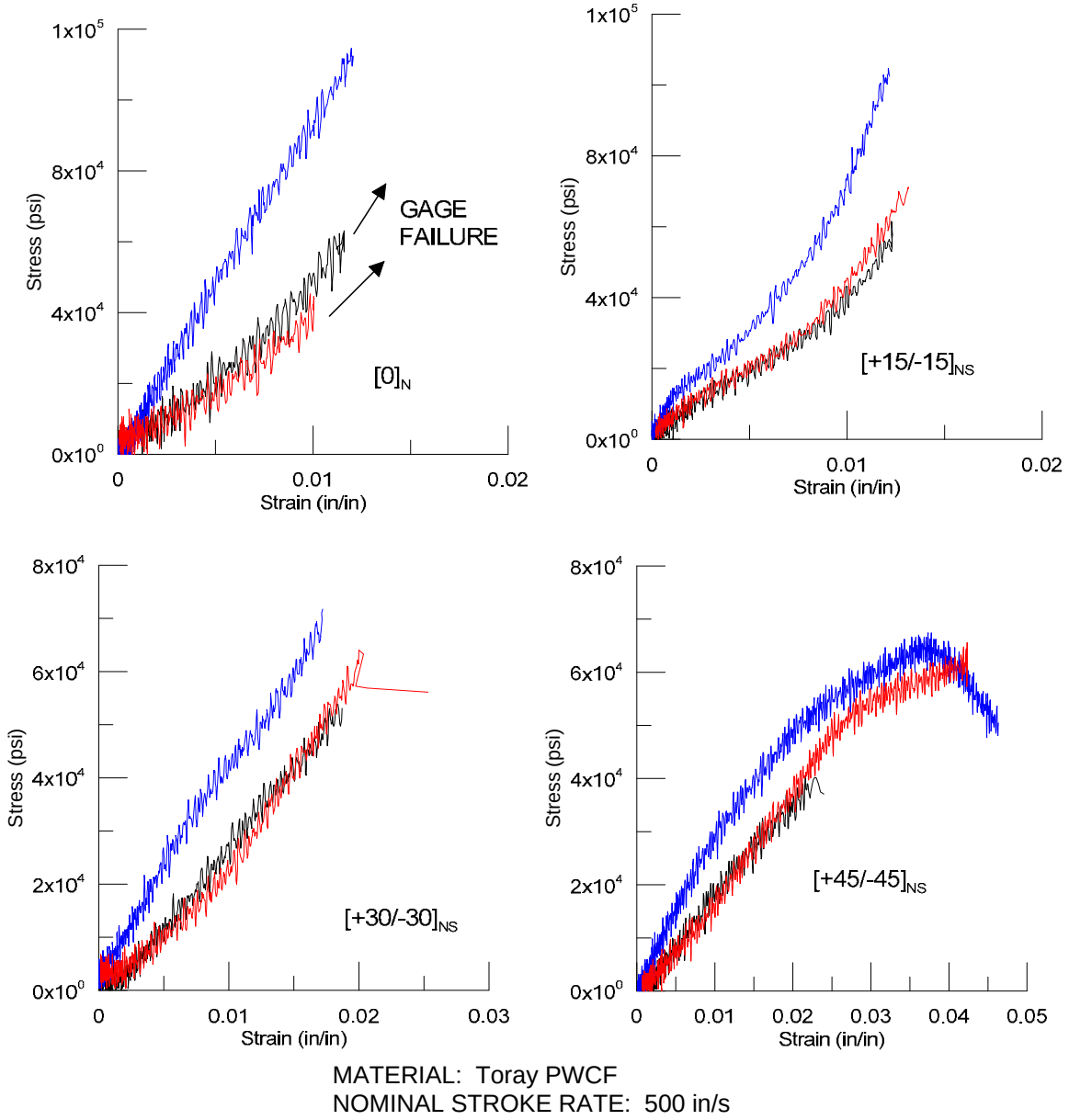

Figure A-37. Stress-Strain Diagrams for Toray PWCF Material Oriented at $[0°]_N$, $[-15°/+15°]_{NS}$, $[-30°/+30°]_{NS}$, and $[-45°/+45°]_{NS}$ and Tested at a Rate of 500 in/s

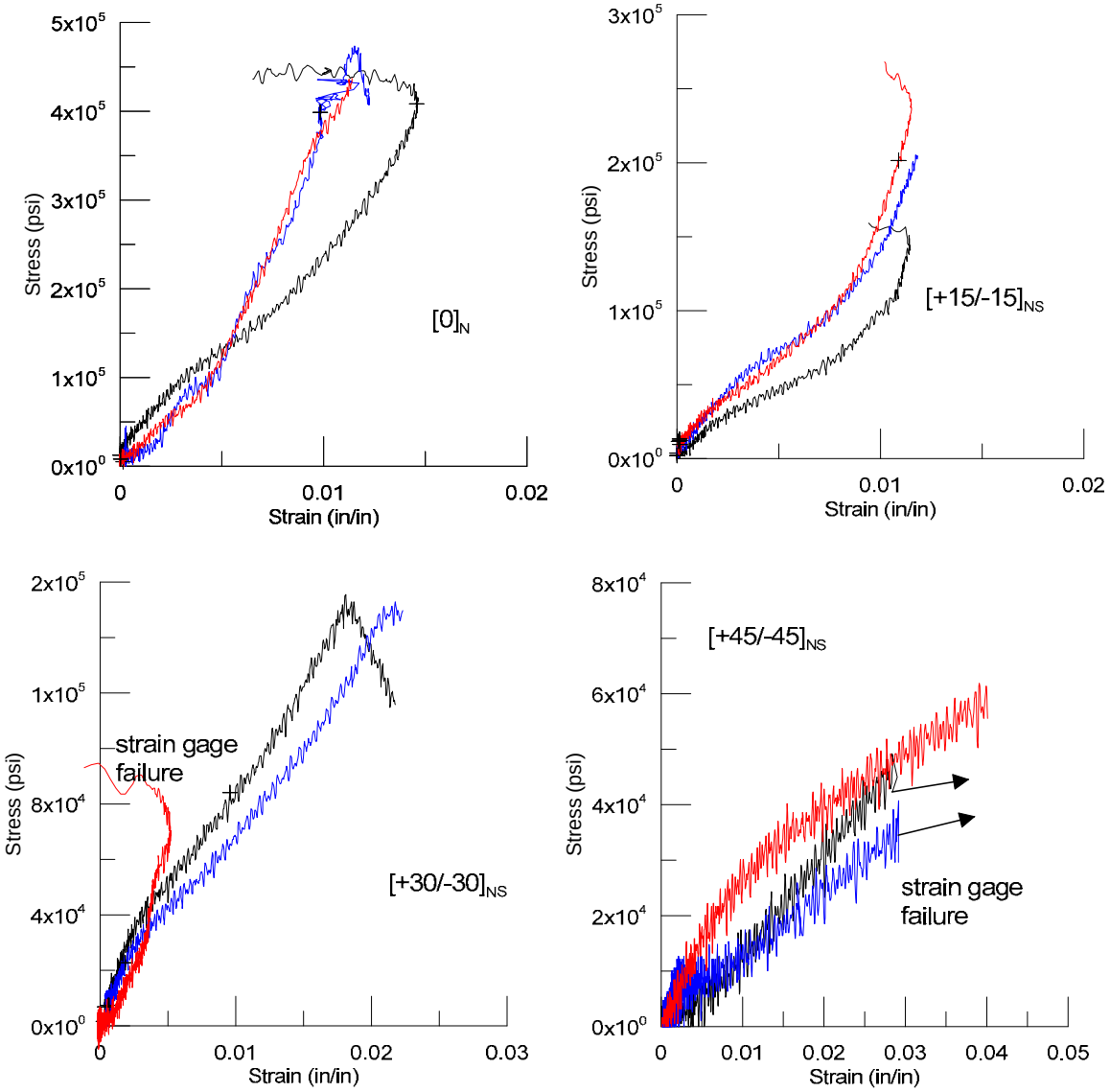

MATERIAL: TR_NCT 321-A-Newport Unitape
NOMINAL STROKE RATE: 500 in/s

Figure A-38. Stress-Strain Diagrams for Newport Unitape Material Oriented at $[0°]_N$, $[-15°/+15°]_{NS}$, $[-30°/+30°]_{NS}$, and $[-45°/+45°]_{NS}$ and Tested at a Rate of 500 in/s

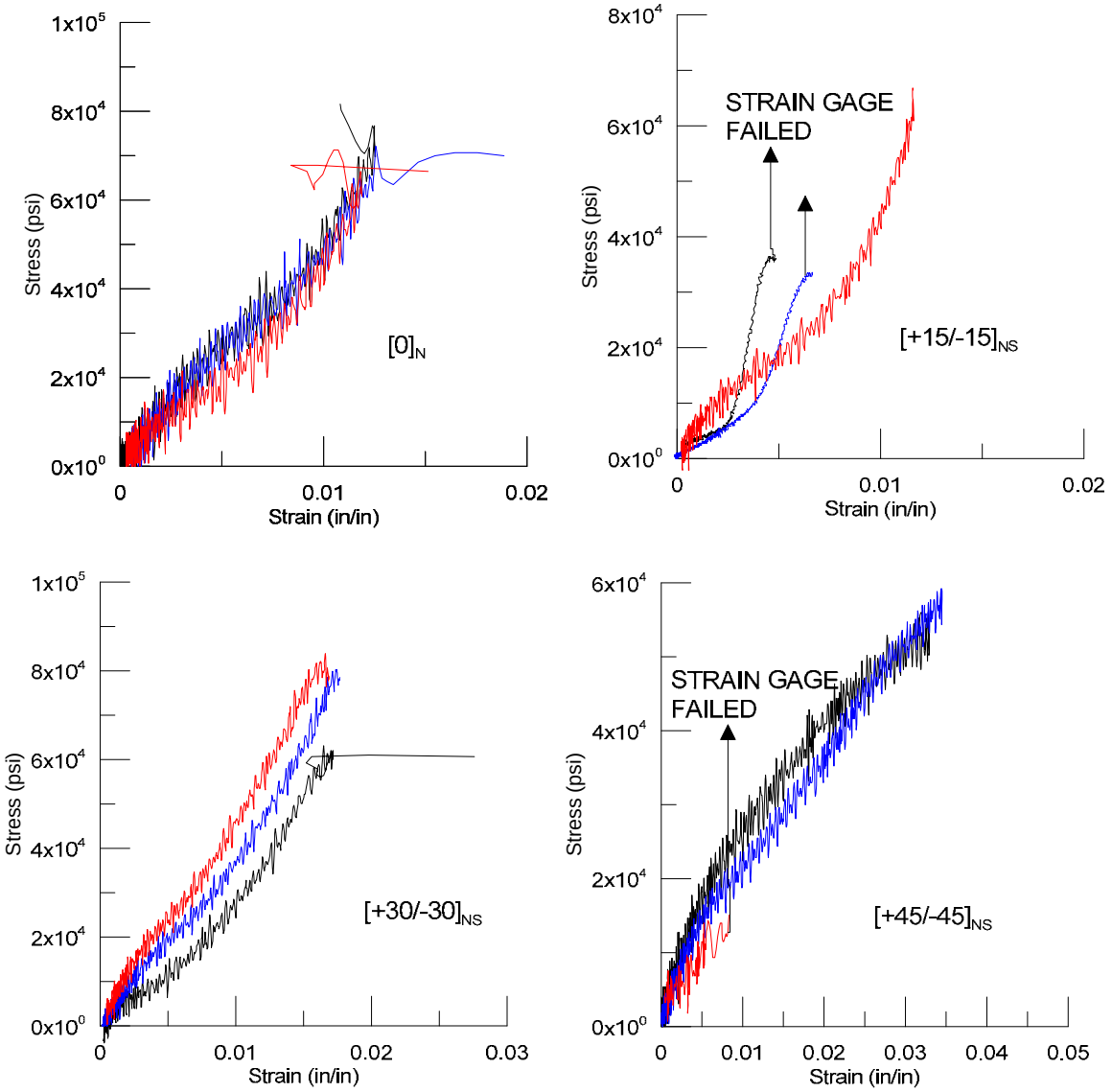

MATERIAL: Newport PWCF
NOMINAL STROKE RATE: 500 in/s

Figure A-39. Stress-Strain Diagrams for Newport PWCF Material Oriented at $[0°]_N$, $[-15°/+15°]_{NS}$, $[-30°/+30°]_{NS}$, and $[-45°/+45°]_{NS}$ and Tested at a Rate of 500 in/s

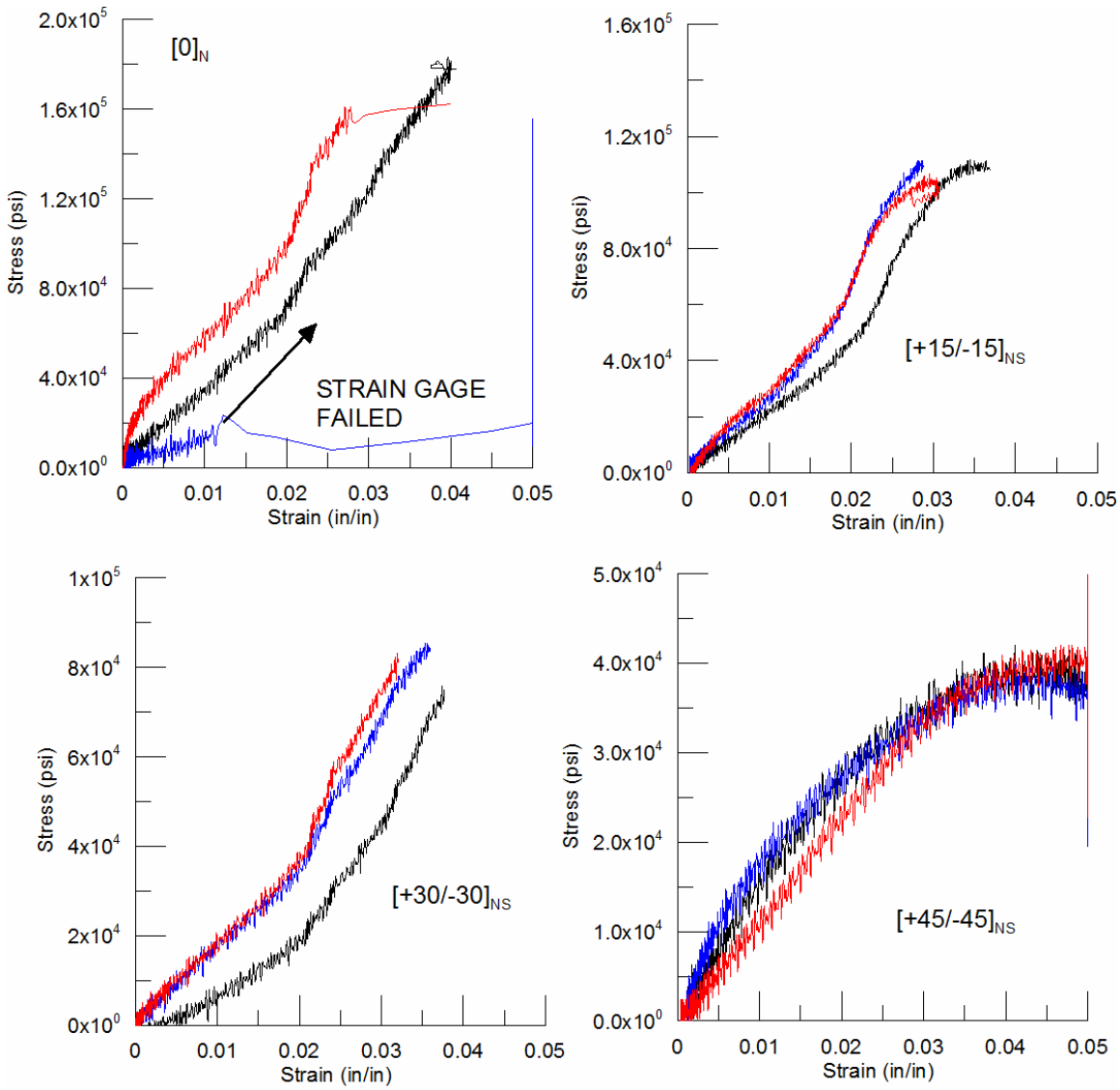

MATERIAL: Newport Glass Fiber
NOMINAL STROKE RATE: 500 in/s

Figure A-40. Stress-Strain Diagrams for Newport Glass Fiber Material Oriented at $[0°]_N$, $[-15°/+15°]_{NS}$, $[-30°/+30°]_{NS}$, and $[-45°/+45°]_{NS}$ and Tested at a Rate of 500 in/s

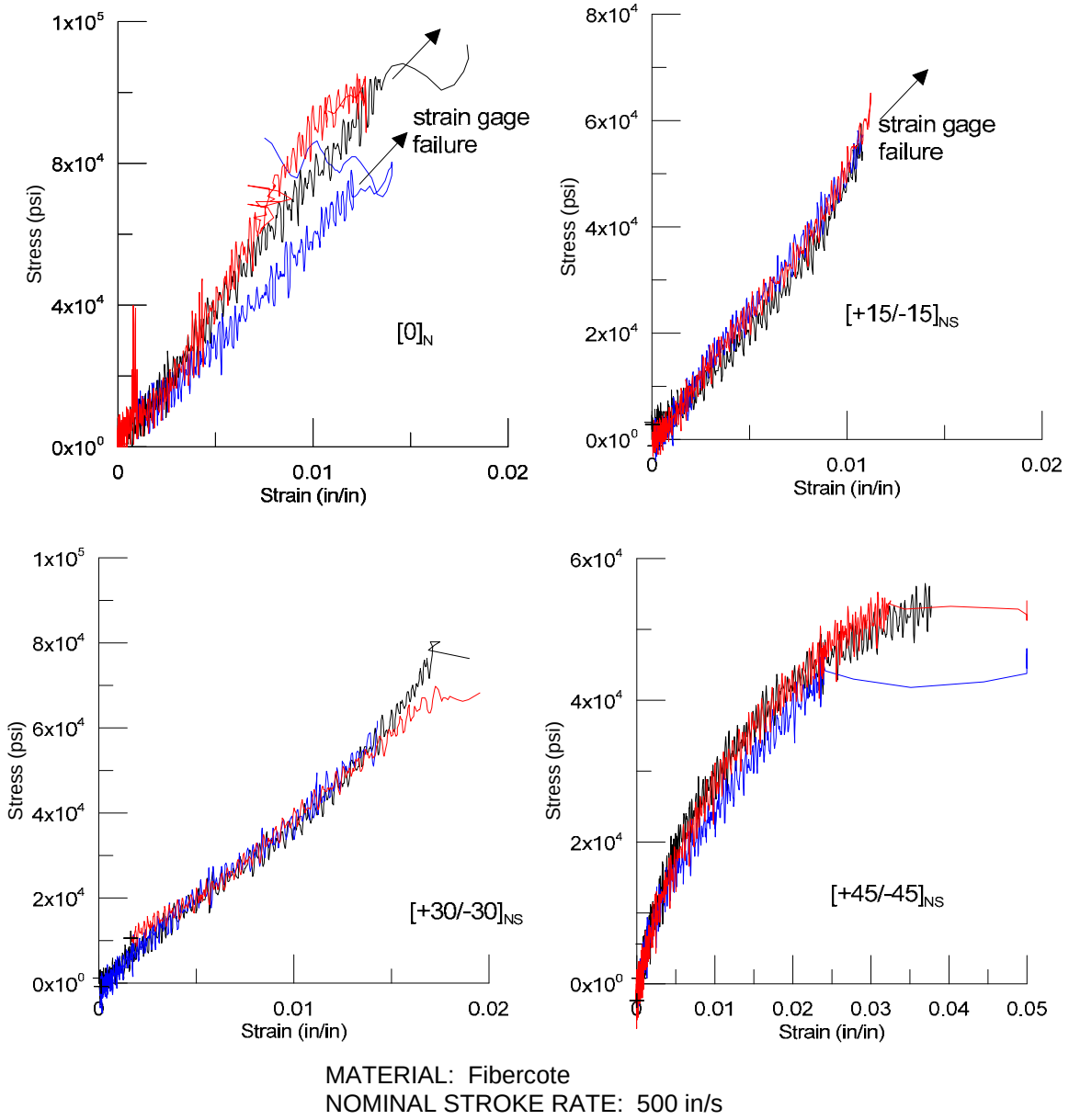

MATERIAL: Fibercote
NOMINAL STROKE RATE: 500 in/s

Figure A-41. Stress-Strain Diagrams for Fibercote Material Oriented at $[0°]_N$, $[-15°/+15°]_{NS}$, $[-30°/+30°]_{NS}$, and $[-45°/+45°]_{NS}$ and Tested at a Rate of 500 in/s

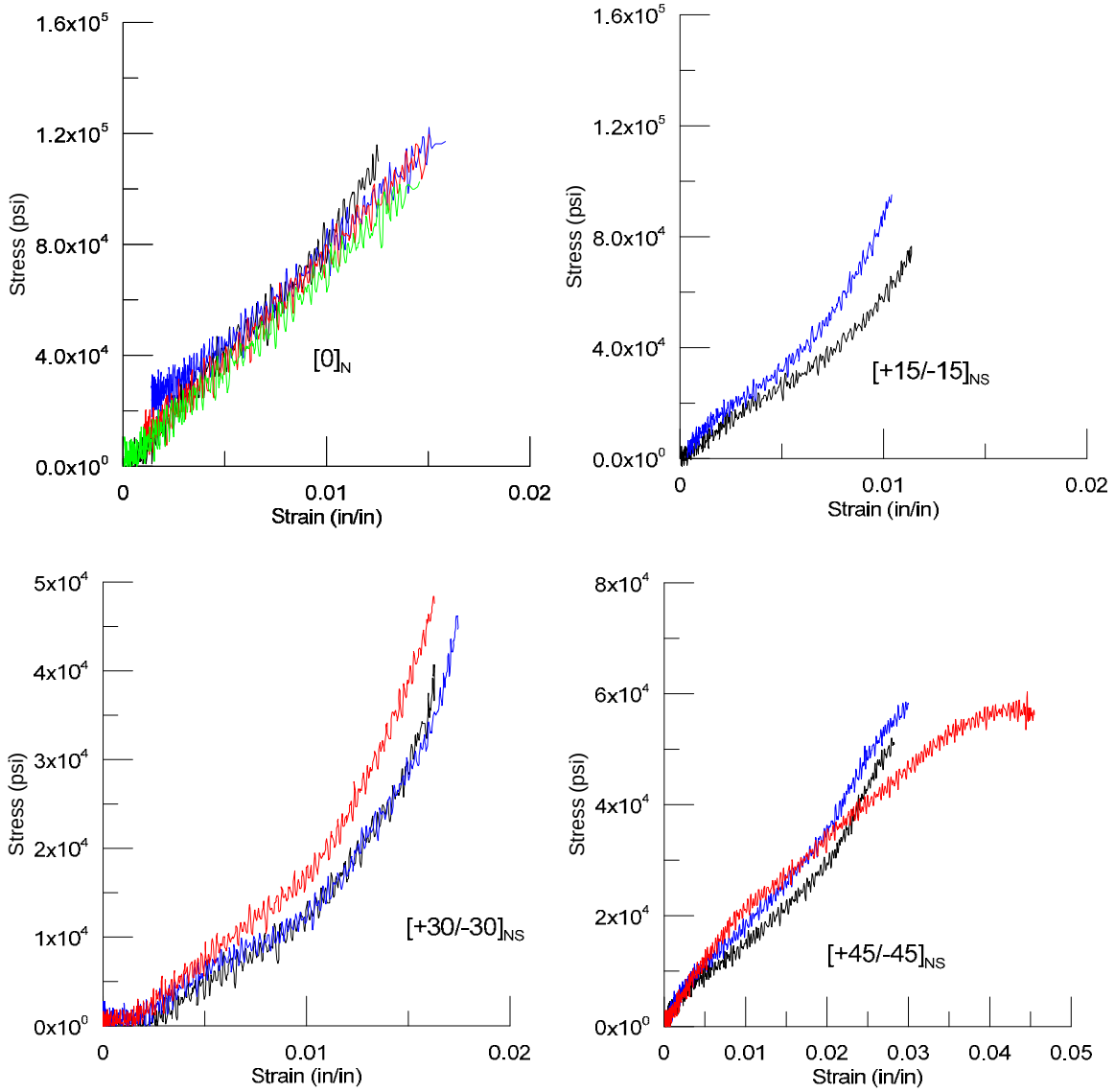

MATERIAL: Cytec
NOMINAL STROKE RATE: 500 in/s

Figure A-42. Stress-Strain Diagrams for Cytec Oriented at $[0°]_N$, $[-15°/+15°]_{NS}$, $[-30°/+30°]_{NS}$, and $[-45°/+45°]_{NS}$ and Tested at a Rate of 500 in/s

APPENDIX B—SHEAR TEST DATA

Table B-1. Shear Strengths at Different Rates of Testing

Material	Nominal Speed (in/s)					
	8×10^{-4}	1	10	100	250	500
Newport NB321/7781	18.06 17.24 18.47	19.86 19.60 20.16	22.33 21.49 22.14	29.28 28.66 28.55	42.85 42.70 42.14	46.62 45.09 35.64
Newport NB321/3K70 PWCF	17.72 17.12	21.54 20.37 19.01	20.83 21.38 20.72	30.51 31.93 30.67	40.94 41.05 42.40	42.60 49.51 45.83
Newport NCT321/G150 Unitape	20.63 17.95	22.81 23.81 22.78	24.19 24.05 24.33	42.23 40.34 41.68	24.39 24.26 24.07	25.47 22.69 23.22
Toray T800S/3900-2B Unitape	18.63 16.87 16.39	22.72 22.61 23.30	27.53 24.51 24.43	35.85 29.74 30.70	37.39 34.03 35.54	29.34 22.30 21.62
Toray T700G-12K-PW/3900-2	20.61 22.89	26.03 26.75 26.19	27.37 27.15 27.16	36.71 40.43 37.51	47.04 52.28 46.41	52.91 58.15 50.30
Fibercote 3KPW-E365 PWCF	22.06 19.05 18.98	21.34 22.74 22.84	24.99 24.84 23.30	39.99 33.02 36.75	29.53 32.48 42.66	25.84 25.31 29.15
Cytec T300/7714AC 3KNT	16.45 16.08 14.55	18.78 18.63 18.56	21.03 21.67 20.59	33.41 29.60 27.32	23.46 24.59 20.67	26.91 — 24.43

Units of strength equal $\times10^3$ psi

Table B-2. Average Shear Strain Rates at Different Rates of Testing

Material	Nominal Speed (in/s)					
	8×10^{-4}	1	10	100	250	500
Newport NB321/7781	0.0005 0.0018 0.0010	1.14 1.16 1.06	9.85 6.88 7.07	220.95 225.76 155.91	335.31 371.59 351.39	374.72 447.97 465.62
Newport NB321/3K70 PWCF	0.0012 0.0016	1.03 0.96 0.88	7.27 7.73 8.26	162.08 155.36 172.67	350.35 412.92 380.32	501.36 494.00 479.94
Newport NCT321/G150 Unitape	0.0016 0.0016	1.21 1.24 0.93	5.64 6.36 9.31	191.02 204.63 213.23	538.42 508.00 483.64	621.83 655.52 649.18
Toray T800S/3900-2B Unitape	0.0023 0.0021 0.0022	0.86 1.18 1.06	6.99 6.86 10.08	190.36 167.37 186.76	391.09 354.58 369.16	619.12 512.32 565.09
Toray T700G-12K- PW/3900-2	0.0015 0.0012	0.79 0.80 0.83	5.79 6.06 6.15	143.38 140.32 139.08	357.14 317.01 363.05	418.43 376.19 428.42
Fibercote 3KPW-E365 PWCF	0.0008 0.0007 0.0005	0.99 0.91 1.02	7.68 7.53 6.84	254.90 310.15 241.91	257.00 490.07 551.55	574.96 708.09 654.82
Cytec T300/7714AC 3KNT	0.0024 0.0013 0.0037	0.98 1.05 0.54	8.25 8.48 8.51	236.9 201.5 216.7	539.1 464.8 588.6	528.3 581.5 588.8

Units of shear strain rate equal rad/s

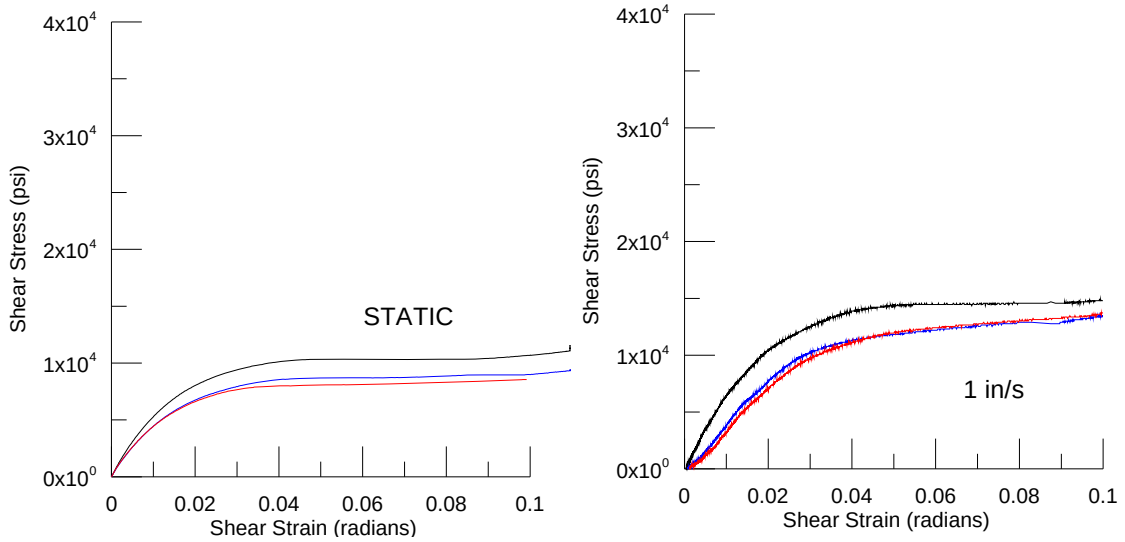

MATERIAL: Toray Unitape

Figure B-1. Shear Stress-Strain Diagrams for Toray Unitape Material Tested at Quasi-Static Rate and at 1 in/s

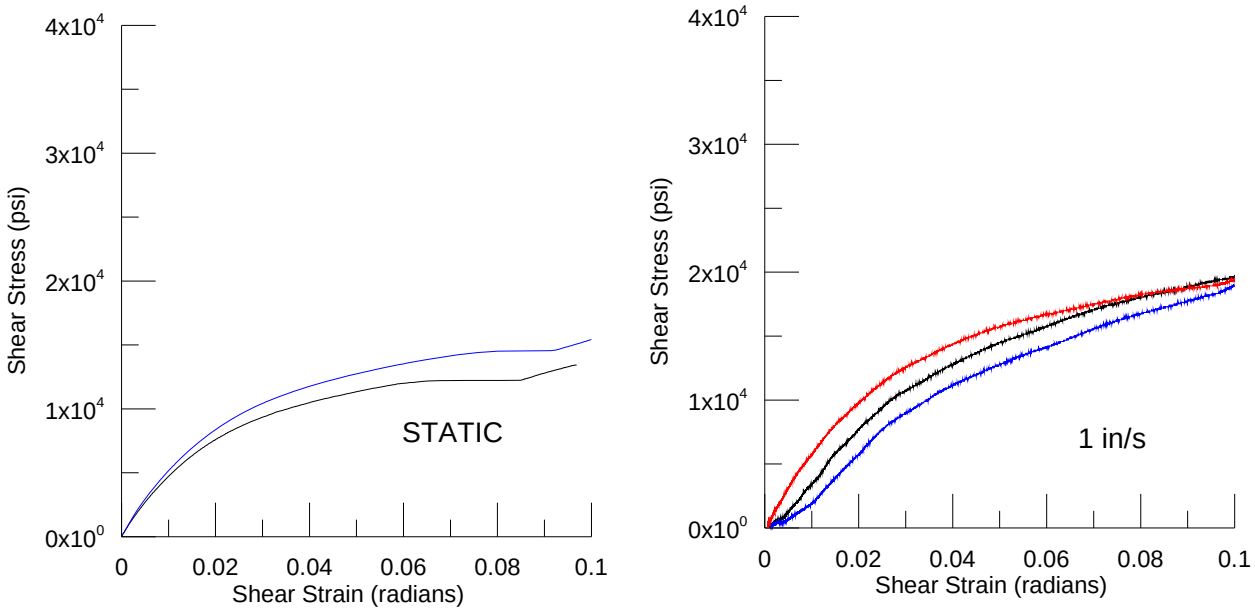

MATERIAL: Toray Fabric

Figure B-2. Shear Stress-Strain Diagrams for Toray Fabric Material Tested at Quasi-Static Rate and at 1 in/s

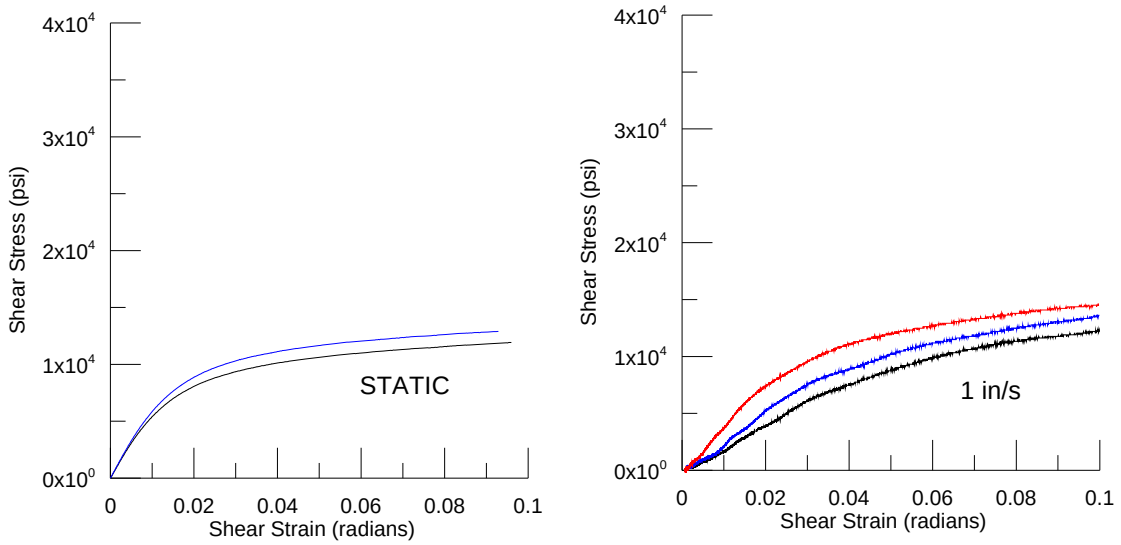

MATERIAL: Newport Unitape

Figure B-3. Shear Stress-Strain Diagrams for Newport Unitape Material Tested at Quasi-Static Rate and at 1 in/s

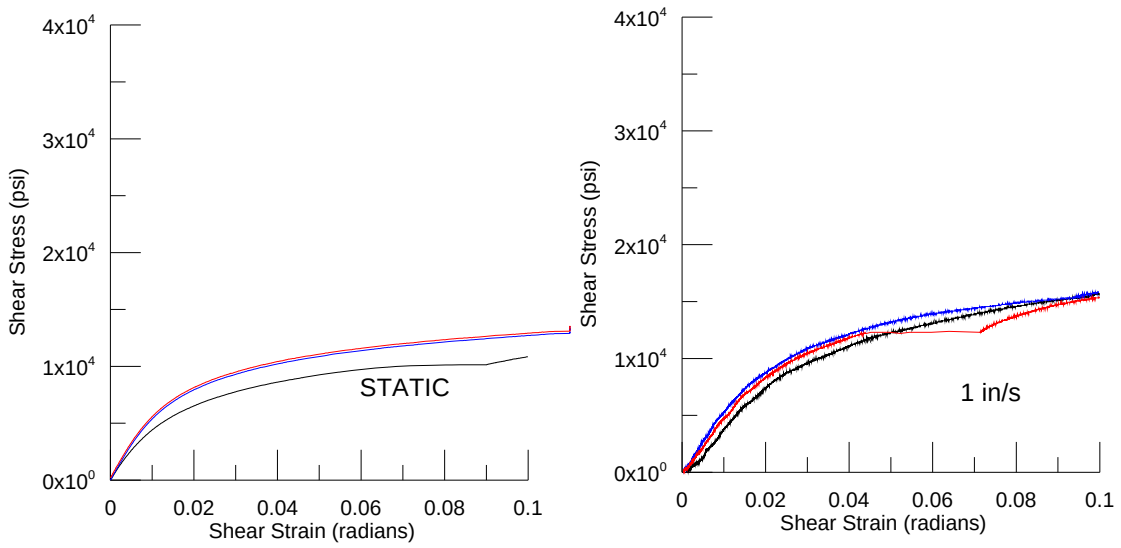

MATERIAL: Newport Carbon Fabric

Figure B-4. Shear Stress-Strain Diagrams for Newport Carbon Fabric Material Tested at Quasi-Static Rate and at 1 in/s

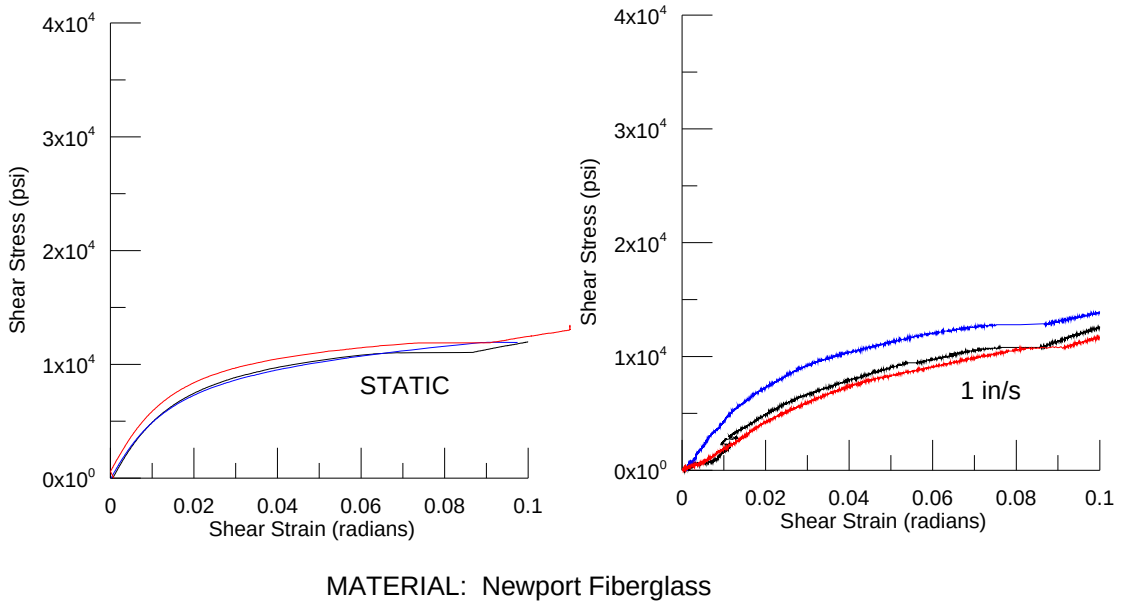

Figure B-5. Shear Stress-Strain Diagrams for Newport Fiberglass Material Tested at Quasi-Static Rate and at 1 in/s

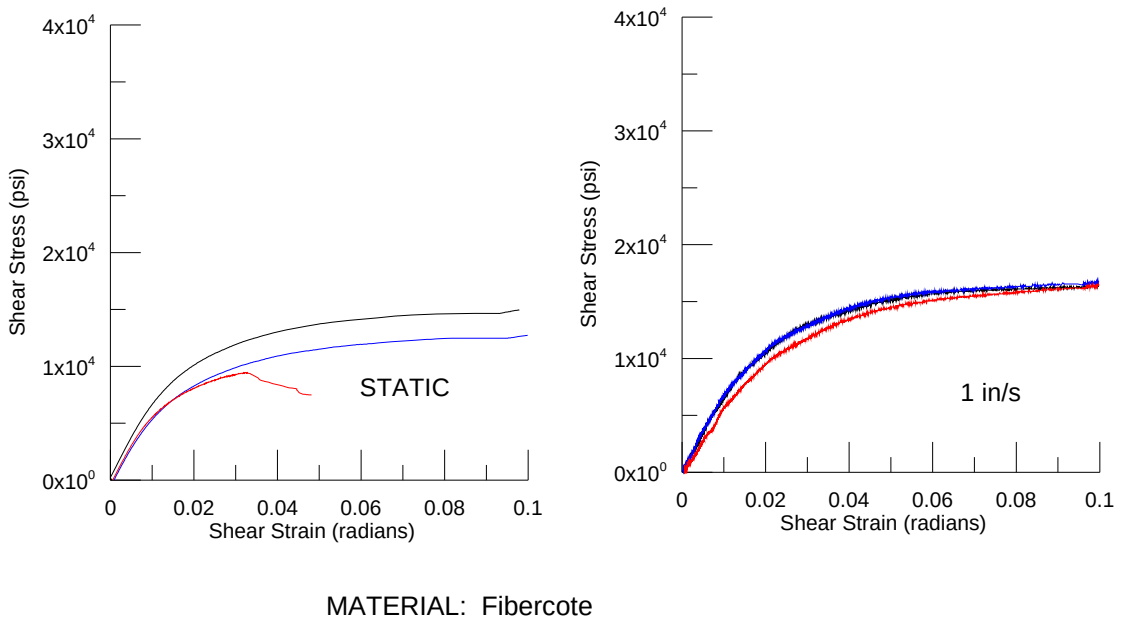

Figure B-6. Shear Stress-Strain Diagrams for Fibercote Material Tested at Quasi-Static Rate and at 1 in/s

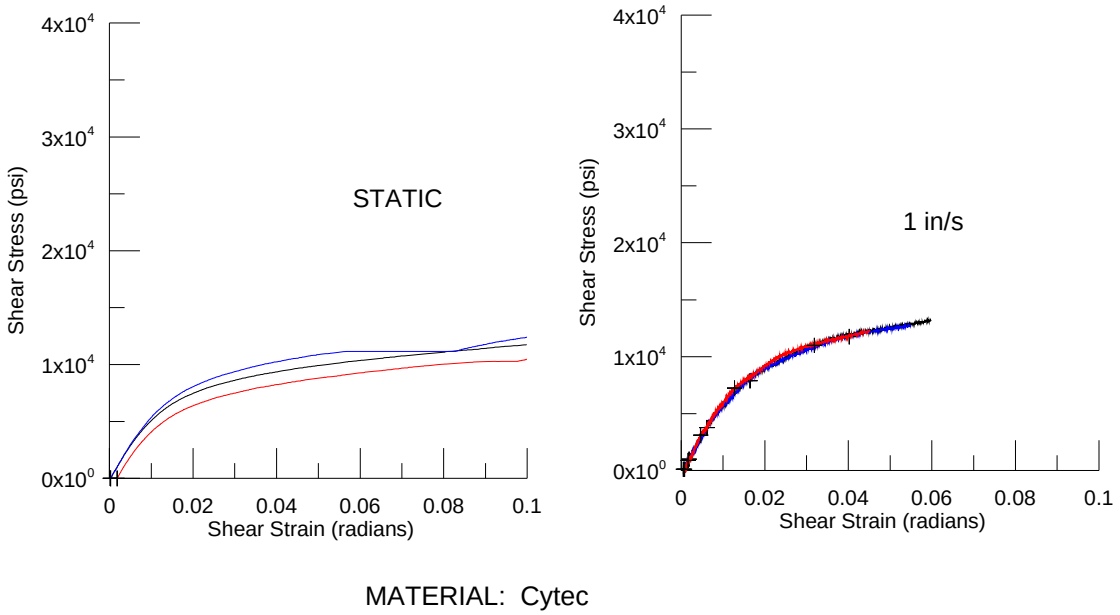

Figure B-7. Shear Stress-Strain Diagrams for Cytec Material Tested at Quasi-Static Rate and at 1 in/s

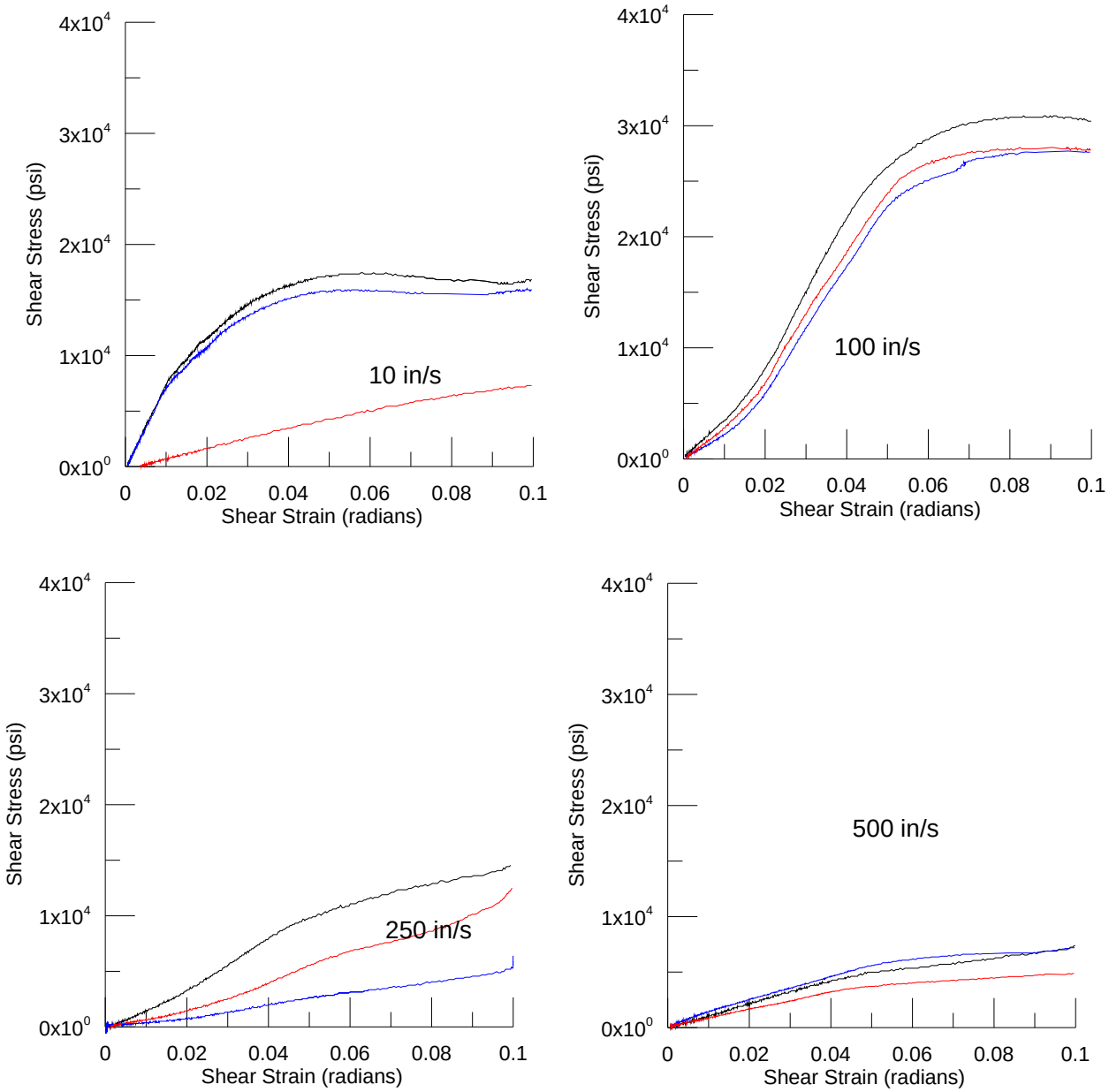

MATERIAL: Toray Unitape

Figure B-8. Shear Stress-Strain Diagrams for Toray Unitape Material Tested at Rates of 10, 100, 250, and 500 in/s

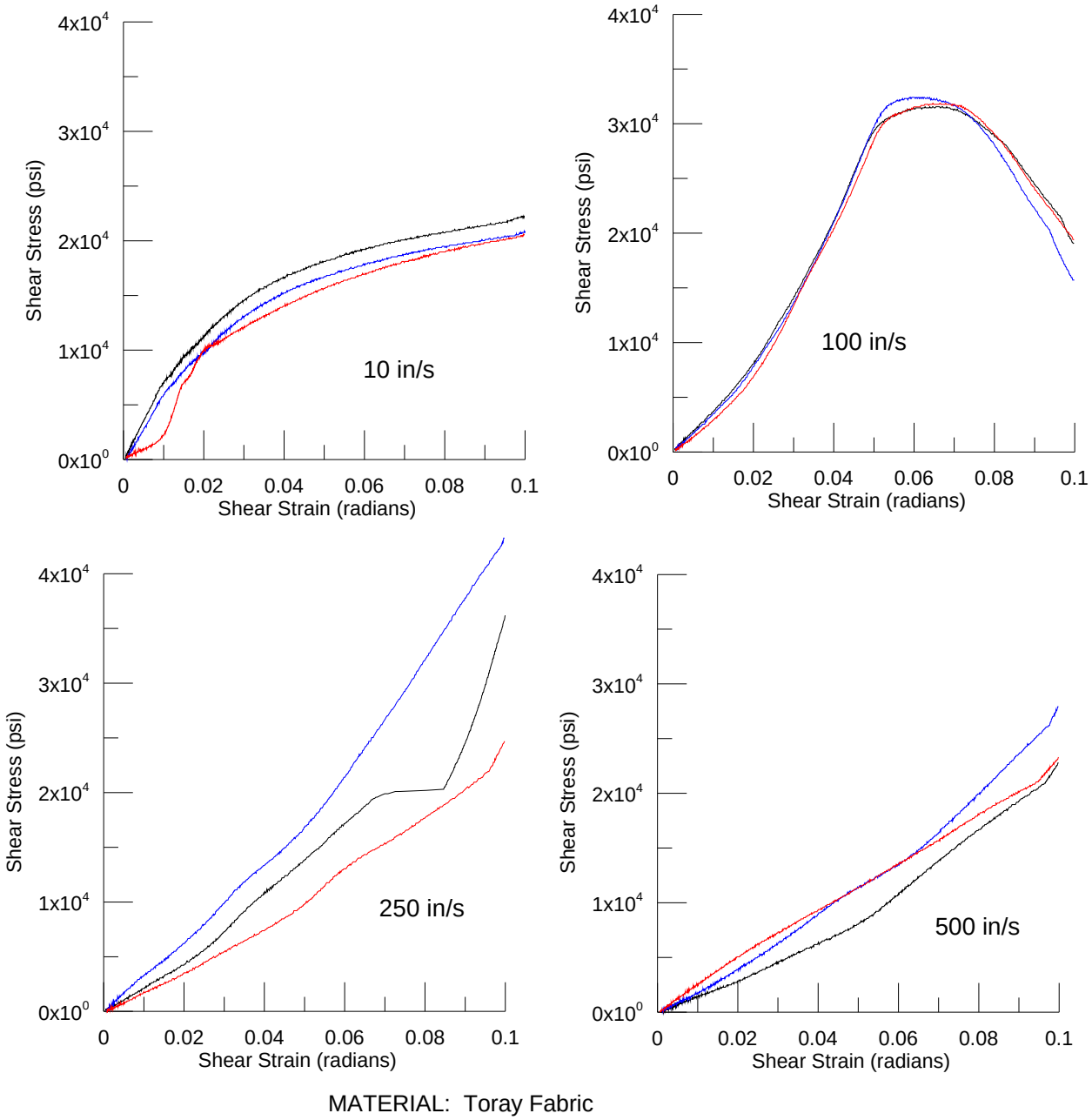

Figure B-9. Shear Stress-Strain Diagrams for Toray Fabric Material Tested at Rates of 10, 100, 250, and 500 in/s

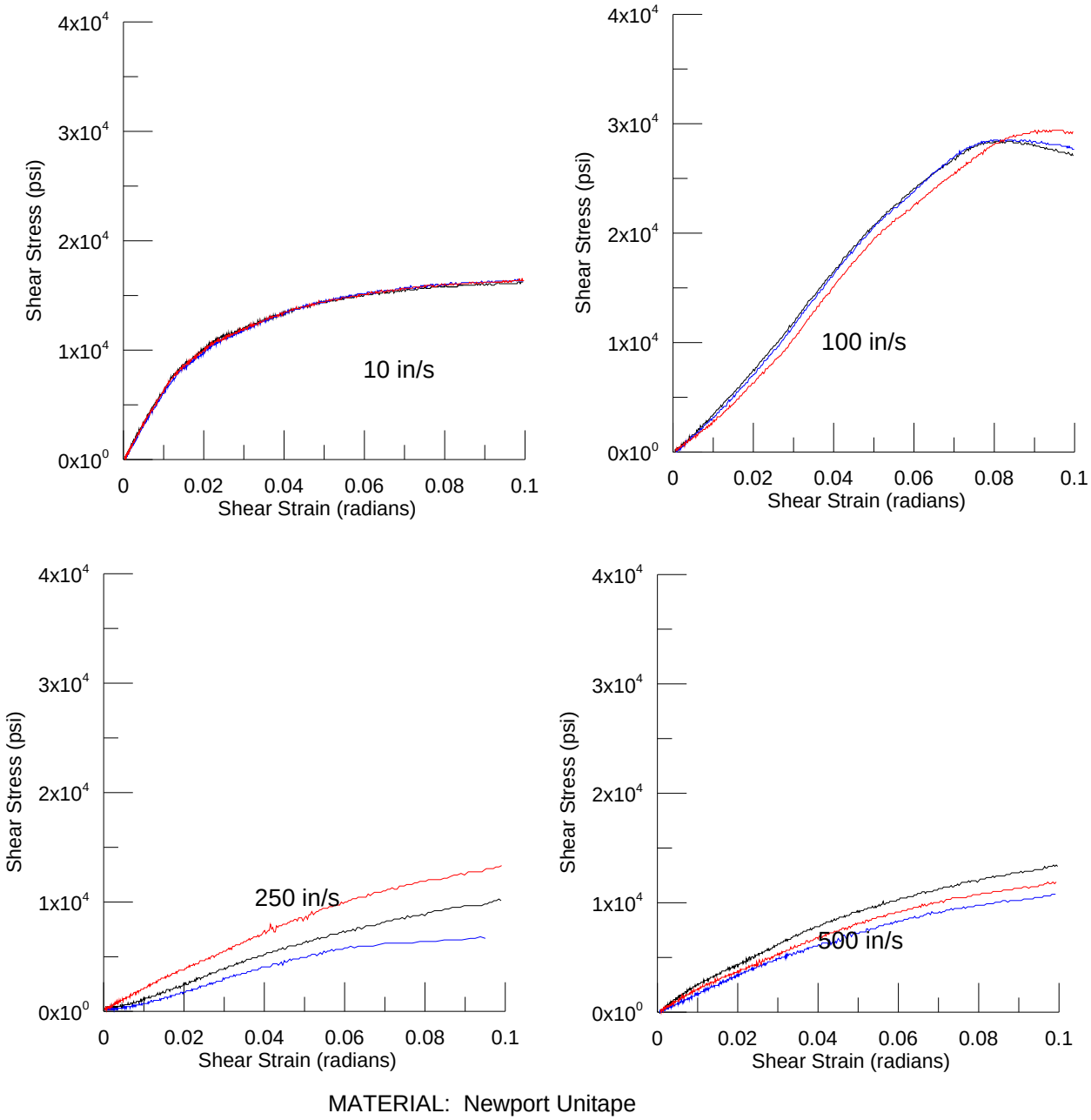

Figure B-10. Shear Stress-Strain Diagrams for Newport Unitape Material Tested at Rates of 10, 100, 250, and 500 in/s

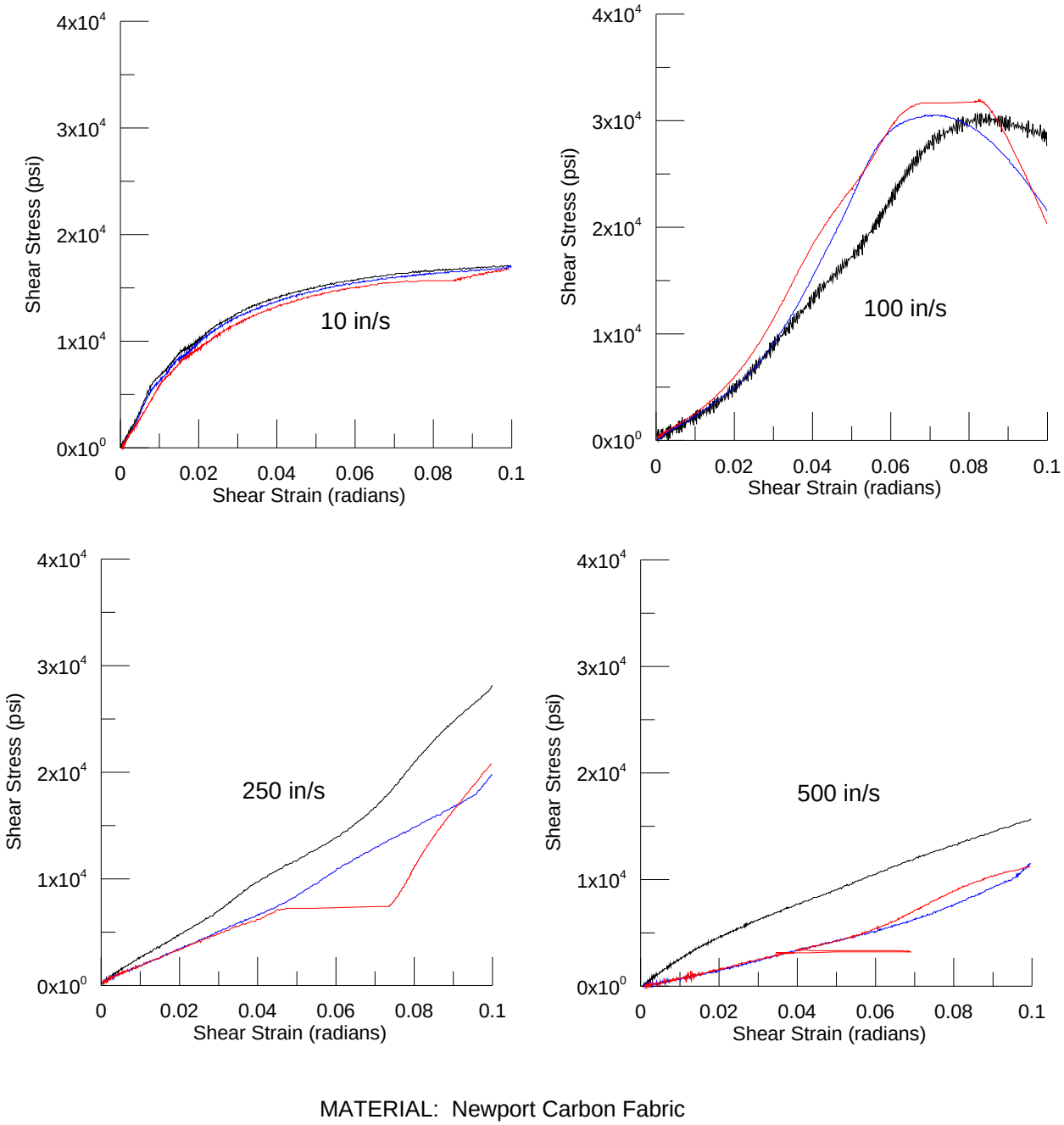

MATERIAL: Newport Carbon Fabric

Figure B-11. Shear Stress-Strain Diagrams for Newport Carbon Fabric Material Tested at Rates of 10, 100, 250, and 500 in/s

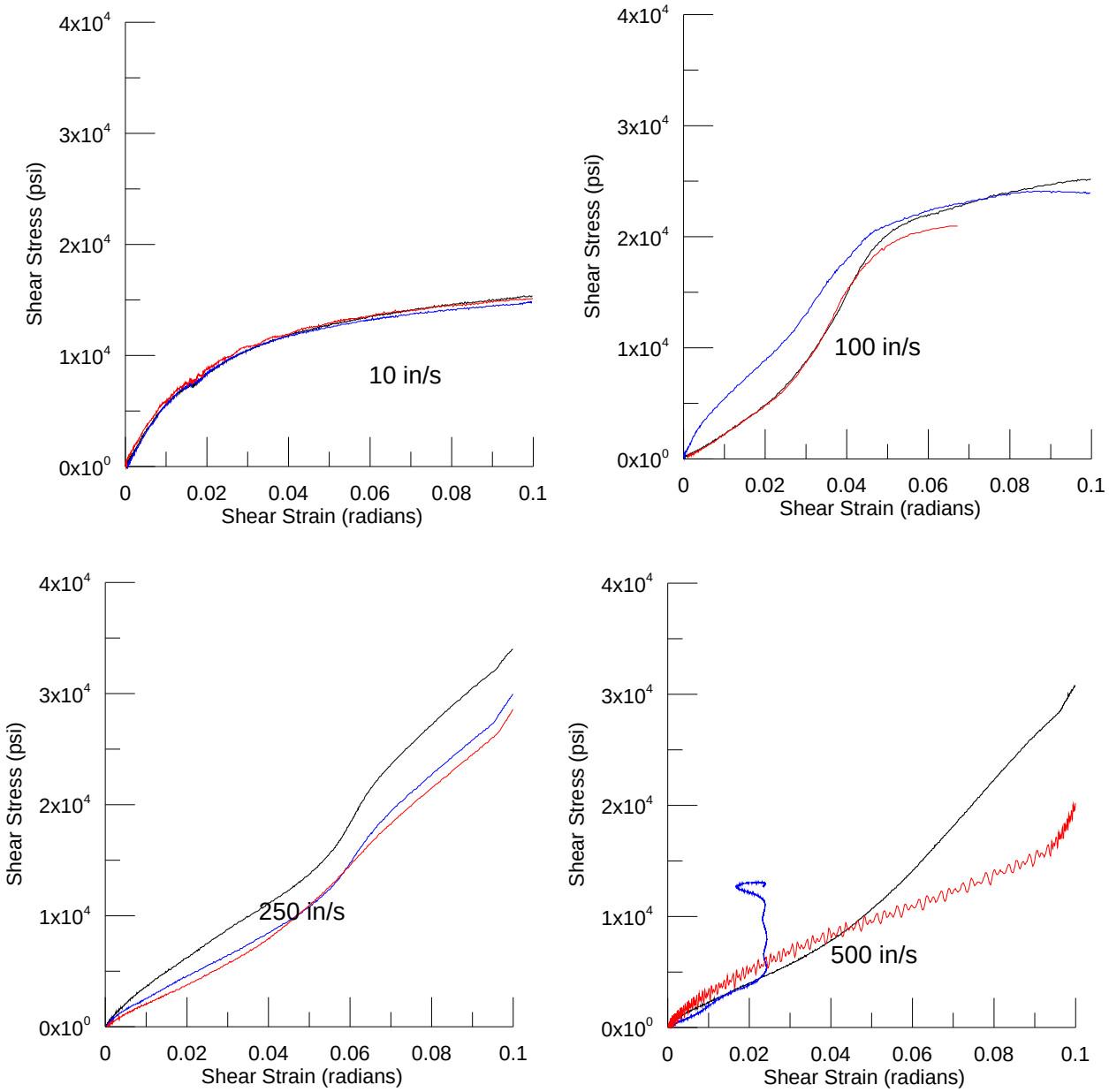

MATERIAL: Newport Fiberglass

Figure B-12. Shear Stress-Strain Diagrams for Newport Fiberglass Material Tested at Rates of 10, 100, 250, and 500 in/s

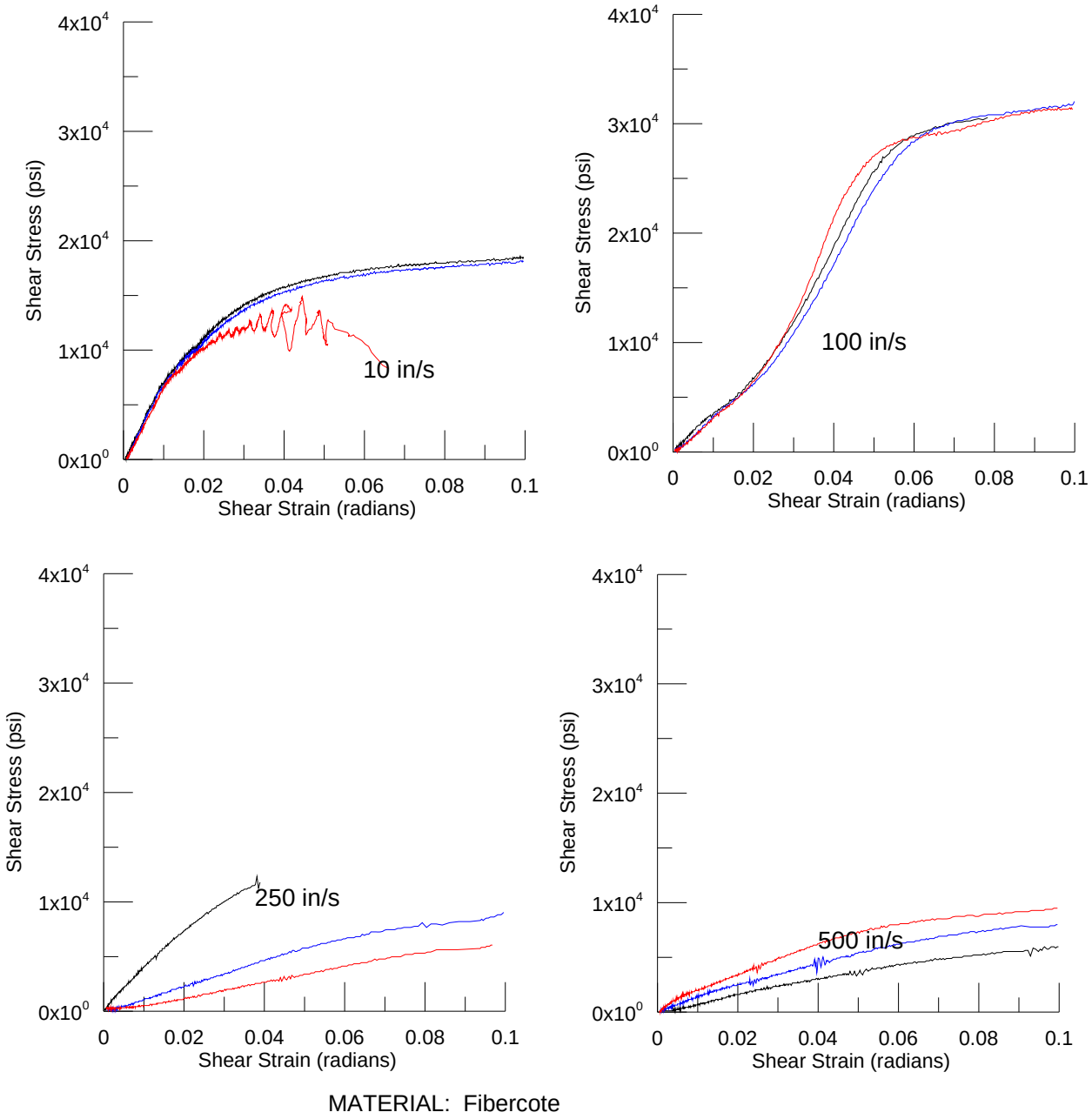

Figure B-13. Shear Stress-Strain Diagrams for Fibercote Material Tested at Rates of 10, 100, 250, and 500 in/s

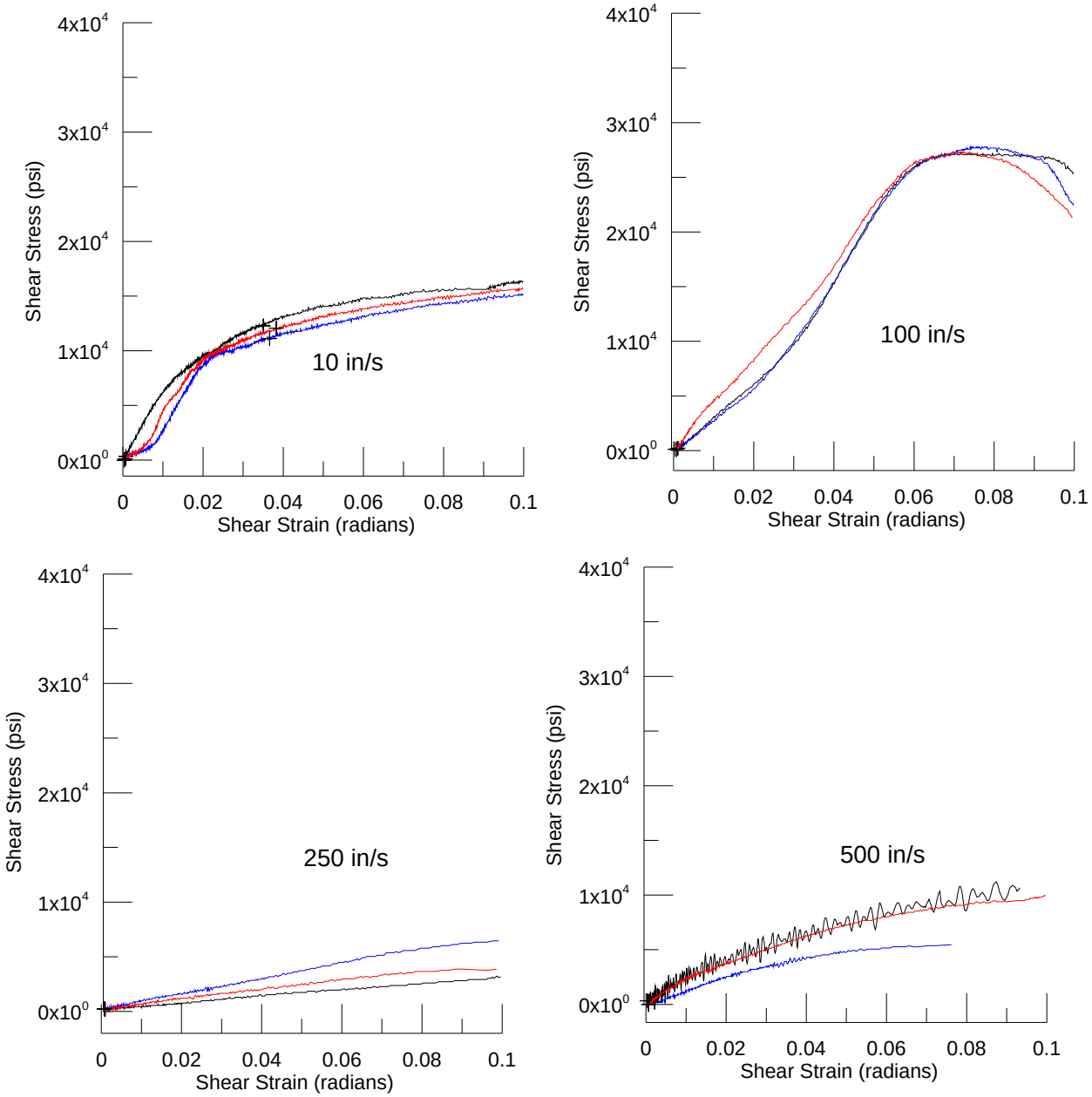

MATERIAL: Cytec

Figure B-14. Shear Stress-Strain Diagrams for Cytec Material Tested at Rates of 10, 100, 250, and 500 in/s

APPENDIX C—COMPRESSION TEST DATA

Table C-1. Summary of Failure Strengths and Strain Rates for Toray T800S/3900-2B Unitape

Orientation (degrees)	Average Strain Rate (1/s)	Actual Strain Rate (1/s)	Failure Strength (psi)	Average Failure Strength (psi)
0	0.00167	0.00167	83,234	79,598
		0.00167	81,837	
		0.00167	73,722	
	1	1	112,111	103,044
		1	93,977	
	450	408	114,491	120,008
		465	123,470	
		476	122,063	
	633	588	118,062	112,108
		667	121,835	
		645	96,428	
	763	714	117,819	116,109
		833	117,594	
		741	112,913	
15	0.00167	0.00167	61,280	68,749
		0.00167	70,804	
		0.00167	74,162	
	1	1	75,937	70,334
		1	64,731	
	456	476	102,632	81,401
		465	79,648	
		426	61,923	
	667	667	94,139	73,847
		690	61,852	
		645	65,551	
	826	769	66,974	73,898
		909	68,325	
		800	86,395	

Table C-1. Summary of Failure Strengths and Strain Rates for Toray T800S/3900-2B Unitape (Continued)

Orientation (degrees)	Average Strain Rate (1/s)	Actual Strain Rate (1/s)	Failure Strength (psi)	Average Failure Strength (psi)
30	0.00167	0.00167	38,920	39,298
		0.00167	39,878	
		0.00167	39,097	
	1	1	25,568	25,462
		1	25,357	
	479	444	49,036	44,163
		465	36,864	
		526	46,590	
	674	690	29,236	37,037
		667	45,665	
		667	36,208	
	834	870	45,189	42,438
		833	39,520	
		800	42,606	
45	0.00167	0.00167	28,886	28,046
		0.00167	25,802	
		0.00167	29,450	
	1	1	33,877	34,071
		1	34,265	
	473	465	31,319	30,843
		488	28,888	
		465	32,324	
	719	800	31,781	31,630
		667	32,232	
		690	30,878	
	812	833	36,417	35,425
		833	34,721	
		769	35,136	

Specimen 1

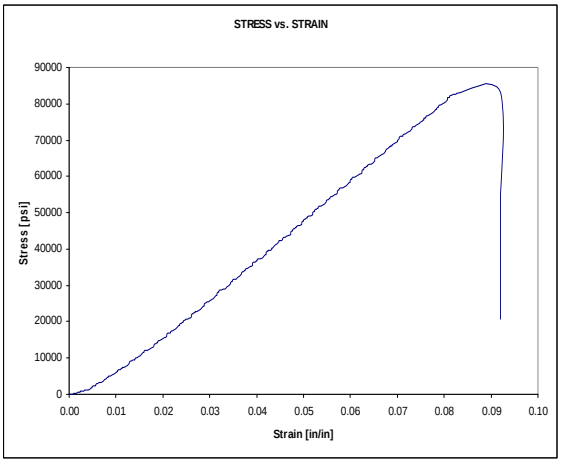

Specimen 2

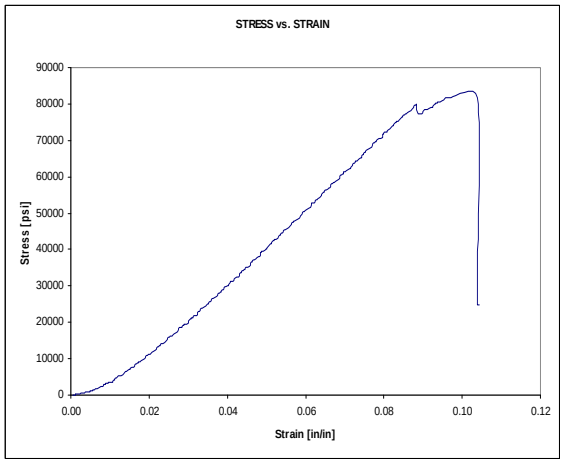

Specimen 3

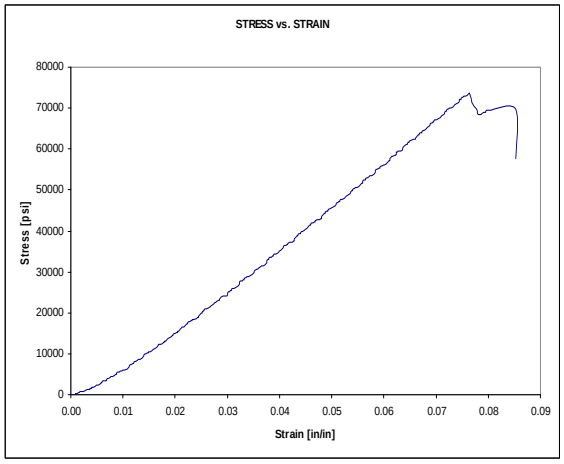

Figure C-1. Stress-Strain Curves for [0°] Toray T800S/3900-2B Unitape Specimens Tested at Average Strain Rate of 0.00167 s^{-1}

Specimen 1

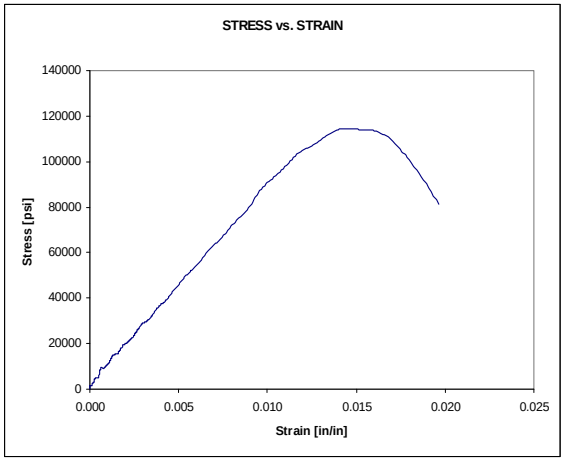

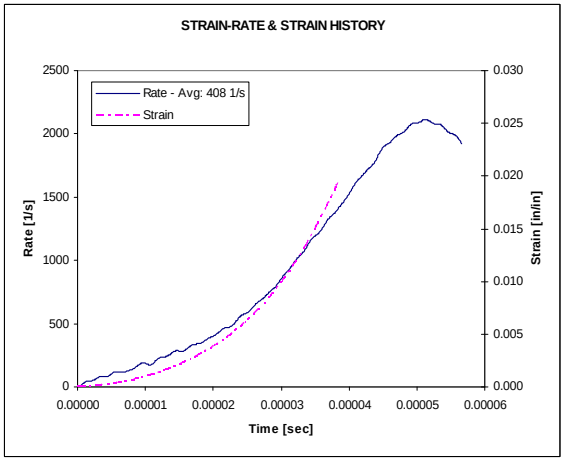

Specimen 2

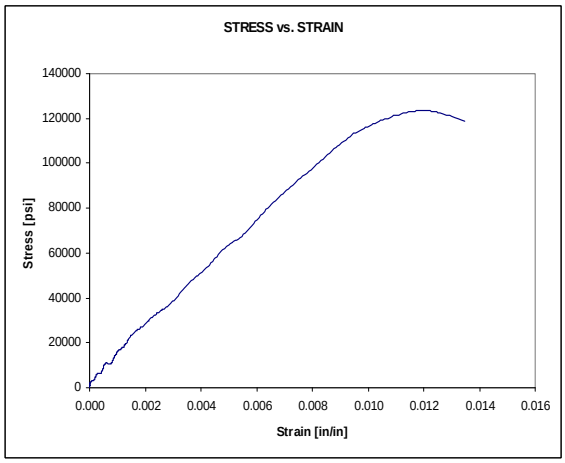

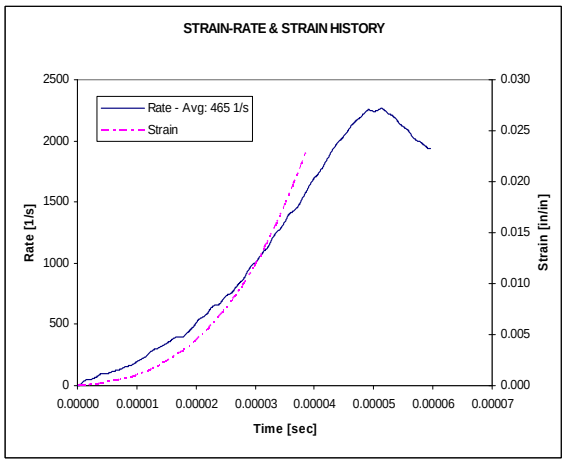

Specimen 3

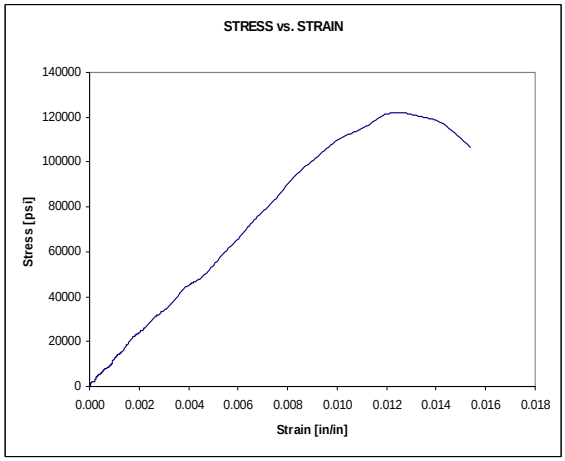

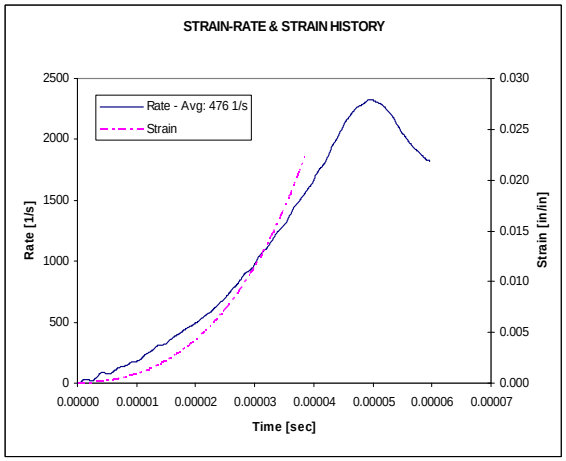

Figure C-2. Stress-Strain Curves for [0°] Toray T800S/3900-2B Unitape Specimens Tested at Average Strain Rate of 450 s^{-1}

Specimen 1

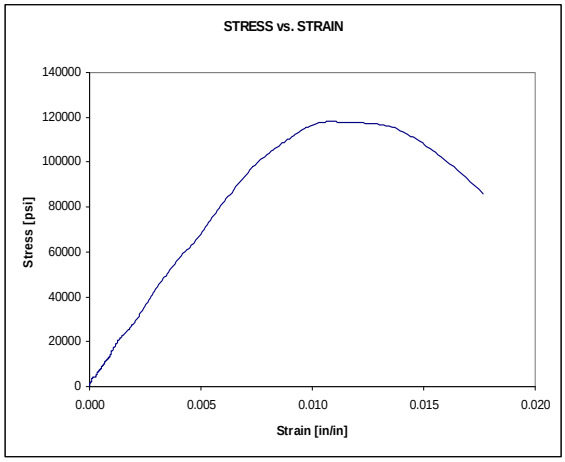

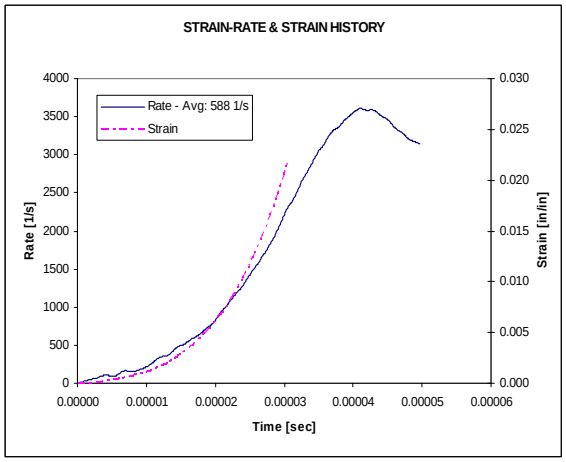

Specimen 2

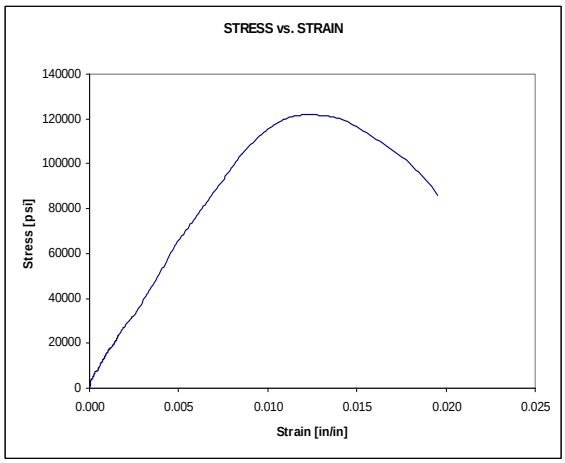

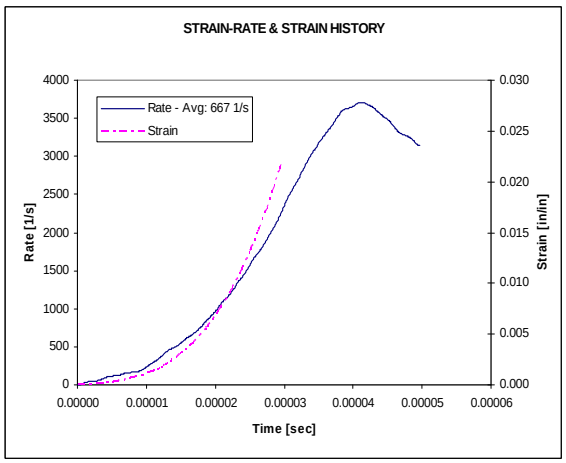

Specimen 3

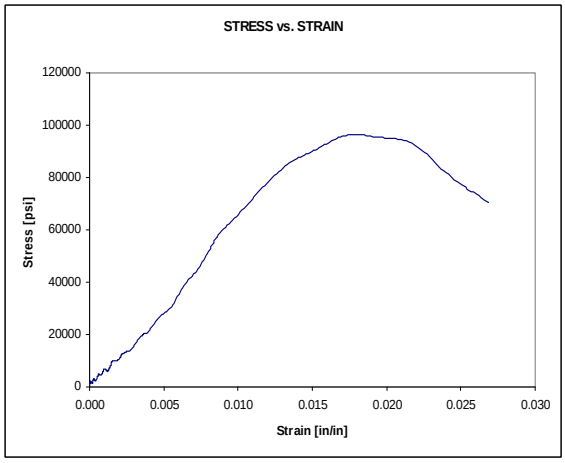

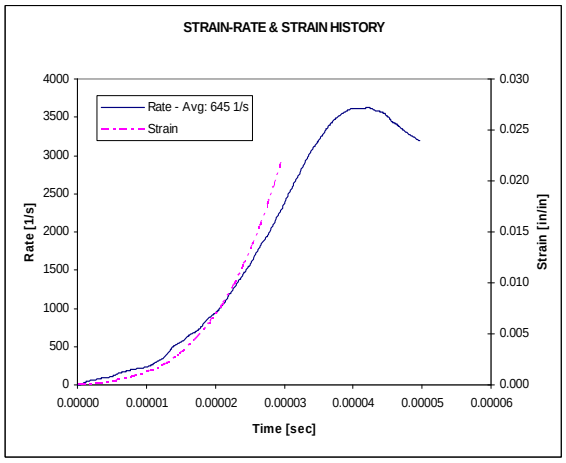

Figure C-3. Stress-Strain Curves for [0°] Toray T800S/3900-2B Unitape Specimens Tested at Average Strain Rate of 633 s^{-1}

Specimen 1

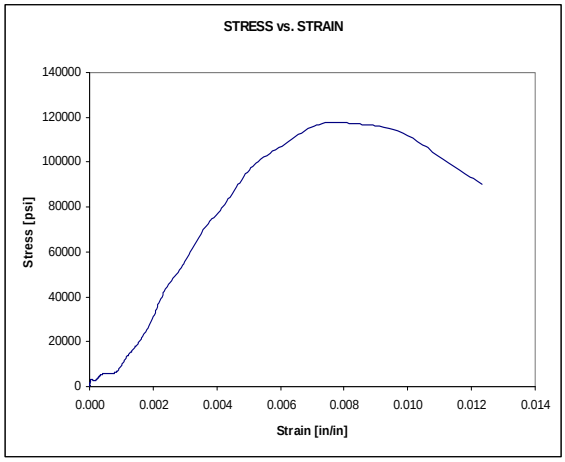

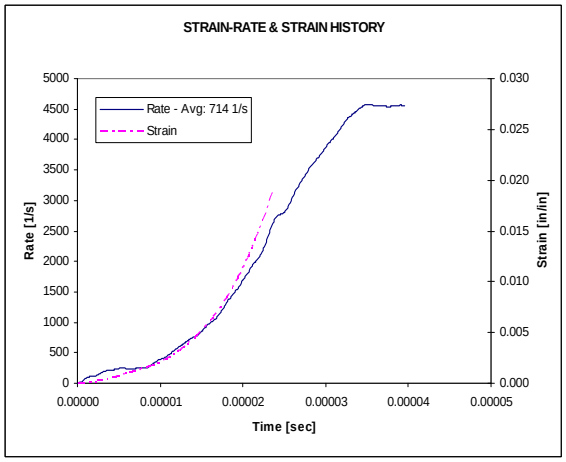

Specimen 2

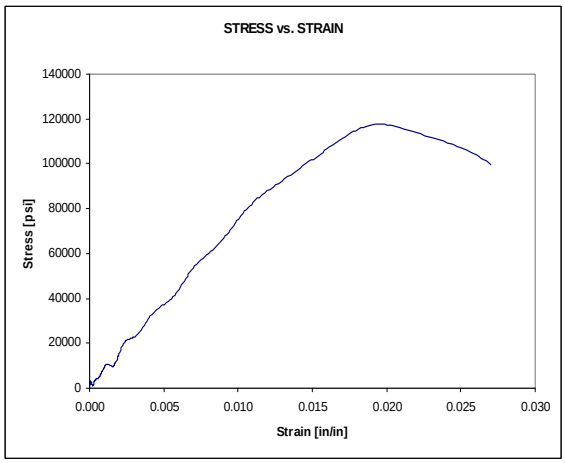

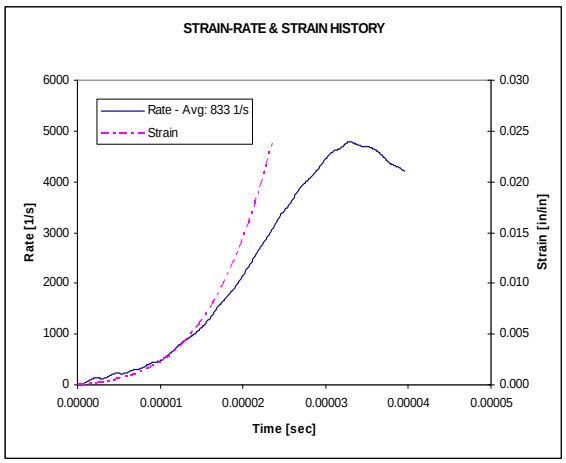

Specimen 3

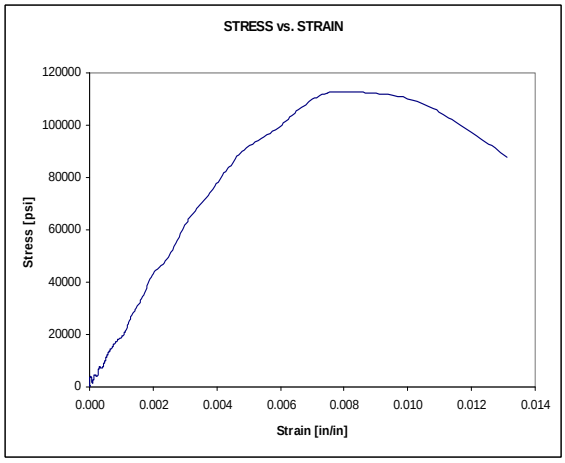

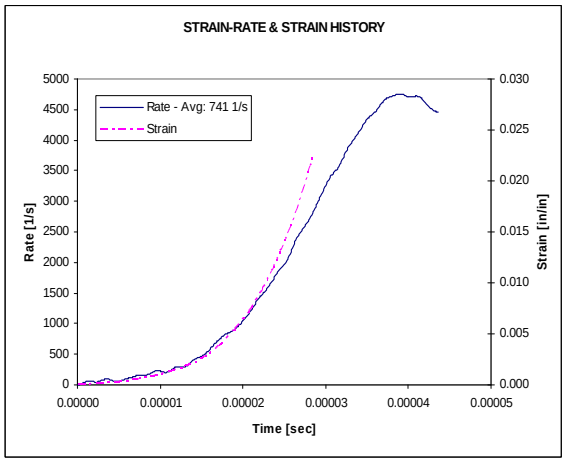

Figure C-4. Stress-Strain Curves for [0°] Toray T800S/3900-2B Unitape Specimens Tested at Average Strain Rate of 763 s^{-1}

Specimen 1

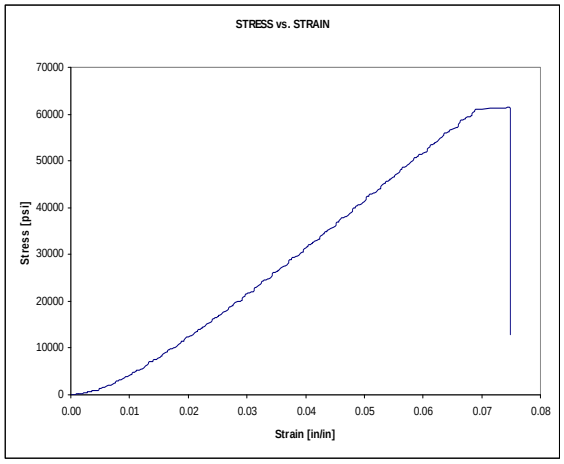

Specimen 2

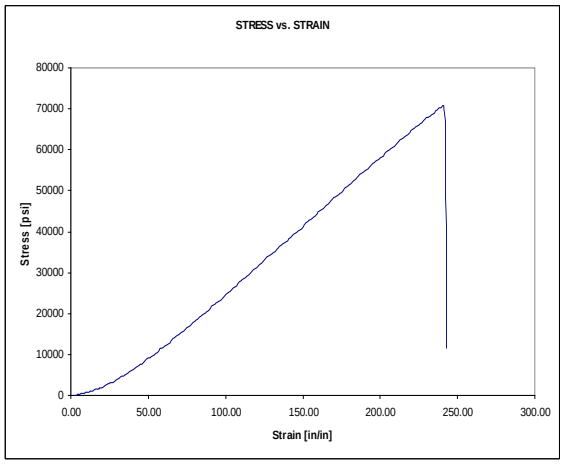

Specimen 3

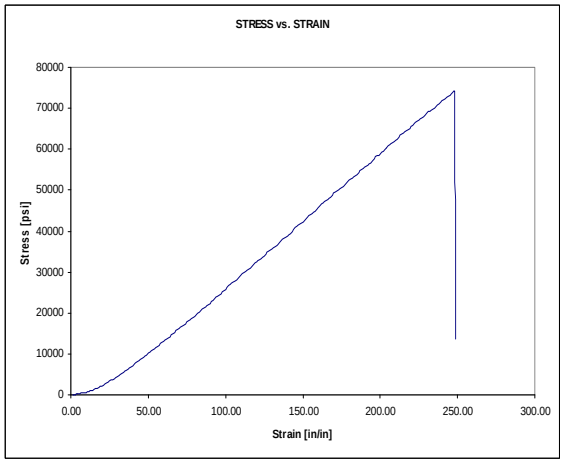

Figure C-5. Stress-Strain Curves for $[+15°/-15°]_{NS}$ Toray T800S/3900-2B Unitape Specimens Tested at Average Strain Rate of 0.00167 s^{-1}

Specimen 1

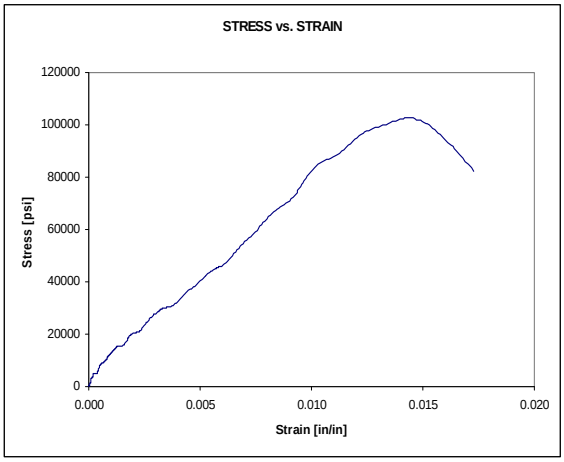

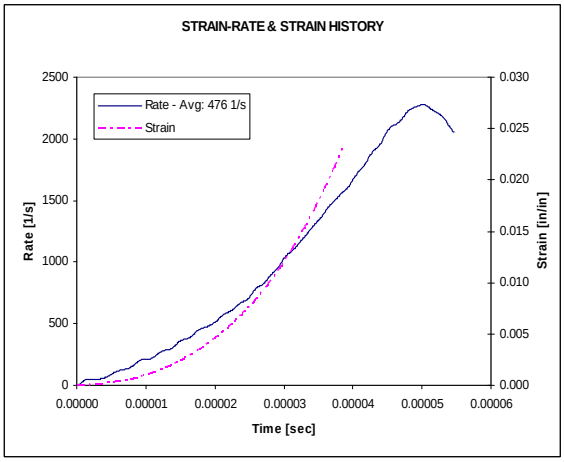

Specimen 2

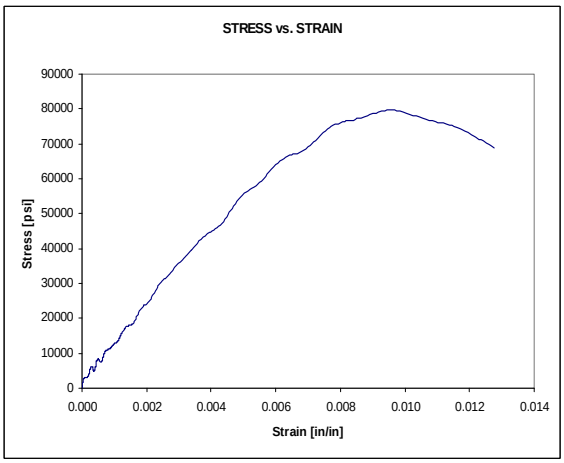

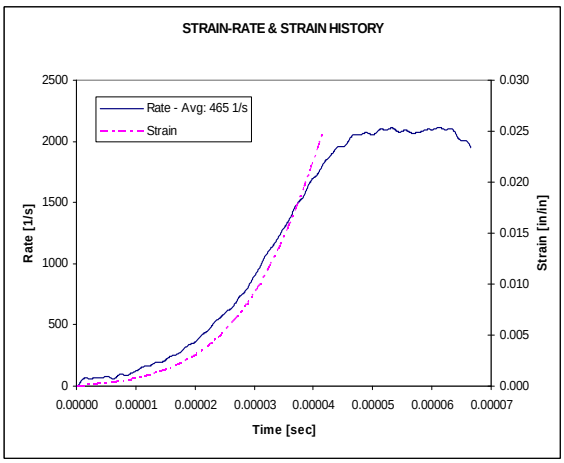

Specimen 3

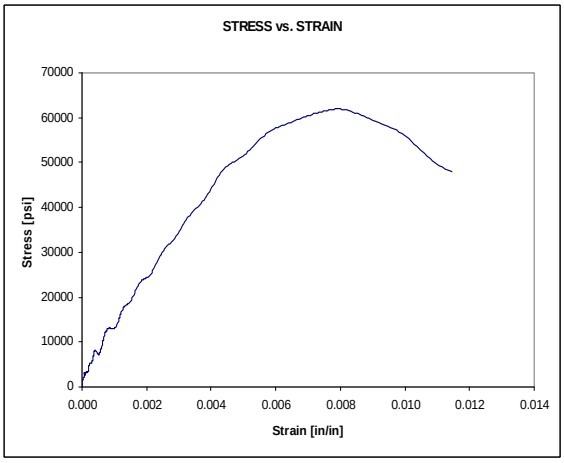

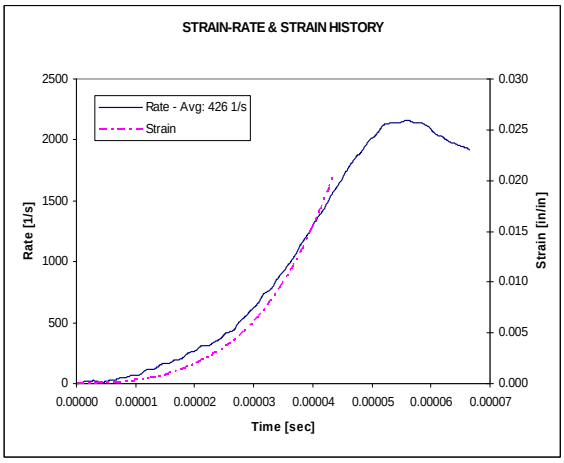

Figure C-6. Stress-Strain Curves for $[+15°/-15°]_{NS}$ Toray T800S/3900-2B Unitape Specimens Tested at Average Strain Rate of 456 s^{-1}

Specimen 1

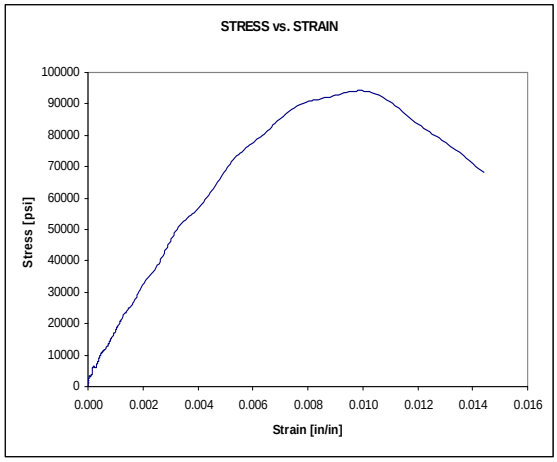

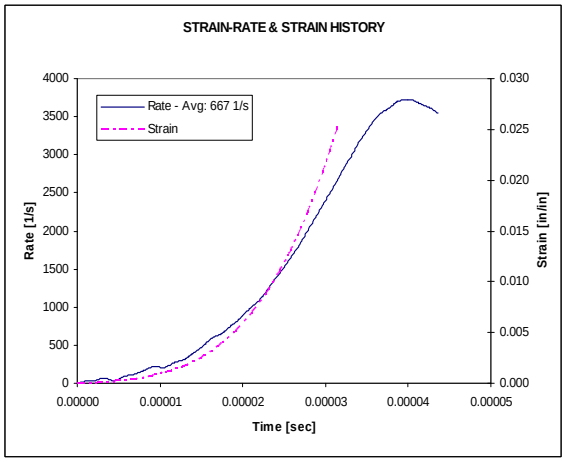

Specimen 2

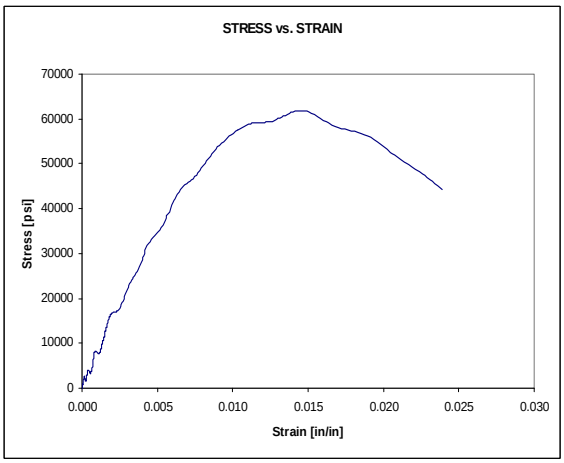

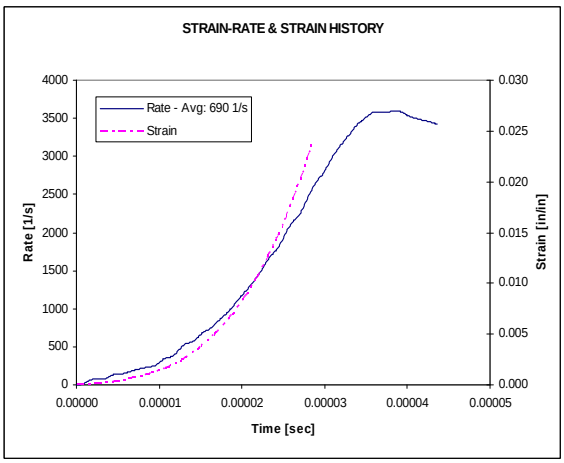

Specimen 3

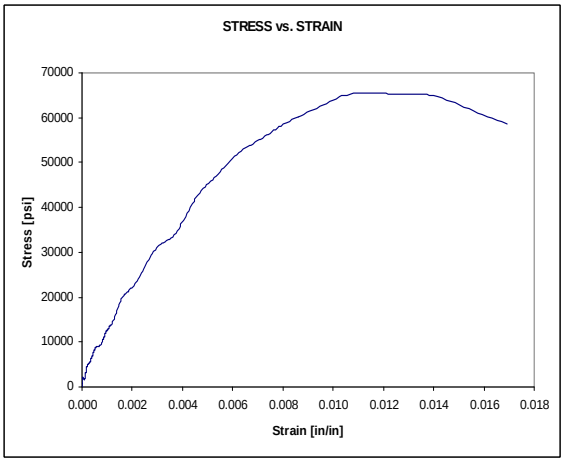

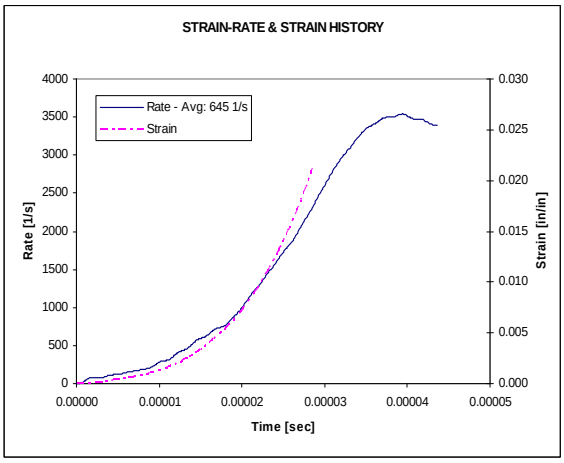

Figure C-7. Stress-Strain Curves for $[+15°/-15°]_{NS}$ Toray T800S/3900-2B Unitape Specimens Tested at Average Strain Rate of 667 s^{-1}

Specimen 1

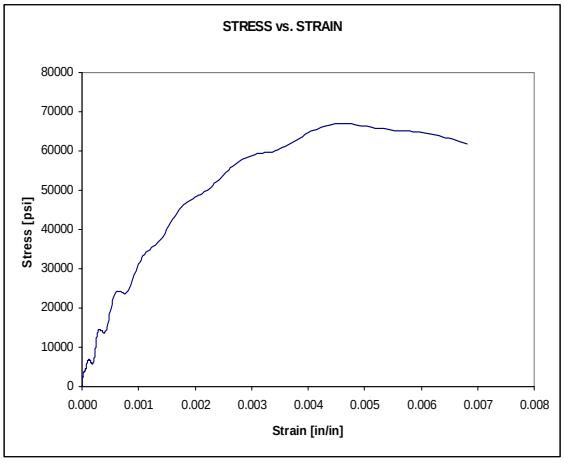

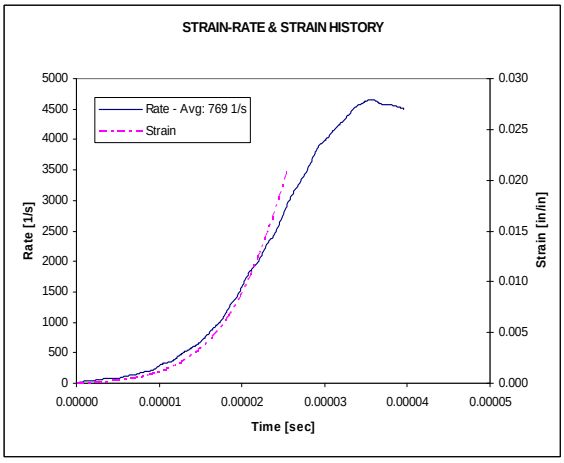

Specimen 2

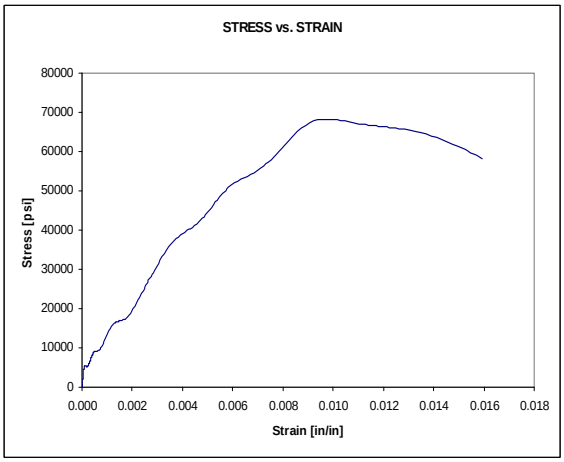

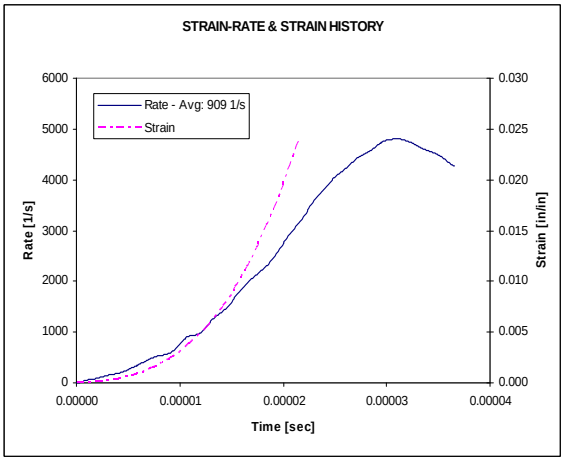

Specimen 3

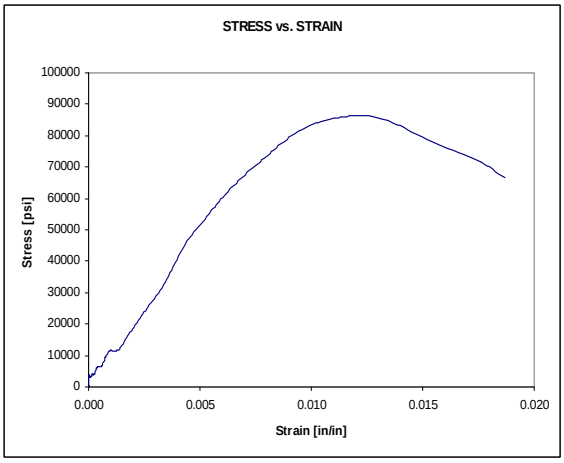

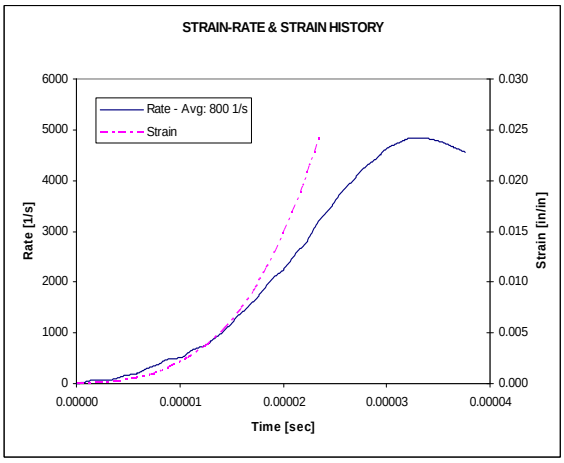

Figure C-8. Stress-Strain Curves for $[+15°/-15°]_{NS}$ Toray T800S/3900-2B Unitape Specimens Tested at Average Strain Rate of 826 s^{-1}

Specimen 1

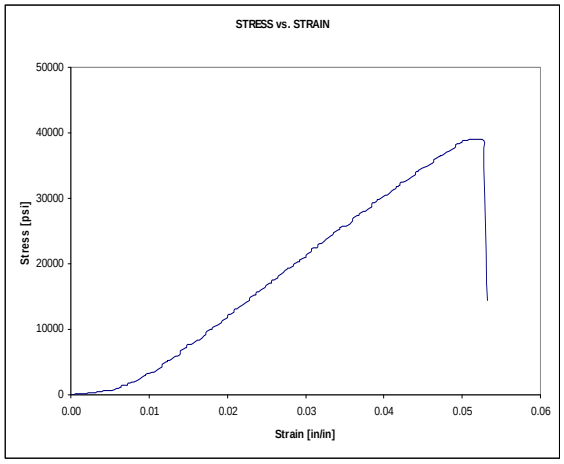

Specimen 2

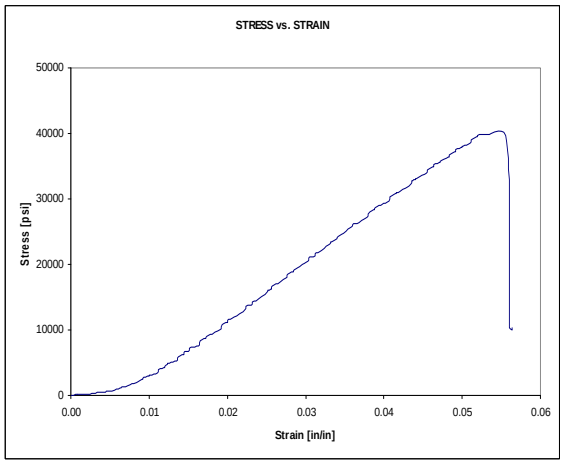

Specimen 3

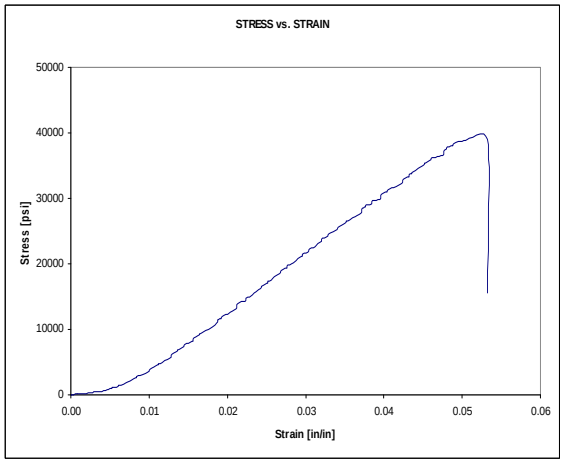

Figure C-9. Stress-Strain Curves for $[+30°/-30°]_{NS}$ Toray T800S/3900-2B Unitape Specimens Tested at Average Strain Rate of 0.00167 s^{-1}

Specimen 1

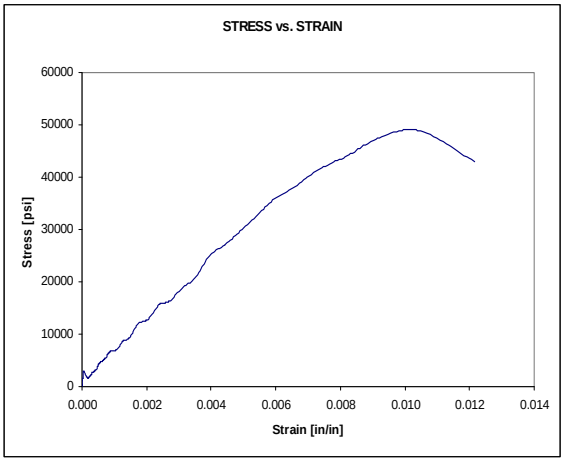

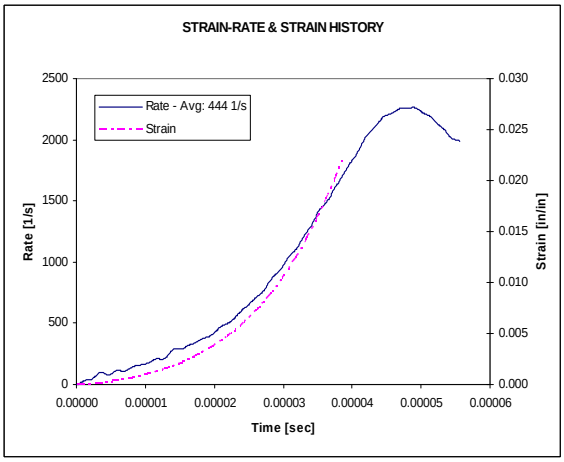

Specimen 2

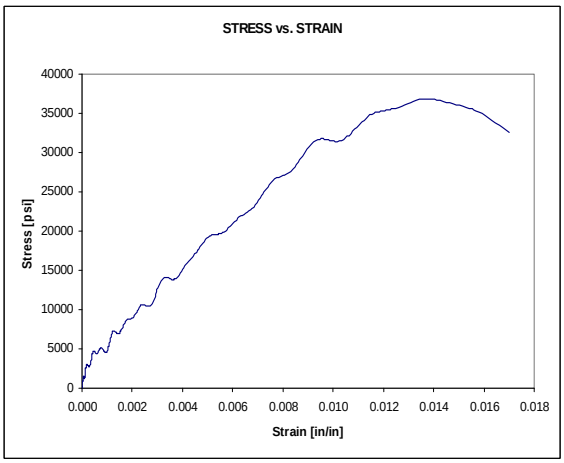

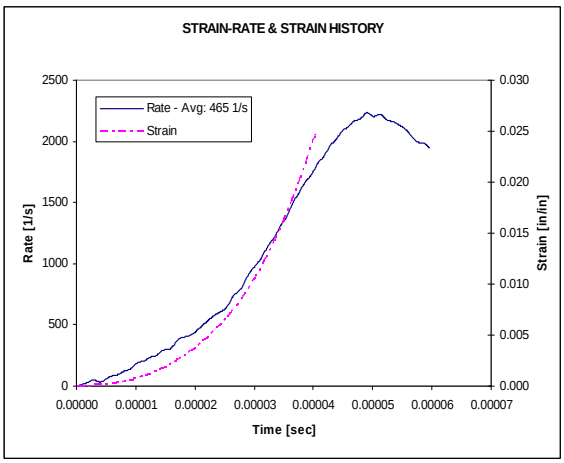

Specimen 3

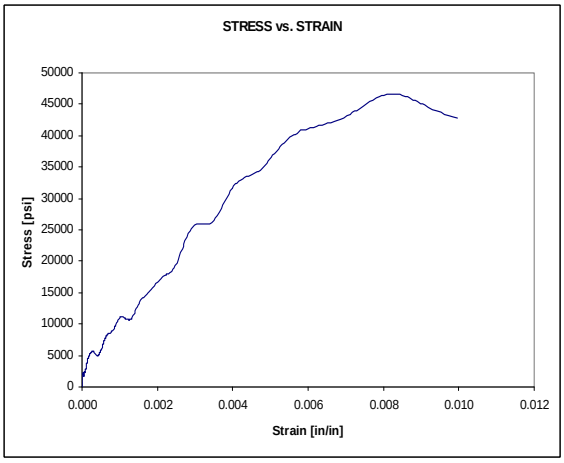

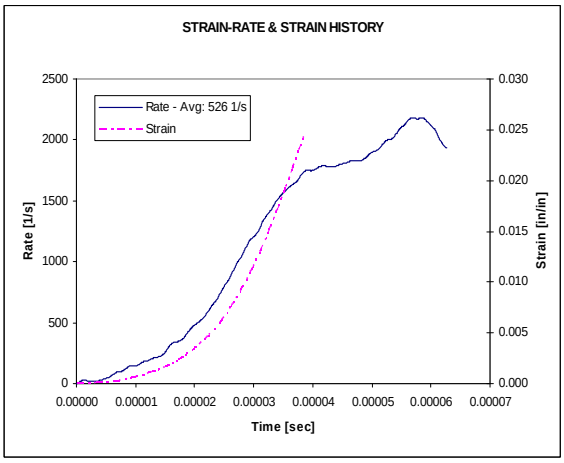

Figure C-10. Stress-Strain Curves for $[+30°/-30°]_{NS}$ Toray T800S/3900-2B Unitape Specimens Tested at Average Strain Rate of 479 s^{-1}

Specimen 1

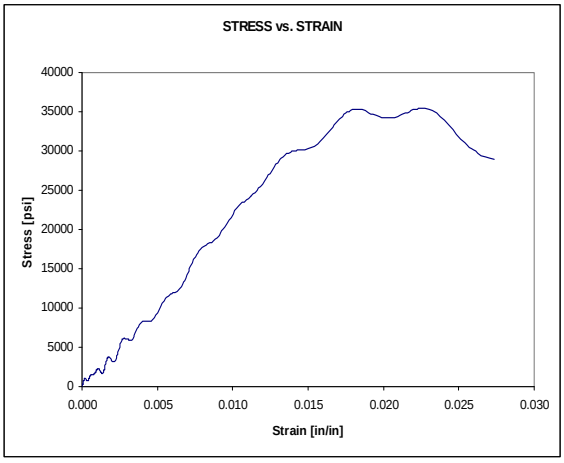

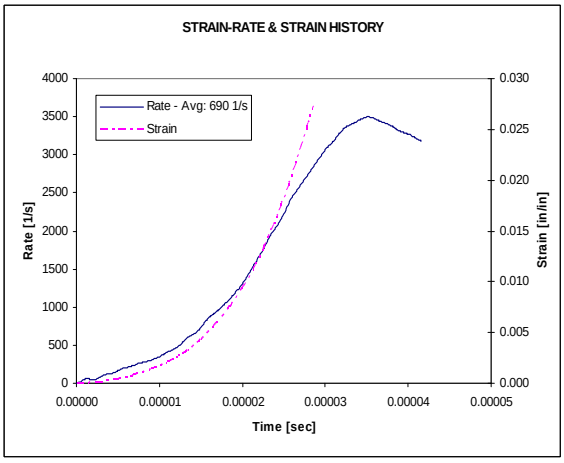

Specimen 2

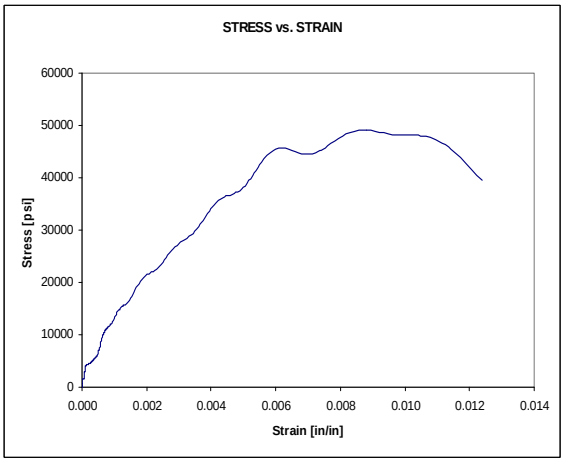

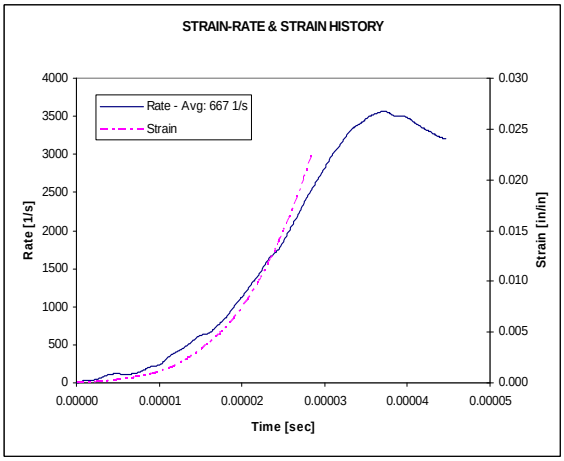

Specimen 3

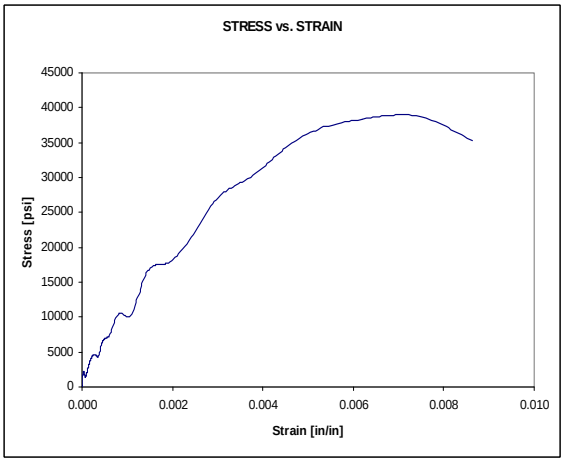

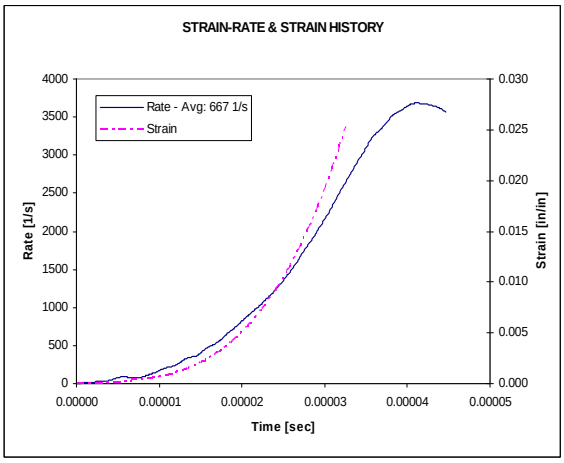

Figure C-11. Stress-Strain Curves for $[+30°/-30°]_{NS}$ Toray T800S/3900-2B Unitape Specimens Tested at Average Strain Rate of 674 s^{-1}

Specimen 1

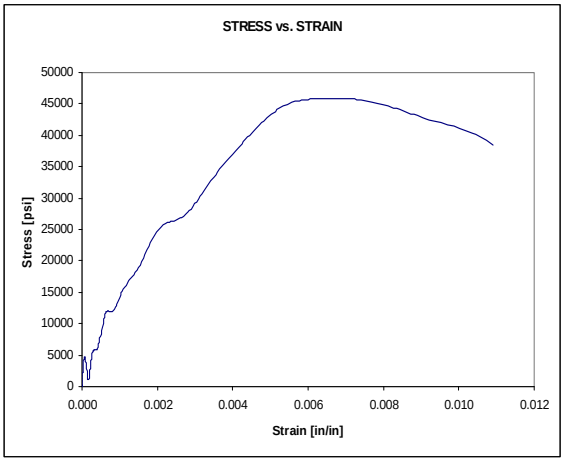

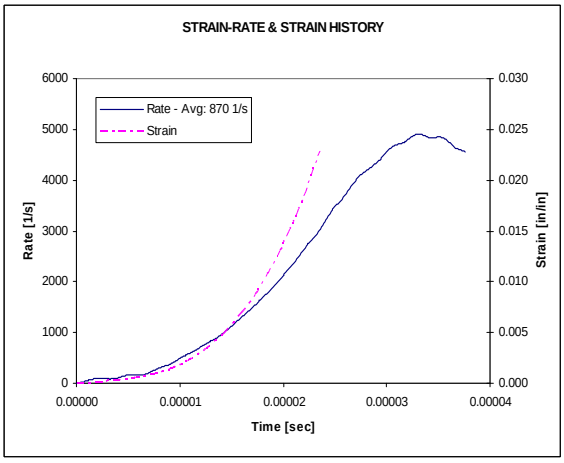

Specimen 2

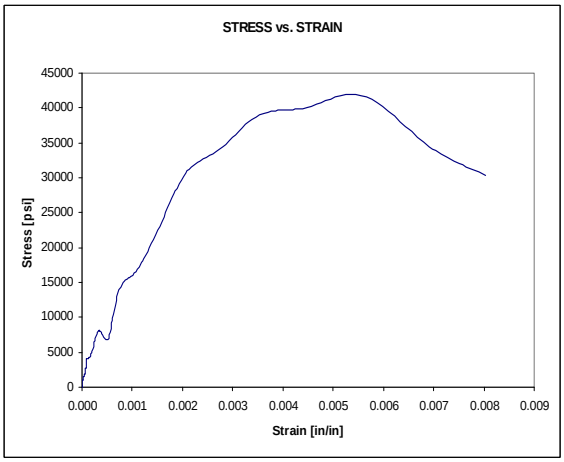

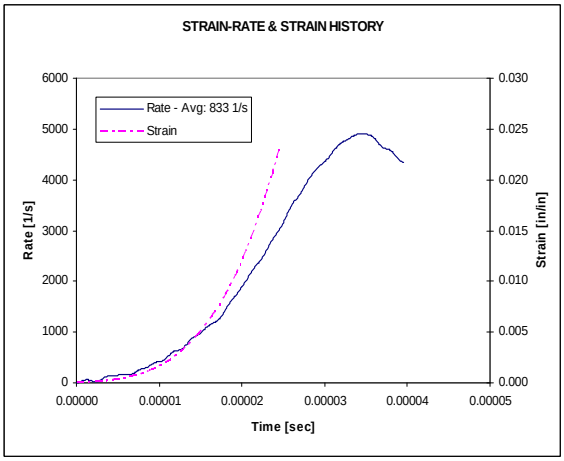

Specimen 3

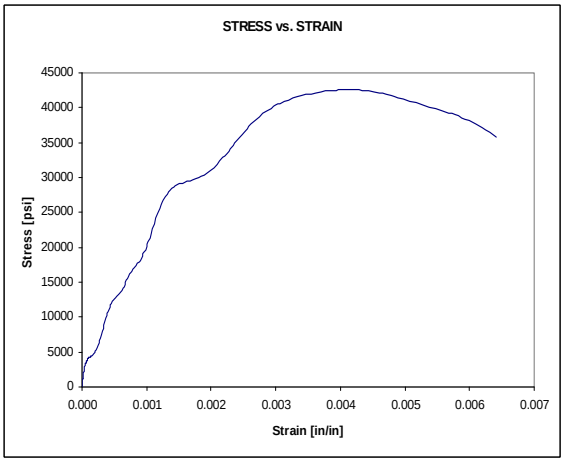

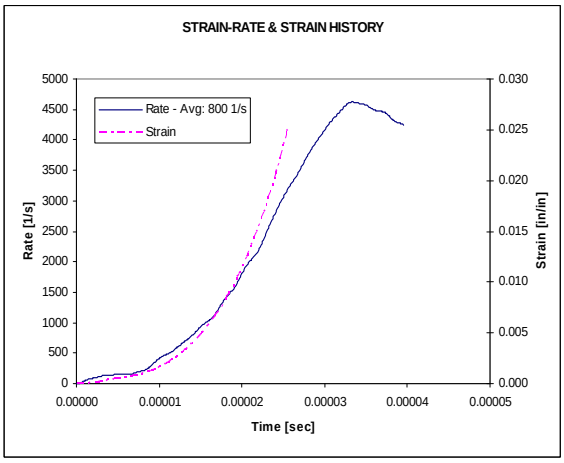

Figure C-12. Stress-Strain Curves for $[+30°/-30°]_{NS}$ Toray T800s/3900-2B Unitape Specimens Tested at Average Strain Rate of 834 s^{-1}

Specimen 1

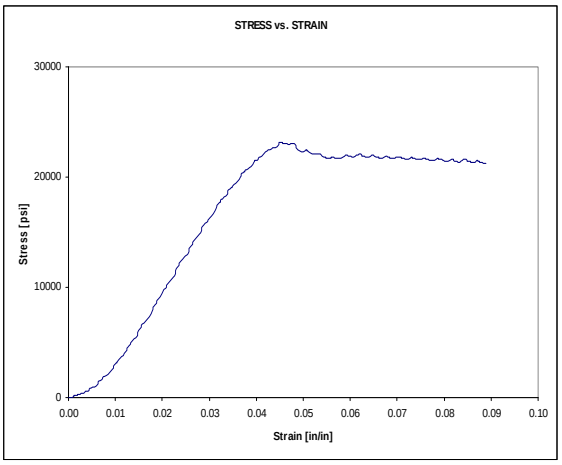

Specimen 2

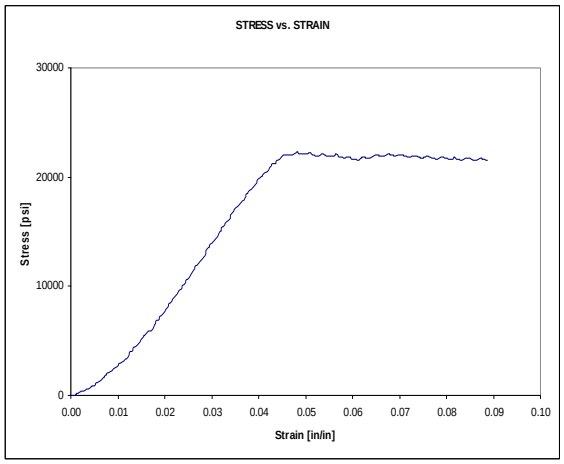

Specimen 3

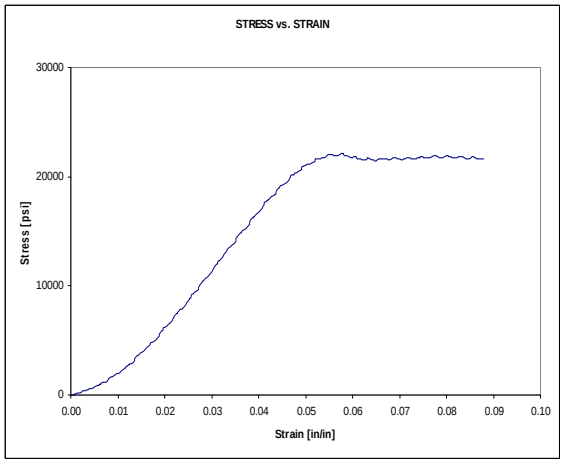

Figure C-13. Stress-Strain Curves for $[+45°/-45°]_{NS}$ Toray T800S/3900-2B Unitape Specimens Tested at Average Strain Rate of 0.00167 s^{-1}

Specimen 1

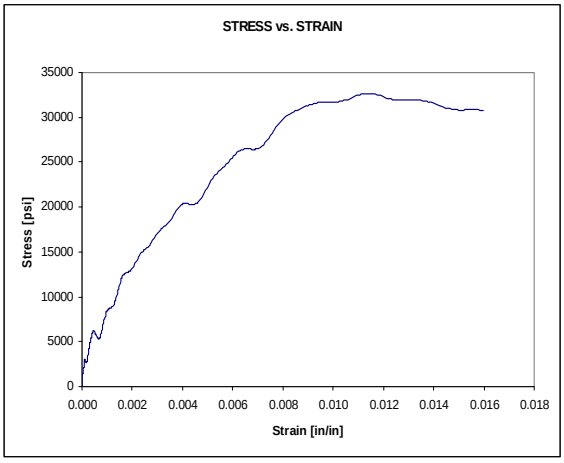

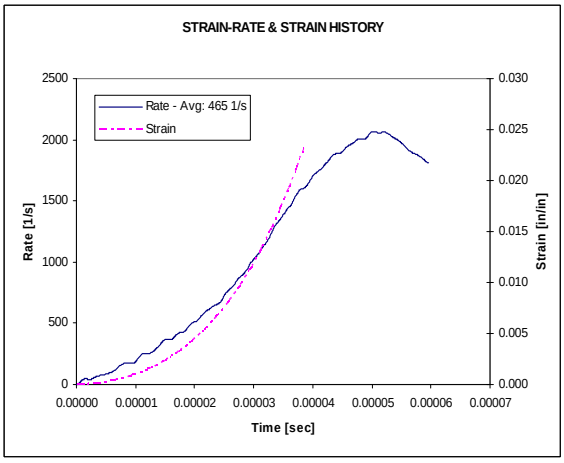

Specimen 2

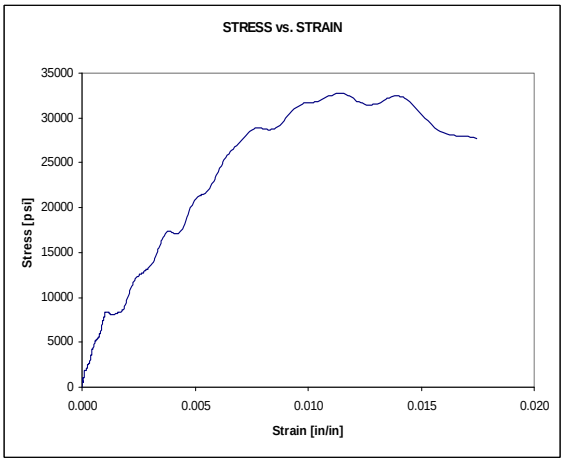

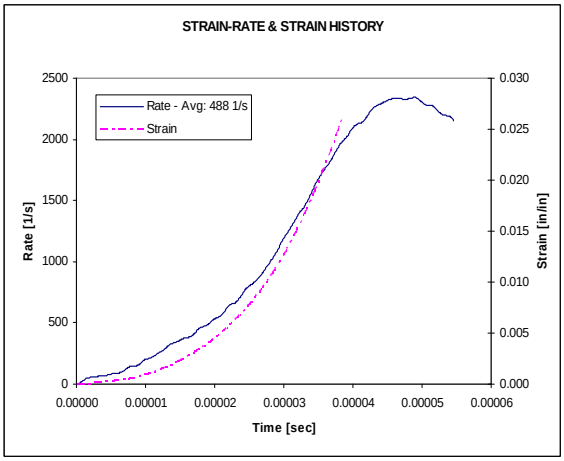

Specimen 3

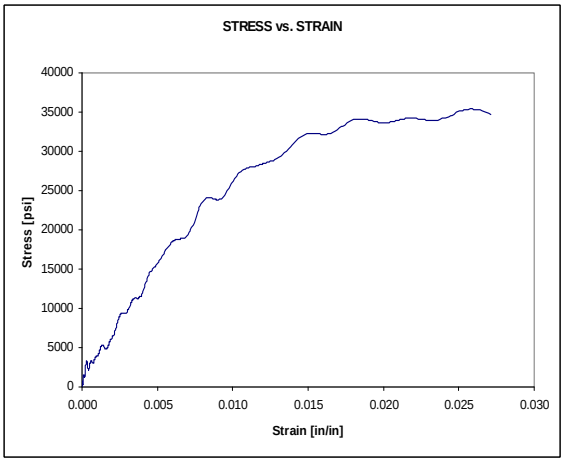

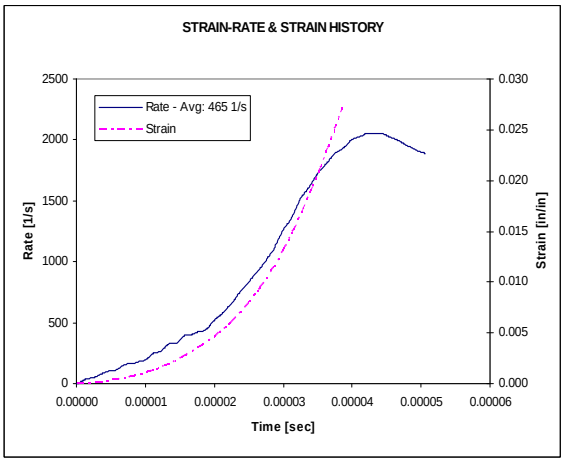

Figure C-14. Stress-Strain Curves for $[+45°/-45°]_{NS}$ Toray T800S/3900-2B Unitape Specimens Tested at Average Strain Rate of 473 s^{-1}

Specimen 1

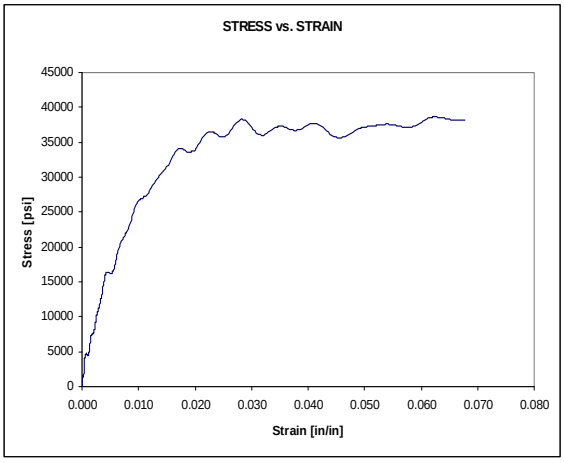

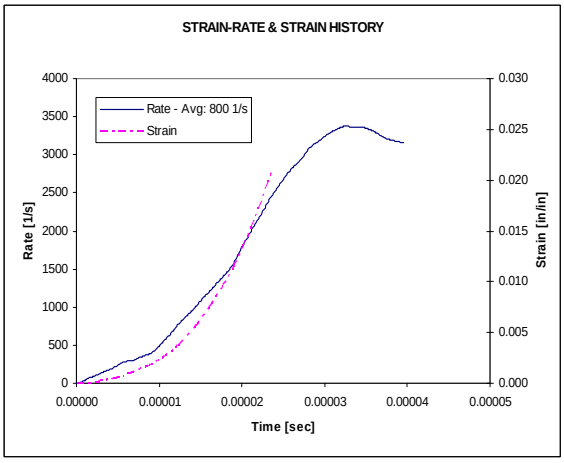

Specimen 2

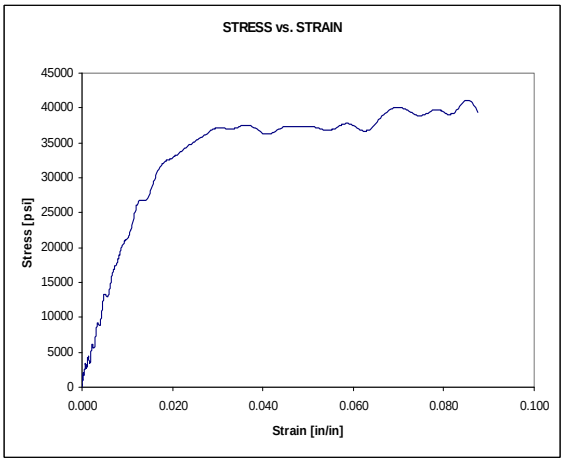

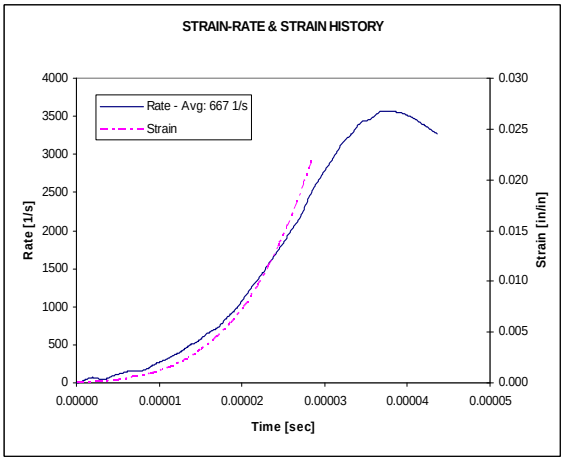

Specimen 3

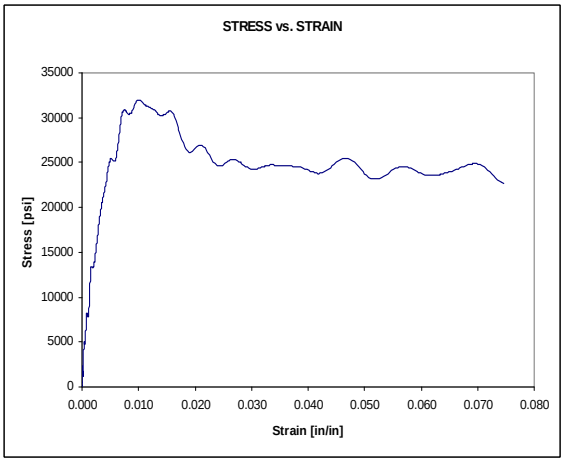

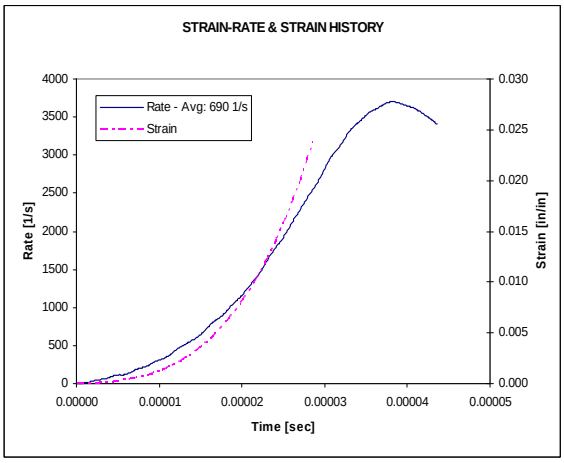

Figure C-15. Stress-Strain Curves for $[+45°/-45°]_{NS}$ Toray T800S/3900-2B Unitape Specimens Tested at Average Strain Rate of 719 s^{-1}

Specimen 1

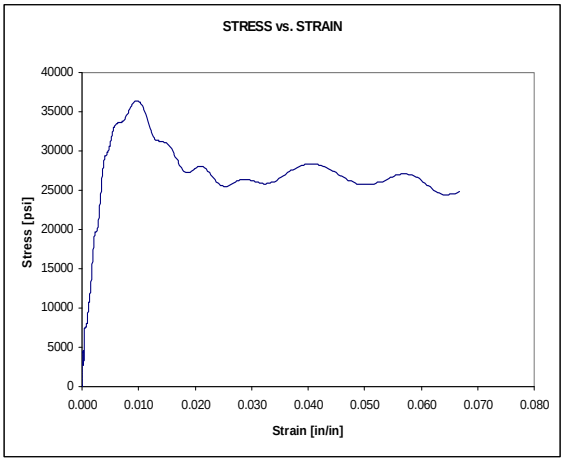

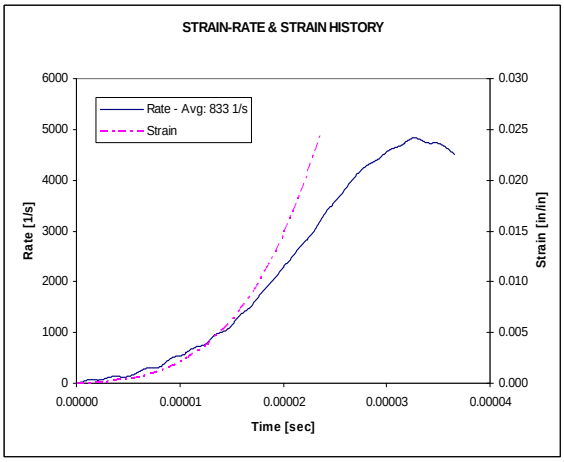

Specimen 2

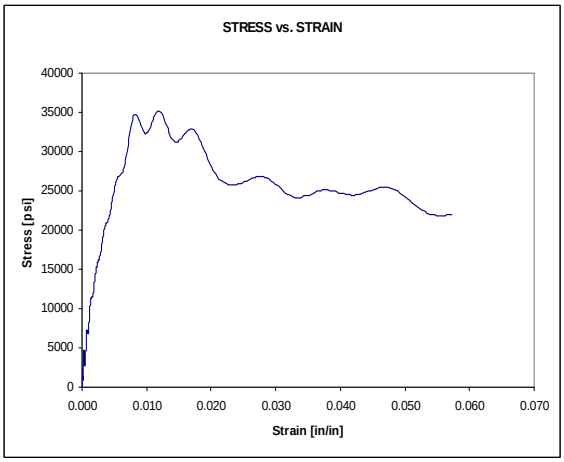

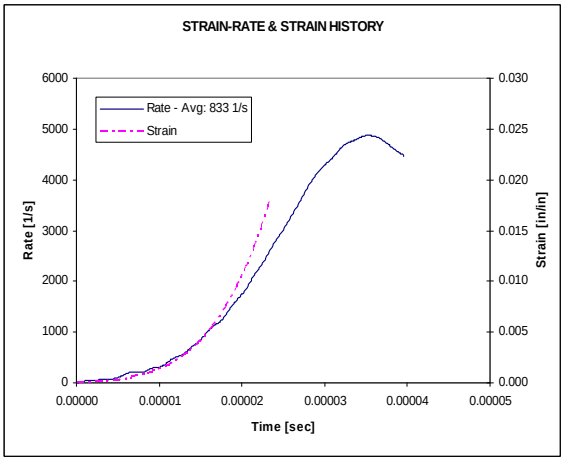

Specimen 3

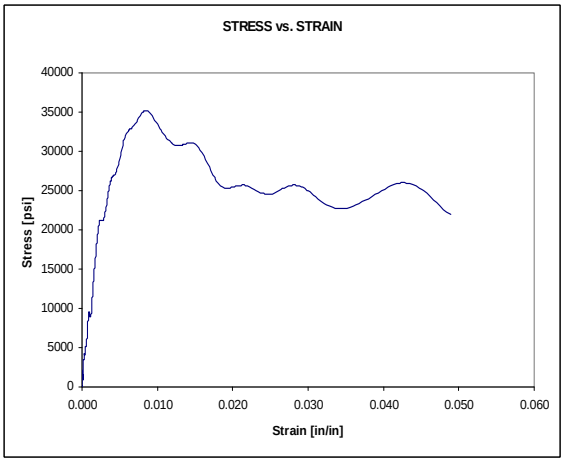

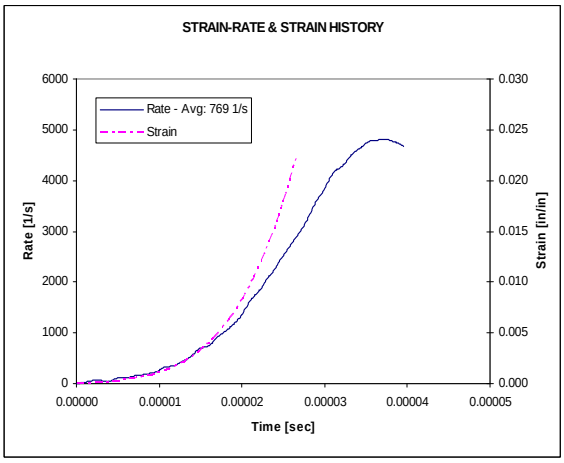

Figure C-16. Stress-Strain Curves for $[+45°/-45°]_{NS}$ Toray T800S/3900-2B Unitape Specimens Tested at Average Strain Rate of 812 s^{-1}

Table C-2. Summary of Failure Strengths and Strain Rates for Toray T700G-12K-50C/3900-2 PWCF

Orientation (degrees)	Average Strain Rate (1/s)	Actual Strain Rate (1/s)	Failure Strength (psi)	Average Failure Strength (psi)
0	0.00167	0.00167	80,888	82,023
		0.00167	80,028	
		0.00167	85,154	
	1	1	81,869	82,947
		1	84,026	
	385	392	96,905	95,930
		370	98,832	
		392	92,053	
	492	333	99,376	96,592
		571	95,242	
		571	95,158	
	706	714	90,635	86,842
		690	91,709	
		714	78,181	
15	0.00167	0.00167	79,389	78,391
		0.00167	78,184	
		0.00167	77,600	
	1	1	81,906	79,459
		1	77,012	
	407	377	87,618	84,638
		417	81,683	
		426	84,613	
	594	606	89,738	87,650
		588	89,909	
		588	83,303	
	675	645	81,203	80,237
		690	78,751	
		690	80,756	

Table C-2. Summary of Failure Strengths and Strain Rates for Toray T700G-12K-50C/3900-2 PWCF (Continued)

Orientation (degrees)	Average Strain Rate (1/s)	Actual Strain Rate (1/s)	Failure Strength (psi)	Average Failure Strength (psi)
30	0.00167	0.00167	58,290	56,839
		0.00167	58,370	
		0.00167	53,858	
	1	1	66,833	64,784
		1	62,736	
	407	377	65,988	66,183
		426	68,834	
		417	63,728	
	594	588	69,230	68,937
		606	66,585	
		588	70,996	
	723	714	65,900	63,922
		741	65,714	
		714	60,152	
45	0.00167	0.00167	37,373	37,657
		0.00167	37,835	
		0.00167	37,764	
	1	1	38,244	38,477
		1	38,710	
	380	370	26,713	28,688
		392	29,272	
		377	30,080	
	577	571	34,049	33,544
		571	32,246	
		588	34,336	
	676	690	39,195	38,500
		714	40,122	
		625	36,184	

Specimen 1

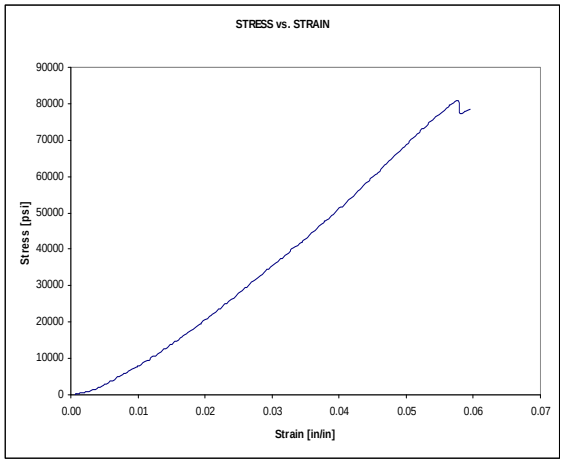

Specimen 2

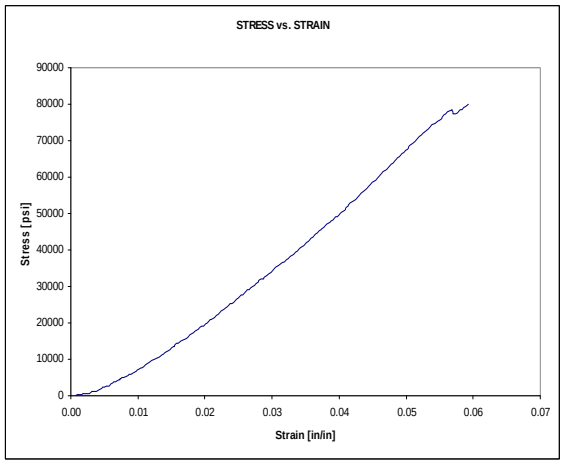

Specimen 3

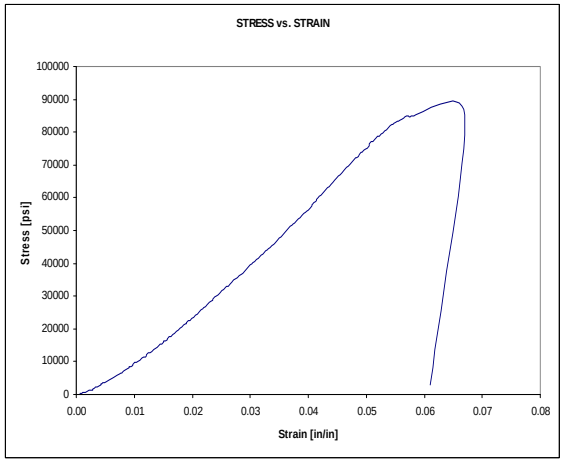

Figure C-17. Stress-Strain Curves for [0°] T700G-12K-50C/3900-2 PWCF Specimens Tested at Average Strain Rate of 0.00167 s^{-1}

Specimen 1

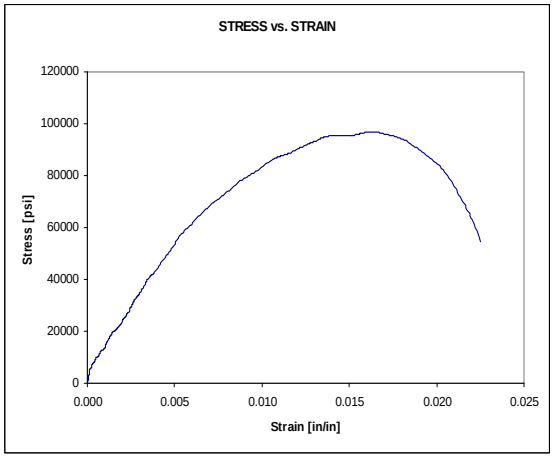

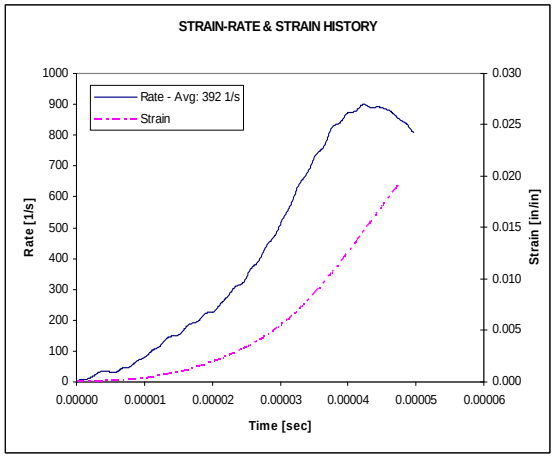

Specimen 2

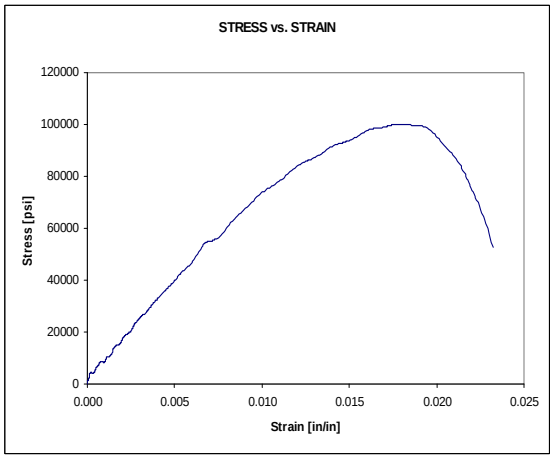

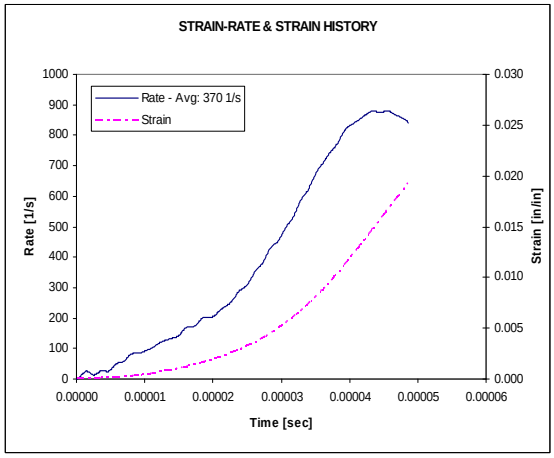

Specimen 3

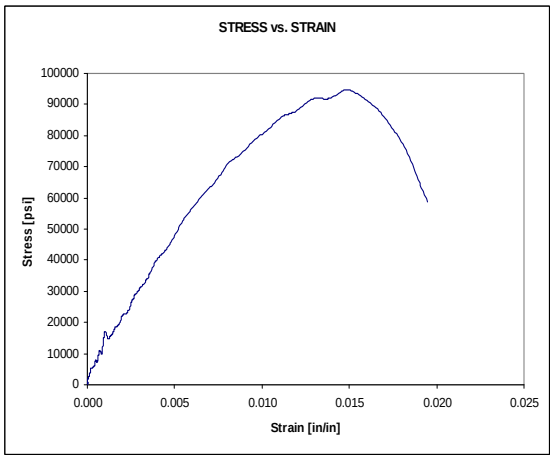

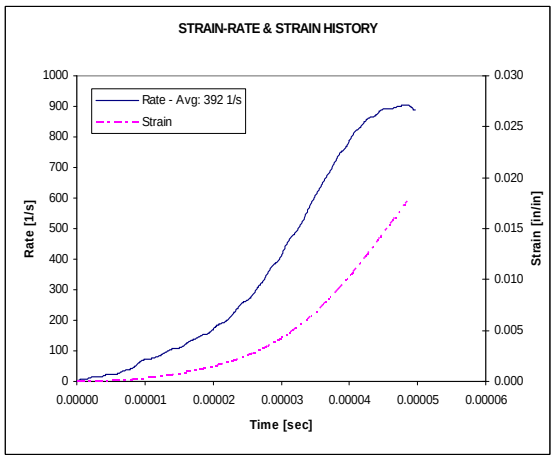

Figure C-18. Stress-Strain Curves for [0°] T700G-12K-50C/3900-2 PWCF Specimens Tested at Average Strain Rate of 385 s^{-1}

Specimen 1

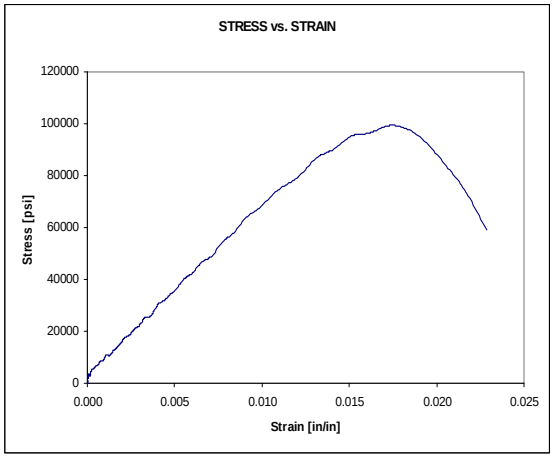

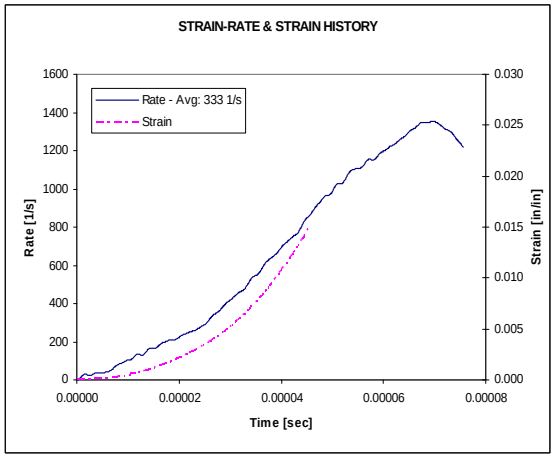

Specimen 2

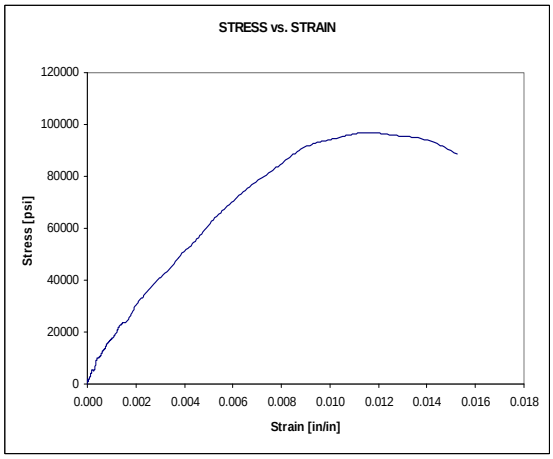

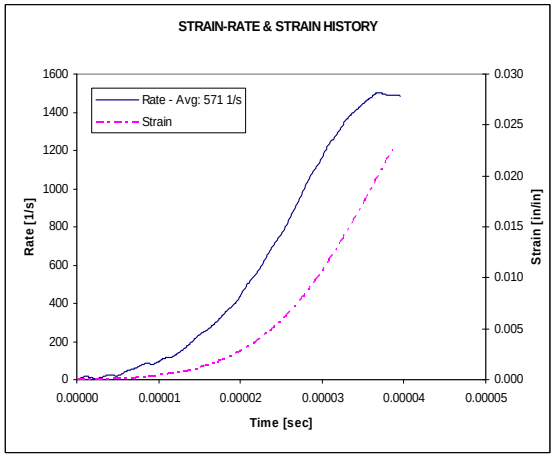

Specimen 3

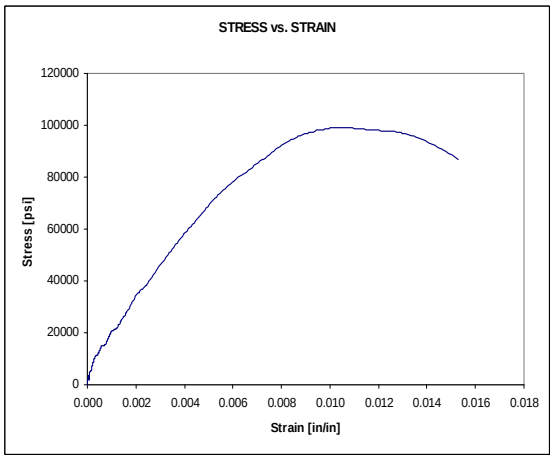

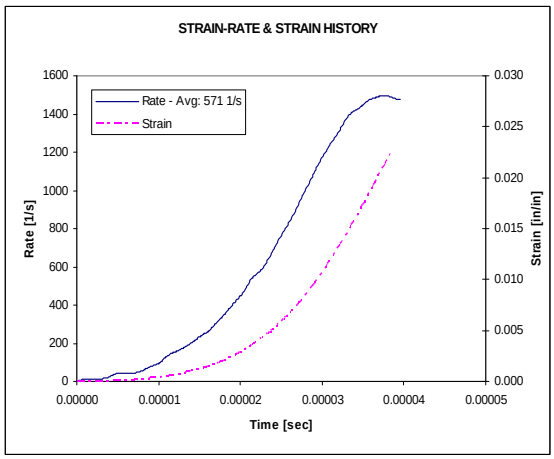

Figure C-19. Stress-Strain Curves for [0°] T700G-12K-50C/3900-2 PWCF Specimens Tested at Average Strain Rate of 492 s^{-1}

Specimen 1

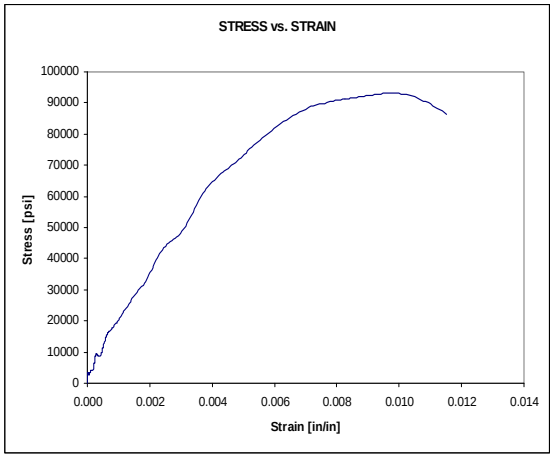

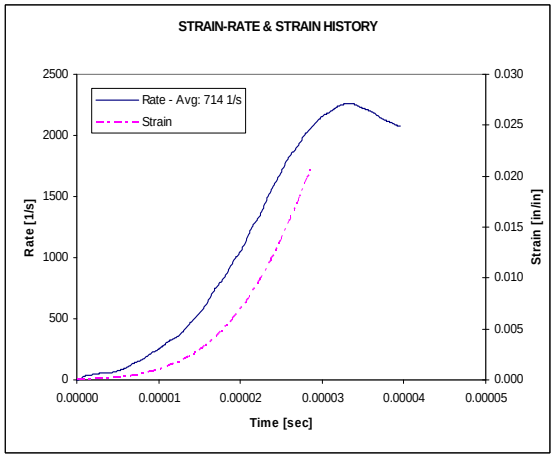

Specimen 2

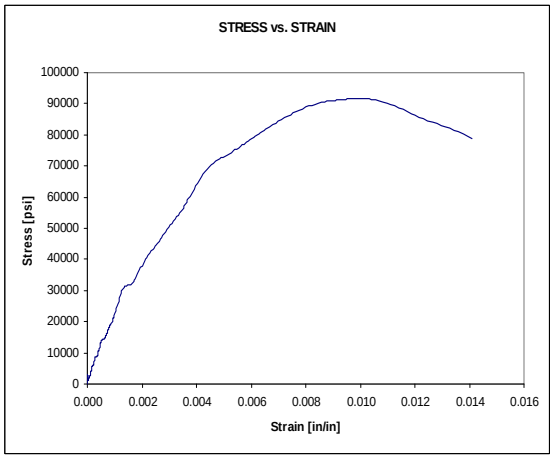

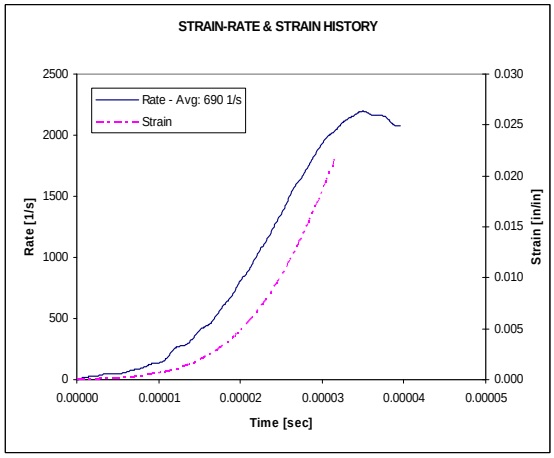

Specimen 3

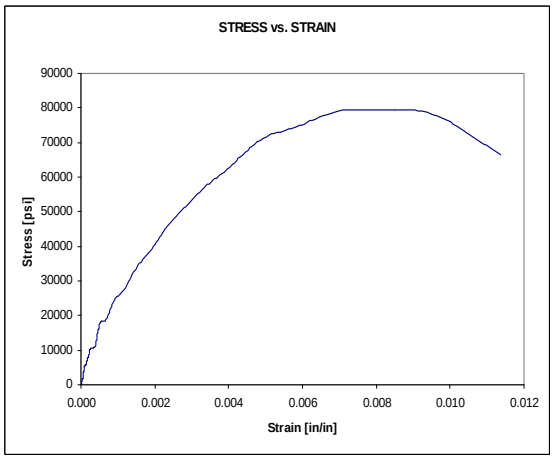

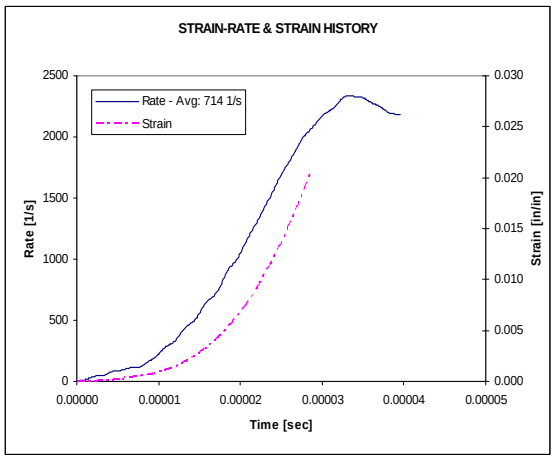

Figure C-20. Stress-Strain Curves for [0°] T700G-12K-50C/3900-2 PWCF Specimens Tested at Average Strain Rate of 706 s^{-1}

Specimen 1

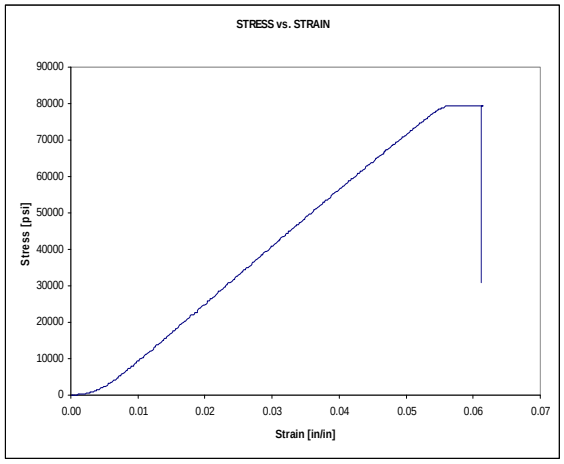

Specimen 2

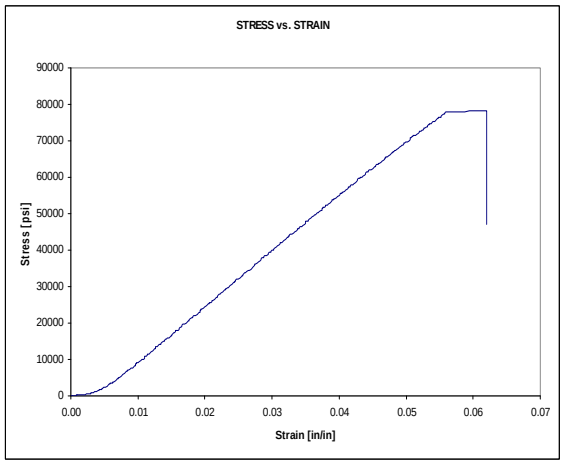

Specimen 3

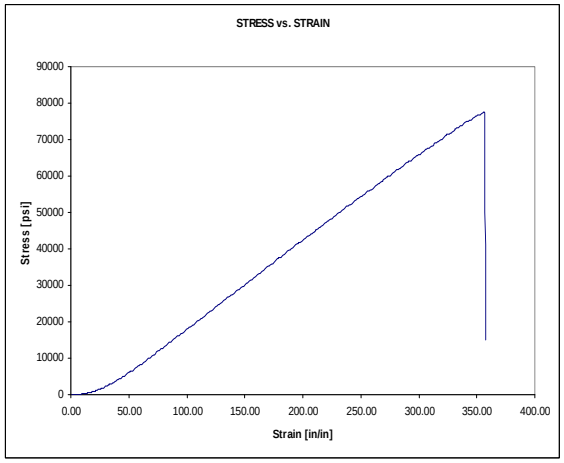

Figure C-21. Stress-Strain Curves for $[+15°/-15°]_{NS}$ T700G-12K-50C/3900-2 PWCF Specimens Tested at Average Strain Rate of 0.00167 s^{-1}

Specimen 1

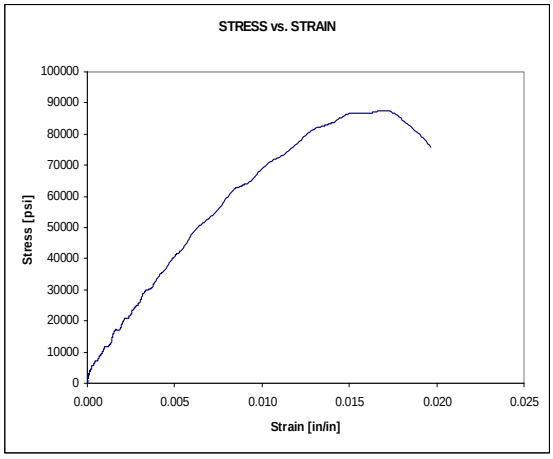

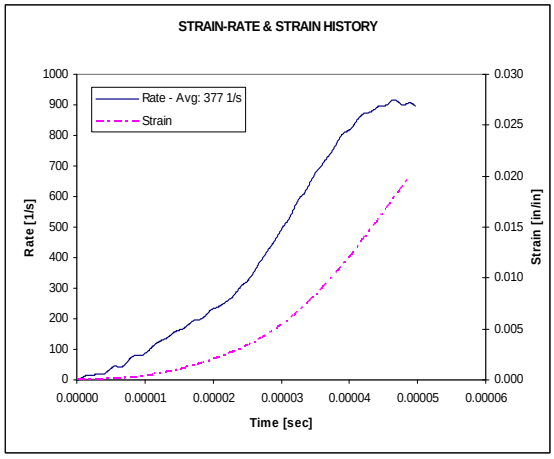

Specimen 2

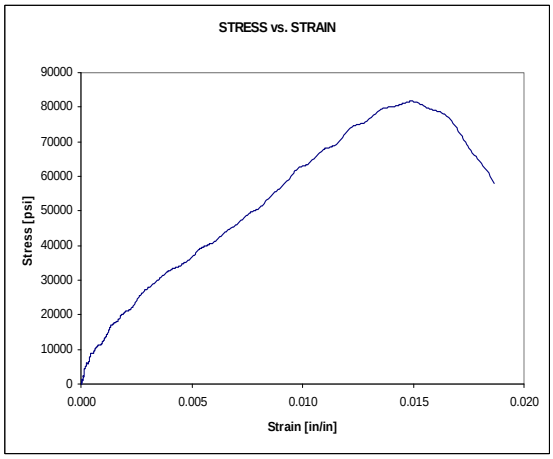

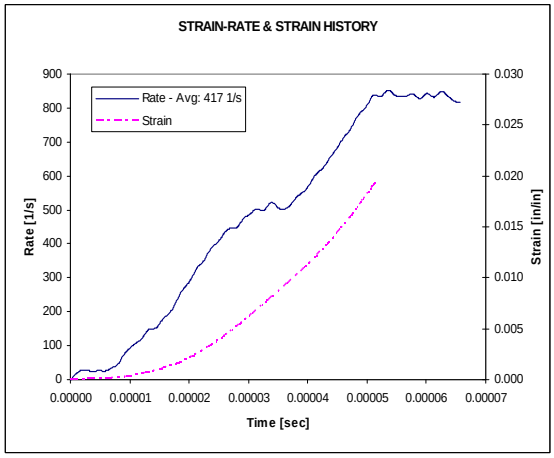

Specimen 3

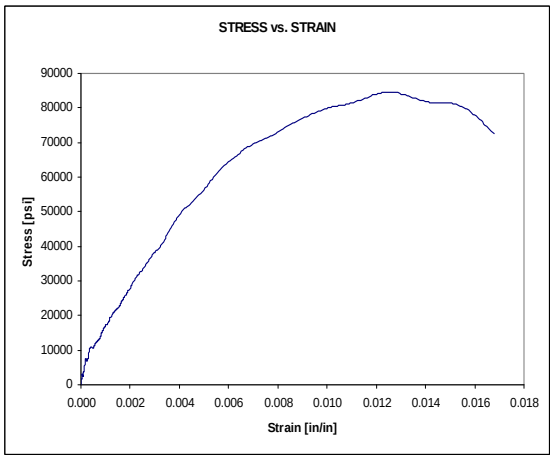

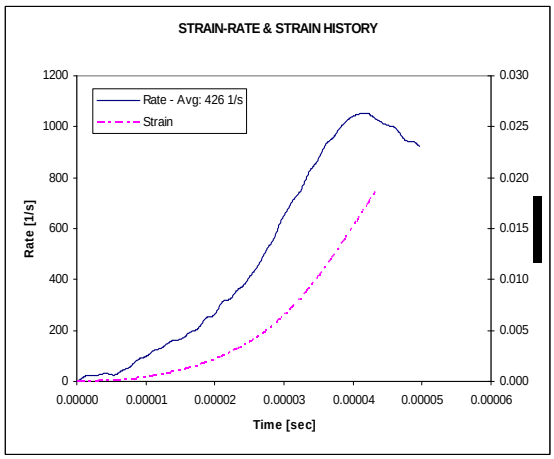

Figure C-22. Stress-Strain Curves for $[+15°/-15°]_{NS}$ T700G-12K-50C/3900-2 PWCF Specimens Tested at Average Strain Rate of 407 s^{-1}

Specimen 1

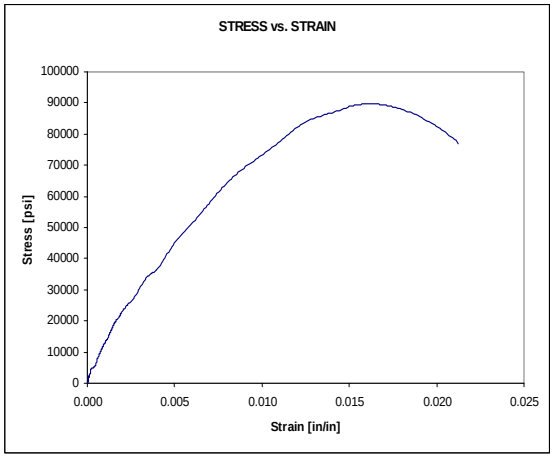

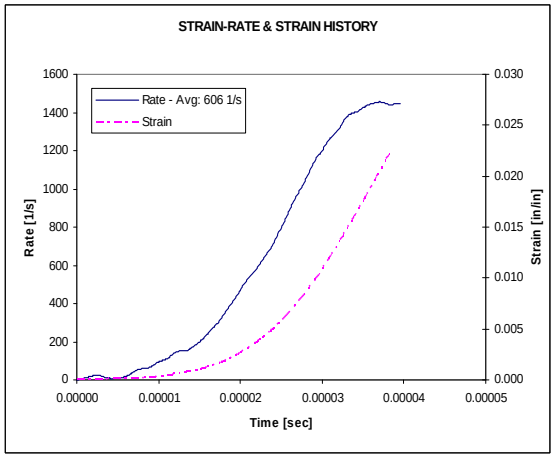

Specimen 2

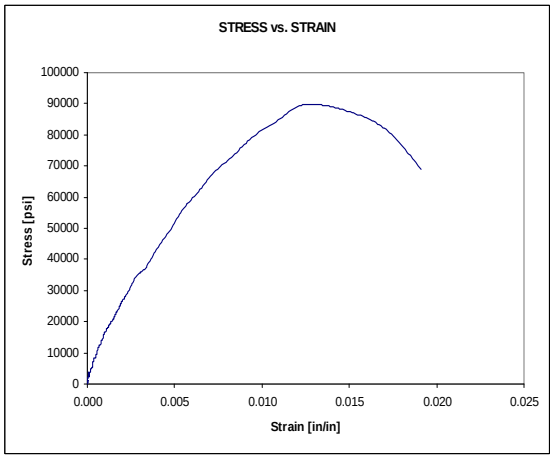

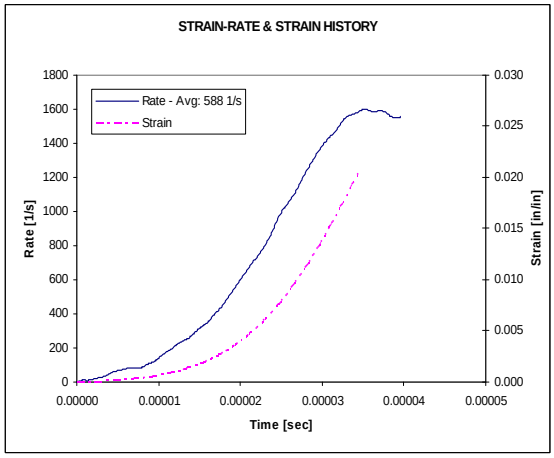

Specimen 3

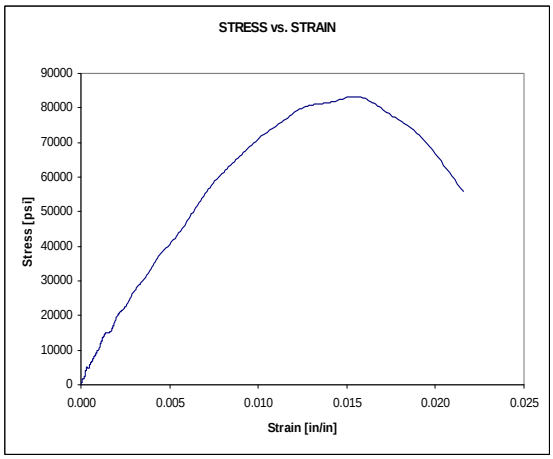

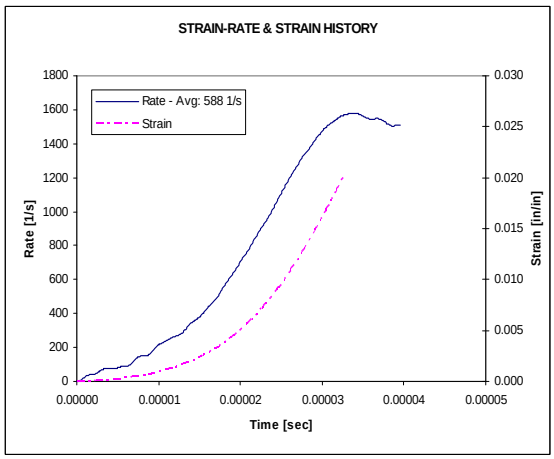

Figure C-23. Stress-Strain Curves for $[+15°/-15°]_{NS}$ T700G-12K-50C/3900-2 PWCF Specimens Tested at Average Strain Rate of 594 s^{-1}

Specimen 1

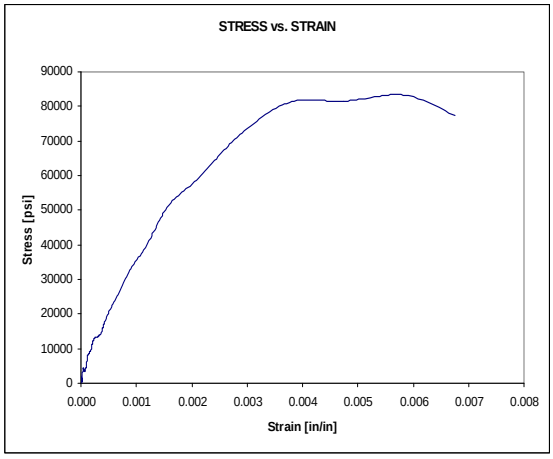

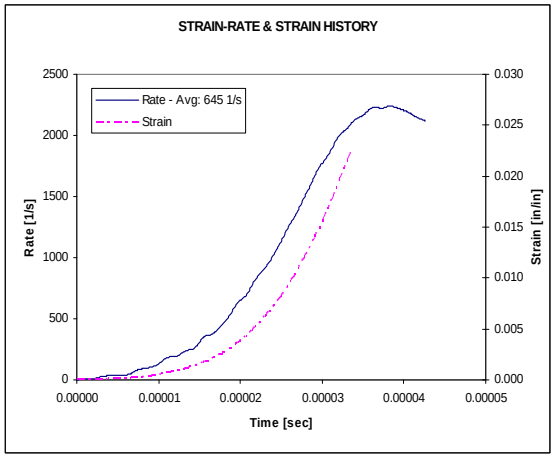

Specimen 2

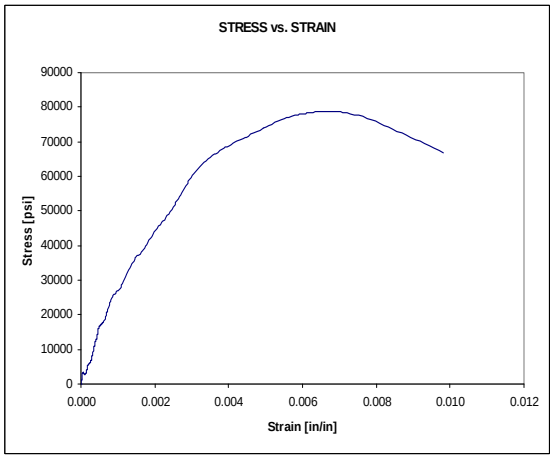

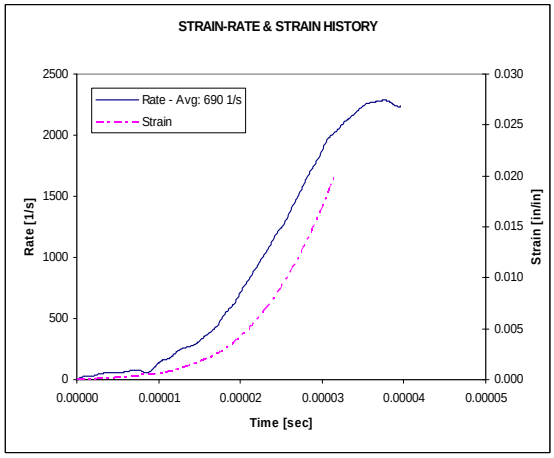

Specimen 3

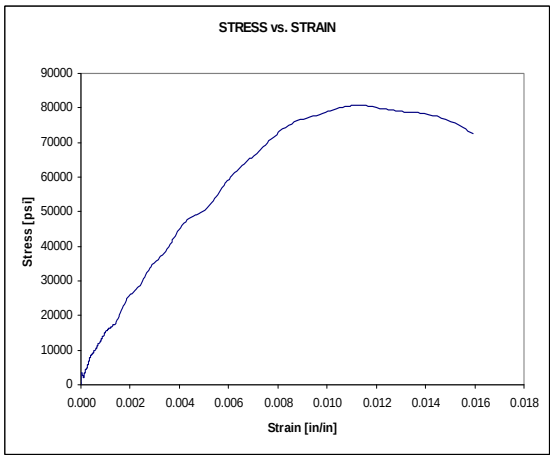

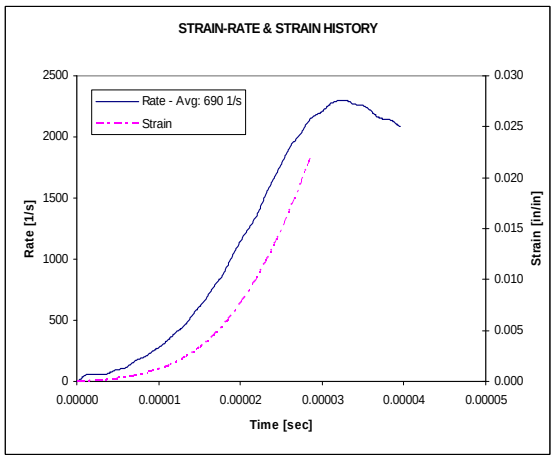

Figure C-24. Stress-Strain Curves for $[+15°/-15°]_{NS}$ T700G-12K-50C/3900-2 PWCF Specimens Tested at Average Strain Rate of 675 s^{-1}

Specimen 1

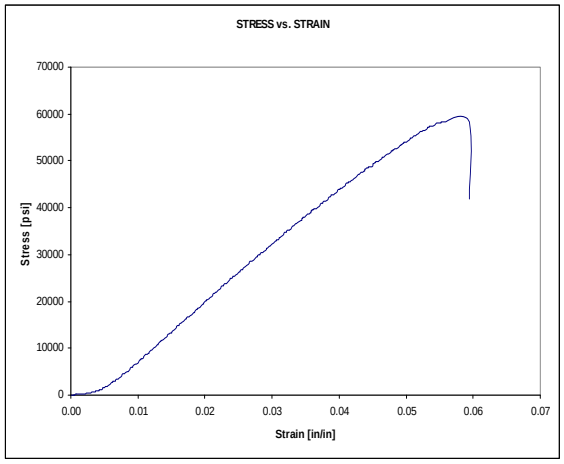

Specimen 2

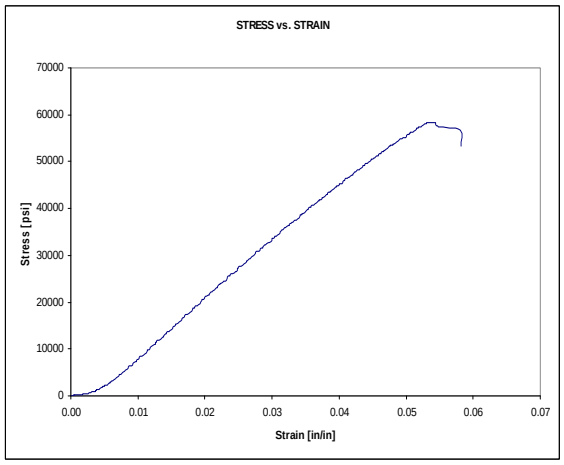

Specimen 3

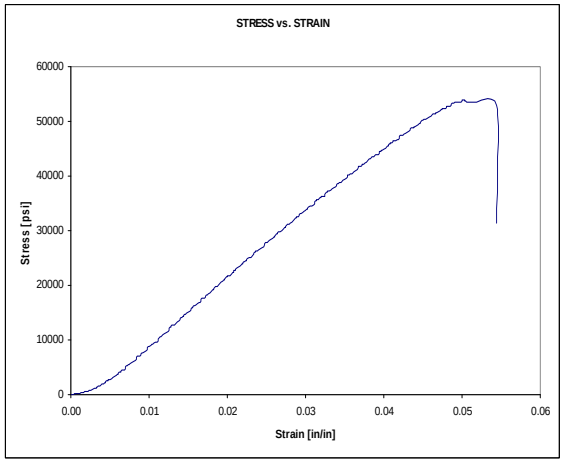

Figure C-25. Stress-Strain Curves for $[+30°/-30°]_{NS}$ T700G-12K-50C/3900-2 PWCF Specimens Tested at Average Strain Rate of 0.00167 s^{-1}

Specimen 1

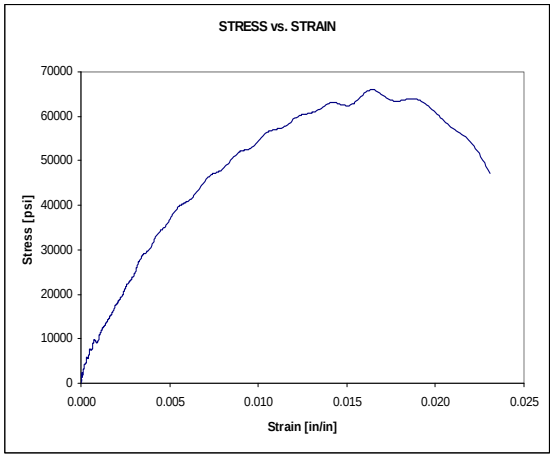

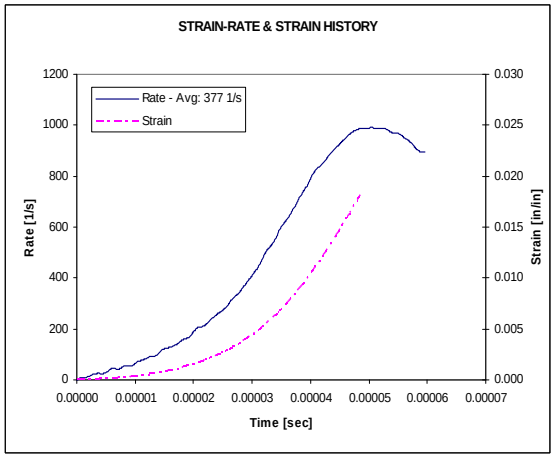

Specimen 2

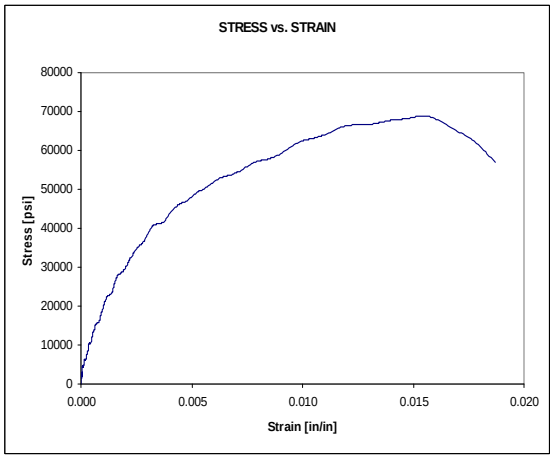

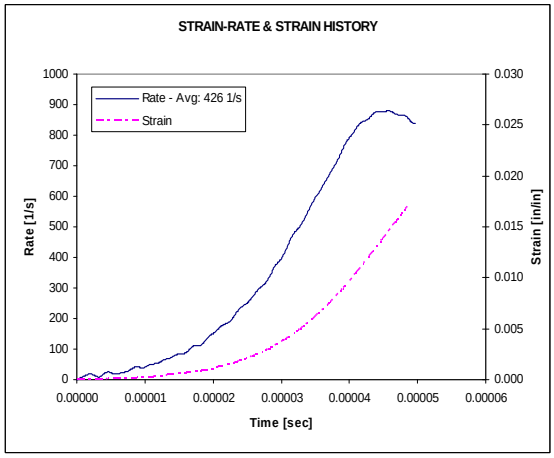

Specimen 3

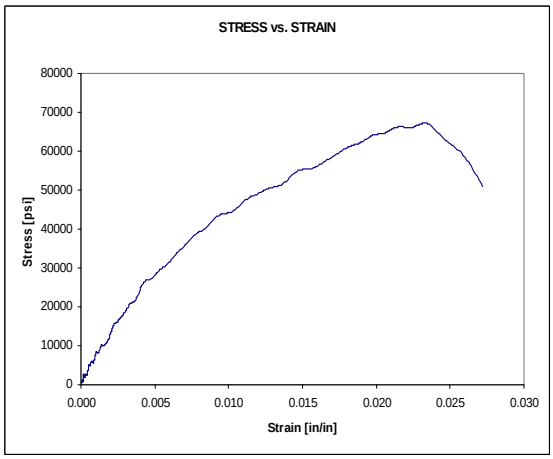

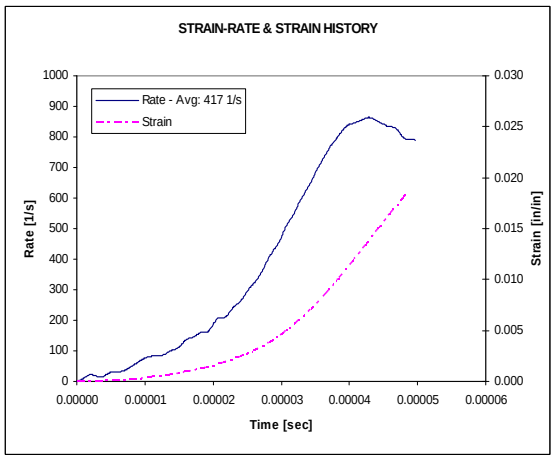

Figure C-26. Stress-Strain Curves for $[+30°/-30°]_{NS}$ T700G-12K-50C/3900-2 PWCF Specimens Tested at Average Strain Rate of 407 s^{-1}

Specimen 1

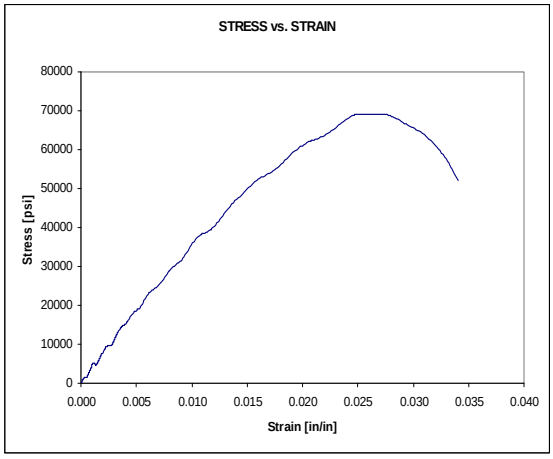

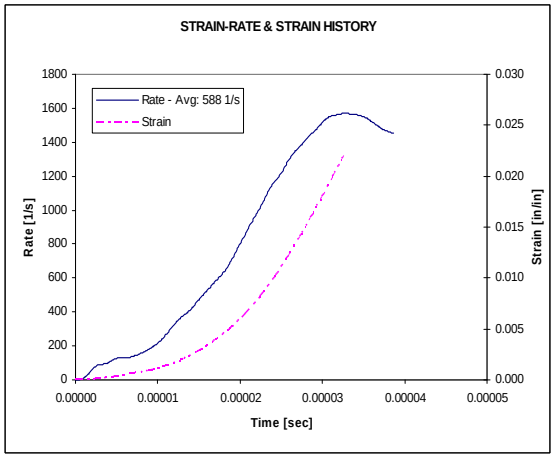

Specimen 2

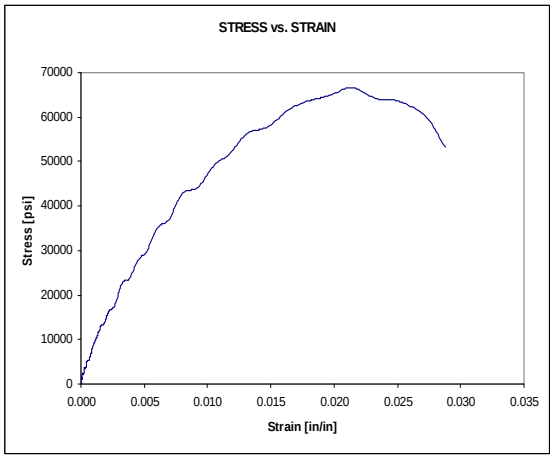

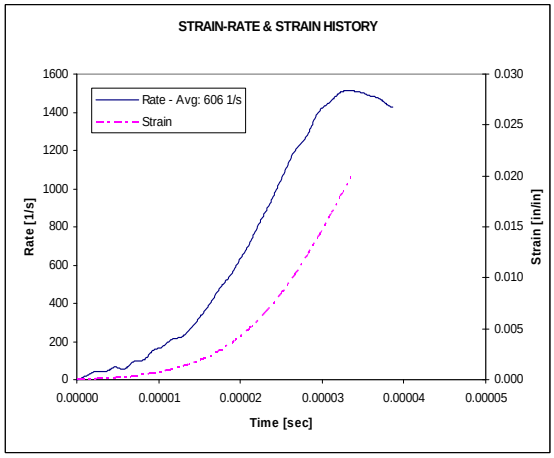

Specimen 3

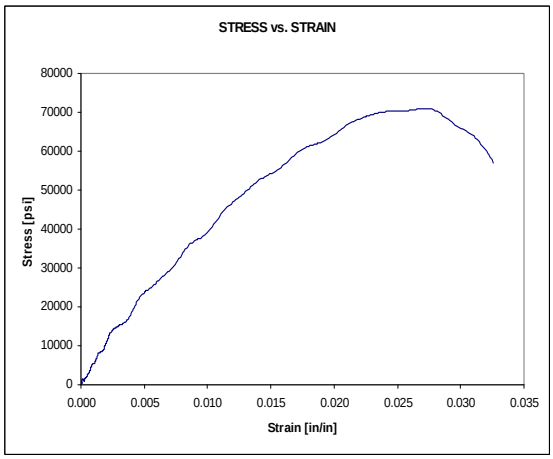

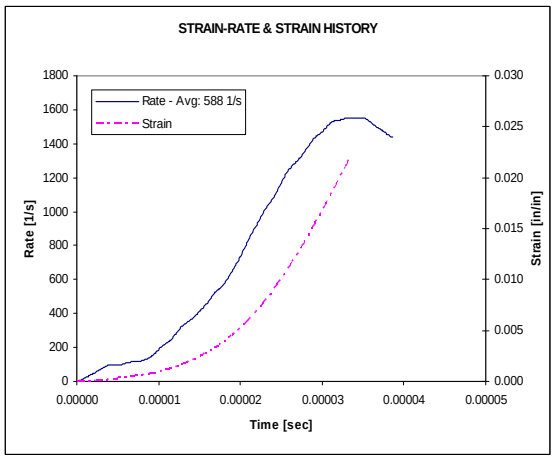

Figure C-27. Stress-Strain Curves for $[+30°/-30°]_{NS}$ T700G-12K-50C/3900-2 PWCF Specimens Tested at Average Strain Rate of 594 s^{-1}

Specimen 1

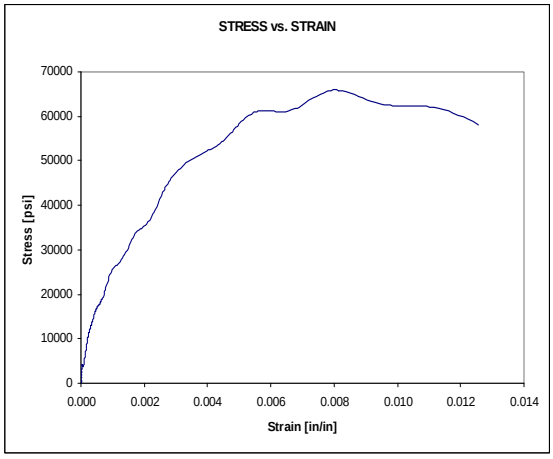

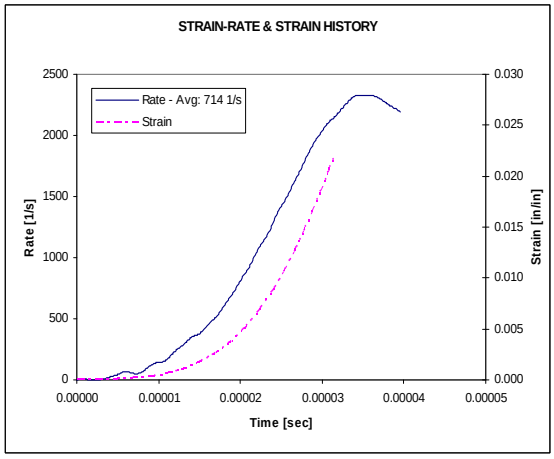

Specimen 2

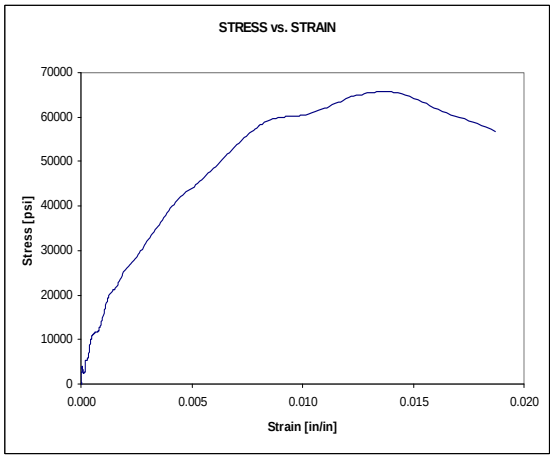

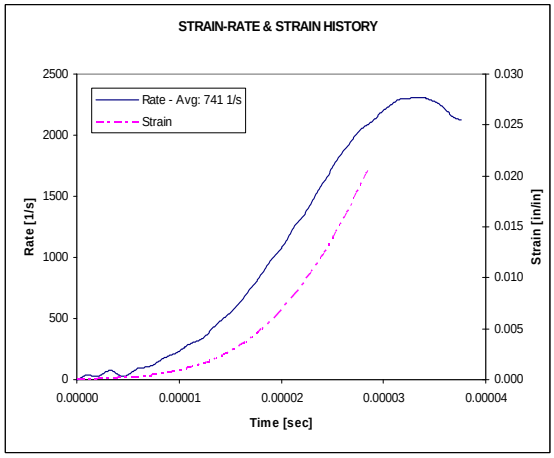

Specimen 3

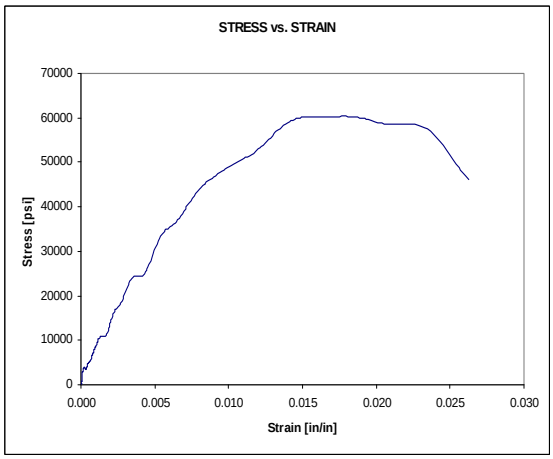

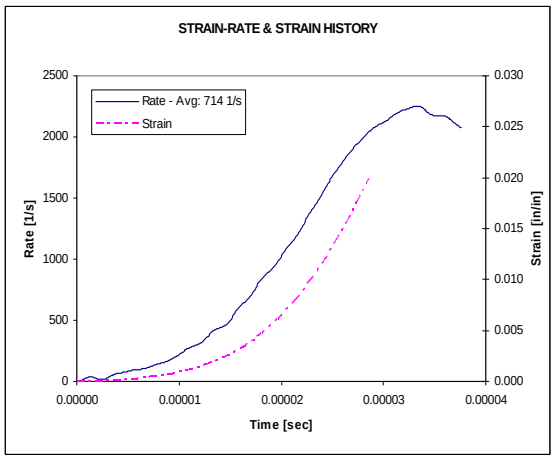

Figure C-28. Stress-Strain Curves for $[+30°/-30°]_{NS}$ T700G-12K-50C/3900-2 PWCF Specimens Tested at Average Strain Rate of 723 s^{-1}

Specimen 1

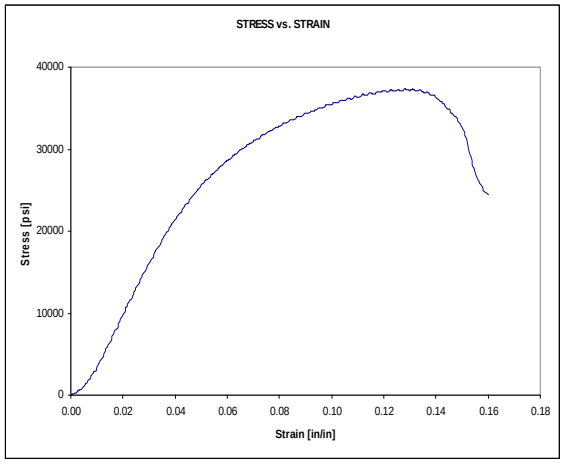

Specimen 2

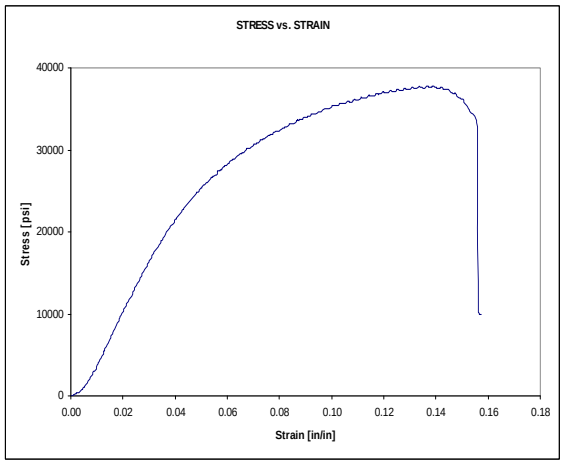

Specimen 3

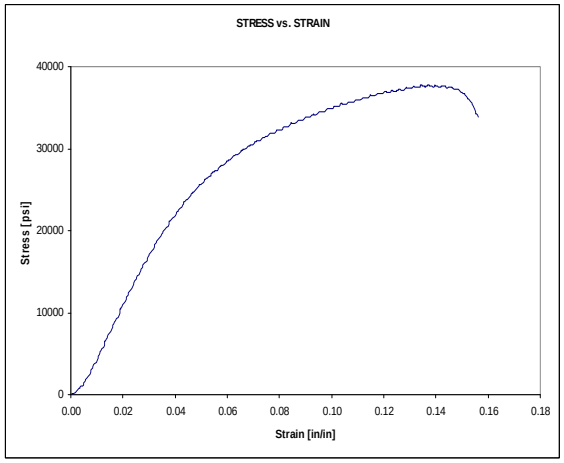

Figure C-29. Stress-Strain Curves for $[+45°/-45°]_{NS}$ T700G-12K-50C/3900-2 PWCF Specimens Tested at Average Strain Rate of 0.00167 s^{-1}

Specimen 1

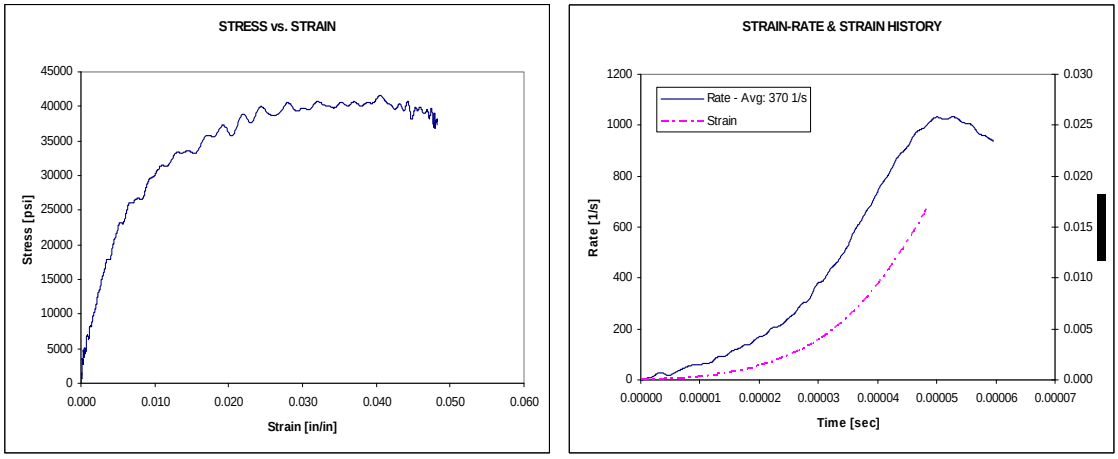

Specimen 2

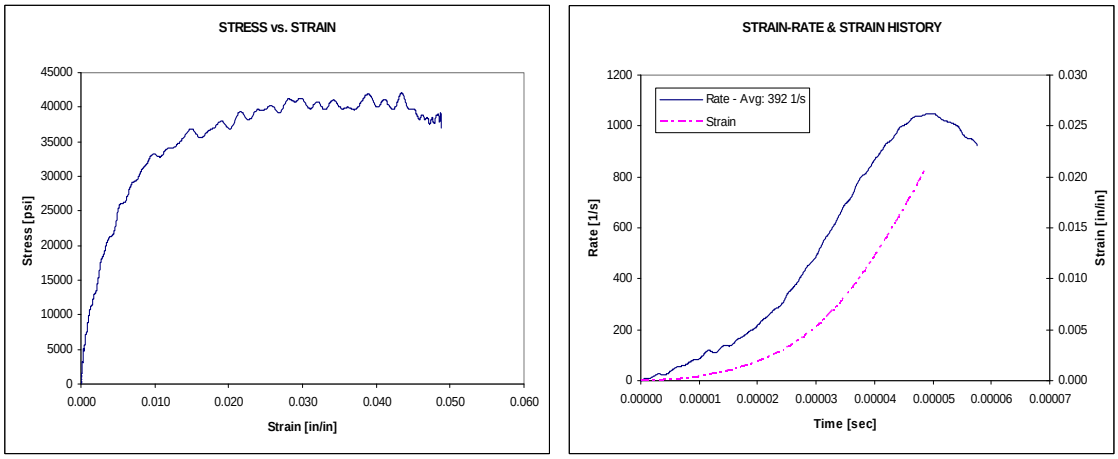

Specimen 3

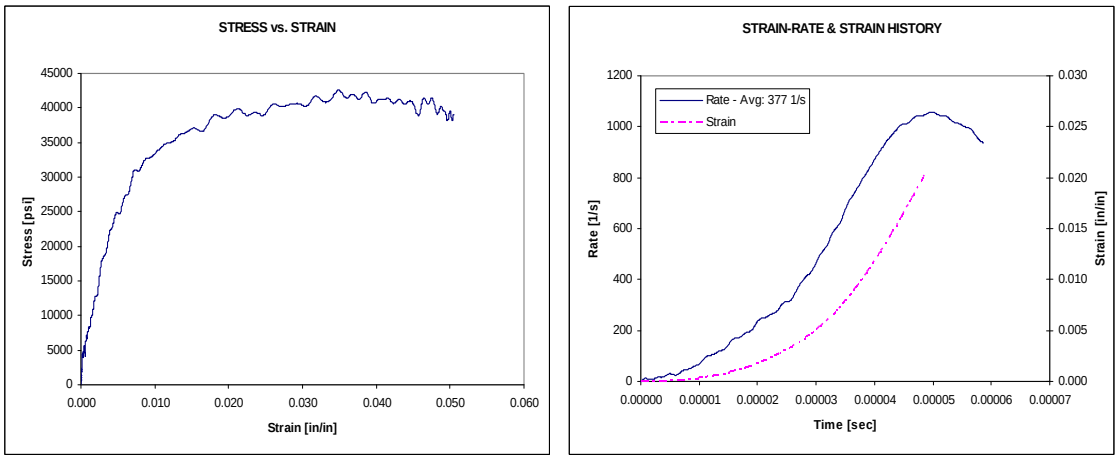

Figure C-30. Stress-Strain Curves for $[+45°/-45°]_{NS}$ T700G-12K-50C/3900-2 PWCF Specimens Tested at Average Strain Rate of 380 s^{-1}

Specimen 1

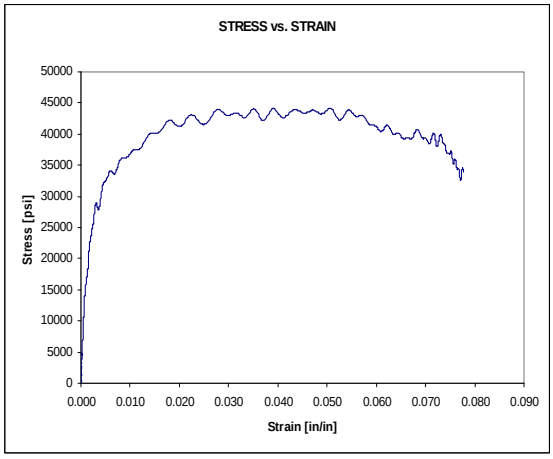

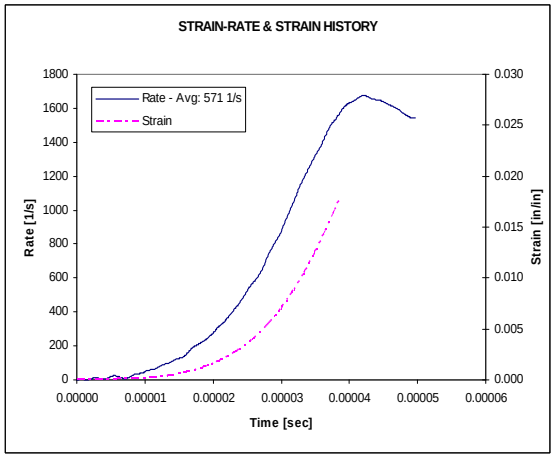

Specimen 2

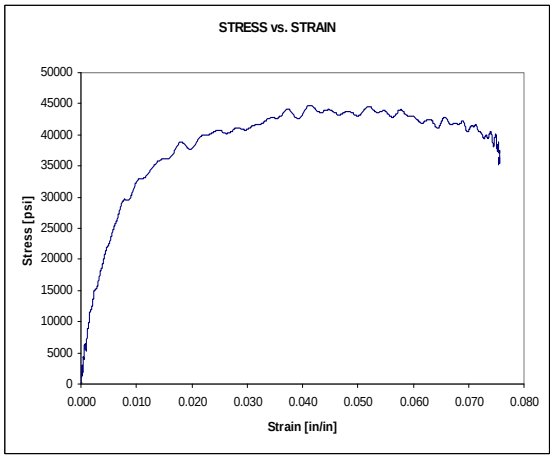

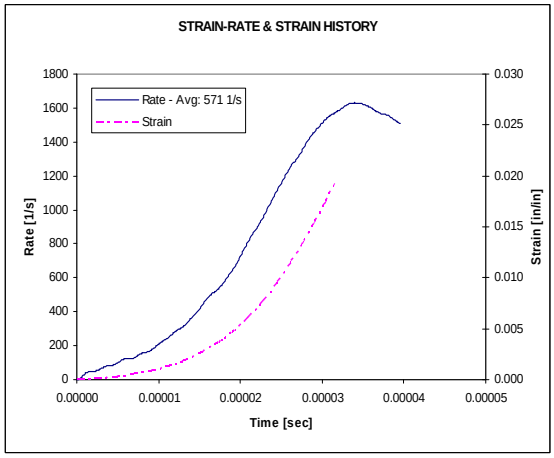

Specimen 3

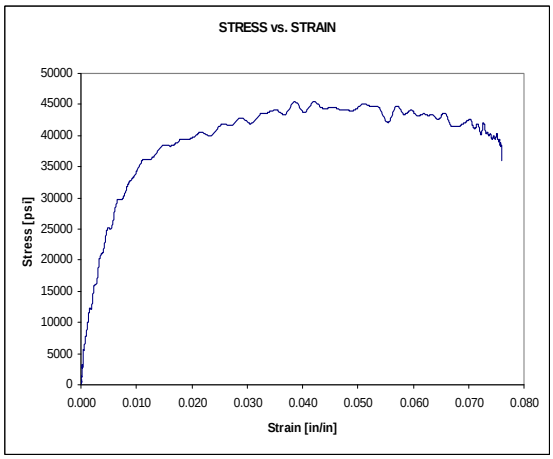

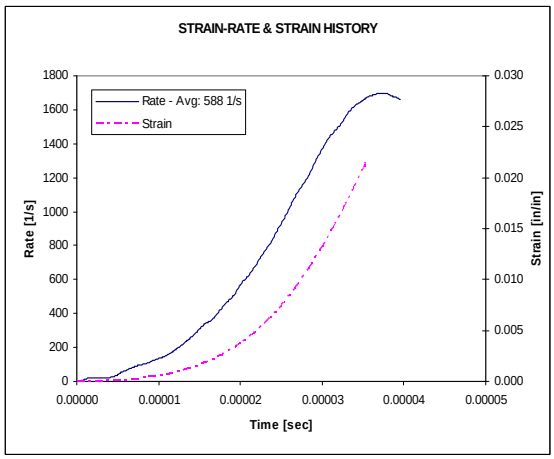

Figure C-31. Stress-Strain Curves for $[+45°/-45°]_{NS}$ T700G-12K-50C/3900-2 PWCF Specimens Tested at Average Strain Rate of 577 s^{-1}

Specimen 1

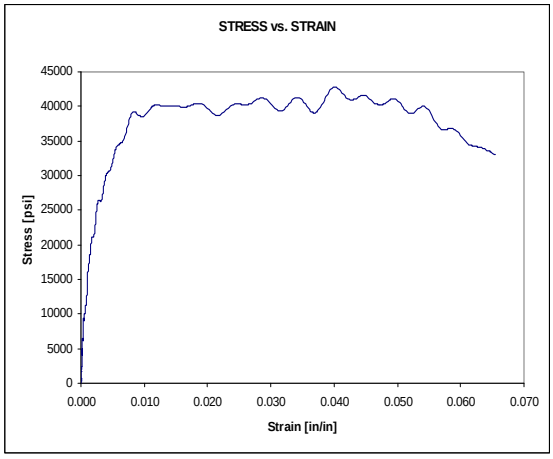

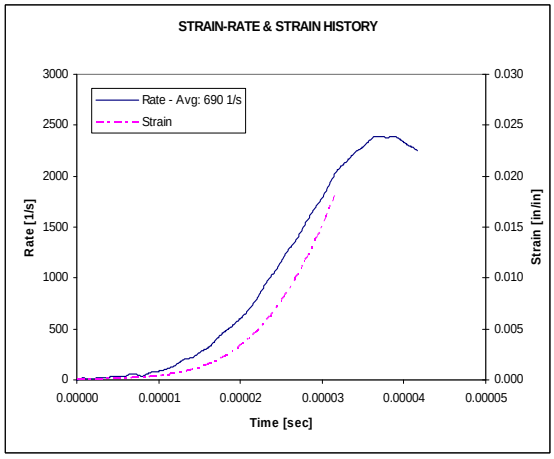

Specimen 2

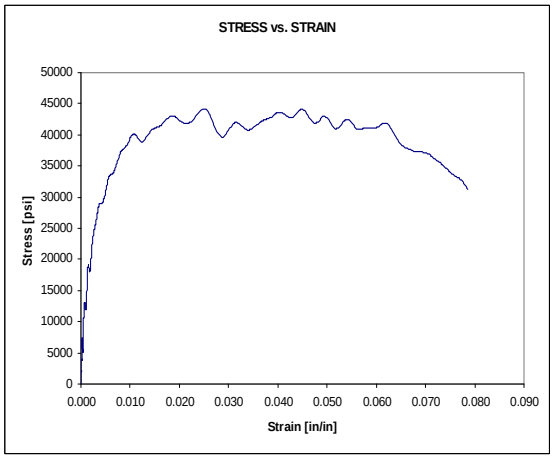

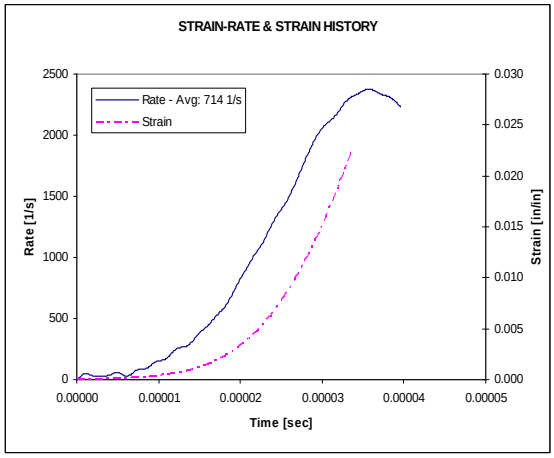

Specimen 3

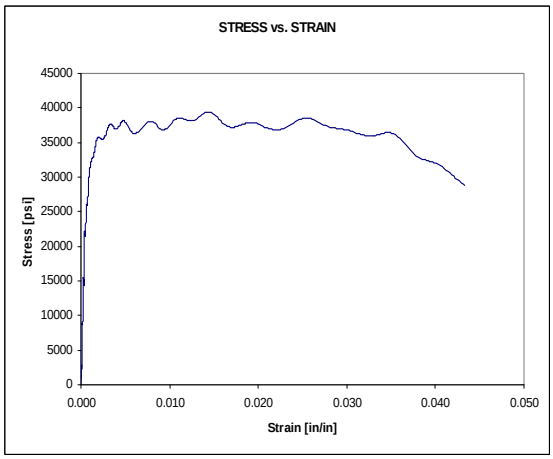

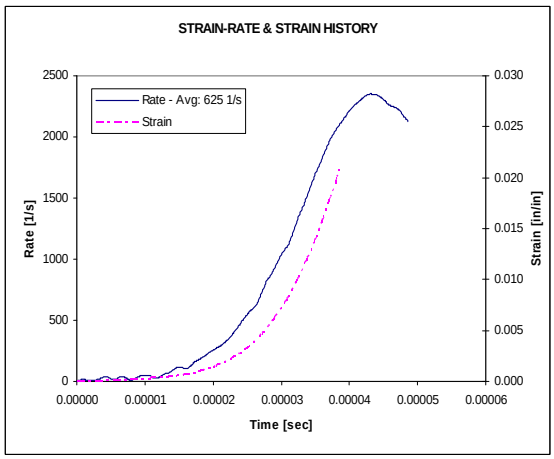

Figure C-32. Stress-Strain Curves for $[+45°/-45°]_{NS}$ T700G-12K-50C/3900-2 PWCF Specimens Tested at Average Strain Rate of 676 s^{-1}

Table C-3. Summary of Failure Strengths and Strain Rates for Newport NB321/7781 Fiberglass

Orientation (degrees)	Average Strain Rate (1/s)	Actual Strain Rate (1/s)	Failure Strength (psi)	Average Failure Strength (psi)
0	0.00167	0.00167	59,353	62,791
		0.00167	63,367	
		0.00167	65,653	
	1	1	72,679	73,081
		1	73,482	
	466	444	68,678	74,528
		455	75,779	
		500	79,128	
	699	690	75,658	75,113
		741	68,490	
		667	81,192	
	823	800	83,196	80,982
		800	78,405	
		870	81,347	
15	0.00167	0.00167	63,664	59,313
		0.00167	62,143	
		0.00167	52,132	
	1	1	63,482	67,990
		1	72,497	
	448	444	69,002	67,115
		465	57,743	
		435	74,600	
	659	667	71,922	73,549
		645	75,341	
		667	73,384	
	812	769	74,763	74,828
		833	74,659	
		833	75,063	

Table C-3. Summary of Failure Strengths and Strain Rates for Newport NB321/7781 Fiberglass (Continued)

Orientation (degrees)	Average Strain Rate (1/s)	Actual Strain Rate (1/s)	Failure Strength (psi)	Average Failure Strength (psi)
30	0.00167	0.00167	44,818	43,029
		0.00167	41,054	
		0.00167	43,215	
	1	1	49,992	50,449
		1	50,905	
	463	435	47,445	46,096
		488	46,176	
		465	44,666	
	692	645	56,909	52,306
		741	45,239	
		690	54,771	
	822	833	53,251	53,281
		800	52,657	
		833	53,936	
45	0.00167	0.00167	24,197	24,471
		0.00167	24,504	
		0.00167	24,713	
	1	1	32,034	31,894
		1	31,753	
	368	392	25,905	25,407
		328	23,475	
		385	26,840	
	572	556	26,280	26,705
		571	26,498	
		588	27,337	
	698	690	30,490	30,639
		690	30,881	
		714	30,547	

Specimen 1

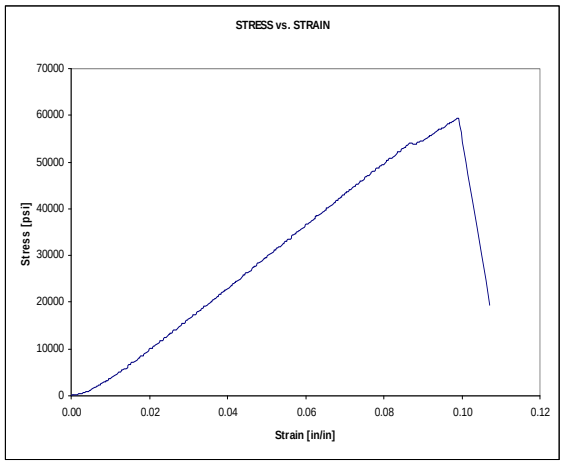

Specimen 2

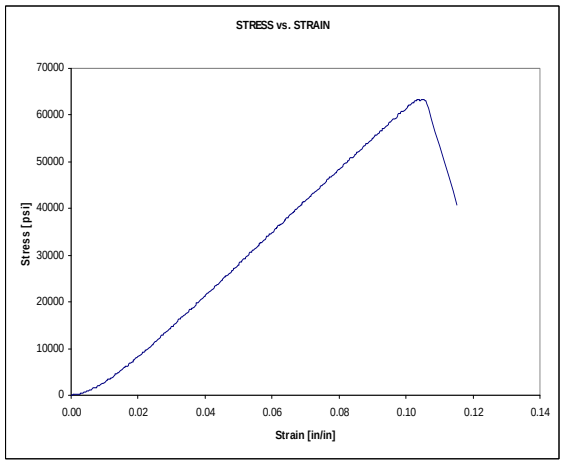

Specimen 3

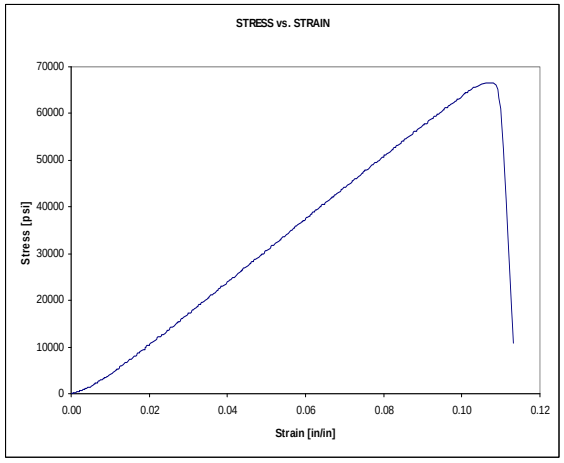

Figure C-33. Stress-Strain Curves for [0°] Newport NB321/7781 Fiberglass Satin Weave Glass Fabric Specimens Tested at Average Strain Rate of 0.00167 s^{-1}

Specimen 1

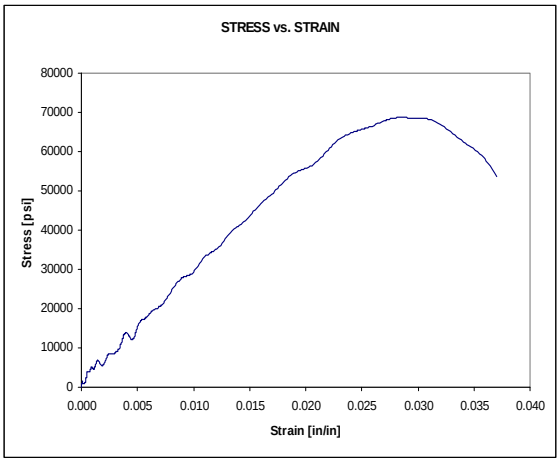

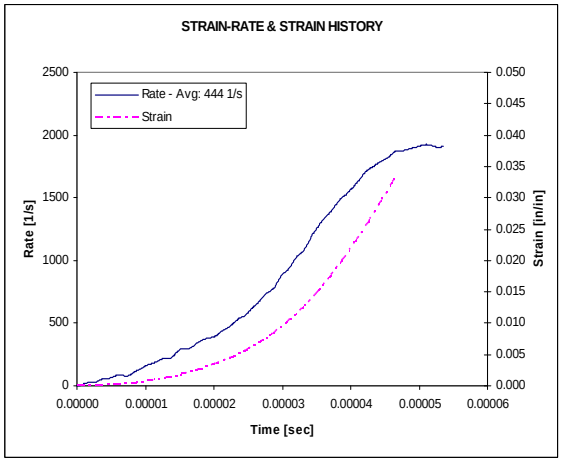

Specimen 2

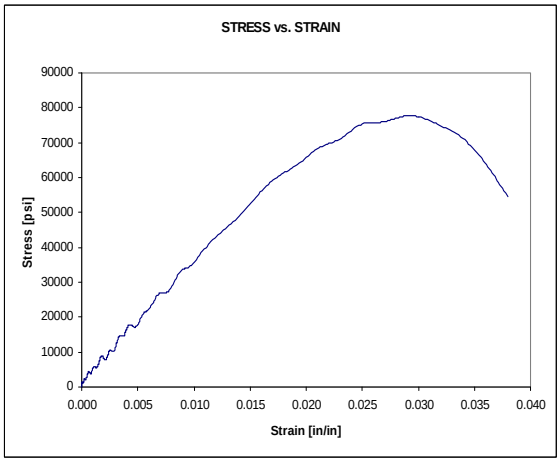

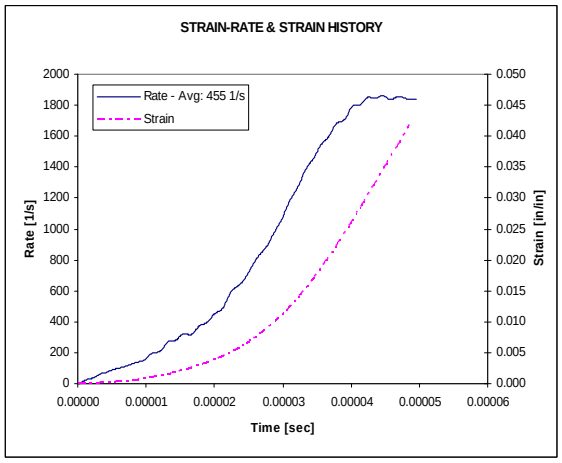

Specimen 3

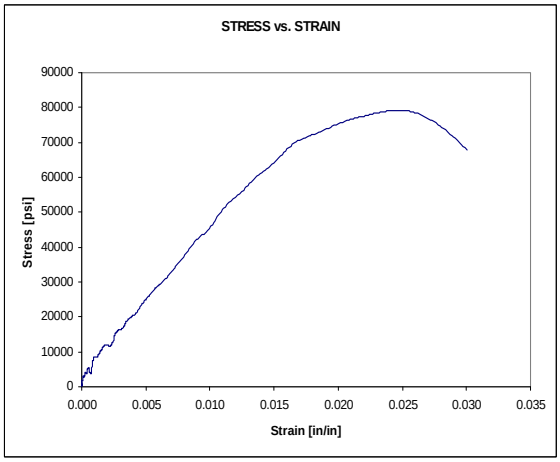

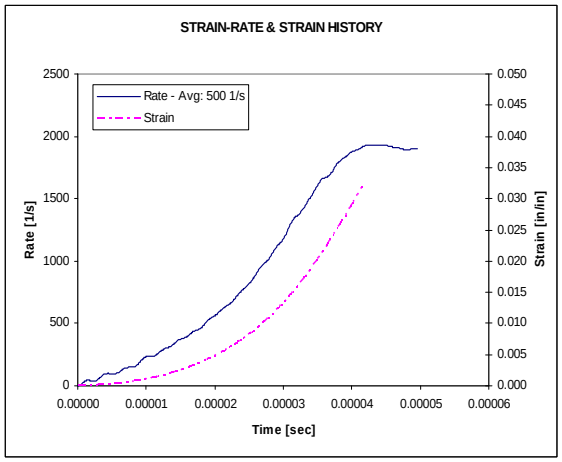

Figure C-34. Stress-Strain Curves for [0°] Newport NB321/7781 Fiberglass Satin Weave Glass Fabric Specimens Tested at Average Strain Rate of 466 s^{-1}

Specimen 1

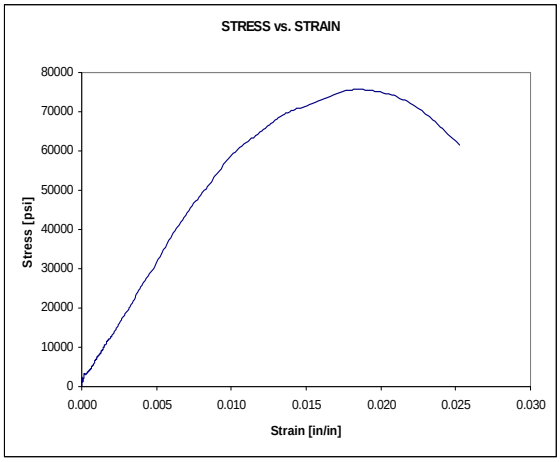

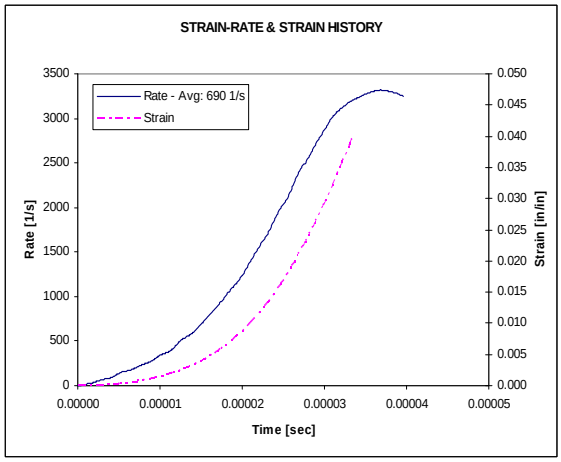

Specimen 2

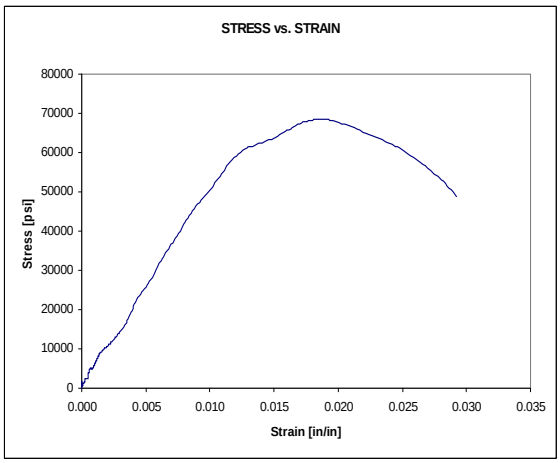

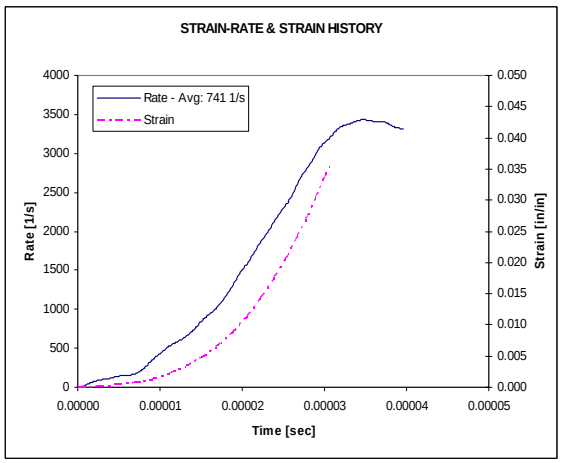

Specimen 3

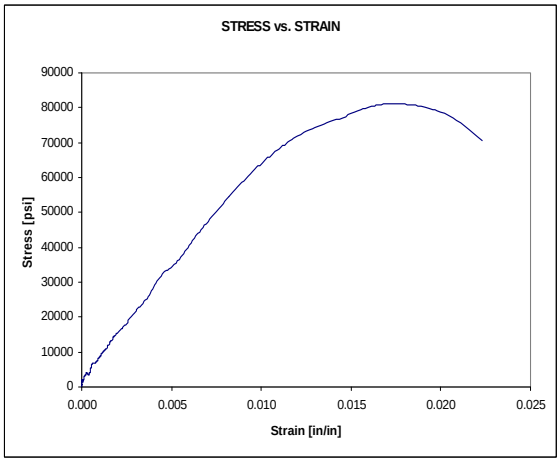

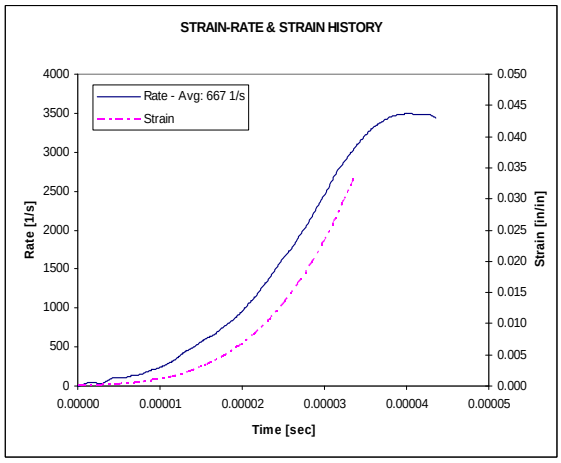

Figure C-35. Stress-Strain Curves for [0°] Newport NB321/7781 Fiberglass Satin Weave Glass Fabric Specimens Tested at Average Strain Rate of 699 s^{-1}

Specimen 1

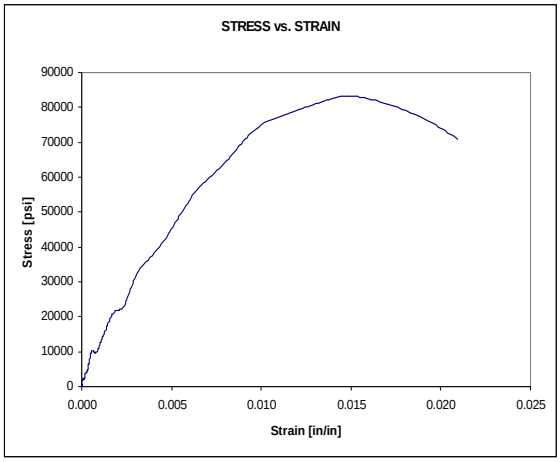

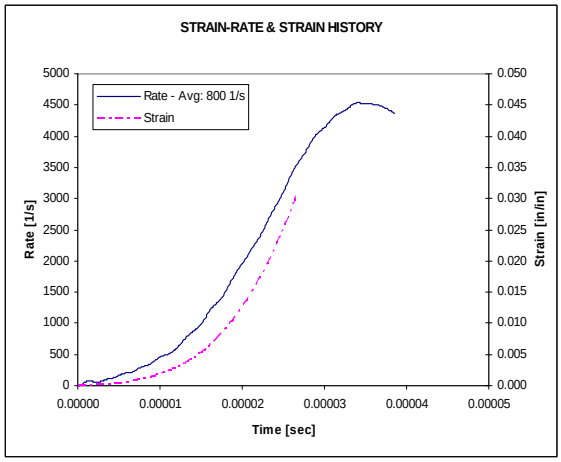

Specimen 2

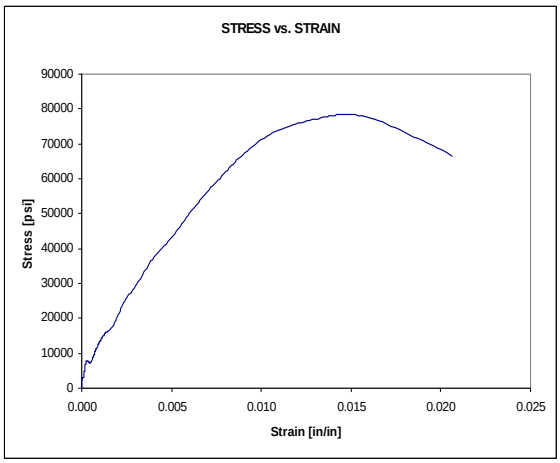

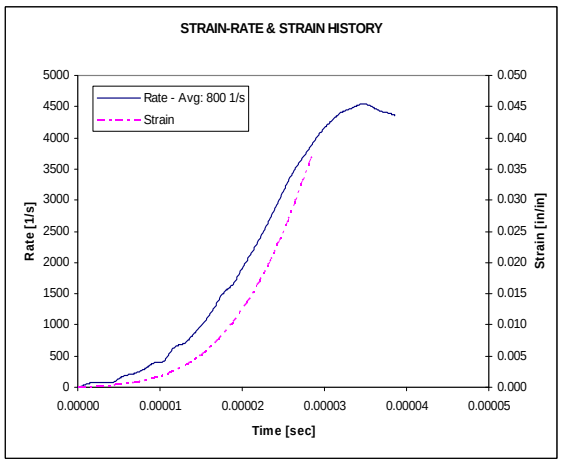

Specimen 3

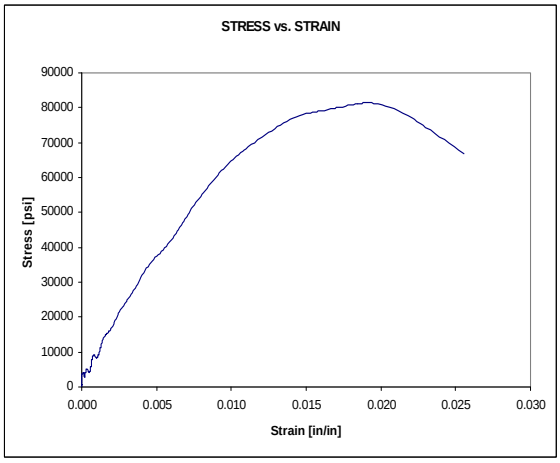

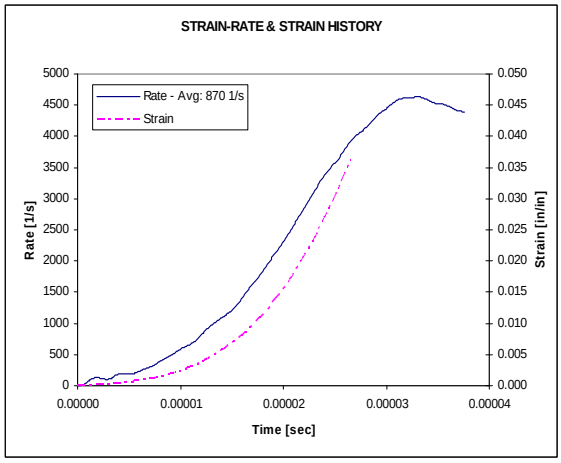

Figure C-36. Stress-Strain Curves for [0°] Newport NB321/7781 Fiberglass Satin Weave Glass Fabric Specimens Tested at Average Strain Rate of 823 s^{-1}

Specimen 1

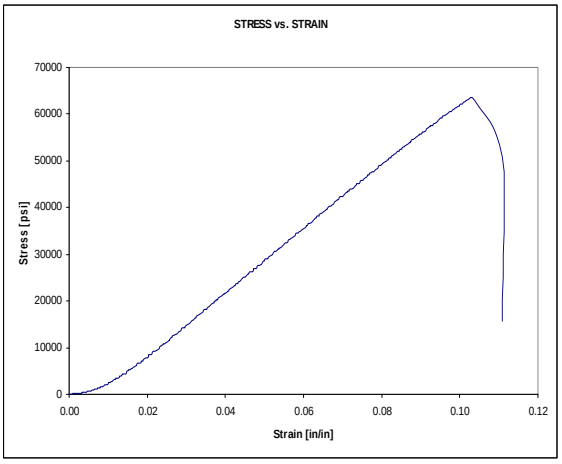

Specimen 2

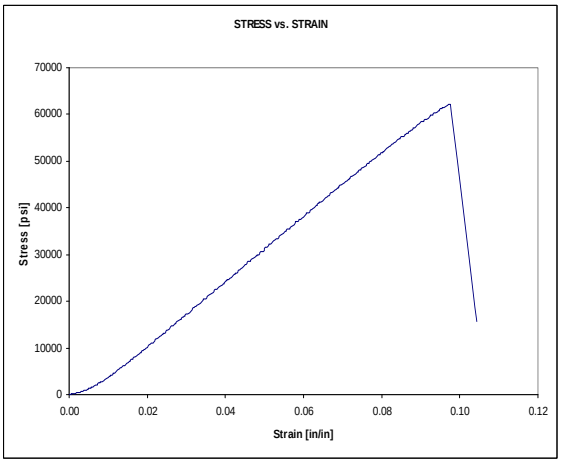

Specimen 3

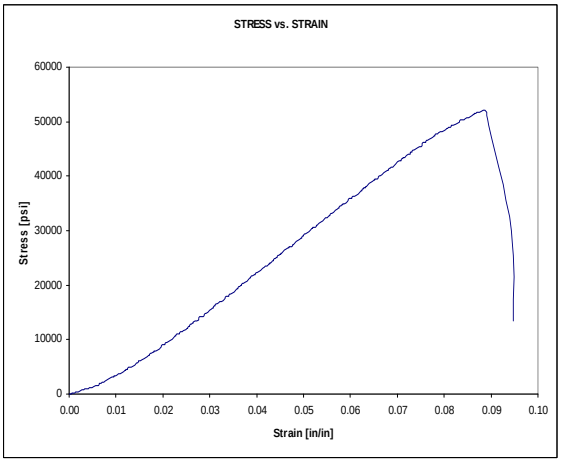

Figure C-37. Stress-Strain Curves for $[+15°/-15°]_{NS}$ Newport NB321/7781 Fiberglass Satin Weave Glass Fabric Specimens Tested at Average Strain Rate of 0.00167 s^{-1}

Specimen 1

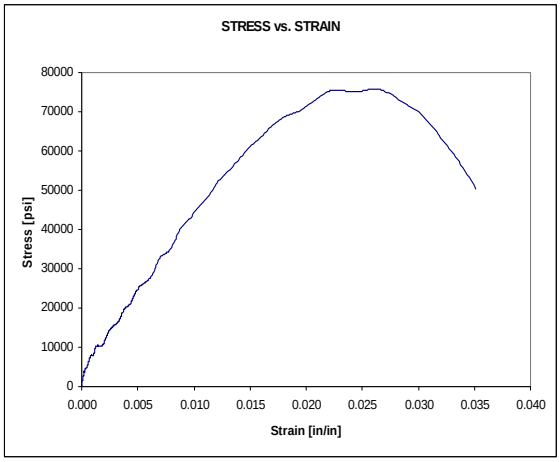

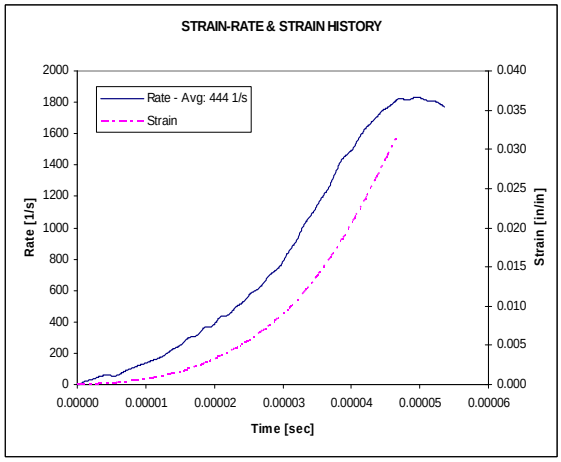

Specimen 2

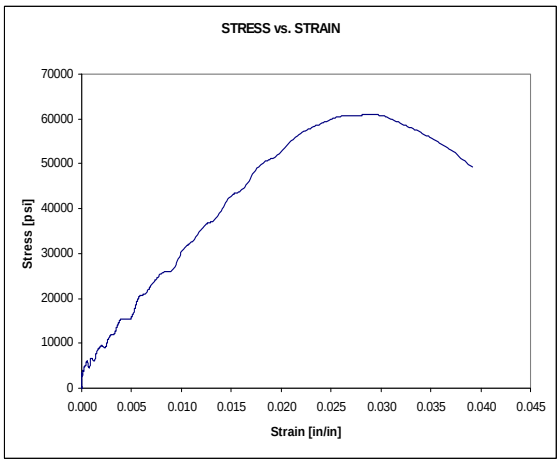

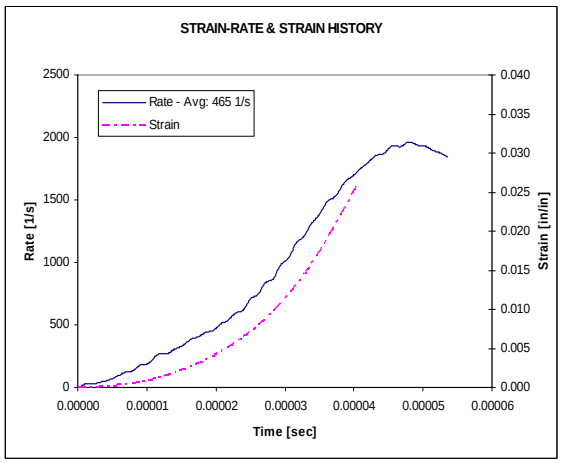

Specimen 3

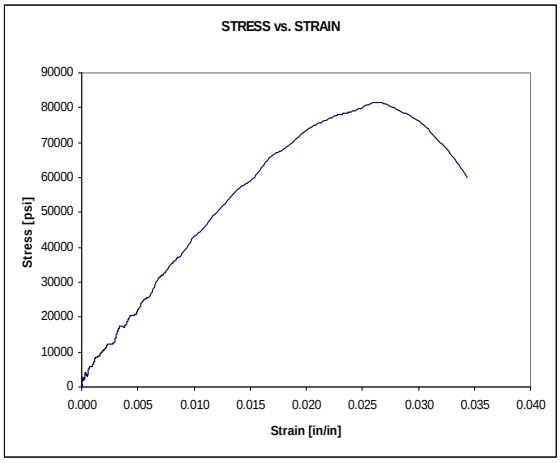

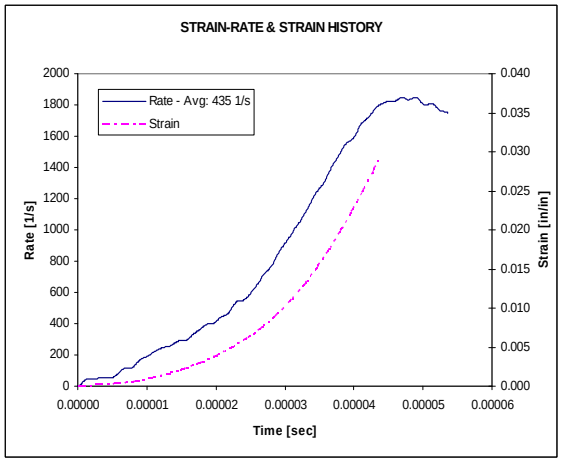

Figure C-38. Stress-Strain Curves for $[+15°/-15°]_{NS}$ Newport NB321/7781 Fiberglass Satin Weave Glass Fabric Specimens Tested at Average Strain Rate of 448 s^{-1}

Specimen 1

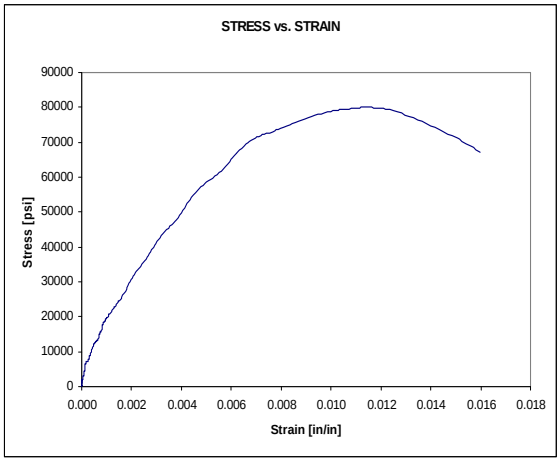

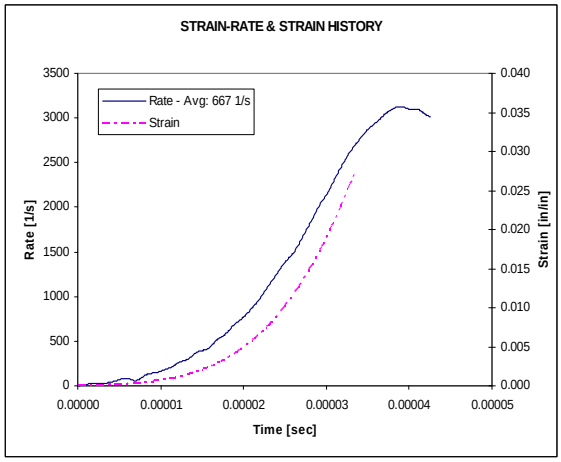

Specimen 2

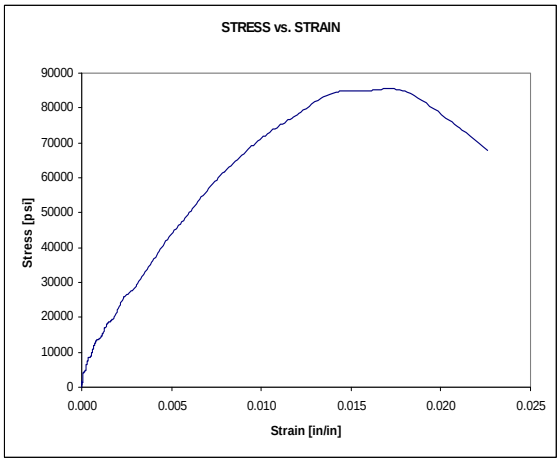

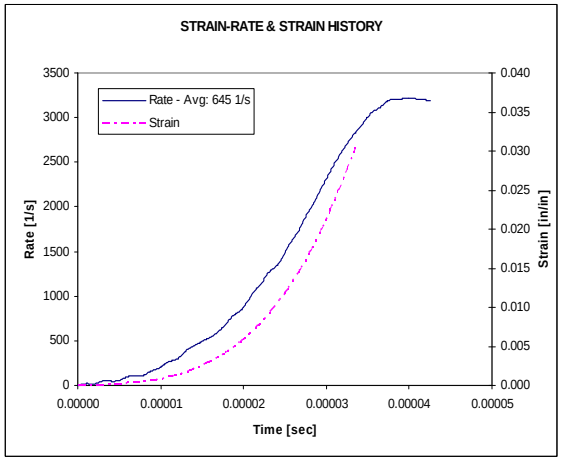

Specimen 3

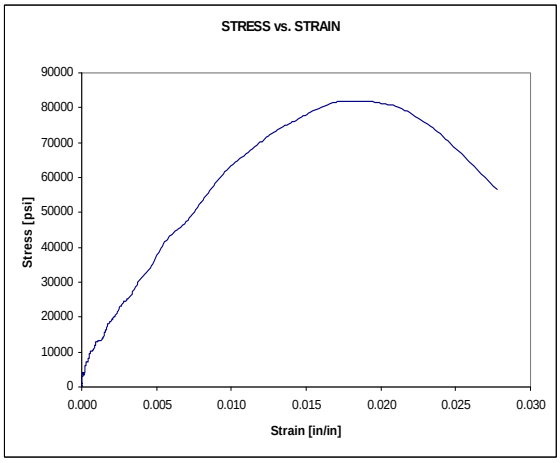

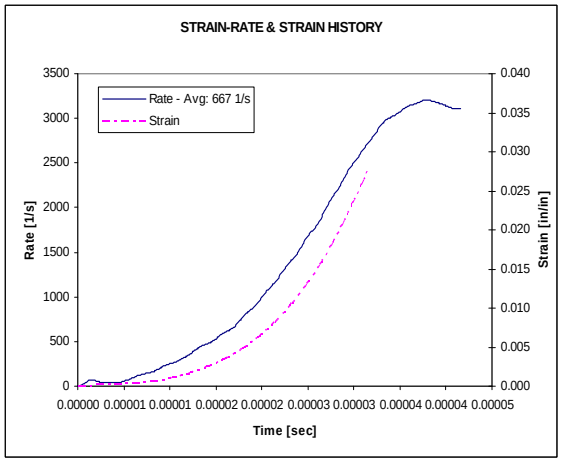

Figure C-39. Stress-Strain Curves for $[+15°/-15°]_{NS}$ Newport NB321/7781 Fiberglass Satin Weave Glass Fabric Specimens Tested at Average Strain Rate of 659 s^{-1}

Specimen 1

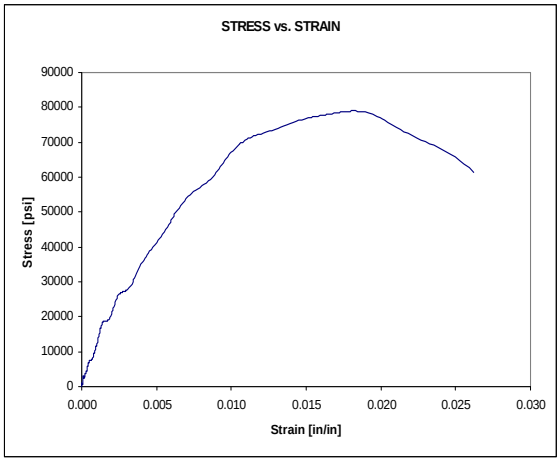

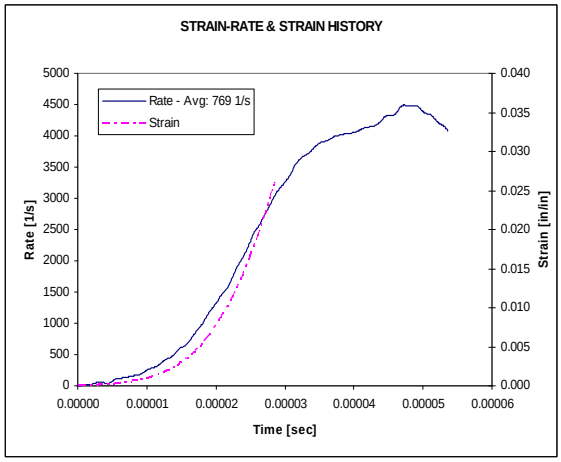

Specimen 2

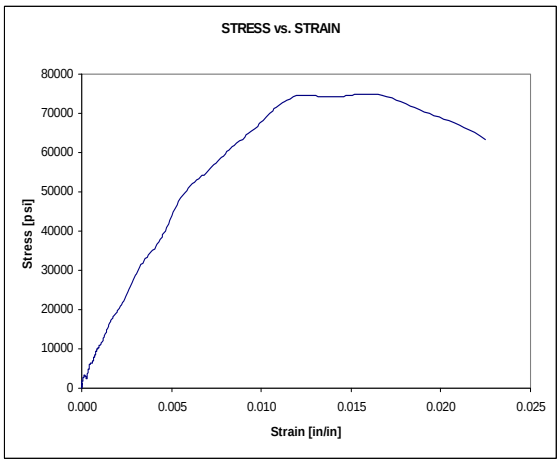

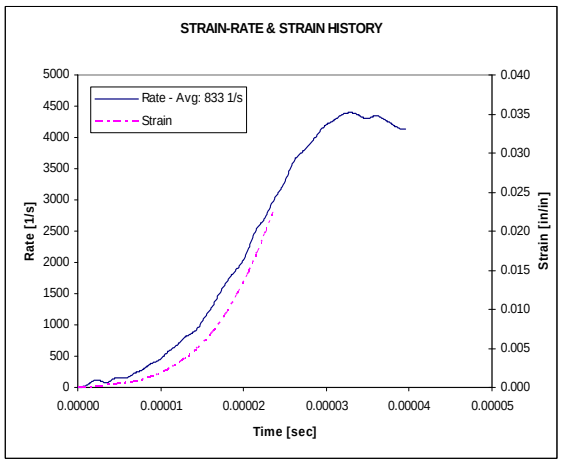

Specimen 3

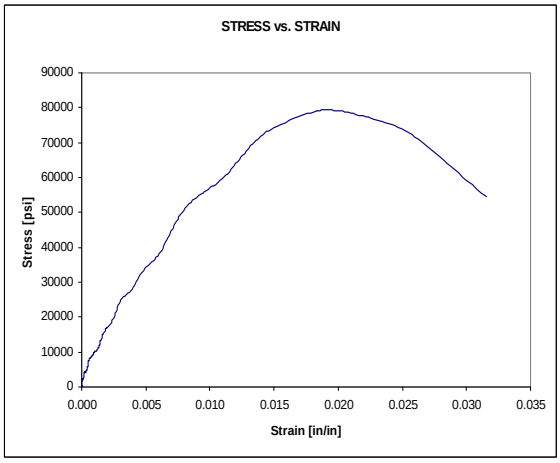

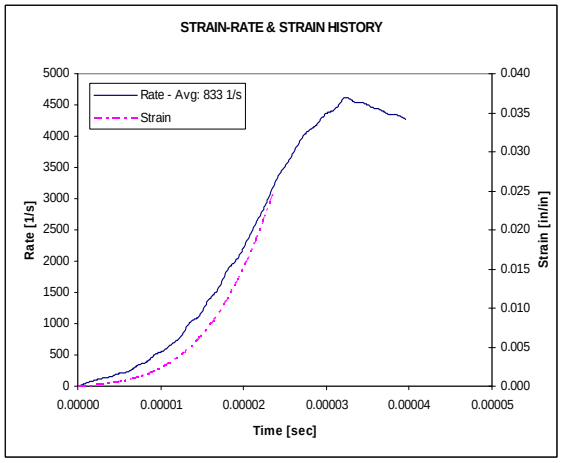

Figure C-40. Stress-Strain Curves for $[+15°/-15°]_{NS}$ Newport NB321/7781 Fiberglass Satin Weave Glass Fabric Specimens Tested at Average Strain Rate of 812 s^{-1}

Specimen 1

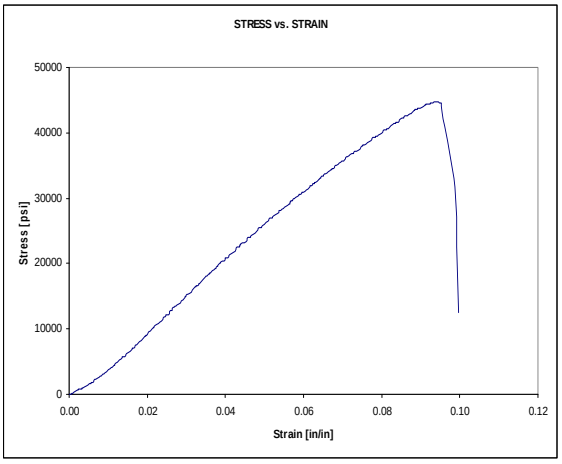

Specimen 2

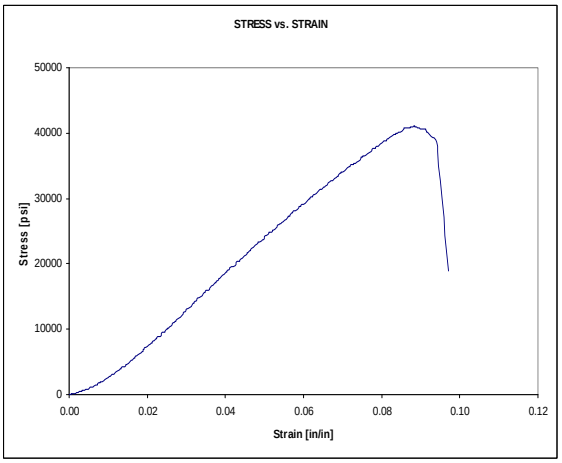

Specimen 3

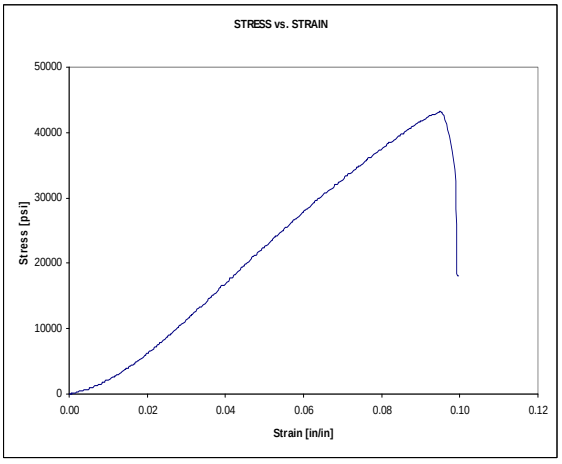

Figure C-41. Stress-Strain Curves for $[+30°/-30°]_{NS}$ Newport NB321/7781 Fiberglass Satin Weave Glass Fabric Specimens Tested at Average Strain Rate of 0.00167 s^{-1}

Specimen 1

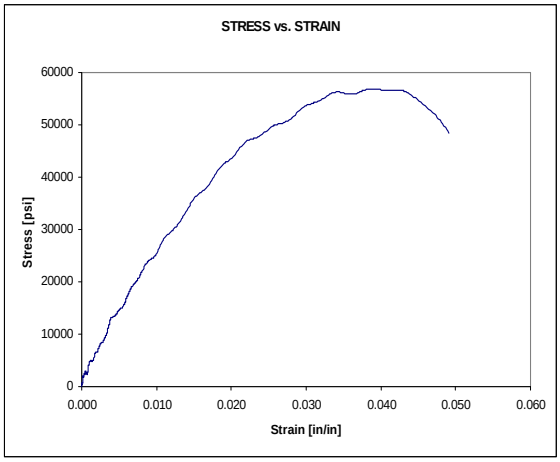

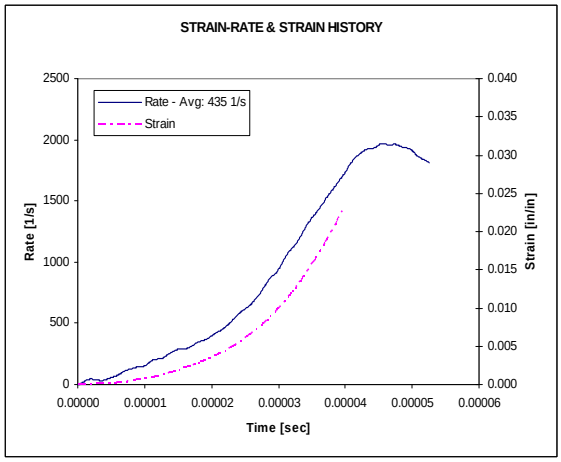

Specimen 2

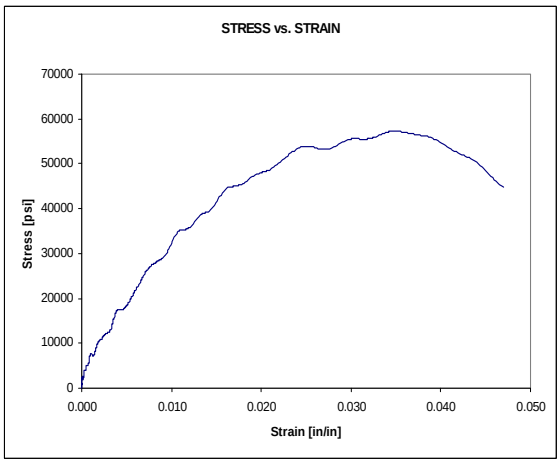

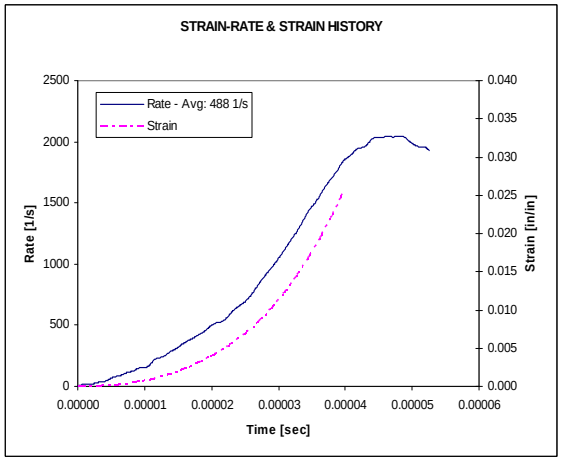

Specimen 3

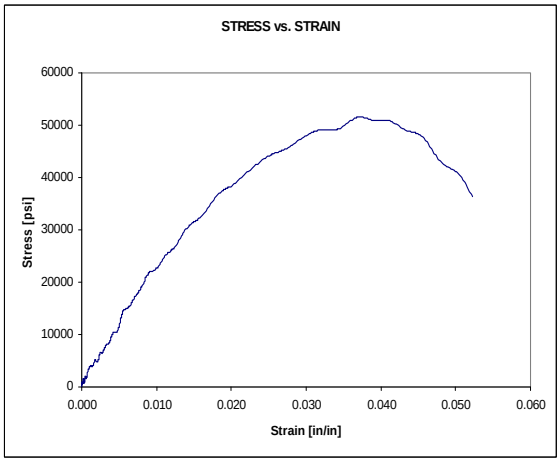

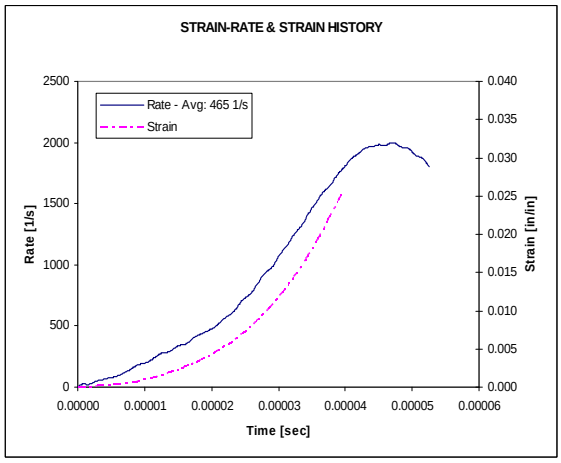

Figure C-42. Stress-Strain Curves for $[+30°/-30°]_{NS}$ Newport NB321/7781 Fiberglass Satin Weave Glass Fabric Specimens Tested at Average Strain Rate of 463 s^{-1}

Specimen 1

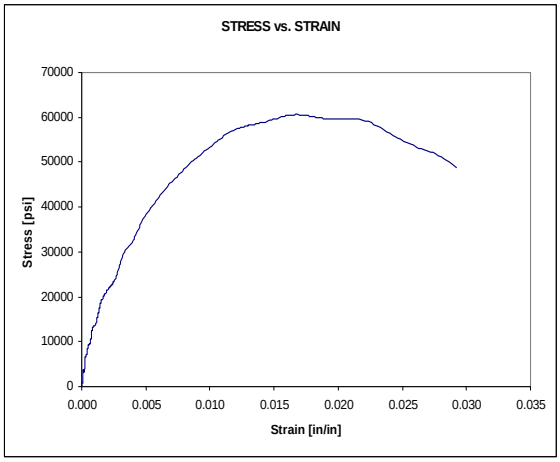

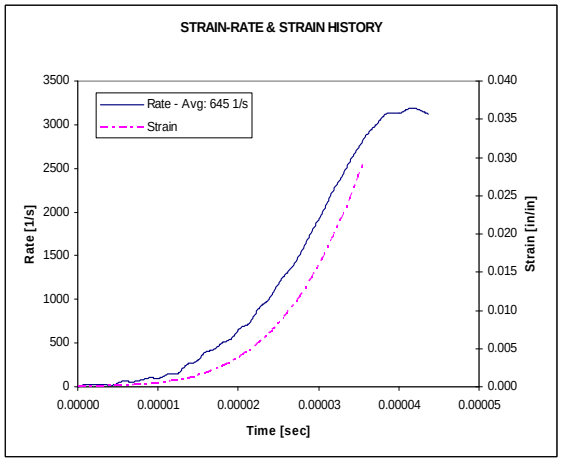

Specimen 2

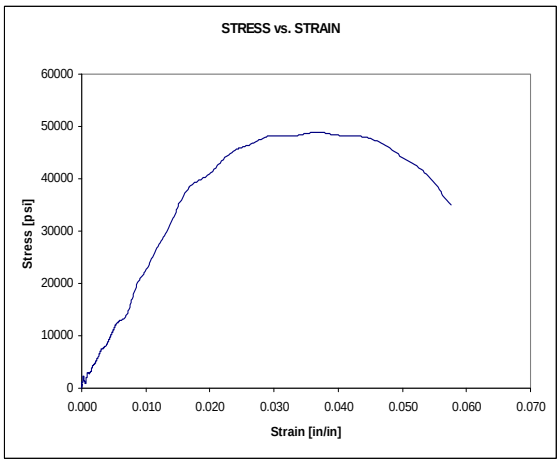

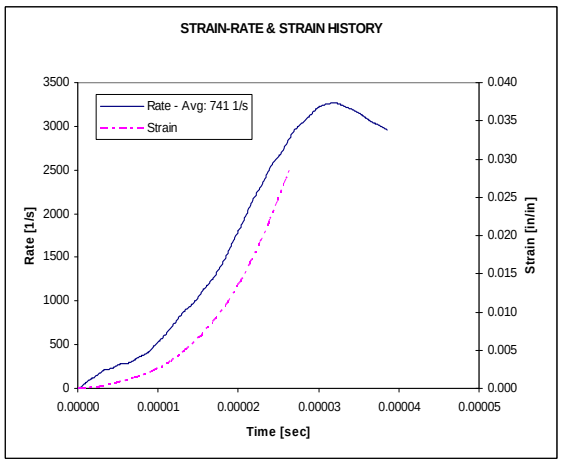

Specimen 3

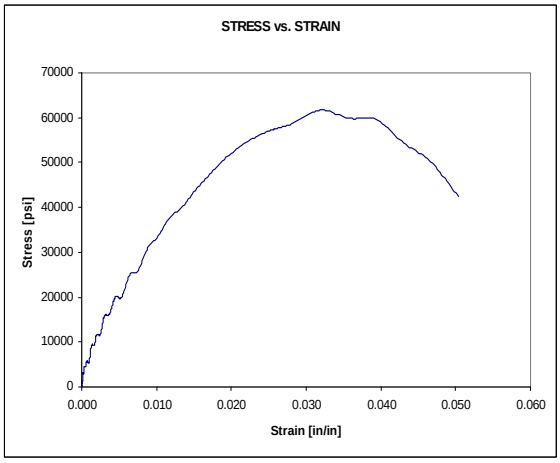

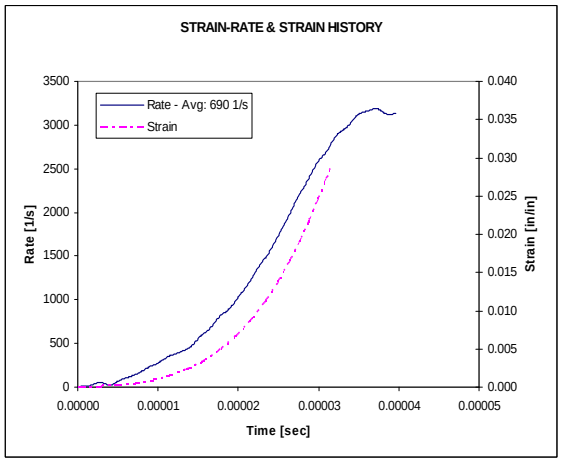

Figure C-43. Stress-Strain Curves for $[+30°/-30°]_{NS}$ Newport NB321/7781 Fiberglass Satin Weave Glass Fabric Specimens Tested at Average Strain Rate of 692 s^{-1}

Specimen 1

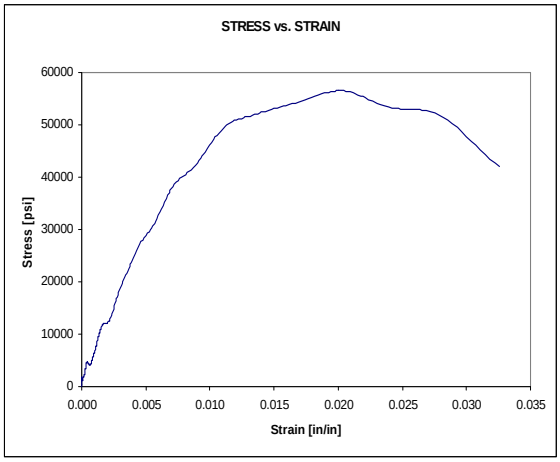

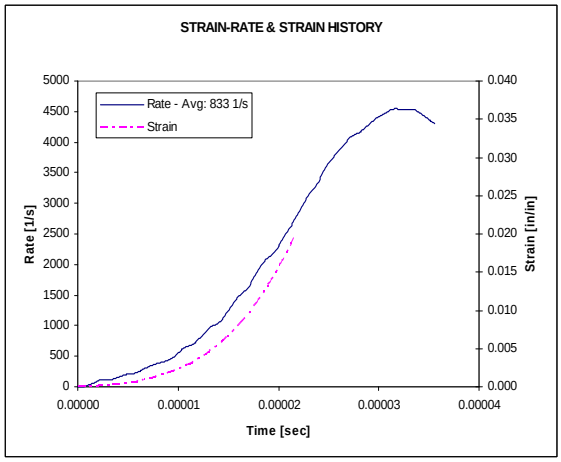

Specimen 2

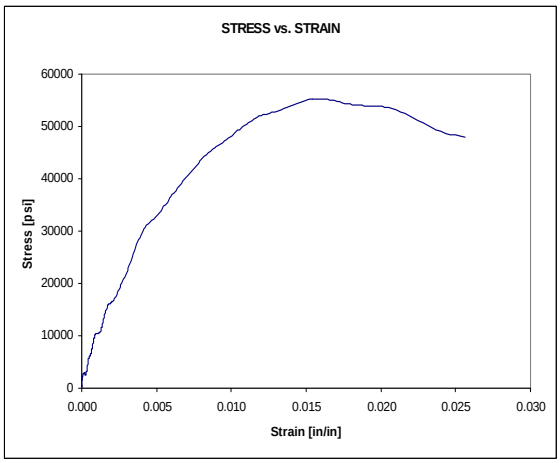

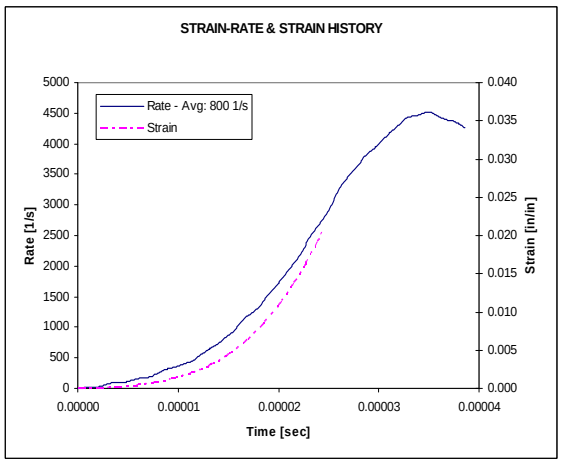

Specimen 3

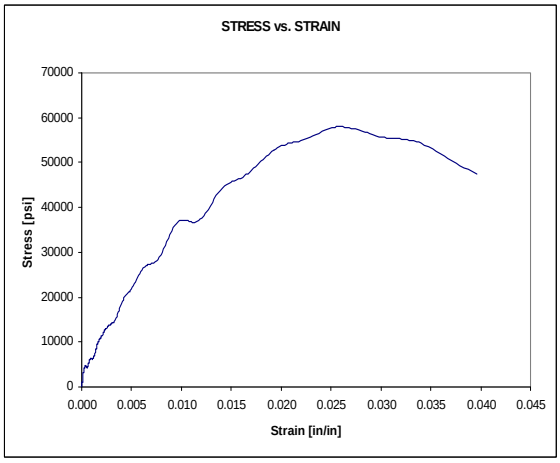

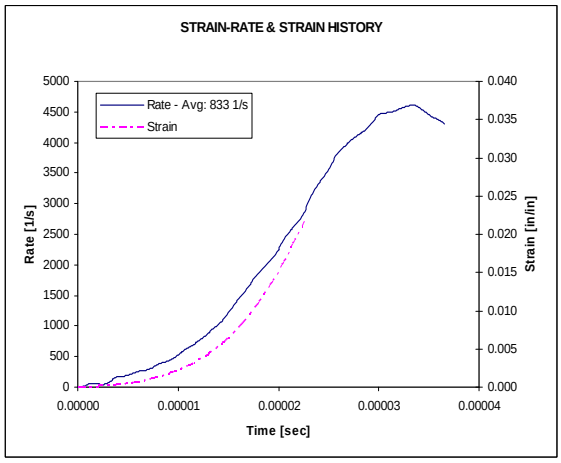

Figure C-44. Stress-Strain Curves for $[+30°/-30°]_{NS}$ Newport NB321/7781 Fiberglass Satin Weave Glass Fabric Specimens Tested at Average Strain Rate of 822 s^{-1}

Specimen 1

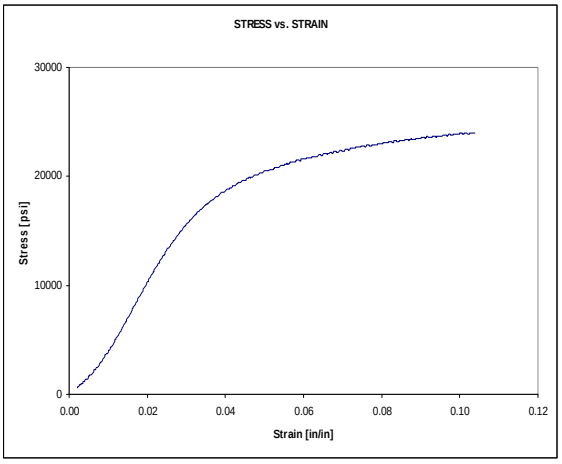

Specimen 2

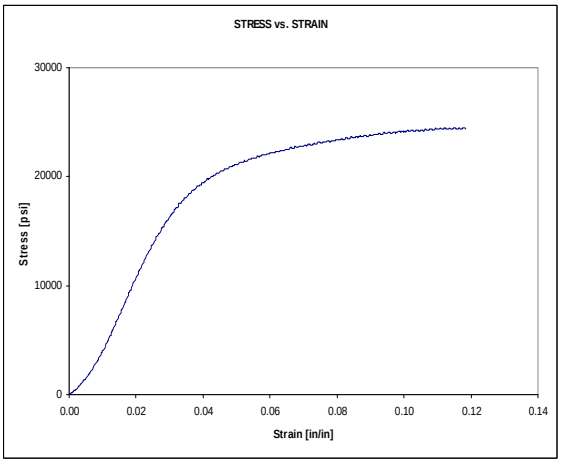

Specimen 3

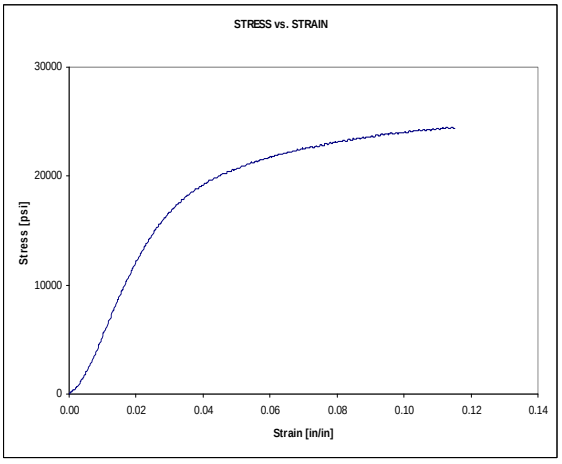

Figure C-45. Stress-Strain Curves for $[+45°/-45°]_{NS}$ Newport NB321/7781 Fiberglass Satin Weave Glass Fabric Specimens Tested at Average Strain Rate of 0.00167 s^{-1}

Specimen 1

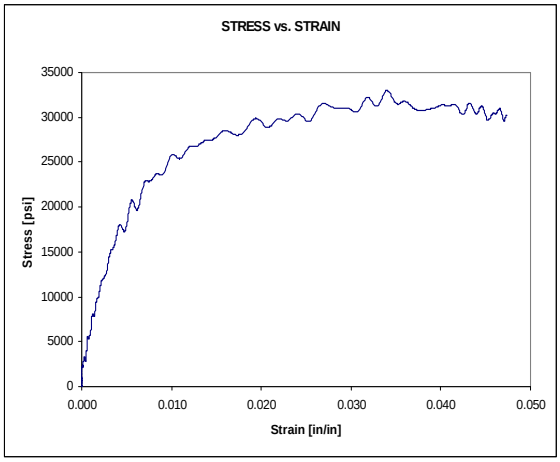

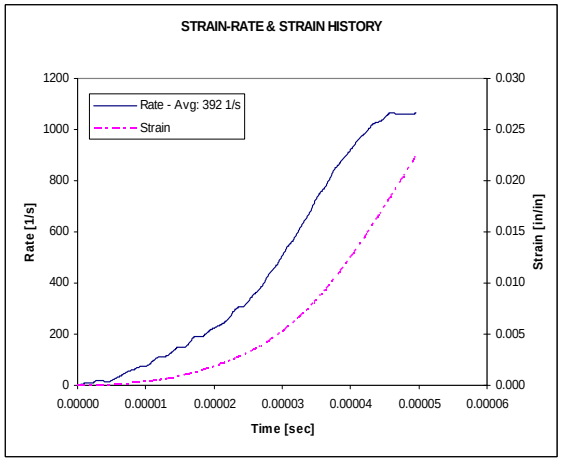

Specimen 2

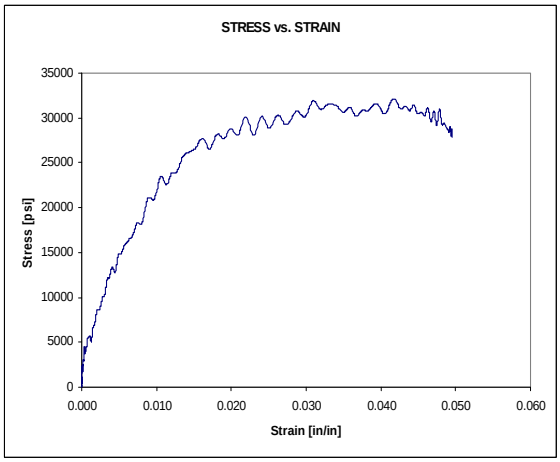

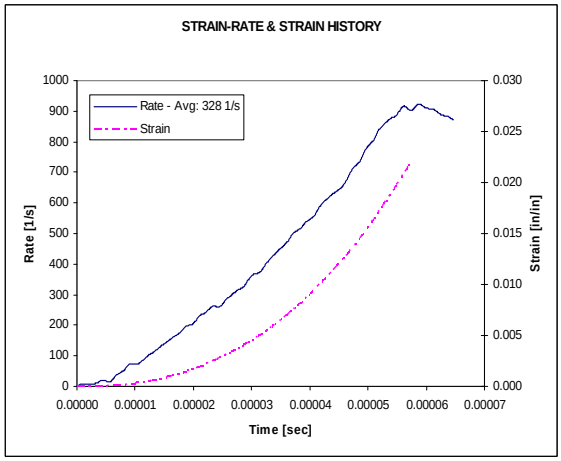

Specimen 3

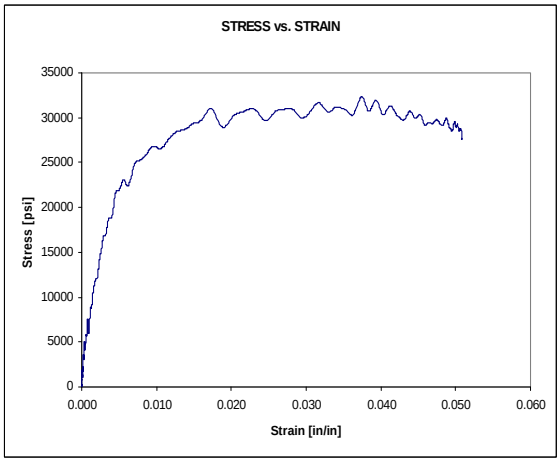

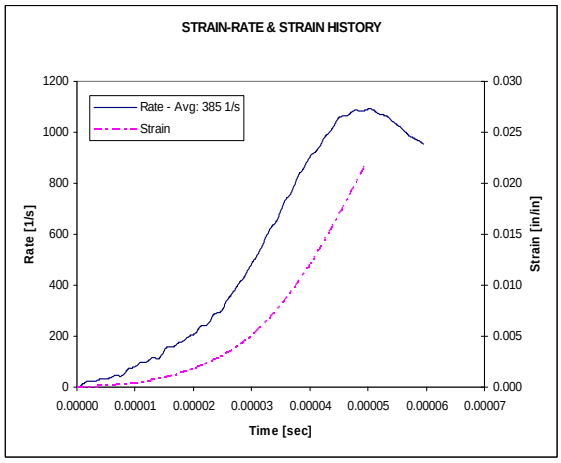

Figure C-46. Stress-Strain Curves for $[+45°/-45°]_{NS}$ Newport NB321/7781 Fiberglass Satin Weave Glass Fabric Specimens Tested at Average Strain Rate of 368 s^{-1}

Specimen 1

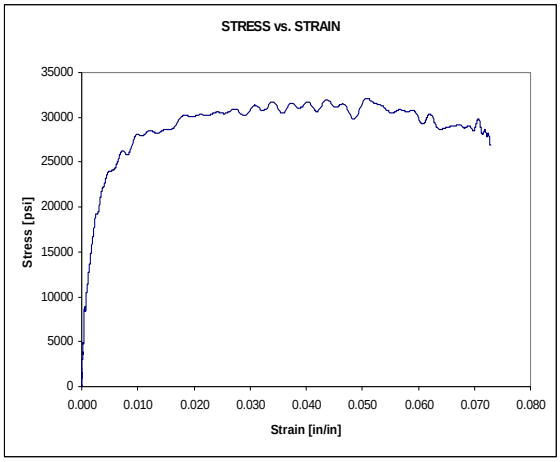

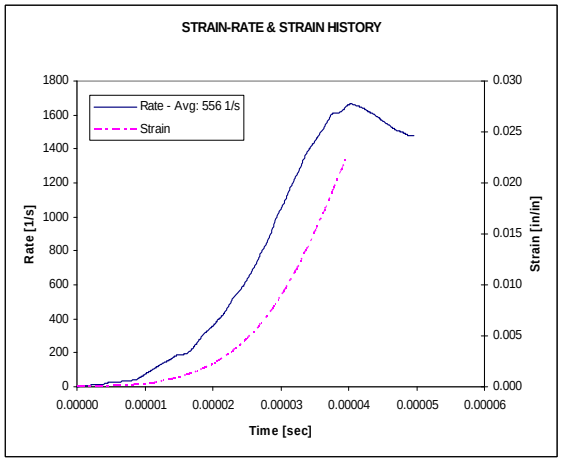

Specimen 2

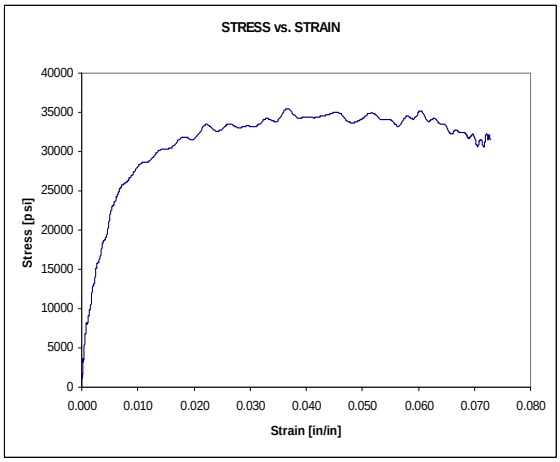

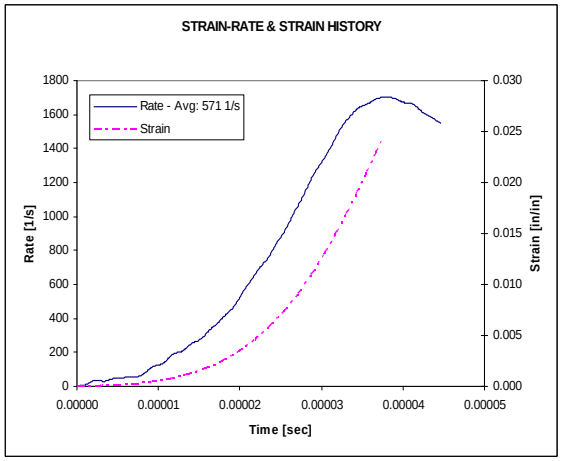

Specimen 3

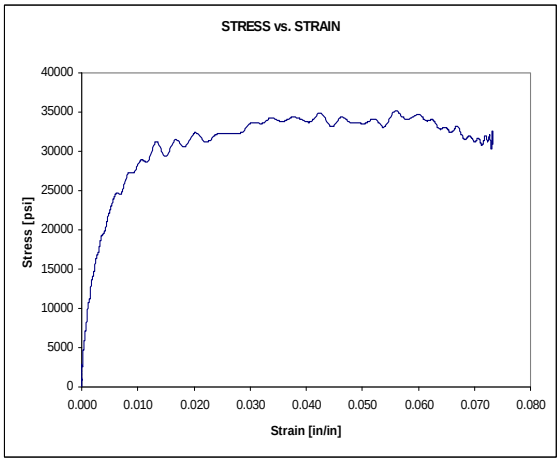

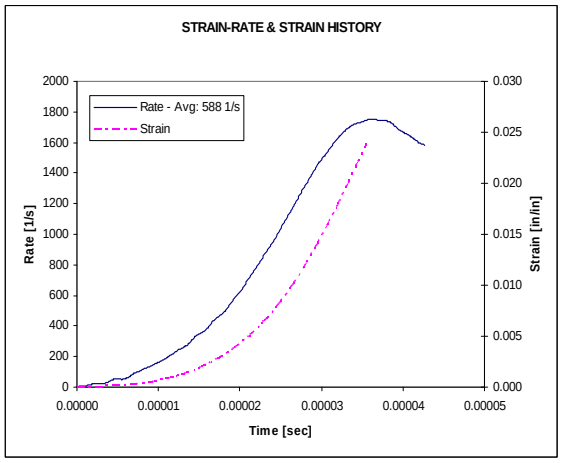

Figure C-47. Stress-Strain Curves for $[+45°/-45°]_{NS}$ Newport NB321/7781 Fiberglass Satin Weave Glass Fabric Specimens Tested at Average Strain Rate of 572 s^{-1}

Specimen 1

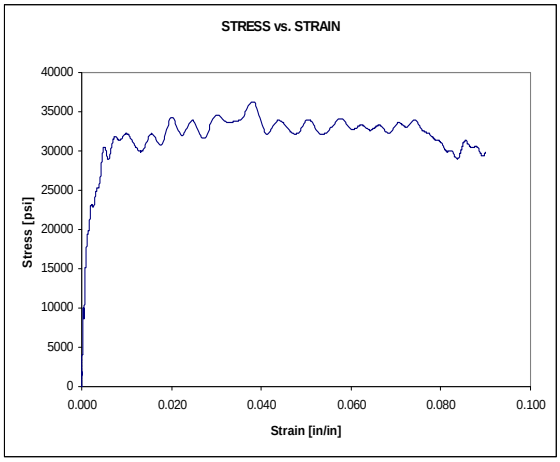

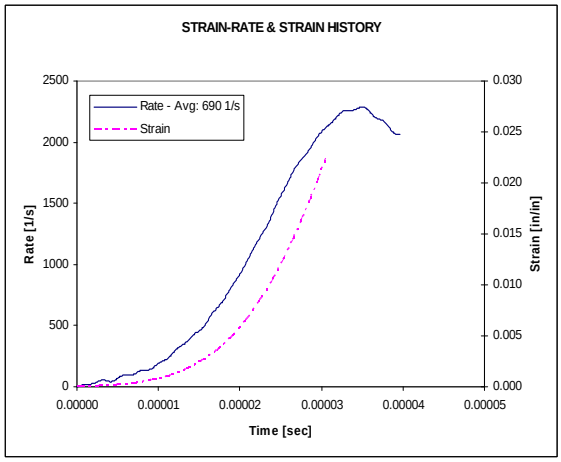

Specimen 2

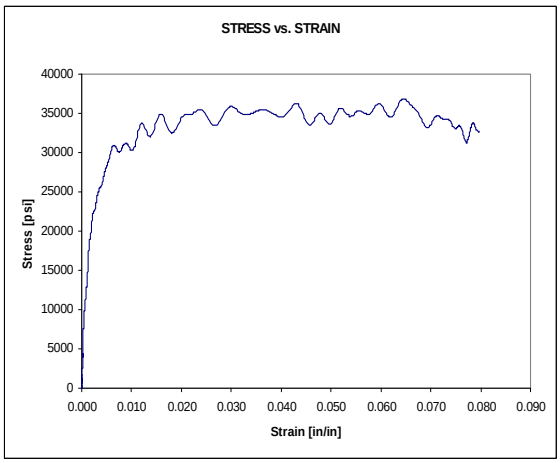

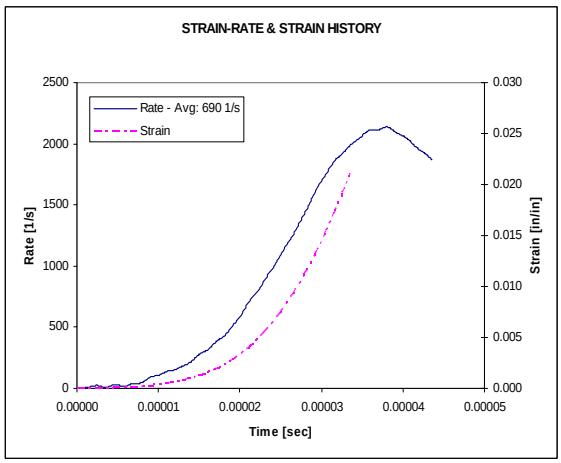

Specimen 3

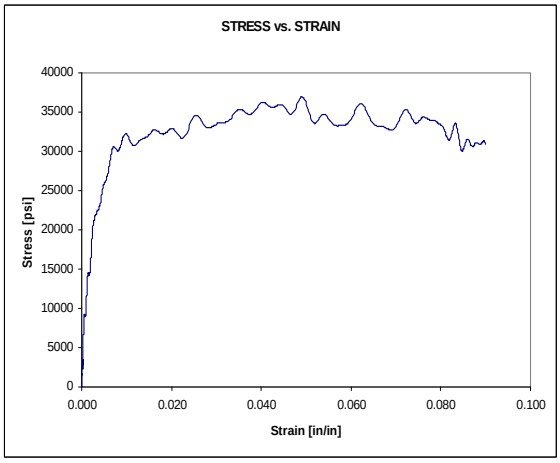

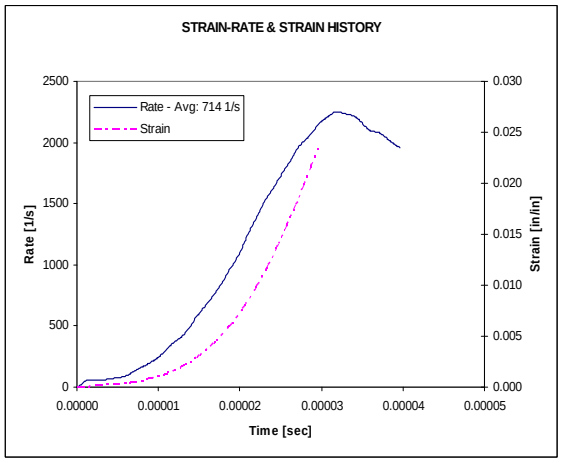

Figure C-48. Stress-Strain Curves for $[+45°/-45°]_{NS}$ Newport NB321/7781 Fiberglass Satin Weave Glass Fabric Specimens Tested at Average Strain Rate of 698 s^{-1}

Table C-4. Summary of Failure Strengths and Strain Rates for Newport NB321/3K70 PWCF

Orientation (degrees)	Average Strain Rate (1/s)	Actual Strain Rate (1/s)	Failure Strength (psi)	Average Failure Strength (psi)
0	0.00167	0.00167	66,110	57,849
		0.00167	50,910	
		0.00167	56,525	
	1	1	66,382	67,993
		1	69,603	
	389	370	55,169	63,527
		370	67,850	
		426	67,562	
	502	313	69,534	71,273
		606	72,712	
		588	71,575	
	781	769	68,286	66,353
		741	66,744	
		833	64,030	
15	0.00167	0.00167	58,777	58,262
		0.00167	57,526	
		0.00167	58,483	
	1	1	63,890	62,633
		1	61,376	
	371	392	58,809	58,122
		370	57,336	
		351	58,220	
	588	588	59,959	59,345
		588	58,221	
		588	59,855	
	674	667	58,158	59,852
		690	61,103	
		667	60,296	

Table C-4. Summary of Failure Strengths and Strain Rates for Newport NB321/3K70 PWCF (Continued)

Orientation (degrees)	Average Strain Rate (1/s)	Actual Strain Rate (1/s)	Failure Strength (psi)	Average Failure Strength (psi)
30	0.00167	0.00167	44,312	44,114
		0.00167	45,152	
		0.00167	42,878	
	1	1	47,399	48,593
		1	49,787	
	365	392	49,028	49,141
		357	46,949	
		345	51,447	
	551	571	51,452	51,343
		526	50,553	
		556	52,024	
	682	667	51,448	53,432
		690	57,264	
		690	51,583	
45	0.00167	0.00167	24,674	25,421
		0.00167	25,466	
		0.00167	26,124	
	1	1	28,819	28,907
		1	28,994	
	413	370	27,101	27,613
		392	27,674	
		476	28,063	
	594	588	31,594	31,008
		606	29,985	
		588	31,445	
	674	690	34,142	32,948
		667	32,808	
		667	31,893	
	851	952	31,893	34,480
		769	31,893	
		833	39,654	

Specimen 1

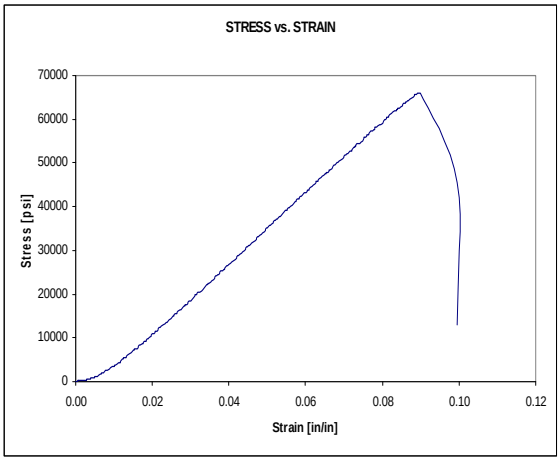

Specimen 2

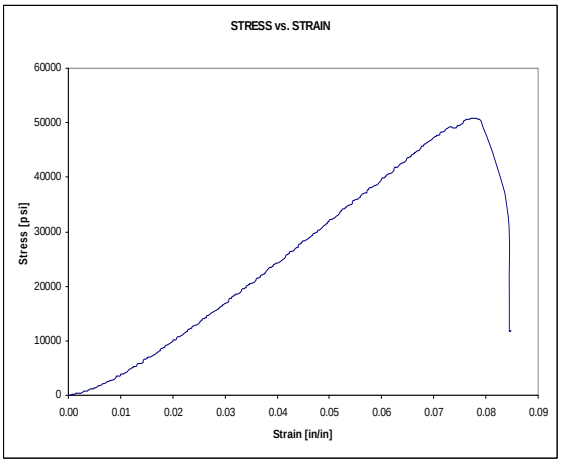

Specimen 3

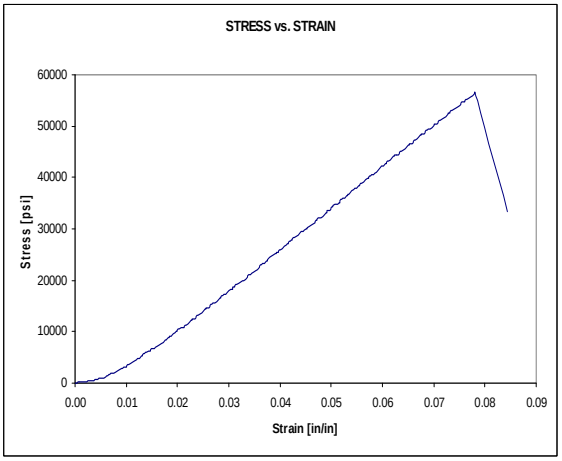

Figure C-49. Stress-Strain Curves for [0°] Newport NB321/3K70 PWCF Specimens Tested at Average Strain Rate of 0.00167 s^{-1}

Specimen 1

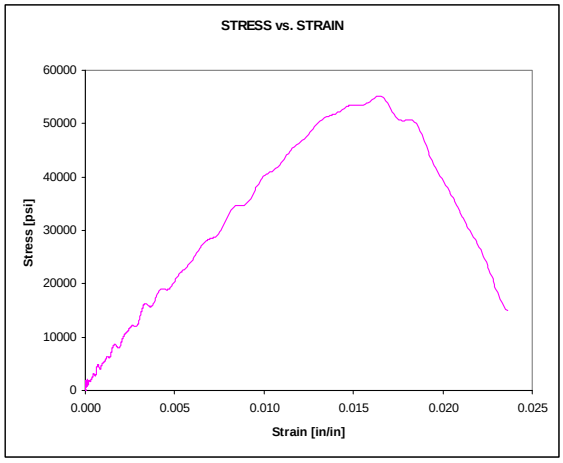

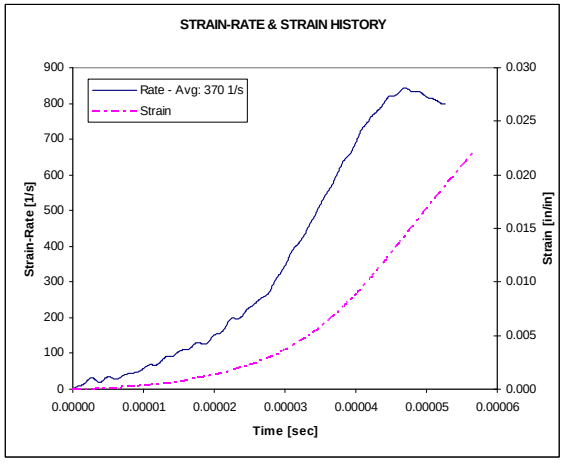

Specimen 2

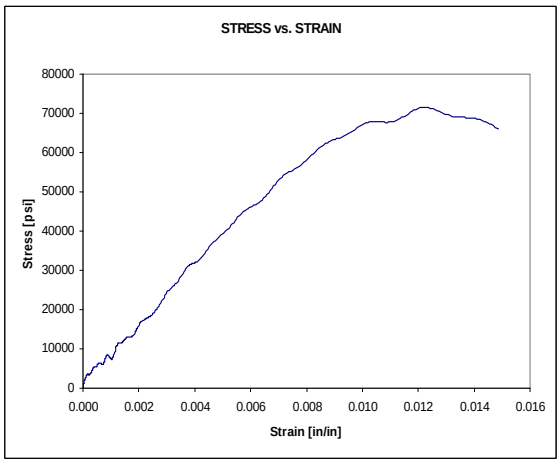

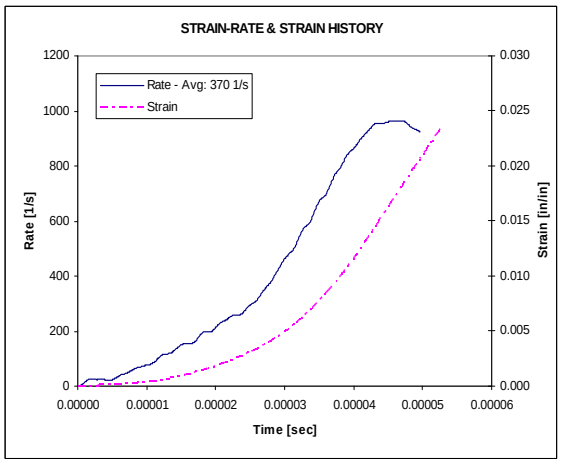

Specimen 3

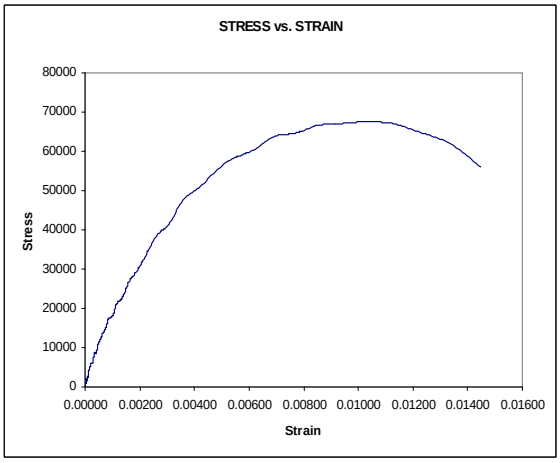

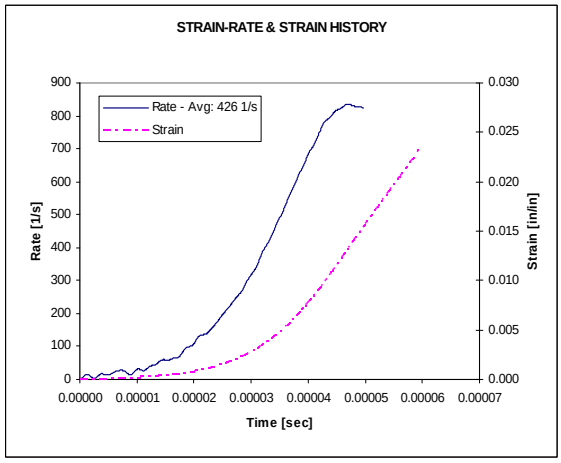

Figure C-50. Stress-Strain Curves for [0°] Newport NB321/3K70 PWCF Specimens Tested at Average Strain Rate of 389 s^{-1}

Specimen 1

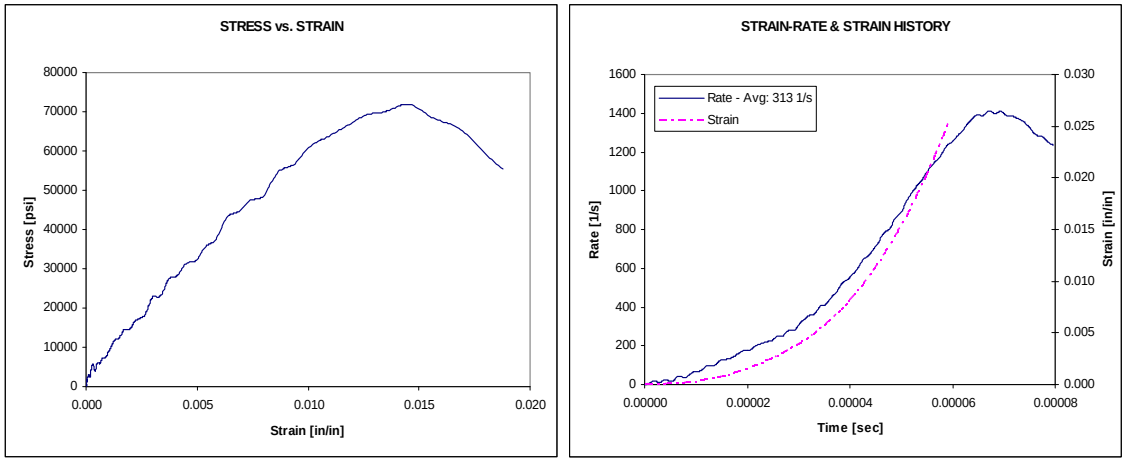

Specimen 2

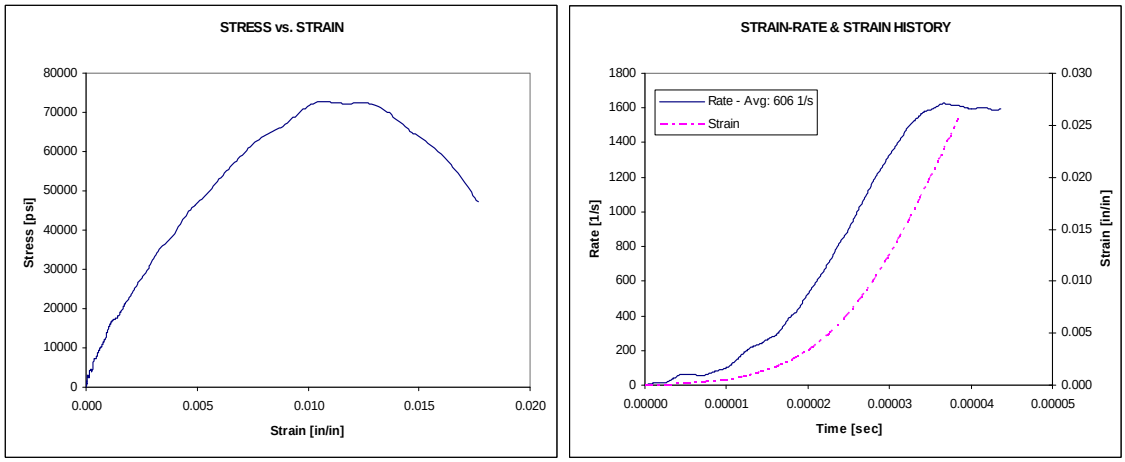

Specimen 3

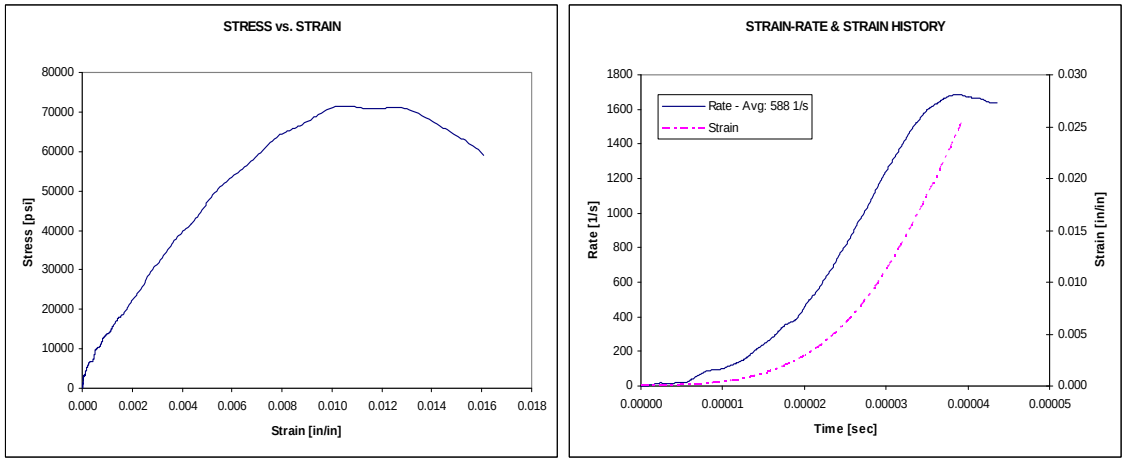

Figure C-51. Stress-Strain Curves for [0°] Newport NB321/3K70 PWCF Specimens Tested at Average Strain Rate of 502 s^{-1}

Specimen 1

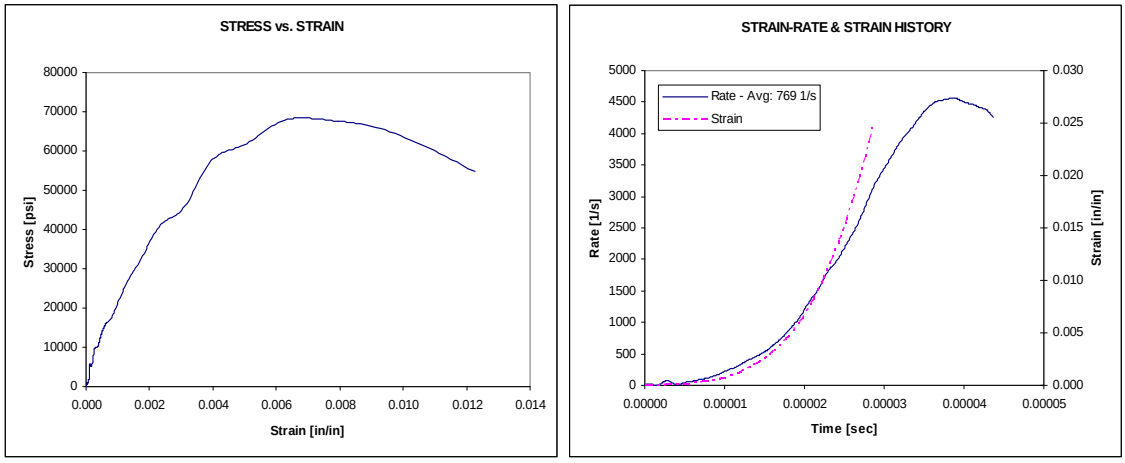

Specimen 2

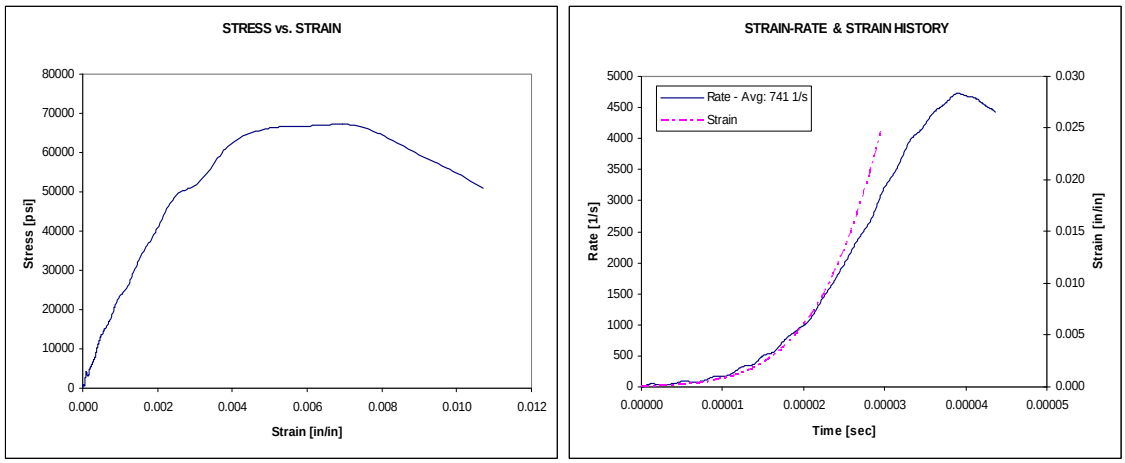

Specimen 3

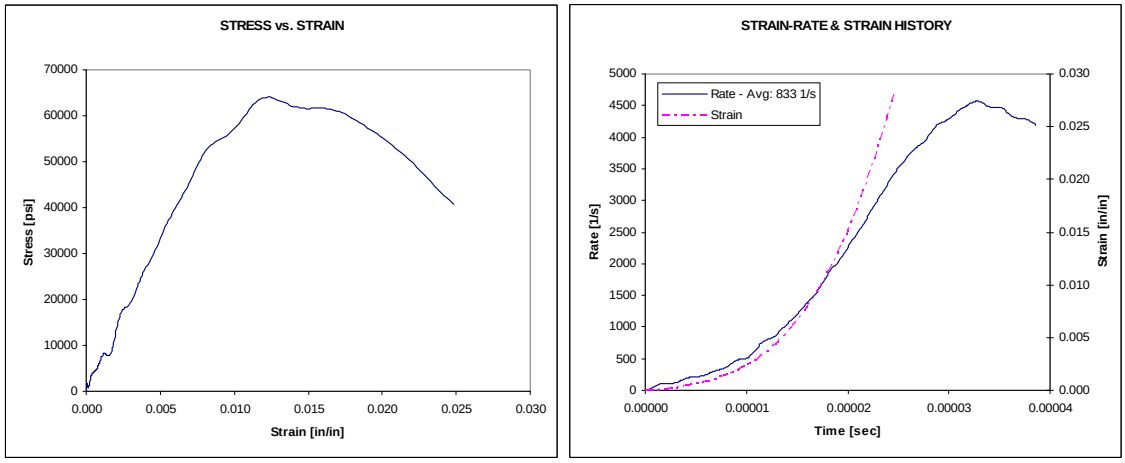

Figure C-52. Stress-Strain Curves for [0°] Newport NB321/3K70 PWCF Specimens Tested at Average Strain Rate of 781 s^{-1}

Specimen 1

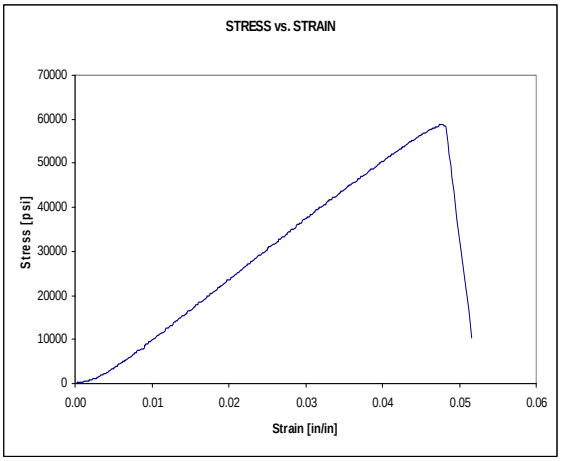

Specimen 2

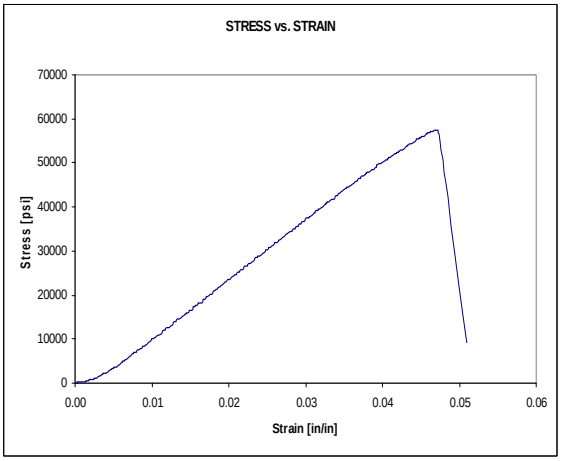

Specimen 3

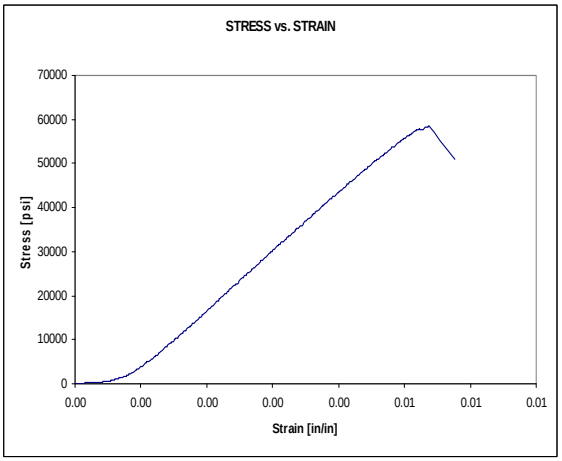

Figure C-53. Stress-Strain Curves for $[+15°/-15°]_{NS}$ Newport NB321/3K70 PWCF Specimens Tested at Average Strain Rate of 0.00167 s^{-1}

Specimen 1

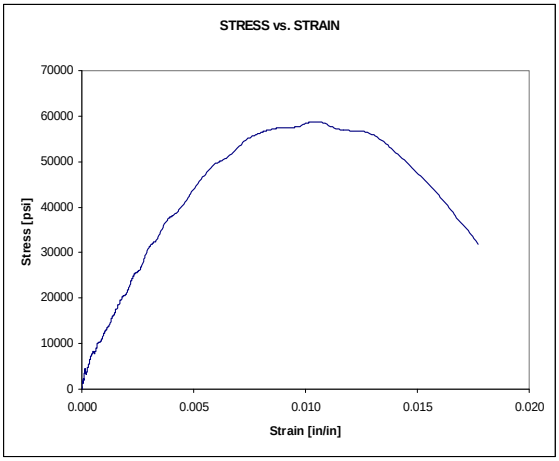

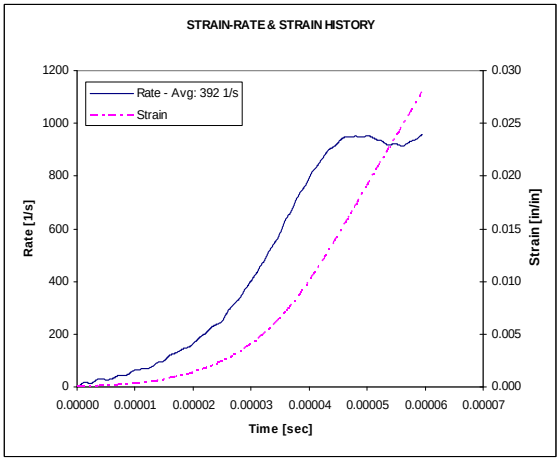

Specimen 2

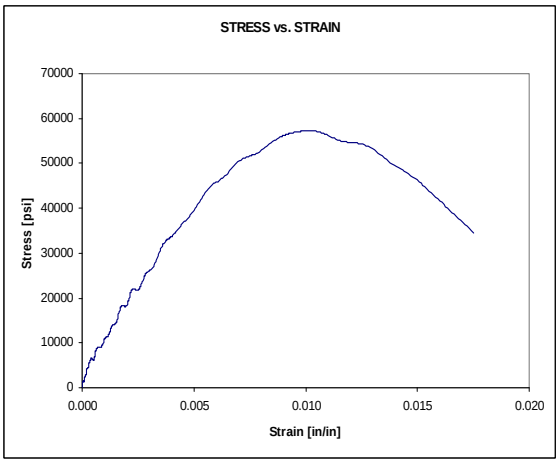

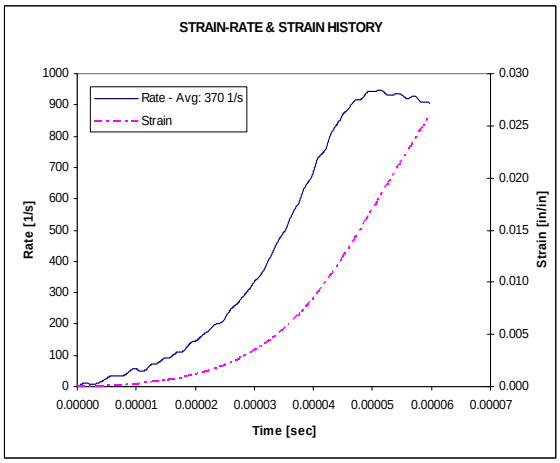

Specimen 3

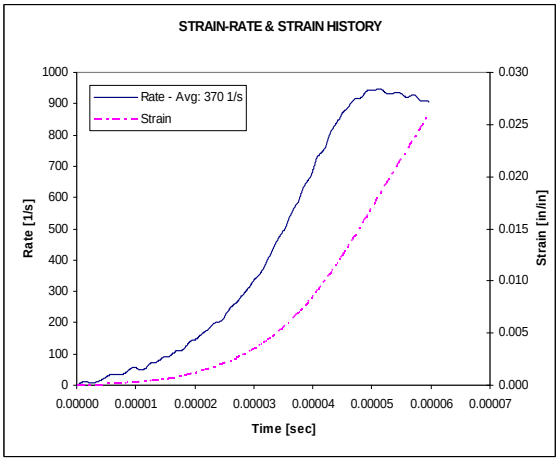

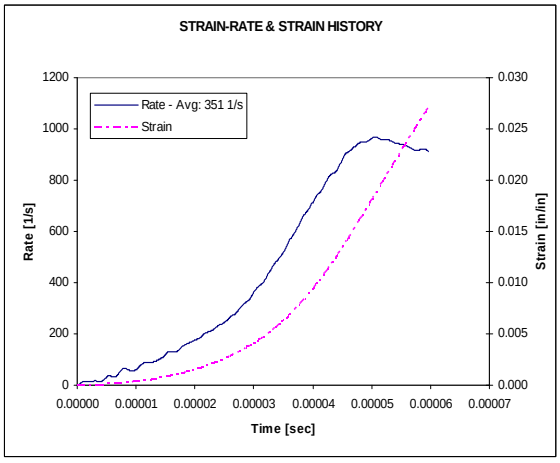

Figure C-54. Stress-Strain Curves for $[+15°/-15°]_{NS}$ Newport NB321/3K70 PWCF Specimens Tested at Average Strain Rate of 371 s^{-1}

Specimen 1

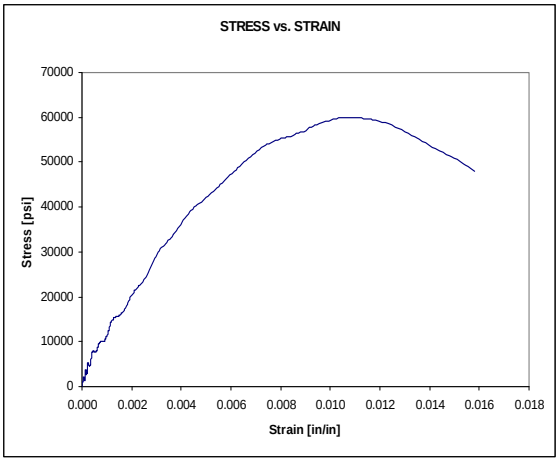

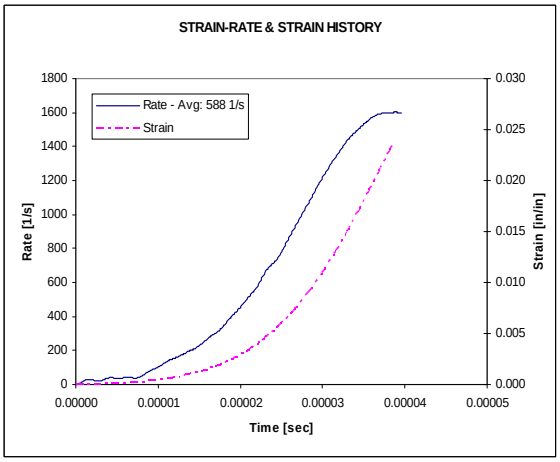

Specimen 2

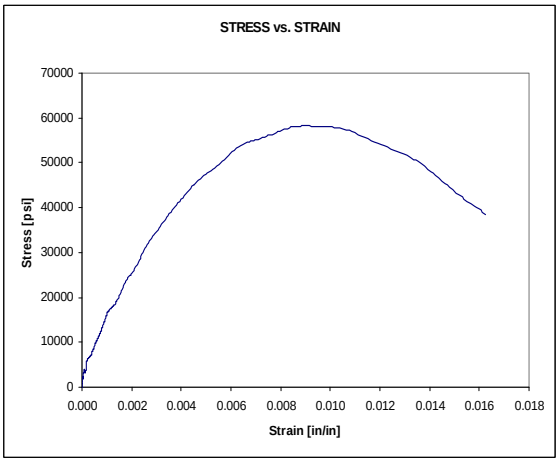

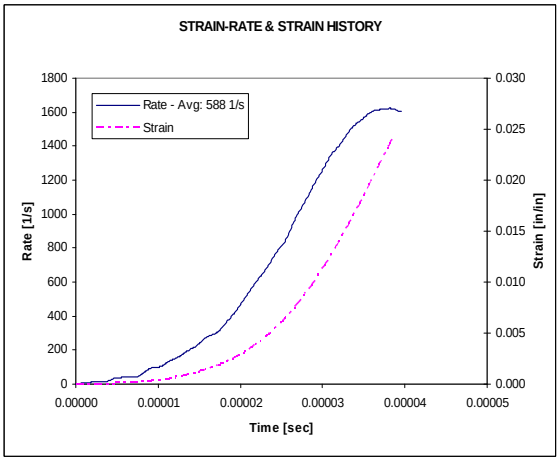

Specimen 3

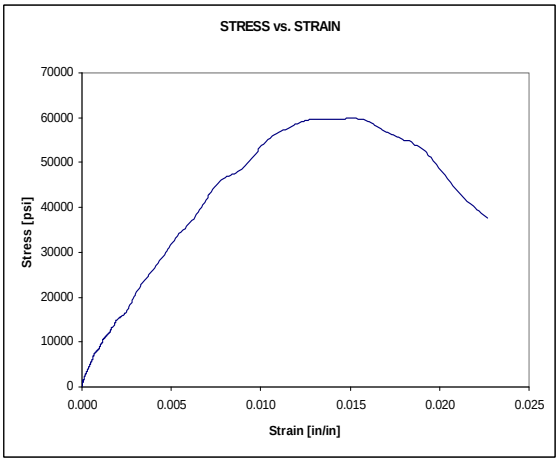

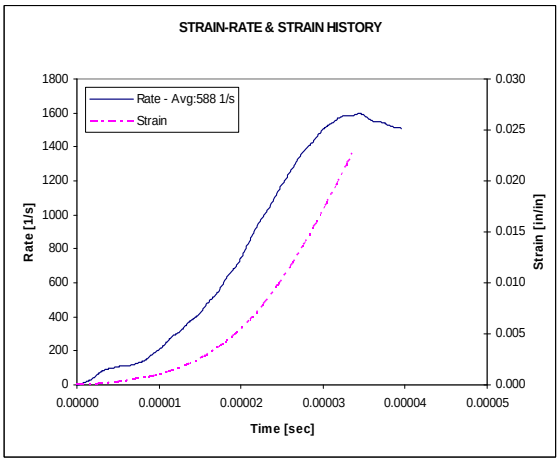

Figure C-55. Stress-Strain Curves for $[+15°/-15°]_{NS}$ Newport NB321/3K70 PWCF Specimens Tested at Average Strain Rate of 588 s^{-1}

Specimen 1

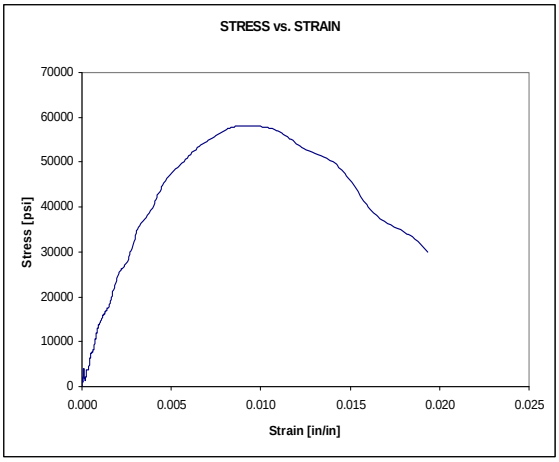

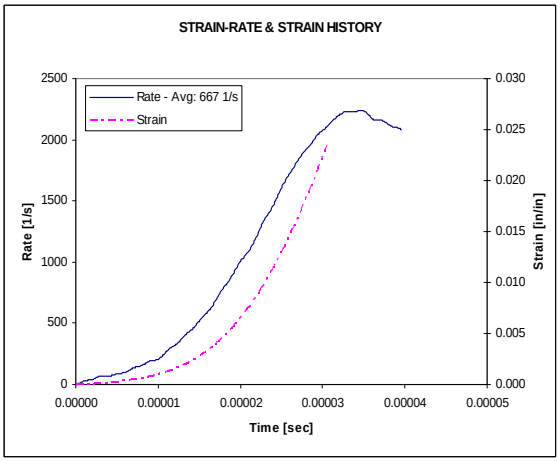

Specimen 2

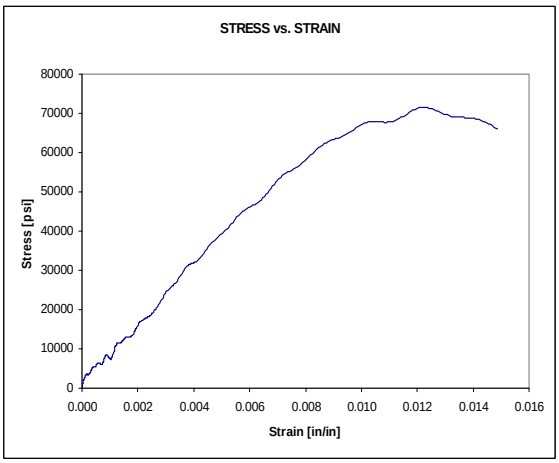

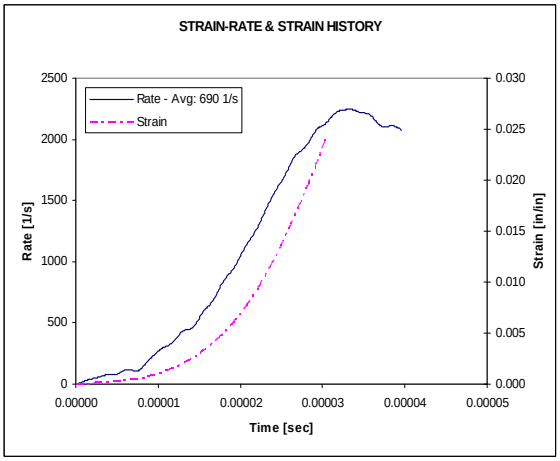

Specimen 3

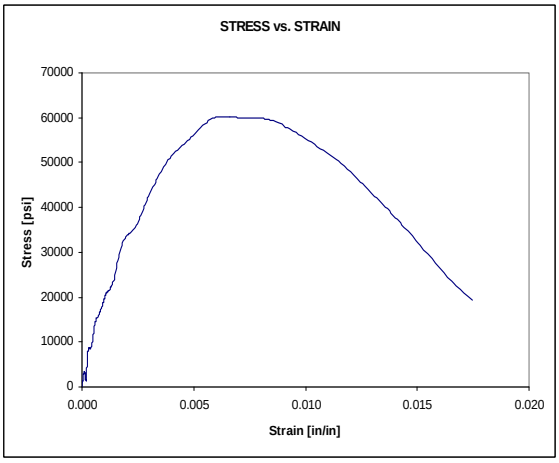

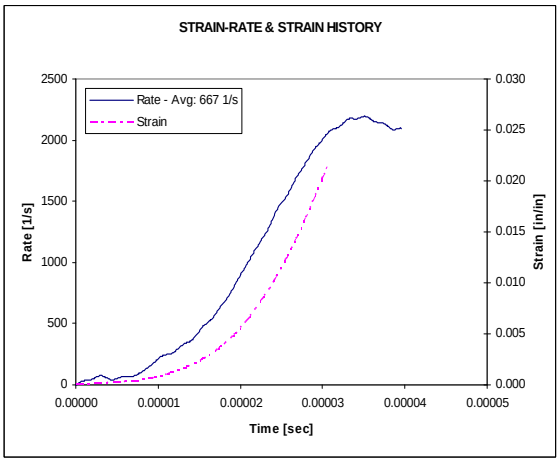

Figure C-56. Stress-Strain Curves for $[+15°/-15°]_{NS}$ Newport NB321/3K70 PWCF Specimens Tested at Average Strain Rate of 674 s^{-1}

Specimen 1

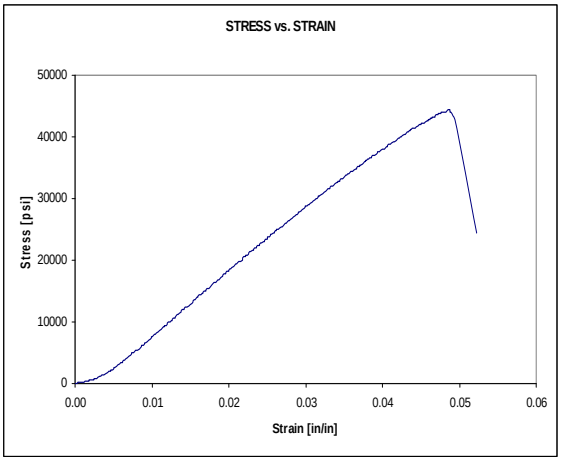

Specimen 2

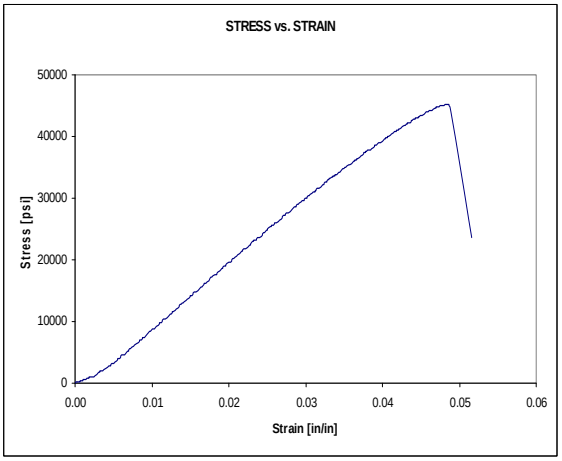

Specimen 3

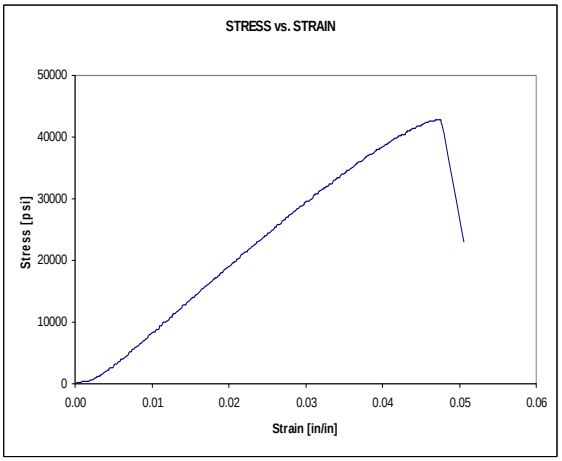

Figure C-57. Stress-Strain Curves for $[+30°/-30°]_{NS}$ Newport NB321/3K70 PWCF Specimens Tested at Average Strain Rate of 0.00167 s^{-1}

Specimen 1

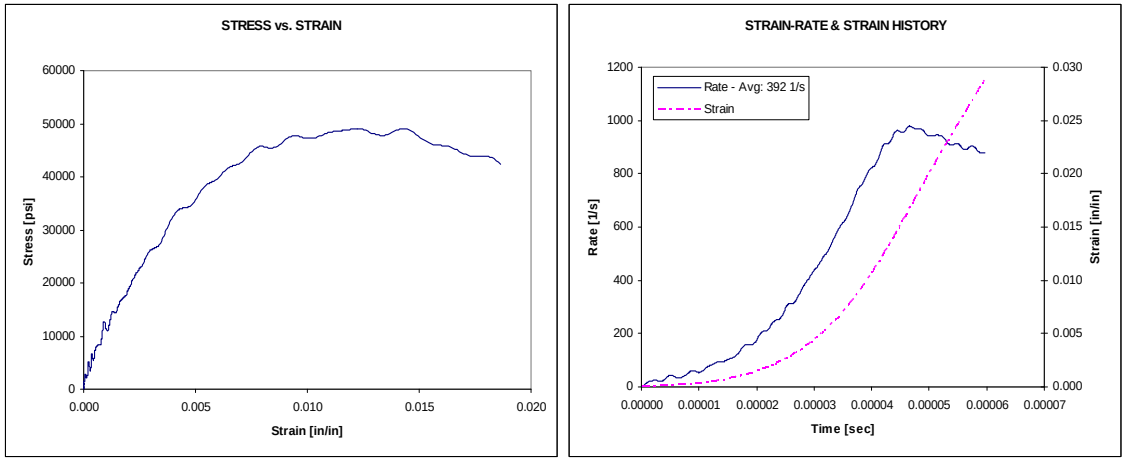

Specimen 2

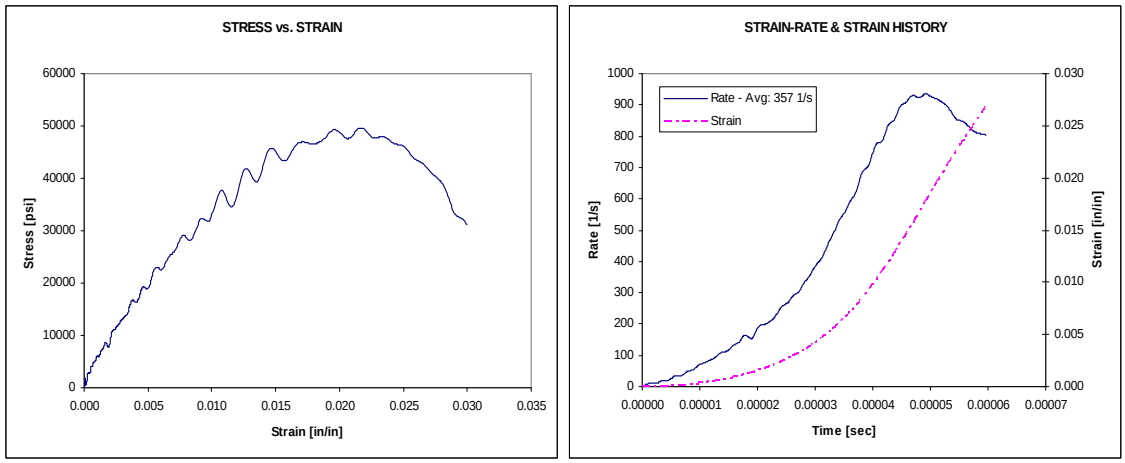

Specimen 3

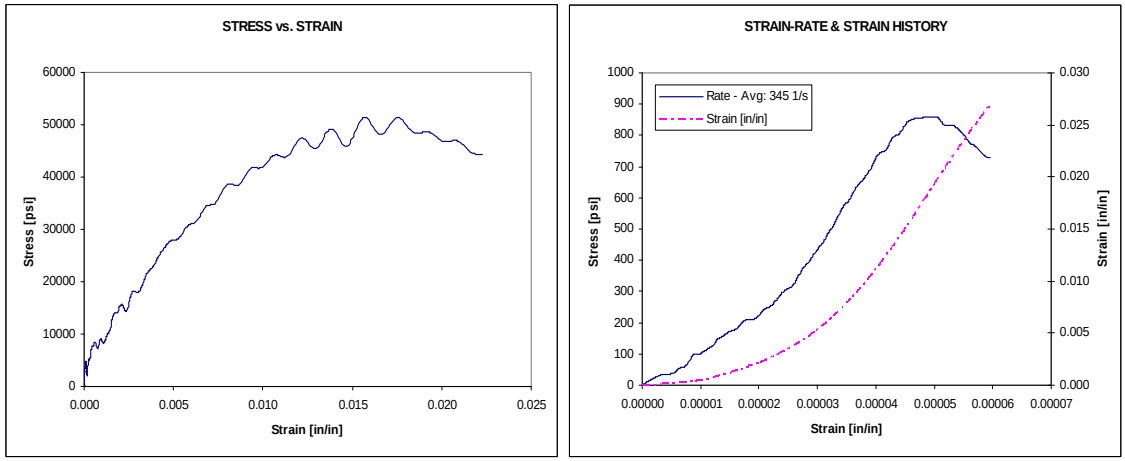

Figure C-58. Stress-Strain Curves for $[+30°/-30°]_{NS}$ Newport NB321/3K70 PWCF Specimens Tested at Average Strain Rate of 365 s^{-1}

Specimen 1

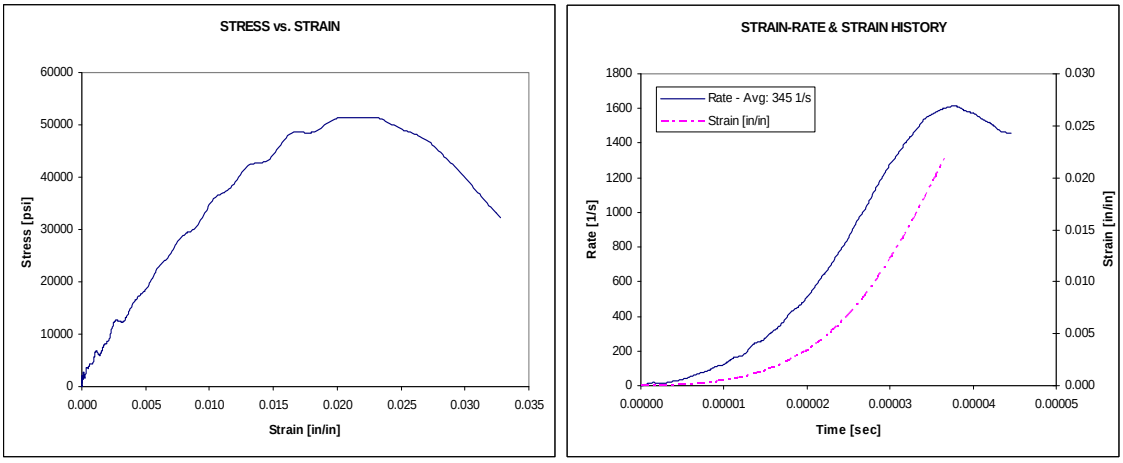

Specimen 2

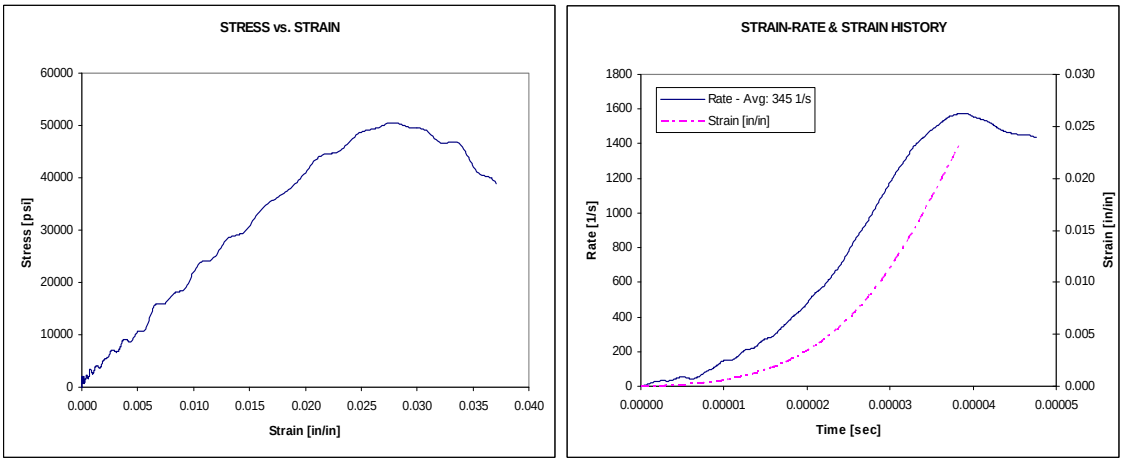

Specimen 3

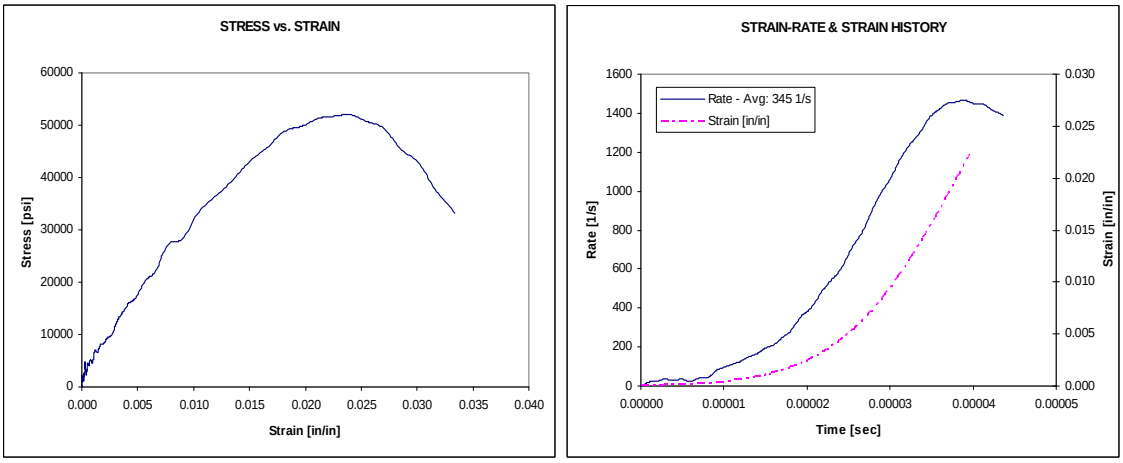

Figure C-59. Stress-Strain Curves for $[+30°/-30°]_{NS}$ Newport NB321/3K70 PWCF Specimens Tested at Average Strain Rate of 551 s^{-1}

Specimen 1

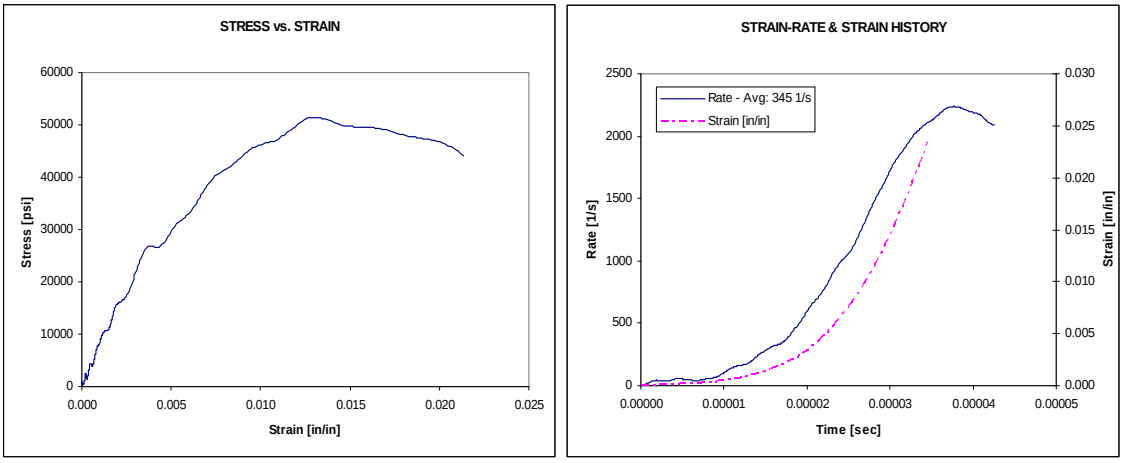

Specimen 2

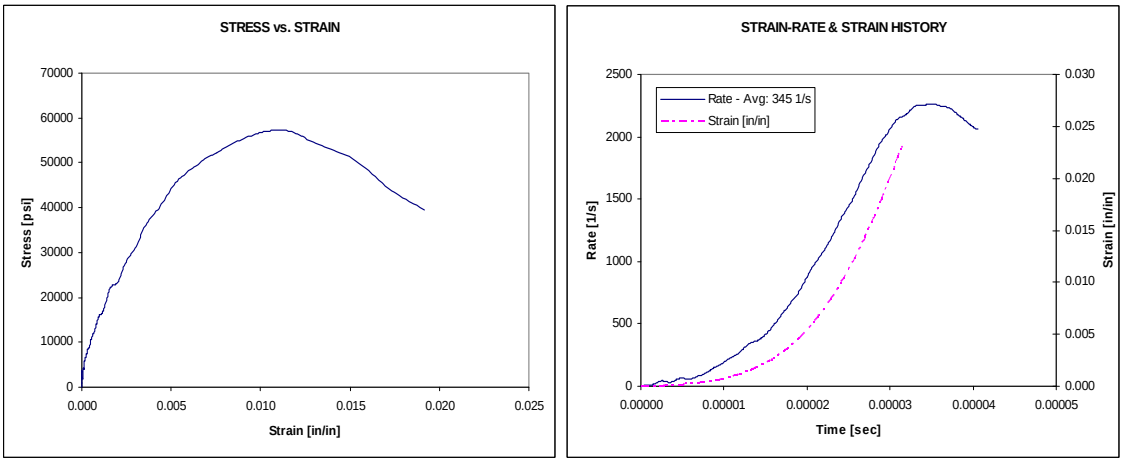

Specimen 3

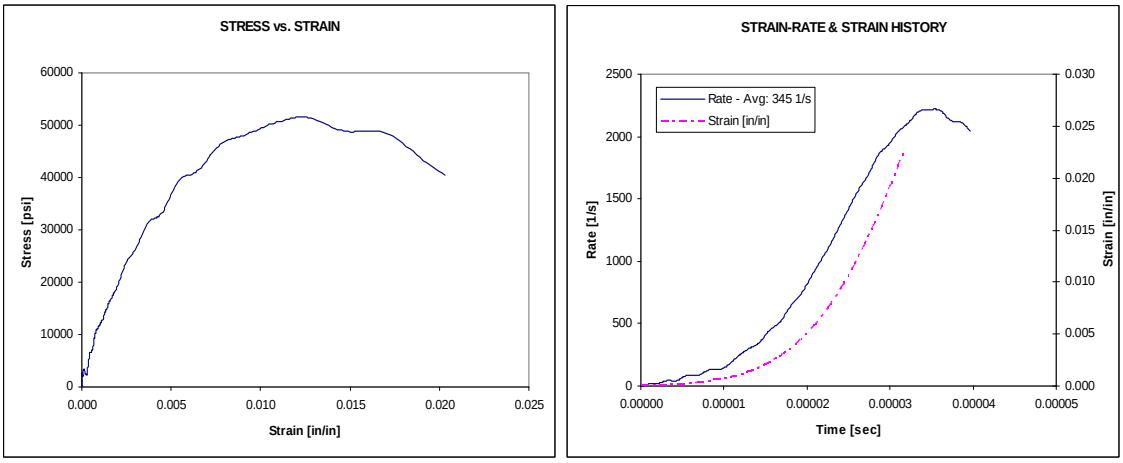

Figure C-60. Stress-Strain Curves for $[+30°/-30°]_{NS}$ Newport NB321/3K70 PWCF Specimens Tested at Average Strain Rate of 682 s^{-1}

Specimen 1

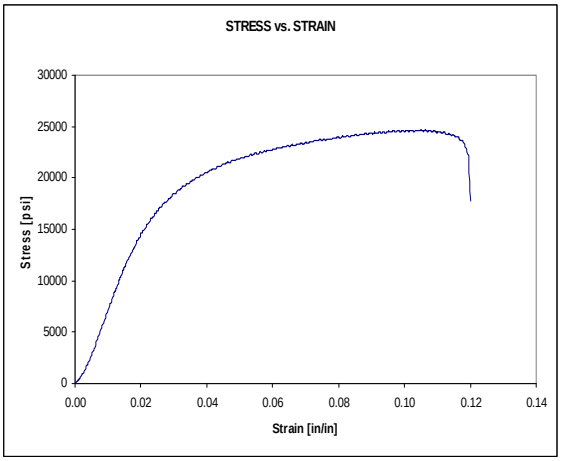

Specimen 2

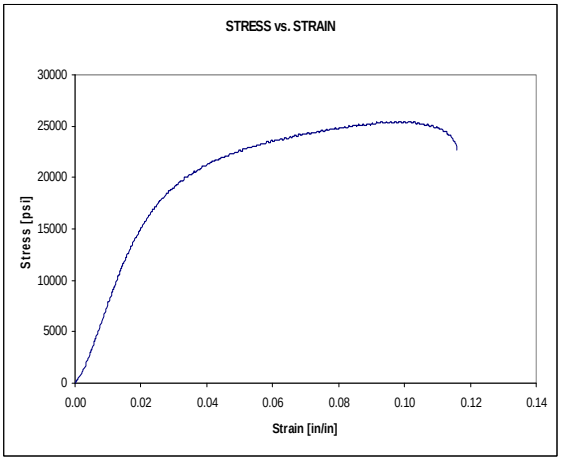

Specimen 3

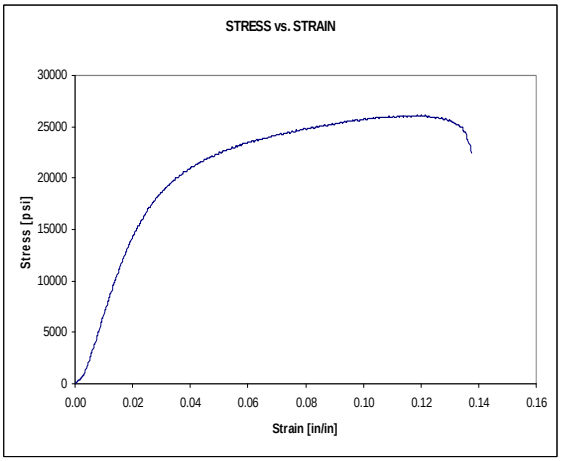

Figure C-61. Stress-Strain Curves for $[+45°/-45°]_{NS}$ Newport NB321/3K70 PWCF Specimens Tested at Average Strain Rate of 0.00167 s^{-1}

Specimen 1

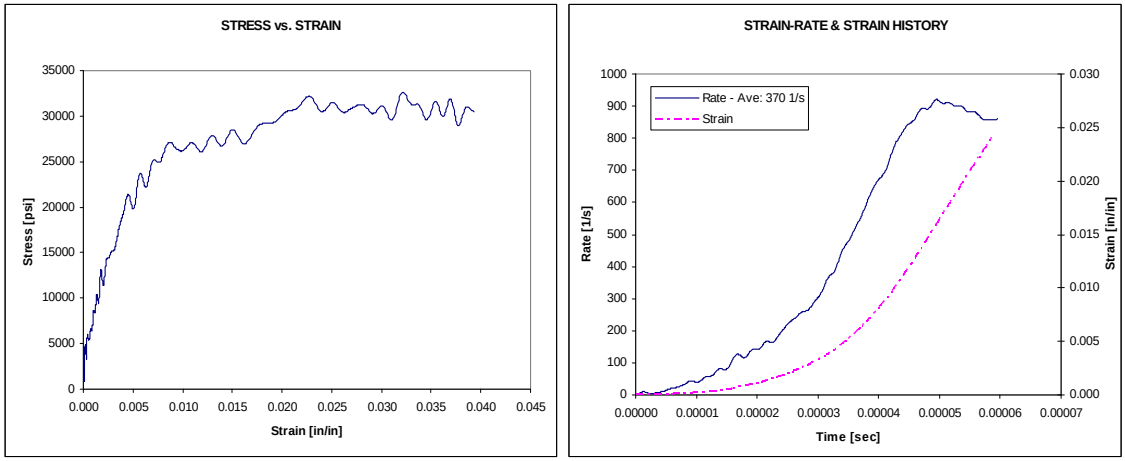

Specimen 2

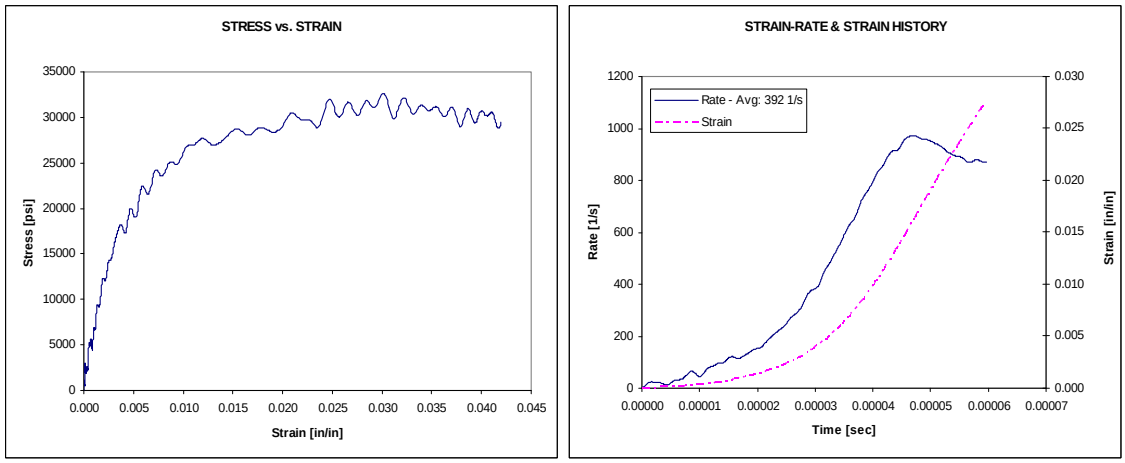

Specimen 3

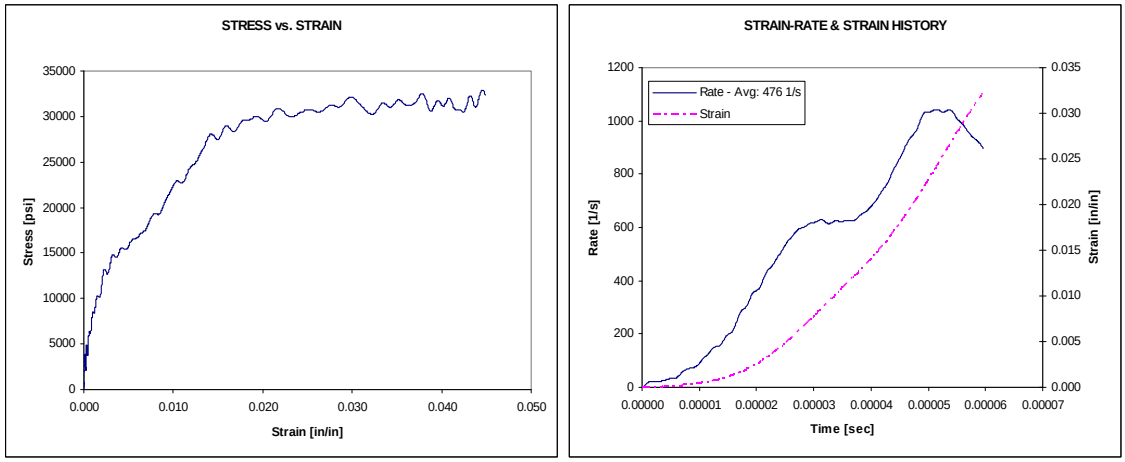

Figure C-62. Stress-Strain Curves for $[+45°/-45°]_{NS}$ Newport NB321/3K70 PWCF Specimens Tested at Average Strain Rate of 413 s^{-1}

Specimen 1

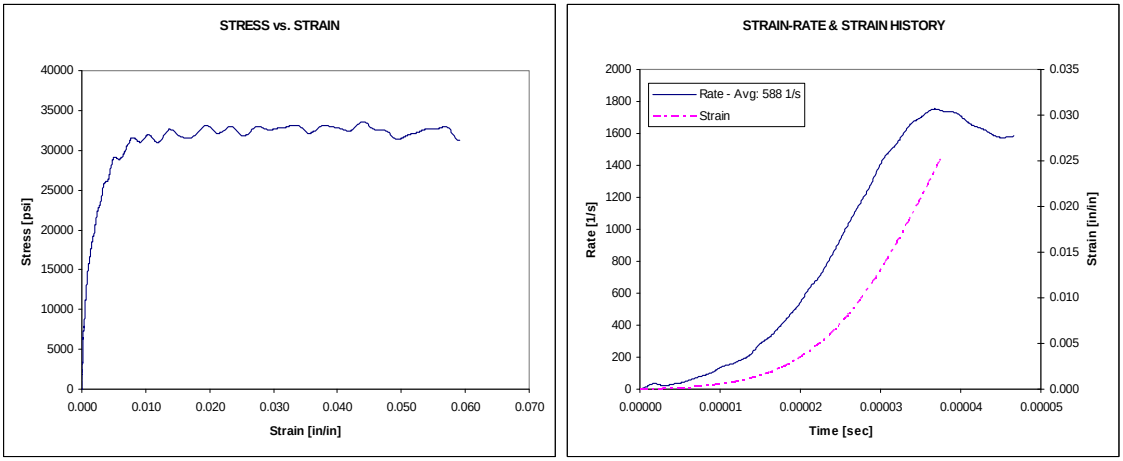

Specimen 2

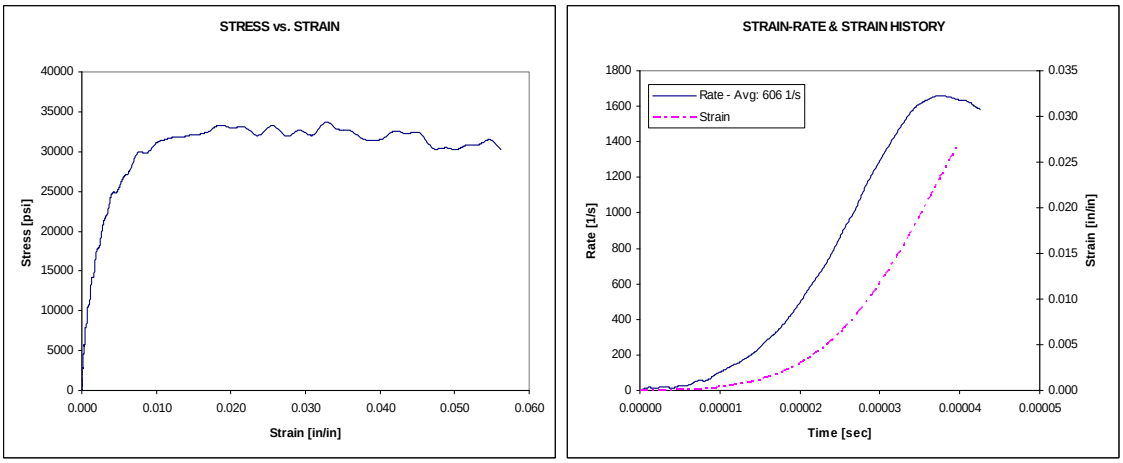

Specimen 3

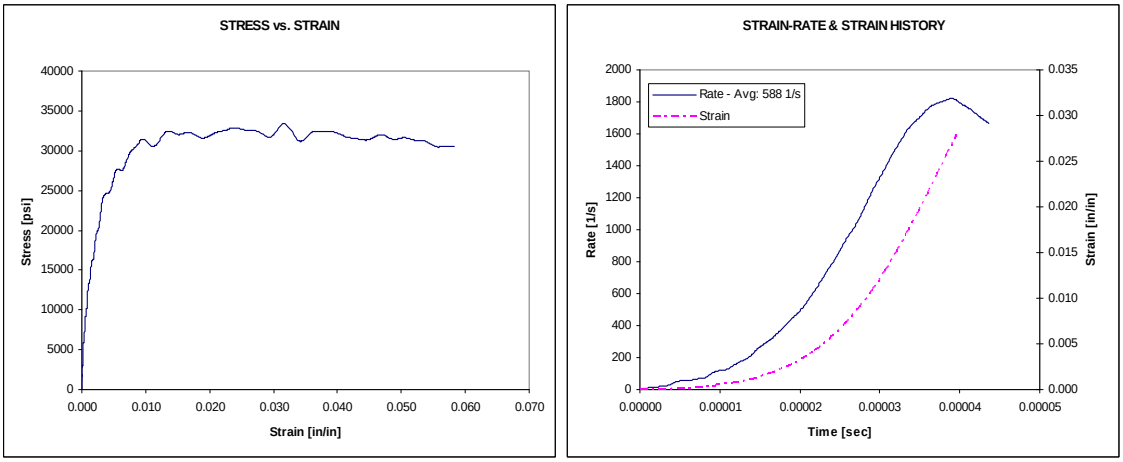

Figure C-63. Stress-Strain Curves for $[+45°/-45°]_{NS}$ Newport NB321/3K70 PWCF Specimens Tested at Average Strain Rate of 594 s^{-1}

Specimen 1

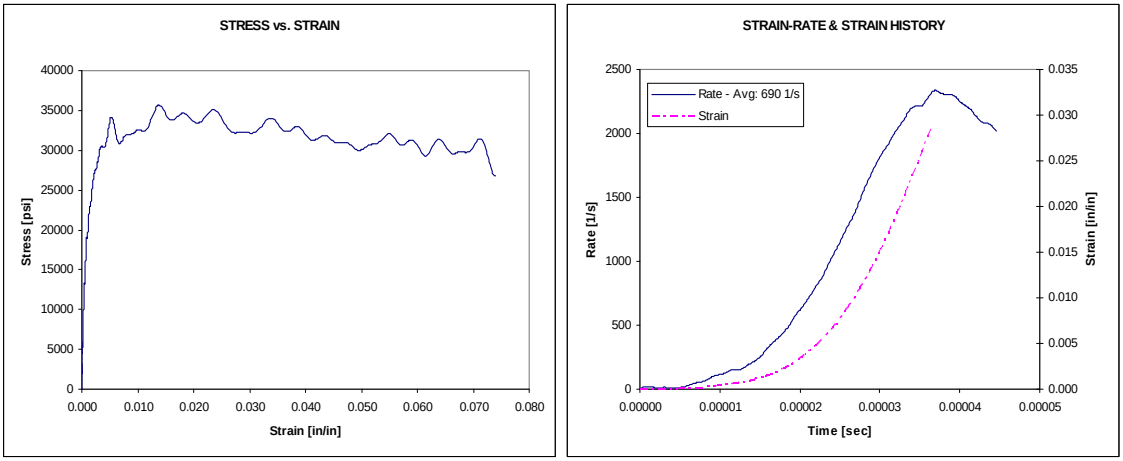

Specimen 2

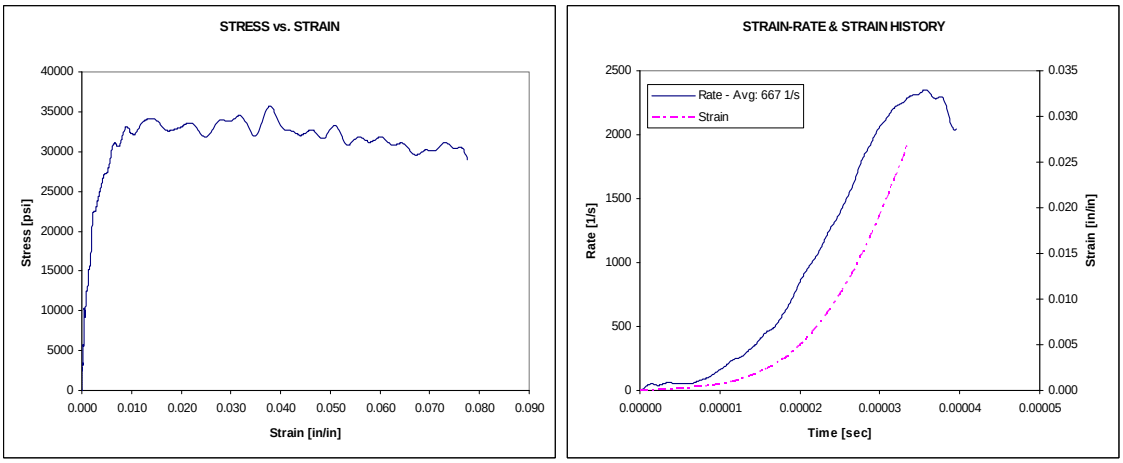

Specimen 3

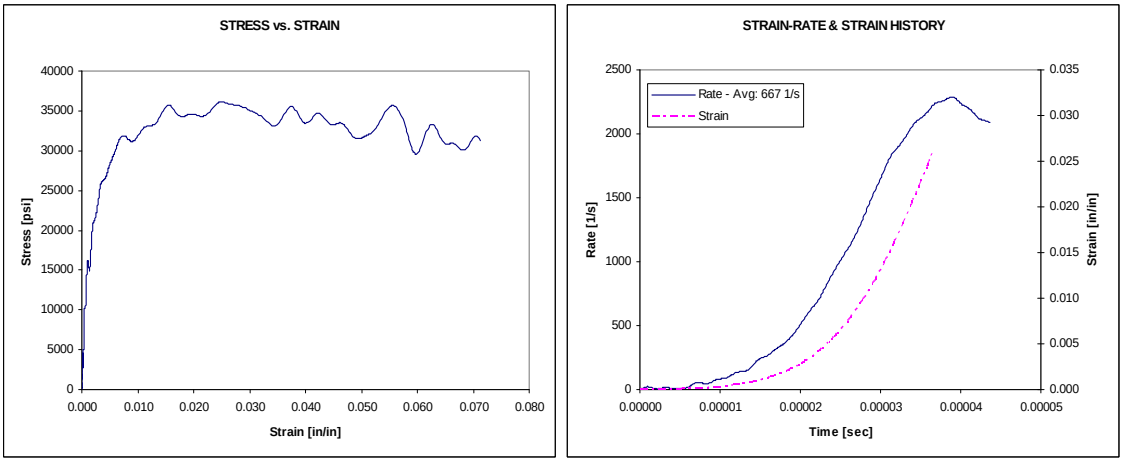

Figure C-64. Stress-Strain Curves for $[+45°/-45°]_{NS}$ Newport NB321/3K70 PWCF Specimens Tested at Average Strain Rate of 674 s^{-1}

Specimen 1

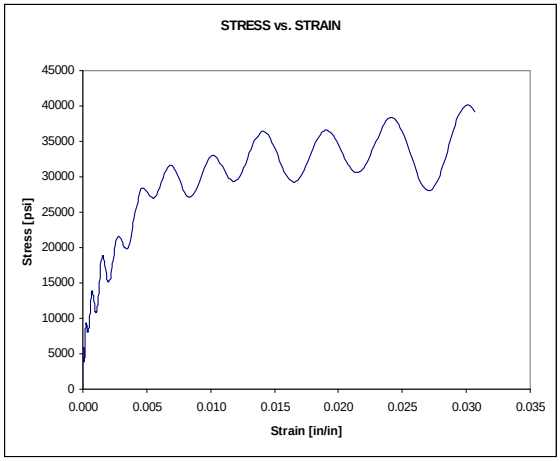

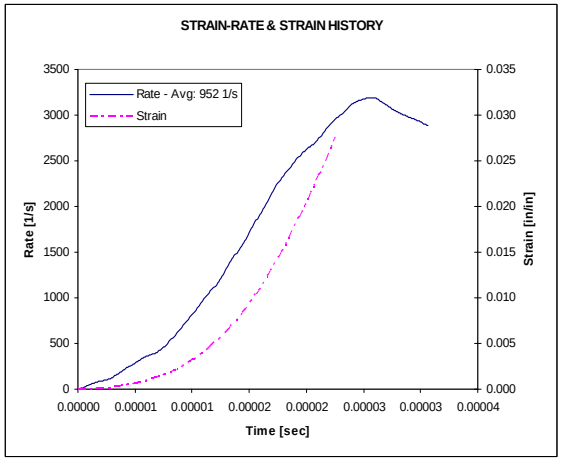

Specimen 2

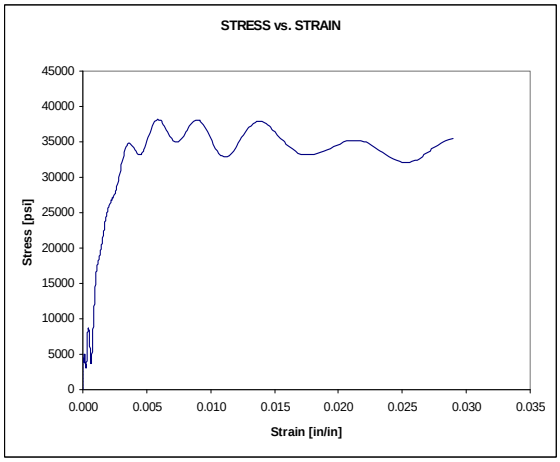

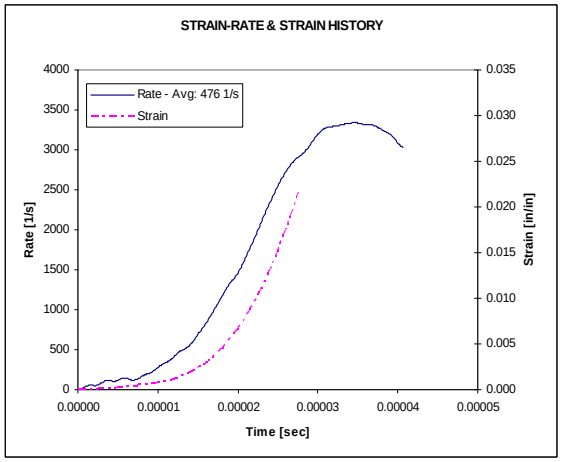

Specimen 3

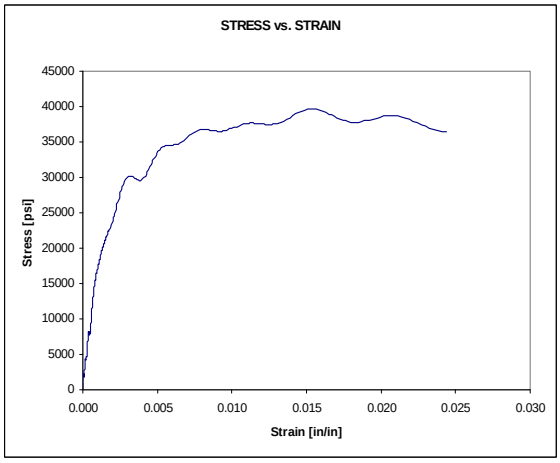

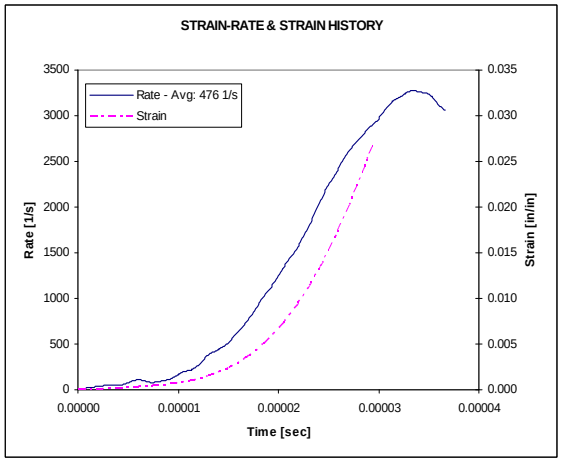

Figure C-65. Stress-Strain Curves for $[+45°/-45°]_{NS}$ Newport NB321/3K70 PWCF Specimens Tested at Average Strain Rate of 851 s^{-1}

Table C-5. Summary of Failure Strengths and Strain Rates for Newport NCT321/G150 Unitape

Orientation (degrees)	Average Strain Rate (1/s)	Actual Strain Rate (1/s)	Failure Strength (psi)	Average Failure Strength (psi)
0	0.00167	0.00167	93,699	96,694
		0.00167	87,586	
		0.00167	108,798	
	1	1	89,136	97,364
		1	105,591	
	423	408	119,070	115,367
		417	101,414	
		444	125,618	
	668	714	130,522	125,603
		645	116,728	
		645	129,560	
	780	800	127,290	124,901
		741	128,620	
		800	118,792	
15	0.00167	0.00167	101,498	101,046
		0.00167	104,945	
		0.00167	96,696	
	1	1	99,074	101,070
		1	103,065	
	404	370	107,881	108,950
		426	111,004	
		417	107,965	
	556	571	120,597	117,772
		541	118,301	
		556	114,419	
	660	645	101,583	96,748
		690	89,783	
		645	98,878	

Table C-5. Summary of Failure Strengths and Strain Rates for Newport NCT321/G150 Unitape (Continued)

Orientation (degrees)	Average Strain Rate (1/s)	Actual Strain Rate (1/s)	Failure Strength (psi)	Average Failure Strength (psi)
30	0.00167	0.00167	36,149	30,716
		0.00167	31,833	
		0.00167	24,167	
	1	1	20,335	26,661
		1	32,987	
	378	364	41,666	41,250
		392	43,983	
		377	38,099	
	594	606	48,293	46,789
		588	47,218	
		588	44,855	
	668	714	45,795	45,276
		645	43,232	
		645	46,800	
45	0.00167	0.00167	30,701	32,350
		0.00167	33,103	
		0.00167	33,247	
	1	1	29,497	28,621
		1	27,744	
	438	455	32,749	33,424
		426	34,667	
		435	32,856	
	699	667	35,108	32,365
		741	31,175	
		690	30,811	
	801	800	40,418	39,027
		833	38,152	
		769	38,511	

Specimen 1

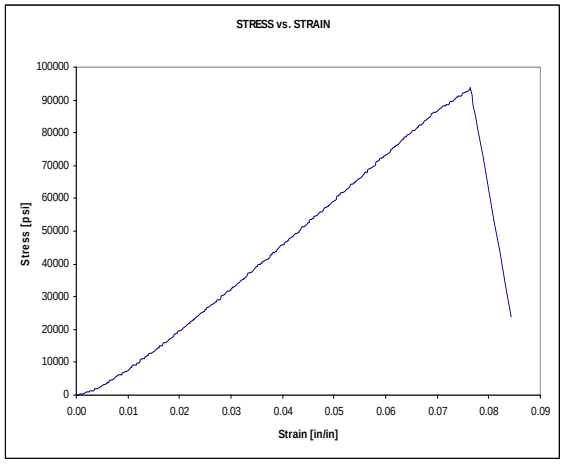

Specimen 2

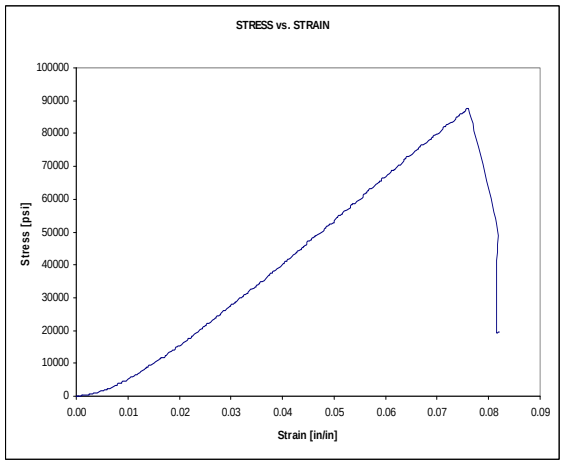

Specimen 3

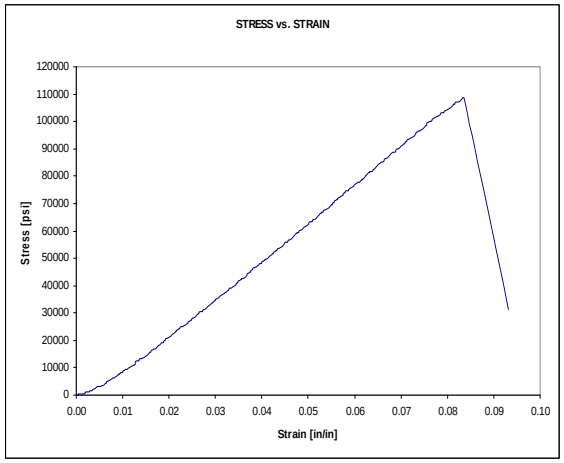

Figure C-66. Stress-Strain Curves for [0°] Newport NCT321/G150 Unitape Specimens Tested at Average Strain Rate of 0.00167 s^{-1}

Specimen 1

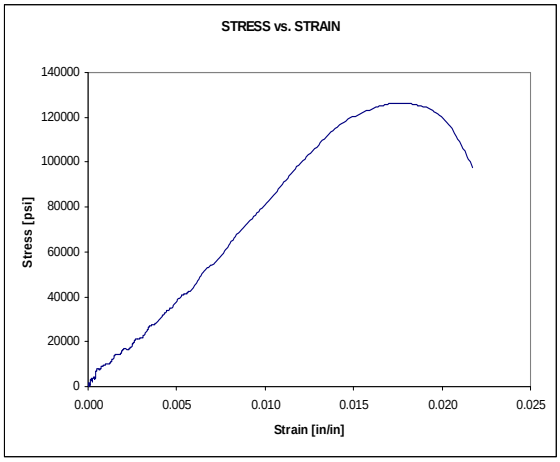

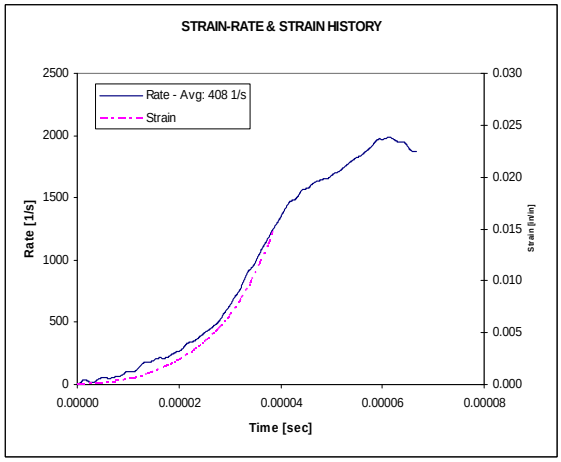

Specimen 2

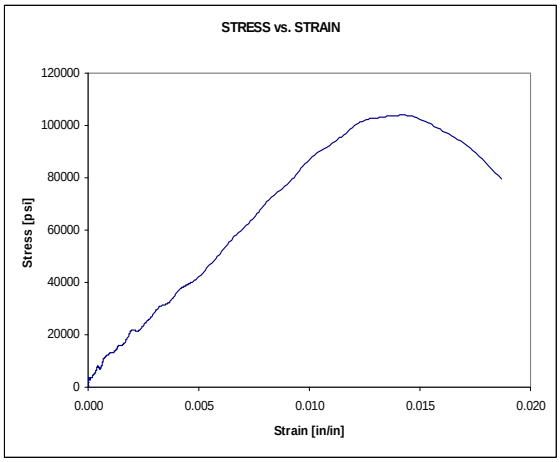

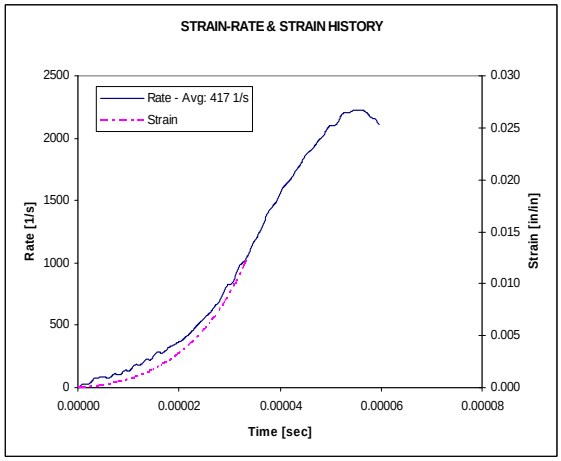

Specimen 3

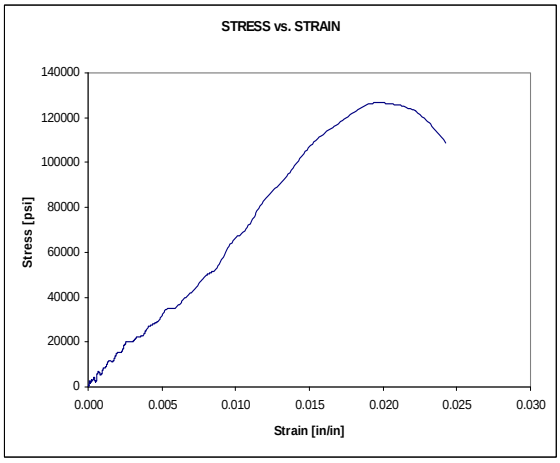

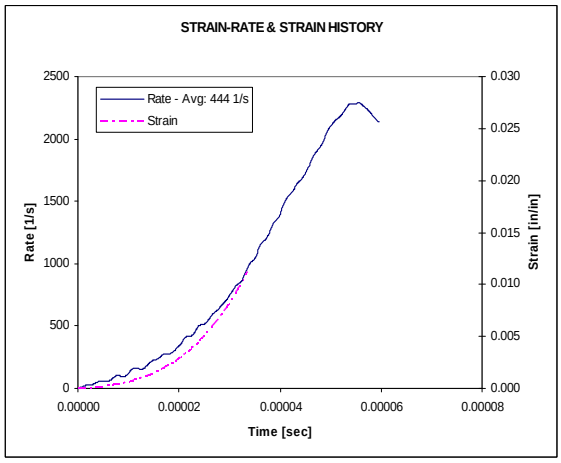

Figure C-67. Stress-Strain Curves for [0°] Newport NCT321/G150 Unitape Specimens Tested at Average Strain Rate of 423 s^{-1}

Specimen 1

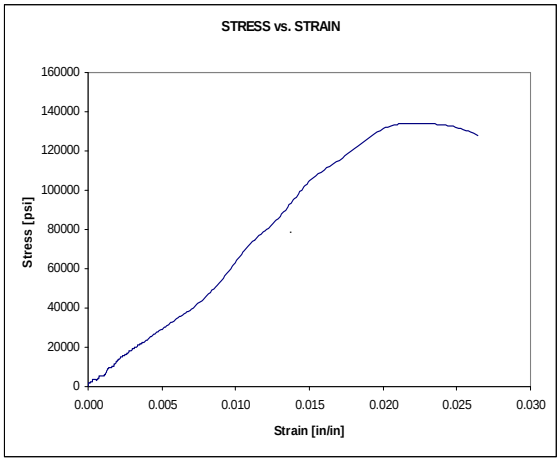

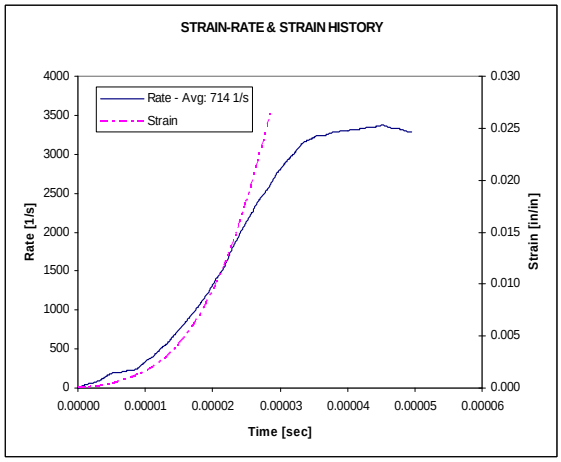

Specimen 2

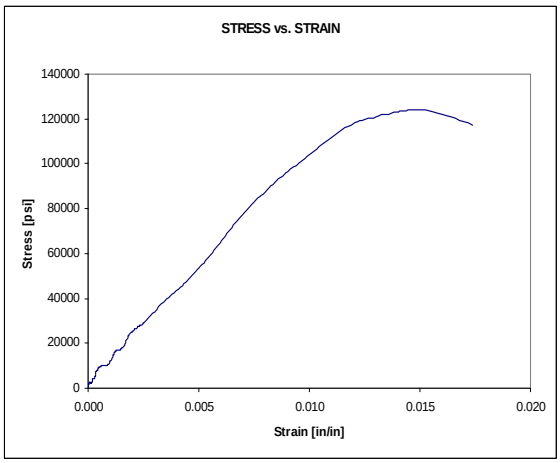

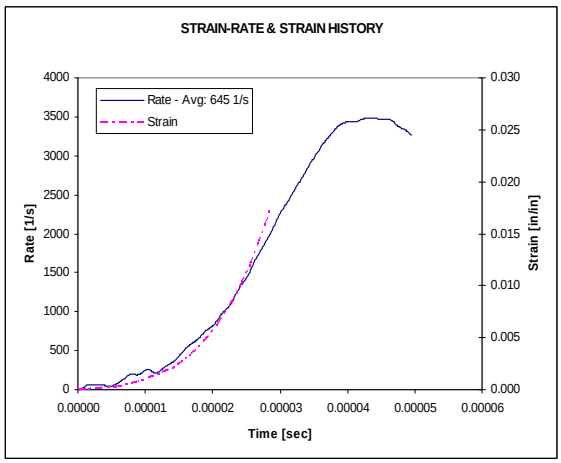

Specimen 3

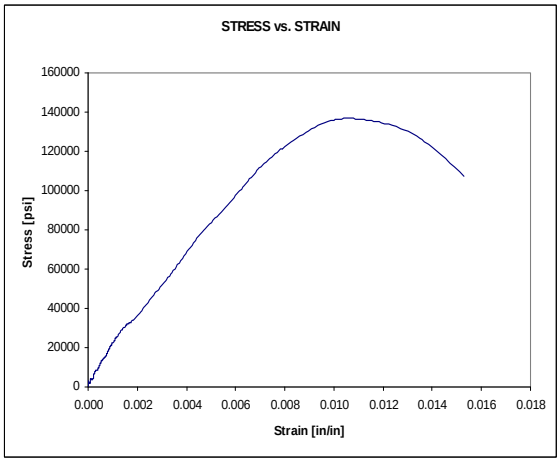

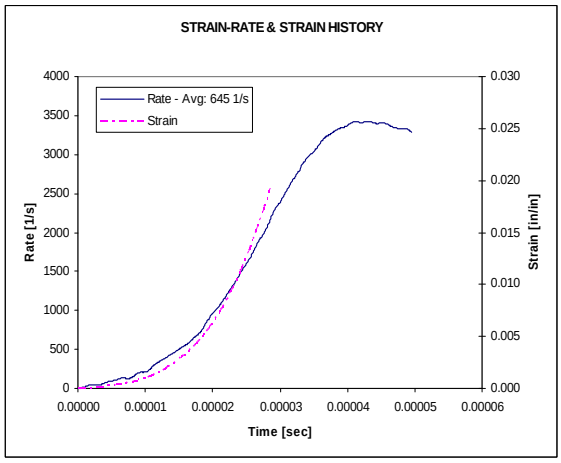

Figure C-68. Stress-Strain Curves for [0°] Newport NCT321/G150 Unitape Specimens Tested at Average Strain Rate of 668 s^{-1}

Specimen 1

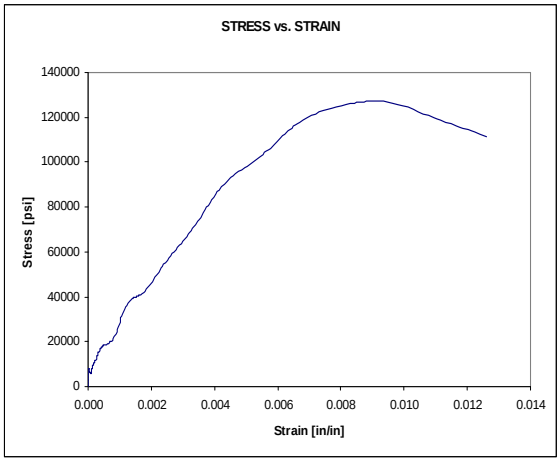

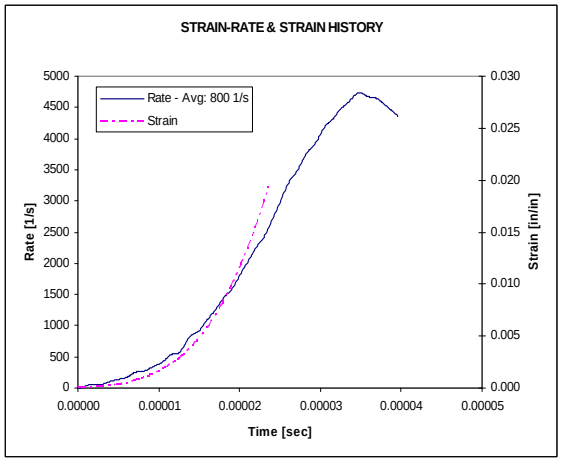

Specimen 2

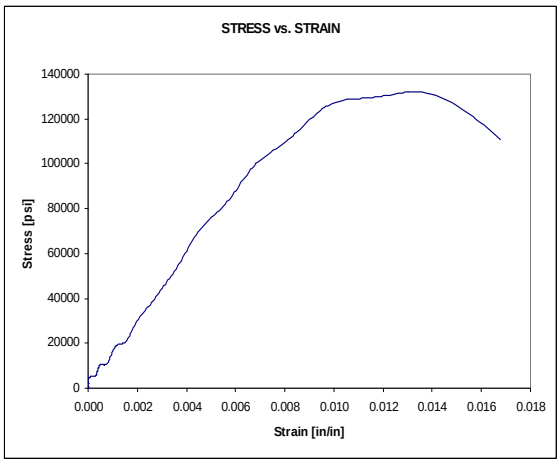

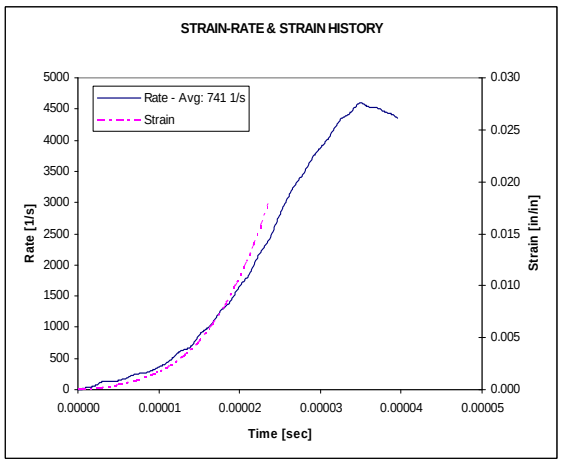

Specimen 3

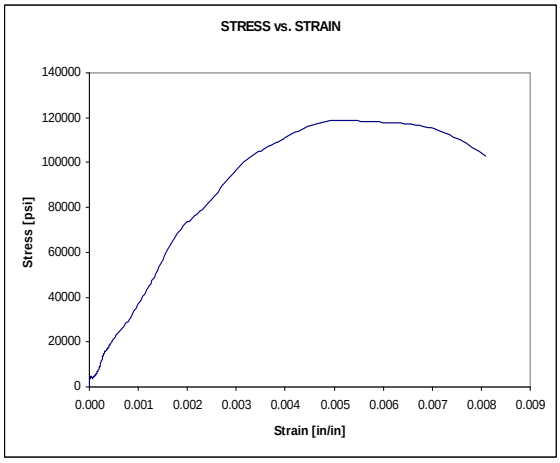

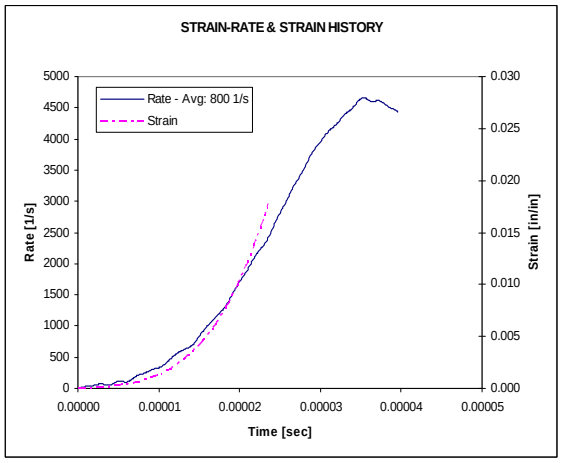

Figure C-69. Stress-Strain Curves for [0°] Newport NCT321/G150 Unitape Specimens Tested at Average Strain Rate of 780 s^{-1}

Specimen 1

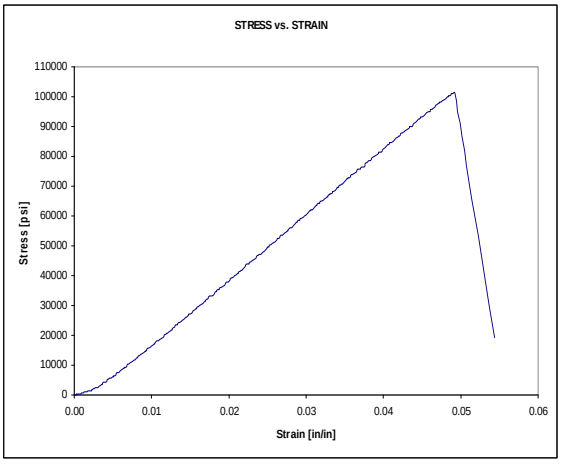

Specimen 2

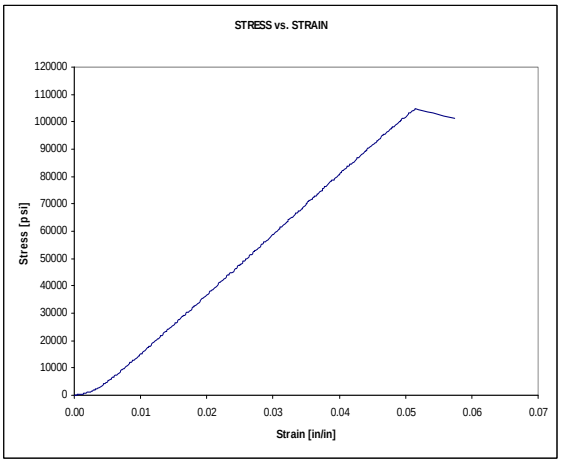

Specimen 3

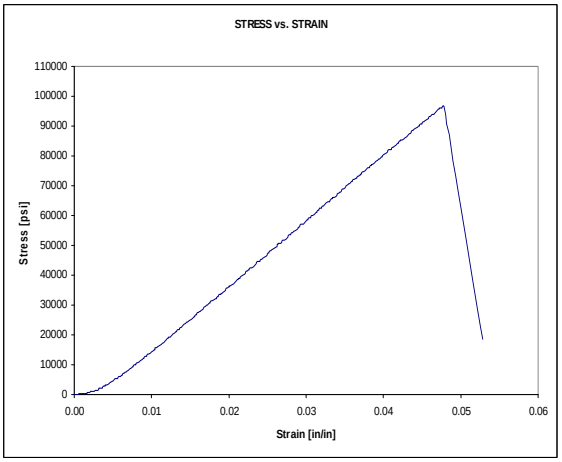

Figure C-70. Stress-Strain Curves for $[+15°/-15°]_{NS}$ Newport NCT321/G150 Unitape Specimens Tested at Average Strain Rate of 0.00167 s^{-1}

Specimen 1

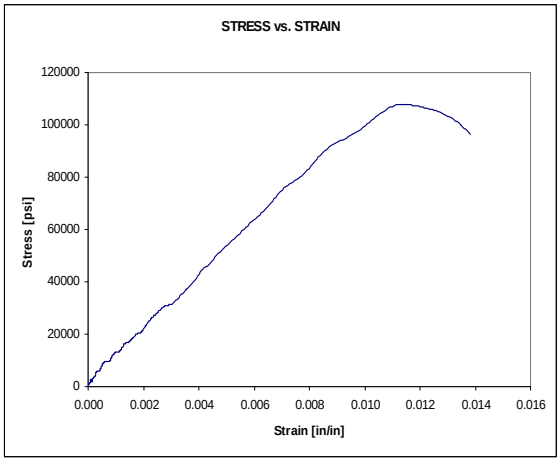

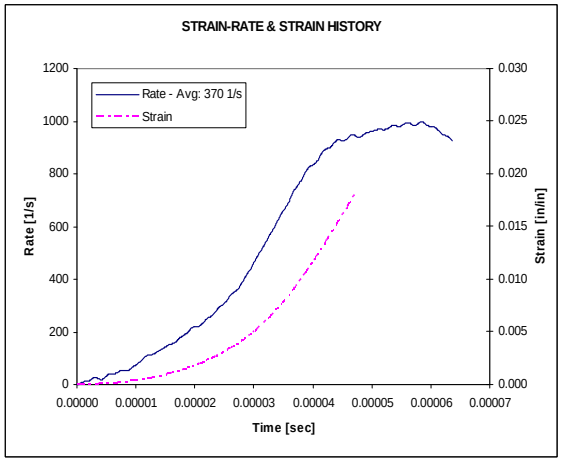

Specimen 2

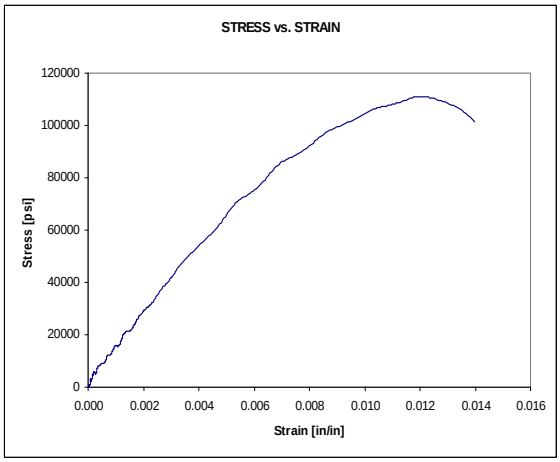

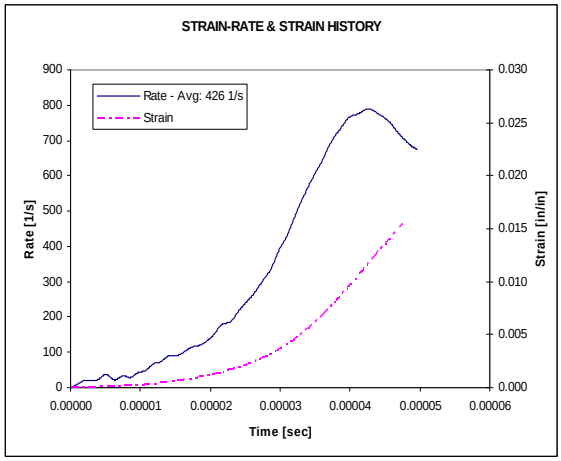

Specimen 3

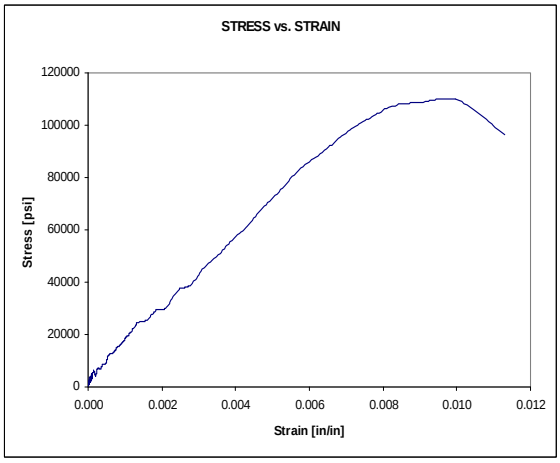

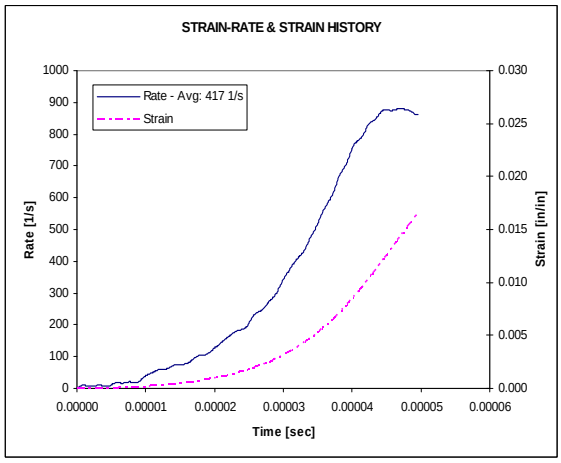

Figure C-71. Stress-Strain Curves for $[+15°/-15°]_{NS}$ Newport NCT321/G150 Unitape Specimens Tested at Average Strain Rate of 404 s^{-1}

Specimen 1

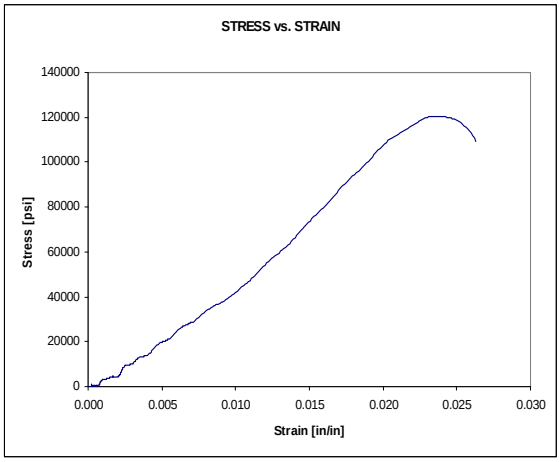

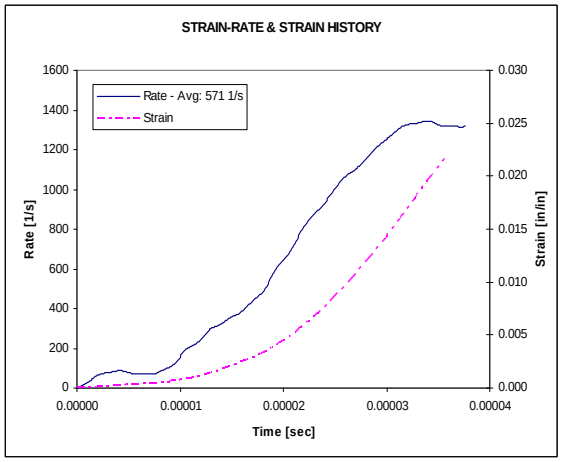

Specimen 2

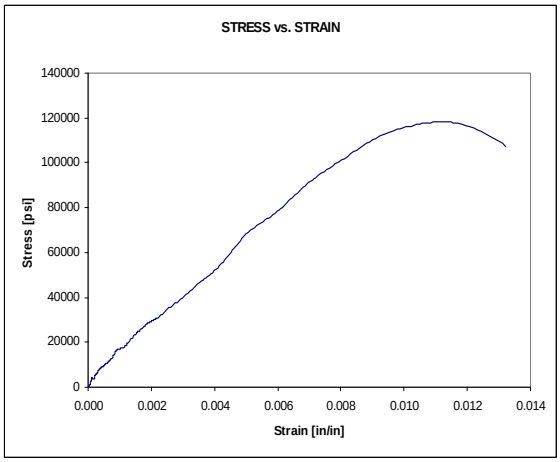

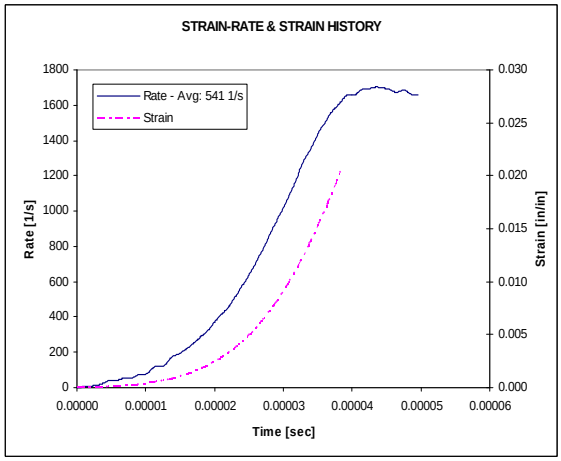

Specimen 3

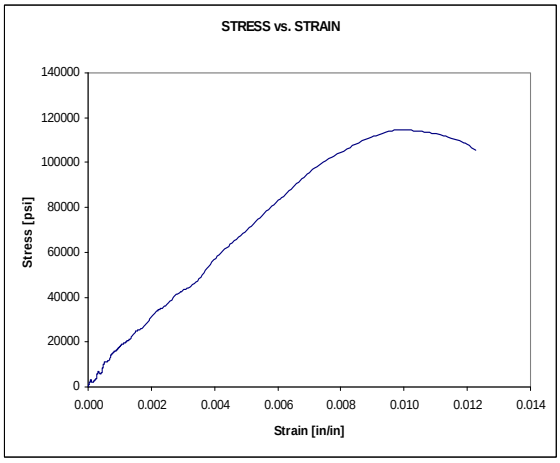

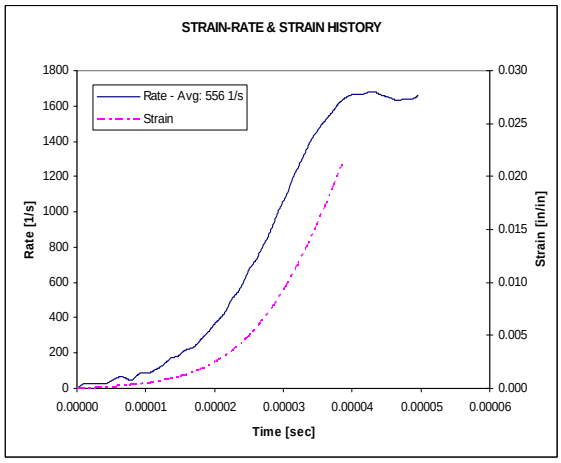

Figure C-72. Stress-Strain Curves for $[+15°/-15°]_{NS}$ Newport NCT321/G150 Unitape Specimens Tested at Average Strain Rate of 556 s^{-1}

Specimen 1

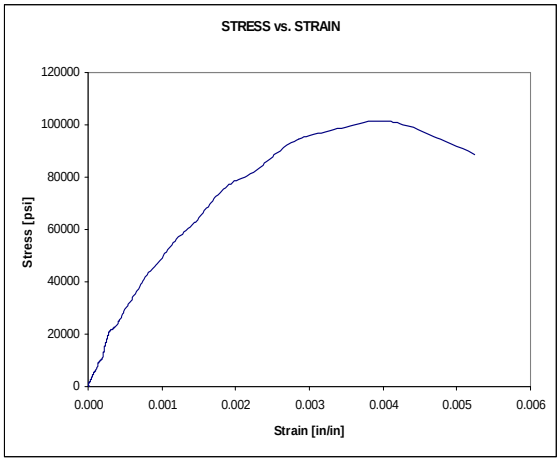

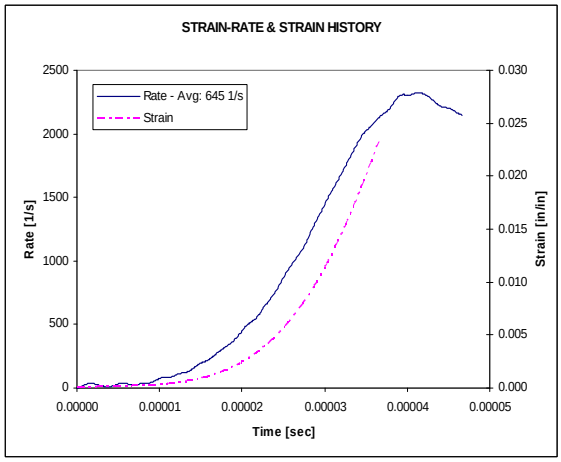

Specimen 2

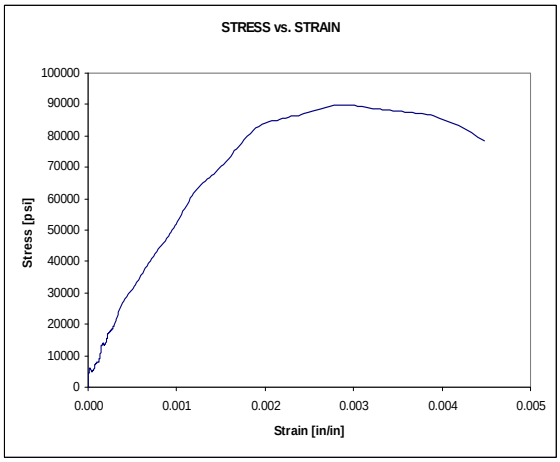

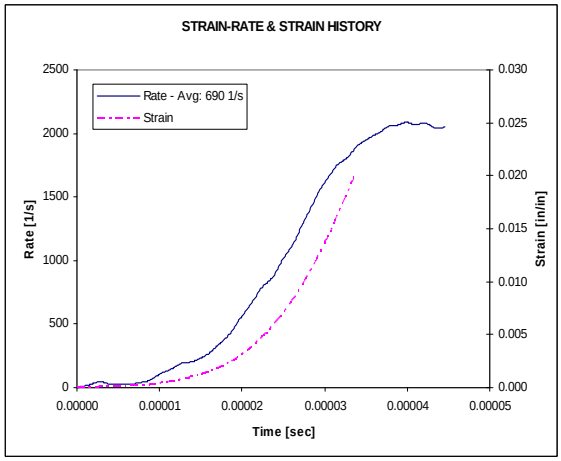

Specimen 3

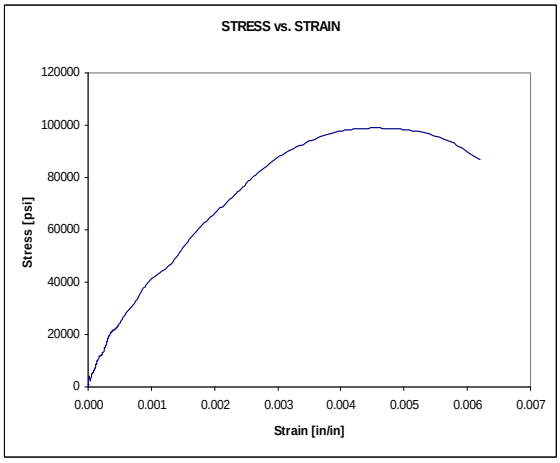

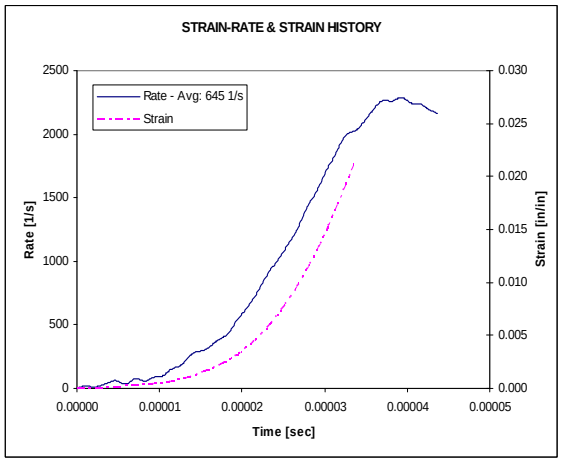

Figure C-73. Stress-Strain Curves for $[+15°/-15°]_{NS}$ Newport NCT321/G150 Unitape Specimens Tested at Average Strain Rate of 660 s^{-1}

Specimen 1

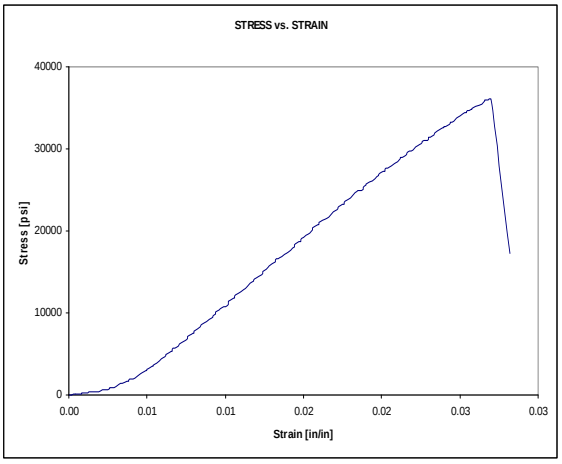

Specimen 2

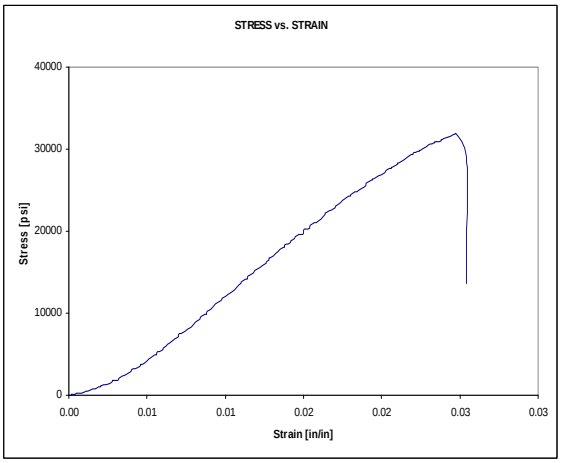

Specimen 3

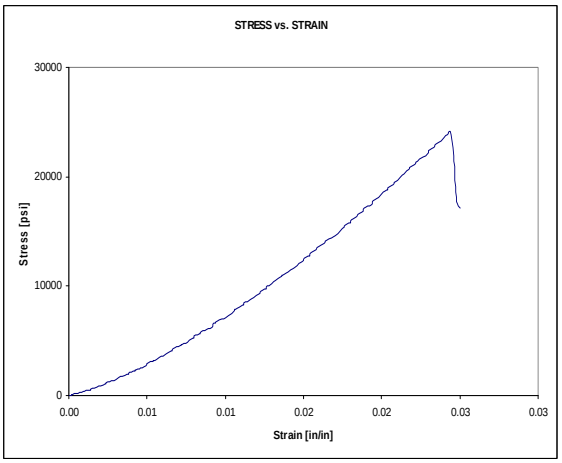

Figure C-74. Stress-Strain Curves for $[+30°/-30°]_{NS}$ Newport NCT321/G150 Unitape Specimens Tested at Average Strain Rate of 0.00167 s^{-1}

Specimen 1

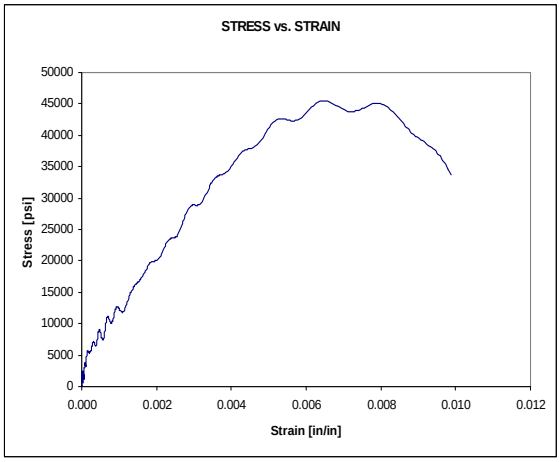

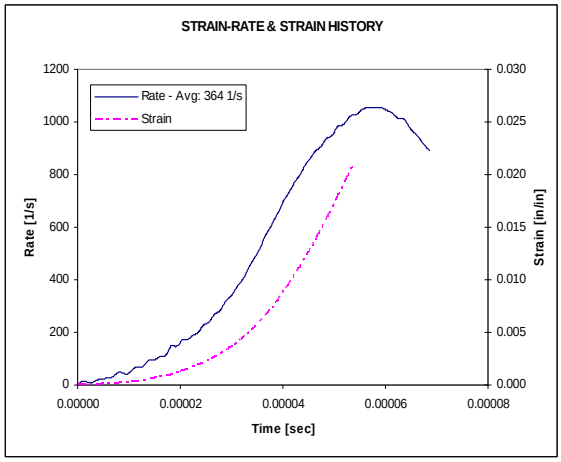

Specimen 2

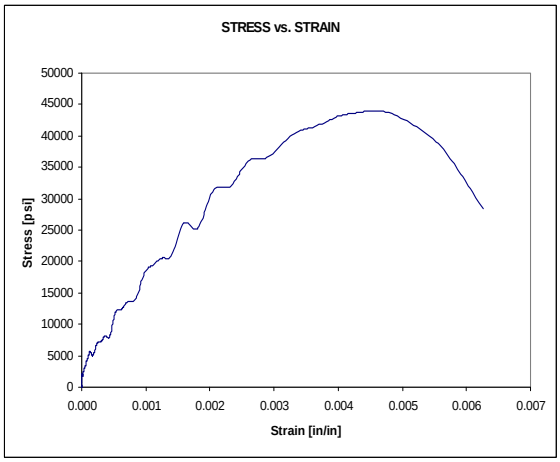

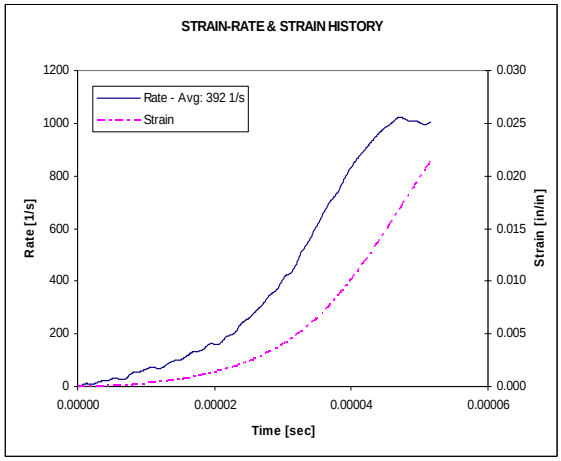

Specimen 3

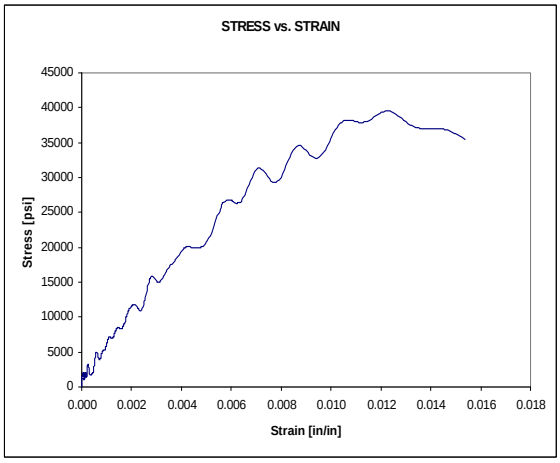

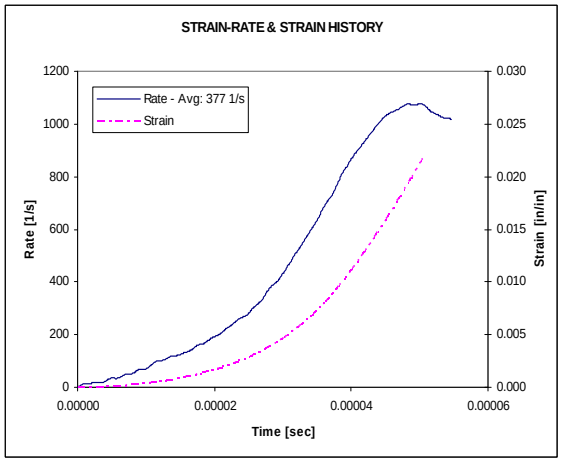

Figure C-75. Stress-Strain Curves for $[+30°/-30°]_{NS}$ Newport NCT321/G150 Unitape Specimens Tested at Average Strain Rate of 378 s^{-1}

Specimen 1

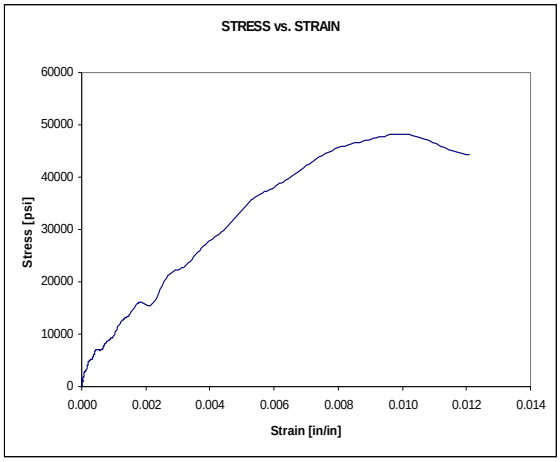

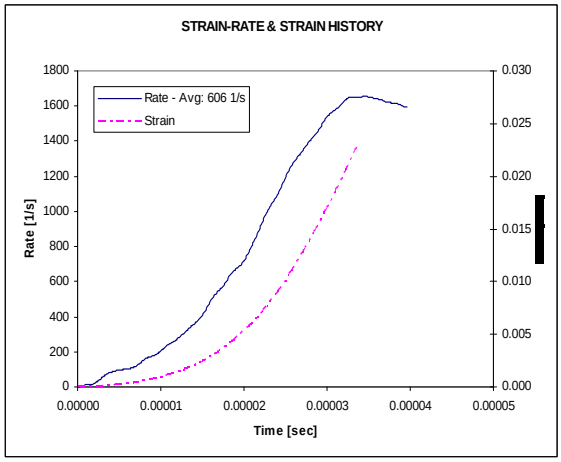

Specimen 2

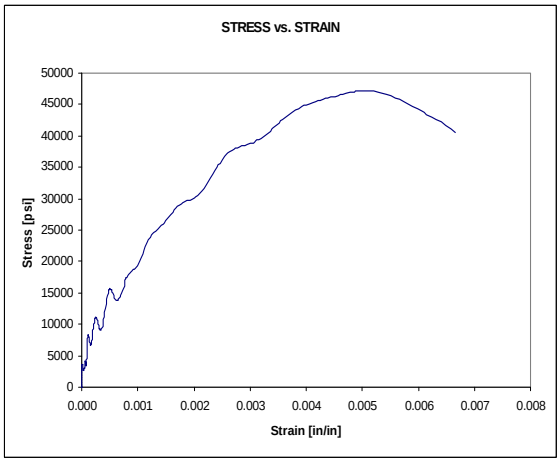

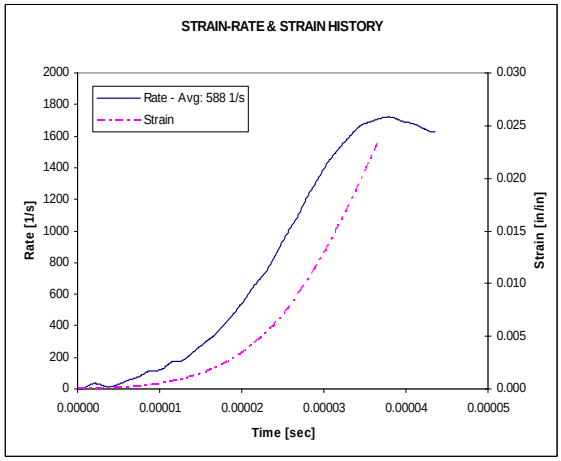

Specimen 3

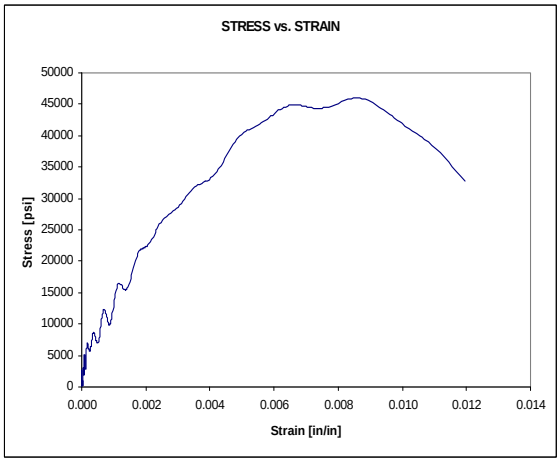

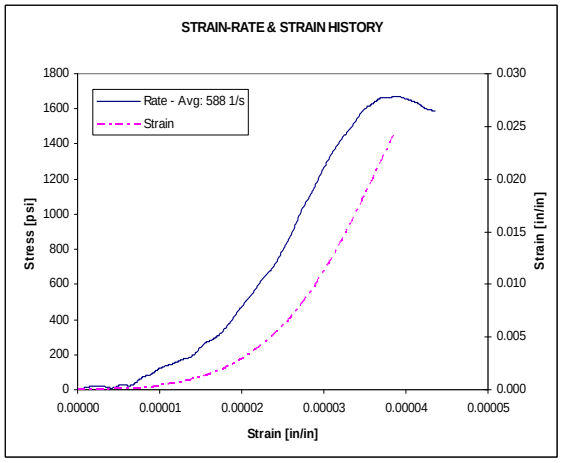

Figure C-76. Stress-Strain Curves for $[+30°/-30°]_{NS}$ Newport NCT321/G150 Unitape Specimens Tested at Average Strain Rate of 594 s^{-1}

Specimen 1

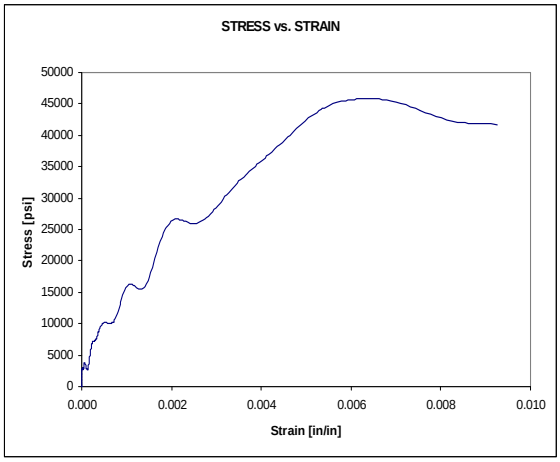

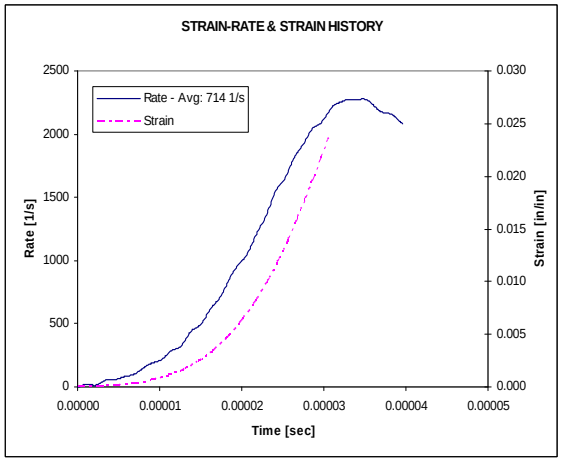

Specimen 2

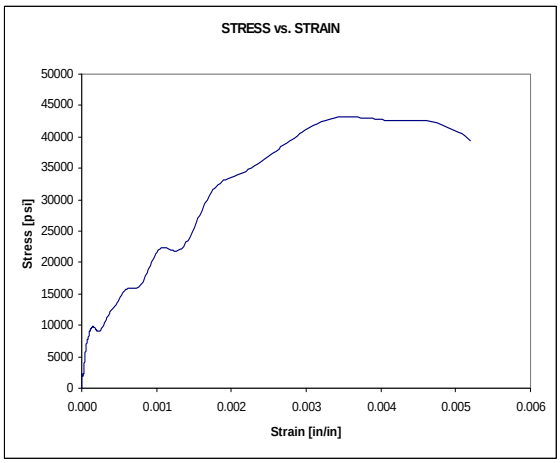

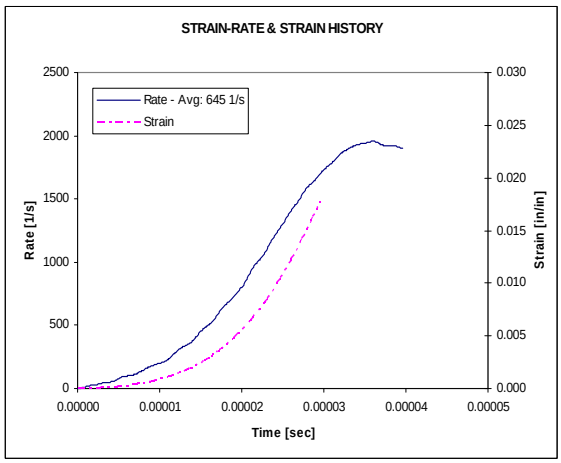

Specimen 3

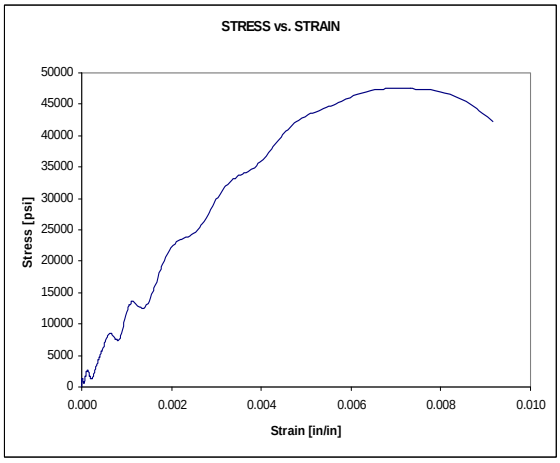

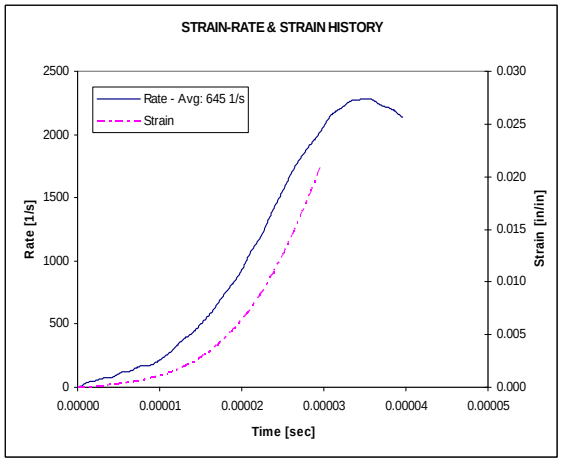

Figure C-77. Stress-Strain Curves for $[+30°/-30°]_{NS}$ Newport NCT321/G150 Unitape Specimens Tested at Average Strain Rate of 668 s^{-1}

Specimen 1

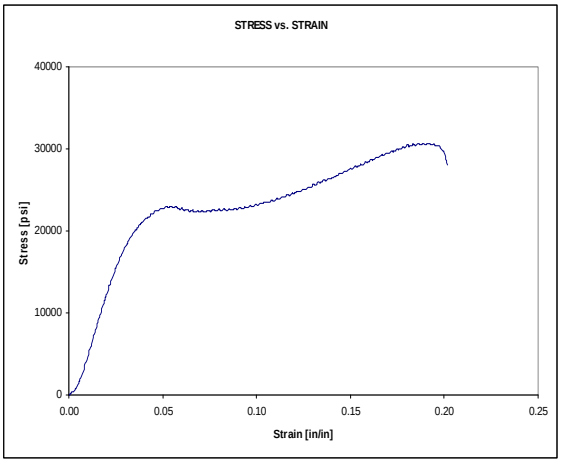

Specimen 2

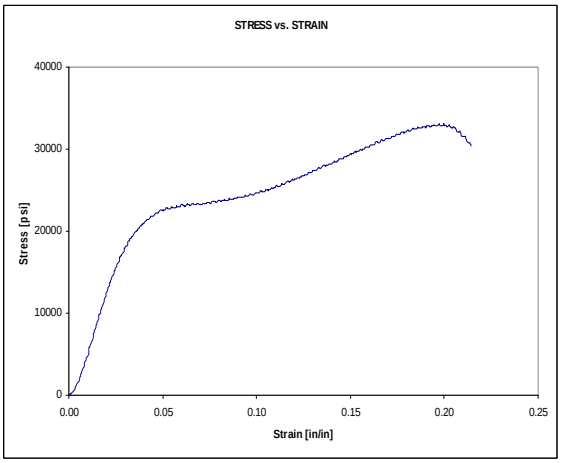

Specimen 3

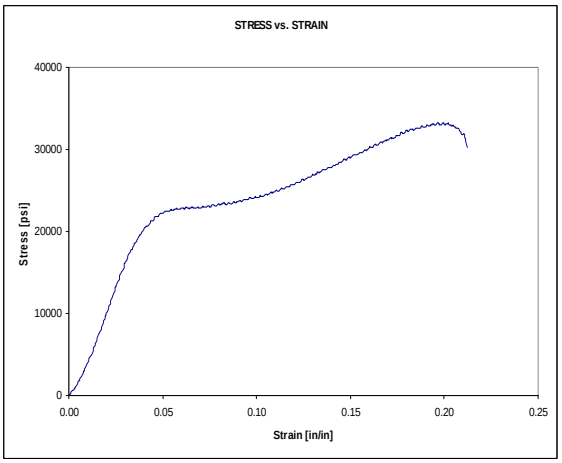

Figure C-78. Stress-Strain Curves for $[+45°/-45°]_{NS}$ Newport NCT321/G150 Unitape Specimens Tested at Average Strain Rate of 0.00167 s^{-1}

Specimen 1

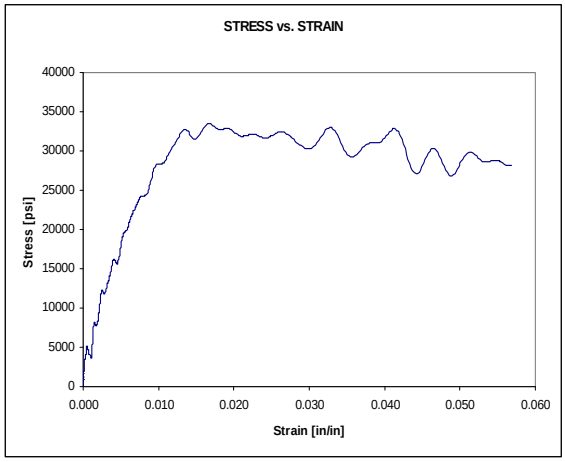

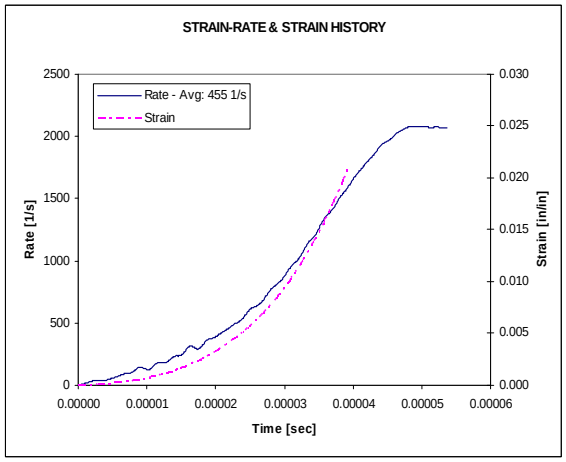

Specimen 2

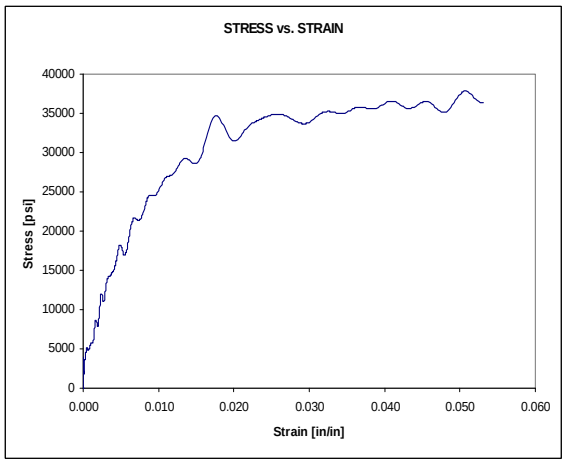

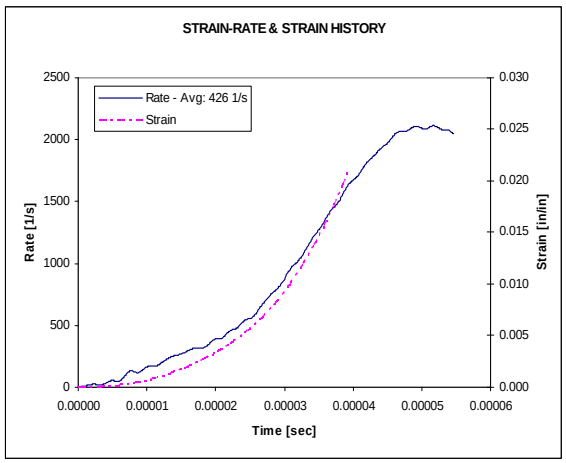

Specimen 3

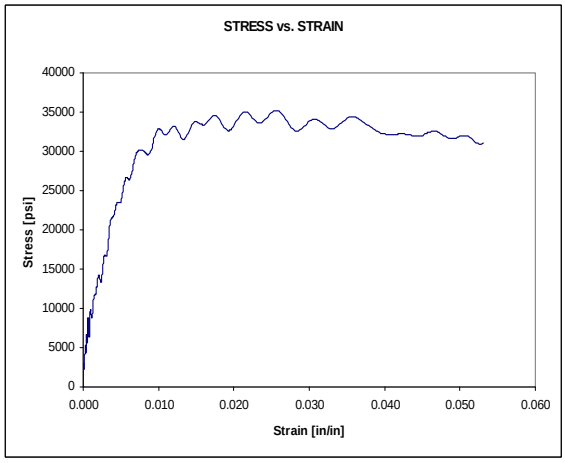

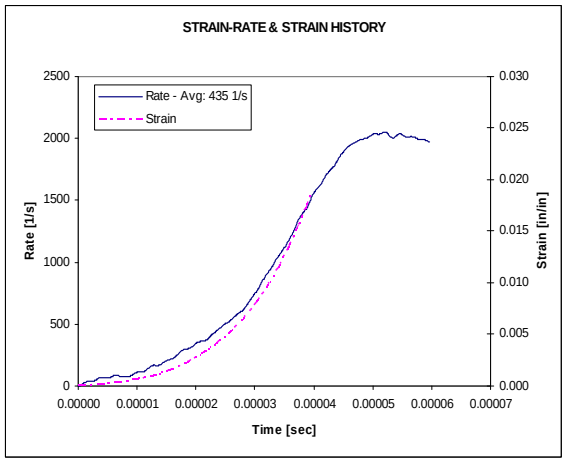

Figure C-79. Stress-Strain Curves for $[+45°/-45°]_{NS}$ Newport NCT321/G150 Unitape Specimens Tested at Average Strain Rate of 438 s^{-1}

Specimen 1

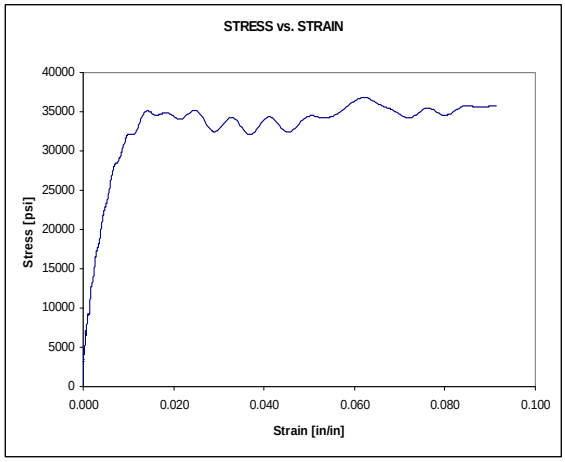

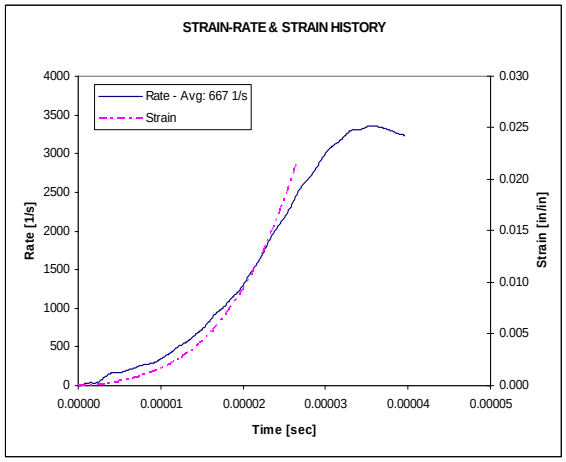

Specimen 2

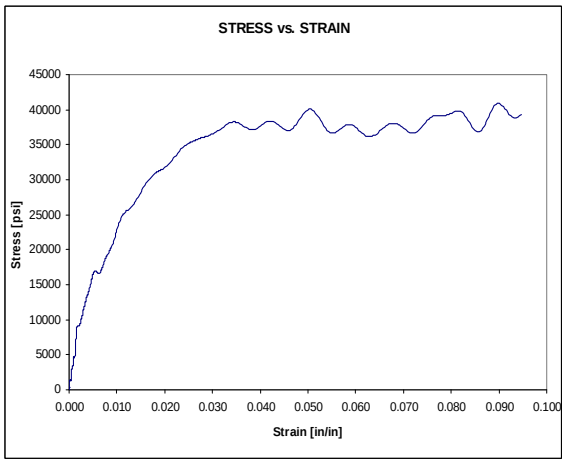

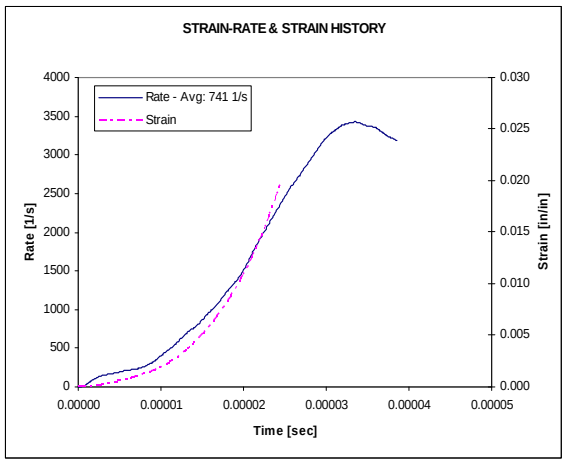

Specimen 3

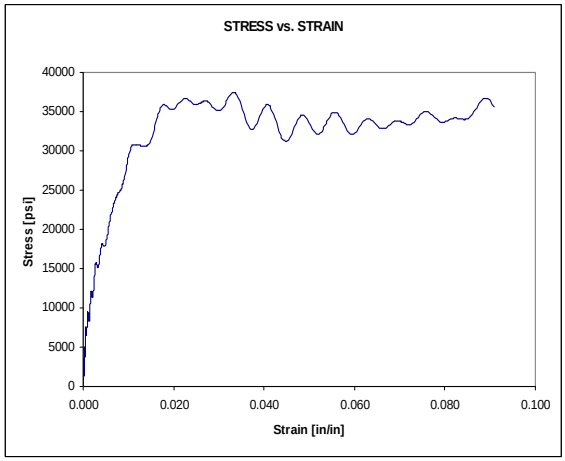

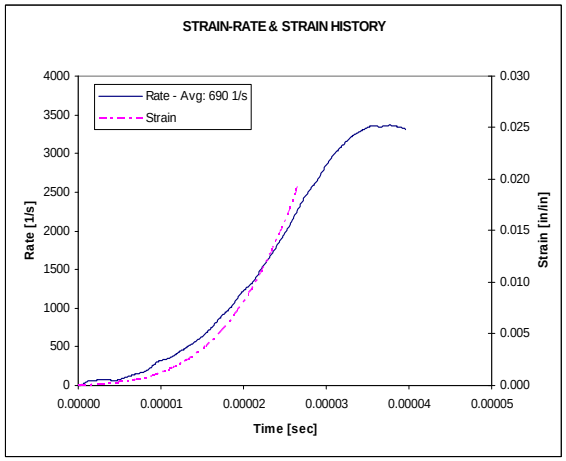

Figure C-80. Stress-Strain Curves for $[+45°/-45°]_{NS}$ Newport NCT321/G150 Unitape Specimens Tested at Average Strain Rate of 699 s^{-1}

Specimen 1

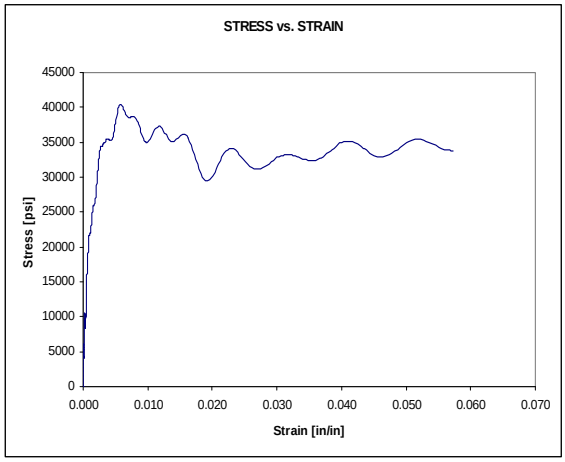

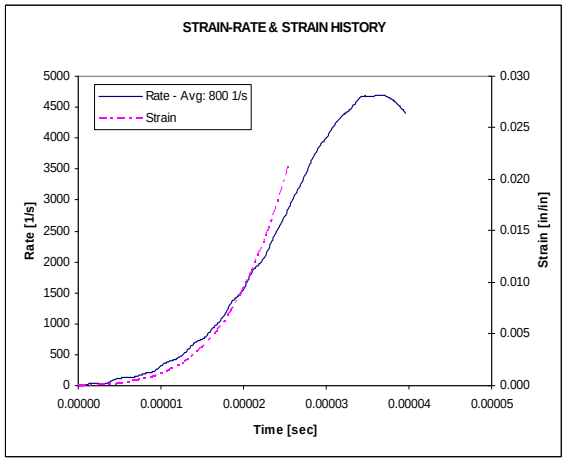

Specimen 2

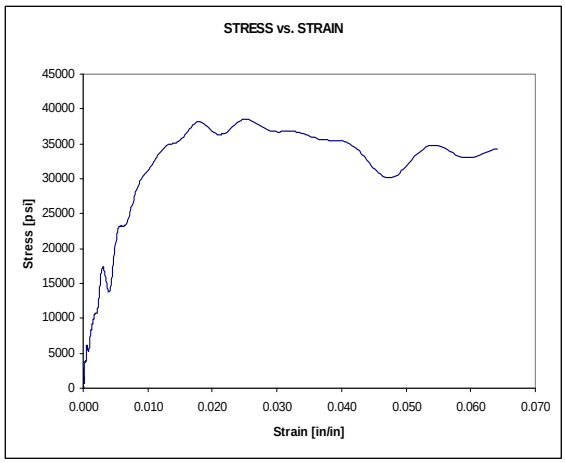

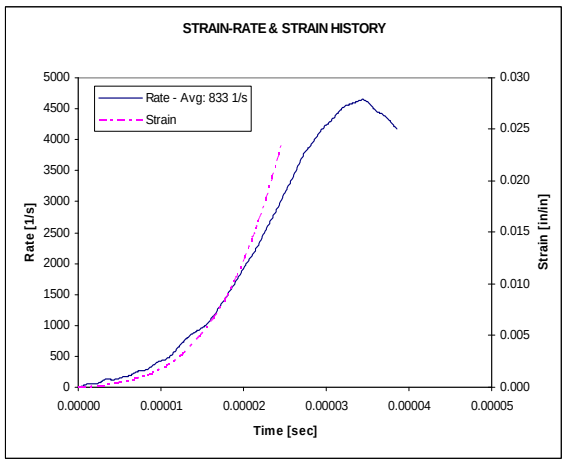

Specimen 3

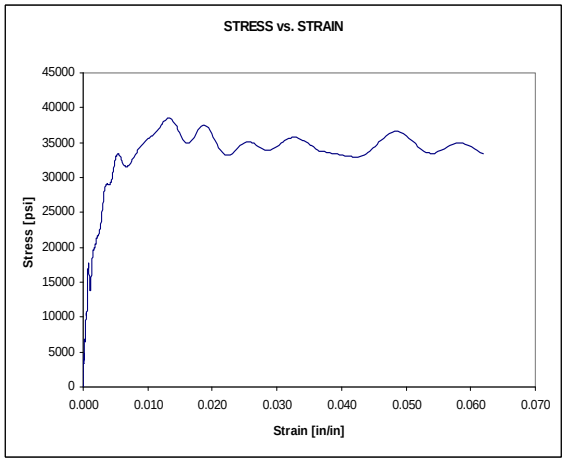

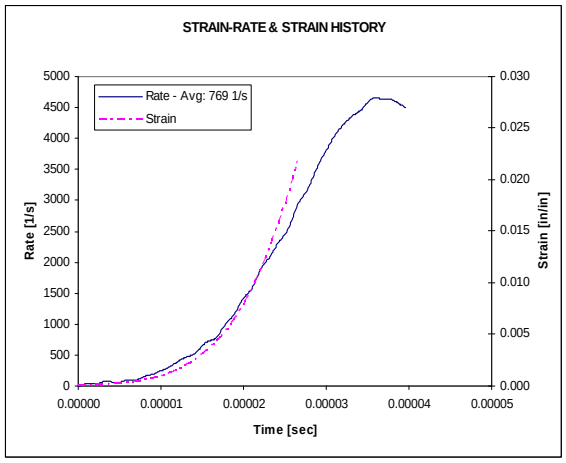

Figure C-81. Stress-Strain Curves for $[+45°/-45°]_{NS}$ Newport NCT321/G150 Unitape Specimens Tested at Average Strain Rate of 801 s^{-1}

Table C-6. Summary of Failure Strengths and Strain Rates for Cytec T300/97714AC 3KNT PWCF

Orientation (degrees)	Average Strain Rate (1/s)	Actual Strain Rate (1/s)	Failure Strength (psi)	Average Failure Strength (psi)
0	0.00167	0.00167	69,895	69,222
		0.00167	64,205	
		0.00167	73,566	
	1	1	81,991	74,110
		1	66,229	
	368	377	72,717	77,242
		357	81,937	
		370	77,070	
	567	588	80,122	80,532
		571	77,728	
		541	83,746	
	653	645	84,432	82,607
		690	83,201	
		625	80,187	
15	0.00167	0.00167	63,463	63,606
		0.00167	67,165	
		0.00167	60,192	
	1	1	71,195	71,036
		1	70,877	
	353	351	66,926	67,853
		351	68,637	
		357	67,997	
	577	571	70,762	68,449
		571	68,238	
		588	66,348	
	698	714	70,339	71,117
		714	71,289	
		667	71,722	

Table C-6. Summary of Failure Strengths and Strain Rates for Cytec T300/97714AC 3KNT PWCF (Continued)

Orientation (degrees)	Average Strain Rate (1/s)	Actual Strain Rate (1/s)	Failure Strength (psi)	Average Failure Strength (psi)
30	0.00167	0.00167	47,655	47,902
		0.00167	48,328	
		0.00167	47,723	
	1	1	51,680	52,815
		1	53,949	
	361	357	53,346	53,971
		364	53,275	
		364	55,293	
	583	588	53,638	53,964
		571	56,623	
		588	51,630	
	667	667	63,521	59,206
		645	57,285	
		690	56,811	
45	0.00167	0.00167	32,678	32,446
		0.00167	33,019	
		0.00167	31,642	
	1	1	31,203	35,564
		1	39,924	
	385	392	26,127	26,628
		392	26,614	
		370	27,142	
	561	556	31,540	32,372
		556	33,461	
		571	32,117	
	691	667	33,735	35,139
		667	34,926	
		741	36,755	

Specimen 1

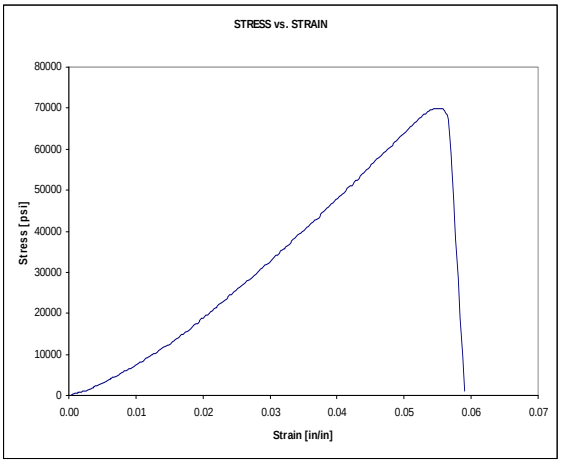

Specimen 2

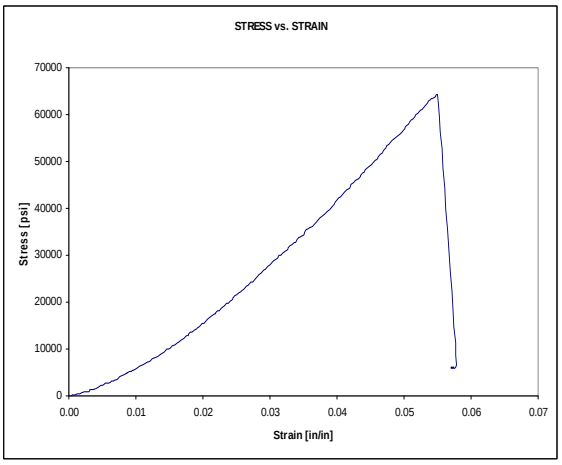

Specimen 3

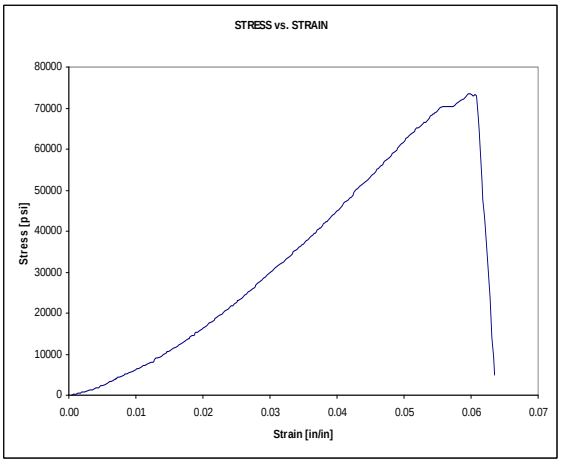

Figure C-82. Stress-Strain Curves for [0°] Cytec T300/97714AC 3KNT PWCF Specimens Tested at Average Strain Rate of 0.00167 s^{-1}

Specimen 1

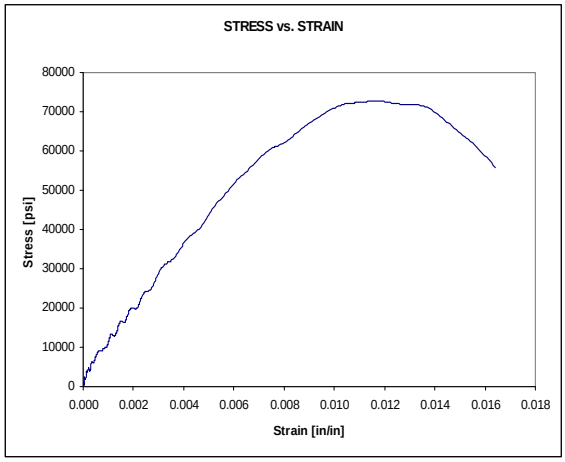

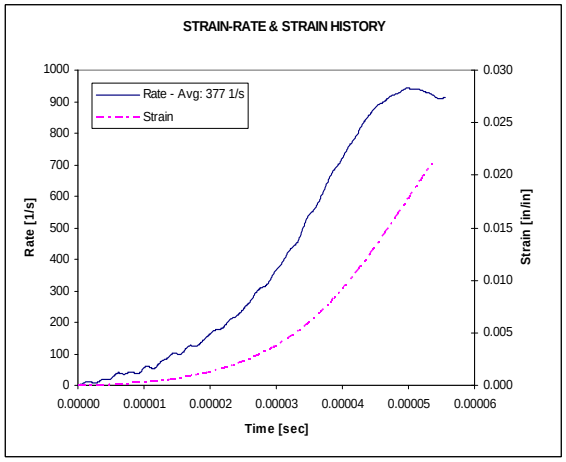

Specimen 2

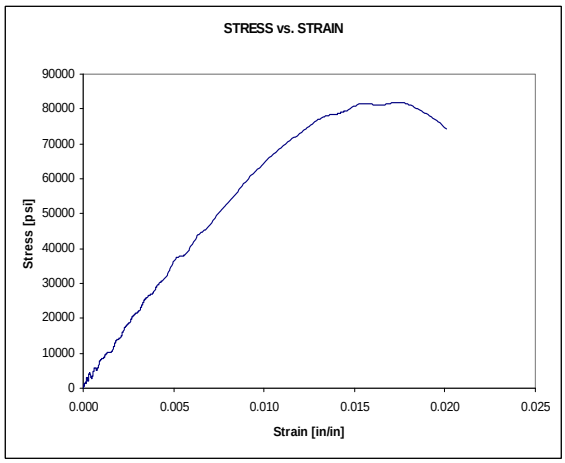

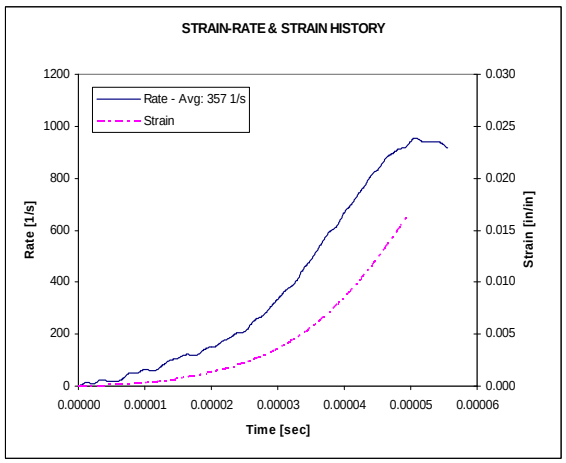

Specimen 3

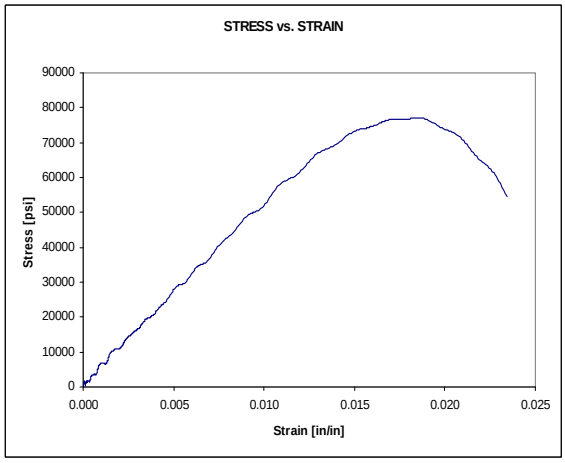

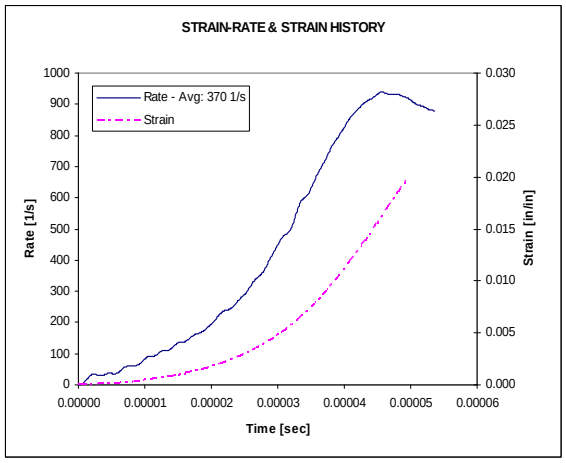

Figure C-83. Stress-Strain Curves for [0°] Cytec T300/97714AC 3KNT PWCF Specimens Tested at Average Strain Rate of 368 s^{-1}

Specimen 1

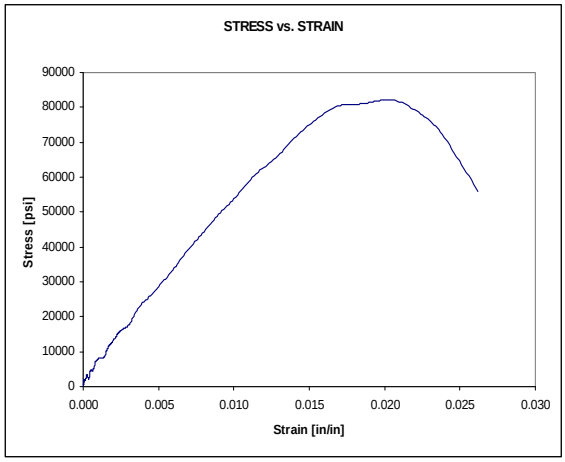

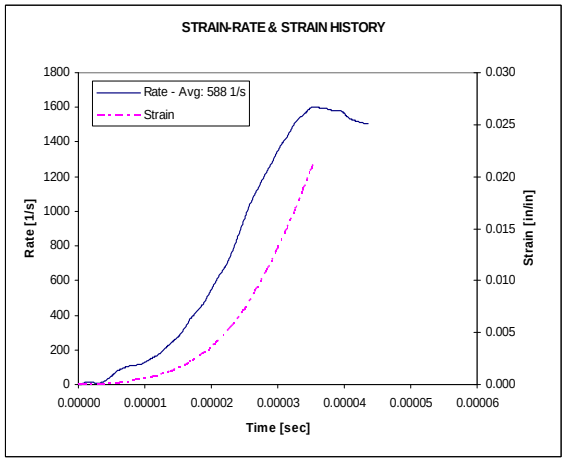

Specimen 2

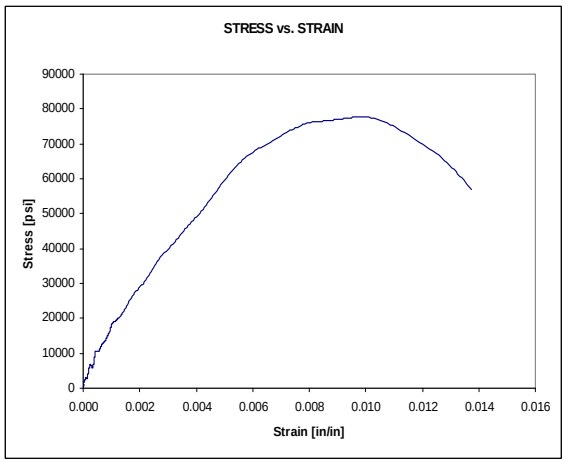

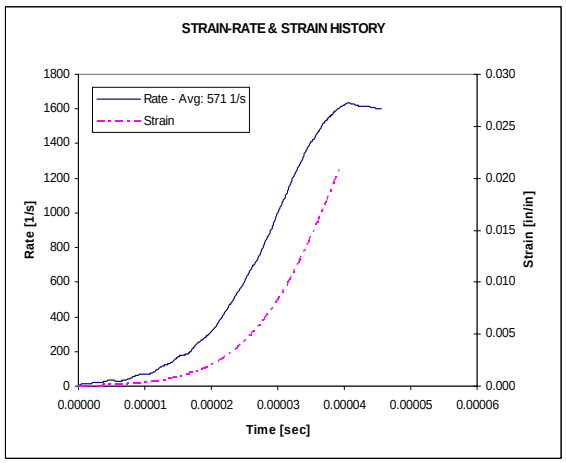

Specimen 3

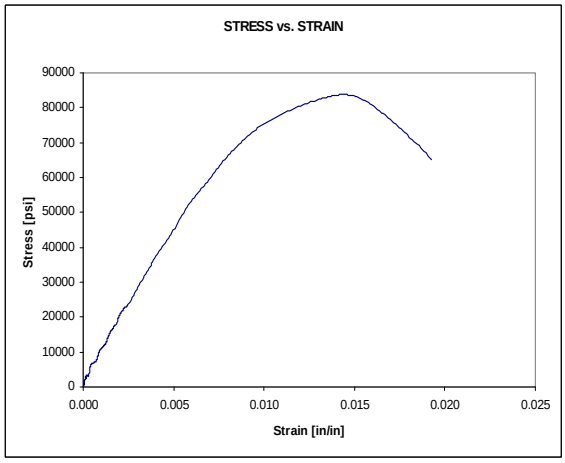

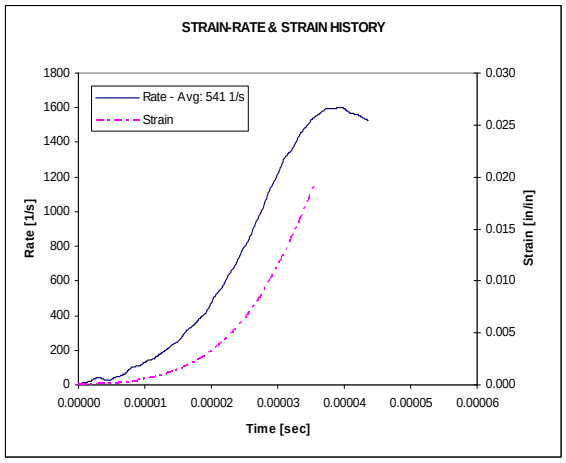

Figure C-84. Stress-Strain Curves for [0°] Cytec T300/97714AC 3KNT PWCF Specimens Tested at Average Strain Rate of 567 s^{-1}

Specimen 1

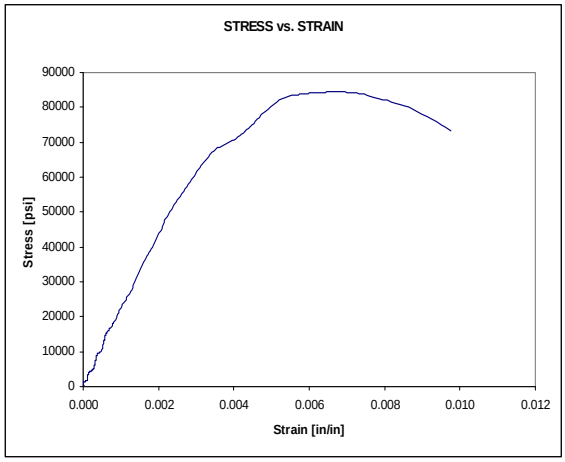

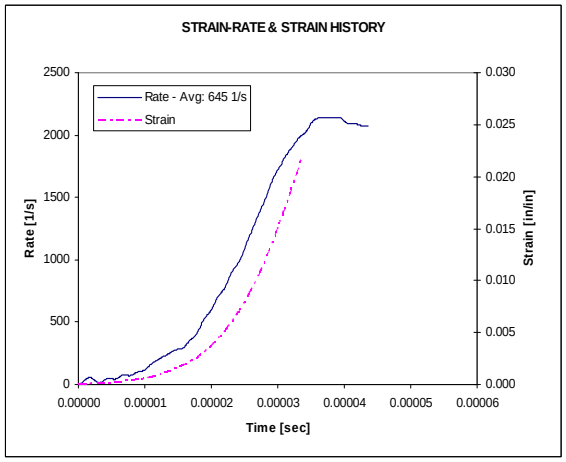

Specimen 2

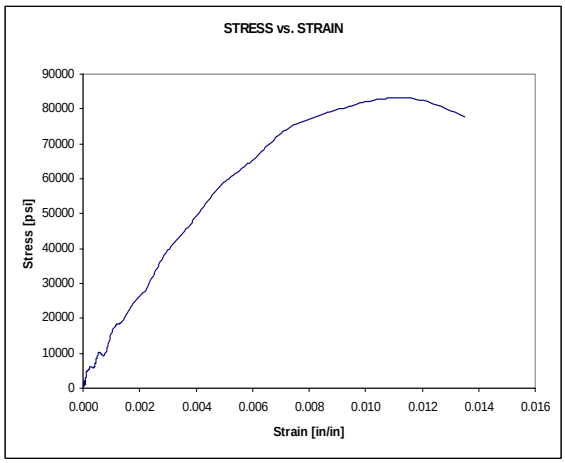

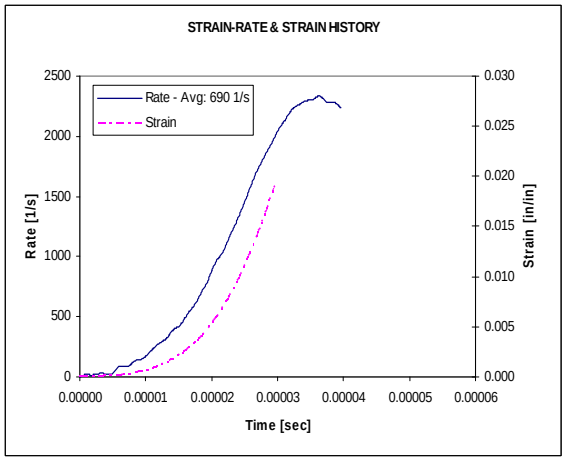

Specimen 3

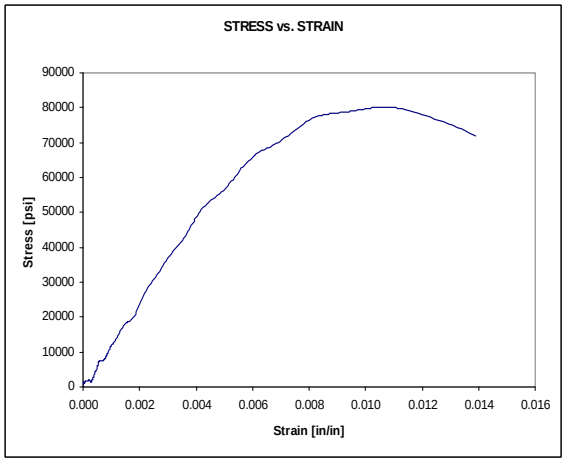

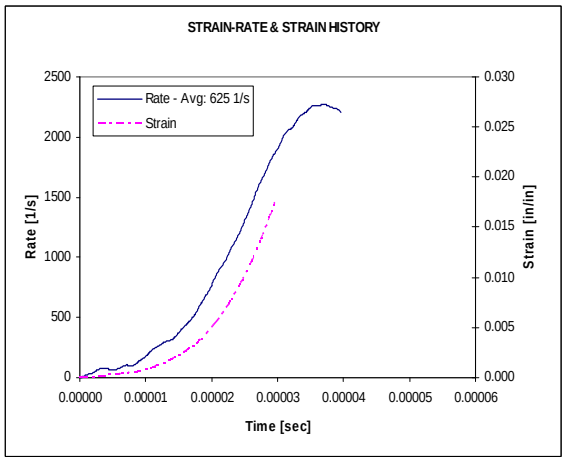

Figure C-85. Stress-Strain Curves for [0°] Cytec T300/97714AC 3KNT PWCF Specimens Tested at Average Strain Rate of 653 s^{-1}

Specimen 1

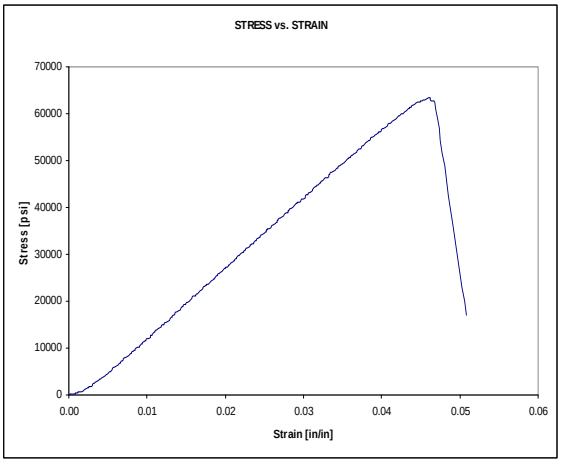

Specimen 2

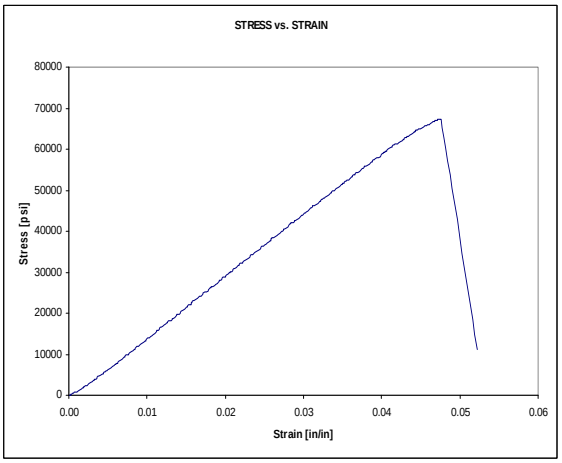

Specimen 3

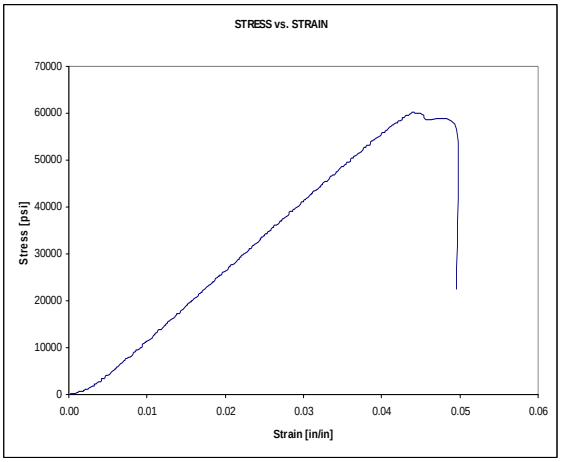

Figure C-86. Stress-Strain Curves for $[+15°/-15°]_{NS}$ Cytec T300/97714AC 3KNT PWCF Specimens Tested at Average Strain Rate of 0.00167 s^{-1}

Specimen 1

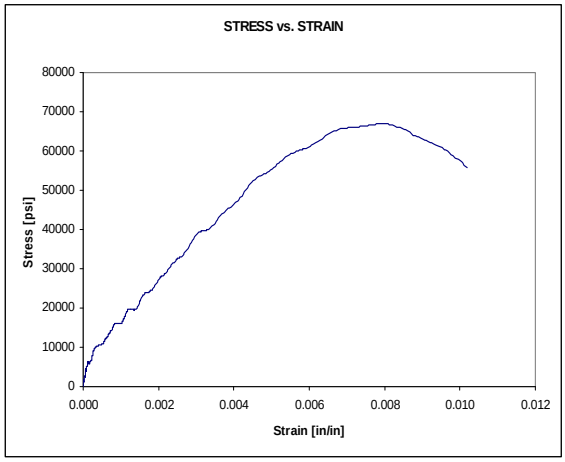

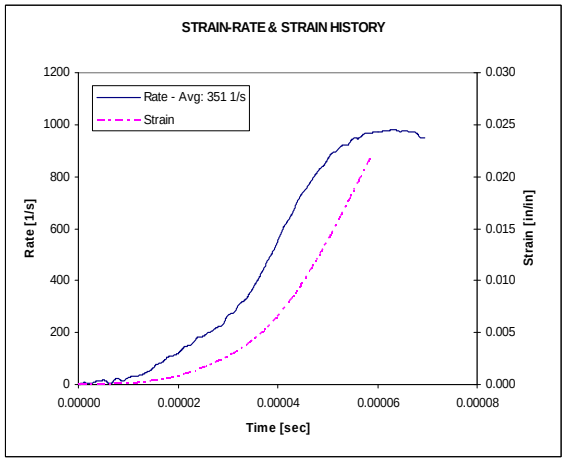

Specimen 2

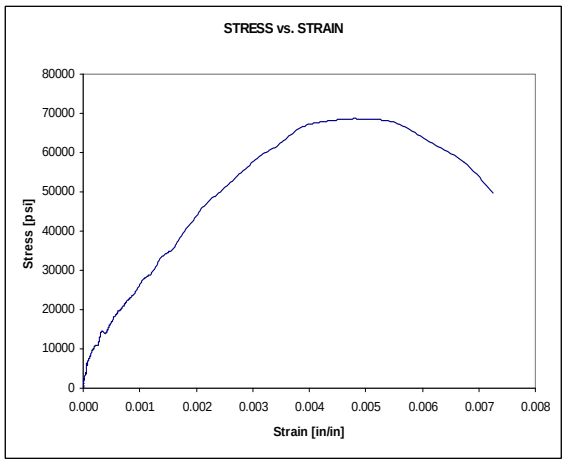

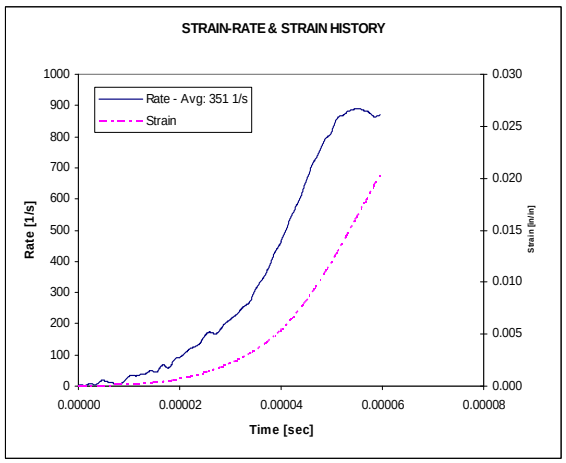

Specimen 3

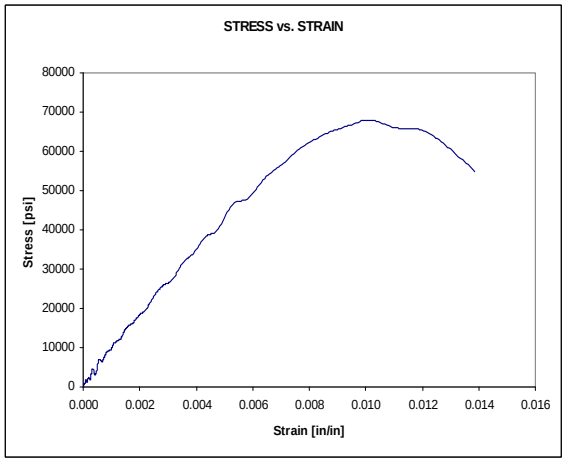

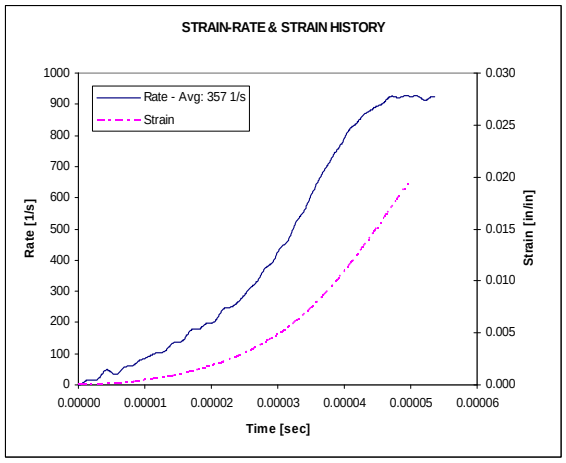

Figure C-87. Stress-Strain Curves for $[+15°/-15°]_{NS}$ Cytec T300/97714AC 3KNT PWCF Specimens Tested at Average Strain Rate of 353 s^{-1}

Specimen 1

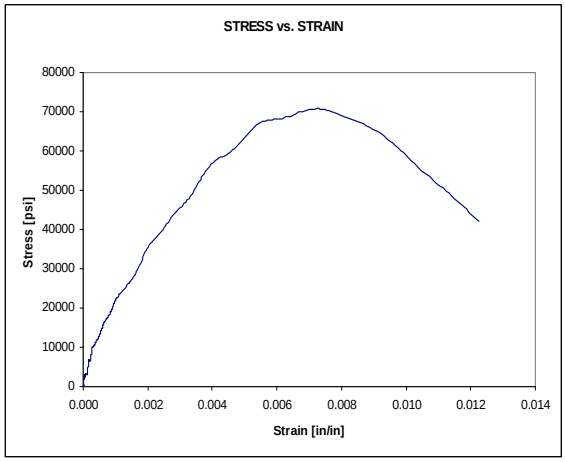

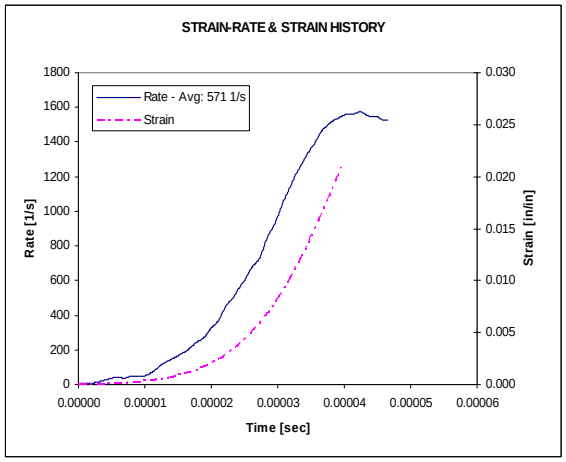

Specimen 2

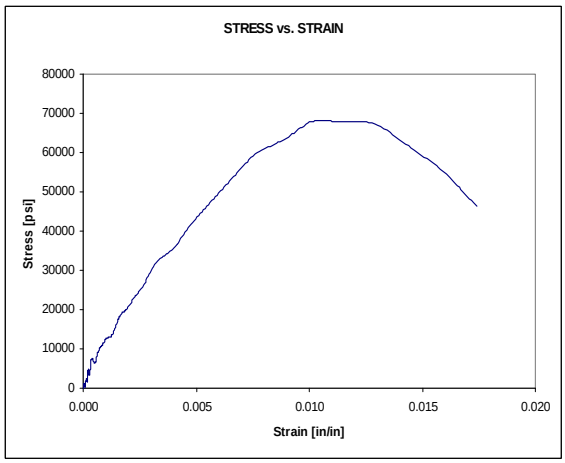

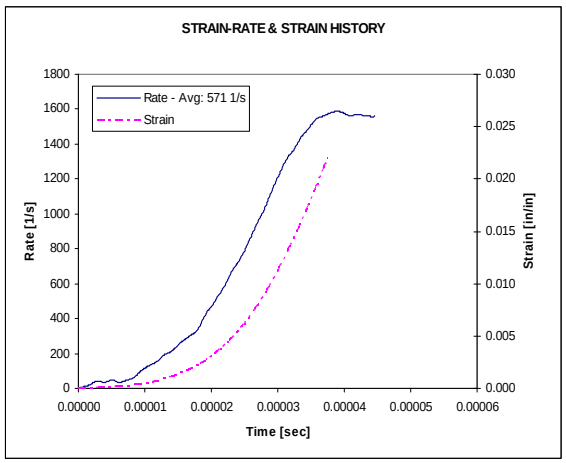

Specimen 3

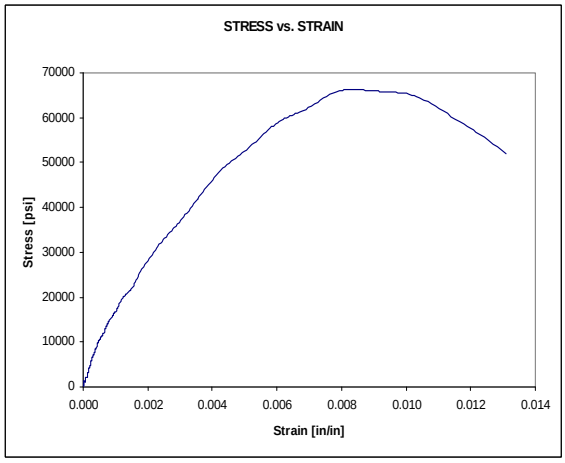

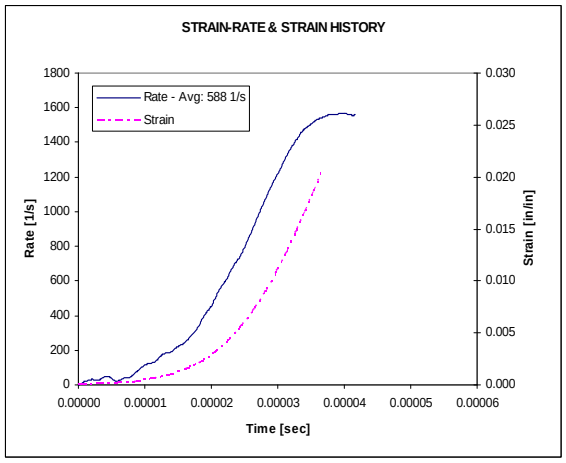

Figure C-88. Stress-Strain Curves for $[+15°/-15°]_{NS}$ Cytec T300/97714AC 3KNT PWCF Specimens Tested at Average Strain Rate of 577 s^{-1}

Specimen 1

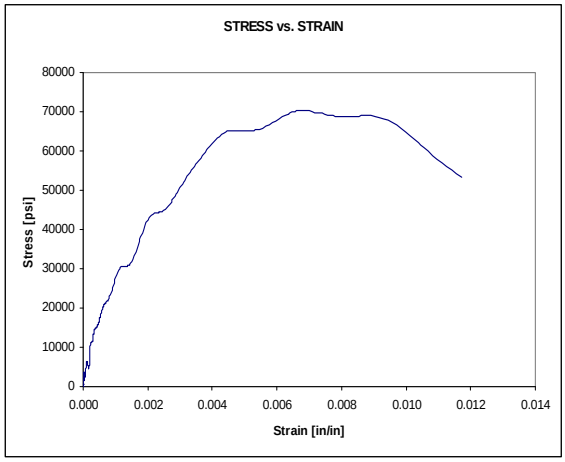

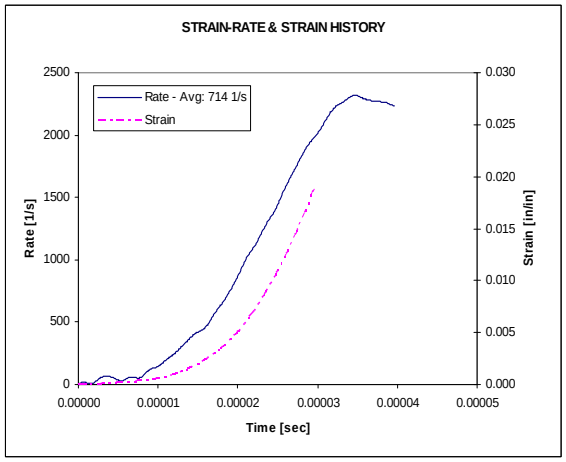

Specimen 2

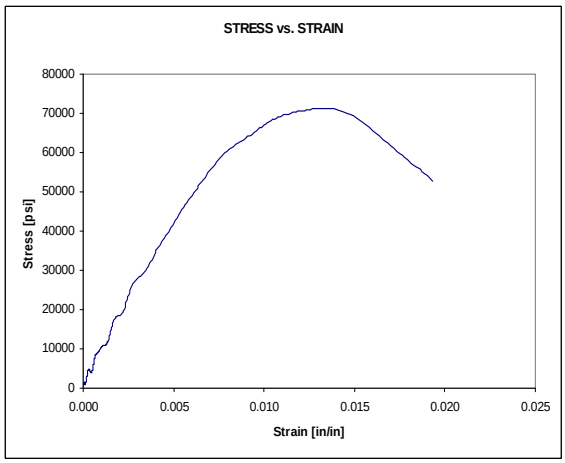

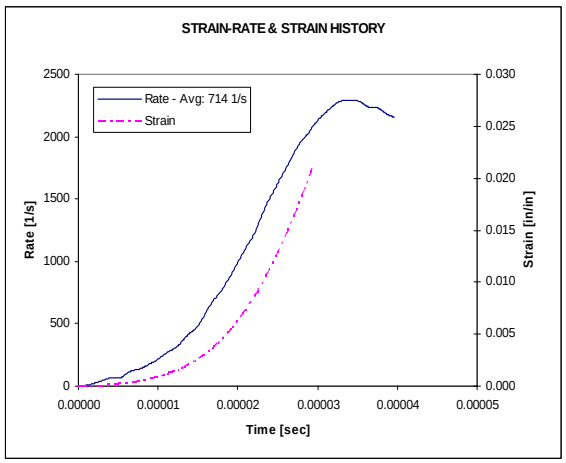

Specimen 3

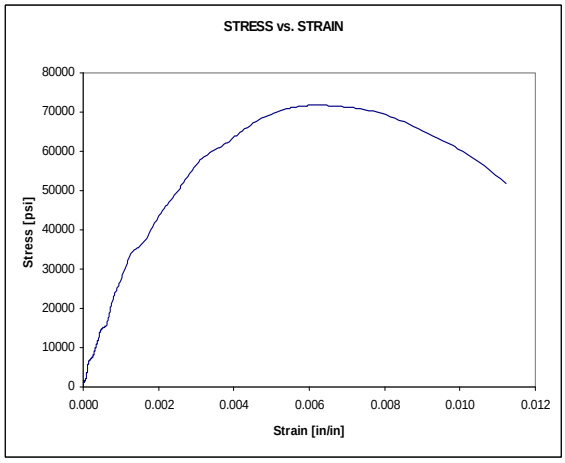

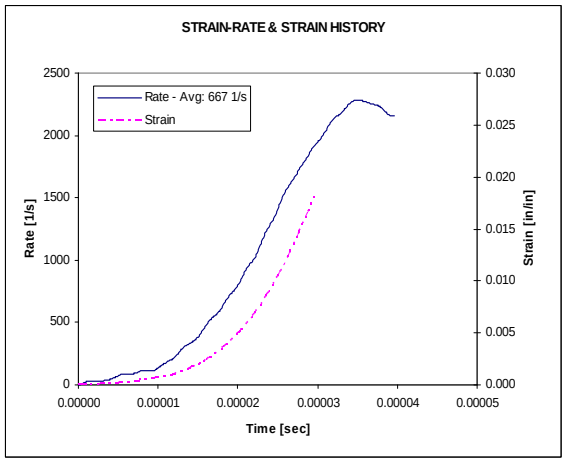

Figure C-89. Stress-Strain Curves for $[+15°/-15°]_{NS}$ Cytec T300/97714AC 3KNT PWCF Specimens Tested at Average Strain Rate of 698 s^{-1}

Specimen 1

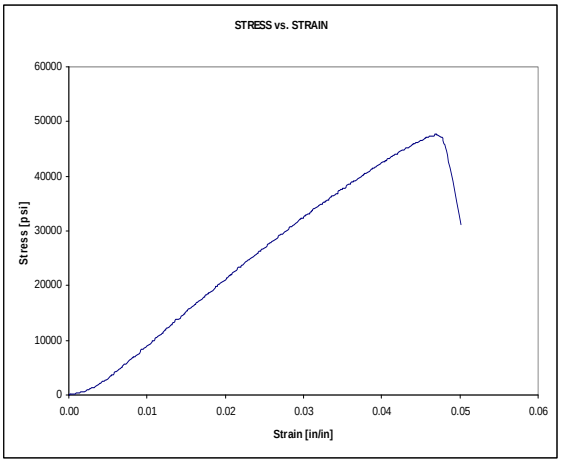

Specimen 2

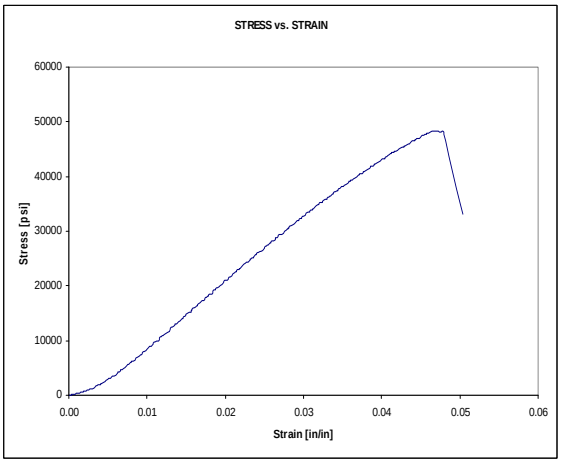

Specimen 3

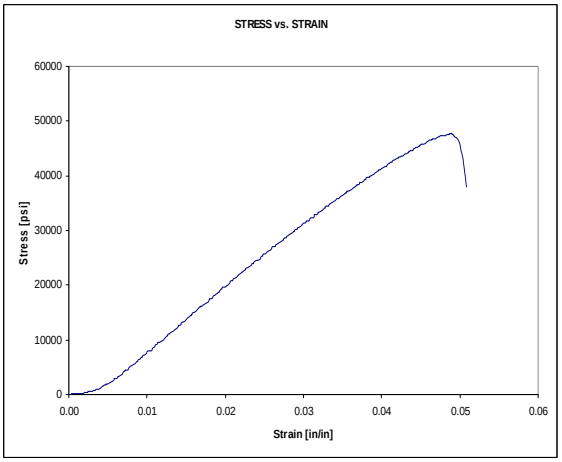

Figure C-90. Stress-Strain Curves for $[+30°/-30°]_{NS}$ Cytec T300/97714AC 3KNT PWCF Specimens Tested at Average Strain Rate of 0.00167 s^{-1}

Specimen 1

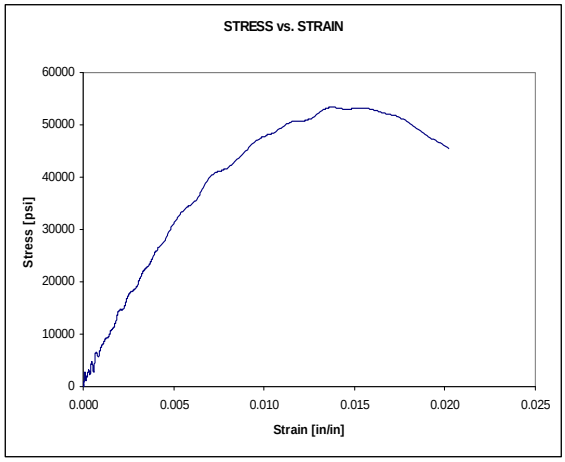

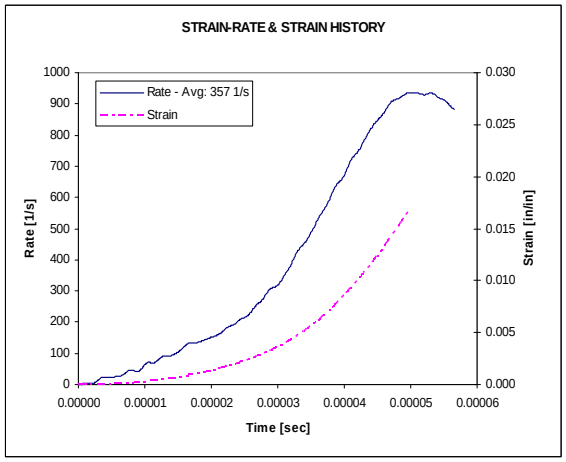

Specimen 2

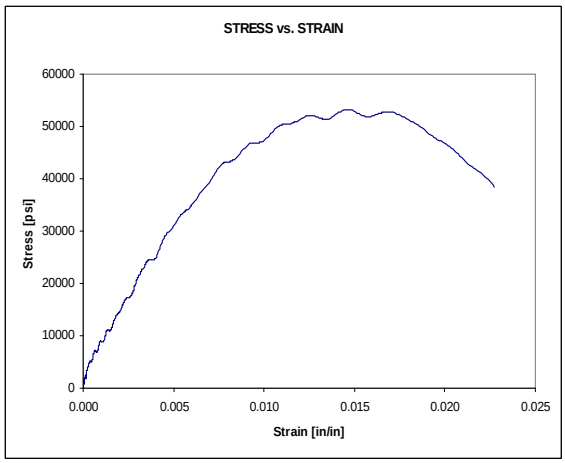

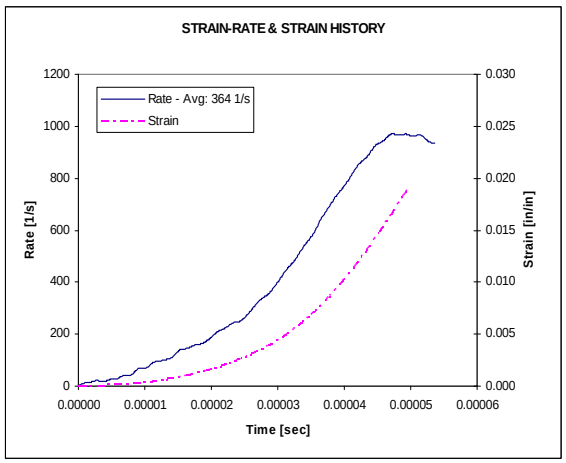

Specimen 3

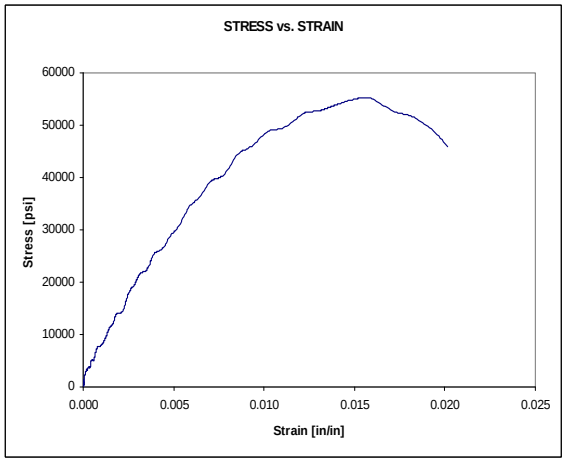

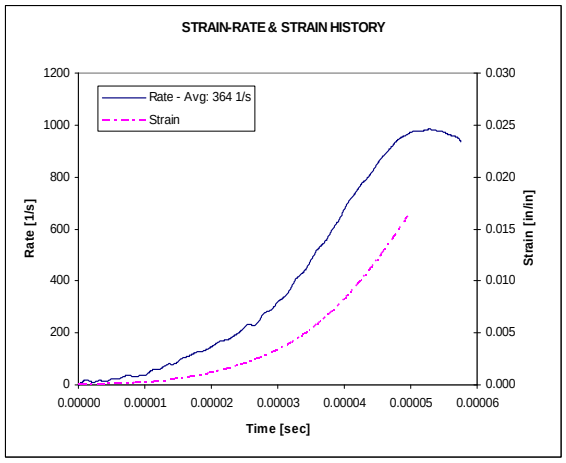

Figure C-91. Stress-Strain Curves for $[+30°/-30°]_{NS}$ Cytec T300/97714AC 3KNT PWCF Specimens Tested at Average Strain Rate of 361 s^{-1}

Specimen 1

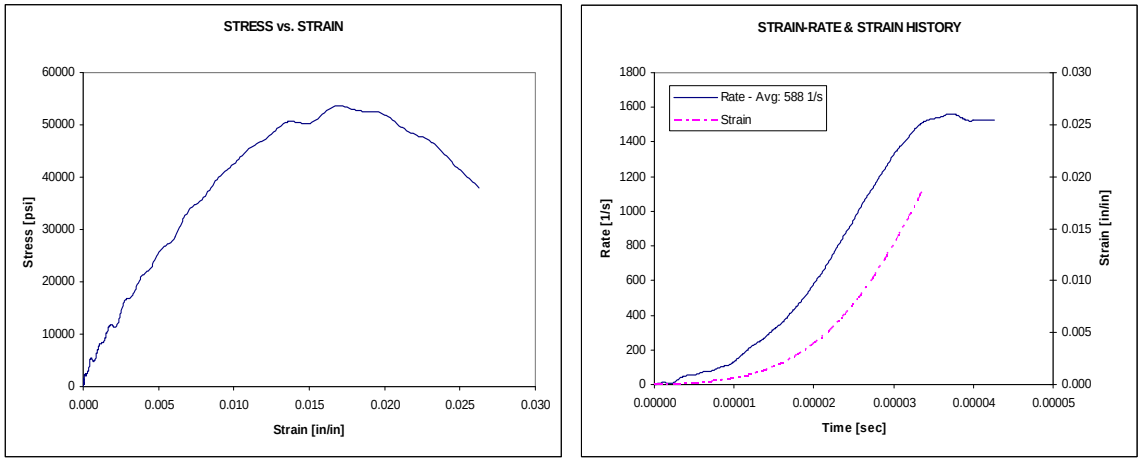

Specimen 2

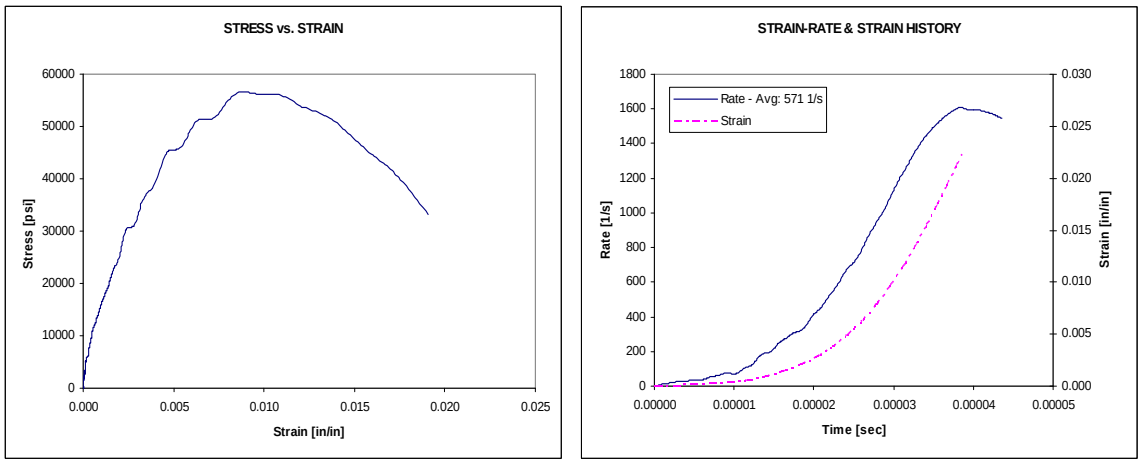

Specimen 3

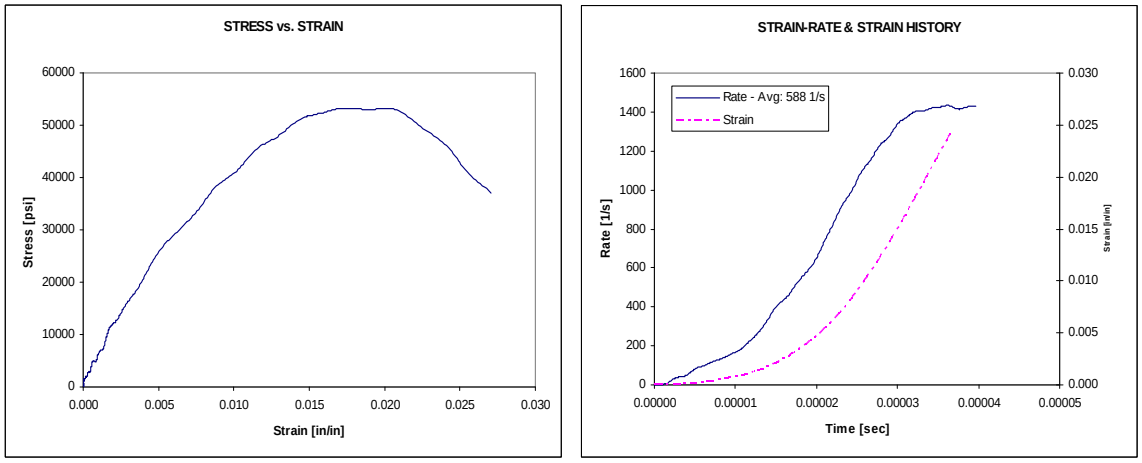

Figure C-92. Stress-Strain Curves for $[+30°/-30°]_{NS}$ Cytec T300/97714AC 3KNT PWCF Specimens Tested at Average Strain Rate of 583 s^{-1}

Specimen 1

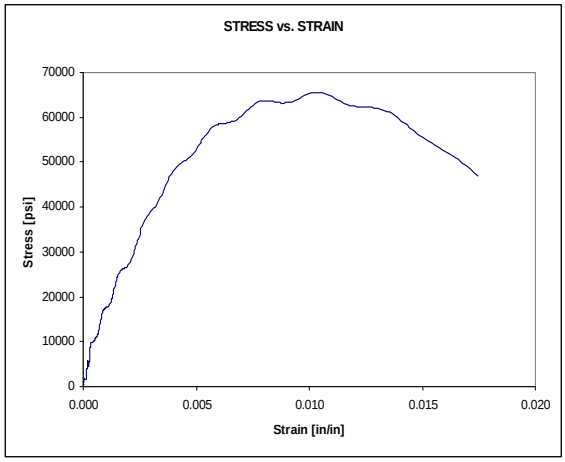

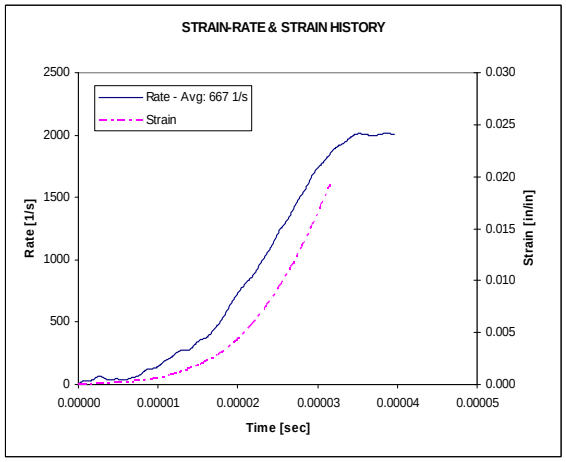

Specimen 2

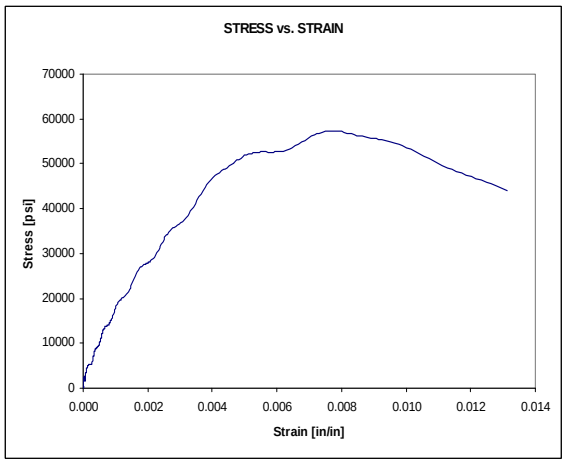

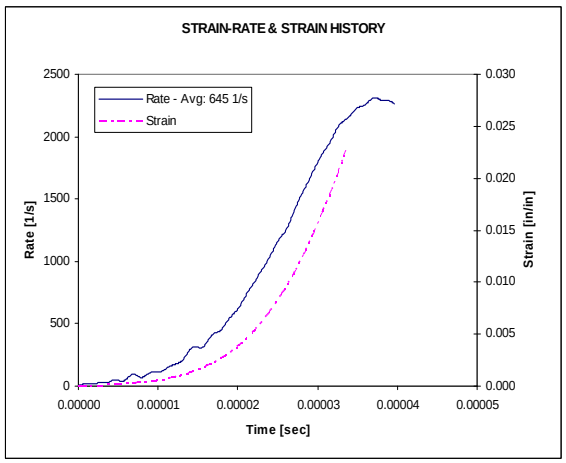

Specimen 3

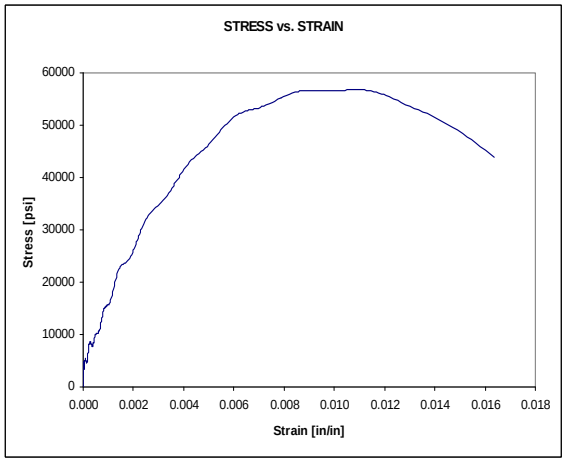

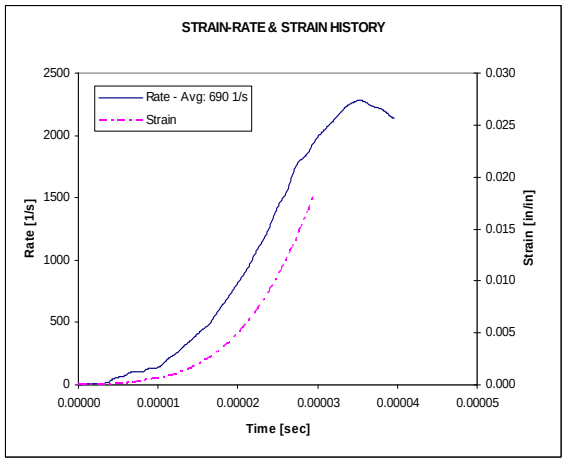

Figure C-93. Stress-Strain Curves for $[+30°/-30°]_{NS}$ Cytec T300/97714AC 3KNT PWCF Specimens Tested at Average Strain Rate of 667 s^{-1}

Specimen 1

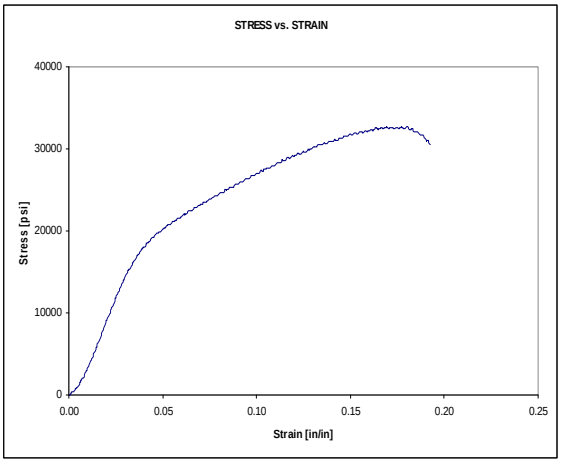

Specimen 2

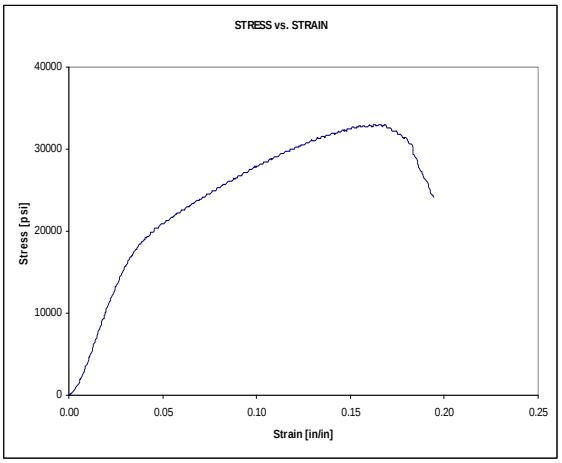

Specimen 3

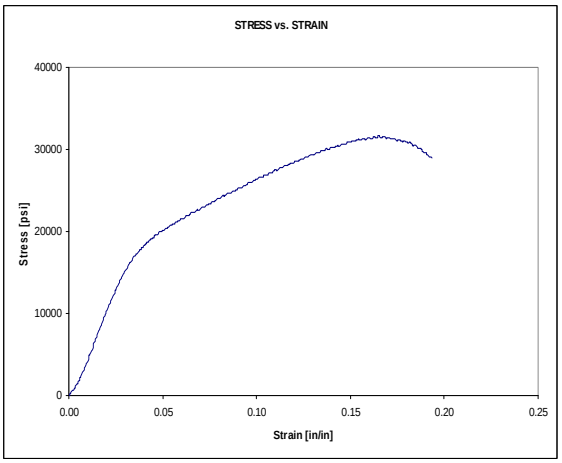

Figure C-94. Stress-Strain Curves for $[+45°/-45°]_{NS}$ Cytec T300/97714AC 3KNT PWCF Specimens Tested at Average Strain Rate of 0.00167 s^{-1}

Specimen 1

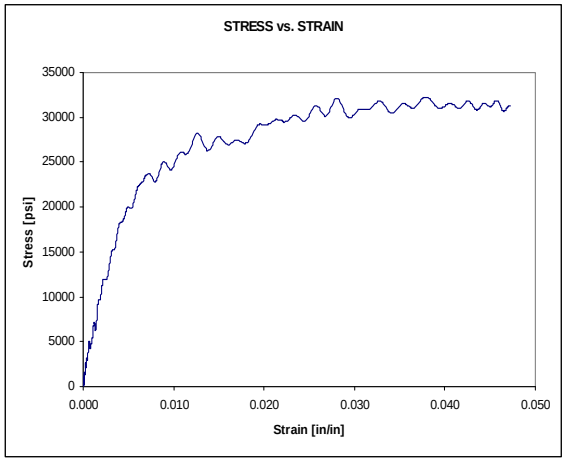

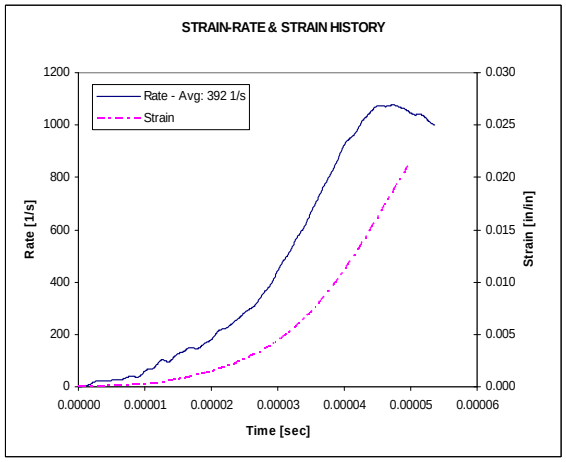

Specimen 2

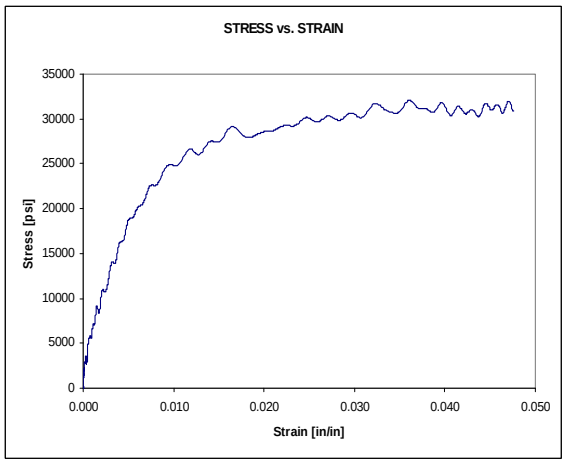

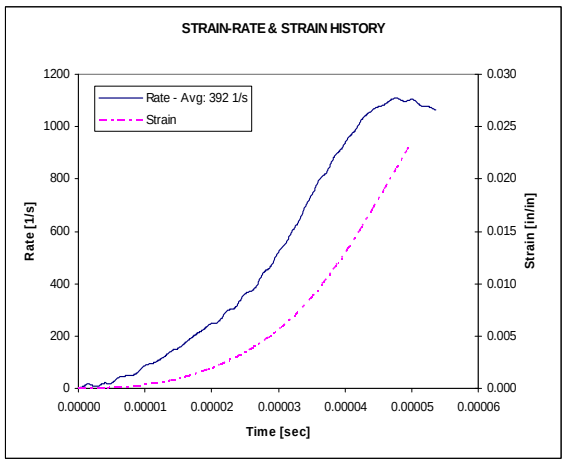

Specimen 3

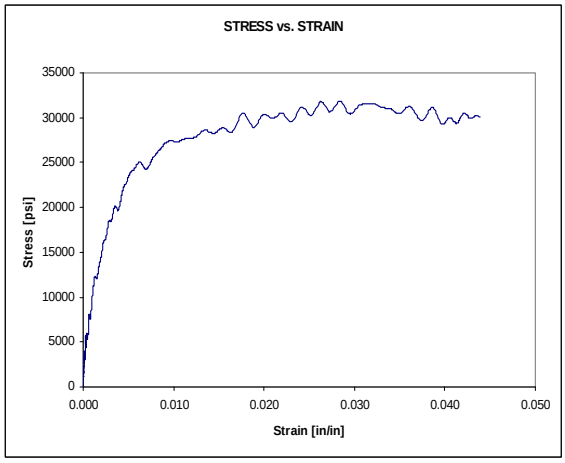

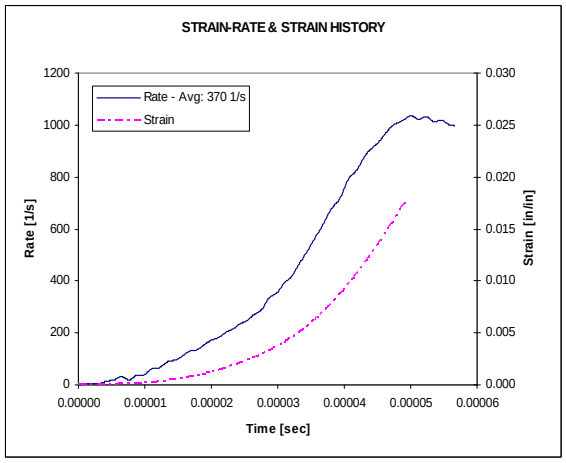

Figure C-95. Stress-Strain Curves for $[+45°/-45°]_{NS}$ Cytec T300/97714AC 3KNT PWCF Specimens Tested at Average Strain Rate of 385 s^{-1}

Specimen 1

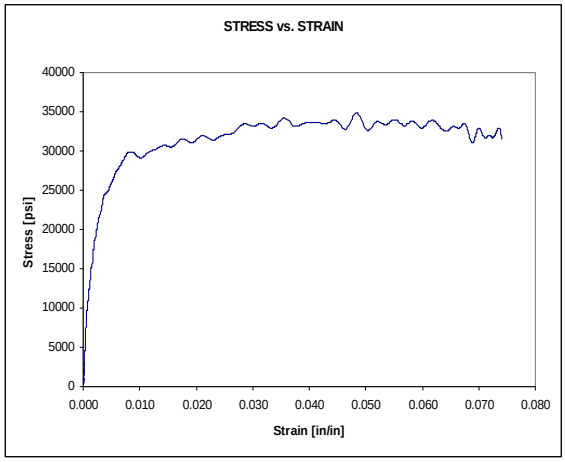

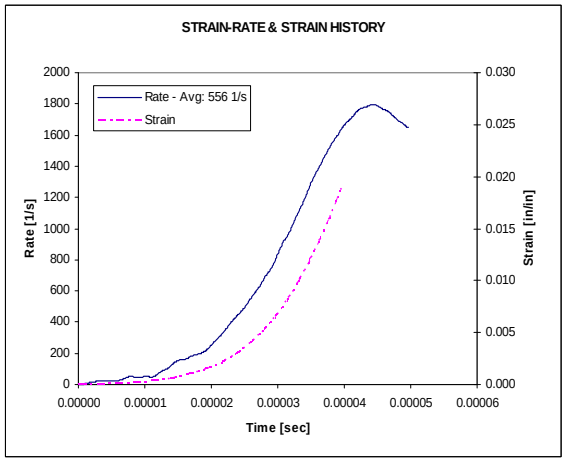

Specimen 2

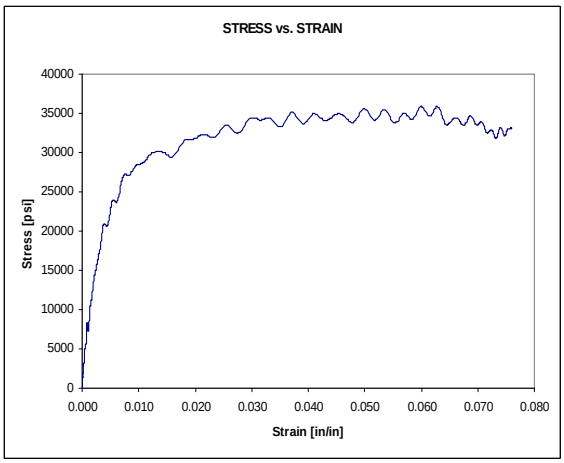

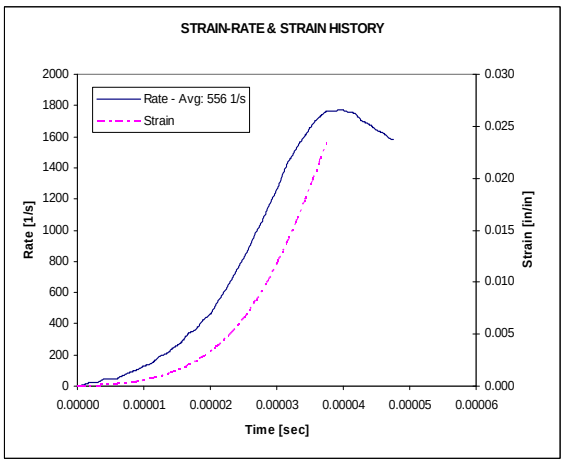

Specimen 3

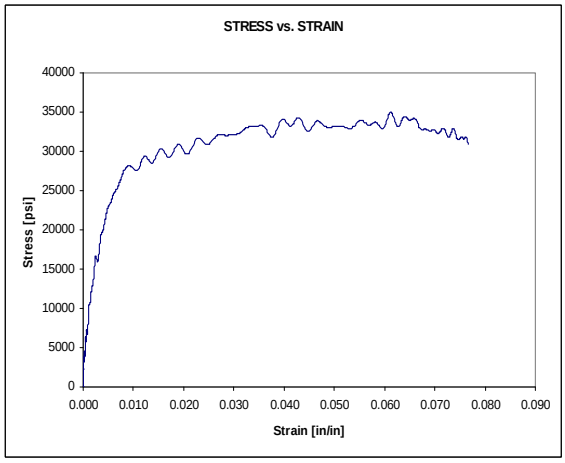

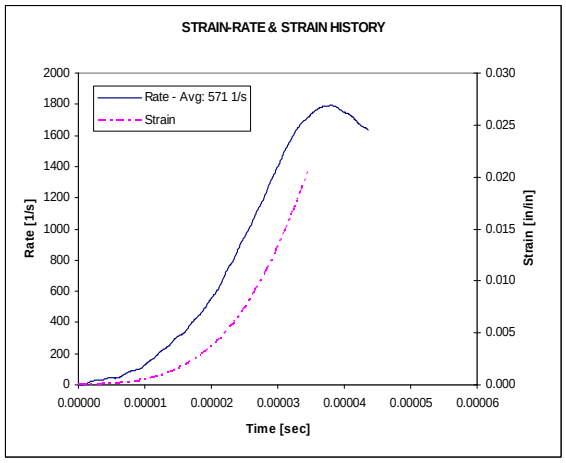

Figure C-96. Stress-Strain Curves for $[+45°/-45°]_{NS}$ Cytec T300/97714AC 3KNT PWCF Specimens Tested at Average Strain Rate of 561 s^{-1}

Specimen 1

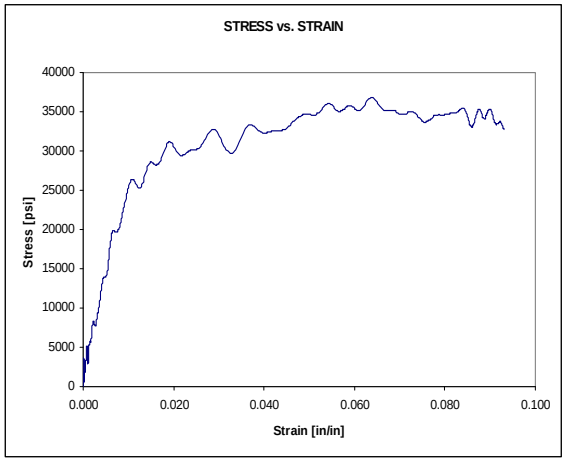

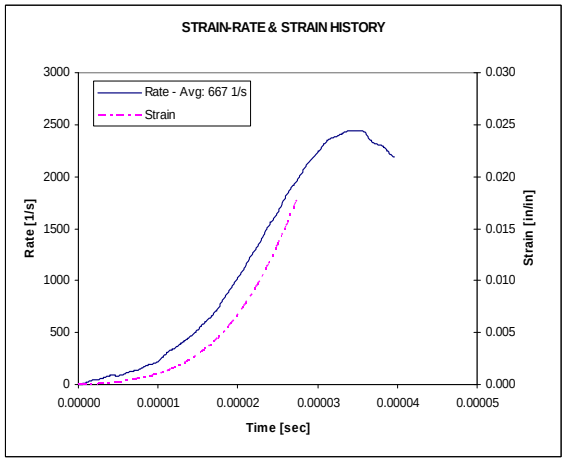

Specimen 2

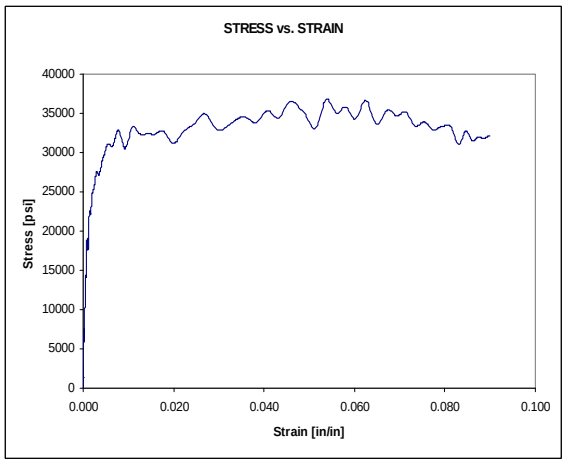

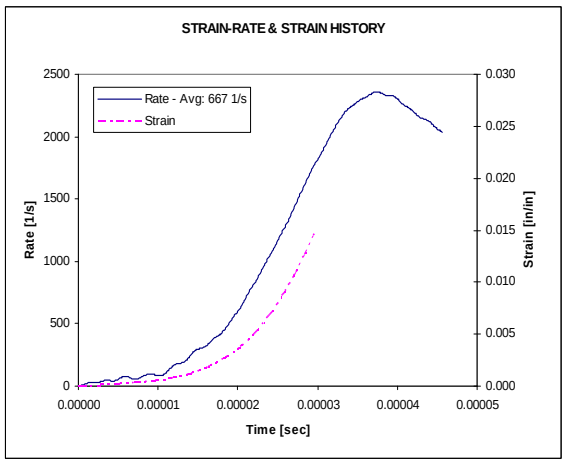

Specimen 3

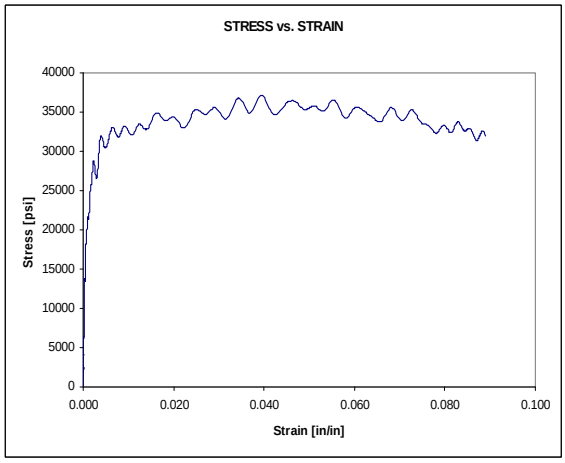

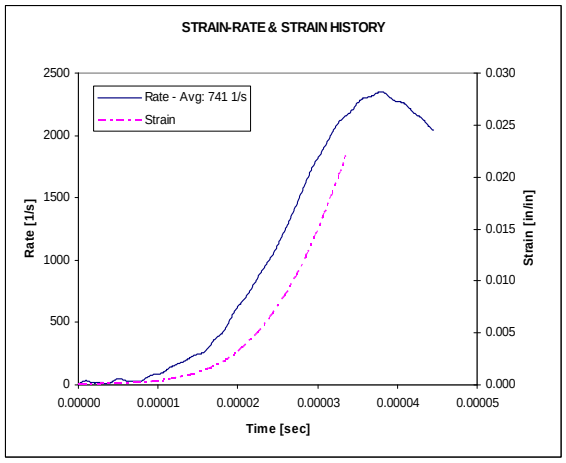

Figure C-97. Stress-Strain Curves for $[+45°/-45°]_{NS}$ Cytec T300/97714AC 3KNT PWCF Specimens Tested at Average Strain Rate of 691 s^{-1}

Table C-7. Summary of Failure Strengths and Strain Rates for Fibercote 3KPW-E365 PWCF

Orientation (degrees)	Average Strain Rate (1/s)	Actual Strain Rate (1/s)	Failure Strength (psi)	Average Failure Strength (psi)
0	0.00167	0.00167	70,152	68,154
		0.00167	62,824	
		0.00167	71,485	
	1	1	88,205	88,925
		1	89,644	
	414	426	86,339	80,467
		408	84,494	
		408	70,567	
	600	606	92,739	90,907
		588	89,441	
		606	90,542	
	674	690	80,395	88,203
		667	93,710	
		667	90,503	
15	0.00167	0.00167	76,385	72,502
		0.00167	71,618	
		0.00167	69,503	
	1	1	64,341	70,940
		1	77,538	
	398	377	80,486	72,318
		417	64,003	
		400	72,465	
	600	606	75,012	78,352
		588	76,469	
		606	83,575	
	692	690	80,890	76,819
		645	77,073	
		741	72,493	

Table C-7. Summary of Failure Strengths and Strain Rates for Fibercote 3KPW-E365 PWCF (Continued)

Orientation (degrees)	Average Strain Rate (1/s)	Actual Strain Rate (1/s)	Failure Strength (psi)	Average Failure Strength (psi)
30	0.00167	0.00167	52,856	54,333
		0.00167	53,921	
		0.00167	56,222	
	1	1	53,634	51,483
		1	49,333	
	385	377	54,857	58,157
		400	59,267	
		377	60,347	
	583	606	61,811	61,365
		556	60,504	
		588	61,781	
	662	714	63,646	62,379
		667	63,187	
		606	60,304	
45	0.00167	0.00167	29,745	30,102
		0.00167	28,263	
		0.00167	32,297	
	1	1	32,111	35,924
		1	39,737	
	404	377	35,370	32,726
		400	29,408	
		435	33,401	
	612	625	36,694	36,236
		606	36,222	
		606	35,793	
	707	690	38,093	37,396
		741	37,492	
		690	36,604	

Specimen 1

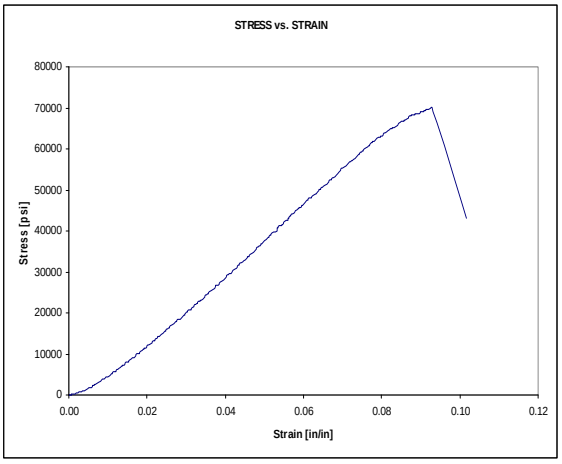

Specimen 2

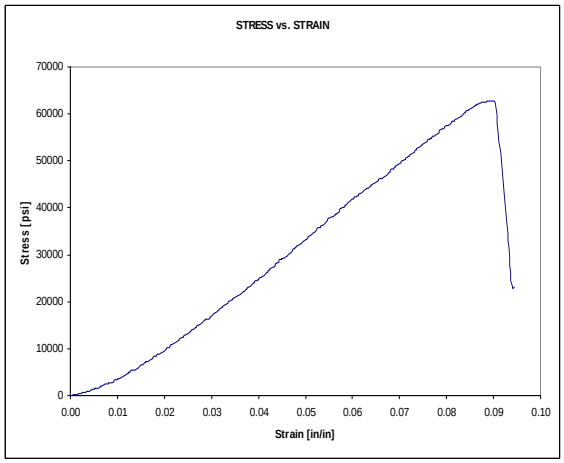

Specimen 3

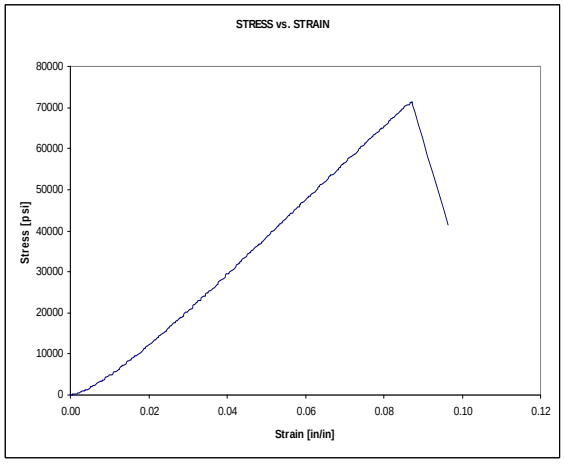

Figure C-98. Stress-Strain Curves for [0°] Fibercote 3KPW-E365 PWCF Specimens Tested at Average Strain Rate of 0.00167 s^{-1}

Specimen 1

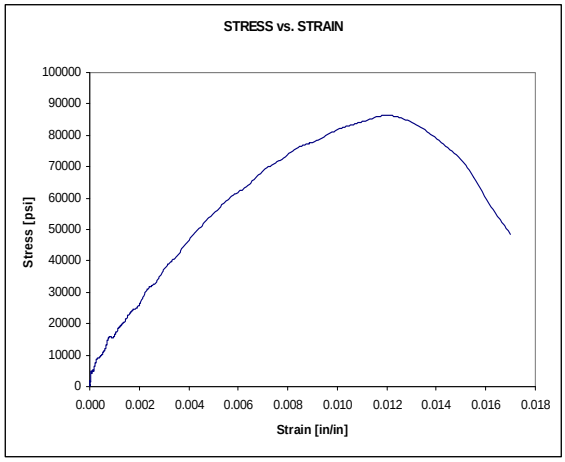

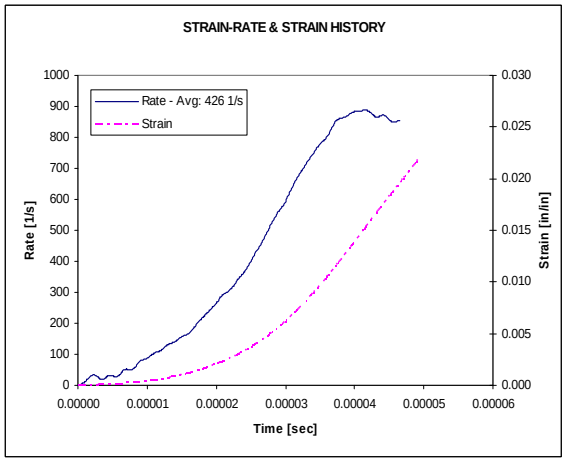

Specimen 2

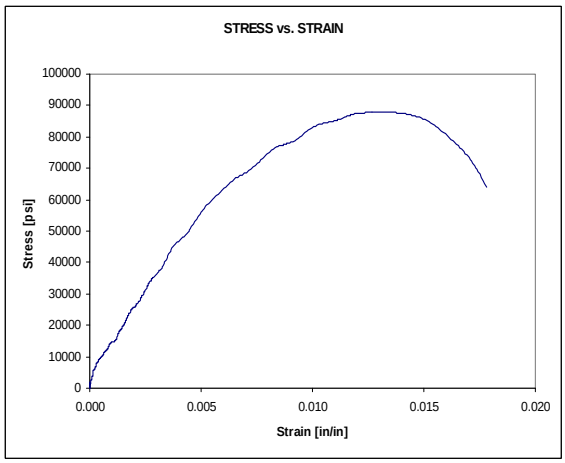

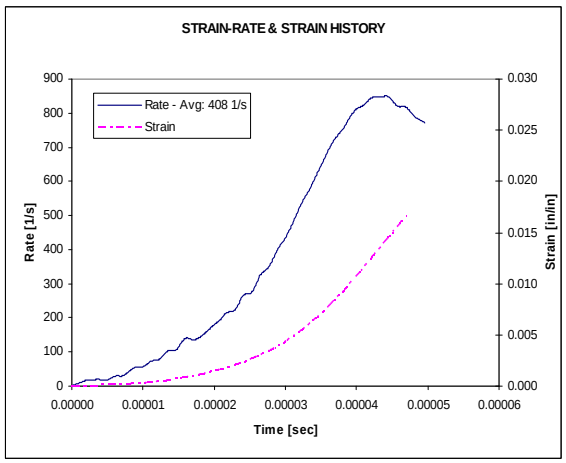

Specimen 3

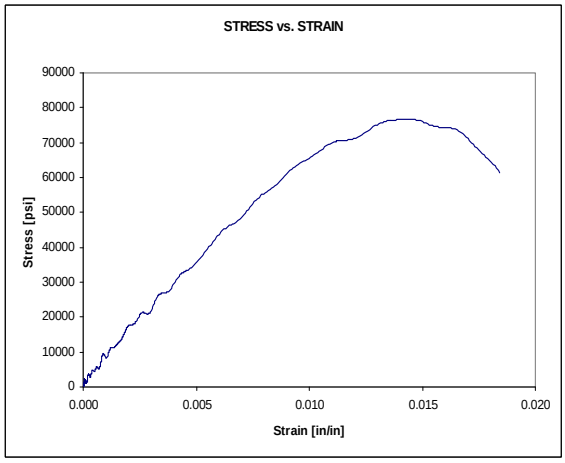

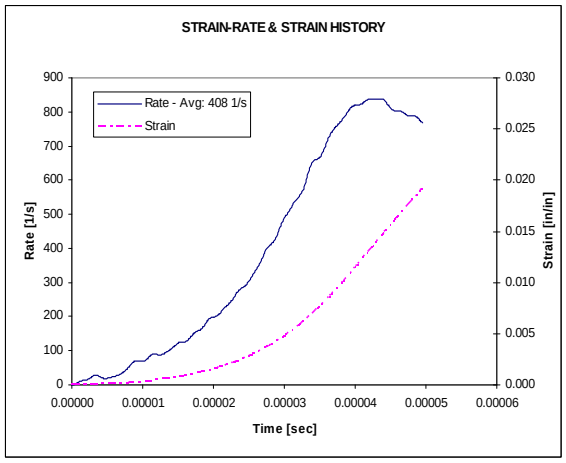

Figure C-99. Stress-Strain Curves for [0°] Fibercote 3KPW-E365 PWCF Specimens Tested at Average Strain Rate of 414 s^{-1}

Specimen 1

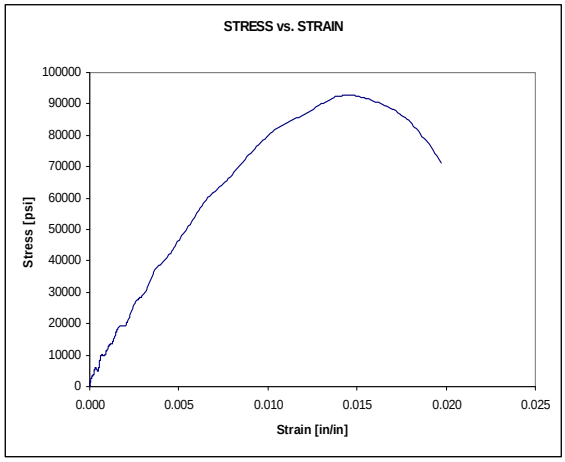

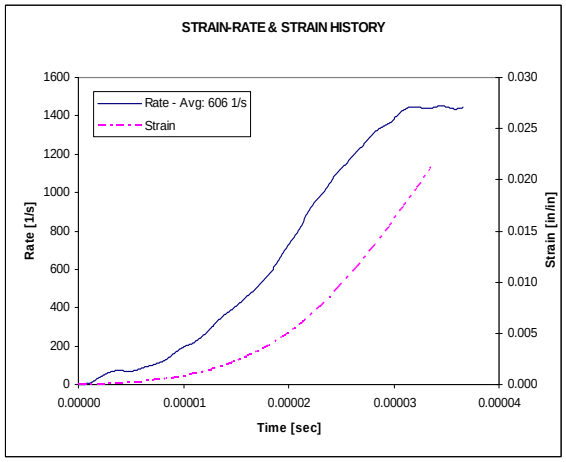

Specimen 2

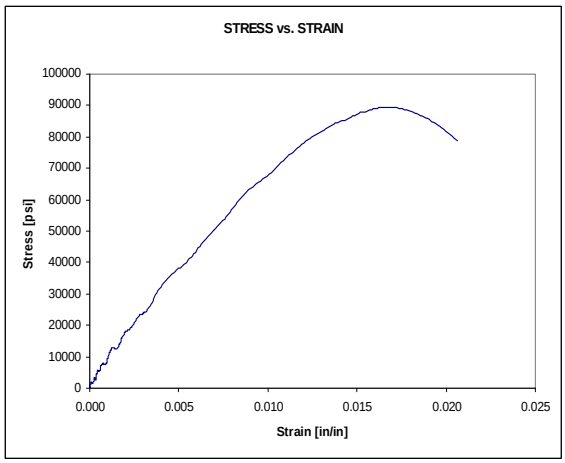

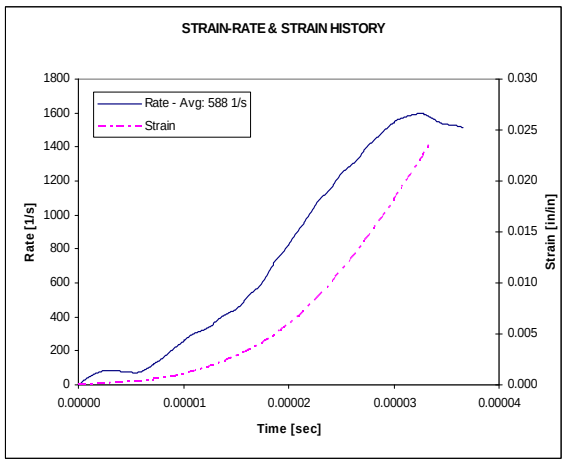

Specimen 3

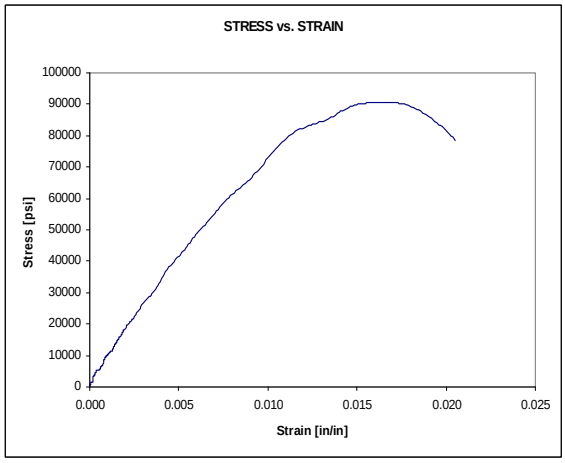

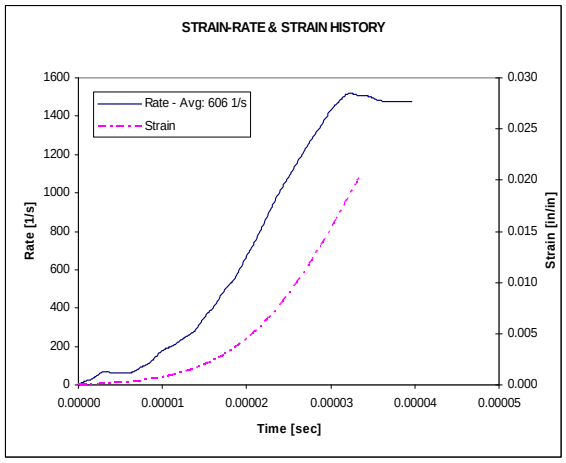

Figure C-100. Stress-Strain Curves for [0°] Fibercote 3KPW-E365 PWCF Specimens Tested at Average Strain Rate of 600 s^{-1}

Specimen 1

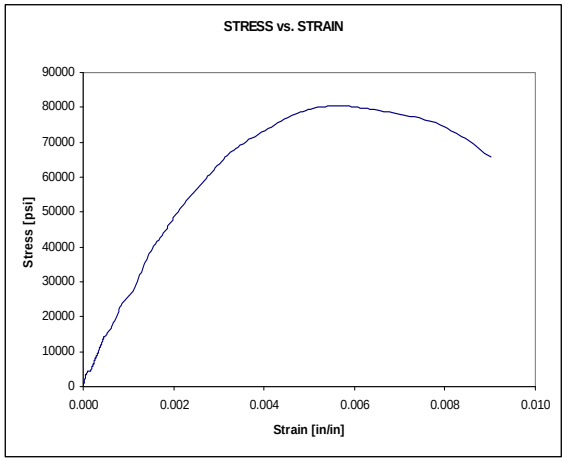

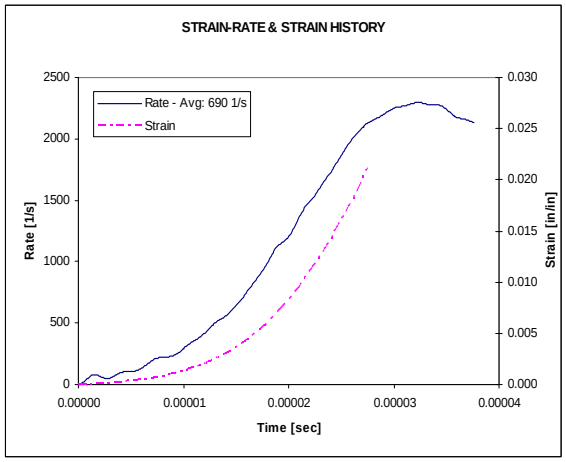

Specimen 2

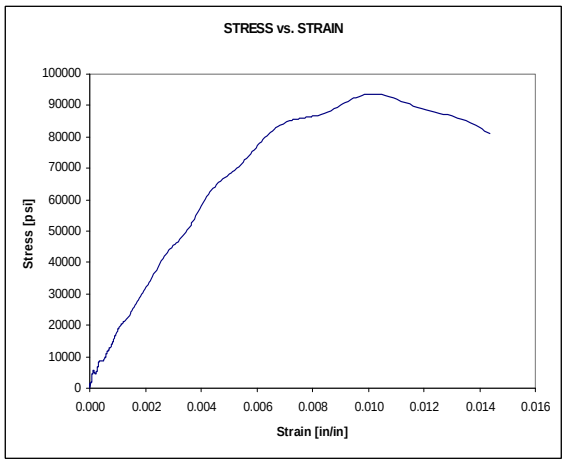

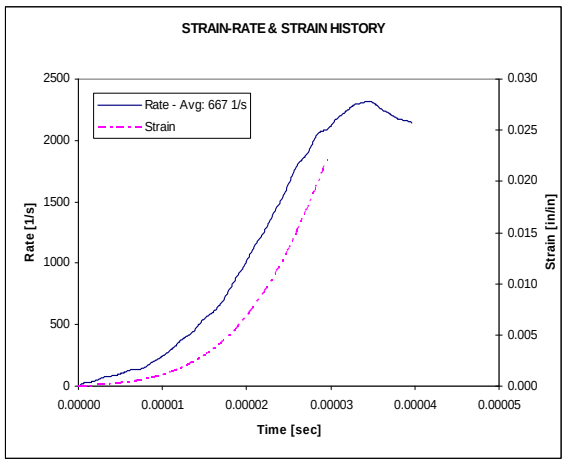

Specimen 3

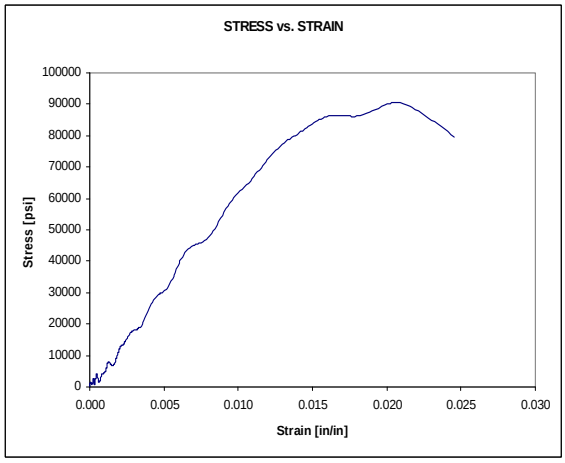

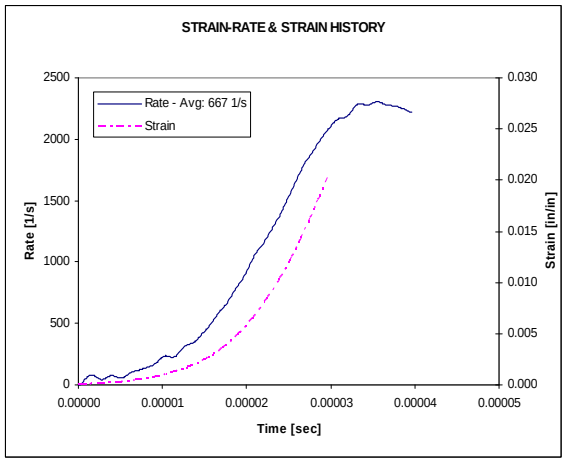

Figure C-101. Stress-Strain Curves for [0°] Fibercote 3KPW-E365 PWCF Specimens Tested at Average Strain Rate of 674 s^{-1}

Specimen 1

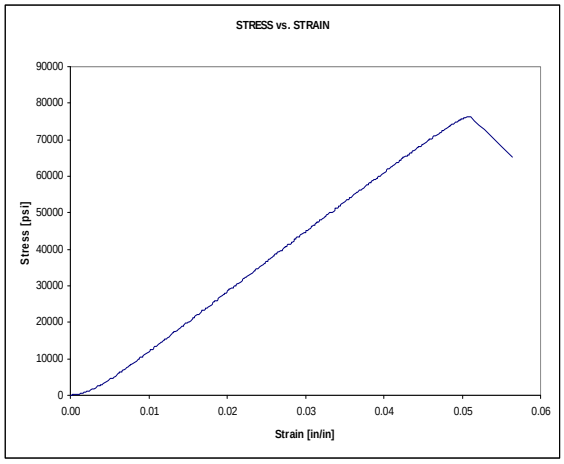

Specimen 2

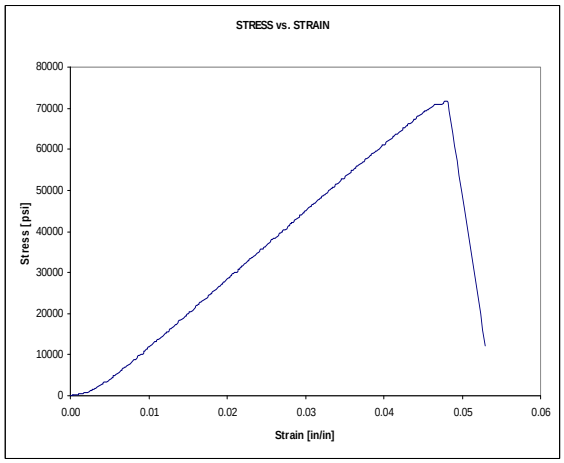

Specimen 3

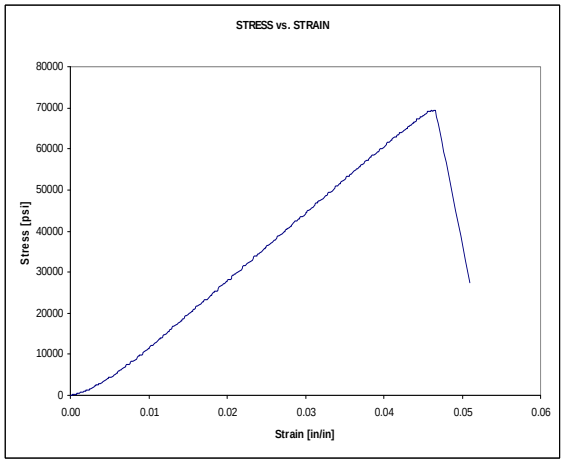

Figure C-102. Stress-Strain Curves for $[[+15°/-15°]_{NS}$ Fibercote 3KPW-E365 PWCF Specimens Tested at Average Strain Rate of 0.00167 s^{-1}

Specimen 1

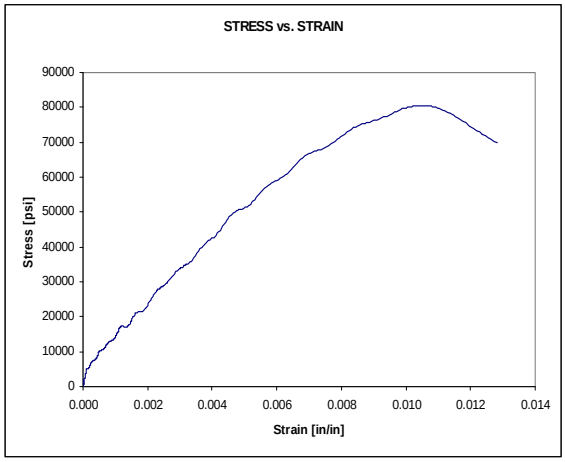

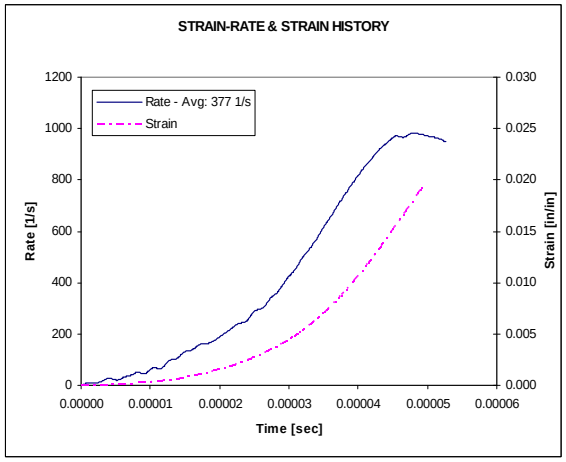

Specimen 2

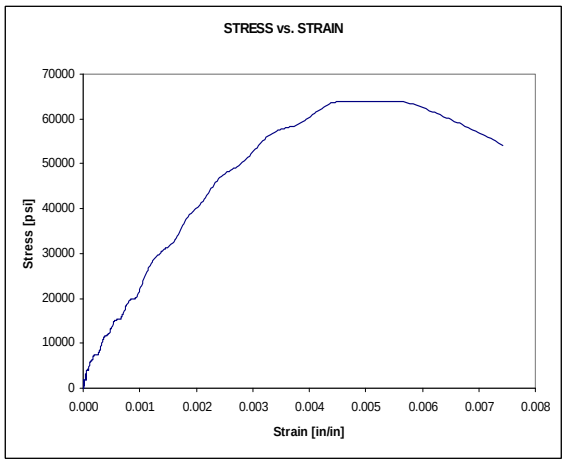

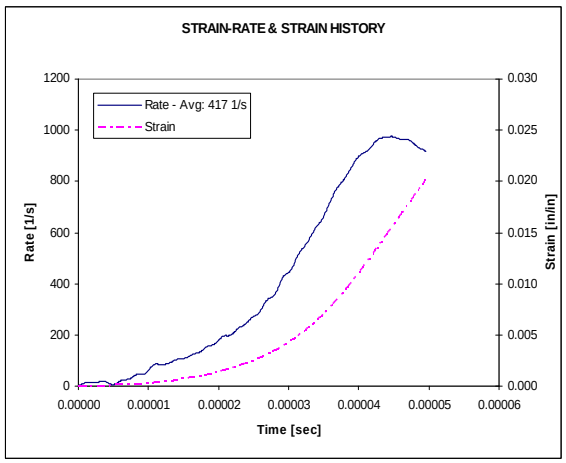

Specimen 3

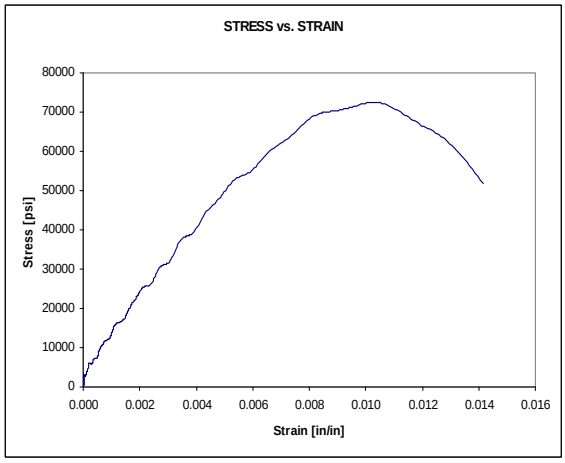

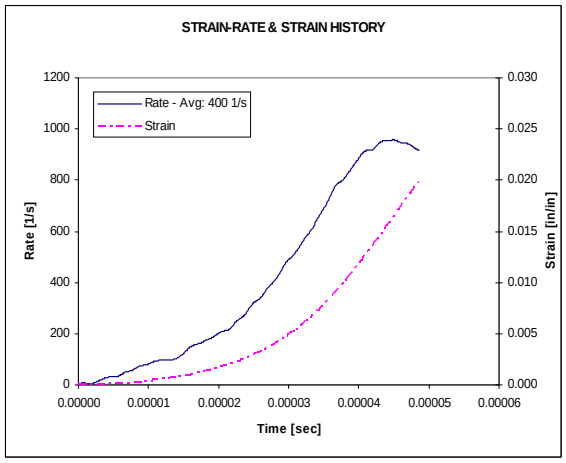

Figure C-103. Stress-Strain Curves for $[+15°/-15°]_{NS}$ Fibercote 3KPW-E365 PWCF Specimens Tested at Average Strain Rate of 398 s^{-1}

Specimen 1

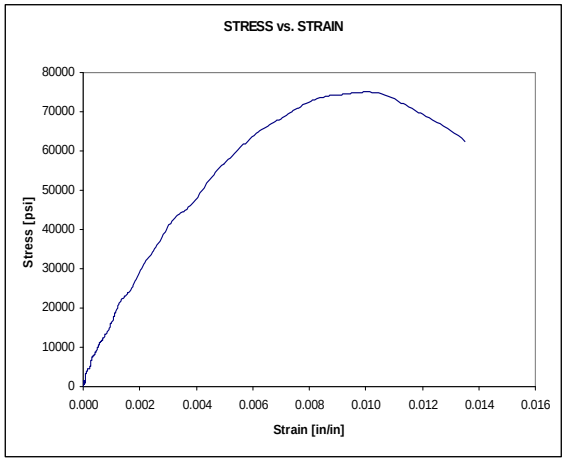

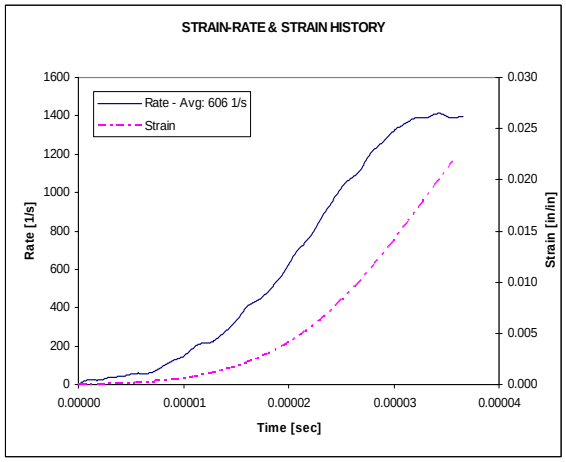

Specimen 2

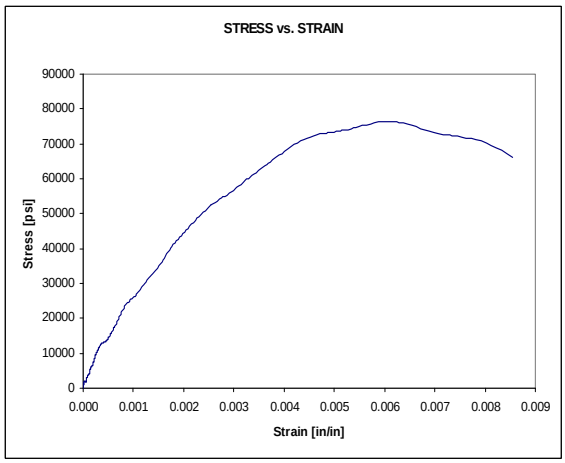

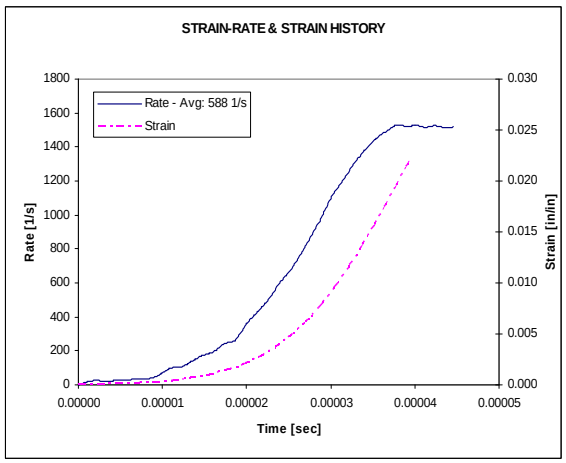

Specimen 3

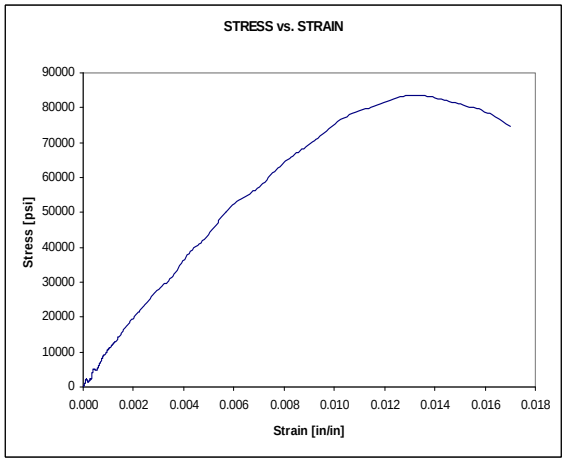

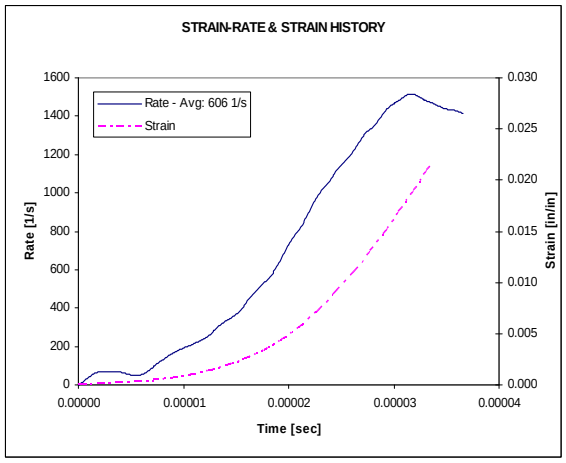

Figure C-104. Stress-Strain Curves for $[+15°/-15°]_{NS}$ Fibercote 3KPW-E365 PWCF Specimens Tested at Average Strain Rate of 600 s^{-1}

Specimen 1

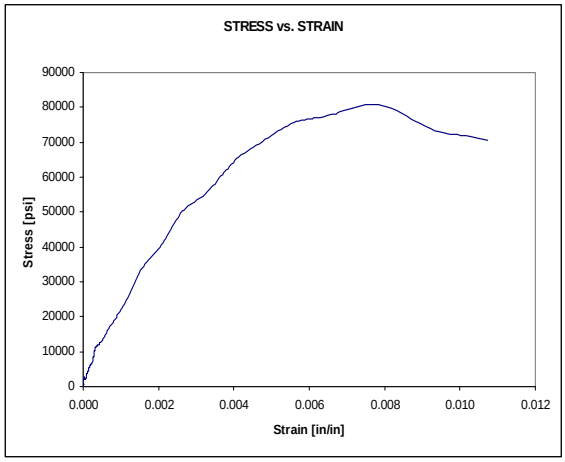

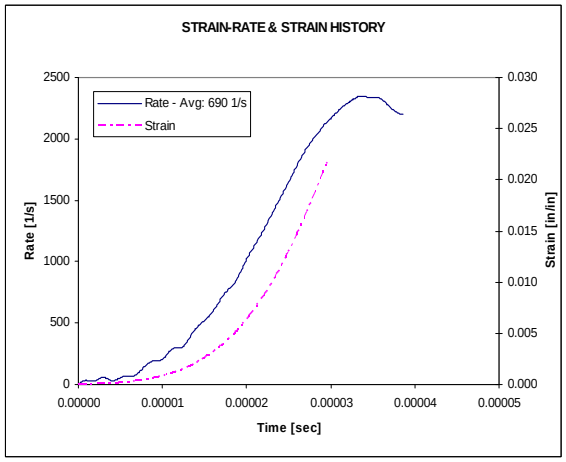

Specimen 2

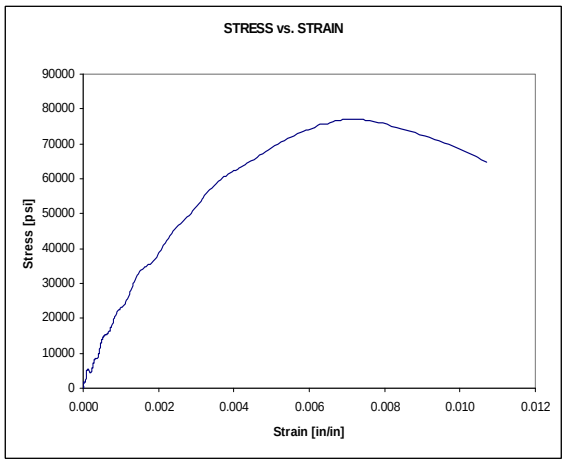

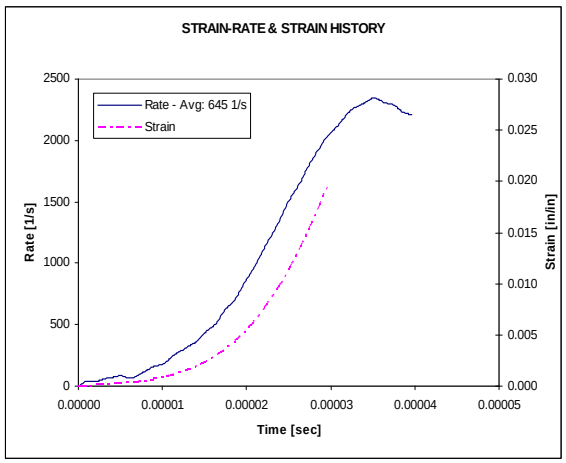

Specimen 3

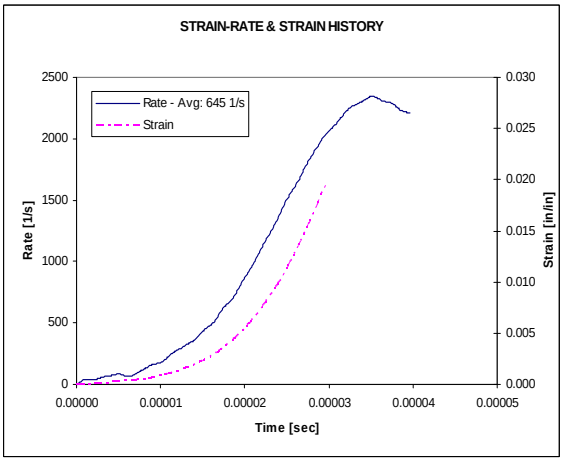

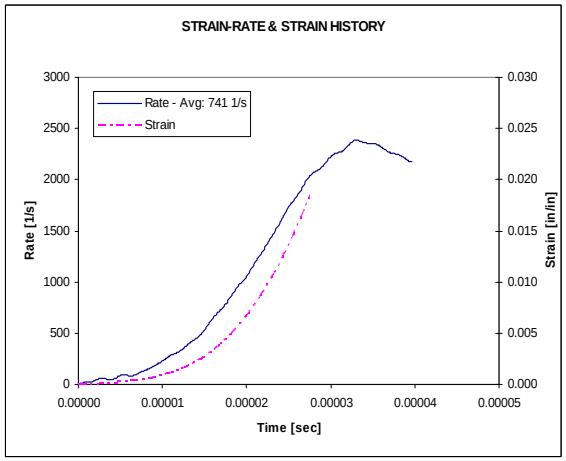

Figure C-105. Stress-Strain Curves for $[+15°/-15°]_{NS}$ Fibercote 3KPW-E365 PWCF Specimens Tested at Average Strain Rate of 692 s^{-1}

Specimen 1

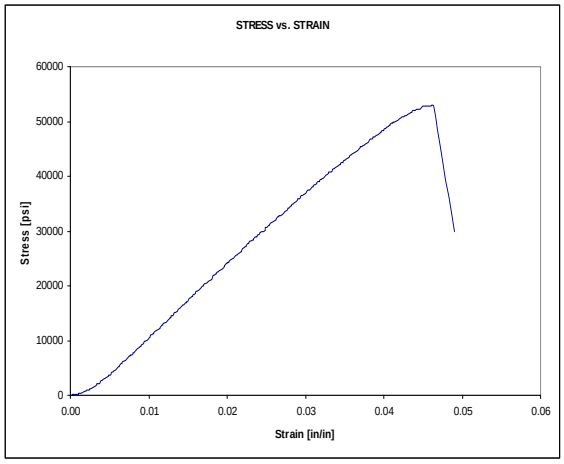

Specimen 2

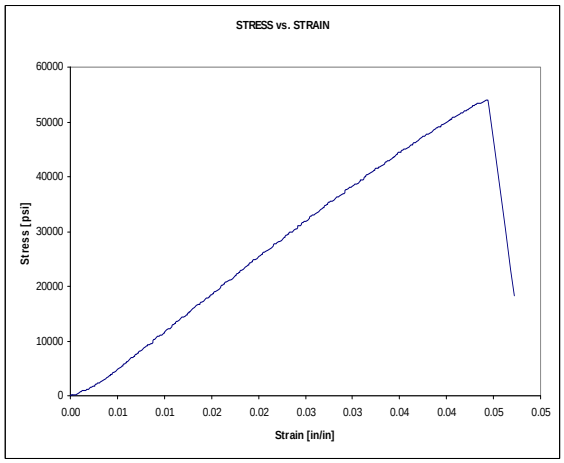

Specimen 3

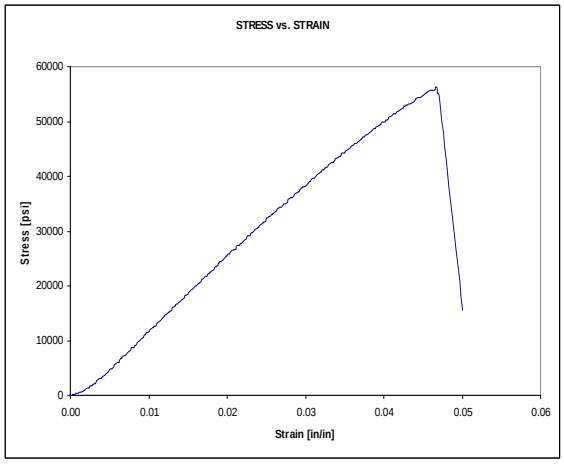

Figure C-106. Stress-Strain Curves for $[+30°/-30°]_{NS}$ Fibercote 3KPW-E365 PWCF Specimens Tested at Average Strain Rate of 0.00167 s^{-1}

Specimen 1

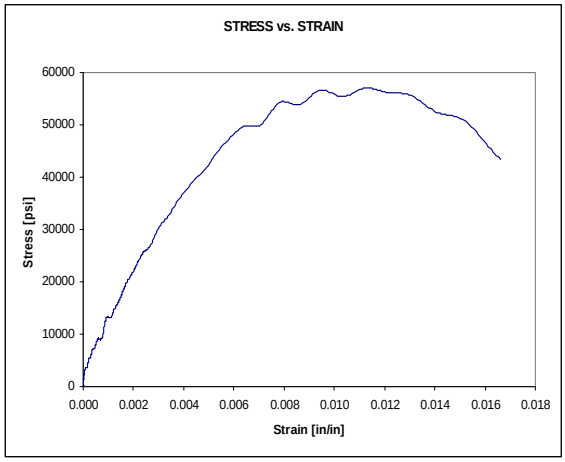

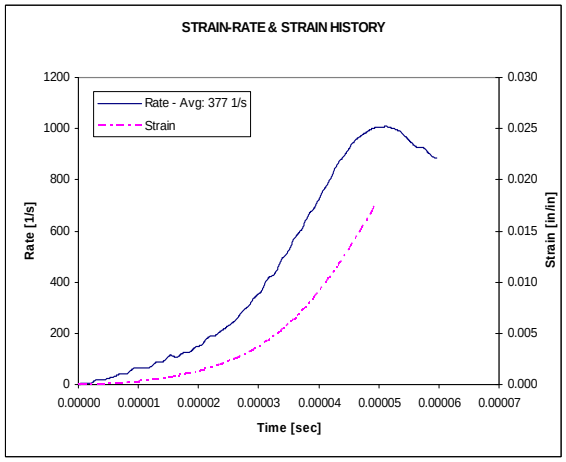

Specimen 2

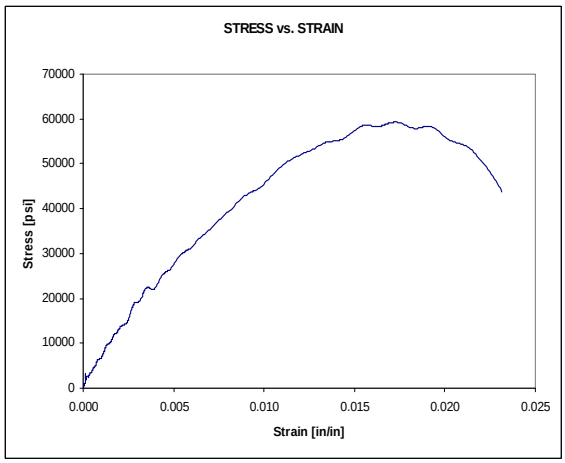

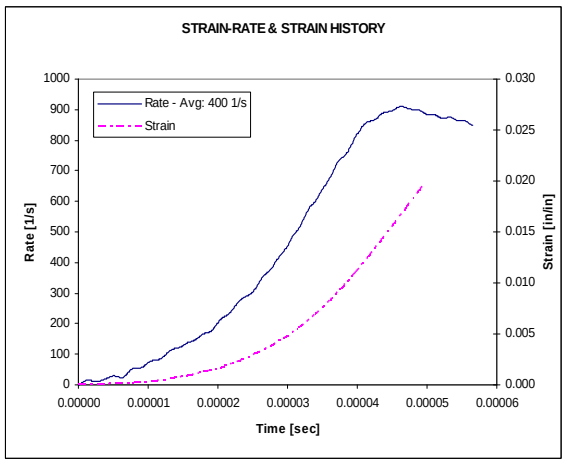

Specimen 3

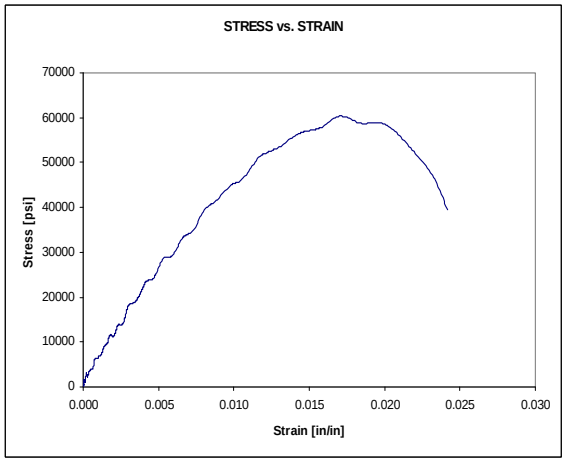

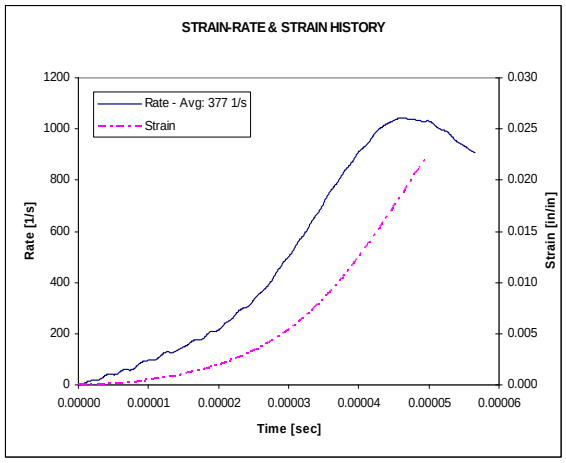

Figure C-107. Stress-Strain Curves for $[+30°/-30°]_{NS}$ Fibercote 3KPW-E365 PWCF Specimens Tested at Average Strain Rate of 385 s^{-1}

Specimen 1

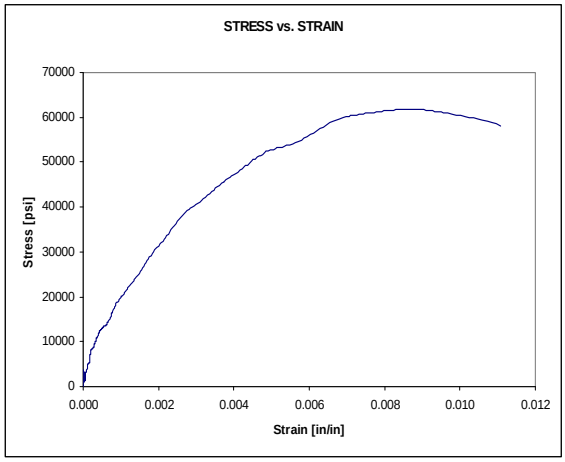

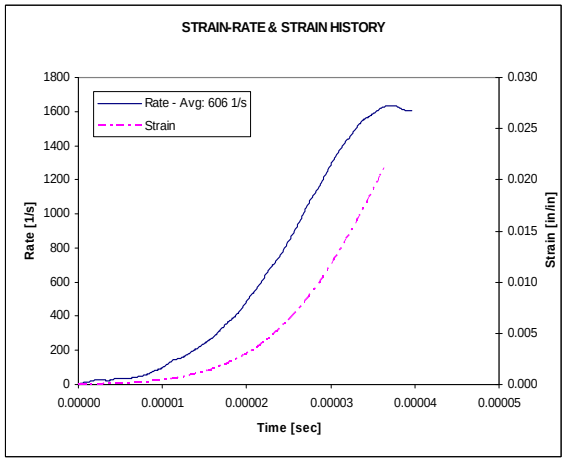

Specimen 2

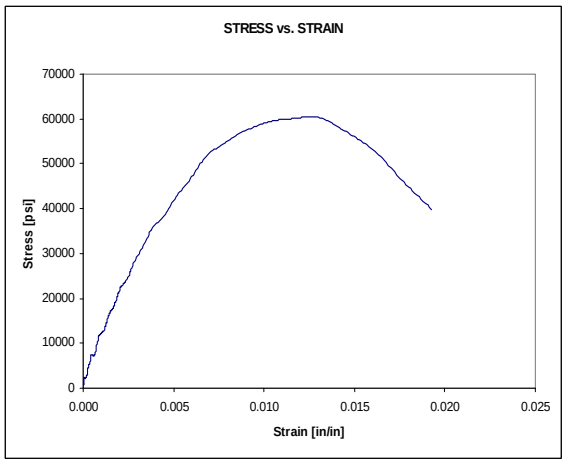

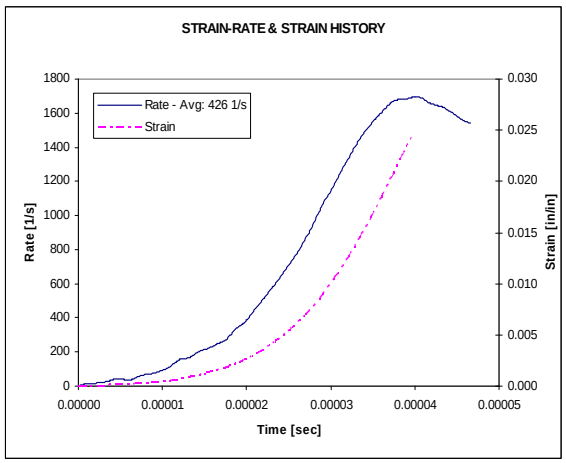

Specimen 3

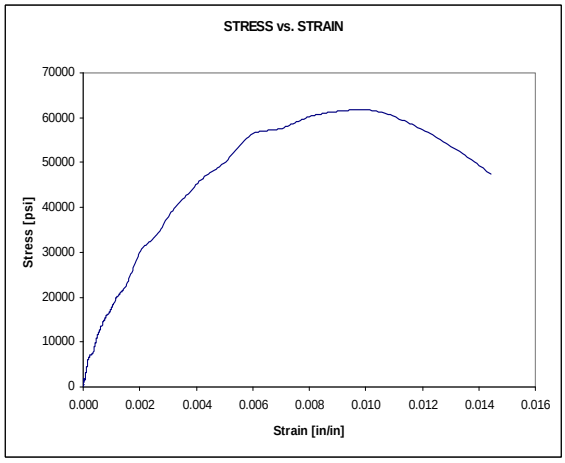

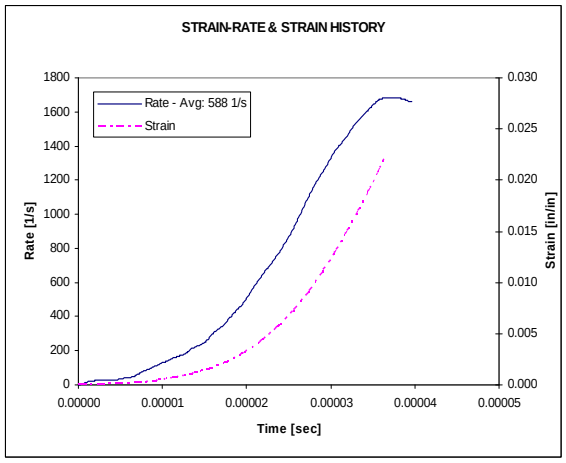

Figure C-108. Stress-Strain Curves for $[+30°/-30°]_{NS}$ Fibercote 3KPW-E365 PWCF Specimens Tested at Average Strain Rate of 583 s^{-1}

Specimen 1

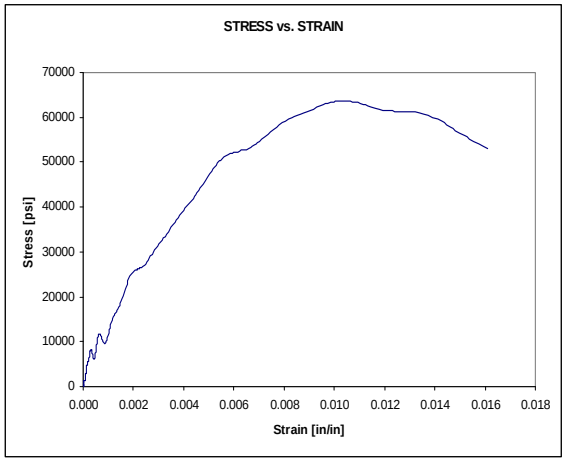

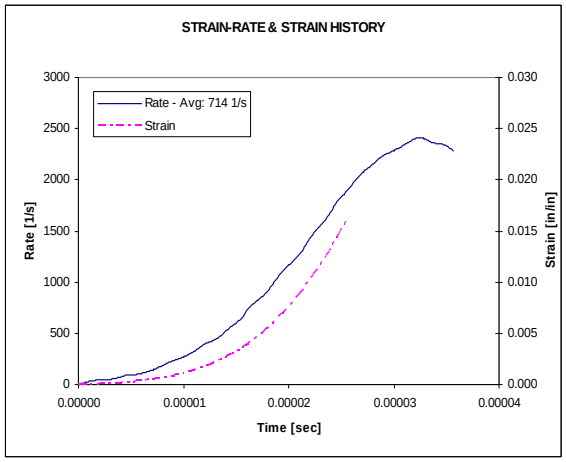

Specimen 2

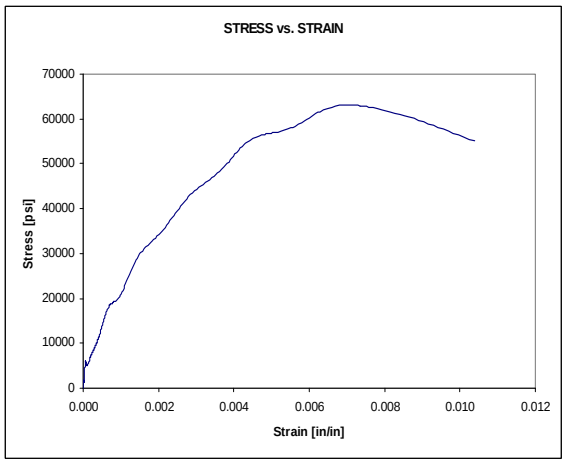

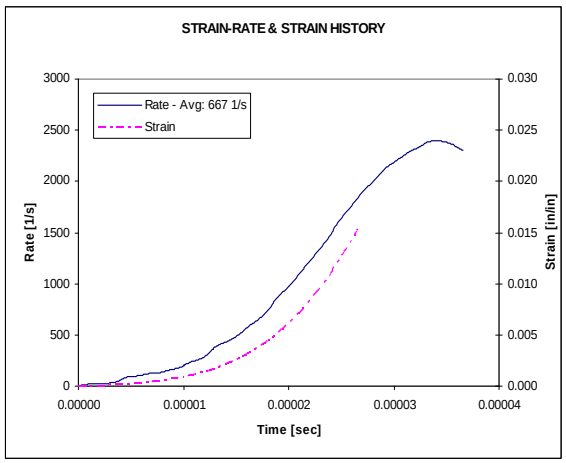

Specimen 3

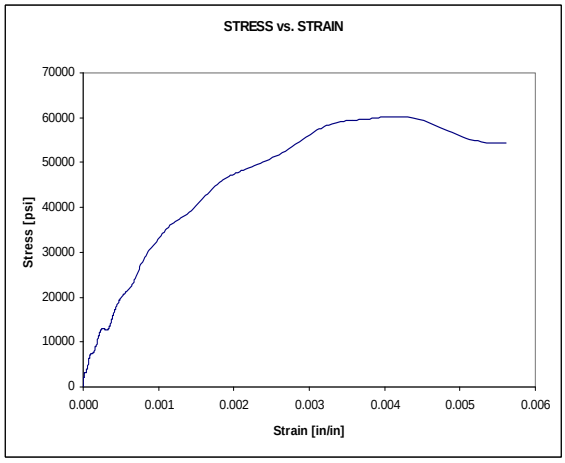

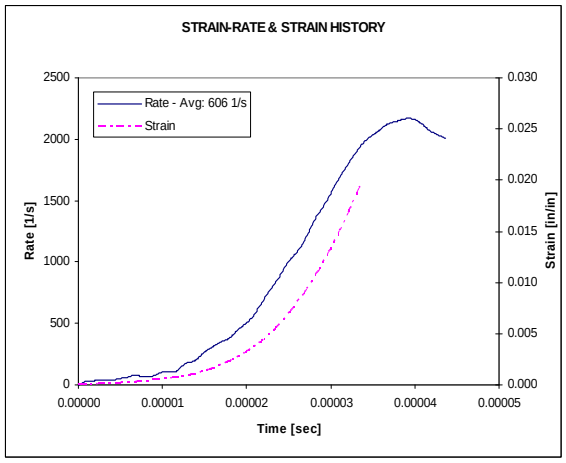

Figure C-109. Stress-Strain Curves for $[+30°/-30°]_{NS}$ Fibercote 3KPW-E365 PWCF Specimens Tested at Average Strain Rate of 662 s^{-1}

Specimen 1

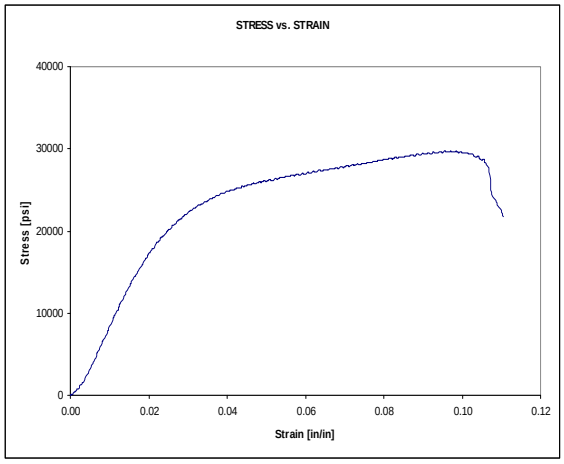

Specimen 2

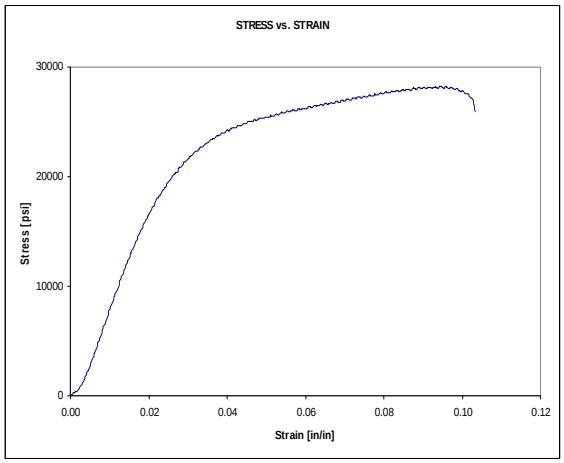

Specimen 3

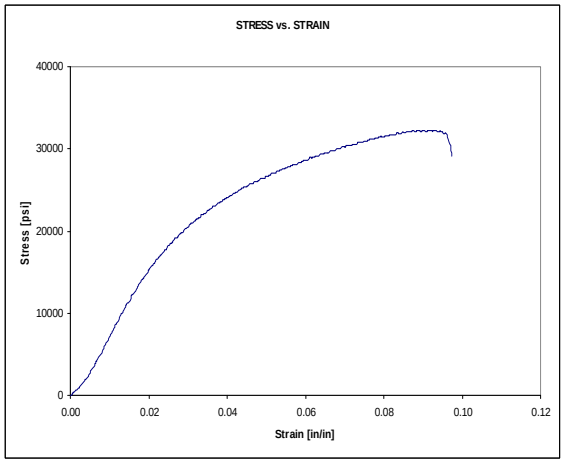

Figure C-110. Stress-Strain Curves for $[+45°/-45°]_{NS}$ Fibercote 3KPW-E365 PWCF Specimens Tested at Average Strain Rate of 0.00167 s^{-1}

Specimen 1

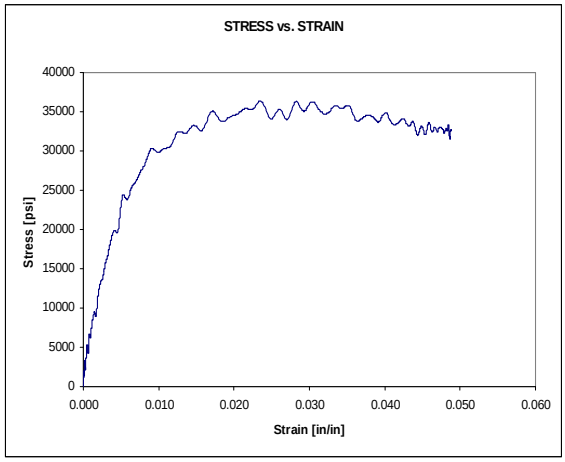

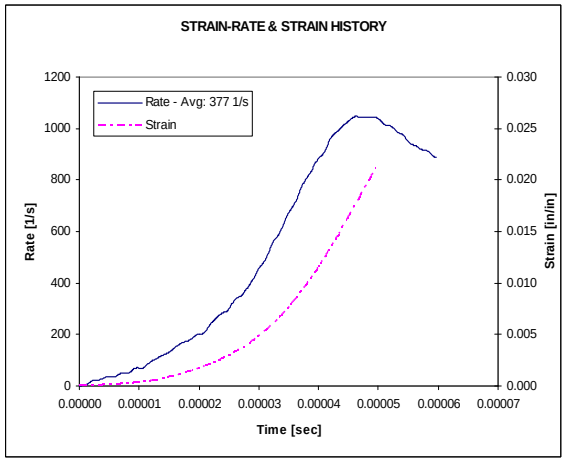

Specimen 2

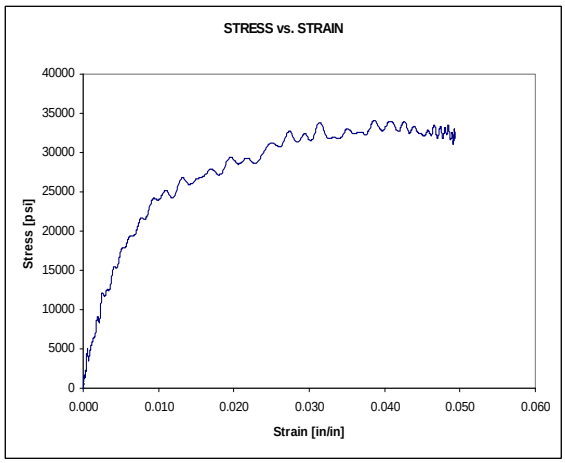

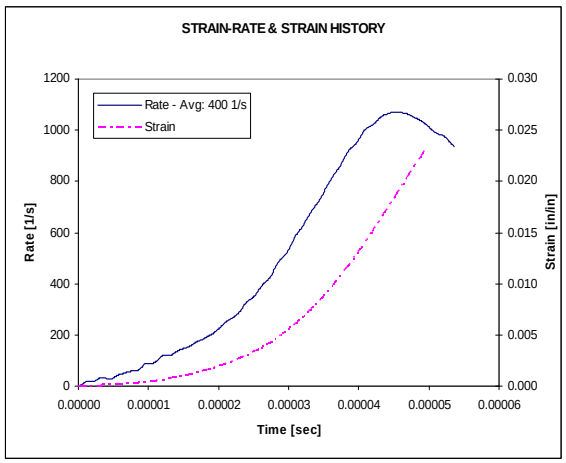

Specimen 3

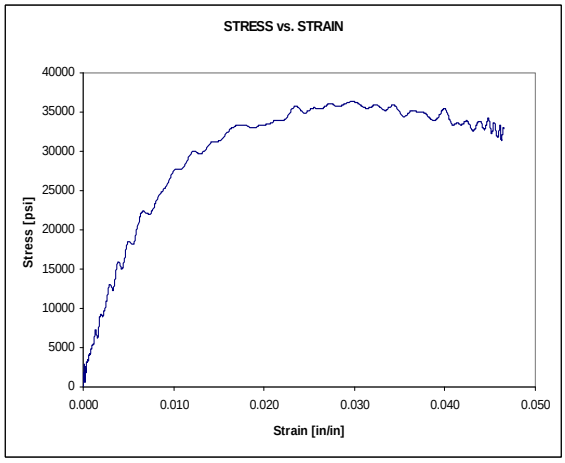

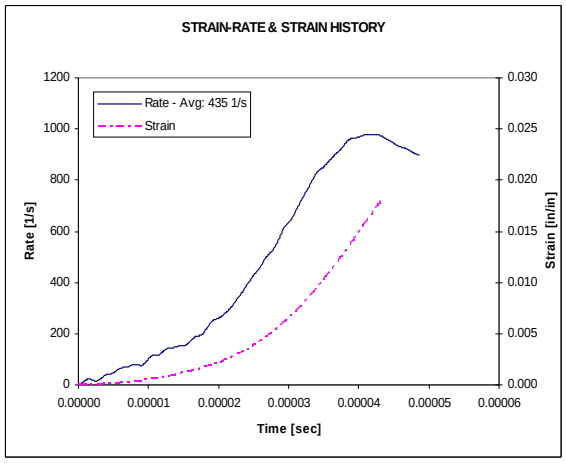

Figure C-111. Stress-Strain Curves for $[+45°/-45°]_{NS}$ Fibercote 3KPW-E365 PWCF Specimens Tested at Average Strain Rate of 404 s^{-1}

Specimen 1

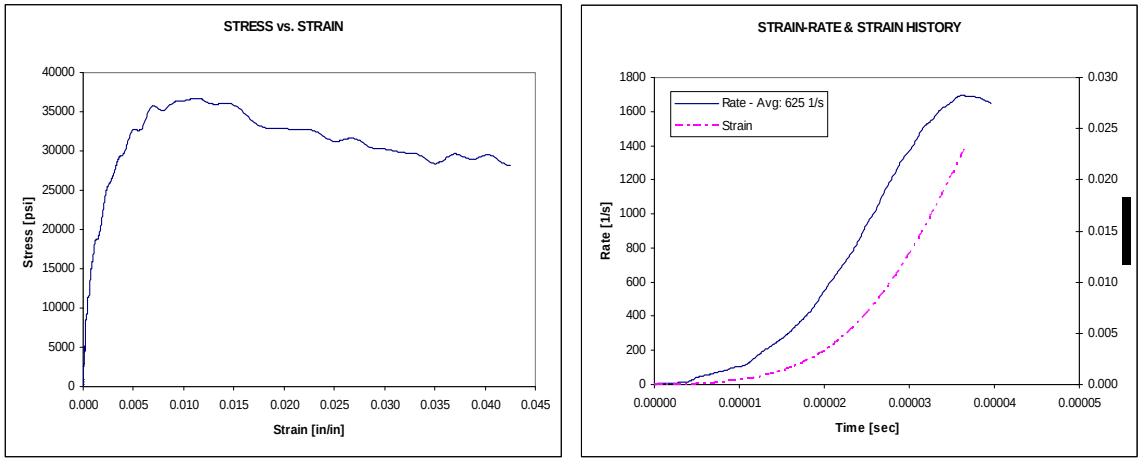

Specimen 2

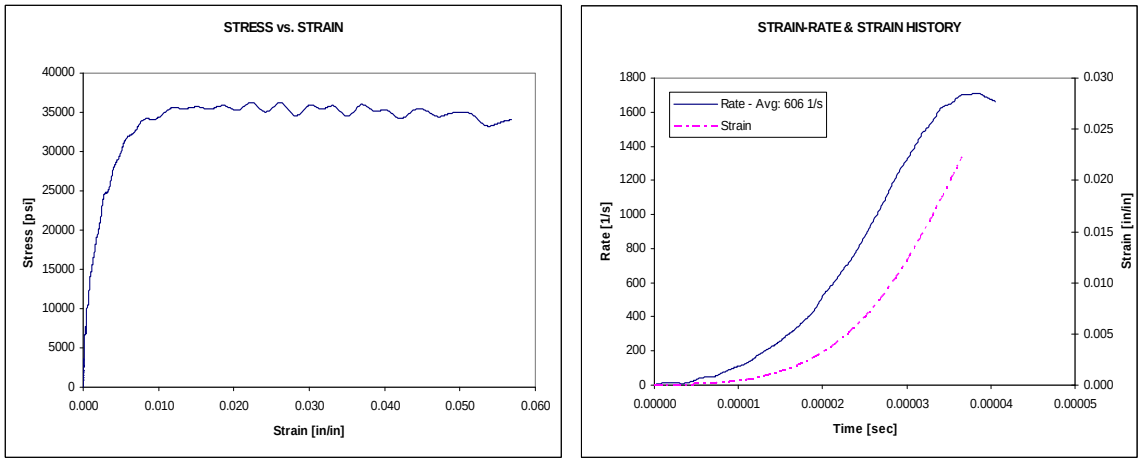

Specimen 3

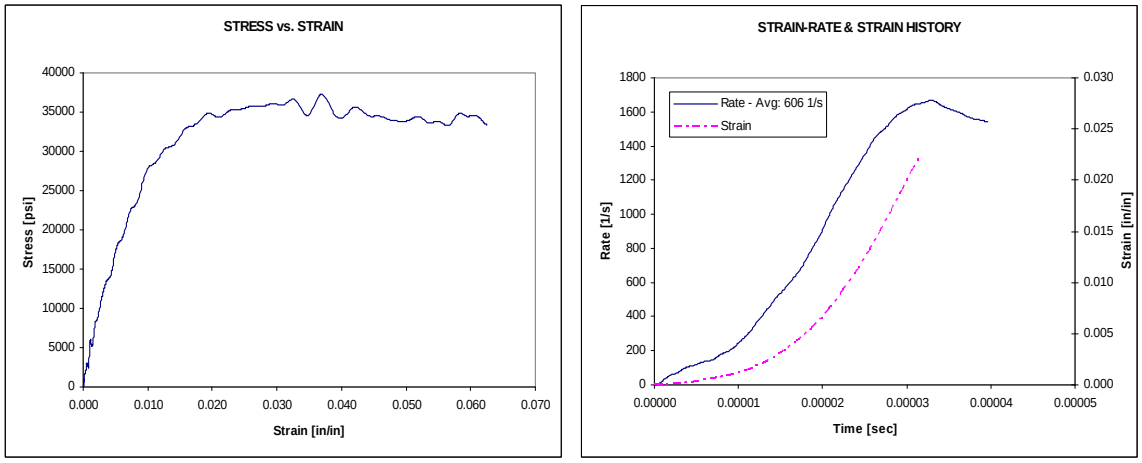

Figure C-112. Stress-Strain Curves for $[+45°/-45°]_{NS}$ Fibercote 3KPW-E365 PWCF Specimens Tested at Average Strain Rate of 612 s^{-1}

Specimen 1

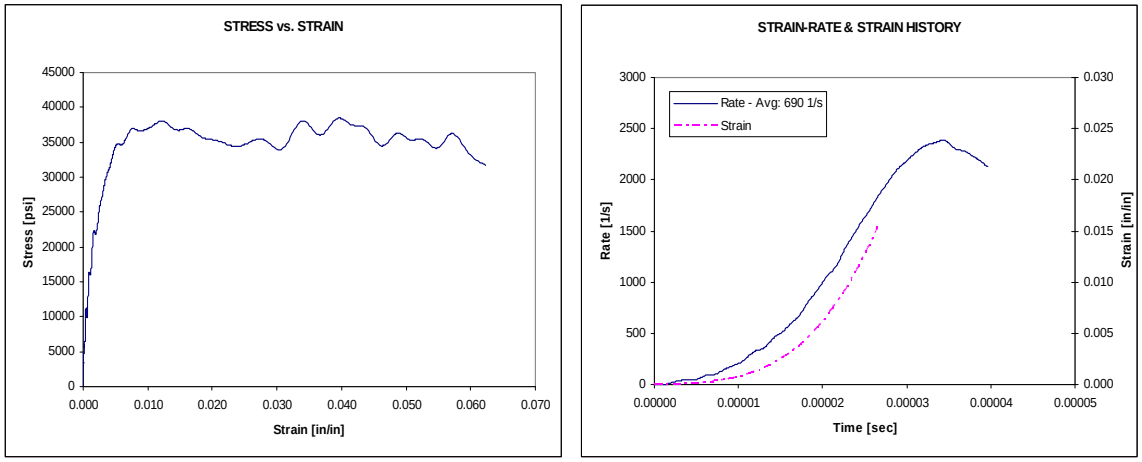

Specimen 2

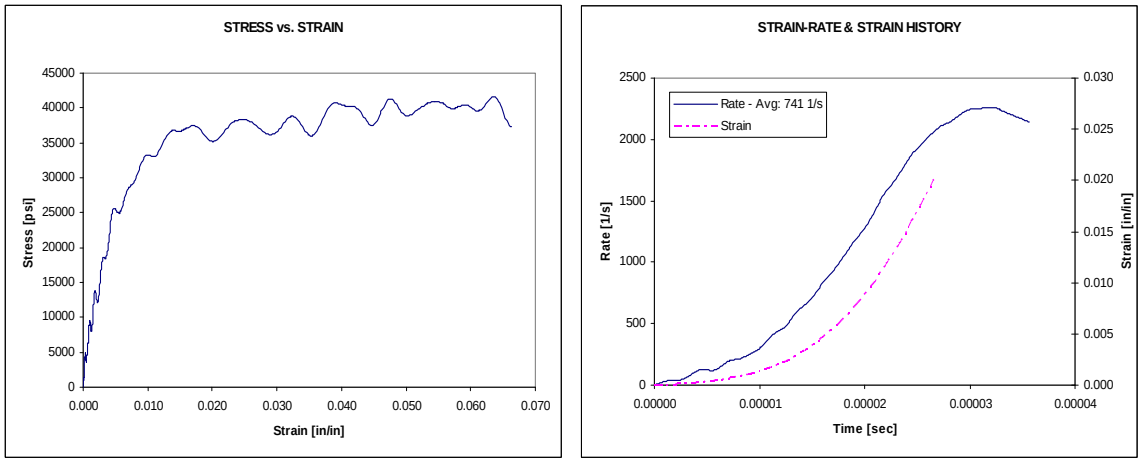

Specimen 3

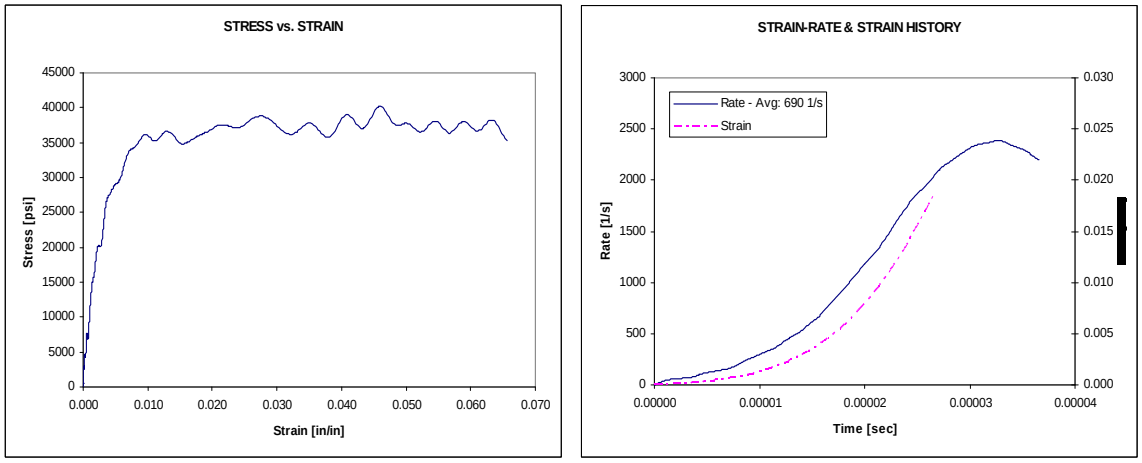

Figure C-113. Stress-Strain Curves for $[+45°/-45°]_{NS}$ Fibercote 3KPW-E365 PWCF Specimens Tested at Average Strain Rate of 707 s^{-1}